# CRACK INITIATION MODELING OF A DIRECTIONALLY-SOLIDIFIED NICKEL-BASE SUPERALLOY

A Dissertation
Presented to
The Academic Faculty

by

Ali Page Gordon

In Partial Fulfillment
of the Requirements for the Degree
Doctor of Philosophy in the
George W. Woodruff School of Mechanical Engineering

Georgia Institute of Technology
May 2006

# CRACK INITIATION MODELING OF A DIRECTIONALLY-SOLIDIFIED NICKEL-BASE SUPERALLOY

Approved by:

Dr. David L. McDowell, Advisor
George W. Woodruff School of Mechanical Engineering
*Georgia Institute of Technology*

Dr. Richard W. Neu, Co-Advisor
School of George W. Woodruff School of Mechanical Engineering
*Georgia Institute of Technology*

Dr. Thomas H. Sanders, Jr.
School of Materials Science and Engineering
*Georgia Institute of Technology*

Dr. Stephen D. Antolovich
School of Materials Science and Engineering
*Georgia Institute of Technology*

Dr. Erian A. Armanios
School of Aerospace Engineering
*Georgia Institute of Technology*

Dr. Min Zhou
George W. Woodruff School of Mechanical Engineering
*Georgia Institute of Technology*

Date Approved:

*To Angelita, Kayla, Celine, and my parents*

*This thesis would be incomplete*
*without a mention of the love, patience and support*
*that you all have given me during this effort*

*Kayla*

*Celine*

# ACKNOWLEDGEMENTS

This thesis would not have been possible without the assistance of a great number of people who have contributed their support during the performance of my graduate studies. For their substantial aid, I would like to express my sincere gratitude to those listed below as well as many others I have failed to mention.

I would like to thank my advisors, Professors David L. McDowell and Richard W. Neu, for their guidance. I will always be very appreciative for Dr. McDowell's support, patience, and encouragement throughout my graduate studies. His technical and editorial advice was essential to the completion of this dissertation. His wisdom and professionalism have taught me innumerable lessons on research, mentorship, and life in general. I have spent a great deal of time drawing from the insights and examples of Dr. Neu. He has shared sound direction in the course of performing experimental research and preparing for an academic career. Both of my advisers' unwavering support has made it an honor to work with them.

My thanks also go to the members of my dissertation reading committee, who are: Drs. Thomas H. Sanders, Jr., Stephen D. Antolovich, Erian A. Armanios, Min Zhou. Their efforts in reviewing drafts of my work have improved the contents of this dissertation.

The help of Dr. Steve Johnson, Mr. Rick C. Brown, and Mr. Robert "Coop" Cooper in the Mechanical Properties Research Laboratory was greatly appreciated. Their expertise and guidance are truly appreciated. The assistance of Mrs. Cecilia Jones was also valuable.

The friendship of Mahesh M. Shenoy and Jayson Mayeur is much appreciated and has led to many interesting and good-spirited discussions relating to and not relating to this research. I am also grateful to my Materials Science and Engineering colleagues Matt D. Trexler, Kip O. Findley, Shelby Highsmith, and Alejandro R. Ibanez for helping considerably with realizing important methods for experimentation involved in this project. Undergraduate students who helped with microscopy are Garry Donaghy and Tam Nguyen. I would like to thank my friends who have greatly enriched my time at Georgia Tech: William C. Patton, III, Byron M. Donald, Kwaku C. Eason, Mikhel E. Hawkins, Jerome D. Coombs-Reyes, Sundiata K. Jangha, and Gregory E. Triplett. Special appreciation and thanks go to the Pattons, the Currys, and the Broyards, who have been like family members to me and my family.

To support my research activities, I have received support from GEM, Ford Motor Company, the Alfred P. Sloan Foundation, Georgia Tech's Presidential Fellowship, NSF-FACES Fellowship, the Office of Naval Research, and the Georgia Space Grant. I am grateful for the support of these entities and their administrators. This research program was supported by General Electric Energy (formerly known as GE Power Systems) under Cooperative Agreement No: DE-FC26-03NT41448.

Last and most importantly, I would like to thank my family. My wife, Angelita, whose love, support, and patience has helped me to finalize this work. Kayla and Celine's presence has also been added motivation. My parents and extended family receive my deepest gratitude for their dedication and the many years of encouragement during my studies.

# TABLE OF CONTENTS

## LIST OF TABLES

## LIST OF FIGURES

# NOMENCLATURE

***Abbreviations:***

| | |
|---|---|
| *Avg* | Average |
| *Cor* | Correlated |
| *Cr* | Creep |
| *Env* | Environment |
| *Eq. or Eqs.* | Equation(s) |
| *Fat* | Fatigue |
| *Fig. or Figs.* | Figure(s) |
| *Ox* | Oxidation |
| *Pre* | Pre-exposed or pre-exposure |

***Acronyms:***

| | |
|---|---|
| *APB* | Anti-phase boundary |
| *ASTM* | American Society for Testing and Materials |
| CC | Continuous cycling |
| *CCG* | Creep crack growth |
| *CPM* | Cycles per minute |
| *CSSC* | Cyclic stress-strain curve |
| *DCA* | Damage Curve Approach |
| *DS* | Directionally-solidified |
| *EBSD* | Electron backscatter diffraction |

| | |
|---|---|
| *EDM* | Electro discharge machining |
| *EDS* | Energy dispersive spectroscopy |
| *FCC* | Face-centered cubic |
| *FE* | Finite element |
| *GB* | Grain boundary |
| *HC* | Hold in compression |
| *HT* | Hold in tension |
| *IGT* | Industrial Gas Turbine |
| *ISV* | Internal state variable |
| *L* | Longitudinal |
| *LCF* | Low cycle fatigue |
| *LMP* | Larson-Miller Parameter |
| *MPRL* | Mechanical Properties Research Laboratory (at Georgia Tech) |
| *OM* | Optical microscopy/metallogrpahy |
| *PC* | Polycrystalline |
| *Ppm* | Parts per million |
| *RT* | Room temperature |
| *SC* | Single crystal |
| *SEM* | Scanning electron microscopy |
| *T* | Transverse |
| $T/C$ | Thermocouple |
| *TBC* | Thermal barrier coating |
| *TEM* | Transmission electron microscopy |

*TMF* Thermomechanical fatigue

*UMAT* User-defined Material

***Experimental Measures, Conditions, and Symbols:***

$\boldsymbol{\varepsilon}$ or $\varepsilon_{ij}$ Strain tensor: $\left[\frac{mm}{mm}\right]$, $\left[\frac{in}{in}\right]$, or $[\%]$

$\varepsilon_{pl}$ Cyclically stable uniaxial plastic strain: $\left[\frac{mm}{mm}\right]$, $\left[\frac{in}{in}\right]$, or $[\%]$

$\varepsilon_{in}$ Uniaxial inelastic strain: $\left[\frac{mm}{mm}\right]$, $\left[\frac{in}{in}\right]$, or $[\%]$

$\varepsilon_{m}$ Uniaxial mechanical strain: $\left[\frac{mm}{mm}\right]$, $\left[\frac{in}{in}\right]$, or $[\%]$

$\varepsilon_{f}$ Uniaxial rupture strain: $\left[\frac{mm}{mm}\right]$, $\left[\frac{in}{in}\right]$, or $[\%]$

$\dot{\varepsilon}$ Uniaxial strain rate: $\left[\frac{mm}{mm \cdot s}\right]$, $\left[\frac{in}{in \cdot s}\right]$, or $\left[\frac{\%}{s}\right]$

$\varepsilon_{t}$ Uniaxial total strain: $\left[\frac{mm}{mm}\right]$, $\left[\frac{in}{in}\right]$, or $[\%]$

$\varepsilon_{th}$ Uniaxial thermal strain: $\left[\frac{mm}{mm}\right]$, $\left[\frac{in}{in}\right]$, or $[\%]$

$\varepsilon_{el}$ Cyclically stable uniaxial elastic strain: $\left[\frac{mm}{mm}\right]$, $\left[\frac{in}{in}\right]$, or $[\%]$

$\Delta\varepsilon$ Uniaxial strain range: $\left[\frac{mm}{mm}\right]$, $\left[\frac{in}{in}\right]$, or $[\%]$

$\phi$ Phasing between mechanical and thermal cycles: $[^{\circ}]$ or $[rad]$

$\Delta\sigma$ Cyclically stable stress range: $[MPa]$ or $[ksi]$

| | |
|---|---|
| $\boldsymbol{\sigma}$ or $\sigma_{ij}$ | Stress tensor: $[MPa]$ or $[ksi]$ |
| $\sigma_m$ | Mean stress: $[MPa]$ or $[ksi]$ |
| $\bar{\sigma}$ | Von Mises effective stress: $[MPa]$ or $[ksi]$ |
| $\sigma_o$ | Yield strength: $[MPa]$ or $[ksi]$ |
| $\frac{da}{dt}$ | Crack growth rate: $\left[\frac{mm}{hr}\right]$ or $\left[\frac{in}{hr}\right]$ |
| $\frac{da}{dN}$ | Crack growth rate per unit cycle: $\left[\frac{mm}{cycle}\right]$ or $\left[\frac{in}{cycle}\right]$ |
| $A_\varepsilon$ | Strain amplitude ratio of the amplitude and mean strain |
| $F_{O_2}$ | Volume fracture of oxygen: $[\%]$ |
| $N$ | Number of cycles endured: $[cycles]$ |
| $N_f$ | Number of cycles to failure: $[cycles]$ |
| $N_i$ | Number of cycles required to initiate a crack: $[cycles]$ |
| $P$ | Applied load: $[N]$ or $[lb]$ |
| $P_{\max}$ | Maximum applied load: $[N]$ or $[lb]$ |
| $P_{O_2}$ | Partial pressure of oxygen: $[atm]$ or $[bar]$ |
| $R^2$ | Square of the Pearson product-moment correlation coefficient |
| $R_\varepsilon$ | Strain ratio of the minimum and maximum strain |
| $T$ | Specimen temperature: $[°C]$, $[°F]$ or $[K]$ |
| $T_{eff}$ | Effective temperature: $[°C]$, $[°F]$ or $[K]$ |

| | |
|---|---|
| $\Delta T$ | Temperature range: $[^\circ C]$, $[^\circ F]$ or $[K]$ |
| $T_m$ | Melting temperature: $[^\circ C]$, $[^\circ F]$ or $[K]$ |
| $t$ | Time: $[s]$ or $[hr]$ |
| $t_{cc}$ | Push-pull or non-hold portion of total cycle period: $[s]$ or $[hr]$ |
| $t_{hc}$ | Dwell period in compression: $[s]$ or $[hr]$ |
| $t_{ht}$ | Dwell period in tension: $[s]$ or $[hr]$ |
| $t_{tc}$ | Total (e.g. sum of dwell and non-hold) cycle period: $[s]$ or $[hr]$ |
| $t_r$ | Rupture time: $[s]$ or $[hr]$ |

***Fracture Mechanics Variables:***

| | |
|---|---|
| $C(t)$ | Path-dependent CCG integral: $\left[\frac{\text{MPa}\cdot\text{mm}}{hr}\right]$ or $\left[\frac{\text{ksi}\cdot\text{in}}{hr}\right]$ |
| $K_I$ | Mode I stress intensity factor: $\left[\text{MPa}\cdot\sqrt{\text{mm}}\right]$ or $\left[\text{ksi}\cdot\sqrt{\text{in}}\right]$ |
| $J$ | Elastic-plastic crack tip integral: $[\text{MPa}\cdot\text{mm}]$ or $[\text{ksi}\cdot\text{in}]$ |

***Fundamental Physical Constants:***

| | |
|---|---|
| $\delta_{ij}$ or $\mathbf{I}$ | Kronecker delta, identity tensor |
| $\pi$ | Pi: $[3.14159\ldots]$ |
| $e$ | Euler's number, base of natural logarithm: $[2.71828\ldots]$ |
| $R$ | Universal gas constant (or molar gas constant): $\left[8.31457\ \frac{J}{K\cdot mol}\right]$ |

***Microstructural Measures and Material Descriptions:***

| | |
|---|---|
| $[001]$ | Primary crystallographic direction |
| $\{001\}$ | Family of crystallographic planes |
| $\langle 001 \rangle$ | Family of primary crystallographic directions |
| $\gamma$ | Matrix phase of superalloy of a Ni-base superalloy |
| $\gamma'$ | Precipitate phase of superalloy of a Ni-base superalloy |
| $a$ | Crack length: $[mm]$ or $[in]$ |
| $a_i$ | Crack initiation length: $[mm]$ or $[in]$ |
| $d$ | Grain size: $[mm]$ or $[in]$ |
| $h$ | Oxide spike depth: $[mm]$ or $[in]$ |
| $\overline{h}_f$ | Critical oxide rupture thickness: $[mm]$ or $[in]$ |
| $l_i$ | Oxide spike depth at crack initiation: $[mm]$ or $[in]$ |
| $L_{OX}$ | Oxide depth: $[mm]$ or $[in]$ |
| $L_{GPD}$ | Precipitate particle depletion depth: $[mm]$ or $[in]$ |
| $\frac{dr}{dt}$ | Rate of coarsening of precipitate particles: $\left[\frac{\mu m}{hr}\right]$ or $\left[\frac{in}{hr}\right]$ |
| $SDAS$ | Secondary dendritic arm spacing: $[mm]$ or $[in]$ |
| $TDAS$ | Tertiary dendritic arm spacing: $[mm]$ or $[in]$ |

***Fatigue Analysis Variables:***

| | |
|---|---|
| $\varepsilon_f'$ | Fatigue ductility coefficient |
| $\sigma_f'$ | Fatigue strength coefficient: $[MPa]$ or $[ksi]$ |
| $b$ | Fatigue strength exponent |
| $c$ | Fatigue ductility exponent |
| $K'$ | Cyclic strength coefficient: $\left[MPa^{-n'}\right]$ or $\left[ksi^{-n'}\right]$ |
| $n$ | Norton creep strain hardening exponent |
| $n'$ | Cyclic strain hardening exponent |

***Material Properties and Modeling Variables:***

| | |
|---|---|
| $\langle x \rangle$ | Macauley brackets defined as: $\langle x \rangle = \begin{cases} 0 & x \le 0 \\ x & x > 0 \end{cases}$ |
| $\alpha_{th}$ or $CTE$ | Coefficient of thermal expansion: $°C^{-1}$ or $\left[°F^{-1}\right]$ |
| $\sigma_0$ or $\sigma_{YS}$ | 0.2 % offset yield strength: $[MPa]$ or $[ksi]$ |
| $\Theta$ | Arrhenius term |
| $\nu$ | Poisson's Ratio |
| $\sigma_{UTS}$ or $UTS$ | Ultimate tensile strength: $[MPa]$ or $[ksi]$ |
| $A$ | Norton's power law (secondary creep) coefficient: $\left[MPa^{-n}\right]$ or $\left[ksi^{-n}\right]$ |
| $C_i$ | Generic constants used in fatigue and fatigue-damage models |
| $E$ | Modulus of elasticity (e.g. Young's modulus): $[GPa]$ or $[Msi]$ |
| $E_i$ | Initial elastic modulus: $[GPa]$ or $[Msi]$ |
| $\mathbf{F}$ or $F_{ij}$ | Deformation gradient |

| | |
|---|---|
| $J_{ijkl}$ or $\mathbf{J}$ | Jacobian matrix: $[MPa]$ or $[ksi]$ |
| $m$ | Constant in the Monkman-Grant relationship |
| $n$ | Norton's power law (secondary creep) exponent |
| $Q$ | Activation energy: $\left[\frac{J}{mol}\right]$ |
| $W_i$ | Weighting parameter |

***Internal State Variables:***

| | |
|---|---|
| $\chi^{\alpha}$ | Backstress stress on the $\alpha^{th}$ slip system: $[MPa]$ or $[ksi]$ |
| $\gamma^{(\alpha)}$ | Shear strain on the $\alpha^{th}$ slip system |
| $\kappa^{\alpha}$ | Threshold stress on the $\alpha^{th}$ slip system: $[MPa]$ or $[ksi]$ |
| $\omega$ | Damage accumulation |
| $\dot{\omega}$ | Damage accumulation rate |

# SUMMARY

Combustion gas turbine components designed for application in electric power generation equipment are subject to periodic replacement as a result of cracking, damage, and mechanical property degeneration that render them unsafe for continued operation. In view of the significant costs associated with inspecting, servicing, and replacing damaged components, there has been much interest in developing models that not only predict service life, but also estimate the evolved microstructural state of the material. This thesis explains manifestations of microstructural damage mechanisms that facilitate fatigue crack nucleation in a newly-developed directionally-solidified (DS) Ni-base superalloy components exposed to elevated temperatures and high stresses. In this study, models were developed and validated for damage and life prediction using DS GTD-111 as the subject material. This material, proprietary to General Electric Energy, has a chemical composition and grain structure designed to withstand creep damage occurring in the first and second stage blades of gas-powered turbines. The service conditions in these components, which generally exceed 600ºC, facilitate the onset of one or more damage mechanisms related to fatigue, creep, or environment.

The study was divided into an empirical phase, which consisted of experimentally simulating service conditions in fatigue specimens, and a modeling phase, which entailed numerically simulating the stress-strain response of the material. Experiments have been carried out to simulate a variety of thermal, mechanical, and environmental operating conditions endured by longitudinally (L) and transversely (T) oriented DS GTD-111. Both in-phase and out-of-phase thermo-mechanical fatigue tests are conducted. In some cases, tests in extreme environments/temperatures were needed to isolate one or at most

two of the mechanisms causing damage. Microstructural examinations were carried out via SEM and optical microscopy. A continuum crystal plasticity model was used to simulate the material behavior in the L and T orientations. The constitutive model was implemented in ABAQUS and a parameter estimation scheme was developed to obtain the material constants. A physically-based model was developed for correlating crack initiation life based on the experimental life data and predictions are made using the crack initiation model. Assuming a unique relationship between the damage fraction and cycle fraction with respect to cycles to crack initiation for each damage mode, the total crack initiation life has been represented in terms of the individual damage components (fatigue, creep-fatigue, creep, and oxidation-fatigue) observed at the end state of crack initiation.

# 1. INTRODUCTION

## *1.1 Background and Motivation*

Land-based gas-powered turbines have been developed using concepts of aircraft jet engine technology. In these systems, super-heated, pressurized gases are aimed at Ni-base superalloy buckets (also referred to as blades) which power the turbine to spin electric generators. Substantive improvements of the thermal efficiency of a gas turbine can be achieved by increasing either the pressure or the temperature directed towards the bucket airfoil. Primary amongst other design considerations, therefore, is the ability of the blades and other hot gas path components to resist high temperature damage mechanisms. Other highly-important attributes are castability and weldability for ease of manufacture and repair, respectively.

Replacing conventionally cast, polycrystalline (PC) Ni-base superalloy components with higher performance materials has been identified by gas turbine manufacturers as a means to attain the needed efficiency gains. Investment casting processes have been modified to enhance the creep strength of Ni-base superalloys beyond what is arguably achievable by means of purely altering the alloying chemistry. Increased resistance to oxidation, hot corrosion, thermal fatigue, and creep in these materials has been achieved by means of directional solidification, a casting technique developed to reduce to the number of grain boundaries (GBs) transverse to the primary stress axis of the bucket.

Even though the high temperature durability of these components has been significantly improved, the combination of cyclic centrifugal forces generated by angular velocities of 3600 *RPM* and temperatures exceeding 600°C and up to 1260°C (Sharke, 2000) can be substantial enough to promote a myriad of microstructural damage mechanisms. This damage causes the formation and growth of low cycle fatigue (LCF) cracks which are the primary reason for premature retirement of directionally-solidified (DS) gas turbine blades.

Fractographic analyses of failed and retired Ni-base superalloy turbine blades revealed that preferential locations of crack initiation are along the trailing edge near cooling holes, at excessively misaligned GBs intersecting the airfoil tip, and along the suction side of the blade (Bulloch and Callegy, 2000; Park et al., 2002; Mazur, et al., 2005). Potential locations of thermal gradients, e.g. hot-spots, are also susceptible to sustaining LCF cracks (Hou et al., 2002; Chang et al., 2003). In fact, cracks found in some ex-service DS GTD-111 (a proprietary material developed by GE Energy) turbine blades were up to 6.35 *mm* along the trailing edge near the first cooling hole and 19 *mm* at the tip of the blade. If undetected, these LCF cracks propagate under fatigue until the remaining ligament is overloaded and ruptures. The ultimate consequences are foreign object damage (FOD) to other components, unplanned outages, additional replacement costs, and most precarious, loss of safety.

## *1.2 Research Objectives*

The majority of the life of a blade is spent in the crack initiation stage; thus, the chief goal of this research will be to characterize the conditions and microstructures

associated with crack initiation in directionally-solidified Ni-base superalloys. While a number of researchers have studied the mechanical behavior of DS Ni-base superalloys, no detailed analyses of the microstructural damage mechanisms and fatigue crack initiation life prediction methodologies have been provided.

The goals of this research are as follows:

**(1) Distinguish the dominant microstructural mechanisms that develop and enhance damage.** Experiments are necessary to develop models to simulate the material behavior at current and planned service conditions. Damage occurring to DS GTD-111 which is responsible for failure has been identified by conducting isothermal and non-isothermal fatigue tests, creep-fatigue tests, isothermal unstressed tests, and creep deformation tests. Temperatures of consideration were from room temperature to 1093ºC (2000ºF).

**(2) Determine the influence of material orientation on crack initiation.** Since LCF crack initiation has been observed parallel and perpendicular to the primary stress axis of the blade, experiments and characterization emphasized the material response in orientations either longitudinal or transverse to the DS axis.

**(3) Define the role of thermal/mechanical pre-exposure on crack initiation life.** An often ignored reality is the existence of pre-existing damage caused during manufacture. Additional testing and characterization were conducted on samples that were pre-exposed (to high temperatures, mechanical loading, and environments either devoid or rich in corrosive contaminants) and then subsequently fatigue-tested.

**(4) Characterize damage mechanisms and relate them to crack initiation behavior.** Microscopic analyses of samples of tested material were coupled with quantitative test data to develop fatigue damage maps and mathematical models.

**(5) Develop a formulation that facilitates estimation of crack initiation behavior under both isothermal and non-isothermal LCF.** The model development was supported by data from experiments that isolated the microstructural mechanisms of creep, fatigue, and oxidation. Finite element simulations and a constitutive model were used to make predictions of the behavior of DS GTD-111.

A primary outcome of this research is a detailed characterization of the reliability and failure mechanisms of DS Ni-base superalloys that can be used in order to enhance the design and efficiency of gas-powered turbine blades. This work will also lead to the improved accuracy of fatigue life predictions of DS GTD-111 and similar Ni-base superalloy components used in electric power generation applications.

## *1.3 Overview of the Thesis*

The content and organization of this work is as follows. Chapter 2 contains a detailed literature review involving advances with damage mechanics and life prediction methodologies for materials exposed to high temperatures. The metallurgical characteristics of the test material, DS GTD-111, are discussed in Chapter 3. This section also contains descriptions of the experimental methodologies employed. In Chapter 4, results in the forms of trends and microstructural characterization obtained from the testing program are described. The constitutive model that was used to predict the mechanical behavior of the material is contained in Chapter 5. Results from simulations of experiments are discussed there as well. Afterwards, in Chapter 6, a mechanistically-based fatigue damage life prediction model is introduced. Crack initiation life correlations are presented there. The remaining sections, Chapters 7 and 8, contain

conclusions and recommendations for future studies, respectively. Finally, Appendices A, B, C, D, and E review experimental and modeling results.

# 2. LITERATURE REVIEW

## 2.1 Application of DS Ni-base Superalloys

Industrial gas turbine (IGT) manufacturers, such as General Electric, Siemens Westinghouse, and Pratt & Whitney, use high strength, temperature resistant superalloys in hot sections of turbines. In order for these electric power generation companies to improve reliability, maintainability, and efficiency of gas turbine blades beyond their current limitations, the advancement of durability and predictability of these materials is required. Although the implications of fulfilling these objectives are far-reaching, immediate savings can be attained by minimizing various expensive resources (e.g. fuel, material, and operator time). An IGT that is currently in production for land-based power generation is the 6FA, shown in Fig. 2.1. To improve the efficiency of this machine and others like it, several decades of research have been devoted to implementing innovative manufacturing techniques that improve the fatigue, corrosion, and temperature-resistance of intermetallic turbine components. Substantial effort has also been expended in identifying the mechanisms responsible for early retirement of these blades.

Difficult-to-machine components such as buckets or vanes are fabricated using the technique of "lost wax casting" a process that dates back at least 3000 years (Sharke, 2000) and has resurged as the method of choice for manufacturing many of the components used in advanced power trains. Variations of the methods can be applied to process Ni-based superalloy turbine components having one of three types of grain

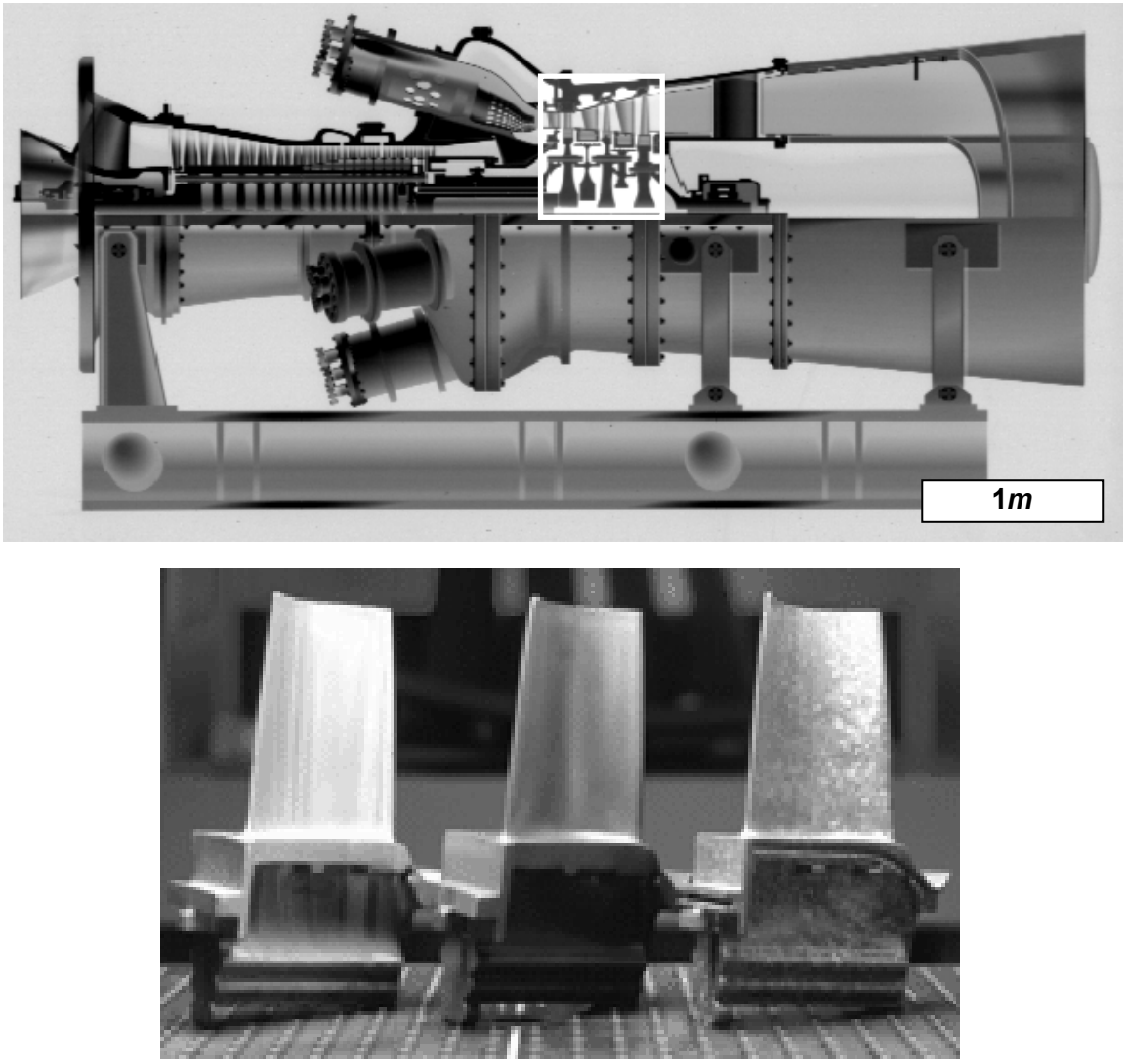


***Figure 2.1:*** *(top) 6FA gas turbine (Ramarchandran and Conway, 1996) with 1st-3rd stage buckets highlighted. (bottom) Visible grain structures in various forms of Ni-base superalloy blades (Sharke, 2000).*

patterns: equiaxed, directionally-solidified, or single crystal. An equiaxed pattern allows for a multitude of grains in the finished casting, but places a tight restriction on their size, depending on their location in the part. A directionally solidified casting restricts the path of grain growth in a part, but not necessarily size. A single crystal is technically the most challenging of the three to grow. Each of these grain patterns can be typically seen in the profiles of gas turbine blades, as shown in Fig. 2.1. The main difference in

processing directionally solidified components is that the bottom cools first so the grains begin growing vertically from the bottom upward. This type of heat releasing process is a so-called exothermic reaction applied to allow the metal to solidify without high porosity.

In the 1970s General Electric Power Systems (known as General Electric Energy since 2004) introduced blades composed of IN-738, a solid strengthened, dual-phase Ni-base superalloy. In 1983, emphasis on tighter processing control for improved creep strength lead to the replacement of first stage IN-738 blades with those composed of equiaxed GTD-111 (Schilke, 2004). Optimizing the chemical composition and implementing crystal orientation control lead to the introduction of directionally-solidified (DS) GTD-111 blades in 1987.

Molten metal is top-filled into a bucket-shaped ceramic mold which is cooled at its bottom. As the planar liquid-solid interface travels longitudinally through the helical grain selector which is located at the bottom of the mold (Fig. 2.2), the number of grains is reduced. Solidification of long and slender grains composed of aligned dendrites (Fig. 2.3) manifests blades with no grain boundaries oriented transversely to the primary axis of the blade. The elimination of these transverse grain boundaries confers additional creep and rupture strength on the material along the longitudinal (blade) direction and the orientation of the grain structure provides a decreased elastic modulus in the longitudinal direction to enhance fatigue life.

A turbine bucket fabricated from this solidification process and constituted of DS GTD-111 is shown in Fig. 2.4. The DS GTD-111 material is currently being used in first stage bucket in the 6FA, 7FA, and 9FA turbines. It is also used in third stage buckets of

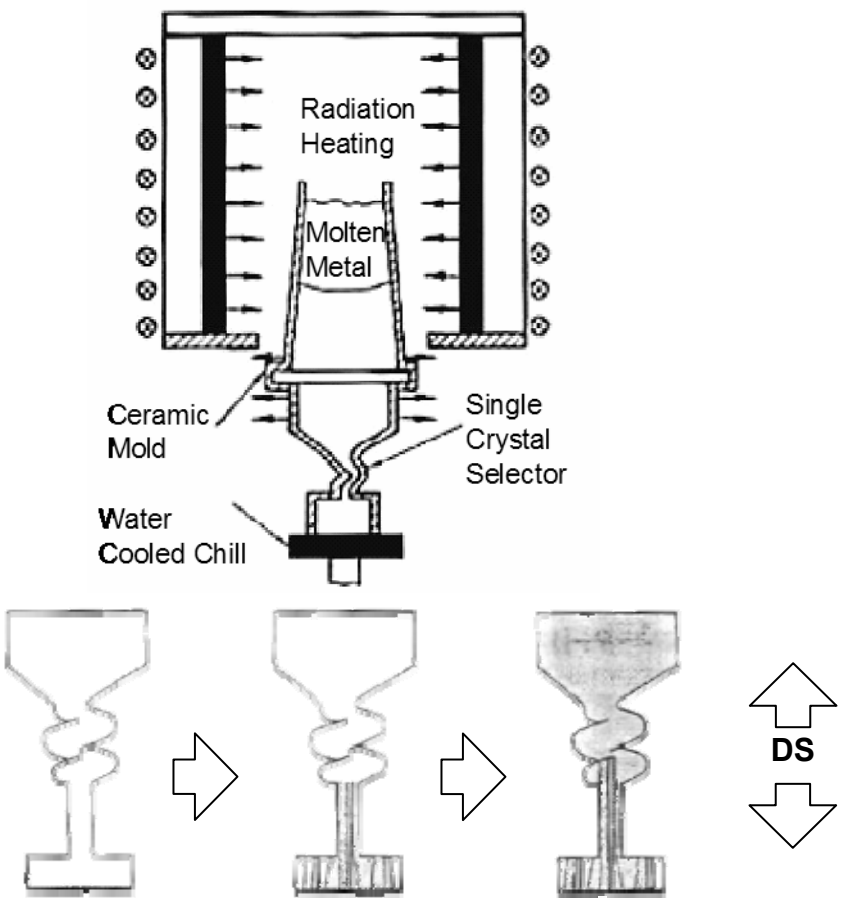


***Figure 2.2:*** *Upward solidification steps resulting from the application of the helical grain selector used crystallographic orientation control.*

7FA and 9FA gas turbines. Careful control ensures that the chemical composition and grain morphology is consistent through the length of the blade. Efficiencies as high as 60% are now achievable because of increased firing temperature coupled with more efficient component and system designs. With even tighter controls over temperature gradients, this process can also be used to cast single crystal (SC) blades devoid of grain boundaries.

The sections of this chapter are devoted to the review of research findings pertaining to the metallurgical, fatigue, oxidation, and creep strength of Ni-base materials

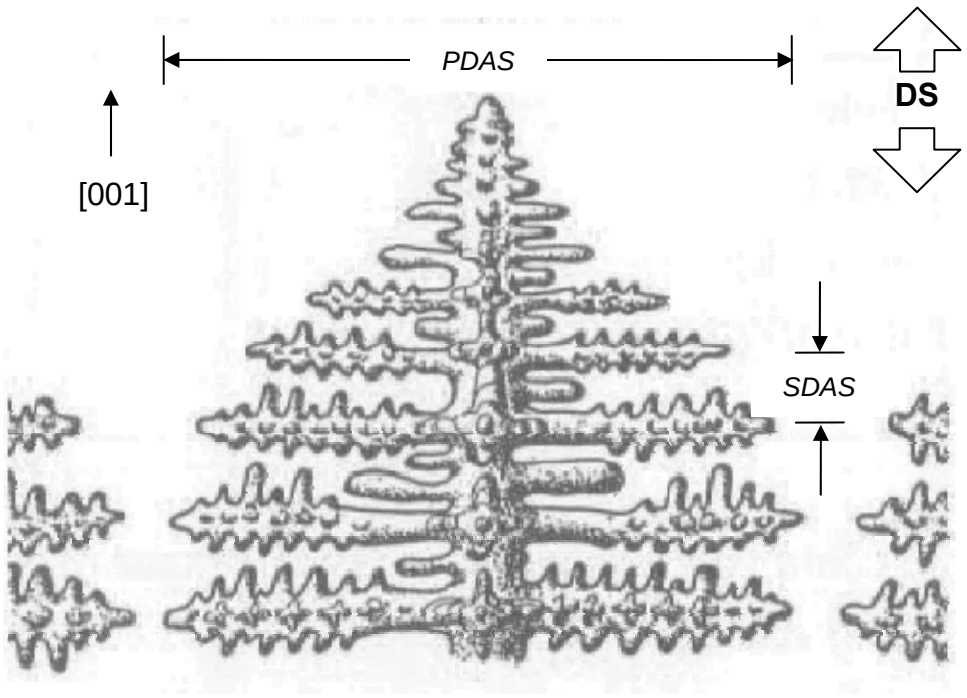


***Figure 2.3:*** *Depiction of the growing dendrites characterized by the primary dendritic arm spacing and the secondary dendritic arm spacing (PDAS and SDAS, respectively) (Kurz and Fisher, 1998).*

with emphasis on those with the DS microstructure. Strategies implemented for modeling the monotonic and cyclic mechanical properties of this class of materials are also detailed.

## *2.2 Brief Description of DS GTD-111*

Directionally-solidified GTD-111 is a relatively recently-developed Ni-base superalloy manufactured by GE Energy for turbine applications. The initial microstructure of a bucket is the product of composition, casting, and heat treatment. Hot isostatic pressing (HIP) can be used to reduce grain boundary (GB) porosity within the bulk. The grains of DS GTD-111 are approximately 5 *mm* in width transverse to the DS

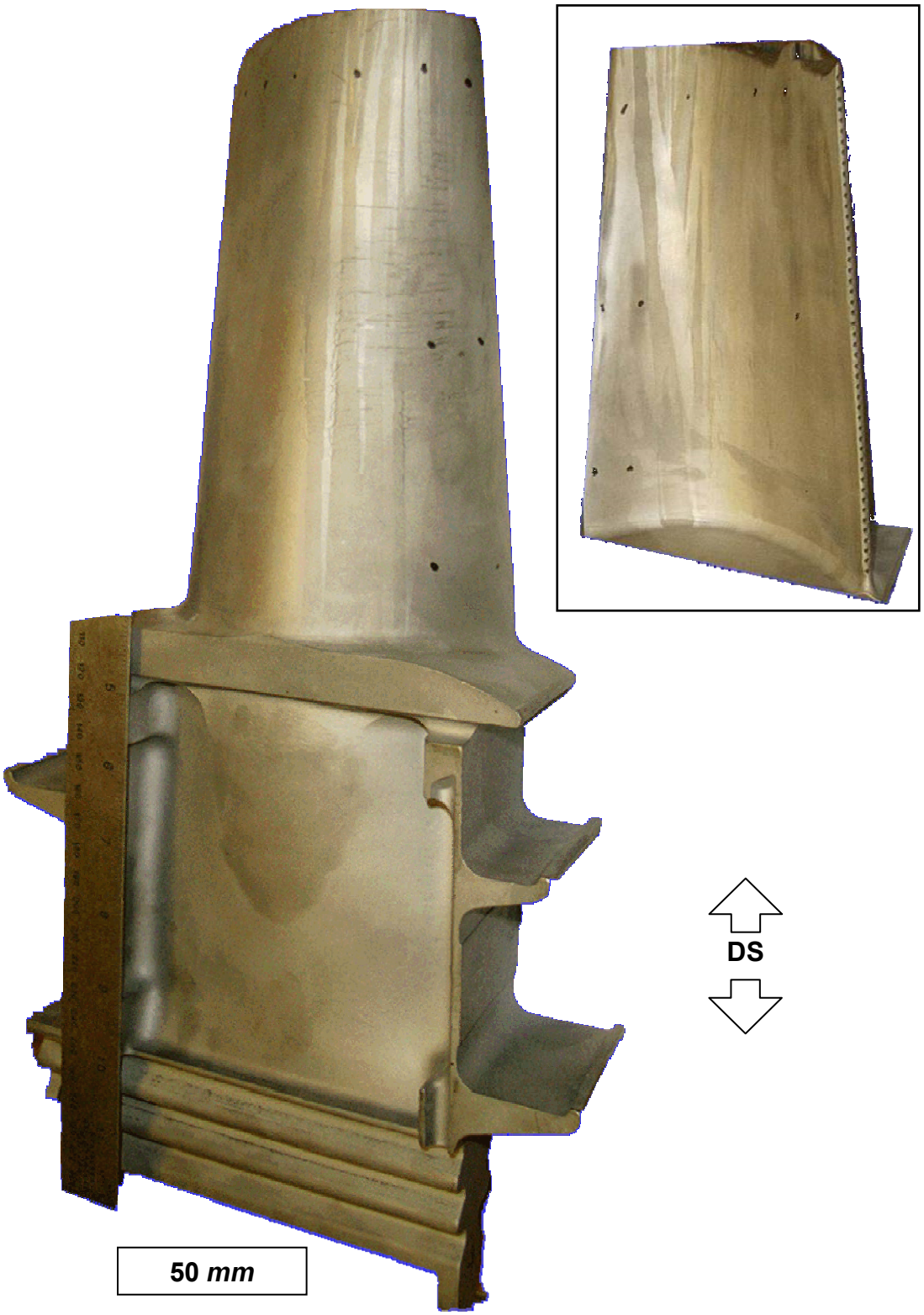


***Figure 2.4:*** *Suction and (inset) pressure sides of a directionally-solidified gas turbine blade.*

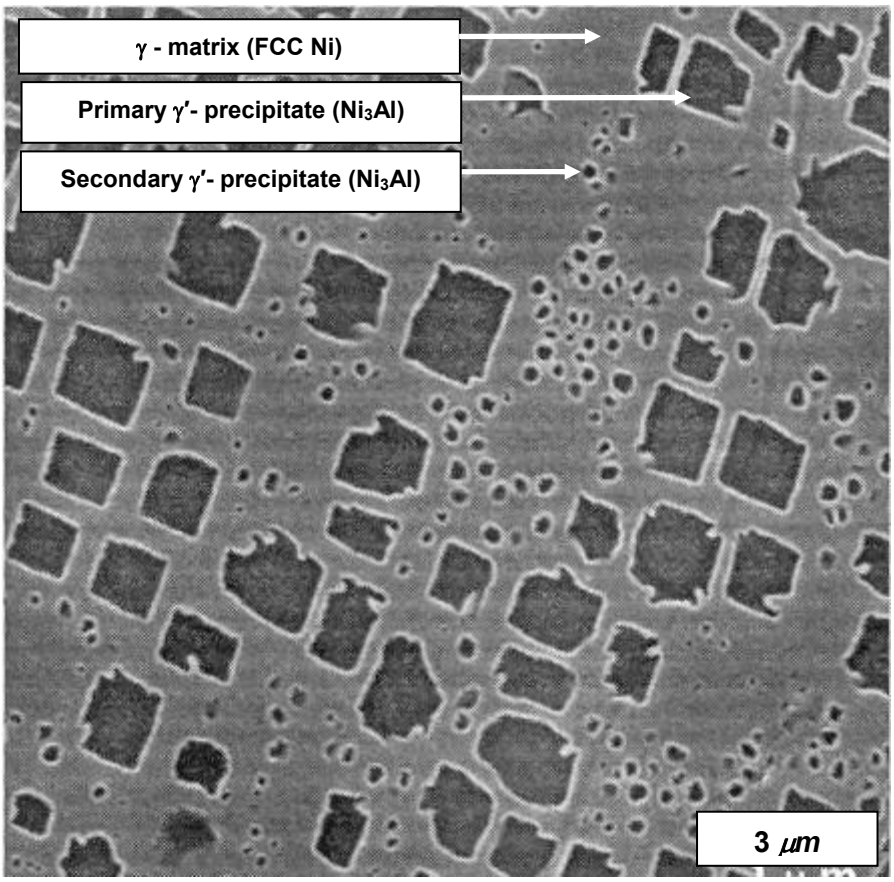


***Figure 2.5:*** *Image of the matrix and (course and fine) precipitate phases of DS GTD-111, a directionally-solidified Ni-base superalloy.*

axis. Like other Ni-base superalloys, DS GTD-111 is a dual-phase intermetallic consisting of a soft matrix and hard precipitates, as shown in Fig. 2.5. The γ matrix phase is FCC austenitic Ni solid solution with strengthening elements. The $L1_2$-structured γ′ precipitate phase is an ordered FCC super-lattice of nickel-aluminide, $Ni_3Al$, having a bimodal distribution. The cuboidal and spherical shapes serve as the main strengthening phase in many Ni-based superalloys (Antolovich, 1981; Nazmy, 1983; Huron, 1986; MacLachlan, 2000; Nomoto, 2000; Sajjadi, 2001; Neuner, 2002; Nategh, 2003). Because a slow cooling rate is applied during processing, DS GTD-111 has large grains and a

supersolvus microstructure consisting of primary cooling cuboidal γ′ precipitate particles averaging 0.5 $\mu m$ in width and secondary cooling spherical γ′ particles average 0.05 $\mu m$ in width (Trexler and Sanders, 2002). Comparatively, primary and secondary precipitates in PC GTD-111 measure 0.86 $\mu m$ and 0.1 $\mu m$, respectively. In each material, precipitates account for between 45-65% of the total volume fraction and are coherent with the matrix. Chromium (Cr) and aluminum (Al) have been added to enhance corrosion resistance. The use of different alloying elements affects the formation of the matrix phase and the precipitates and the overall material properties.

Directional solidification creates microstructures with columnar grains typically averaging 100 *mm* in length and between 0.1 *mm* and 4 *mm* in width (Huron, 1986; Marchionni, 1996; Yao, 1997); however, the average dimensions of grains in DS GTD-111, a superalloy developed are approximately 5×5×125 *mm*. During the solidification process, primary dendrite stems grow parallel to the solidification direction (Fig. 2.3). These stems are accompanied by secondary and tertiary dendrite arms that grow outward along [100] and [010] directions. The secondary arm spacing is a function of the temperature gradient at the nearby liquid/solid interface and velocity. This grain structure improves various aspects of the mechanical behavior found in PC Ni-base materials (Shahinan, 1989; Tong, 2001). For example, void nucleation and sliding at the GBs are each limited in DS Ni-base superalloys since the presence of GBs perpendicular to the primary stress direction is eliminated. Ni-base superalloys with DS structure are anisotropic and have superior creep properties than those with PC microstructures. The collection of long dendrites within grains serve as a fracture toughening mechanism since

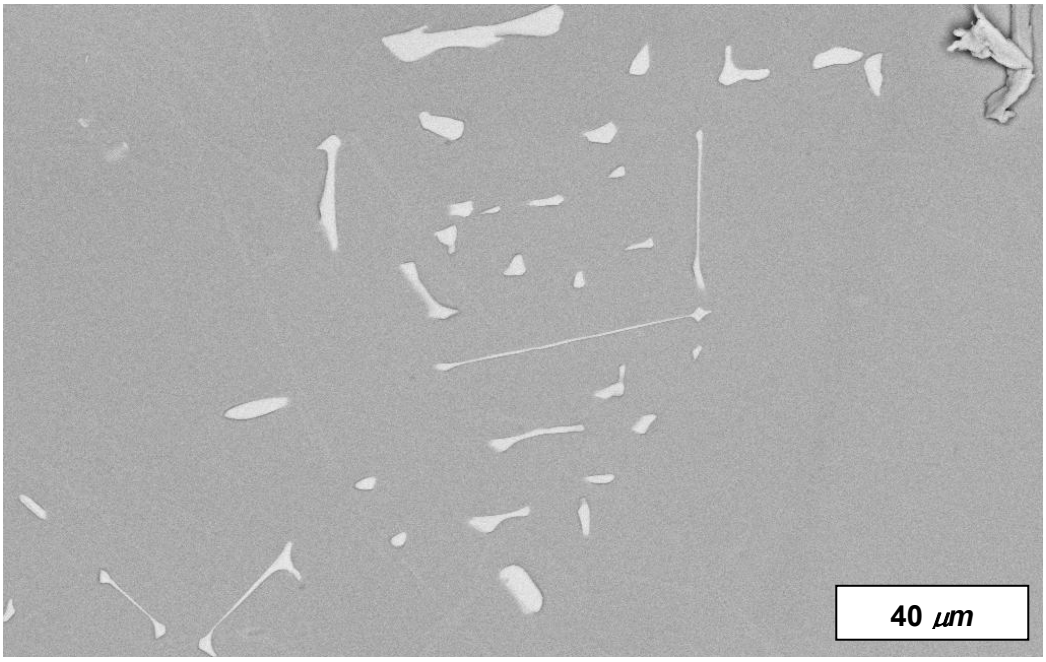


***Figure 2.6:*** *Several MC-type carbides with the Chinese script morphology in DS GTD-111, a directionally-solidified Ni-base superalloy.*

propagating cracks are often deflected toward GB interfaces, resulting in significant out-of-plane crack extension (Ibanez, 2003).

Directionally-solidified GTD-111 contains MC-type carbides that are present just after casting, and also contains $M_{23}C_6$–type of carbides which develop during ageing. Each type of inclusion particle is most prevalent between adjacent dendrites (e.g. in the so-called interdendritic region), in the γ matrix, along GBs, and near air-exposed surfaces (Nazmy, 1983; Nakasone, 1992). Figure 2.6 illustrates a collection of MC-type carbides that are likely interconnected on planes above and below the viewing plane. Titanium (Ti) and Cr are prone to forming hard, orientation-independent carbides that increase the fracture toughness of the material and reduce GB sliding (MacLachlin, 2000). The carbides are 50 to 150 $\mu m$ long with a high aspect ratio (~10:1 or greater).

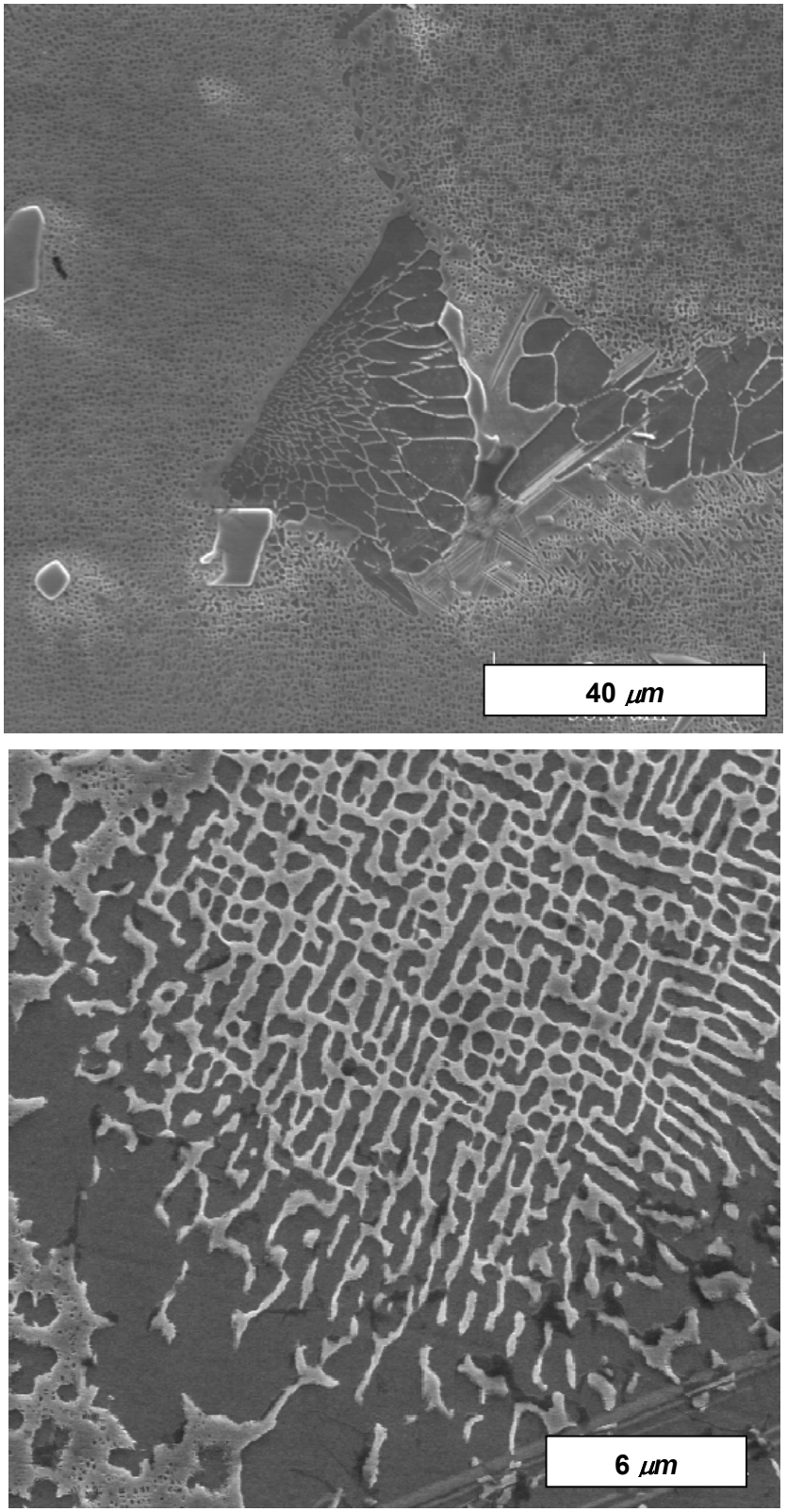


***Figure 2.7:*** *Image of interdendritic eutectic nodule found in directionally-solidified GTD-111.*

Eutectics nodules of γ-γ′ are also present in the material (Fig. 2.7). They are ductile and vary in size from 30 to 150 $\mu m$, and they can act as local stress concentrators under remotely applied loading.

The convention for describing the crystallographic orientation of samples extracted from either blades or slabs of DS GTD-111 is shown in Fig. 2.8. Longitudinal (L) specimens are fabricated so that the direction of the columnar grains (i.e., the DS axis) is parallel to the loading axis, whereas transverse (T) specimens are oriented so that the grains are perpendicular to the loading direction. The grain structures found in cross sections perpendicular to the primary stress axis of DS GTD-111 blades resemble those of equiaxed or polycrystalline GTD-111.

## 2.3 Prior Research on forms of GTD-111

GTD-111, a polycrystalline (PC) superalloy, was developed and patented by GE in the mid-1970s for 1st stage buckets and has grains between 0.67 *mm* and 1.5 *mm* (Sajjadi and Nategh, 2001). Equiaxed GTD-111 is an advancement from René 80 and General Electric Co. has reported that the alloy has an advantage of approximately 20°C (36°F) in creep rupture over the industry standard blading material IN-738 because of its greater percentage of solid solution strengthening precipitate particles (Embley and Russell, 1984; Schilke, 2004). It is equally corrosion resistant. GTD-111 is also superior to IN-738 in terms of low cycle fatigue (LCF) strength. The design of the GTD-111 superalloy utilized phase stability and other predictive techniques to balance the levels of critical elements (Cr, Mo, Co, Al, W and Ta), thereby maintaining the local hot corrosion resistance of IN-738 at higher strength levels without compromising phase stability and

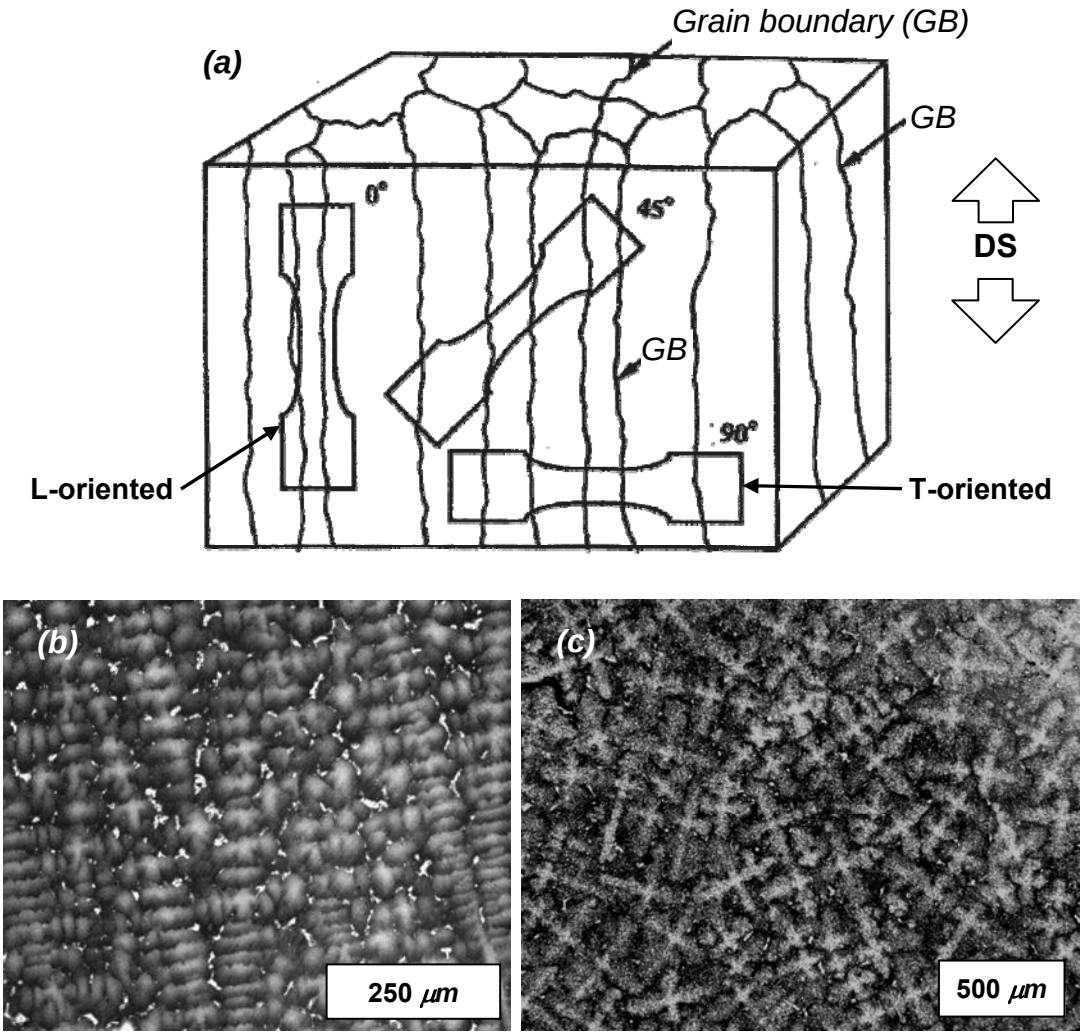


***Figure 2.8:*** *Sketch of grain boundaries and sectioning convention (a) and grain structures of sections (b) || and (c) ⊥ to the primary stress axis of directionally-solidified Ni-base specimens.*

castability. The nominal chemical compositions of each of these Ni-base superalloys are given in Table 2.1. A major difference between IN-738 and GTD-111 is compositional; there is a higher amount of Nb contained in IN-738. The compositions of René 80 and GTD-111 are the same except for slight modifications to the proportions of the elements C, Ta, and Mo. Each of these superalloys has an $L1_2$ structured precipitate phase contributing to anti-phase boundary (APB) strengthening in which the cuboidal

precipitate are separated by narrow matrix channels. In the late-1980's, DS GTD-111 was introduced as an advancement relative to the equiaxed GTD-111.

***Table 2.1:*** *Chemical compositions of some Ni-base superalloys*

| Material | Cr | Co | Ti | W | Al | Mo | Ta | C | Ni | Reference |
|---|---|---|---|---|---|---|---|---|---|---|
| René80 | 14.0 | 9.5 | 4.8 | 4.0 | 3.0 | 4.0 | - | 0.17 | Bal. | Daleo and Wilson, 1998 |
| IN-738 | 15.8 | 8.3 | 3.6 | 2.65 | 3.5 | 1.8 | 2.3 | 0.13 | Bal. | Lvova and Norsworthy, 2001 |
| GTD-111 | 13.8 | 9.5 | 4.8 | 3.9 | 2.9 | 1.5 | 2.9 | 0.10 | Bal. | Sajjadi et al., 2004 |
| DS GTD-111 | 14.0 | 9.5 | 4.9 | 3.8 | 3.0 | 1.6 | 2.8 | 0.10 | Bal. | Ibanez, 2003 |

Under real or simulated service conditions, turbine blade materials undergo various microstructural changes that usually facilitate degradation of mechanical properties such as tensile strength, creep resistance, etc. The following list highlights some of the microstructural changes and deformation mechanisms that have been reported for the temperature-resistant DS and PC GTD-111:

- Dislocation climb and looping around precipitate particles at high homologous temperatures (above $0.6T_m$) and under intermediate stress levels (Sajjadi and Nategh, 2001; Sajjadi et al., 2002; Nategh and Sajjadi, 2003; Sajjadi et al., 2004).
- Precipitate shearing at low homologous temperatures (below $0.6T_m$) and under high stress levels (above 300 *MPa*) (Sajjadi and Nategh, 2001; Sajjadi et al., 2004).
- Diffusional creep at low stresses (below 300 *MPa*) (Sajjadi and Nategh, 2001).
- Precipitate coarsening, coalescence, and loss of coherency at the γ-γ′ interfaces (above 1000°C) (Daleo and Wilson, 1998; Lvov et al., 2004).
- Transgranular and intergranular primary carbide particle degeneration (above 1000°C) (Trexler and Sanders, 2002; Lvov et al., 2004).

- Embrittlement and cracking at grain boundaries that intersect surfaces (Woodford and Stiles, 1997, Saxena, 2001).

Basic mechanical and metallurgical property tests were conducted on either as-cast and heat treated, or service-exposed material. In most cases, the as-cast or heat-treated materials were subjected to conditions that bracketed the operating conditions of a turbine blade.

In a series of investigations, correlations were developed to characterize the temperature and stress-dependence of mechanical properties of GTD-111 (Daleo and Wilson, 1998; Sajjadi and Nategh, 2001; Sajjadi et al., 2002; Nategh and Sajjadi, 2003; Sajjadi et al., 2004). For example, it is widely-known that both the yield and ultimate strengths slightly increase with temperature near 760°C (1400°F) for GTD-111. The variation of the yield strength (Sajjadi et al., 2004) and ultimate strength (Daleo and Wilson, 1998) is due to the contributions of the matrix and precipitate phases. While the yield strength of pure $\gamma$ generally decreases with increasing temperature, that of pure $\gamma'$ increases with temperature and is maximum at nearly 900°C (1652°F). When subjected to a constant strain rate of $10^{-4}\ s^{-1}$ and temperature of 800°C, a homogeneous dislocation network forms and slip bands extend through precipitate particles, as shown in Fig. 2.9b. This leads to high yield strength. Plastic deformation at 650°C (1202°F) produces high densities of dislocations that pile up at matrix-precipitate interfaces. These dislocation tangles impede dislocation motion and lead to the lowest yield strength (Fig. 2.9a). At higher temperatures, such as 800°C (1472°F), a homogeneous distribution of dislocations were observed in the matrix, while $\gamma'$ particles were rarely disturbed, as shown in Fig. 2.9c. Orowan dislocation loops formed around precipitate particles.

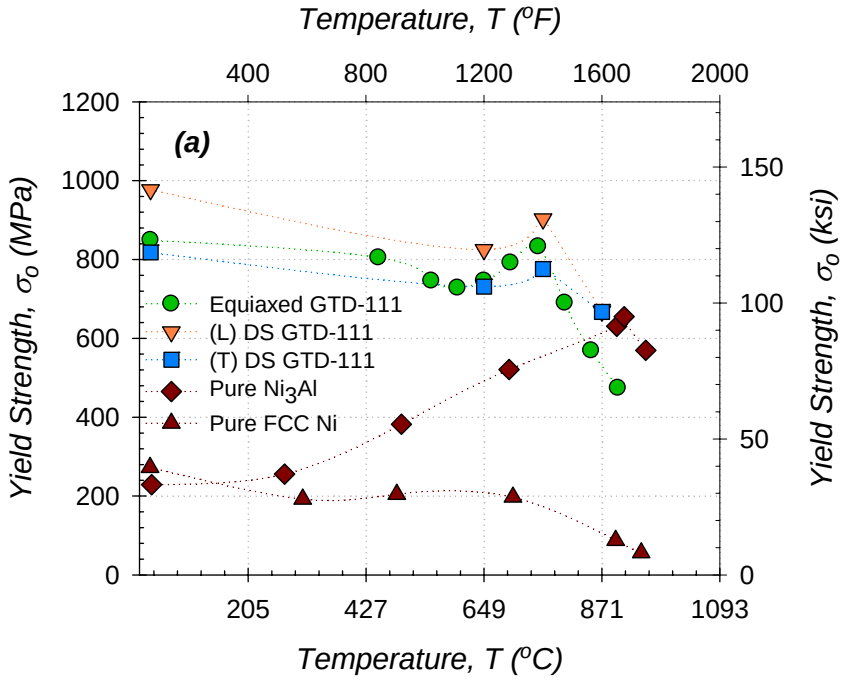


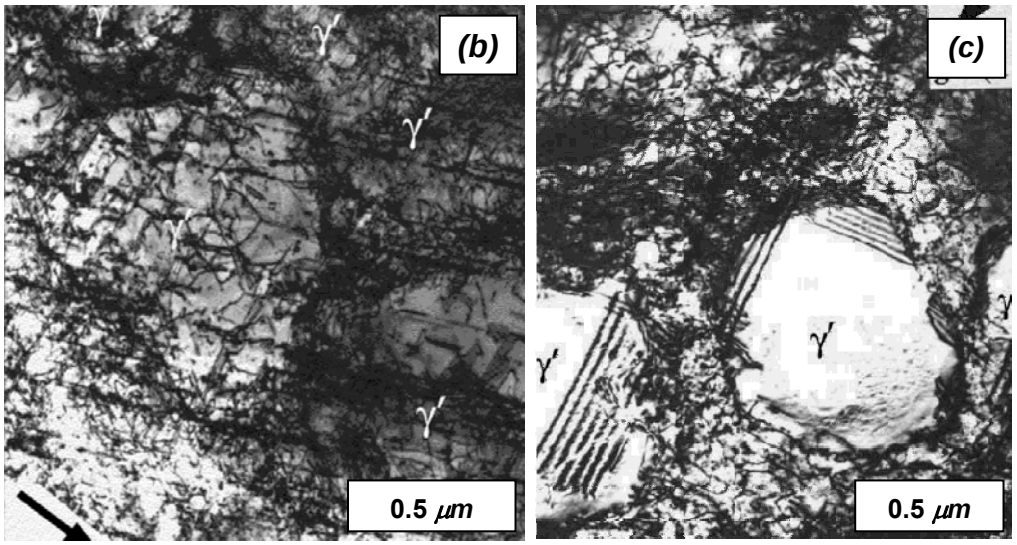


***Figure 2.9:*** *(a) Temperature-dependent yield strength behavior of conventionally cast (Sajjadi et al., 2004) and directionally-solidified (Ibanez, 2003) GTD-111 compared with pure nickel-aluminide and nickel (Beardmore et al., 1969). Dislocation morphology occurring in tensile-tested GTD-111 at (b) 550°C and (c) 800°C. For each case the strain rate was $10^{-4}$ $s^{-1}$ (Sajjadi et al., 2004).*

The uniaxial tensile material properties of DS GTD-111 have been determined using both monotonic (Ibanez, 2003) and cyclic experiments (Gordon et al., 2002). The

elastic modulus of the L- and T-oriented materials, like most other materials, decrease with increasing temperature, as listed in Table 2.2. The modulus versus temperature curve of the L-oriented case falls below that of the T-oriented DS GTD-111 case. The yield strength in the both grain directions, however, exhibits an increase between 649°C and 760°C, as shown in Fig. 2.9a. The material is generally more ductile in the longitudinal direction than in the transverse.

***Table 2.2:*** *Tensile Properties of DS GTD-111*

| Temperature | | Elastic Modulus, *E* | | Yield Strength, $\sigma_0$ † | | Elongation |
|---|---|---|---|---|---|---|
| (°C) | (°F) | (GPa) | (Msi) | (MPa) | (ksi) | (%) |
| 21 | 70 | - | - | 977 | 142 | 7.0 |
| 649 | 1200 | 126 | 18 | 825 | 120 | 7.0 |
| 760 | 1400 | 116 | 17 | 903 | 131 | 12.9 |
| 871 | 1600 | 108 | 16 | 669 | 97 | 23.1 |
| 982 | 1800 | 96 | 14 | - | - | - |
| 1038 | 1900 | 90 | 13 | - | - | - |
| 21 | 70 | - | - | 817 | 119 | 10.0 |
| 649 | 1200 | 180.5 | 26 | 731 | 106 | 9.8 |
| 760 | 1400 | 169 | 25 | 776 | 113 | 7.8 |
| 871 | 1600 | 157 | 23 | 666 | 97 | 9.1 |
| 982 | 1800 | 130.6 | 19 | - | - | - |
| 1038 | 1900 | 125 | 18 | - | - | - |

†*Displacement Rate = 0.0042mm/s (0.0017in/s)*

The temperature dependent dislocation network formed under tensile loading is analogous to that formed under creep deformation. Under creep loading at high temperatures and low stresses, dislocations migrate mainly within the matrix at γ-γ′ interfaces, while at low temperatures and high stresses dislocations cut through γ′ particles by stacking fault (SF) formation and anti-phase boundary (APB) coupled dislocation pairs (Sinharoy et al., 2001; Sajjadi et al., 2002; Nategh and Sajjadi, 2003). Under high stresses and low homologous temperatures deformation is associated with

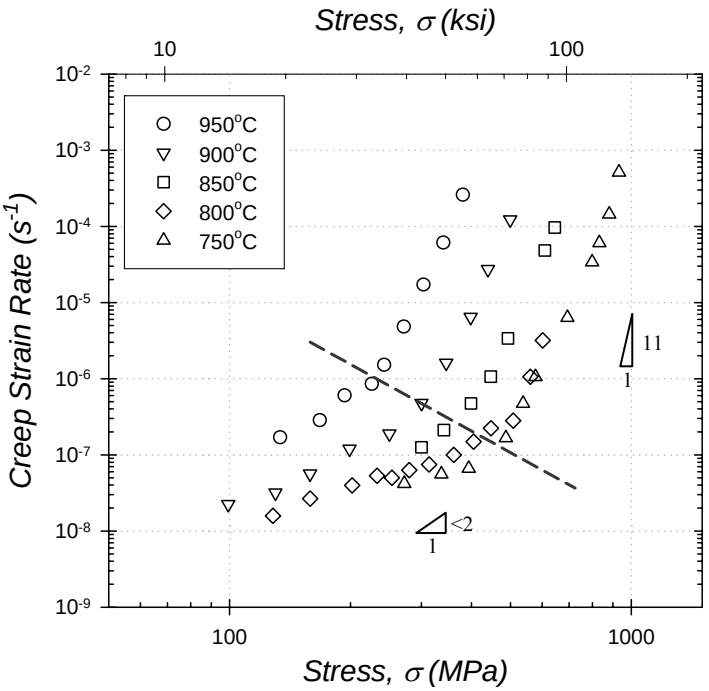


***Figure 2.10:*** *Stress-dependent power law breakdown of the steady state creep rate of equiaxed GTD-111 at different temperatures (Sajjadi and Nategh, 2001).*

precipitate particle shearing mechanism and anti-phase boundary creation. Under low stresses and high homologous temperatures, a precipitate particle bypass mechanism (looping and climb) dominate. The transition between deformation mechanisms at intermediate temperatures and stress levels is abrupt, and is best characterized by plots of the steady state creep rate, $\dot{\varepsilon}$, versus the applied stress (Sajjadi and Nategh, 2001). In Fig. 2.10, the data clearly show a breakdown in the power law creep relationship. The stress-temperature-dependence of these mechanisms is best characterized using a deformation mechanism map, as illustrated in Fig. 2.11. It should be noted that under very low stresses a diffusion creep mechanism is also operative.

With sustained exposure to mechanical loading and isothermal temperatures, dual-phase Ni-base superalloys never reach a state of equilibrium (Nabarro et al., 1996;

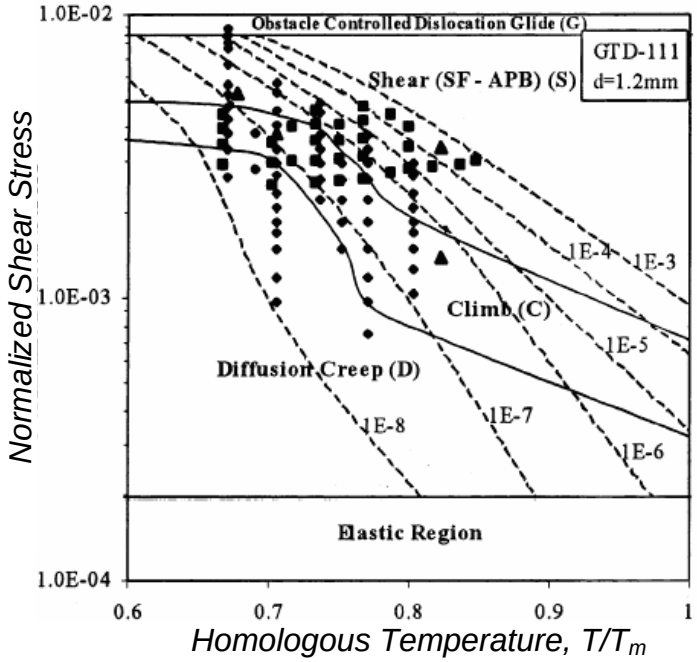


***Figure 2.11:*** *Deformation mechanism map for equiaxed GTD-111. Dashed contours represent* $\dot{\varepsilon}$ *with units* $s^{-1}$ *(Sajjadi and Nategh, 2001).*

Daleo and Wilson, 1998; Sajjadi and Nategh, 2001). Precipitate particles change shape via high temperature creep. Under remote applied loading, development of internal stresses are strongly controlled by the lattice and elastic constants of the two phases. The lattice misfit, $\delta$, is determined by lattice parameters for the precipitate and matrix phases ($a_{\gamma'}$ and $a_{\gamma}$, respectively), i.e. (Nabarro et al., 1996), i.e.,

$$\delta = 2\frac{a_{\gamma'} - a_{\gamma}}{a_{\gamma'} + a_{\gamma}}. \qquad (2.1)$$

In Ni-base superalloys, the lattice constant of the ordered precipitate phase is smaller than the lattice constant of the matrix phase, thus causing the lattice misfit to be negative.

Consequently, under a tensile stress at reasonably high homologous temperatures, the resultant local stresses in horizontal matrix channels (transverse to the load axis) are higher than those in the vertical channels (parallel to the load axis). The resulting elastic strain energy density gradient in the channels drives the diffusion process. Nickel atoms travel to horizontal channels and Al travels to vertical channels. Each cuboidal γ′ particle shortens along the transverse axis. Adjacent particles make contact and coalesce. Thus, tensile creep promotes the directional coarsening precipitates perpendicular to the applied stress, a process often called rafting. Compressive creep loading, conversely, causes the rafts to form parallel to the load axis.

Above RT, the rate of coarsening of γ′ in GTD-111 (Daleo and Wilson, 1998) follows the classical Lifshitz-Slyozov-Wagner theory of diffusion-controlled coarsening (Lifshitz and Slyozov, 1961; Wagner, 1961) that assumes a constant volume fraction of precipitates, i.e.,

$$r^3 - r_i^3 = Kt\,. \tag{2.2}$$

Here $t$ is time in seconds and $r$ is the average particle radius in *nm*. The constant, $r_i$, is the average starting radius and $K$ is a rate constant given by

$$K = \left[\frac{1}{T}\exp\left(B - \frac{Q}{RT}\right)\right], \tag{2.3}$$

where $B$ is a constant, $R$ is the gas constant, and $T$ is absolute temperature.

The major differences in PC and DS GTD-111 relates to the total GB area, interdendritic area, and the morphology (i.e., size, shape, and distribution) of the inclusions at those locations. Chromium-rich MC-type carbides are considered to be the primary carbides formed during the solidification of the alloy. Since DS GTD-111 has a slightly higher composition of carbide-forming elements (Cr and Mo) than other Ni-base superalloys, it has considerably more transgranular carbides than that of conventionally cast GTD-111 (Ibanez, 2003). In each material, the carbides have the "Chinese-script" morphology and have a volume fraction of less than 1.2% in DS GTD-111; thus, along any plane, the nominal shapes of carbides can appear as rounded with a diameter of a few microns or as elongated, measuring up to 150 $\mu m$ in length. Eutectic γ' and MC-type (and some $M_6C$) carbides are often strung along grain boundaries and interdendritic areas as shown in Figs. 2.12. The eutectics can also be scattered throughout the matrix.

In addition to the γ′-particle coarsening typically found after exposure to nominally creep conditions, carbide degeneration from $M_6C$ to $M_{23}C_6$ was also observed. Reduced stability of the virgin metal contributes to carbide evolution. Using Energy Dispersive Spectroscopy (EDS), several groups of researchers studied MC-carbide decomposition in several Ni-base superalloys (IN-738, PC GTD-111, and DS GTD-111) after long-term exposures to service conditions (Daleo and Wilson, 1998; Lvova and Norsworthy, 2001; Trexler and Sanders, 2002; Lvov et al., 2004). At a location experiencing elevated temperature such as the blade tip, the migration of Cr to the boundary leaves the matrix locally enriched in Ni, Al, Ti, and other γ′-forming elements. The MC-type carbides degenerate forming $M_{23}C_6$ carbides around the periphery of the

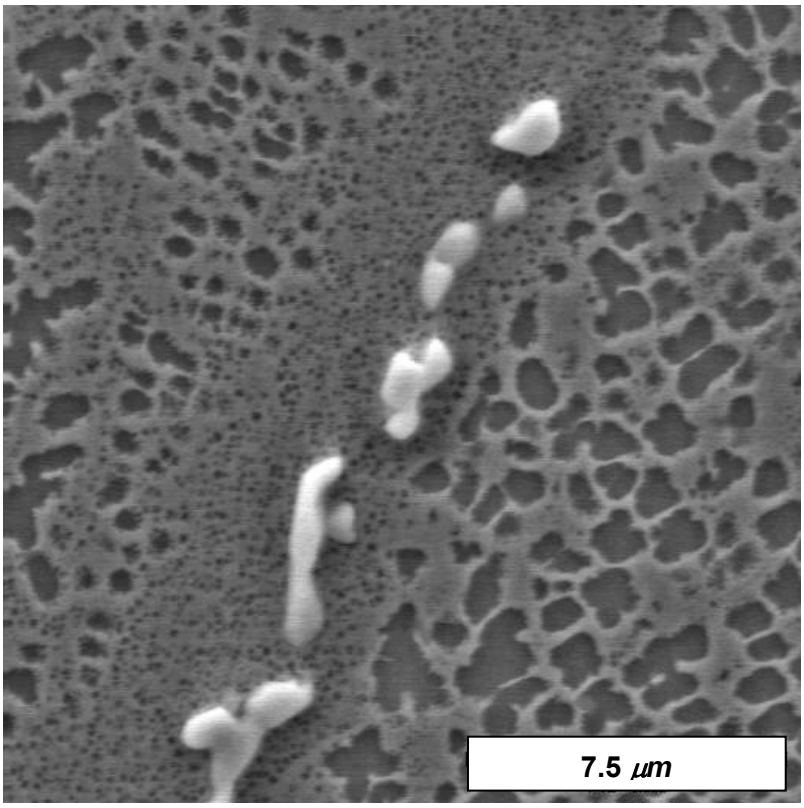


***Figure 2.12:*** *Image of grain boundary in DS GTD-111 showing MC-type carbides (bright particles) strung along the boundary as well as the $\gamma'$-depleted zone along the boundary.*

MC carbides (Daleo and Wilson, 1998; Lvova and Norsworthy, 2001). Diffusion of Cr from the primary carbide particles causes the following reaction to proceed:

$$MC + \gamma \rightarrow M_{23}C_6 + \gamma' . \tag{2.4}$$

The degeneration of the primary carbides to form the secondary Ta-rich $M_{23}C_6$–type carbides has been observed between 760°C (1400°F) and 980°C (1800°F) (Lvova and Norsworthy, 2001) and between 816°C (1500°F) and 899°C (1650°F) for 5000*hr* (Daleo and Wilson, 1998). Additionally, the outward diffusion of Ta and the inward diffusion

on Ni form nearby $DO_{19}$-structured η-phase ($Ni_3Ti$), so the overall reaction for the primary carbide degeneration may be written as

$$MC + \gamma \rightarrow M_{23}C_6 + \eta . \tag{2.5}$$

Maximum secondary $M_{23}C_6$ carbide precipitation occurs at 845°C in GTD-111 and IN-738 (Lvova and Norsworthy, 2001). In either case, the degenerated MC is typically surrounded by a well-defined decomposition zone, with discrete $M_{23}C_6$–carbide precipitation initially forming on the MC-γ interface.

Since diffusion is more rapid along GBs, carbide particles at these locations decompose more quickly than transgranular carbides. With continued opportunity for diffusion, the $M_{23}C_6$ carbide particles coarsen and coalesce forming continuous films along sections of the grain boundaries. The built-up carbide morphology at the grain boundary reduces sliding (Lvova and Norsworthy, 2001), and may provide preferential sites for crack initiation. Mismatches in coefficients of thermal expansion (CTE) of carbides and the nearby material cause shear stresses at carbide/metal interfaces at high temperatures. Local concentrations of stress affect the crack tip stress triaxiality and subsequently alter the crack tip trajectory and growth rate. These tortuous crack paths add to the overall fracture toughness of the material (Trexler and Sanders, 2002).

The processes leading the tensile creep failure in DS GTD-111 depends on the grain orientation. In the longitudinal direction creep crack growth (CCG) is transgranular, while in the transverse direction CCG is interdendritic (Woodford and Stiles, 1997), as illustrated in Fig. 2.13. In either case, cracks can initiate at the surface

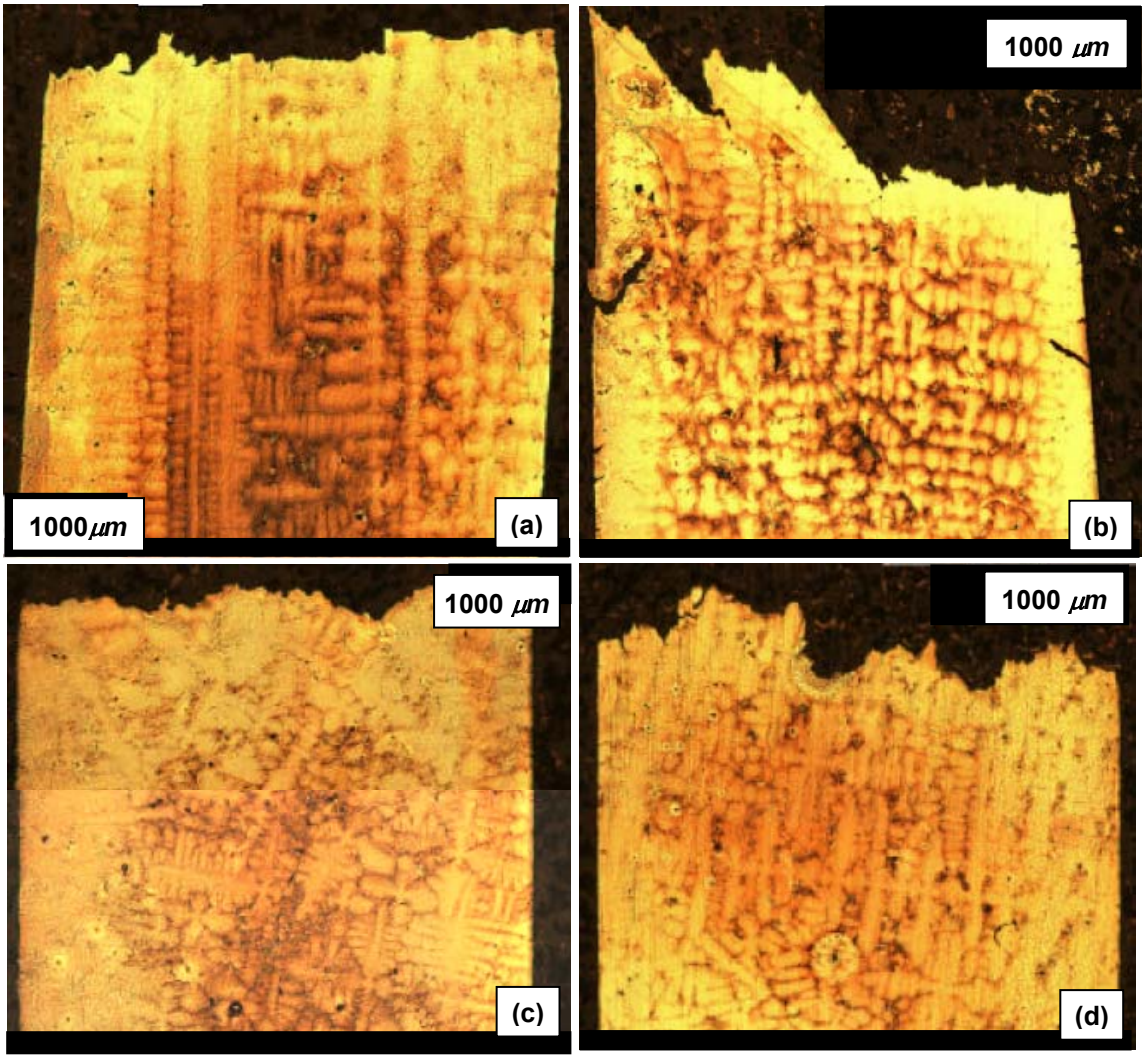


***Figure 2.13:*** *Micrographs of creep-tested (a-b) L-oriented and (c-d) T-oriented DS GTD-111. Stresses and temperatures for each of the cases (a) 614 MPa (89 ksi), 760°C (1400°F), (b) 290 MPa (42 ksi), 871°C (1600°F), (c) 614 MPa, 760°C, and (d) 290 MPa, 871°C (Ibanez, 2003).*

near oxidized grain boundaries or within the bulk at microstructural discontinuities. Because the grain boundaries along the stress axis present obstacles to crack propagation, the longitudinal orientation shows a longer creep life than the transverse material. Creep behavior consistently shows a very short primary creep regime, followed by a steady-state region that accounts for more than half of the creep life. The tertiary creep is

responsible for the majority of the accumulated creep strain. Woodford (1996) and Ibanez (2003) independently determined that above 900°C the creep strength of the L-oriented DS and PC (or off-axis DS materials) versions of GTD-111 appear to be about the same and independent of the loading direction.

Intergranular cracking found near the tips of ex-service buckets (blades) has been associated with an intergranular embrittlement mechanism (Woodford and Stiles, 1997). Creep rupture properties of PC GTD-111 degraded significantly after thermal exposures. The dissolution of the secondary precipitate particles and the increase in the size of the primary particles tends to lower the creep strength and possibly the fatigue resistance of the material. At 871°C the cracking mechanism was assisted by oxidation at the grain boundary. Gas phase embrittlement (GPE) by oxygen occurs when the material is exposed to air at high temperature (Woodford, 1996). This embrittlement may also be due to the segregation of embrittling species (e.g. degenerated MC-type carbides) from the grain interior instead of external sources (Woodford and Stiles, 1997). For an exposure at 1000°C for 24 hours, the ductility in the longitudinal direction reduced by 30% and ductility in off-axis directions dropped to near zero. For exposures at 850°C and lower for at least a week, no embrittlement occurs. Though in a study on PC GTD-111 for a much longer length of time [5000 hours (208 days)] at 816°C and then creep tested at 871°C and stress of 297 *MPa*, an intergranular fracture mechanism assisted by oxidation of grain boundaries is observed (Daleo and Wilson, 1998).

There are several types of thermomechanical fatigue cycles used to evaluate high temperature fatigue strengths of blading superalloys. The most complex cycle is that experienced in actual service conditions of gas turbine startup and shutdown, known as

the engine cycle. For the most critical regions, such as cooling holes, the strain-temperature profiles are shown in Fig. 2.14a and 2.14b. The linear cycles are representative of what is experienced in many parts of the blade. For example, the linear out-of-phase (OP) TMF cycle is a reasonable approximation for the leading edge of the blade. Of all of the types of cycles, the linear OP cycle has the most deleterious because of the high tensile strains generated at low temperatures (Embley and Russell, 1984). A considerable amount of testing was carried out using simple and simulated operating cycles to evaluate IN-738 and the then-new GTD-111 Ni-base superalloy. They determined that wave shape can have an overriding effect on life. Of the isothermal experiments conducted those with two minute compressive holds lead to the shortest lives. Maximum tensile stress and maximum cycle temperature were identified as critical parameters for correlating crack initiation life. For example, increasing the maximum temperature for OP TMF cycling shortens the life, as shown in Fig. 2.14c.

In application, combustion turbine blades are generally coated with a diffusion overlay to improve oxidation and corrosion resistance. Thermal barrier coatings (TBCs), such as CoNiCrAlY, are protective shrouds that are bonded to potential hot sections of gas turbine engine components to limit diffusion mechanisms at higher temperatures and aggressive combustion gases. In two studies by Chan and colleagues (Chan et al., 1999; Cheruvu et al., 2000), GTD-111 coated with either MCrAlY, PtAl, or a duplex coating (over-aluminized GT29+ or GT33+) were cyclically oxidized between room temperature and a peak temperature of either 954°C (1750°F), 1010°C (1850°F), or 1066°C (1950°F). Weight change analysis and microscopy were used to demonstrate that the degradation of Al content in the coating best correlates the life service coat. In a subsequent study,

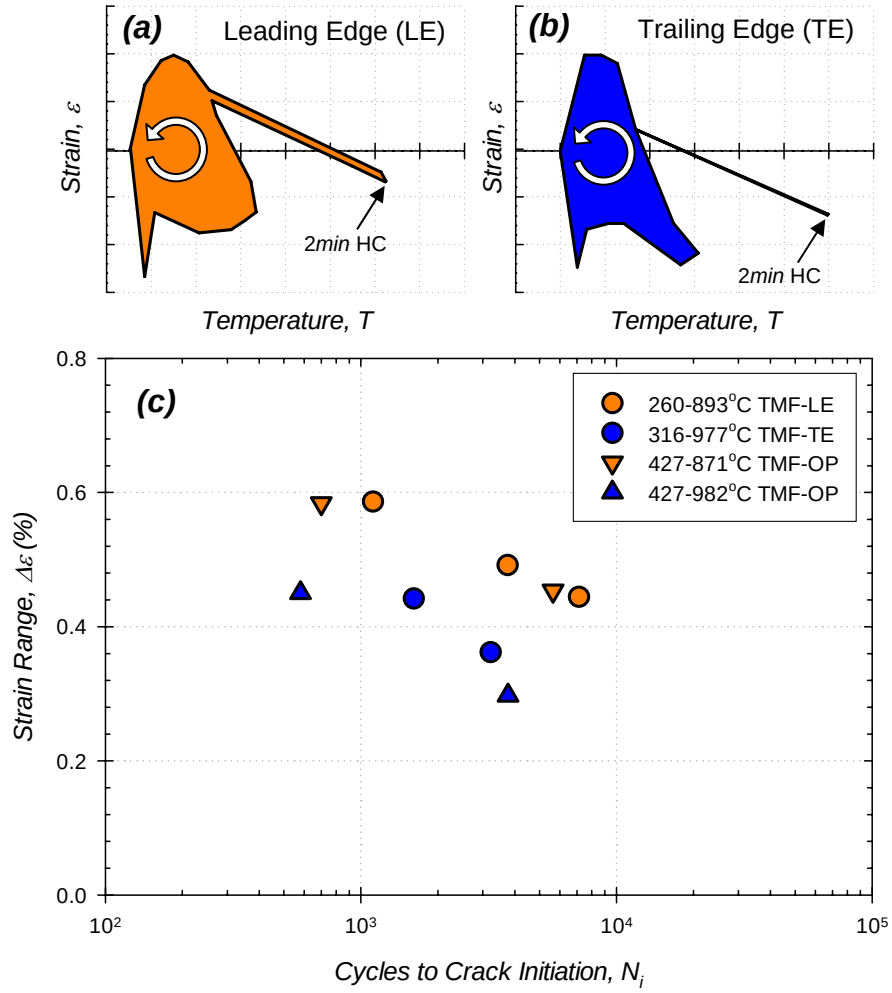


***Figure 2.14:*** *Two types of "engine" cycles used operative in (a) leading and (b) trailing edge locations of turbine blades. (c) Crack initiation life of PC GTD-111 under various forms of thermomechanical fatigue (TMF) cycling (Embley and Russell, 1984). Engine cycling (a-b) commences at the minimum temperature and zero strain in both cases.*

Chang and coworkers (Chang et al., 2003) used visual inspection, metallography, and finite element analysis to determine the cause of failure of a first stage DS GTD-111 turbine blade coated with GT33+. Thermal overloading in the form of a temperature gradient (300°C over a 30 *mm* section) near the tip of the leading edge of the bucket

induced a complex stress state. This resulted in phase instability, surface damage, and eventual crack formation.

## *2.4 Fatigue Behavior of Ni-base Superalloys*

Over the past three decades there has been numerous fatigue studies conducted on various forms of Ni-base superalloys. Key goals in many of investigations have been the determination of life exhausted during either the crack initiation or propagation phases. To measure fatigue life (i.e., both initiation and propagation phases), the fatigue life is usually taken as cycles until specimen rupture or a 50% drop in the saturated tensile load. Criteria for measuring cycles to initiation, $N_i$, are more complex and, as such, more varied. For example, Okada et al. (1992) defined $N_i$ to occur with the initial appearance 10 $\mu m$ deep surface cracks. This measure is conservative compared to Rémy and coworkers who in separate studies defined the end of the crack initiation phase to occur when observed cracks measured 25 $\mu m$ (Reger and Rémy, 1983), 300 $\mu m$ (Reger and Rémy, 1988), or up to 1000 $\mu m$ (Fleury and Rémy, 1993). Crack initiation depths ranging from 300 $\mu m$ to 1000 $\mu m$ have also been applied (Boubidi and Sievert, 2002). Carrying out fatigue tests until the desired surface condition is reached requires iterative test interruption and surface replication and microscopy. Several studies (Antolovich et al., 1981; Nazmy, 1982; Hasebe et al., 1992) define crack initiation to occur when the tensile stress response drops off from the initial saturated stress or is no longer symmetric with the compressive stress response.

A general observation from research focusing on both phases where both crack initiation life and fatigue were obtained is that trends in $N_f$ are dually reflective of trends

in $N_i$ (Reger and Rémy, 1988; Wright, 1988; Fleury and Rémy, 1994). Another important observation is that the majority of life is spent in the initiation phase; afterwards, the stress response drops off rapidly (Antolovich et al., 1981). A discussion of the phenomenological fatigue trends in Ni-base superalloys follows.

*Continuous Cycling Low Cycle Fatigue Behavior*

To establish baseline fatigue behavior, push-pull fatigue data for Ni-base superalloys are often obtained and then interpolated using either stress or strain-based laws. For example, at 600°C (1112°F) a two-component power law can be used to interpolate fatigue life data of two DS superalloys (René 80 and CM247LC) (Okazaki et al., 1990). The strain-life approaches, such as the classic Basquin and Coffin-Manson power laws, can also be applied. At 850°C, the total strain life of DS CM247LC could be decomposed into elastic and plastic strain range components (Marchionni et al., 1996). The fatigue strength exponent, $b = 0.15$, and the fatigue ductility exponent, $c = 0.68$. The plastic strain amplitude versus fatigue life of René 77 (a PC Ni-base superalloy) subjected to 927°C (1700°F) could be modeled with the Coffin-Manson law with slope of -0.67. The average plastic energy is defined as

$$\Delta W = \frac{\Delta\sigma\Delta\varepsilon_p}{1+n'}. \tag{2.6}$$

This expression has units of $kJ \cdot m^3$ and correlated fatigue life data with much accuracy (Antolovich, 1981b).

Low cycle fatigue failures originate from the specimen surface or near surface sites above certain transition strain ranges, while below the transition strain range, the failure initiation is dominated by crack formation at internal defects (Hyzak and Bernstein, 1982a; Hyzak and Bernstein, 1982b). The surface-subsurface transition strain range is dependent on test conditions (rate and temperature) and properties of the superalloy (composition and size and volume fraction of defects).

*Orientation Dependence*

The isothermal uniaxial fatigue life of single crystal Ni-base superalloys (AM1 and MAR-M200) stressed along the [001] orientation displayed a much longer life than those oriented along the [101] and [111] directions. Orientation plays a strong role in the dependence of fatigue life on mechanical strain; however, orientation dependence is not as clearly apparent when relating fatigue life to stress amplitude (Chieragatti and Rémy, 1991; Fleury and Rémy, 1994). The greatest difference in life usually occurs at lower mechanical strain ranges. A difference by nearly a factor of 7.5 was recorded at $\Delta\varepsilon_m = 1.0\%$ at 950°C (1742°F). At a lower strain range of 0.5% and/or lower temperatures, the life difference escalates to two orders of magnitude.

Several studies have been conducted on the orientation dependence of DS Ni-base superalloys as well. In CM247LC and René N4, L-oriented specimens subjected to temperatures above 950°C displayed the longest fatigue lives, while T-oriented samples exhibited the shortest fatigue lives (Marchionni et al., 1996; Wright and Anderson, 1980). René N4 samples in between those orientations, such as 45°-specimens, exhibited total lives in between those orientations. At a temperature of 1000°C, the L, T, and 45°-

oriented samples of the DS material MAR-M247 were subjected to load-controlled tensile creep-fatigue conditions (Okada et al., 1998); the life of the L-oriented sample outlasted both of the T and 45°-oriented specimens by nearly factors of 7 and 3, respectively. In DS René 120 at 982°C, the T-oriented specimen had a plastic strain life differing from both the L and 45°-oriented specimens by nearly a factor of 20 (Huron, 1986), as shown in Fig. 2.15a. The variation in these discrepancies could be related to a number of experimental (temperature, frequency) or microstructural aspects (grain size, inclusion volume fraction) that influence crack nucleation at grain interfaces. With regard to the current research, the most relevant study of off-axis-oriented isothermal LCF behavior was carried out by Hasebe et al., (1992). The subject of this investigation was that of the crack initiation behavior of MAR-M247LC, which was fatigued at L, T, and 45° orientations (Fig. 2.15b). Compared to L and T-oriented samples, 45°-oriented samples displayed the lowest crack initiation lives.

One explanation for the differences in fatigue lives is based on the anisotropic nature of the mechanical properties. The orientations with the lower elastic modulus, e.g. [001] for SCs and L-oriented for DS materials, result in a reduced cyclic stress range and lower level of cyclic plasticity. This is verified by the observation that orientation-dependence is less apparent when fatigue life data are plotted in terms of cyclic plastic strain range.

Another explanation is associated with grain structure. Cracks in the L-oriented samples initiate within the grain typically along secondary dendrite arms. Resistance to crack propagation is high in these samples since dendrite boundaries represent obstacles fracture. Cracks in the T and 45°–specimens initiated along grain boundaries and

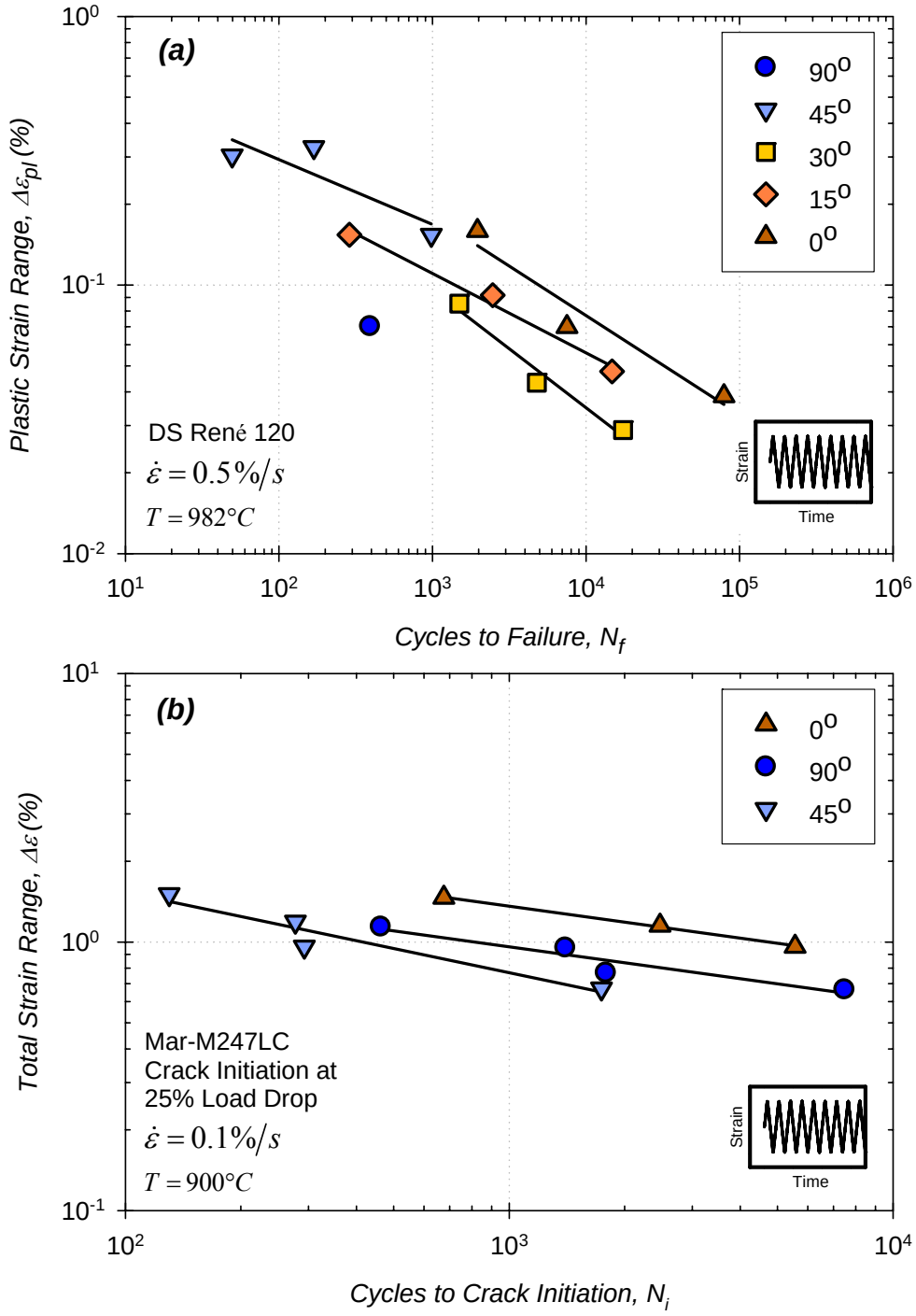


***Figure 2.15:*** *Orientation dependence of (a) plastic and (b) total strain life of two DS Ni-base superalloys (DS René 120 – Huron, 1986) and Mar-M247LC – Hasebe et al., 1992). For each case $R_\varepsilon$=-1.*

typically propagated rapidly due to the larger quantity of grain boundaries transverse to the loading axis (Okada et al., 1998).

*Temperature-Dependence*

The temperature dependence of the fatigue life of AM1, a SC Ñibase superalloy, was determined by Fleury and Rémy (1994). As temperature increases, the coefficient of the power law applied to interpolate stress range versus life data decreases while the exponent nearly stays the same. In DS materials (MAR–M246 and CM247LC), however, the coefficient of the cyclic plastic strain versus life law increases with increasing temperature from 704°C (1300°F) to 1093°C (2000°F). The exponent remins in the range of $0.68 < c < 0.78$ (Huron, 1986; Marchionni et al., 1996).

*Strain Rate/Frequency Effects*

The most notable effect of strain rate on deformation properties is the effect on flow stress (Leverant et al., 1971). As the strain rate is decreased, the peak yield strength of the material decreases. The most apparent consequence of the rate–dependent yield strength is demonstrated by means of fatigue cycling. Under LCF conditions, in situations with peak stress exceeding the yield strength, the cyclic stress range determines the plastic strain range. As such, total strain versus fatigue life curves shift toward longer lives with increasing cycling frequency.

The rate dependence of the yield strength is related to the reduced importance of creep in the fatigue cycle. There is a crossover is in the damage mechanism from "surface-dominated" at cyclic frequencies of 20 *CPM* and below to "integranular"

between 180 and 600 *CPM* in U-700, which is a polycrystalline Ni-base superalloy at 760°C (1400°F) and 586 *MPa* (85 *ksi*) (Organ and Gell, 1971). Whereas low frequencies favor surface intergranular crack initiation and propagation, high frequencies favor subsurface initiation at grain boundary inclusions. Life increases by nearly a factor of 100 by increasing the rate from 2 *CPM* to 600 *CPM*. A DS Ni-base superalloy known as René 120 was subjected to two strain rates ($\dot{\varepsilon} = 0.0083\%/s$ and $0.83\%/s$) at three temperatures ($T = 704°C$, $927°C$, and $1093°C$) (Huron, 1986). Although more data are needed to draw a general conclusion concerning rate dependent cyclic properties of the material, a few trends are as follows. At intermediate temperatures, specimens cycled at low rates had shorter lives than those cycled at high rates. The difference is most likely due to the influence of oxidation damage. At high temperatures, samples cycled at low strain rates had longer lives than those cycled at high rates. No explanation was given for this unexpected finding. An identical trend was also observed under nearly zero-to-tension cycled ($R_\varepsilon = 0.05$) PC René 80 at 871°C and 982°C (Antolovich et al., 1980; Antolovich et al., 1981a).

Mechanical strain versus total life curves do not exhibit this anomalous trend. At both 500°C and 871°C an increase in the cyclic frequency increased the mechanical strain versus fatigue life on the order of 2 to 4 times. Increased life under increased strain rate is attributed to a decrease in both the environmentally induced damage and creep damage in MAR-M247 (Sehitoglu and Boismier, 1990a).

*Thermomechanical Fatigue Effects*

Single crystal Ni-base superalloy samples of AM1 were subjected to high temperature "aeronautical" non-isothermal fatigue cycling (CCD-TMF). The deformation response depends on the temperature-dependent mechanical properties: modulus, yield stress, and cyclic hardening/softening behavior (Fleury and Rémy, 1994). It should be noted, however, that the most detrimental TMF cycle type to overall life is that of OP cycling (Embley and Russell, 1984).

Typically, the stress or strain range versus fatigue life curves of TMF data are bracketed between those of the isothermal fatigue life at the minimum and maximum temperatures. Out-of-phase TMF test results correspond well with isothermal fatigue tests conducted at the peak temperature (Sehitoglu and Boismier, 1990a). TMF life data are best correlated with in-phase (IF) life data using strain-life data since stress-based (e.g. stress range or maximum stress) correlations are affected by temperature.

Under TMF cycling (500°C ⇆ 871°C) at high mechanical strain ranges, IP cycling leads to shorter lives than OP TMF cycling. A crossover in life occurs at $\Delta\varepsilon = 0.5\%$, and a drop-off trend for OP-TMF life at low strain ranges is evidence of the increased role of oxidation damage occurring at longer lives. Crack initiation under IP-TMF is aided by the residual tensile stresses found around the inclusions because their coefficient of thermal expansion (CTE) is less than the CTE of the alloy; also, they have a higher modulus of elasticity than the surrounding alloy, resulting in an additional stress concentration around the inclusions.

In the presence of a mean stress, thermomechanically fatigue-tested IN-100 has a fatigue crack initiation life that decreases with increasing stress ratios at 1000°C. Stress versus life data can be normalized using the stress ratio, *R*, (Rémy et al., 1993).

*Creep-Fatigue Effects*

Of the various forms of fatigue cycling, that with superimposed dwell periods in tension shortens crack initiation lives of various forms of Ni-base superalloys (Reger and Rémy, 1988; Koster et al., 2002). The total strain life curve in CMSX4 at 950°C, shifts towards shorter lives when tensile dwell periods are increased (Koster et al., 2002). Under tensile creep fatigue conditions sites of crack initiation are often at stress concentrations, such as pores, eutectic inclusions, and coarsening precipitate particles. This was the case for the SC, CMSX-2 [001], cycled according to $\Delta\sigma = 600\ MPa$, $R_\sigma = -1$, and $t_{ht} = 60\ s$ at 950°C (Okazaki and Yamazaki, 1999).

Dwell periods in compression promote environmentally dominant forms of damage, discussed below.

*Environmental Effects*

Oxidation plays an important role in the crack initiation behavior of Ni-base superalloys at high temperatures. A PC Ni-base superalloy, IN-100, was used to determine the influence of environment on test frequency at 1000°C between 379 *MPa* (55 *ksi*) and 861 *MPa* (125 *ksi*). Tests in vacuum (pressurized to $10^{-4}\ N \cdot m^{-2}$) result in a much higher crack initiation life than in air for low test frequencies. The difference in life was nearly a factor of 100 for $\Delta\varepsilon_{in} \approx 0.1\%$ and a frequency of 3 *CPM* (Reger et al.,

1988). The fracture surfaces of a single crystal (MAR-M200) were markedly different for the two cases. In vacuum-exposed samples, the surface is covered with small equiaxed dimples produced by local necking. In air-tested samples, the surface has steps and river lanes. At high stresses the fracture surfaces appeared identically dimpled (Duquette and Gell, 1971). These morphological differences indicate that environmentally-controlled diffusion kinetics are involved in the local damage processes.

The inelastic strain range curves for samples exposed to air are insenstive to tensile hold times at low cyclic test frequency (Reger and Rémy, 1988). If the test temperature is decreased, then the oxygen effects decrease. For example decreasing the temperature from 927°C (1700°F) to 760°C (1400°F) closed the gap between stress-life curves of MAR-M200 tested in air and vacuum (Duquette and Gell, 1972). Alternately, for IN-738, compressive dwells are equally detrimental to life as the most damaging form of non-isothermal fatigue type (e.g. OP cycling) (Embley and Russell, 1984). Slower frequency cycling and tensile conditions that allow cracking of brittle surface grown oxides accelerate the crack initiation process (Wright, 1988).

One method for controlling the influence of oxygen content without using a vacuum is surrounding the fatigue sample while testing in an inert gas environment. In this manner it was demonstrated that a consistent increase in fatigue life could be achieved with decreasing oxygen level (Wright, 1988). Oxidation has a significant effect on the high temperature fatigue of single crystal superalloy René N4 tested at 1093°C (2000°F) along [001] in various environments. At 20 *CPM* (0.3%/s) the material showed

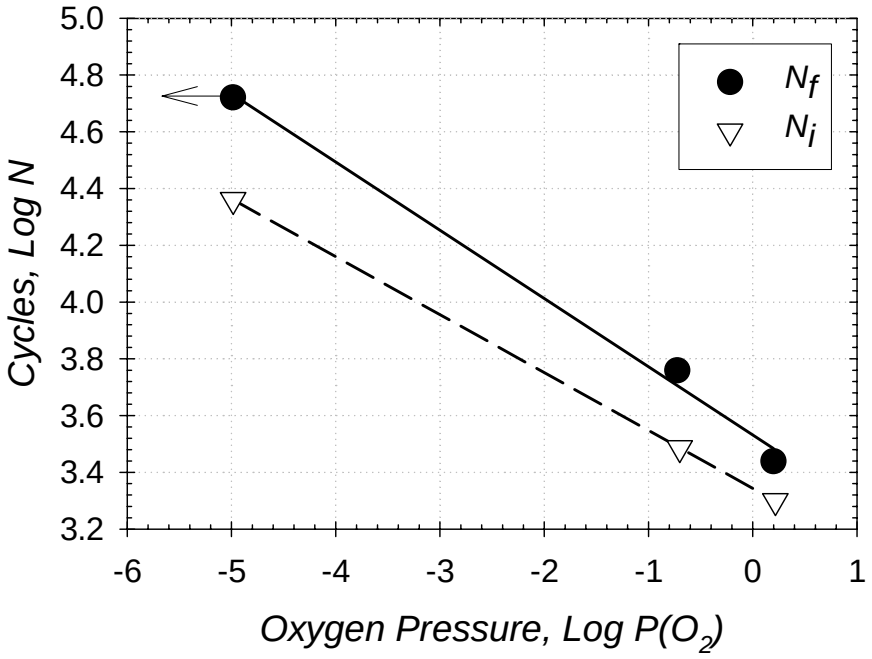


***Figure 2.16:*** *Effect of oxygen pressure on life of a single crystal (René N4) at 1093°C cycled at 20 CPM (Wright, 1988).*

the best resistance to fatigue in helium (~61K cycles) , in air (~8K cycles) For a constant strain range, the test parameter of oxygen pressure can be used to correlate fatigue life, i.e.,

$$N_f = K\left(P_{O_2}\right)^{-0.23} \tag{2.7}$$

The same relation, albeit with difference constants, can be used for crack initiation life as shown in Fig. 2.16. This data were taken for a total strain range of 0.45%.

*Pre-Exposure Effects on Fatigue*

Engineering components are commonly subjected to pre-straining due to manufacturing processes or unintentional overstrains. This type of prior deformation and

exposure can potentially damage a component by altering the surface condition or deteriorating the microstructure. Deformation properties that might be degraded (or improved in some cases) are the yield properties, creep strength and/or crack initiation life (Ott and Mughrabi, 1999; Nazmy et al., 2003). In order to investigate this phenomenon, two load level tests are normally conducted. The first stage, referred to as the pre-exposure, is typically exposure of a sample to some sustained level of temperature and/or strain. Next in the sequence is fatigue testing. The main limitation involved when trying to determine the effects of pre-exposure is that more material constants are needed. Model constants must be determined from a considerable amount of testing, and the number of calculations can be cumbersome in complicated histories.

Pre-straining effects on the PC superalloy IN-718 were investigated at RT (Kalluri et al., 1996). The investigators applied the Damage Curve Approach (DCA), which was originally developed by Manson and Halford (Manson and Halford, 1981; Manson and Halford, 1985). The damage fraction for a two-level fatigue tests was used to account for sequence effects, i.e.,

$$D = \left(\frac{n_1}{N_1}\right)^P + \left(\frac{n_2}{N_2}\right), \tag{2.8}$$

where $N_1$ and $N_2$ are the fatigue lives at the first and second load levels, $n_1$ is the number of cycles applied in the first level, and $n_2$ is the number of remaining cycles in the second level. To convert pre-creep data into pre-fatigue data, $n_1$ was assumed to be a quarter cycle with a strain range equal to twice the magnitude of the pre-strain. The corresponding $N_1$ (typically very short) can be determined from baseline strain life

results. The exponent $P$ is a function of stress level that falls in the range of 0 and 1. The reduced life, $n_2$, could be predicted within a factor of 2. Additionally, compressive pre-straining up to 2% has virtually no effect on life.

Dislocation structures formed in a SC and PC Ni-base superalloys due to prior exposure were examined by TEM (Rong et al., 1997; Christ and Schöler, 2004). The results suggest that temperature and inelastic deformation during pre-loading affect creep and fatigue resistance. Pre-deformation at low ambient temperatures lowers creep resistance because it introduces a high density of mobile dislocations. During the fatigue portion of the test, prior load history effects increase with increasing temperature, and decreasing plastic strain amplitude (Christ and Schöler, 2004). Intermediate temperature (520°C) pre-straining work hardens the material, and thus increases the creep resistance of the material (Rong et al., 1997).

At high temperatures, the precipitate morphology is also significantly affected. Ott and Mughrabi (1999) conducted fatigue tests on pre-crept SC Ni-base materials (CMSX-4 and CMSX-6) to demonstrate that precipitate particle coarsening affects crack propagation behavior. Pre-raft structures parallel to the stress axis hinder the crack propagation along the stress axis and forces the cracks to deviate. The consequence is longer fatigue life. On the other hand, rafts lying perpendicular to the stress axis developed from tension pre-creeping facilitate crack propagation and therefore lead to shorter lives. Figure 2.17 illustrates pre-deformed microstructures that lead to either improvements or reductions in the fatigue life.

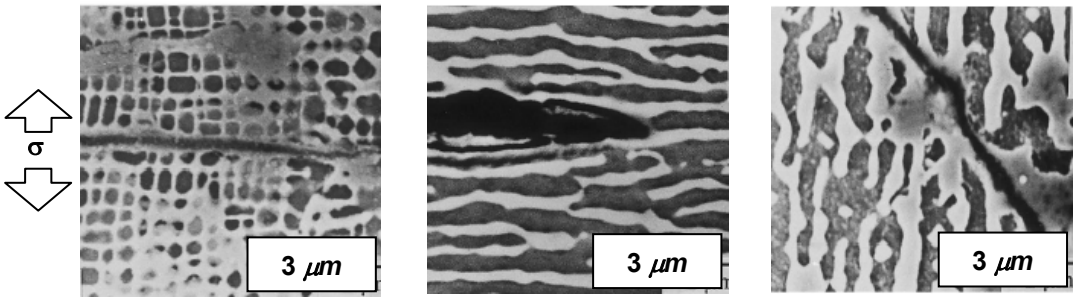


CMSX4 As-cast: ($\Delta\varepsilon_m$=0.9%, $N_f$=4000)

Tension Pre-crept: ($\Delta\varepsilon_m$=0.9%, $N_f$=2750)

Compression Pre-crept: ($\Delta\varepsilon_m$=0.9%, $N_f$=6500)

***Figure 2.17:*** *Effect of pre-creeping on the microstructure and fatigue life of a single crystal Ni-base superalloy (CMSX-4) fatigued at 1050℃ cycled at* $\dot{\varepsilon} = 0.9\%/s$ *(Ott and Mughrabi, 1999). Pre-deformation was conducted in a vacuum at 1100℃ and 115 MPa (17 ksi).*

Crack initiation life depends on the prior exposure condition (e.g temperature environment, mechanical load). Pre-exposures of IN-738 in air at 1000°C cause the most drastic reduction to life, whereas lowering the temperature and/or removing all of the air from the environment affects life to a lesser extent. For example, the $N_i$ of René N4 cycled at, $\Delta\varepsilon = 0.45\%$ $\dot{\varepsilon} = 0.3\%/\text{s}$ with R = -1 at 1093°C (2000°F) was reduced by a factor of 2.1 when pre-exposed to static air at 1093°C for 100 *hr* (Wright, 1988); however, fatigue lives of pre-exposed sample can be significantly increased after the surface layer is machined away (Fig. 2.18). This was observed in PC René 80 subjected to a prior exposure of 982°C and 97 *MPa* (14 *ksi*) in tension and fatigue cycling with $\Delta\varepsilon_{pl} = 0.05\%$ at 0.33 *Hz* at 871°C (Antolovich et al., 1980).

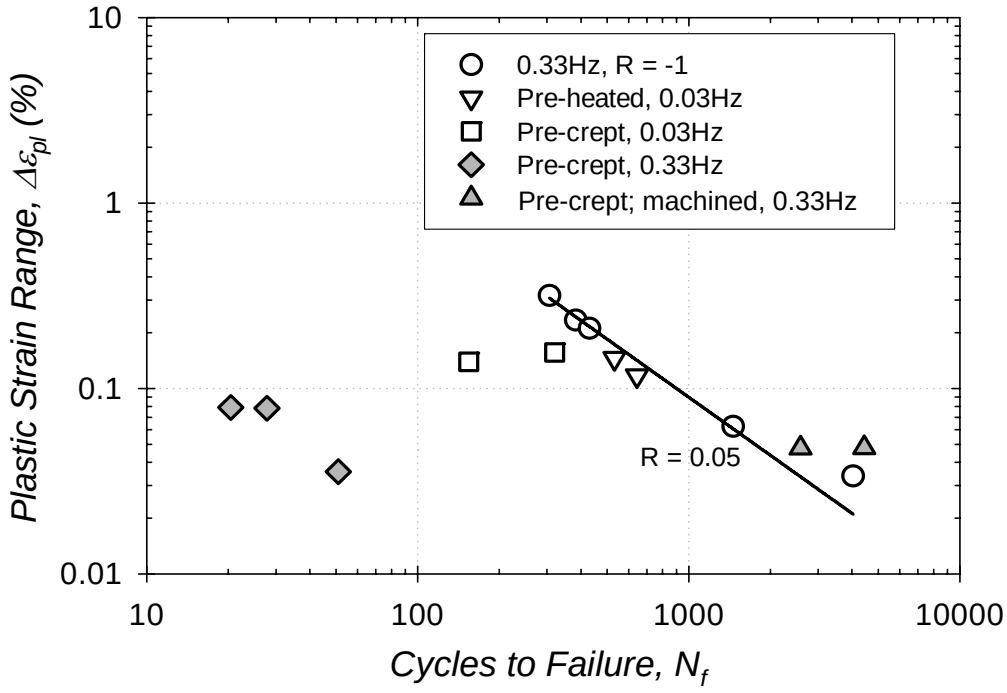


***Figure 2.18:*** *Effects of pre-exposure and maching on plastic strain-life of René 80 isothermal cycled at 871℃ with R=0.05 except as noted. Pre-heating was carried out at 982℃ for 100 hr, and pre-creeping was carried at 982℃ and 97 MPa (14 ksi) for 100 hr (Antolovich et al., 1980).*

## *2.5 Creep Deformation Behavior of Ni-base Superalloys*

The uniaxial creep deformation and rupture behavior has been the focus of investigations of a variety of intermetallic Ni-base superalloys. The testing conditions ranges involved are those that best represent the conditions in operation. Temperatures ranged from 649°C to 1100°C, while stresses ranged from 250 *MPa* to 700 *MPa*. Early in the creep life of dual-phase Ni-base superalloys, the ductile matrix becomes filled with a stable network of interfacial dislocations and very little precipitate shearing occurs unless the test temperature is low. Afterwards, steady state creep occurs due to continued dislocation generation and microcracking at interdendritic inclusion particles and casting

porosities. Precipitate shearing is also introduced in this stage. This is accompanied by cavitation in conventionally cast materials with a polycrystalline microstructure. Stress concentrations at the sites sustained damage leads to the onset of tertiary creep which is associated with the coalescence of microcracks. Precipitate shearing is also dominant.

In addition to the results on variations of GTD-111 that have been reviewed in Sec. 2.3, creep of materials has been conducted on a plethora of Ni-base superalloys with various microstructures and chemical compositions. While most investigations have been focused on the mechanics of creep deformation and rupture, many have introduced mathematical formula that correlate the stress-strain response with experiments.

Depending on the experimental configurations, creep tests take a long time to perform. If the applied stress is low enough, tests can last beyond 1000 *hr*. The Larson-Miller parameter (Larson and Miller, 1952) has been established to prediction of creep rates or creep rupture times to longer times than have been measured. This is derived by using the Arrhenius equation for steady state creep:

$$\dot{\varepsilon} = D \exp\left( -\frac{Q_c}{RT} \right) \tag{2.9}$$

Here $Q_c$ is the activation energy for steady state creep, $R$ is the universal gas constant, and $D$ is a constant. Assuming that the majority of life is used up during steady state creep (e.g. $\varepsilon \approx \dot{\varepsilon} \cdot t_r$), Eq. (2.9) can manipulated into the Larson-Miller parameter, LMP, i.e.,

$$LMP = T\left(C + \log t_r\right)/1000 \tag{2.10}$$

where $t_r$ is the time to rupture (in hours) and $C$ is constant. The temperature, $T$, is measured in Kelvin ($K$). The LMP is typically used as a design parameter against creep rupture. Using this type of parameter would be helpful in optimizing the volume fraction of γ′, which is nearly 65% (Harada et al., 1982; Murakumo et al., 2004) for TMS-75 (SC) and IN-713C (PC) near 900°C (1652°F) or 1000°C (1832°F) and 137 *MPa* (20 *ksi*).

Creep rupture data from experiments on transversely and longitudinally-oriented directionally-solidified GTD-111 are compared with those of equiaxed and single crystal materials in Figs. 2.19a and 2.19b, respectively, via a plot of stress versus LMP. For a given stress, LMP data of the L-oriented DS GTD-111 lie slightly to the right of data generated for the T-oriented and PC materials. This small difference corresponds to an increase of resistance to creep rupture of nearly 25°C (45°F). Alternatively, given a lifetime required at a specified temperature, LMP can be calculated and the maximum allowed stress interpolated on the graph. Because of its ease in implementation, inspection intervals of turbine blades are based on estimates of LMP determined from nominal operating conditions (e.g. thermal, mechanical, and environmental loading histories).

Experimental results from isotropic PC materials (Harada et al., 1982; Kim et al., 1992; Srinivas et al., 1995; Ai et al., 1998; Sajjadi et al., 2004) and anisotropic SC materials (Harada, et al., 1982; Gunturi et al., 2000; MacLachlan et al., 2001; MacLachlan et al., 2002; Murakumo et al., 2004) exhibit similarity to results of DS materials (Ohno et al., 1992; Woodford, 1997; Ibanez, 2003). Generally, the creep

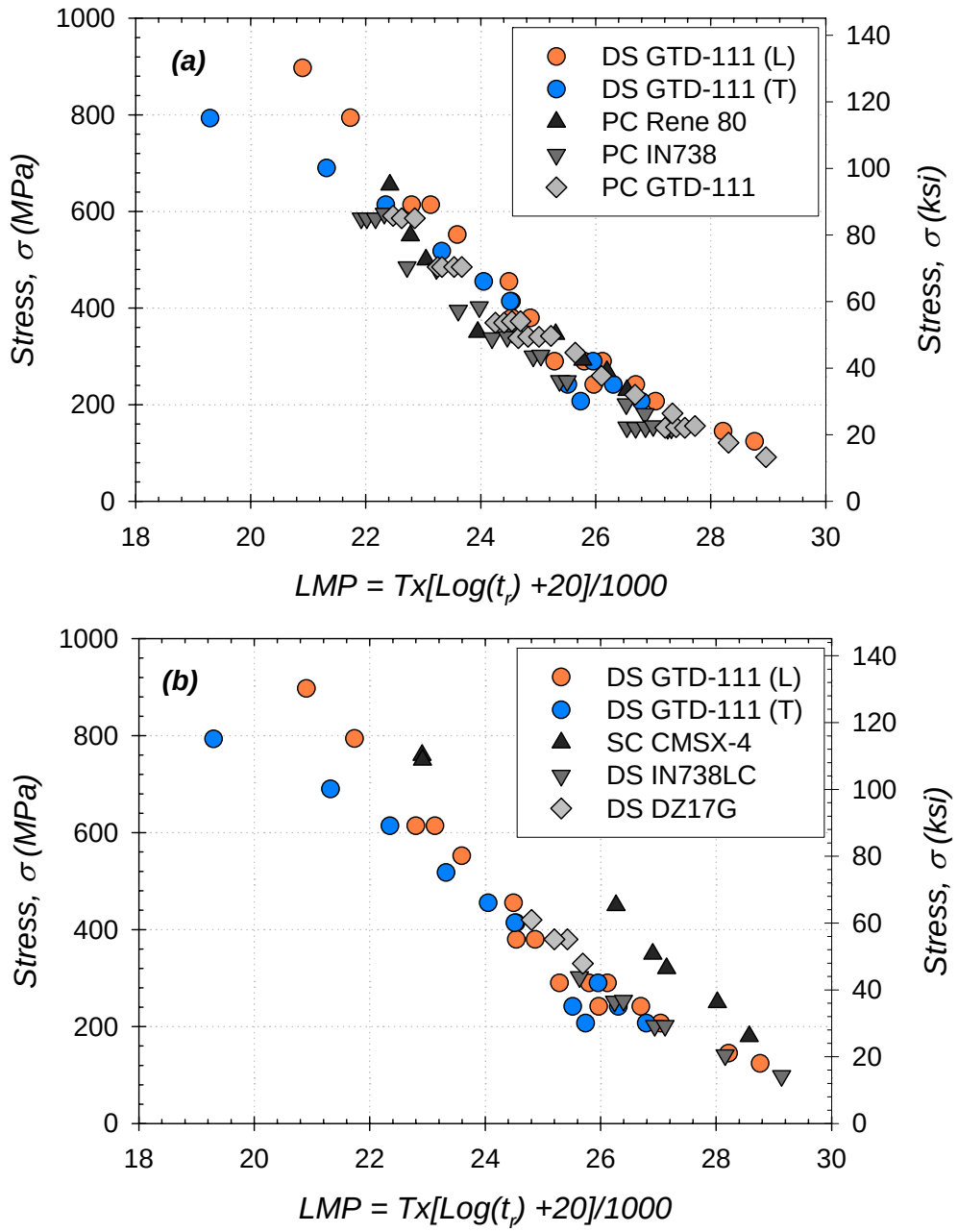


***Figure 2.19:*** *Larson-Miller Parameter (LMP) for L- and T-oriented DS GTD-111 compared with (a) polycrystalline (PC) materials [René80 – (Kim et al., 1992); IN-738 (Woodford, 1997)]; PC [GTD-111 (Daleo and Wilson, 1998)] and (b) directionally-solidified (DS) [DZ17G (Guo et al., 2001), IN-738LC (Castillo et al., 1987)], and single crystal (SC) [CMSX-4 (MacLachlan et al., 2001)] materials.*

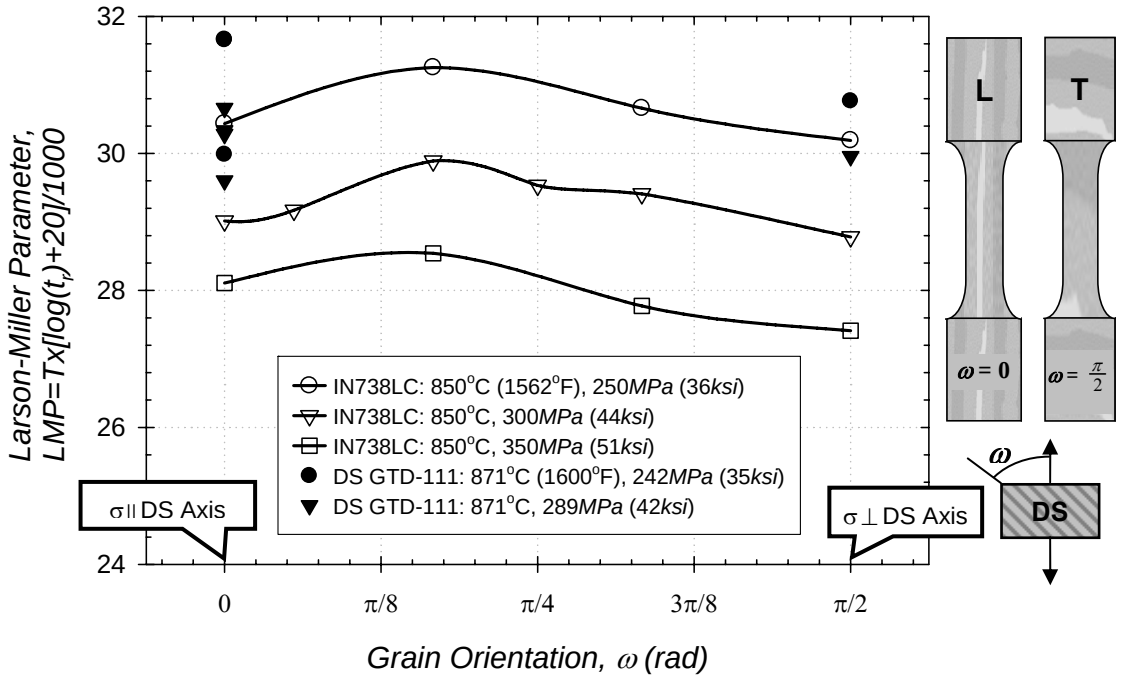


***Figure 2.20:*** *Larson-Miller Parameter (LMP) for multiaxially-crept IN738LC under constant stress levels (Ohno et al., 1992) compared to uniaxially-crept DS GTD-111 (Ibanez, 2003).*

curves show limited primary and secondary creep and extensive tertiary creep. By increasing the temperature, oxidation plays an enhanced role (Srinivas et al., 1995). Embrittled grain boundaries are denuded of precipitate particle and rich in cavities along grain boundaries. This is especially the case at grain interfaces that intersect the specimen surface (Ai et al., 1998). The macroscopic response to this cavitation is the hastening of microcracking and the increase of the creep rate of the material at lower stress levels. Coalescence of these grain boundaries microcracks signals the onset of the tertiary creep stage. Rupture typically occurs when the cross-sectional are fraction covered by the cracks reaches 0.6 (Kim et al, 1992).

In an investigation of the off-axis creep rupture behavior of the DS Ni-base superalloy IN738LC, Ohno and coworkers (1992) determined that the creep strength of

the material along intermediate orientations of the material exceeded that of the L and T orienteations, as shown in Fig. 2.20. The peak value of the LMP typically occurred for specimens with the grains oriented $\pi/6$ from the stress axis.

In cases where there are no grain boundaries at which a surface crack can initiate, rupture can occur at stress concentrations (Fig. 2.21) or at interdendritic regions. The observation that this is more prevalent at higher temperatures is an indication of the contribution of surface oxidation for either orientation. Compared to L-oriented material, T-oriented samples have similar creep strength at low stresses and high temperature, but its creep strength is lowered at higher stresses (Woodford, 1997).

Deformation of the material is the consequence of crystallographic slip. Slip is generally dictated by the resolved shear stresses along the favorable crystallographic slip planes. There are two slip systems that are appropriate for FCC single crystal Ni-base superalloys: octahedral slip on {111}<110> (12 slip systems) and cube slip systems {100}<110> (6 slip systems). While octahedral slip is active throughout the temperature range, cube slip is mainly active at high homologous temperatures. Macroscopic cube slip is a manifestation of multiple crossings of octahedral slip along matrix channels (Bettge and Österle, 1999) producing zig-zag dislocation lines. MacLachlin and colleagueas investigated the uniaxial creep strength of several single crystal materials (R2200, CMSX-4, and SRR99) (Gunturi et al., 2000; MacLachlin and Knowles, 2000; MacLachlin et al., 2001) at either 750 or 950°C. They determined that specimens oriented along the [111] pole deform by the {111}<112> octahedral slip systems toward the [001]-[111] boundary.

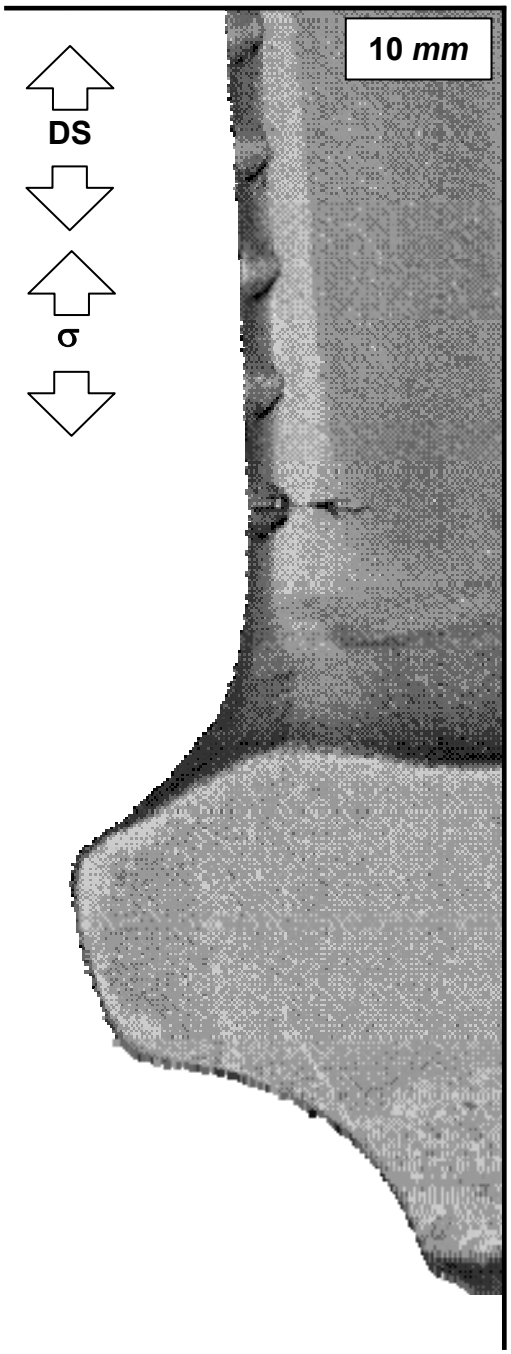


***Figure 2.21:*** *Low cycle fatigue (LCF) crack at the 1st cooling hole of a Ni-base gas turbine blade.*

For cases where the macroscopic response of the material is the focus, there are two classifications of modeling approaches implemented. The first is an extension of the *phenomenological* isotropic creep models. The second is *slip system* modeling that considers slip on specific planes associated with the face-centered cubic phase of material. The modeling is based on crystal plasticity theory. The primary distinction between the two is that quantified observations of material microstructure are the underpinning of the latter approach. For each modeling regime, several models have been presented to include descriptions for the accumulation of damage in the form of void growth and coalescence. In so doing, tertiary creep (i.e., creep softening) is accounted for. In situations where the evolution of the microstructure needs to be quantified (e.g., precipitate rafting or coherency loss) the two phase microstructure must be explicitly considered.

To model the uniaxial behavior of conventional castings and DS materials (Guo et al., 2001; Ibanez, 2003), investigators have used models based on isotropic power law rules that accurately correlates the temperature and stress-dependence of steady-state creep deformation, i.e.,

$$\dot{\varepsilon}_{cr} = A\left(\bar{\sigma}\right)^{n}. \tag{2.11}$$

Here, $A$ is referred to as the steady-state creep coefficient, and $n$ is the creep exponent. The coefficient of Norton's Law for secondary or steady-state creep [Eq. (2.11)] was modified to account for temperature-dependence, i.e.,

$$\dot{\varepsilon}_{cr} = \left[ B \exp\left( -\frac{Q_c}{RT} \right) \right] (\bar{\sigma})^n . \tag{2.12}$$

Equation (2.12) is known as the Bailey-Norton Law. The activation energy for creep is $Q_c$ is measured in *J/mol*, and $R$ is the universal gas constant with units of *J/mol-K*. Only a limited number of experiments at one temperature are required to determine the material properties, $A$, $B$, and $n$; however, $Q_c$, must be determined from tests at a series of isothermal temperatures. In order to fit most power law relations, the least-squares method was used.

For DS GTD-111, the activation energy for the creep process was reported as 3773 *kJ/mol* for the L-oriented material and 3636 *kJ/mol* for the T-oriented material (Ibanez, 2003); however, only considering the creep results recorded above 649°C (1200°F) yields smaller estimates of $Q_c$. Figure 2.22 plots creep coefficients versus the reciprocal of temperature for L- and T rupture tests. The energy for the process is 1674 *kJ/mol* and 1558 *kJ/mol* for L- and T-oriented DS GTD-111, respectively. The observation that $Q_c$ is slightly higher for L-oriented DS GTD-111 is consist with previous findings (Ibanez, 2003). This temperature dependence was also observed in equiaxed GTD-111 (Sajjadi and Nategh, 2001), which has a considerably lower activation energy below 900°C ($Q_c$ =106 *kJ/mol* below 900°C , $Q_c$ = 675 *kJ/mol* above 900°C). In another DS material called DZ17G, $Q_c$ = 540 *kJ/mol* (near 1050°C) (Guo et al., 2001). In other PC materials having a similar chemical composition but smaller grain size than GTD-111, such as Rene 80 (Kim et al., 1992) and K417 (Ai et al., 1998), activation energies for creep ranged from 283 *kJ/mol* (760-871°C) to 445 *kJ/mol* (700-900°C), respectively.

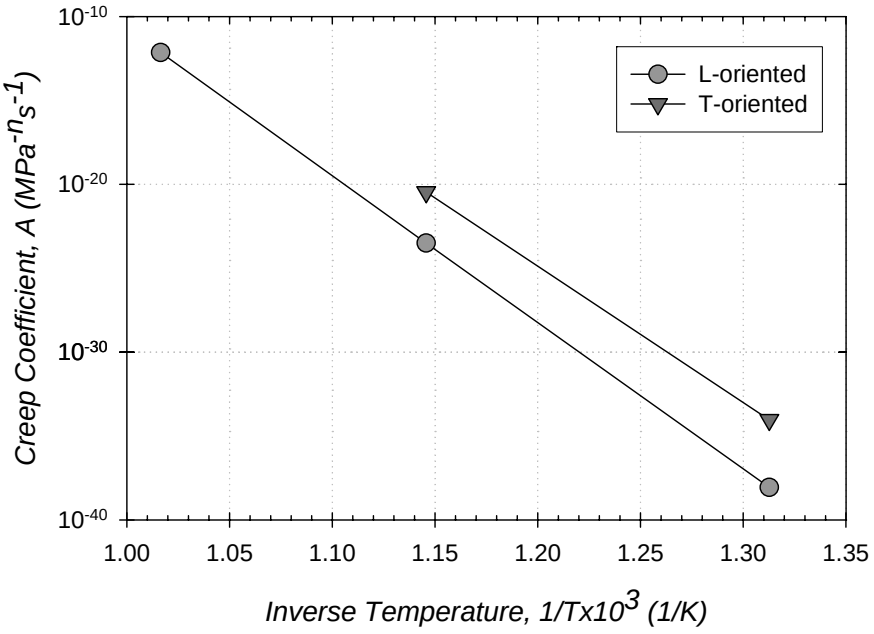


***Figure 2.22:*** *Temperature dependence of activation energies of L- and T-oriented DS GTD-111 above 649°C.*

In single crystal Mar-M200, $Q_c$ = 627 *kJ/mol* (near 760°F) (Leverant and Bernard, 1970). Pure face-centered cubic Nickel has an energy of 276 *kJ/mol*.

Based on microstructural observations, the temperature dependence (or stress-dependence) is due to the transition from diffusional creep (high temperature or low stress) to dislocation creep (low temperature or high stress). The Orowan stress has been used to account for this breakdown in power law creep, i.e.,

$$\bar{\sigma}_{th} = \alpha \frac{Gb_b}{r}, \tag{2.13}$$

where $G$ is the shear stress, $b_b$ is Burger's vector for grain boundary dislocations, $r$ is the spacing of precipitate particles, and $\alpha$ is a proportionality constant. Physically, $\sigma_{th}$ is the

resistance stress for creep, and is implemented in Eq. (2.12) using a piecewise continuous function that explicitly accounts for the individual creep regimes. For example, the following relation can be applied to account for the crossover in creep processes of PC materials (Guo et al., 2001; and Sajjadi and Nategh, 2001):

$$\bar{\sigma} = \begin{cases} \sigma_a - \sigma_{th} + 170MPa; & \sigma_a > \sigma_{th} \\ \dfrac{\sigma_a - \sigma_{th}}{3} + 170MPa; & \sigma_a < \sigma_{th} \end{cases}. \tag{2.14}$$

Here $\sigma_a$ is the uniaxial applied stress, and $\sigma_{th} \approx 240\ MPa$ (39 *ksi*).

In some cases, the off-axis macroscopic creep response of the anisotropic material is needed. Anisotropic creep behavior has been implemented using Hill's anisotropic yield function to describe interpolate the multiaxial material response from a series of uniaxial rupture tests. The yield function is given as

$$\tilde{q}(\sigma) = \sqrt{F(\sigma_y - \sigma_z)^2 + H(\sigma_z - \sigma_x)^2 + I(\sigma_x - \sigma_y)^2 + 2L\tau_{yz}^2 + 2M\tau_{zx}^2 + 2N\tau_{xy}^2} \tag{2.15}$$

where the constants $F$, $H$, $I$, $L$, $M$, and $N$ are independent for fully orthotropic creeping solids. Since DS materials can be assumed as isotropic in the plane transverse to the DS axis, uniaxial creep tests could only be performed in the transverse ($x$ and $z$) and longitudinal ($y$) axes. Using power law creep, stress for the uniaxial creep tests in the $x_i$-direction yields

$$\dot{\varepsilon}_{cr}^{(x_i)} = A_{x_i}\left(\sigma_{x_i}\right)^n = A\left(\tilde{q}\right)^n \tag{2.16}$$

where $A_{x_i}$ and $\sigma_{x_i}$ is the steady-state creep coefficient and normal stress, respectively, in the $x_i$-direction. The relationships between the anisotropic creep coefficients and the equivalent creep coefficient are obtained by combining Eqs. (2.16) and (2.17). Without any loss of generality, if the DS and *y* axes are aligned, the mechanical properties are isotropic in the *xz*-plane. As a result, $A_x=A_z=A_T$. Setting $A=A_y=A_L$ results in the following:

$$H = I = \frac{1}{2}\left(\frac{A_T}{A}\right)^{\frac{2}{n}} \quad , \quad F = \left(\frac{A_L}{A}\right)^{\frac{2}{n}} - H \, . \tag{2.17}$$

Constants related to the shear stresses, *L*, *M*, and *N,* were identically assumed to be unity (Gardner et al., 2001). Data from uniaxial creep tests on L- and T oriented DS GTD-111 (Ibanez, 2003) can be used here. It is important to note that the use of this approach allows for different creep coefficients to accommodate the material anisotropy, but the creep exponent is assumed to be identical in every direction.

In order to accurately correlate the macroscopic deformation based on the level of slip activity, single crystal micromechanical modeling was employed. This approach assumes that the material is homogenized γ-γ′ structure as a single phase continuum having a periodic structure. The methodology accounts for the discrepancies in the thermal and mechanical response between the phases as well as the complex response of dislocations in dual-phase Ni-base superalloys.

Crystal plasticity approaches have been used extensively in modeling single crystal superalloys (Sheh and Stouffer, 1988; Meric, 1991; Osterle, 2000; Shenoy et al., 2005). A simple expression of the creep strain rate due to shearing on all of the slip systems can be written as

$$\dot{\varepsilon}_{ij}^{c} = \sum_{\alpha=1}^{N} \dot{\gamma}^{(\alpha)} V_{ij}^{(\alpha)} \tag{2.18}$$

where $V_{ij}^{(\alpha)}$ is an orientation tensor determined by the slip direction and the slip plane for the $\alpha^{th}$-slip system. The flow rule, which relates the shear strain rate on a on a slip system, $\dot{\gamma}^{(\alpha)}$, can be mathematically expressed in a number of ways to incorporate stress, temperature, threshold stress, etc. In fact, the creep curves of single crystal CMSX-4 at 750°C were correlated accurately using a relation similar to Eq. (2.18) with only the {111}<112> slip systems (Gunturi et al., 2000). This methodology is applicable to off-axis specimens as well.

Damage accumulation during tertiary creep has also been accounted for in DS Ni-base superalloys. Equation (2.18) was modified to include the damage variable (Yue et al., 1996), i.e.,

$$\dot{\varepsilon}_{ij}^{c} = \left(\frac{1}{1-\omega}\right)^{p_2} \sum_{\alpha=1}^{N} \dot{\gamma}^{(\alpha)} V_{ij}^{(\alpha)}, \tag{2.19}$$

where $p_2$ is a material constant. Implementing any of the formulations listing in Eqs. (2.11) - (2.20) is computationally inexpensive. As a result, they have been utilized in modeling oxide/metal systems for which the response of the typically brittle oxide is the primary objective (Evans and Taylor, 1997). Other recent approaches that have been implemented to correlate the behavior of dual-phase Ni-base superalloys are discussed in Sec. 2.7 of this chapter.

## *2.6 Oxidation Behavior of Ni-base Superalloys*

Surfaces of materials exposed to corrosive environments are prone to reactions. Such is the case with superalloys in which exposed regions sustain compositional changes that alter the local properties. High strength Ni-base superalloys have been developed primarily for use in aero-engine structures operating at temperatures up to and beyond 1093°C (2000°F) in environments that contain any of the following elements: oxygen, hydrogen, sulfur, or nitrogen. In oxygen-rich environments, the result of oxidation and other reactions leads to surface embrittlement. Under mechanical loading, the affected surfaces fracture, or spall in some cases, then subsequently expose virgin material to reactants in the ambient environment. Diffusion kinetics of Ni-base superalloys has been characterized via a series of experiments and microscopy (Das et al., 2003; Li et al., 2003); furthermore, effort has also been devoted to quantify the results of oxidation during mechanical loading (Bouhanek et al., 1997).

Oxidation intrusion of bare Ni-base samples generally consists of two stages (Das et al., 2003): (i) rapid growth during the initial transition period, and (ii) slow stable growth during the subsequent period. This saturation behavior classifies the material as

one that passivates. During the transient period, oxide penetration increases rapidly with the diffusion of various alloy constituents toward the surface, leading to the formation of protective scales. Alloy constituents diffuse from grain boundaries, interdendritic regions, and γ′ particles in close proximity to the external surface. The formation of several adjacent oxide scales in the form of $TiO_2$, $Cr_2O_3$, $Al_2O_3$, etc., depend on the initial concentration of Ti, Cr, Al, etc., respectively, in the alloy. The accumulated oxidation clogs diffusion pathways, thereby slowing oxide formation to a steady-state. With continued exposure time, the external scales can be measured via various forms of microscopy. A continuous chromia layer typically forms on the outer surface and is separated from the metal by non-uniform alumina particles. Formation of subsurface nitrides has been observed in combustive environments (Dong, 2001). As the result of Al and Ti being stripped from γ′ particles, a ductile γ matrix layer, referred to as the γ′-depleted zone, is formed beneath the cumulative oxide scale. At room temperature, the Vickers hardness of the γ′-depleted zone is less than that of the unaffected material (Park et al., 2002).

Using thermogravimetric analysis (TGA) and X-ray energy dispersive spectroscopy (EDS) the temperature-dependence of oxidation penetration rates has been linked with the temperature-dependence of the diffusion behaviors of oxide formers (Bouhanek et al., 1997; Li et al., 2003). For example, below 900°C (1652°F) the nominal chemical compositions of the oxide layers are dominantly Cr, Ta, and Ti-rich, whereas above 900°C, the oxides are rich with Al. The oxide $Al_2O_3$ has the best overall protective properties due to its high thermodynamical stability and its slow growth rate (Dettenwanger et al., 1997); however, under certain conditions, $Cr_2O_3$ scales thin by

evaporation of $CrO_3$, resulting in the continuous thinning of the protective $Cr_2O_3$ scale. The instantaneous change of scale thickness is due to the competition of thickening due to diffusion and thinning due to volatilization (Birks and Meier, 1983). As a result, oxidation rates of Ni-base superalloys are largely dependent on the Cr-, Ti, and Al-content (Bouhanek et al., 1997; Krupp and Christ, 2000). Since the different reactants in the alloy have varied affinities for oxygen, reflected by the different free energies of formation of the oxides, the various metal ions will have different mobilities in the various oxide phases; hence, the oxidation process in alloys is much more complex than in pure metals. The Pilling-Bedworth ratio (PBR), which is the ratio of the volume of the metal ion in the oxide to the volume of the metal atom in metal, characterizes the protectiveness of the oxide. The PBRs for $Al_2O_3$, $Cr_2O_3$ , and $TiO_2$ are 1.28, 2.07, and 1.95, respectively. Surface-grown alumina causes the smallest change to surface specific volume, while in the latter metal oxides, large compressive stresses leading to buckling and spalling are likely to occur.

Diffusion is also decelerated at locations where pathways for atomic motion are limited. Densely packed regions, such as dendritic cores, have lower diffusion rates and are thus sites with lower concentrations of segregated impurities.

Diffusion kinetics models for dual-phase Ni-base superalloys have been developed for temperatures between 800°C (1472°F) and 1200°C (2192°F) by measuring weight gain using TGA or by directly recording oxidation penetration depths at cross-sections of exposed surfaces. Three types of laws have been applied to interpolate the diffusion rates: logarithmic, linear, and parabolic (Antolovich et al., 1981a; Birks and Meier, 1983; Reuchet and Rémy, 1983). The cumulative oxidation rates of Ni-base

superalloys are sub-parabolic (Bouhanek et al., 1997; Li et al., 2003) below 1000°C (1832°F) while at higher temperatures the rates approach the parabolic form (Das et al., 2003). Penetration data has been interpolated using a power law fit in terms of temperature levels and exposure times (Reuchet and Rémy, 1983), i.e.,

$$L_{OX} = \alpha\left(\Theta_{OX} t\right)^{m}, \tag{2.20}$$

where $\alpha$ is a geometric constant determined from stress-free experiments, $t$ is exposure time, and $\Theta_{OX}$ is the diffusivity. For narrow temperature ranges, the rate exponent $m$, is assumed constant. For René 80 from 760°C (1400°F) to 982°C (1800°F), $m$ = 0.5 (Antolovich et al., 1981a); however, $m$ ranges from nearly quartic ($m$ = 0.25) at 760°C (1400°F) to nearly linear ($m$ = 1.0) at 1093°C (2000°F) for equiaxed GTD-111 from $10^4$ to $10^5$ *hr*. The temperature dependence of $m$ can be expressed as

$$m\left(T\right) = \left[m_0 T\right]^{n_T} \tag{2.21}$$

Here $m_0$ and $n_T$ are experimentally-determined constants that are used to obtain oxide depth isolines. The temperature dependence of the diffusivity is expressed in Arrhenius form, i.e.,

$$\Theta_{OX}\left(T\right) = \Theta_0 \exp\left(-\frac{Q_{OX}}{RT}\right) \tag{2.22}$$

where $\Theta_0$ is a material property, $Q_{OX}$ is the activation energy for oxidation, $T$ is the ambient isothermal temperature measured in Kelvin, and $R$ is the universal gas constant (8.314 *J/mol-K*). For a varying temperature history, *T(t)*, the diffusion coefficient was restated as an effective oxidation constant (Birks and Meier, 1983), defined as

$$\Theta_{OX}^{eff}(T,t) = \frac{1}{t_c}\int_0^{t_c} \Theta_0 \exp\left(-\frac{Q_{OX}}{RT(t)}\right) dt \tag{2.23}$$

where $t_c$ is the cycle time. Under hypothetical linear temperature cycling between $T_1$ and $T_2$, where $T_1 < T_2$, using Eq. (2.23) predicts

$$L_{ox}\left(\frac{T_1+T_2}{2}\right) \le L_{ox}\left(T_1 \rightleftarrows T_2, t\right) \le L_{ox}\left(T_2\right) \tag{2.24}$$

For example, an effective isothermal temperature, $T_{eff}$, of 838ºC (1540ºF), predicts the identical level of oxidation as that achieved during linear temperature cycling between 538ºC (1000ºF) and 927ºC (1700ºF). Although no relation describing the time and temperature dependencies of precipitate particle depletion have been developed, several measurements have been reported (Wright, 1988; Das et al., 2003). The magnitude of the thermal stresses generated in the adherent oxide under free expansion has been estimated as (Bruce and Hancock, 1969)

$$\sigma_{OX} = \frac{E_{OX}\Delta T\left(\alpha_{OX}-\alpha_M\right)}{1+2\left(\frac{E_{OX}}{E_M}\frac{L_{OX}}{L_M}\right)} \tag{2.25}$$

where $E$, $\alpha$, and $L$ are the modulus, CTE, and depth, respectively, of either the metal (M) or the oxide (OX). Manipulating either the species in the ambient environment or the chemical composition to produce oxides with lower elastic modulii would result in the decrease of $\sigma_{OX}$.

In actual service environments, coal particles add a large wear factor to corrosion rate. Sulfur attack of superalloys is far more aggressive than oxygen ingression, as evidenced by the parabolic rate constants listed in Table 2.3. Generally, the rate of corrosion in sulfur is often several orders of magnitude greater than that corrosion in air. For reasons noted by Khanna (2002), higher diffusion rates of sulfur, low melting eutectic formation, low solubility, and similar energies of formation at high dissolution pressure all contribute to this enhanced corrosion rate in sulfur.

***Table 2.3:*** *Parabaolic rate contsants for diffusion of various metals*

| Type of Diffusion | | Metal | | | |
|---|---|---|---|---|---|
| | | Ni | Co | Fe | Cr |
| Oxidation | ($gm^2cm^{-4}s^{-1}$) | 9.10E-11 | 1.60E-09 | 5.50E-08 | 4.50E-12 |
| Temperature | (°C) | 1000 | 950 | 800 | 1000 |
| | (°F) | 1832 | 1742 | 1472 | 1832 |
| Sulfidation | ($gm^2cm^{-4}s^{-1}$) | 8.50E-04 | 6.70E-06 | 8.10E-06 | 8.10E-07 |
| Temperature | (°C) | 650 | 720 | 800 | 1000 |
| | (°F) | 1202 | 1328 | 1472 | 1832 |

## *2.7 Damage Mechanisms of Ni-base Superalloys*

Numerous damage mechanisms lead to the generation and early propagation of cracks in materials subjected to high temperature fatigue. In fact, several types were found in ex-service first stage buckets of gas turbines made from GTD-111-DS and similar materials (Saxena, 2001). Damage mechanisms can be classified as uncoupled and coupled. Uncoupled mechanisms are observed as the result of purely creep or purely fatigue conditions; meanwhile, coupled mechanisms arise from two or more interacting mechanisms. In some cases, a crack that has been initiated by one uncoupled damage mechanism may experience accelerated growth due to the involvement of a different uncoupled mechanism. The most relevant uncoupled, coupled, and enhanced microstructural damage mechanisms relevant to Ni-base superalloy are discussed next.

*Uncoupled Mechanisms*

**Slip Band Formation** - It is generally accepted that cyclic dislocation activity leads to the creation of localized slip generation between dominant crystalline slip planes. The intense shear deformation, known as slip bands, typically occurs in direction of maximum shear strain amplitude (Hertzberg, 1996). Cracks initiate along these slip bands according to crystallographic orientation. In Ni-base superalloys at lower temperatures, the microcracks are located along the primary {111} slip planes. This mechanism is dominant for PC (Schöler and Christ, 1998), DS (Okazaki et al., 1990; MacLachlan and Knowles, 2000), and SC (Boubidi and Sievert, 2002) alloys at lower homologous temperatures (below 600°C) and higher frequency of loading when planar dislocation slip operates.

**Enhanced Slip at Defects** – A variety of stress concentrators (casting pores, inclusions, and grain boundaries) typically exist within the bulk of cast Ni-base superalloys. Fatigue cycling leads to enhanced slip band formation and cracking at these sites. Microcracks can originate from micropores formed due to the nature of the solidification processes. Carbide inclusions or other large "nodules", especially those which are plentiful at grain boundaries, can fracture or debond. Under creep conditions, multiple cracks coalescence leading to transgranular crack growth and failure of Ni-base superalloys (Sehitoglu and Boismier, 1990a; Okazaki et al. 1990; MacLachlan and Knowles, 2000). This mechanism can also operate near the surface such as at cooling holes in direction normal to the loading axis (Saxena,. 2001), as shown in 2.18. This damage process is the common cause of cracks found along the leading edge of blades. When this mechanism operates, the size distribution of rogue inclusions, pores, and surface features are important parameters in life predictions.

**Bulk Diffusion** - Under the driving force of the applied stress, atoms diffuse from the sides of the grains to the tops and bottoms. The grain becomes longer as the applied stress does work. The rate controlling mechanism is vacancy diffusion or self-diffusion. This type of damage mechanism is most active under sustained loading conditions. For histories with cyclic loading, this mechanism dominates when the life is completely controlled by time and is independent of the number of cycles. This is typical in Ni-base superalloys under sustained tensile dwell periods at very high temperatures when the stress amplitude is small and cycling occurs infrequently (Okada et al. 1998). As such,

key factors are temperature and time. The process will be faster at high temperatures as there are more vacancies.

**Surface Diffusion** – Alloy constituents located along grain interfaces of Ni-base superalloys diffuse along the boundary and react with other atoms. This is important at high temperatures, in which metal atoms diffuse from the boundary and react with atoms in the environment.

*Coupled Environmental-Mechanical Mechanisms*

**Oxide Spiking** – Oxide layers display brittle characteristics in the operating temperatures of hot path turbine blades; therefore, in the presence of mechanical loading, or even thermal unloading, surface oxides may fracture suddenly. Under tensile deformation, the mismatch in elastic modulus at the oxide/metal interface results in localized stresses that often exceed the critical fracture strength of the oxide (Valerio et al., 1994; Srinivas et al., 1995; Evans and Taylor, 1997). Scale fracture exposes the local subjacent virgin metal which itself oxides and cracks. The cumulative effects of oxidation-assisted surface crack initiation are oxide spikes that protrude into the bulk material (Fig. 2.23a). Under isothermal fatigue conditions (Antolovich et al., 1981a; Reuchet and Rémy, 1983; Wright, 1988), oxide spiking lowers the overall ductility of the material. Superimposing increased tensile strain with a temperature drop, such as the case with linear out-of-phase (OP) TMF cycling, results in uneven thermal strain distribution across the oxide/metal interface, which accelerates the accumulation of oxide spikes in bare (Sehitoglu and Boismier; 1990a; Beck et al., 2002) and coated (Zamrik and Renauld; 2000) Ni-base

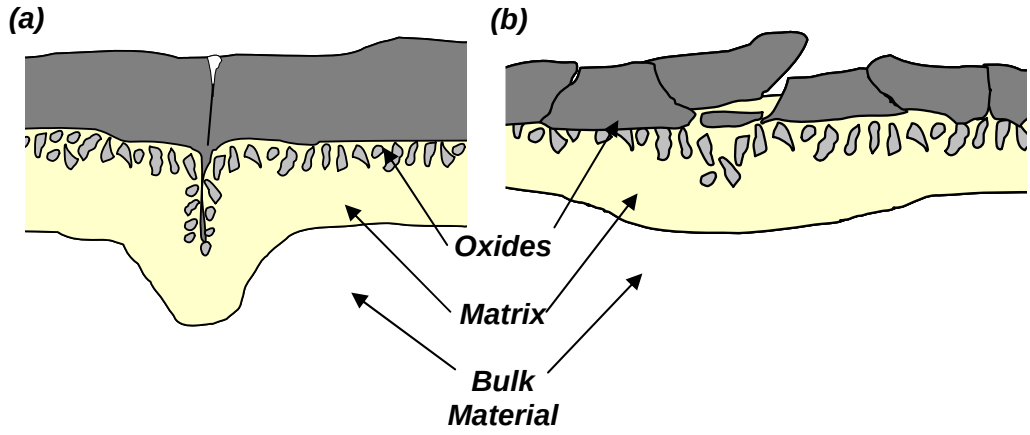


***Figure 2.23:*** *Surface oxidation and mechanical interaction in intermetallic superalloys (a) oxide spiking and (b) oxide spallation.*

alloys. Microcracks nucleate early along the surface due to the lower fracture toughness of this surface layer. Eventually a few of these oxide-spikes penetrate into the bulk material, possibly due to interdendritic oxidation (relating to the heterogeneity of the local oxidation kinetics), one or more of which form the catastrophic crack.

**Oxide Spallation** – Oxide scales grown on the metal during maximum tensile conditions of thermomechanical fatigue reversals experience the largest stresses at the minimum strain level. Oxide wedging results from compressive conditions and mismatches in thermal contraction (Evans, 1994; Nicholls et al., 1996; Evans and Taylor, 1997). Superimposing the compressive strain with a temperature drop, such as the case in linear in-phase (IP) TMF cycling, results in uneven thermal strain distribution across the interface, which accelerates oxide wedging (Fig. 2.23b). A threshold model has been developed to predict the temperature drop that leads to the onset of wedging (Evans, 1994). With time, wedged oxide particles detach or spall at the oxide/metal interface and

expose unoxidized material. If the oxide layer is not adherent, fatigue cycling may only cause the gradual loss of ductility. Adhesive oxide scales, like those deposited on bare (Wright, 1988; Malpertu and Rémy, 1990; Rémy et al., 1993; Vasseur and Rémy, 1994) or coated (Kowalewski and Mughrabi 2000) Ni-base superalloys are prone to surface roughening and pitting with fatigue cycling. This leads to increased local oxidation rates promoting the crack initiation process and channels of damage penetrating into the material. With cycling, these channels form of a crack and, eventually, fatigue-dominant microcrack growth overtakes the oxidation and rupture mechanism.

**Oxidized Slip Bands** – A non-inert gas environment can reduce the fatigue lives of alloys subjected to elevated temperature. A mechanistic interpretation has been used to rationalize the strong effect of the gaseous environment on the surface initiation of fatigue cracks (Thompson et al., 1956). If the magnitude of tensile loading is substantial enough to induce crystallographic slip, then the formation of an oxide layer makes slip reversal difficult. Surface roughening enhances oxygen transport into the bulk of the material along freshly formed slip steps, as shown in Fig. 2.24. The penetrating oxygen atoms inhibit slip reversal, thereby leading to slip bands. The consequence is the nucleation of surface cracks along slip bands. Both oxygen content and temperature of the test environment enhance slip irreversibility under cyclic loading.

**Embrittled Grain Boundary Sliding and Cracking** – This damage mechanism occurs under nominally creep conditions in either PC or off-axis oriented DS Ni-base superalloys (Sehitoglu and Boismier, 1990a; Schöler and Christ, 1998; Beck et al., 2002).

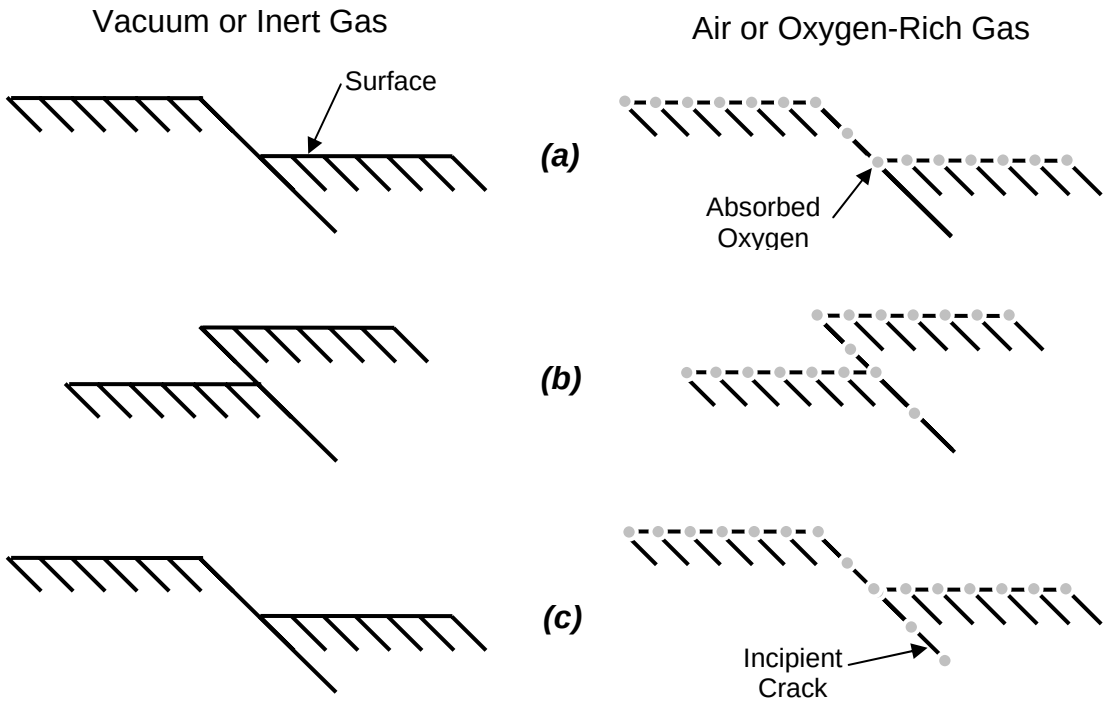


***Figure 2.24:*** *Enhanced penetration and fatigue crack nucleation near a free surface after (a) tensile loading, followed by (b) compressive loading, and ending with (c) tensile loading (Thompson et al., 1956).*

Microstructural evolution at either internal grain boundaries or those intersecting the free surface can degrade creep strength. At these locations, crack formation at elevated temperatures (above 800°C) can result. For example, under high temperature in moist air environments the mechanism of grain boundary sliding which occurs under shear stresses acting on grain interfaces facilitates void formation. Boundaries lying at about 45° to the applied tensile stress experience the largest shear stress and relative shear motion. Rounded and wedge shaped voids are seen mainly at grain edges, and when these coalesce creep rupture occurs. The presence of atomic oxygen reduces the frictional resistance on the grain boundaries inclined to the applied stress direction (Hayes et al., 1994). This allows for extensive grain boundary sliding on the inclined boundaries,

which redistribute the stresses to the grain boundary triple junctions. Microcrack propagation is therefore intergranular. The high stresses acting at these locations cause accelerated cavity nucleation and growth, leading to eventual rupture. The contribution of this mechanism increases with higher temperature and tensile stress combinations and decreasing grain size. This damage process of intergranular cracking at embrittled grain interfaces is commonly observed near the blade tip where grain boundaries are plentiful (Saxena, 2001).

*Sequential Uncoupled Mechanisms*

In complex cyclic stress-strain-temperature blocks, one uncoupled damage process may potentially be subsequently enhanced by one or more other another uncoupled mechanisms. The result is accelerated nucleation and early growth of cracks. For example, fatigue cracks that have initially formed on grain boundaries (MacLachlan and Knowles, 2000) or stress concentrators (Gallerneau et al.; 1996) can experience accelerated growth by the presence of grain boundary creep-induced voids. Conversely, voids that have initially formed along grain boundaries due to creep can act as stress concentrators and subsequently experience accelerated growth via fatigue damage. It should be noted that the damage mechanism may change from fatigue-dominant to creep-dominant, depending on the strain-temperature-time histories and the current state of damage.

Even though the environmental damage mechanism cannot operate independently to initiate a crack, it can accelerate fatigue and creep damage. For example, any oxide spike is also a stress concentrator, resulting in magnification of local cyclic plasticity.

The influence of oxidation may be less significant after crack growth becomes governed by the cyclic loading. Grain boundaries are preferentially oxidized because they are paths of rapid diffusion. Carbides that often reside along the grain boundaries oxidize, providing further weakening. Each of these processes describes an oxidation-assisted fatigue-dominant crack initiation mechanism observed in Ni-base superalloys subjected to isothermal fatigue at intermediate cycles (Antolovich et al., 1980a; Sehitoglu and Boismier, 1990a).

## *2.8 Fatigue Life Prediction Methodologies*

Under temperature and strain histories representative of service conditions, the process of LCF crack initiation enhanced by thermal strains and environment is the primary damage mechanism in turbine blades. Conventional isothermal prediction of cyclic life at a single temperature is not alone sufficient to determine fatigue life due to dramatic deleterious effects of the combination of strain and temperature cycling on life. Fatigue life predictions can be accomplished by means of two types of modeling frameworks: phenomenologically-based and physically-based. Phenomenological models are well-suited for situations where test data are limited to a narrow range of conditions. Physically-based models consider the underlying microstructural damage mechanisms leading to failure. Although each methodology attempts to reduce scatter/uncertainty between correlations and observations, neither provides an exact description. In fact, the distinction of the two is a bit of a blur. It should be noted that physically-based forms and phenomenologically-based forms can actually have the

identical form. The methodology in which the models were derived is the key distinction between the two.

*Phenomenological Models*

Several phenomenological total life and crack initiation prediction models based on hysteresis response (e.g. stress, strain and/or, energy) have been developed for turbine blade materials at high temperatures (Taira, 1973; Coffin, 1977; Bernstein et al. 1993; Zamrik and Renauld, 2000). The Coffin-Manson law was modified to include environmental effects via a frequency factor (Coffin, 1977). This approach is based on the assumption that high temperature fatigue damage is mainly due to environmental effects, i.e.,

$$N_f = C_1 \left(\Delta\varepsilon_{in}\right)^{C_2} \left(\frac{1}{t_c + t_h}\right)^{C_3}, \tag{2.26}$$

where $C_1$, $C_2$, $C_3$, are temperature-dependent material constants, $t_c$ is the cycle time during loading and unloading, and $t_h$ is the hold time in compression or tension. Bernstein and colleagues (Bernstein et al., 1993) developed a semi-empirical formulation based on total strain range, i.e.,

$$N_f = C_1 \left(\Delta\varepsilon_t\right)^{C_2} \left(t_h\right)^{C_3} \exp\left(\frac{C_4}{A_\varepsilon}\right), \tag{2.27}$$

where the strain-amplitude ratio, $A_\varepsilon$, ($\varepsilon_{amp}/\varepsilon_{mean}$) accounts for mean strain effects.

In order to describe effects resulting from non-isothermal conditions, a damage coefficient can be introduced in the Manson-Coffin law which was written as (Taira, 1973)

$$\frac{1}{N_f} = C_1 \lambda(T_{eff})(\Delta\varepsilon_{in})^{C_2} . \tag{2.28}$$

For a given inelastic strain range, $\Delta\varepsilon_{in}$, life results from a series of TMF experiments were correlated with a series of isothermal fatigue tests. Using a time-weighted integration scheme, linear temperature cycling histories from non-isothermal experiments have been used to calculate an effective temperature, $T_{eff}$. The correlation factor, $\lambda\left(T_{eff}\right)$, relates lives of TMF tests to those determined under isothermal conditions. In an identical manner, a recent formulation (Zamrik and Renauld, 2000), compensates for temperature effects via an Arrhenius term, i.e.,

$$N_f = C_1 \left( \frac{\sigma_{\max}\varepsilon_{ten}}{\sigma_u \varepsilon_f} \right)^{C_2} \left( 1 + \frac{t_h}{t_c} \right)^{C_3} \Theta\left(T_{eff}\right). \tag{2.29}$$

The use of the products of the maximum stress, $\sigma_{\max}$, and the maximum tensile strain, $\varepsilon_{ten}$, over from a stabilized hysteresis loop qualifies Eq. (2.30) as an energy-based method based on the Smith-Watson-Topper (SWT) parameter (1971). Using this model

requires that monotonic test data are available. Both the ultimate tensile strength, $\sigma_u$, and the fracture strain of the material, $\varepsilon_f$, are required at each $T_{eff}$.

Regression analysis is needed to determine the constants in Eqs. (2.27) - (2.30). With field data from a series of experiments, the material parameters in each of the methods are curve-fit to correlate with fatigue lives. For a given set of data, the best-fit curves of a given type are generally non-unique; therefore, the curve with a minimal deviation from all data points is desired. Appropriate schemes are the least squares method, $n^{th}$-order splines, and Lagrange polynomials. As a rule of thumb, these interpolation techniques have great accuracy within the bounds of the test data. As a consequence, however, they are generally not appropriate outside the range of testing conditions for which they have been fit.

Although the combination of parameters in these models is intuitively reasonable, phenomenological modeling does not attempt to account for the underlying microstructural mechanisms leading to failure. Additionally, since these models only require macroscopic information (hysteresis response and test control variables), phenomenological models can be easily adapted to correlate the crack initiation stage instead of $N_f$.

*Mechanistic Models*

Mechanistic models describe fatigue damage that can be observed at microstructural scales. Several mechanistically-based approaches have been developed to predict the reduction of fatigue life due to environmental effects (Antolovich et al.,

1981a; Reuchet and Rémy, 1983, Rémy et al. 1993; Koster et al. 2002). Each was developed to predict the behavior of PC Ni-base superalloys.

Antolovich and colleagues introduced a critical oxide depth approach to model the coupled fatigue-environment oxidation spiking mechanism observed in René80 (Antolovich et al., 1981a). Their methodology is based on the observation that the oxidation spiking depth at crack initiation, $l_i$, can be parameterized by hysteresis variables, i.e.,

$$l_i^{C_0} = C_1\left[\sigma_m + C_2\left(\Delta\varepsilon_{pl}\right)^{C_3}\right], \tag{2.30}$$

where $\sigma_m$ is the mean stress, and $C_0$, $C_0$, … , $C_3$ are material constants that exhibit temperature dependence. Assuming the initial interdendritic growth kinetics of surface oxides follow a simple power law, the relation was rewritten as

$$N_i = C_4\left(\frac{t_c}{t_c + t_h}\right)\left[\sigma_m + C_2\left(\Delta\varepsilon_p\right)^{C_3}\right]^{C_5}\Theta\left(T\right), \tag{2.31}$$

Each of these approaches relies on microstructural observations from fatigue-tested samples that exhibited oxidation ranging from negligible to significant. It should be noted that Eq. (2.32) resembles the phenomenological models that were developed for isothermal conditions.

Several life prediction models have been introduced to account for the interaction of fatigue, creep, and environmental damage mechanisms resulting from

thermomechanical fatigue (TMF) cycling. These schemes have been developed to account for either (1) fatigue crack nucleation or total fatigue life (Neu and Sehitoglu, 1989b; Sehitoglu and Boismier, 1990b) or (2) microcrack growth rates (Reuchet and Rémy, 1983; Riedel, 1987; Miller et al., 1992). In order to accurately account for damage processes in material microstructures, these models include separate terms to represent the individual damage micromechanisms. These terms are derived using both hysteresis data from obtained from experiments and observations from at least one form of microscopy of fatigue-tested samples. As such, the form of the chosen term is often dictated by the particular damage mechanism.

Typically, fatigue life damage models are expressed in terms of damage increment per cycle, i.e.,

$$\frac{dD}{dN} = f\left(D, \xi_1, \xi_2, \ldots, \xi_n\right), \tag{2.32}$$

where the $\xi_i$ terms represent various controlling parameters, such as stress, temperature, etc. Equation (2.32) is only linear if the dependence on $D$ vanishes and there does not exist a $\xi_i$ that is a function of the damage variable, $D$. The rate equation for the measure of damage in microcrack growth models is usually represented as

$$\frac{da}{dD} = f\left(a, D, \xi_1, \xi_2, \ldots, \xi_n\right), \tag{2.33}$$

where $a$ denotes an effective microcrack length. For some mechanisms it is more convenient to relate the damage evolution relations [Eqs. (1) and (2)] as an integration over time, e.g.

$$\frac{dD}{dt} = f\left(a, D, \xi_1, \xi_2, \ldots, \xi_n\right) \tag{2.34}$$

or

$$\frac{da}{dt} = f\left(a, \xi_1, \xi_2, \ldots, \xi_n\right) \tag{2.35}$$

The form and controlling parameters used in Eqs. (2.32) - (2.35) are designed to account for the mechanisms most often observed in experiments.

*Mechanics-Based Fatigue Damage Modeling*

When the effects of creep and oxidation are negligible, prediction models use so-called fatigue damage terms to capture the effects of pure fatigue. In crack initiation models, a simple strain-life relationship is often applied if the process is dependent on the mechanical strain range, e.g. (Neu and Sehitoglu 1989b) e.g.,

$$\left.\frac{dD}{dN}\right|_{fat} = C\left(\Delta\varepsilon_m\right)^d \tag{2.36}$$

The fatigue damage term assumes the Coffin-Manson strain-life relation, which is largely physically-based. This term was later adapted to predict cycles to crack initiation of PC Ni-base superalloys by Sehitoglu and Boismier (1990b).

In microcrack growth models, the contribution of fatigue leads to crack advance under tensile conditions. One example is based on the current crack length and the maximum stress (Reuchet and Rémy, 1983)

$$\left.\frac{da}{dN}\right|_{fat} = \Delta\varepsilon_{in}\left(\frac{1}{\cos\left(\frac{\pi}{2}\cdot\frac{\sigma_{\max}}{\sigma_u}\right)}-1\right)a \tag{2.37}$$

The Miller-McDowell-Oehmke (MMO) model (Miller et al., 1992) for crack advance consists of a simple power law relationship using fracture mechanics parameters, i.e.,

$$\left.\frac{da}{dN}\right|_{fat} = C_f\,\Delta J^{m_f}\,, \tag{2.38}$$

where $C_f$ and $m_f$ are constants, and $\Delta J$ is taken as

$$\Delta J = 2\pi Y^2\left[\frac{\Delta\sigma\Delta\varepsilon_{el}}{2}+\frac{f\left(n'\right)\Delta\sigma\Delta\varepsilon_{pl}}{2\pi}\right]a\,. \tag{2.39}$$

Here $f(n')$ is a function of the of the cyclic hardening exponent. It should be noted that $\Delta J$ is appropriate for elastic-plastic materials.

*Mechanics-Based Creep Damage Modeling*

Several mathematical models have been developed to account for creep damage under non-isothermal conditions. In all of the models below creep damage is uncoupled from the effects of push-pull fatigue cycling, and as such, most models relate creep damage in terms of the maximum or averaged tensile experienced during the cycle. In the Neu-Sehitoglu (1989b) and Sehitoglu-Boismier (1990b) models, the creep damage term depends on the stress response during the cycle as well as the phasing of strain and temperature, i.e.,

$$\left.\frac{dD}{dN}\right|_{cr} = \frac{1}{t_c}\int_0^{t_c} A\phi_{crp} \exp\left(-\frac{Q_{cr}}{RT(t)}\right)\left(\frac{\alpha_{eff}\sigma_{eff} + \alpha_H\sigma_H}{K}\right)^m dt\,. \tag{2.40}$$

where $\sigma_{eff}$ is the effective stress, $\sigma_H$ is the hydrostatic stress, $K$ is a scaling factor related to the drag strength, $Q_{cr}$, $A$ and $m$ are material constants. The scaling factors, $\alpha_{eff}$ and $\alpha_H$, are designed to represent the relative amount of damage occurring in tension and compression in a uniaxial experiment. Since it was experimentally observed that limited creep damage occurred in compression, $\alpha_{eff}$ and $\alpha_H$ were set to 1/3 and 1, respectively, so that the term $\alpha_{eff}\sigma_{eff} + \alpha_H\sigma_H$ reduced to 0 for compressive conditions

(Neu and Sehitoglu, 1989b). The phasing factor is a Gaussian curve with a maximum value of unity occurring during in-phase TMF cycling at $\dot{\varepsilon}_{th}/\dot{\varepsilon}_m = 1$, i.e.,

$$\phi_{crp} = \exp\left[-\frac{1}{2}\left(\frac{\left(\dot{\varepsilon}_{th}/\dot{\varepsilon}_m\right)-1}{\xi_{crp}}\right)^2\right] \tag{2.41}$$

Here $\phi_{crp}$ and the material constant $\xi_{crp}$ are determined from TMF tests, such that $\dot{\varepsilon}_{th}/\dot{\varepsilon}_m \neq 0$. Alternatively, as the mechanical strain rate approaches zero, $\phi_{crp}$ converges to 0.

To couple creep with other forms of damage experienced during fatigue, a conventional Rabotnov-Kachanov damage model can be assumed to influence the effective stress range,

$$\Delta\tilde{\sigma} = \frac{\Delta\sigma}{\left(1-D_{cr}\right)}. \tag{2.42}$$

This equation is based on the observation that remotely applied stresses are raised in the local vicinity of microcracks formed by creep deformation. The incremental evolution in creep damage is obtained by integrating

$$\frac{dD_{cr}}{dt} = \left(1-D_{cr}\right)^{-k}\left(\frac{\sigma}{A}\right)^r. \tag{2.43}$$

All constants ($k$, $A$, and $r$) are temperature dependent. A special term can be included to account for creep in compression (Gallerneau et al., 1996).

Conventional creep macrocrack growth parameters are used to correlate cyclic microcrack propagation. For example, in the MMO model, creep microcrack growth is correlated by (Miller et al., 1992)

$$\left.\frac{da}{dN}\right|_{crp} = C_c \hat{C}^{m_c} \tag{2.44}$$

where $\hat{C}$ is a very simple form of the stress power release rate, i.e.

$$\hat{C} = \left\langle a\left[\frac{1}{t_t}\int_0^{t_t} \sigma\dot{\varepsilon}_c dt - \frac{1}{t_c}\int_0^{t_c} \sigma\dot{\varepsilon}_c dt\right]\right\rangle \tag{2.45}$$

where $\dot{\varepsilon}_c$ is the creep strain rate, $t_t$ is the time within the cycle during which tensile strain accumulates, and $t_c$ is the time within the cycle during which compressive strain accumulates. With this form, a compressive hold period does not contribute creep damage and compressive creep strain counteracts tensile creep strain in a fully reversed test. In this manner, the possibility of healing of damage under compression is accounted for. Further, $\hat{C}$ is non-zero for in-phase TMF but $\hat{C}$ = 0 for out-of-phase TMF.

A model for creep crack growth is based on the $C^*(t)$ -integral (Riedel, 1987),

$$\left.\frac{da}{dN}\right|_{crp} = F\left(\int_0^{t_{ten}} C^*(t)\, dt\right) \tag{2.46}$$

where $t_{ten}$ is the time during the cycle when stress is tensile. Here, the function $F$ depends on the creep damage mechanism (e.g. alternating dislocation slip or cavity nucleation, growth, and coalescence). It should be noted that Eq. (2.46)

*Physics-Based Environmental (Fatigue-Oxidation) Damage Models*

Environmental fatigue damage is the most complex of all of the individual physics-based damage modules. In addition to the CSSC data that is needed to make predictions, diffusion kinetics data, specific to the material involved, must be incorporated.

The surface diffusion kinetics occurring in Mar-M247, a PC Ni-base superalloy, necessitated that the environmental damage term account for oxidation and γ′ depletion (Sehitolglu and Boismier, 1990b). This term is based on the observation that environmentally-induced microcracks, e.g. oxide spikes, are the result of repeated rupture and oxidation of a critical ligament of fresh material ahead of the crack tip observed by Neu and Sehitoglu (1989b). The rate of growth of this microcrack is given by

$$\frac{dh}{dN} = \frac{dh}{dt}\frac{dt}{dN} = \frac{dh}{dt} t_{tc}\,, \tag{2.47}$$

where $t_{tc}$ is the total cycle period. When the ligament of material adjacent to the crack of length $h$ fractures, crack advance is parameterized not only by the oxidation and γ′

depletion kinetics, but also depends on the total mechanical strain range, the mechanical strain rate, and the phasing between the thermal and mechanical strain rate. A possible relationship is given as (Sehitolglu and Boismier, 1990b)

$$h = \left[ \frac{B\Phi_{env}\left(K_{OX} + K_{GPD}\right)}{\delta_o} \right] \frac{\left(\Delta\varepsilon_m\right)^2}{\left(\dot{\varepsilon}_m\right)^{-b}} t^{\beta}, \tag{2.48}$$

where $B$, $\beta$, $b$, and $\delta_0$ are material constants determined from TMF and isothermal fatigue tests. The averaged diffusivity constants, $K_{OX}$ and $K_{GPD}$, separately describe the surface diffusion under non-isothermal cycling, and are defined by

$$K_j = \frac{1}{t_{tc}} \int_0^{t_{tc}} \Theta_{0_j} \exp\left( -\frac{Q_j}{RT(t)} \right) dt . \tag{2.49}$$

where $j=OX, GPD$. Upon integration, the resulting term becomes (Sehitoglu and Boismier, 1990b)

$$\left.\frac{dD}{dN}\right|_{env} = \left[ \frac{B\Phi_{env}\left(\bar{K}_{h,ox} + \bar{K}_{h,\gamma'}\right)}{h_{cr}\delta_o} \right]^{\frac{1}{\beta}} \frac{2\left(\Delta\varepsilon_m\right)^{\frac{2}{\beta}+1}}{\left(\dot{\varepsilon}_m\right)^{1-\frac{b}{\beta}}} \tag{2.50}$$

The phasing factor, $\Phi_{env}$, is based on the phenomenon that coupled environment-fatigue damage is typically only detrimental to life for out-of-phase TMF cycling. Similar to Eq. (2.41), Eq. (2.50) depends on the ratio of the thermal and mechanical strain rates. The

value of $\Phi_{env}$ ranges from zero to one. If the value of $\Phi_{env}$ is zero, there is no environmental damage from the phasing and if the value of $\Phi_{env}$ is one, the coupling of the environment and phasing is most detrimental to life. The phasing factor is defined

$$\Phi_{env} = \frac{1}{t_c}\int_0^{t_c} \phi_{env} dt \tag{2.51}$$

where $\phi_{env}$ is a Gaussian curve of the form

$$\phi_{env} = \exp\left[-\frac{1}{2}\left(\frac{\left(\dot{\varepsilon}_{th}/\dot{\varepsilon}_m\right)+1}{\xi_{env}}\right)^2\right] \tag{2.52}$$

and $\dot{\varepsilon}_{th}/\dot{\varepsilon}_m$ is the ratio of thermal to mechanical strain rates. For isothermal fatigue, $\dot{\varepsilon}_{th}/\dot{\varepsilon}_m$ = 0; for out-of-phase TMF, $\dot{\varepsilon}_{th}/\dot{\varepsilon}_m$ = -1; for in-phase TMF, $\dot{\varepsilon}_{th}/\dot{\varepsilon}_m$ = 1. The parameter $\xi_{env}$ is a measure of the relative amount of damage associated with different phasings. The framework for linear cumulative damage given in Eqs. (2.47) - (2.52) is a modification of that presented by Neu and Sehitoglu (1989b)

A model that predicts oxidation up to crack nucleation was presented as a damage rate equation dependent on the loading and applied stress (Gallerneau et al., 1996), e.g.,

$$\left.\frac{dD}{dt}\right|_{ox} = \frac{1}{2D_{ox}}\left(\frac{k_{ox}}{e_o}\right)^2\left[1+\left\langle\frac{X^{ox}-\sigma_{lox}(\bar{\sigma})}{B}\right\rangle\right]^{2m} \tag{2.53}$$

where $\sigma_{lox}$ is the stress above which the oxidation kinetics are accelerated, $k_{ox}$ is an oxidation constant, and m and B are material constants.

The environmental damage rate presented as part of the MMO model (Miller et al., 1992) represents a coupling process between fatigue and environmental degradation. The form of the relationship is

$$\left.\frac{da}{dN}\right|_{env} = C_o' \exp\left[\frac{-\left(Q_{env} - B\hat{\sigma}^k\right)}{RT_{eff}}\right] \Delta J^{m_o}\, \Delta t^{(1/2-\xi)} \tag{2.54}$$

where

$$\hat{\sigma} = \left\langle \sigma_{T_{\min}} \right\rangle \tag{2.55}$$

and the effective cycle temperature, $T_{eff}$, is defined by

$$\exp\left[\frac{-Q_{env}}{RT_{eff}}\right] = \frac{1}{\Delta t}\int_{t_{\min}}^{t_{\max}} \exp\left[\frac{-Q_{env}}{RT(t)}\right] dt \tag{2.56}$$

Here, $t_{\min}$ and $t_{\max}$ are the times within the cycle at which the minimum and maximum temperatures occur and $\Delta t = t_{\max} - t_{\min}$. The parameters $C_o'$, $m_o$, $B$, $k$, and $\xi$ are constants and $Q_{env}$ is the activation energy of the controlling crack tip environmental degradation process.

A unique method that provides an incubation period for crack growth increment instead of simply assuming that an increment of fracture occurs each cycle has also been presented to account for fatigue-oxidation interaction. The model is formulated by considering the number of cycles to allow a microcrack, measured by $a$, to completely fracture a local element of size $\lambda$ (Rémy et al., 1993; Koster et al., 2002), i.e.,

$$\frac{da}{dN} = \frac{\lambda}{N(\lambda)} \tag{2.57}$$

where $N(\lambda)$ is the number of cycles to fracture a local element. One particular model that accounts for the influence of creep has been developed (Rémy et al., 1993) This model can also be applied for crack initiation.

$$N(\lambda) = \left(\frac{\Delta\tilde{\sigma}}{2\sigma_c}\right)^M \left(\frac{\sigma_c}{(1-R)(\sigma_c - \sigma_{\max})}\right)^\alpha \tag{2.58}$$

Here $M$ and $\alpha$ are material constants, and $R$ is a piecewise continuous expression of the load ratio. The model accounts for stress relaxation due to creep via the effective stress term, $\Delta\tilde{\sigma}$ from Eq. (2.42). Then, using this relation, the parameters are adjusted to incorporate the effect of creep and oxidation. The model is also applicable to TMF. With exposures to high temperatures during the TMF cycle oxidizes the material at the crack tip; then, high stress ranges at medium temperatures give rise to fatigue damage in the material that has been embrittled by oxidation. As such, the diffusion kinetics of the

material have been included via, $\sigma_c$, a term that combines oxidation properties as well as the critical fracture stress of the oxide. For example, Rémy and coworkers (Rémy et al. 2000) defined $\sigma_c$ based on a rule of mixtures for the penetration of the influence of microcrack of size $\lambda$, i.e.,

$$\sigma_c = \sigma_{c,virgin}\left(1-\frac{Pl_{ox}}{\lambda}\right)+\sigma_{c,embrittled}\left(\frac{Pl_{ox}}{\lambda}\right) \tag{2.59}$$

here, $P$ is a constant, $\sigma_{c,virgin}$ represents the critical stress virgin (unoxidized) material, and $\sigma_{c,embrittled}$ is the reduced critical stress for the embrittled material along crack path. The term $l_{ox}$ is the depth of oxidation penetration influence, which may also be influenced by the microstructure (grain boundaries or interdendritic regions). The depth of oxide is given by a rate equation that includes a fatigue interaction factor (Reuchet and Rémy, 1983), i.e.,

$$dl_{ox} = \alpha_o \Theta(T) dt^{\rho} \cdot f(\Delta\varepsilon) \tag{2.60}$$

where $\alpha_o$ and $\rho$ are constants, and $f(\Delta\varepsilon)$ is a function that describes the influence of the interaction between the cyclic strain and oxidation kinetics. Equation (2.61) is integrated over the entire thermal-mechanical cycle. Generally, $\alpha_o$ and $\rho$ are determined from metallurgical examination of specimens exposed to temperatures in the desired environment under no load. Then $f(\Delta\varepsilon)$ is deduced from low frequency isothermal

LCF. In general, the relationship between oxidation penetration and time is quartic for Ni-base superalloys (i.e. $\rho \approx 0.25$), and $\rho$ exhibits slight temperature dependence. Even though this model uses rather simple relationships fatigue and oxidation, it has been shown to account for LCF life of wrought Waspaloy under several loading and temperature conditions (Koster et al., 2002; Rémy et al., 2000).

## *2.9 Constitutive Modeling of DS GTD-111*

The methodology referred to as crystal plasticity has been used to modeling slip activity in single crystal superalloys (Meric et al., 1991; Vitek et al., 1996; Osterle et al., 2000; Shenoy et al., 2005). This method relies on a multiplicative rule used for describing the deformation gradient, **F**, given as (Bilby et al., 1955; Lee, 1969; Sheh and Stouffer, 1988)

$$\mathbf{F} = \mathbf{F}^e \cdot \mathbf{F}^p \tag{2.61}$$

where the deformation gradient is composed of elastic, $\mathbf{F}^e$, and plastic, $\mathbf{F}^p$, deformation gradients. The former elastic term is associated with reversible elastic stretch and rigid body rotation of the crystal lattice, while the latter plastic term accounts for dislocation motion and the associated shape change of the grain but not its crystal lattice. For a given crystal lattice, the close-packed planes act as the slip planes with unit normal vector, $\underset{\sim}{m}_o^\alpha$, in the reference configuration for each of the $\alpha$ slip systems, along which the dislocations glide in the slip direction in the reference configuration with unit vector, $\underset{\sim}{s}_o^\alpha$. This is depicted in Fig. 2.25.

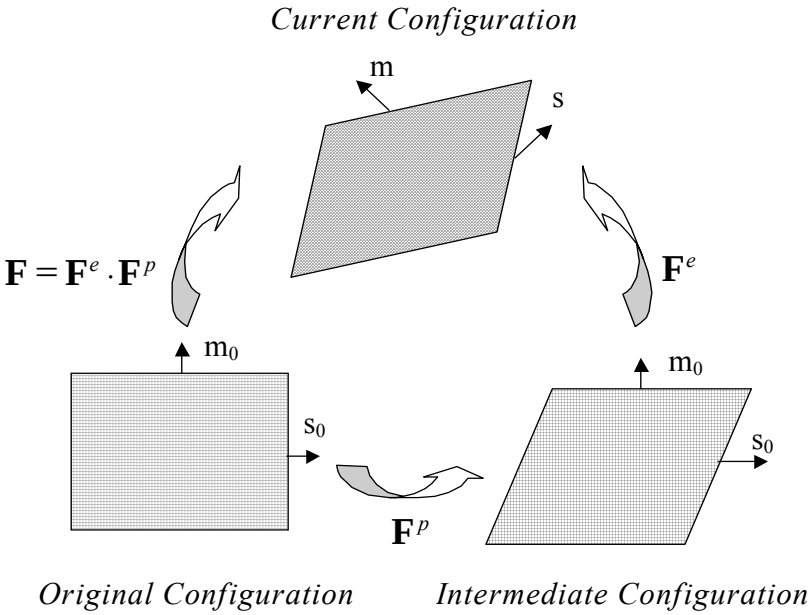


***Figure 2.25:*** *Elasto-plastic decomposition of the deformation gradient (Lee, 1969; Sheh and Stouffer, 1988).*

The shearing rates along each of the active slip systems, $\dot{\gamma}^{\alpha}$, depend on the resolved shear stress on the slip systems. The macroscopic plastic velocity gradient is obtained by summing over all slip systems in the intermediate relaxed configuration according to

$$\mathbf{L}^{\mathbf{p}} = \sum_{\alpha=1}^{N_{slip}} \dot{\gamma}^{\alpha} \left( \underset{\sim}{s}_o^{\alpha} \otimes \underset{\sim}{m}_o^{\alpha} \right) \tag{2.62}$$

The homogenous crystal plasticity framework described in Eqs. (2.62) and (2.63) was used to describe the deformation of the dual-phase Ni-base superalloys DS GTD-111 (Shenoy et al., 2005). The model explicitly accounts for the crystallographic orientations, though it does not explicitly account for the distinct matrix and precipitate phases. The

viscoplastic flow rule accounts for the macroscopic deformation of a grain is accurately described using the underlying temperature and strain rate dependent dislocation behavior. The twelve octahedral <110> slip systems are active for the entire range of conditions. It has been observed, however, that at high homologous temperatures octahedral slip in a typical single crystal Ni-base superalloy occurs in a zig-zag motion in matrix channels separating precipitate particles (Bettge and Osterle, 1999). The consequence is the manifestation of six macroscopic cube slip systems of the {100}<110> type. Actual cube slip has been observed in precipitate particles at higher temperatures (Sun and Hazzledine, 1996).

Based on these findings, a flow rule for the slip system shearing rate has been developed to capture the temperature, stress, and strain dependence exhibited in the material given as (Shenoy et al., 2005)

$$\dot{\gamma}^{\alpha} = \dot{\gamma}_{o}\Theta(T)\left\langle\frac{\tau_{v}^{\alpha}}{D^{\alpha}}\right\rangle^{n}\exp\left\{B_{o}\left\langle\frac{\tau_{v}^{\alpha}}{D^{\alpha}}\right\rangle^{n+1}\right\}\mathrm{sgn}\left(\tau^{\alpha}-\chi^{\alpha}\right) \tag{2.64}$$

where the slip system viscous overstress, $\tau_{v}^{\alpha}$, is given in terms of the resolved shear stress, $\tau^{\alpha}$, by

$$\tau_{v}^{\alpha} = \left|\tau^{\alpha}-\chi^{\alpha}\right| - \kappa^{\alpha}\frac{\mu}{\mu_{o}}. \tag{2.65}$$

Here $\mu$ is the shear modulus, and $\mu_{o}$ is the shear modulus at absolute zero. Both $\chi^{\alpha}$ and $\kappa^{\alpha}$ are internal state variables that describe the hardening of each slip system. Each

product in Eq. (2.65), aside from the constant reference shearing rate, $\dot{\gamma}_o$, accounts for some factor affecting the slip system activity. For example, the temperature-dependent term, $\Theta(T)$, is the diffusivity parameter given by

$$\Theta(T)=\begin{cases}\exp\left(-\dfrac{Q_o}{RT}\right) & \text{for } T \geq \dfrac{T_m}{2} \\ \exp\left\{-\dfrac{2Q_o}{RT_m}\left[\ln\left(\dfrac{T_m}{2T}\right)+1\right]\right\} & \text{for } T \leq \dfrac{T_m}{2}\end{cases} \tag{2.66}$$

where $Q_0$ is the activation energy for thermally-activated dislocation bypass of obstacles, $R$ is the universal gas constant, and $T_m$ is the absolute melting point temperature measure in Kelvin. The next factor governs the power law creep regime. Here the power law exponent, $n$, is constant. The fourth factor of Eq. (2.65) accounts for the power law breakdown behavior at higher strain rates where the response becomes nearly rate independent. The coefficient, $B_0$, is constant, and $D^\alpha$ is the drag stress that only weakly depends on the history of temperature and viscoplastic deformation.

Internal state variables were used in Eqs. (2.65) and (2.66) to describe the size and shift of the yield surface of each slip system. Both internal state variables depend on the history of temperature and viscoplastic deformation. The back stress, denoted here as $\chi^\alpha$, accounts for the shift of the viscoplastic flow potential of the $\alpha^{th}$ slip system. The back stress manifests a directional dependence and is associated with several features of the heterogeneous material at the microscale, including internal stresses that develop with deformation due to dislocation pile-up at obstacles (e.g. inclusion particles, grain boundaries). The back stress evolution has been written as (Shenoy et al., 2005)

$$\dot{\chi}^{\alpha} = h_{\chi}\left|\dot{\gamma}^{\alpha}\right|\mathrm{sgn}\left(\tau^{\alpha} - \chi^{\alpha}\right) - h_{\chi d}\chi^{\alpha}\left|\dot{\gamma}^{\alpha}\right| + \left(\frac{1}{R_{\chi}}\frac{\partial R_{\chi}}{\partial T} + \frac{1}{h_{\chi d}}\frac{\partial h_{\chi d}}{\partial T}\right)\chi^{\alpha}\dot{T} - \Omega_{\chi}^{\alpha} \tag{2.67}$$

where

$$\Omega_{\chi}^{\alpha} = h_{\chi s}(T)\left|\chi^{\alpha}\right|^{r_{\chi s}} \tag{2.68}$$

is the static thermal recovery terms with several material constants, $h_{\chi}$, $h_{\chi d}$, $h_{\chi s}$, $r_{\chi s}$, and $R_{\chi} = h_{\chi}/h_{\chi d}$. The temperature rate dependent term is necessary to properly model hysteresis behavior under thermomechanical fatigue (TMF) (McDowell, 1992).

The threshold stress corresponds to the size of the viscoplastic flow potential. As such, the threshold stress may be viewed as the resistance to plastic flow arising from statistical strengthening mechanisms associated with increase of dislocation density, solid solution strengthening, etc. The threshold stress is given as

$$\kappa^{\alpha} = \kappa_{c}^{\alpha} + \kappa_{e}^{\alpha} \tag{2.69}$$

where

$$\begin{aligned} \kappa_{c}^{\alpha} &= \kappa_{o}^{\alpha}(T) + h_{pe}\tau_{pe}^{\alpha} + h_{se}\tau_{se}^{\alpha} + h_{cb}\left|\tau_{cb}^{\alpha}\right| \\ \dot{\kappa}_{e}^{\alpha} &= h_{o}\sum_{\beta=1}^{N_{slip}} q^{\alpha\beta}\left|\dot{\gamma}^{\beta}\right| - h_{\kappa s}\kappa^{\alpha}\sum_{\beta=1}^{N_{slip}}\left|\dot{\gamma}^{\beta}\right| - h_{s}\Theta(T)\left\langle\kappa^{\alpha} - \kappa_{th}\right\rangle^{r_{s}} \end{aligned} \tag{2.70}$$

Here $\tau_{pe}$, $\tau_{se}$, and $\tau_{cb}$ are the shear stresses on the primary, secondary and cube slip systems, respectively. Prior to any deformation, both the back stress and the threshold stress are initially zero (i.e., $\chi^{\alpha}(0) = \kappa_e^{\alpha}(0) = 0$). The constants for DS GTD-111 used in this study are given are from literature (Shenoy et al., 2005).

# 3. EXPERIMENTAL PROCEDURE

Numerous experiments were performed as a part of this research. These tests include isothermal low cycle fatigue (LCF) tests, creep-fatigue tests, thermomechanical fatigue (TMF) tests, and stress-free oxidation tests. While most tests were conducted on samples in the as-cast form, several were pre-exposed to elevated temperature and stress. Testing environments were either static laboratory air or an inert gas (e.g. argon). Following a brief description of the material used in this study, the experimental procedure applied for each type of test is detailed in this chapter. All experiments were conducted in the Mechanical Properties Research Laboratory (MPRL) at Georgia Tech.

## *3.1 Test Material*

Material removed directly from a blade casting would be the most suitable for testing since results could be reported for the exact microstructure and composition as that used in service conditions. The shape and size of the blades do not lend themselves to test specimens of sufficient size. Specimens were obtained from several batches of cast rectangular slabs of DS GTD-111 and heat treated to obtain a representative microstructure.

A total of three batches of DS GTD-111 blocks were fabricated to make test specimens. Slabs were specially cast to rectangular shapes comparable in size to first stage turbine blades. The dimensions of these slabs were also designed for machining a

large number of specimens and are shown in Table 3.1. In every case, the solidification axis was along the longest axis of the slabs. For each of the test batches involved, similar

***Table 3.1:*** *Slab dimensions in units of mm (in)*

| Batch | Length | Width | Depth |
|---|---|---|---|
| 1 | 178 | 76 | 16 |
| | (7.00) | (3.00) | (0.63) |
| 2 | 254 | 197 | 32 |
| | (10.00) | (7.75) | (1.25) |
| 3 | 229 | 127 | 16 |
| | (9.00) | (5.00) | (0.63) |

machining and heat treatments were carried out which are described as follows. For Batch 1, Electro Discharge Machining (EDM) was used to make specimens. Afterwards, heat treatment consisted of two steps both of which were carried out at Georgia Tech after specimen machining. First a solution annealed at 1121°C (2050°F) for 2 hours in a vacuum furnace and cooled to room temperature (RT) in inert gas environment at a rate not less than 42°C (75°F) per minute. They were subsequently aged for 4 hours at a temperature of 843°C (1550°F) and then cooled in inert gas environment to ambient conditions at a rate not less than 14°C (25°F) per minute. In the same manner, Batches 2 and 3 slabs were fully heat treated at Cincinnati Testing Laboratory and Metcut Research Associates, respectively, prior to any specimen machining. Since, each batch of material was cast into different slab sizes, there is the potential for small variability in the microstructure (e.g. grain sizes) and mechanical properties among the different batches; hence, each batch is identified separately.

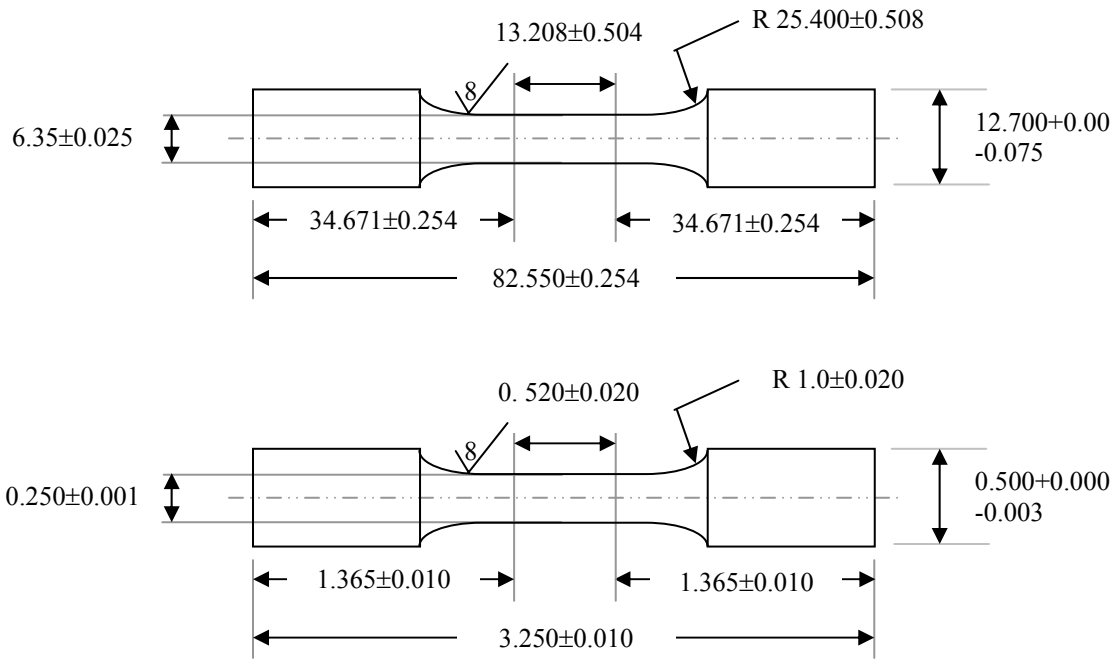


***Figure 3.1:*** *LCF specimen design with (top) dimensions in mm and (bottom) dimensions in inches. Drawings are not to scale.*

The specimens were prepared by Cincinnati Testing Laboratories (CTL) according to ASTM Standards (ASTM E606, 1998, and ASTM E139, 1996). Cylindrical pieces were sectioned from either the longitudinal or transverse axis of the cast plates, denoted as L- or T-oriented bars, respectively. Solid specimens, such as those shown in Fig. 3.1, had a uniform gage length of 12.7 *mm* (0.5 *in*) and a diameter of 6.35 *mm* (0.25 *in*). The resulting ratio of the gage section length to the gage section diameter satisfy the recommended dimensions for strain-controlled low cycle fatigue testing (ASTM E606, 1998). Specimens were prepared so that the diameter at any axial location of the gage section was measured to an accuracy of 0.025 *mm* (0.001 *in*). Longitudinal (L) specimens are fabricated so that the direction of the columnar grains (i.e., the DS axis) is parallel to the loading axis, whereas transverse (T) specimens are oriented so that the

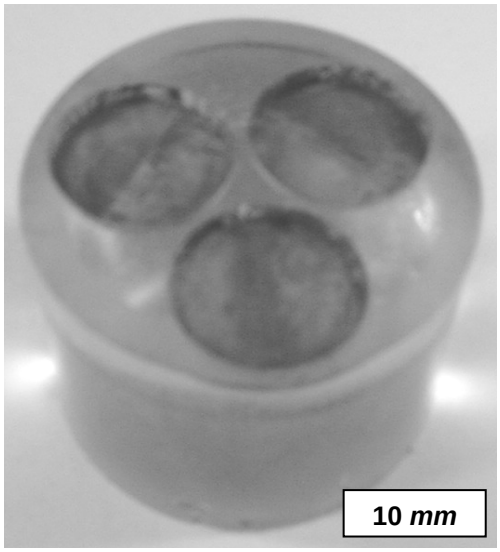


***Figure 3.2:*** *Epoxy resin holder used for polishing oxidation samples.*

grains are transverse to the loading direction. Each shank of every specimen was subsequently engraved and identified with a specimen identification number including an L or T.

For the comparison study of thermal exposure, small specimen discs were used. They measured 12.7 *mm* in diameter and 2.3 *mm* in thickness and were machined from unused shank sections of fatigue specimens. Since these smaller specimens were difficult to hand polish, an epoxy resin mount was specially fabricated. Shown in Fig. 3.2, the holder made it possible to sand multiple samples simultaneously using semi-automated metallographic polishing equipment.

Fatigue and oxidation specimen surfaces were finished by first grinding to 600 grit FEMA SiC paper (1200 for use with surface replication). Each fatigue specimen was visually inspected to ensure that all residual and polishing marks, if any, were along the stress axis, following ASTM Standard E606. Specimens were then degreased in acetone, ultrasonically bathed in alcohol, and air dried. The final cleaning of all specimens for

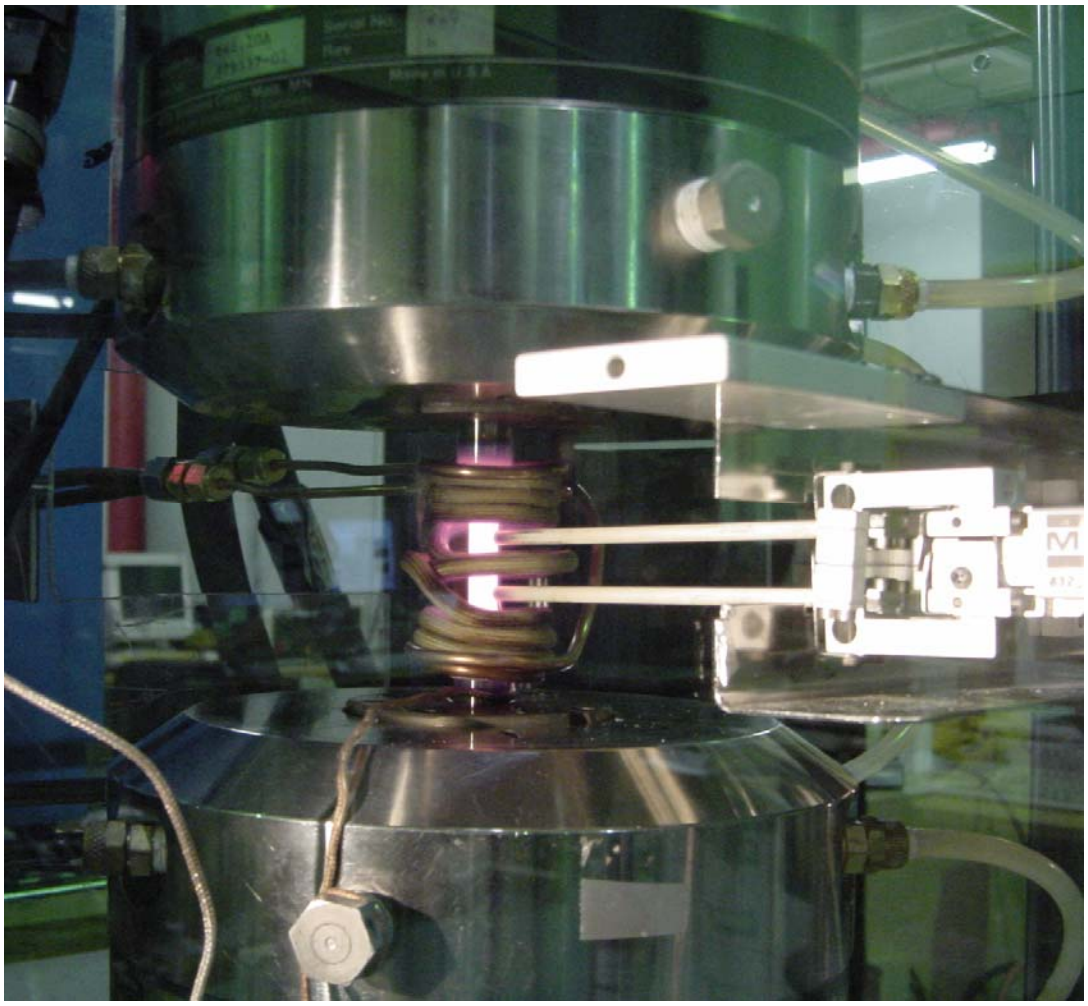

***Figure 3.3:*** *Arrangement of specimen within the collet grips and induction coils.*

testing (or samples for mounting) was carried out with either methanol or ethanol. Methanol is considered to be better because it evaporates more rapidly than other alcohols. Acetone was avoided as the final cleaning step since it can leave a residual film on the surface, although that solvent can be used in the first step of a cleaning process.

## *3.2 Low Cycle Fatigue Tests*

All low cycle fatigue (LCF) tests of L- and T-oriented DS GTD-111 were performed using a 10 *kip* axial servo-hydraulic MTS® testing machine with a dual-channel controller and TestStar software (Testware SX® 4.0D). The load cell resolution was ±0.22 *kN*. Tests were conducted under mechanical strain control, isothermal conditions, and static, room temperature laboratory air. One set of K-type (Omega® model GG-K-26-SLE) thermocouples having 0.404 *mm* (0.0159 *in*) diameter leads were spot welded to the end of the gage section to monitor the temperature within the gage section. The lower end of the specimen was fastened within the lower grip (MTS® model 646), which is positioned by the hydraulic actuator. The specimen gage section was raised to fit within the top collet grip and the heating element. A nominal hydraulic pressure of 10 *MPa* was applied to the grips. The arrangement of a specimen within the grips is shown in Fig. 3.3. A high temperature extensometer (MTS® model 632.52E-14) with 12.7 *mm* (0.5 *in*) gage length. The 5.0 *mm* (0.2 *in*) diameter ceramic rods with pointed tips were seated into the dimples, formed by an indentation jig shown in Fig. 3.4, using light taps of a hammer. The extensometer and specimen configuration is illustrated in Fig. 3.5.

Heat was supplied to the specimen using a radio frequency (RF) induction heater (Ameritherm single phase 2 *kW*). Closed-loop feedback control of the specimen temperature was maintained with a PID controller (Watlow® model 945A-2FK5-A000). The temperature control resolution was ±1ºC. Forced cooling, which is generally used for tubular specimens, was not applied since heat could be rapidly conducted from the

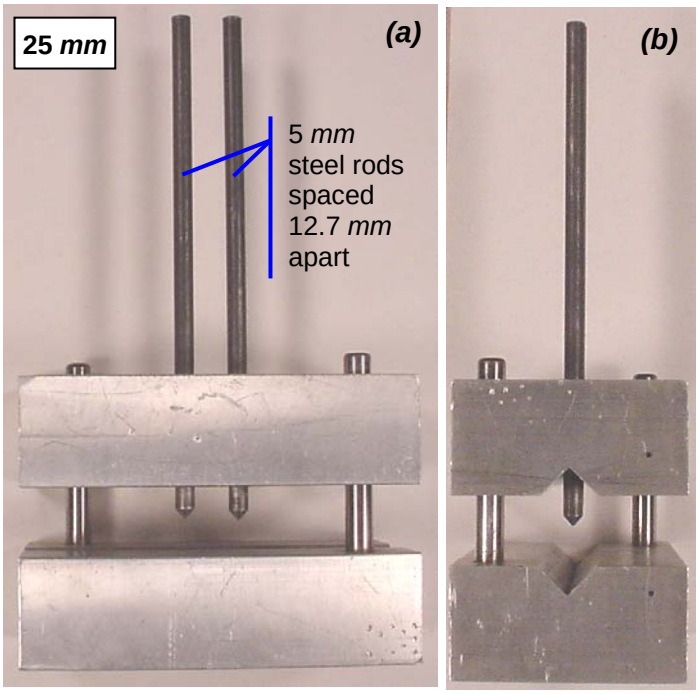


***Figure 3.4:*** *Aluminum holder used for indenting fatigue specimens (a) front view (b) side view.*

specimen via the water-cooled grips. Tests were started approximately 5 *min* after the set-point temperature stabilized.

Numerous continuously cycled (CC), LCF tests were conducted on L- and T-oriented specimens sectioned from each batch of DS GTD-111. Since each of these tests is isothermal, the mechanical strain range ($\Delta\varepsilon_m$) is equal to the total strain range ($\Delta\varepsilon_t$). Each test differed by isothermal temperature ($T$), strain range, or strain ratio ($R_\varepsilon = \varepsilon_{min}/\varepsilon_{max}$). Since the majority of the cracks occurring in DS GTD-111 components are transverse to the DS axis, the majority of the experiments were conducted on L-oriented specimens. The majority of the tests were carried out between 871°C (1600°F) and 1038°C (1900°F) with a few select tests at 650°C (1200°F) and 427°C (800°F). Example strain histories are shown in Fig. 3.6(a). For the majority of tests, the strain rate was held

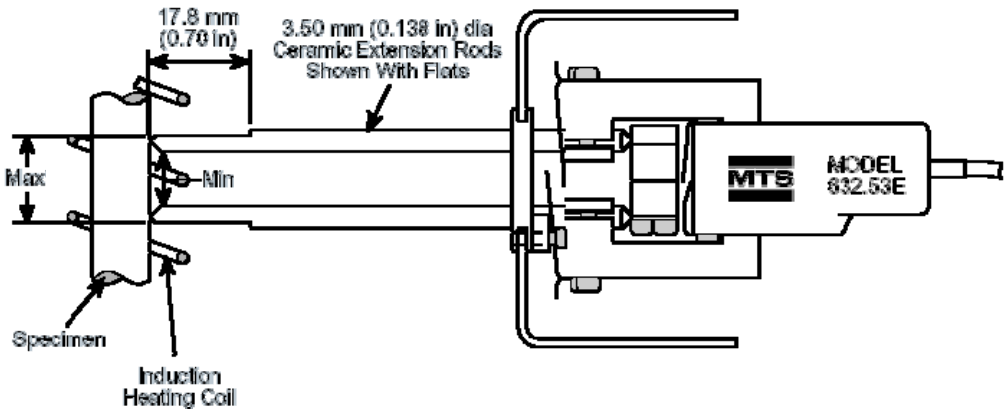


***Figure 3.5:*** *Extensometer and specimen configuration.*

constant at $0.5\%/s$ (in two cases $\dot{\varepsilon} = 0.01\%/s$) during loading and unloading ramps. Using a fixed strain rate (as opposed to a fixed cycle period) eliminates the influence of strain rate dependence from the material response. Triangular waveforms were used in all tests.

Sampling frequency of data acquisition was sufficient to insure correct definition of the hysteresis loop (especially in the regions of reversals). Typically 200 points per cycle is desired; however, since the strain rate was held constant for each test, data was digitally stored at 25 *Hz* to minimize the required disk space. Force (*N*), strain (*mm/mm*), displacement (mm), and temperature (°C) were recorded for each of the first 100 cycles. Thereafter, data was recorded every $100^{th}$ cycle. The peak and valley forces were recorded for each cycle. Data from the first cycle of loading was used to conduct an elastic modulus check. Afterwards, the stress history was periodically analyzed to determine if failure had occurred.

In the current study, crack initiation is assumed to include the process of crack formation (i.e., crack incubation) and microcrack growth to a small size (i.e., early

propagation). For Ni-base superalloys, an appropriate crack initiation depth, $a_i$, is between 0.5 *mm* and 1 *mm*. At this length range, the incubation and early propagation of cracks is typically limited to one grain. Since the gage sections of the specimens have an

initial cross-sectional diameters ($d_0$) averaging 6.35 *mm*, the load corresponding to crack initiation can be estimated as

$$P_i = P_0 \left[ 1 - \left( \frac{a_i}{d_0} \right)^2 \right], \tag{3.1}$$

where $P_0$ is the stabilized maximum load determined from previously recorded initial cycling data. For this investigation, the cycle during which the tensile load dropped 20% from $P_0$ is used to define the crack initiation life ($N_i^{20\%}$ or $N_i$). Additionally, whenever possible the crack initiation life at 10%, 50%, and 100% load drop (i.e., $N_i^{10\%}$, $N_i^{50\%}$, and $N_f$, respectively) were determined. In many instances, however, the cycle with the critical load drop-off coincided with complete fracture of the gage section ($N_f$). At the completion of each test, specimens were cooled by natural convection to room temperature and then sectioned for microscopy. Each specimen was handled delicately to minimize disturbing the surface oxide layer generated during the test.

All LCF tests were performed according to ASTM standard E606 (2003) that recommends at least 10 specimens be used to generate the fatigue properties. Validity of isothermal LCF tests is achieved when the following two critical criteria are satisfied:

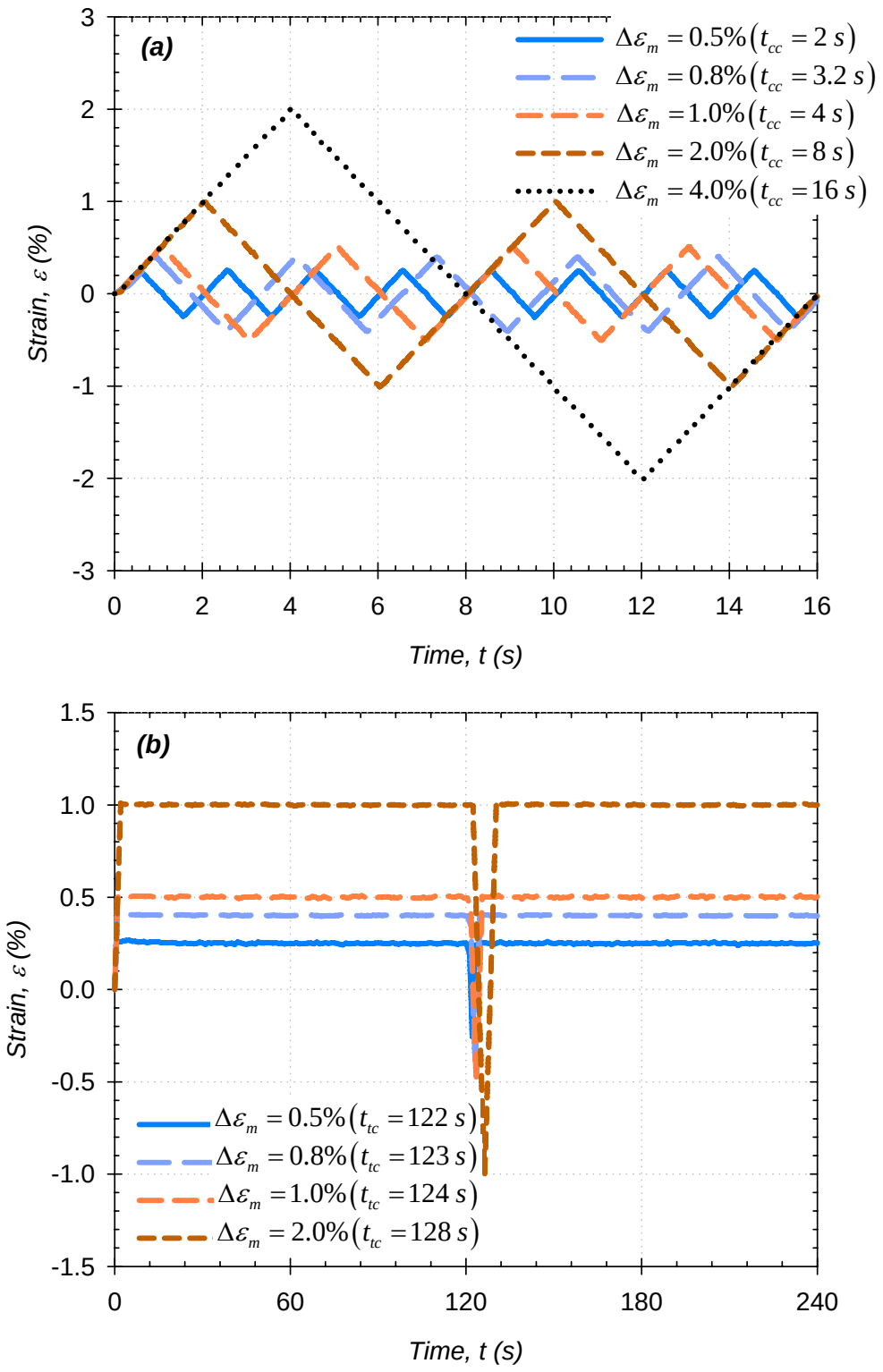


***Figure 3.6:*** *Initial strain histories for (a) continuous cycling and (b) cycling with hold times in tension.*

*Criterion #1:* The temperature throughout the gage section must be within $T_n \pm \Delta T$, where $T_n$ is the nominal test temperature in °C, and $\Delta T$ is 2°C or $1\%T_n$, whichever is greater.

*Criterion #2:* Strain range deviation must be less than 1% of the strain range throughout the life of the test.

Achieving Criterion #1 required that a test coil be iteratively reshaped and the temperature within and surrounding the gage section are checked. Five K-type thermocouples (Omega® model XC-K-24-SLE) were spot-welded to a trial specimen (3 within the gage section) which was then fastened within the collet grips and heated to $T_n$. Typical temperature distributions are illustrated in Fig. 3.7. The temperature distribution is designed so that the maximum temperature occurs in the center of the gage section. This temperature concentration guarantees that crack nucleation is prompted within the extensometer tips. As shown in Fig. 3.7, for increasing isothermal temperature, the axial temperature gradient within the gage section is higher. Two induction coils were fabricated for lower (RT to 760°C) and higher (871°C and 1038°C) isothermal temperature ranges. Images of each type are shown in Fig. 3.8. Each coil was constructed from copper tubing having a 4.7 *mm* (0.188 *in)* outer diameter and brass Swagelok® fittings. The inner diameter of each turn was at least 23 *mm* (0.9 *in*).

It should be noted that the procedure to determine the axial temperature distribution was only carried-out prior to a series of LCF tests. During actual tests, however, only one thermocouple was needed to maintain accurate feedback temperature control. After each LCF test, data was obtained and analyzed to ensure that the maximum mechanical strain range did not exceed a deviation of $1\%\Delta\varepsilon_m$.

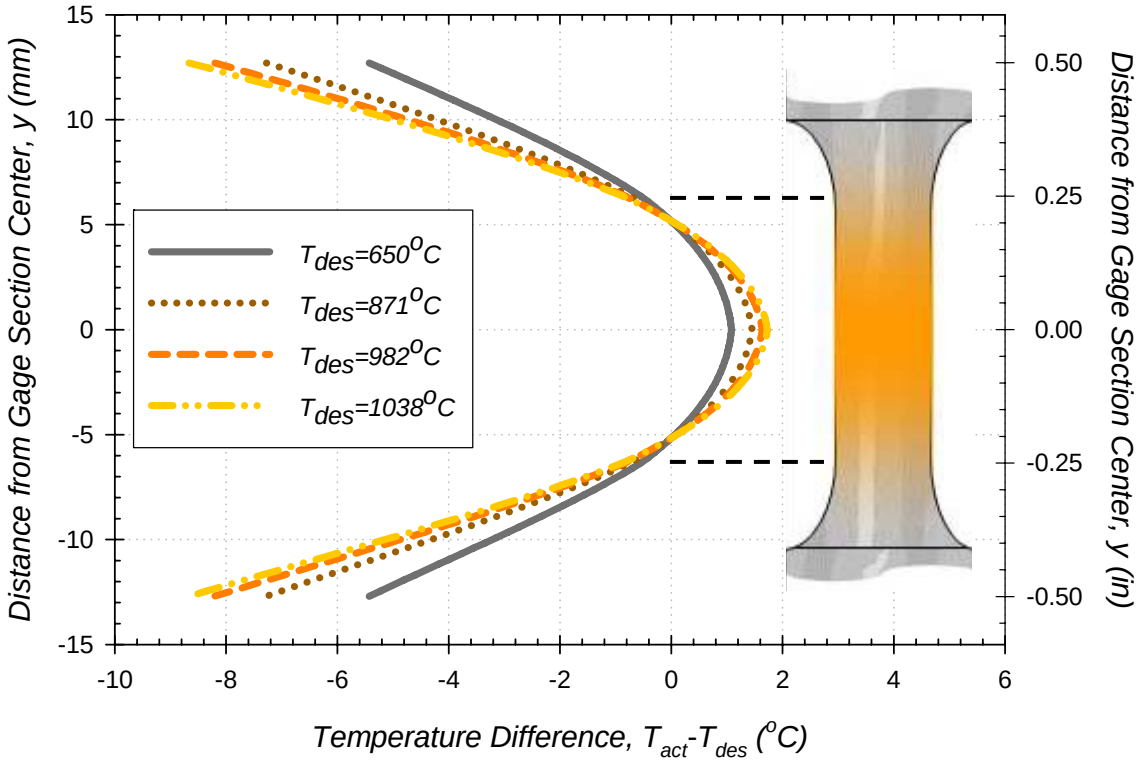


***Figure 3.7:*** *Typical axial temperature gradients within specimen gage section for various desired temperature set points (specimen not drawn to scale).*

## *3.3 Low Cycle Creep-Fatigue Tests*

The experimental procedure for conducting low cycle creep-fatigue tests is identical to LCF tests except for the addition of dwell periods. For tests with tensile dwell periods, the specimen is held at the peak tensile strain for a time period, $t_{ht}$. Similarly, for tests with compressive holds, the specimen is held at the peak compressive strain for a time period, $t_{hc}$. The time to complete one cycle with a tensile hold is given as

$$t_{tc} = t_{ht} + t_{cc} \tag{3.2}$$

With a compressive hold it is totaled as

$$t_{tc} = t_{hc} + t_{cc} \tag{3.3}$$

where $t_{cc}$ is the loading and unloading time.

Various temperatures and strain range combinations were used to conduct tests on L- and T-oriented DS GTD-111 specimens. Each test was carried out until a 20% load drop occurred. Examples of the strain histories for several LCF tests with holds in tension are shown in Fig. 3.6(b). With a strain rate of 0.5%/s for each test, a 2 *min* hold period accounts for at least 85% of the total cycling time even for large strain ranges.

## *3.4 Thermomechanical Fatigue Tests*

The same specimen and test procedures used in isothermal LCF were installed for thermomechanical fatigue (TMF) tests. In strain-controlled TMF experiments (ASTM E2368, 2004), a specimen is subjected to a combined temperature (i.e., thermal strain) cycle and mechanical strain cycle. Although the frequencies of each cycle were the same in the test program, there can exist a difference in phasing between mechanical and thermal strain cycles. This is defined as the waveform shift ($\phi$, expressed in degrees) between the maximum temperature response as measured on the specimen and the maximum mechanical strain response. Two baseline TMF tests are typically conducted

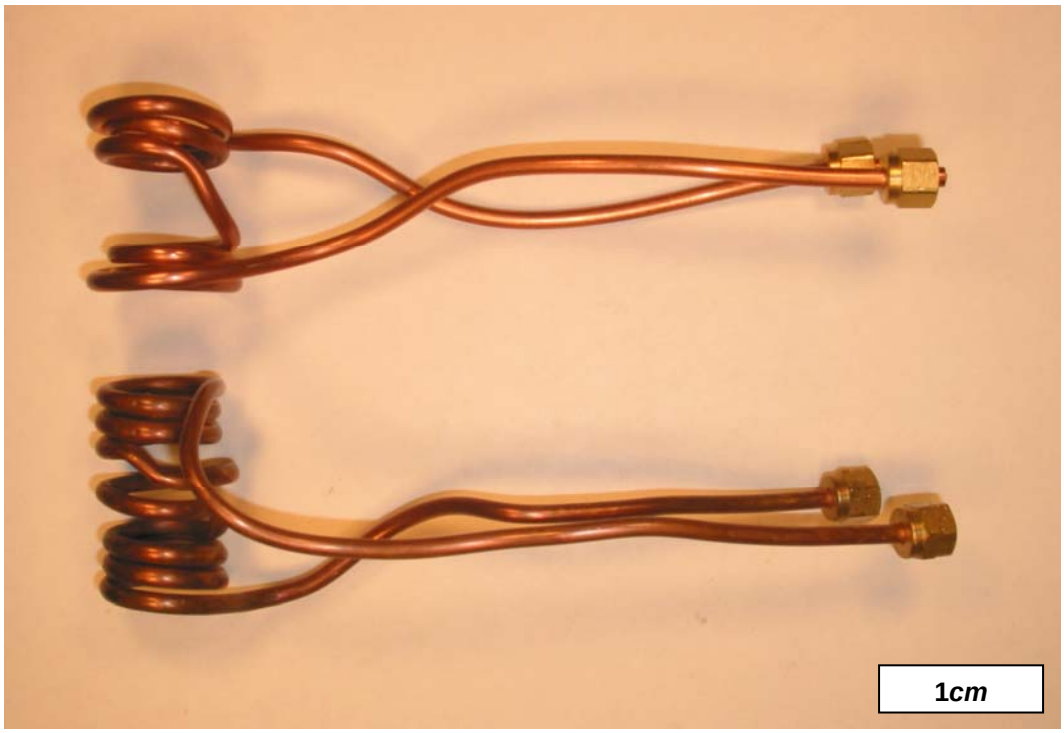


***Figure 3.8:*** *Copper tube coils used for induction heating (top)* 2½-0-2½ turns *for low isothermal temperatures (i.e., between room temperature and 760ºC), and (bottom)* 2½-1-2½ turns *for high isothermal temperatures (i.e., between 871ºC and 1038ºC) and non-isothermal experiments.*

in the laboratory: linear in-phase (IP), with the maximum mechanical strain at the maximum temperature, and linear out-of-phase (OP), with the maximum mechanical strain reached at the minimum temperature. For reference purposes, $\phi$ is considered positive if the temperature response maximum leads the mechanical strain response maximum by 180° or less; otherwise, the phase angle is considered to be negative. Other thermomechanical cycle types are implemented to simulate other service conditions. Examples of two TMF cycle types are shown in Fig. 3.9. For each case the mechanical strain range is 1.0%, while the 0.5% thermal strain peaks and valleys are shifted to cause

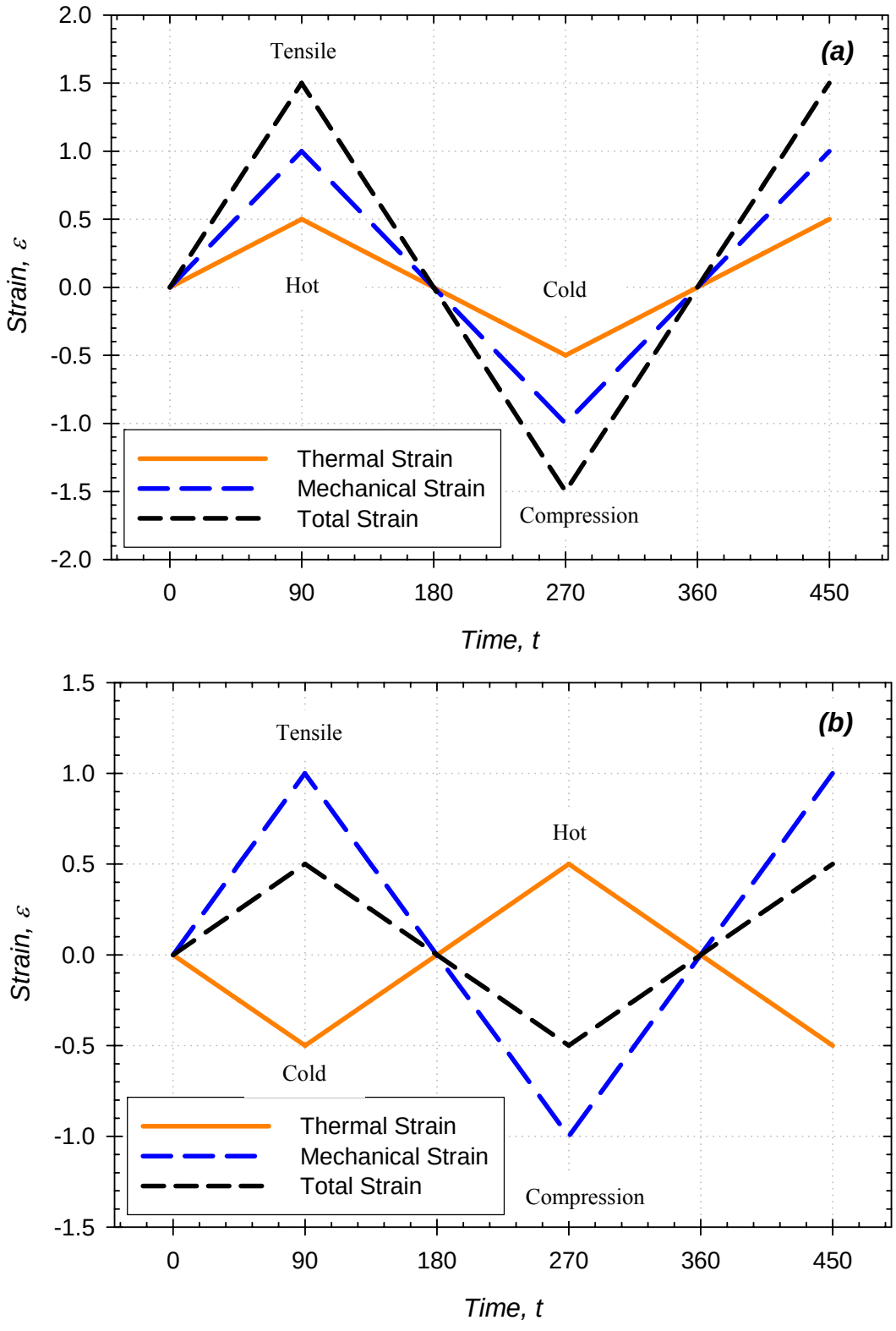


***Figure 3.9:*** *Strain history for (a) in-phase and (b) out-of-phase strain-controlled thermomechanical fatigue cycling.*

either IP ($\phi$ = 0°) or OP ($\phi$ = 180°) cycling. An isothermal LCF test is essentially a special case of TMF with a constant temperature (i.e., $\Delta\varepsilon_{th} = 0$).

In mechanical strain-controlled TMF tests, the mechanical strain component is determined as the difference of total strain measured on the test specimen and the thermal strain, i.e.,

$$\varepsilon_m = \varepsilon_t - \varepsilon_{th}, \tag{3.4}$$

where the linear relationship between temperature range and thermal strain,

$$\varepsilon_{th} = \alpha\left(T - T_{ref}\right), \tag{3.5}$$

is governed by the coefficient of thermal expansion, $\alpha$. The reference temperature, $T_{ref}$, is RT. In application, however, this conventional linear relationship is not sufficient for high temperature ranges. A non-linear relationship is typical for dual phase Ni-base superalloys (Sung and Poirier, 1998). Furthermore, under continuously varying temperature cycling, the thermal strains during cooling and heating may differ.

For a temperature range of 500ºC and a cycle time of 3 *min*, $\varepsilon_{th}$ during cooling and heating phases are clearly distinct near the minimum and maximum temperatures, as shown in Fig. 3.10. Axial and radial thermal gradients cause this disparity. The error in thermal strain approximation is interpreted as an over- or under-estimation of mechanical strain. This causes additional compressive axial force during heating and additional tensile axial force during cooling. Any uncertainty in either $\varepsilon_t$ or $\varepsilon_{th}$ directly propagates

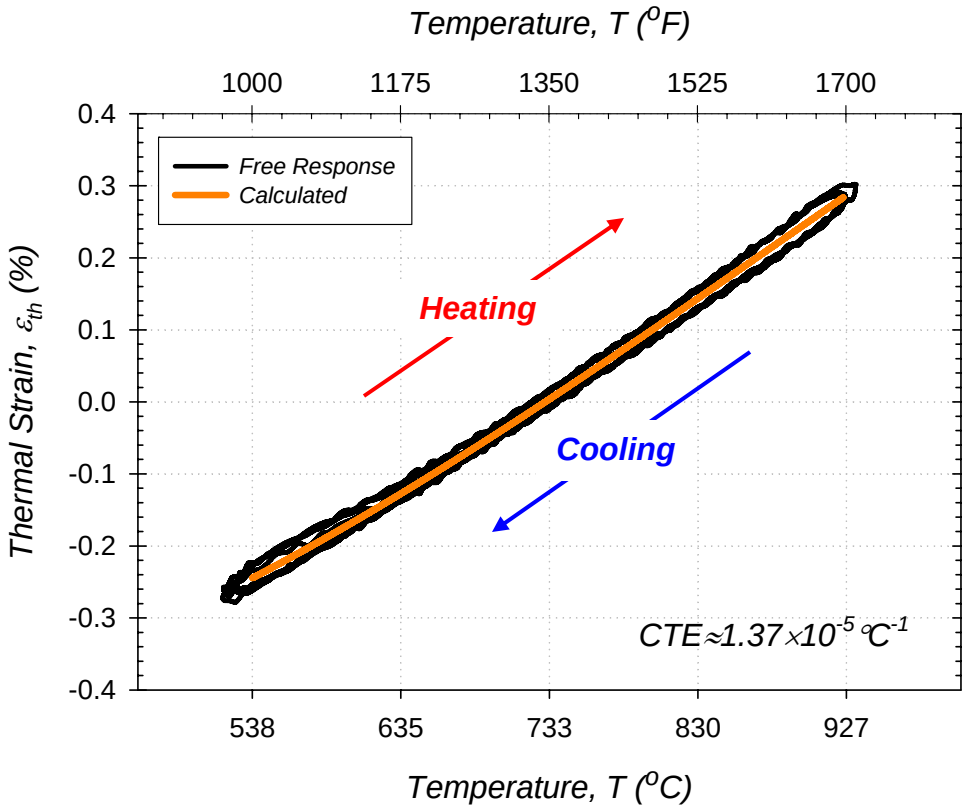


***Figure 3.10:*** *Thermal strain generated during free expansion under temperature cycling at zero load.*

to $\varepsilon_m$. Errors in approximating the thermal strain can, therefore, potentially influence deformation and life estimates. Test parameters (e.g. temperature range and cycle time) and experimental equipment (e.g. induction coil) were designed to minimize thermal gradients.

Strain-controlled TMF tests are more easily executed on axial test frames with dual independent channel servo-loop controllers. The current setup allowed for real-time calculated variable control. Mechanical strain controlled tests were achieved using the independent total strain signal, $\varepsilon_t$, and calculated thermal strain, $\varepsilon_{th}$, implemented via Eq. (3.4). In the identical manner as isothermal LCF tests, axial deformation in the gage section of the specimen is measured with an extensometer. The relationship for thermal

strain was determined from free expansion (no mechanical strain) of the specimen. As per the TMF standard (ASTM E2368), the explicit temperature-based compensation of thermal strains, shown in Fig. 3.10, is given as a polynomial, i.e.,

$$\varepsilon_{th} = \sum_{i=0}^{n} a_i \left(T_{T/C}\right)^i \tag{3.6}$$

A 3rd order polynomial relationship based on temperature is used to fit 5 cycles of free expansion thermal strain data. The specimen temperature reading from the thermocouple ($T_{T/C}$) was retransmitted to the TestStar controller and used to calculate the components of thermal and thus mechanical strain. It was later verified that the thermal strain hysteresis during the zero-load cycling was below $5\%\Delta\varepsilon_{th}$.

A flow chart illustrating the equipment and the transmitted signals used for this experimental setup is shown in Fig. 3.11. Since two or more devices in the arrangement are connected to a common ground through different paths, a ground loop may occur. To avoid this problem, the signals from these devices were feed through an isolation amplifier, fabricated at Georgia Tech. The circuit diagram for this device is given in Fig. 3.12.

In this study, the mechanical strain cycles were either in-phase (0°) or out-of-phase (180°) with the thermal strain cycles. For every experiment, a cycle time of 3 *min* was applied. This quantity was selected based on the maximum capable heating rate of the induction heating system and the maximum cooling rate via natural convection in laboratory air. Since no hold times were applied, from either Eq. (3.2) or Eq. (3.3), $t_{tc} = t_{cc}$ under TMF.

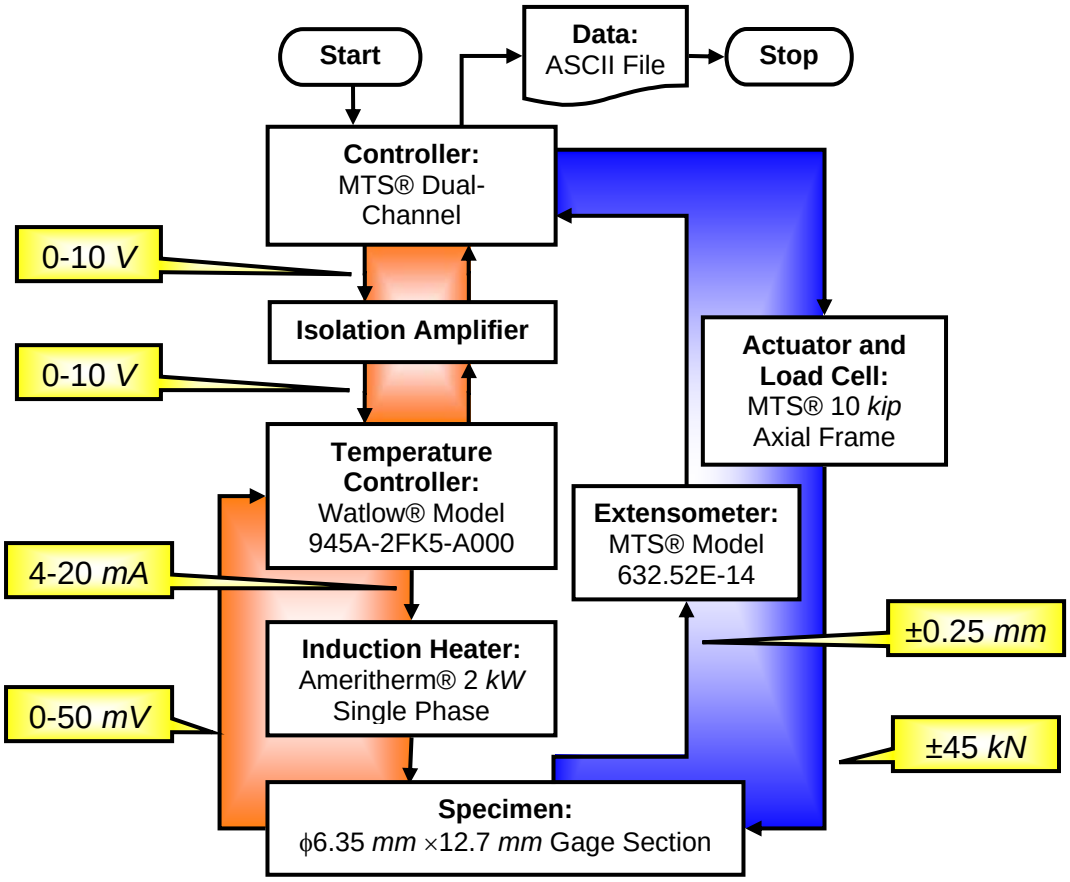


***Figure 3.11:*** *Components and respective signals transmitted in dual closed loop feedback control, thermomechanical fatigue testing system.*

The identical test parameters from isothermal LCF experiments (i.e., strain range, $\Delta\varepsilon$, strain ratio, $R_\varepsilon$, and strain rate, $\dot{\varepsilon}$) correspond to those of the mechanical cycling for TMF experiments (i.e., mechanical strain range, $\Delta\varepsilon_m$, mechanical strain ratio, $R_{\varepsilon_m}$, and strain rate, $\dot{\varepsilon}_m$). Since each of these tests is non-isothermal, the mechanical strain range ($\Delta\varepsilon_m$) is not equal to the total strain range ($\Delta\varepsilon_t$). Completely reversed (i.e., $R_{\varepsilon_m} = -1$), mechanical strain ranges of 0.5% or 1.0% were used, and since the total cycle time was fixed at 180 *s*, $\dot{\varepsilon}_m$ during loading or unloading was either 0.0056%/*s* or 0.0112%/*s*.

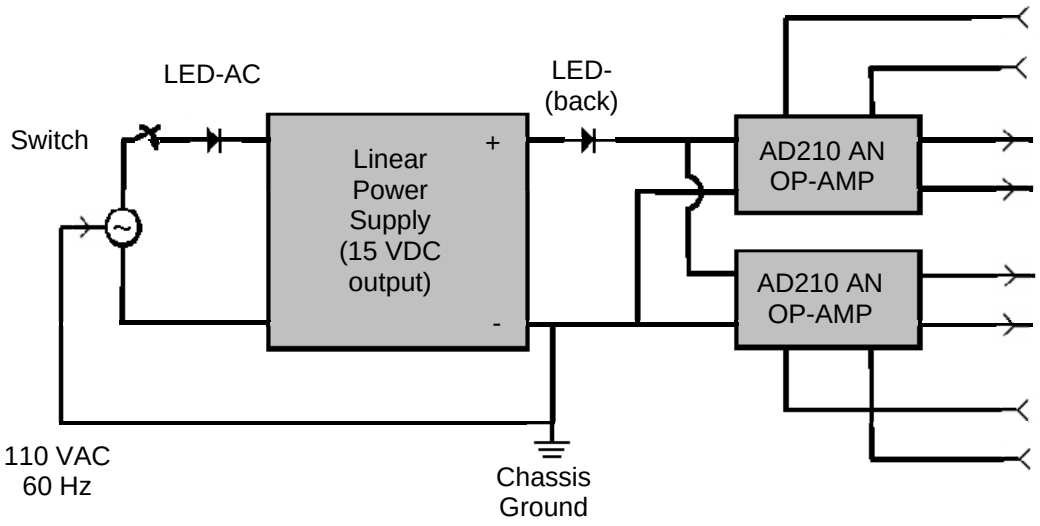


***Figure 3.12:*** *Circuit diagram for isolation device.*

The thermal strain range, $\Delta\varepsilon_{th}$, and thermal strain rate, $\dot{\varepsilon}_{th}$, depend the minimum temperature, $T_{min}$, and maximum temperature, $T_{max}$. Both $T_{min}$ and $T_{max}$ were selected to simulate the temperature range in nominal service conditions of 1st stage Ni-base turbine buckets. For a typical TMF experiment, temperature was continuously cycled from 538°C (1000°F) to 927°C (1700°F) or from 538°C to 1038°C (1900°F). These temperature ranges correspond to thermal strain ranges of 0.55% and 0.89%, respectively. Since a fixed 3 *min* cycle period was used, the rates during either heating or cooling had a magnitude of either 4.32°C/*s* (7.78°F/*s*) or 5.55°C/s (10°F/*s*).

All TMF tests were performed according to an ASTM standard (ASTM E2368, 2004). Validity of each test was achieved when the following critical criteria were satisfied:

*Criterion #1:* The $\varepsilon_{th}$ hysteresis existing at any given temperature point in the cycle under zero force conditions shall be no greater than 5% of the thermal strain range induced.

*Criterion #2:* The maximum allowable axial temperature gradient over the gage section at any given instant in time within the cycle shall be the greater of $\pm 1\% \times T_{max}$ or $\pm 3°K$. Here $T_{max}$ is the maximum cyclic temperature given in °K and measured under dynamic conditions.

*Criterion #3:* The mechanical strain range shall not deviate from the desired value by more than $2\% \Delta\varepsilon_m$ at any given instant in time throughout the duration of the test.

*Criterion #4:* Throughout the duration of the test, the error between the temperature/mechanical strain phasing shall not exceed the bounds of $\phi = 5°$ where $\phi$ is the desired phase shift for the test. No cumulative error is permitted.

The potential for temperature lags experienced during heating and cooling reversals exists. Conduction in the water-cooled collet grips and natural convection from static air were the only methods used to cool the specimen; consequently, the heating rate had to be adjusted to mirror the cooling rate of the material. Both the temperature range ($\Delta T$) and cycle time ($t_{tc}$) were adjusted to achieve Criterion #1. Satisfaction of this criterion only needed to be checked once prior to a series of tests with identical temperature cycles. Ideally, no hysteresis should exist. Forced air cooling is generally not desired with solid specimens due to the potential for radial temperature gradients (i.e., skin effects) within the gage section.

The same techniques used to minimize static axial temperature gradients in isothermal LCF testing were used for minimizing dynamic axial temperature gradients in TMF testing. Although there is no standard practice for determining the dynamic temperature distribution of the gage section, a systematic procedure was carried out in order to satisfy Criteria #2. Temperature readings were recorded from an analog K-type thermocouple reader (Omega Model 199) at 10 intervals during the free response of a calibration specimen under temperature cycling. These readings were analyzed to determine excessively hot or cold spots along the gage section. Any of the following aspects of the induction coil turns were then modified to reduce the dynamic temperature gradients: number of turns, spacing between turns, and diameter of the turn. This process was repeated until the criterion was satisfied. Several iterations of temperature reading and coil modifying were typically needed for a combination of $\Delta T$ and $t_{tc}$. Large $\Delta T$ and small $t_{tc}$ lead to large axial temperature gradients. Since Eq. (3.6) is used to approximate both the heating and cooling curves, error in thermal strain approximation propagates as an over- or under-estimation of mechanical strain. This causes additional compressive axial force during heating and additional tensile axial force during cooling. One measure of the accuracy and uniformity of the cyclic temperature control can be associated with the amount of force generated from the specimen resulting from thermally cycling when the specimen is maintained at zero mechanical strain control.

In reference to Criterion #3, the free response of the specimen under a thermal cycle was obtained from the calibration specimen after it was subjected to a sufficient number of TMF cycles. Evolution of the thermal expansion of the material was determined to be insignificant throughout the life of these experiments. Since the TMF

tests, therefore, were performed under $\Delta\varepsilon_m$ control, deviation of $\Delta\varepsilon_m$ was negligible throughout the life of the material.

Under continuously varying temperature cycling, the thermal strains during cooling and heating may differ with the presence of even slight axial and radial thermal gradients. The lag between temperature command and thermal strain response was assessed prior to initiating TMF cycling. Phase lag compensation, which is built into the TestStar control software, was used to offset the heating/cooling lag to obtain the desired phasing between mechanical and thermal strain cycles. Both the mechanical strain and the temperature should remain cyclically synchronized throughout the duration of the test. A phase lag compensation ($\phi_{la\ g}$) of -6° (3 *s*) was applied so that Criterion #4 was satisfied when cycling the temperature from 538°C to 927°C and $\dot{T} = 4.3°C/s$. When cycling at a higher maximum temperature (i.e., 538°C to 1038°C and $\dot{T} = 5.6°C/s$), more lead-time (i.e., $\phi_{lag}$=-26° (13 *s*)) was needed for the specimen to follow the desired temperature cycle.

## *3.5 Pre-Exposure-Fatigue Tests*

Some of the LCF specimens were pre-exposed in either lab air at high temperature and in some cases a static load was applied. To simulate the corrosive effects of the syngas environment, several specimens were subjected to a sulfur-rich pre-exposure. Pre-exposure consisted of a specified temperature (982°C for all cases), mechanical load (0, ±75 *MPa*, or ±100 *MPa*), and environment (air or simulated syngas) for 100 *hr*. Pre-exposure in the simulated syngas environment was conducted using $N_2$ with 100 *ppm* $H_2S$ at CC Technologies (Dublin, OH). In the stressed cases that were

carried out on the servo-hydraulic machine, creep deformation occurred and was recorded. The specimens were subsequently tested under LCF conditions to determine the effect of pre-exposure on fatigue crack in initiation life.

It should be noted that the standard specimen shape for creep deformation and rupture testing (ASTM E139, 1996) calls for a ratio of the specimen gage section length to the gage section diameter of four. This ratio has been established to ensure accurate strain measurements for long term creep tests. In the current study, specimens have gage section lengths of 12.7 *mm* and gage section diameters of 6.35 *mm*. Since a highly-accurate, direct contact extensometer was employed to measure strain, accurate creep deformation measurements were expected and obtained.

Data from creep rupture and deformation tests that were conducted in an earlier study are also relevant to the current investigation. These tests were performed on a creep frame in accordance with an ASTM standard E139 (1996) and documented by Ibanez (2003).

## *3.6 Semi-Inert Environment Tests*

Nickel-base superalloys exhibit considerable resistance to diffusional degradation. Surface corrosion reactions in these metals are dictated by the composition of the ambient environment. Each of the test configurations described in the previous sections of this chapter were conducted in a laboratory containing static air. By percent volume, this gas has four main constituents: nitrogen, $N_2$ (78.08%), oxygen, $O_2$ (20.95%), argon, Ar (0.93%), and carbon dioxide, $CO_2$ (0.04%). Typical air pressure, $P_{air}$, of these experiments was 1.013 *bar* (1 *atm*) or 101.3 *kPa* (14.69 *psi*). Traces of ideal gases, most

notably He, Ne, Kr, and Xe, can also be found. Significantly modifying the balance of these gases in the envelope surrounding a specimen will alter the surface corrosion process. As a consequence, if the dominant damage mechanism is influenced by the environment, crack initiation will be altered.

A series of experiments was conducted in gases that were either rich in or devoid of oxygen. For brevity, the collection of environments is referred to as *alternate environments.* The experimental setup that was used for isothermal low cycle fatigue testing was modified to conduct these experiments. A description of the test system that was designed for these experiments follows.

A semi-closed chamber was fabricated from a sheet of 0.76 *mm* (0.030 *in*) thick, transparent Lexan® glass (a polycarbonate material) to house the specimen, induction coils, and extensometer tips. The sheet was cut to shape and bent to form a cylinder having an inner diameter of 170 *mm* (6.7 *in*) and a height of 170 *mm* (6.7 *in*). The chamber was then clamped to the upper hydraulic collet grip as shown in Fig. 3.13. Circular and elliptical holes were cut out of the sheet to accommodate sets of copper tubes, gas flow lines, extensometer tips, and bolts as shown in Fig. 3.14. The lower actuating grip was free to slide along the axis of the specimen at the bottom opening of the chamber.

The contents of a 17.0 *kL* (300 $ft^3$) gas cylinder was transported to the chamber using short lengths of PUR tubing [6.35 *mm* OD × 4.32 *mm* ID (25 *in* × 0.17 *in*)] fastened by Swagelok® brass and plastic (PFA - perfluoroalkoxy) fittings. Gas is transported from the chamber to a laser-based oxygen sensor (Oxigraf® model O2L) in the same manner. A schematic of the gas transport is shown in Fig. 3.15a. Depending on the test,

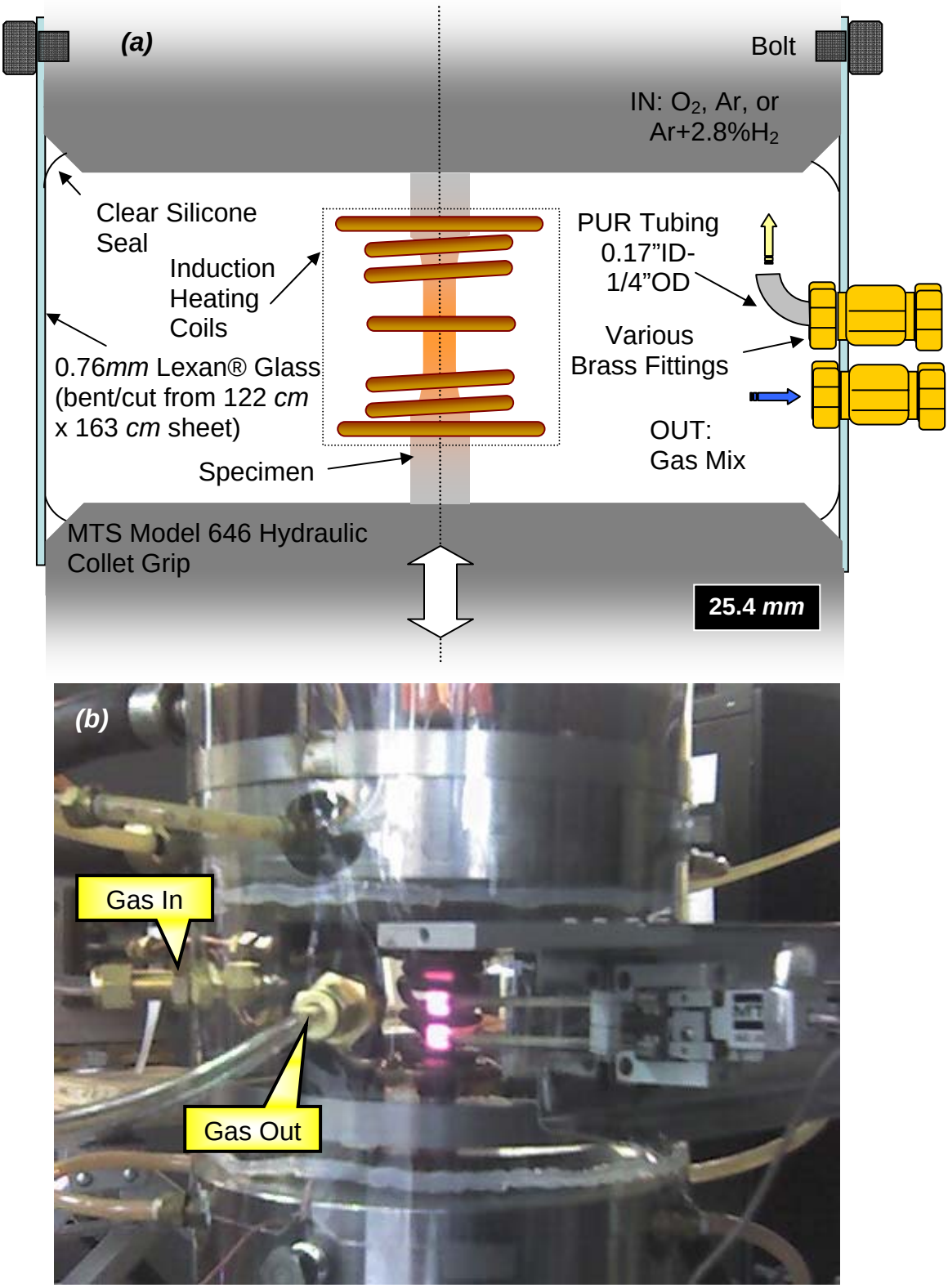


***Figure 3.13:*** *(a) Schematic and (b) photograph of front view of chamber used in alternate environment low cycle fatigue testing of DS GTD-111.*

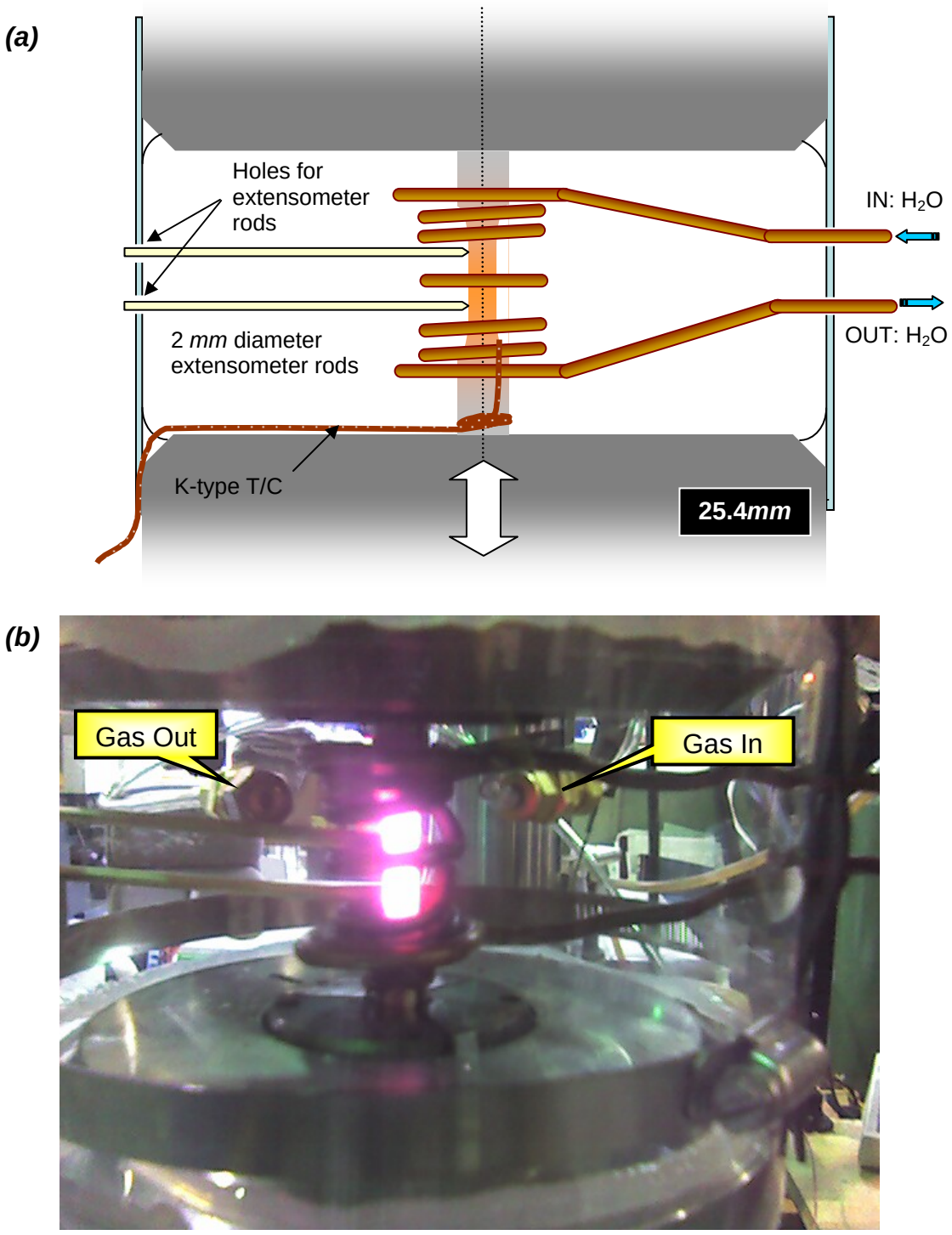


***Figure 3.14:*** *(a) Schematic and (b) photograph of side view of chamber used for alternate environment low cycle fatigue testing of DS GTD-111.*

one of three types of gases were supplied: (a) industrial grade 99.99% pure argon, (b) a two-component mix containing argon and 2.8% hydrogen to minimize oxidation and (c) industrial grade, 99.99% pure oxygen to maximize oxidation. A small amount of hydrogen in the vicinity of the heated specimen acts as an oxygen getter to remove oxygen near the specimen by precipitating into water. Because the extensometer tips and lower grip are required to move freely relative to the chamber, static laboratory air could leak into the chamber. To prevent this, the semi-closed chamber was flooded with the gas prior to, during, and shortly after each fatigue experiment was carried out. Positive pressure of nearly 34 *kPa* (5 *psi*) was maintained by the regulator; therefore, gas would always be flowing out of the chamber.

Oxygen contents of unknown gas mixtures are quantified using oxygen sensors. These sensors are categorized as electrochemical, paramagnetic, or laser-based. Oxygen sensors that utilize the relatively new laser diode absorption spectroscopy gas analysis technology are capable of measuring oxygen content from 0 to 100%. This measurement methodology is not affected by the presence of Ar, $H_2O$, or $CO_2$. The model used for this study automatically adjusts with slight variations of pressure and temperature. The minimum and maximum oxygen levels that can be detected are 0.01% and 99.99%, respectively. The model is capable of operating at any temperature between -142°C (-224°F) and 79°C (175°F).

The gas mixture contained in the Lexan® chamber was transported to the sensor sample inlet using PUR tubing. An internal pump delivered gas across the sensor and back into the chamber at a flow rate between 50 and 600 *ml/min*. Via an analog BNC connector, 0 to1 *V* measurements signaling oxygen content were reported to the MTS

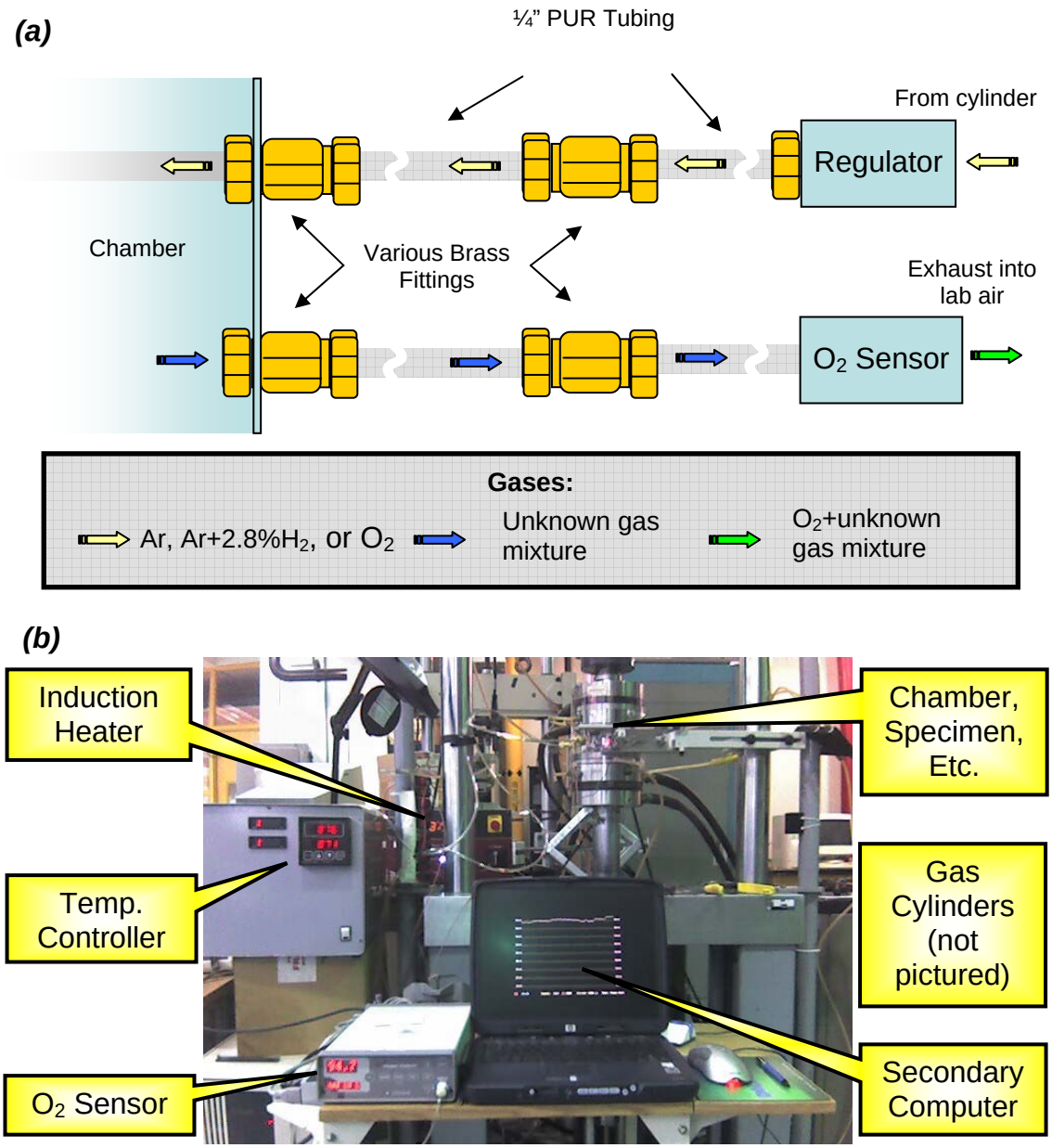


***Figure 3.15:*** *(a) Gas flow diagram for system. (b) Photograph of equipment setup.*

controller every 0.0016 *s* and digitally recorded. Major components of this system are shown in Fig. 3.15b. Oxygen content, sensor pressure and temperature were reported to a secondary computer at a rate of 9.6 *kbaud* via COM1 by way of an RS232 serial connector. The real-time oxygen content history was plotted on a secondary computer

and was used to manually adjust gas flow to the chamber. The data flow chart for this modified test system is illustrated in Fig. 3.16. Readings were continuously taken for the duration of each experiment.

Using the known gas pressure exerted on the sensor, oxygen content was reported as a volume fraction in percentage, $F_{O_2}$. When testing with pure $O_2$, the oxygen content of the chamber was typically 95%. When testing with either pure Ar or Ar+2.8%$H_2$, the oxygen content of the chamber was near 5%.

## *3.7 Stress-Free Oxidation Testing*

After the small disc-shaped oxidation specimens shown in Fig. 3.2 were polished and cleaned, the samples were arranged on an alumina float (Fig. 3.17a) and heated in a 3-zone tubular electric resistance furnace (Lindberg 240 *V* Model: 59744-A) shown in Fig. 3.17b. Samples were exposed to various combinations of temperature [871°C (1600°F), 927°C (1700°F), 982°C (1800°F), and 1038°C (1900°F), 1093°C (2000°F)] and time (1.0 *hr*, 3.1 *hr*, 10.0 *hr*, 31.6 *hr*, 100.0 *hr*, 316.2 *hr*, 1000.0 *hr*) in static air. Since a significant length of the thermocouple was subjected to high temperature, thermocouple wiring insulated with temperature resistance braided sleeving (Omega® model XC-K-24-SLE) was necessary. After the elapsed test time, specimens were removed from the furnace and cooled to room temperature. Samples were then prepared for microscopy.

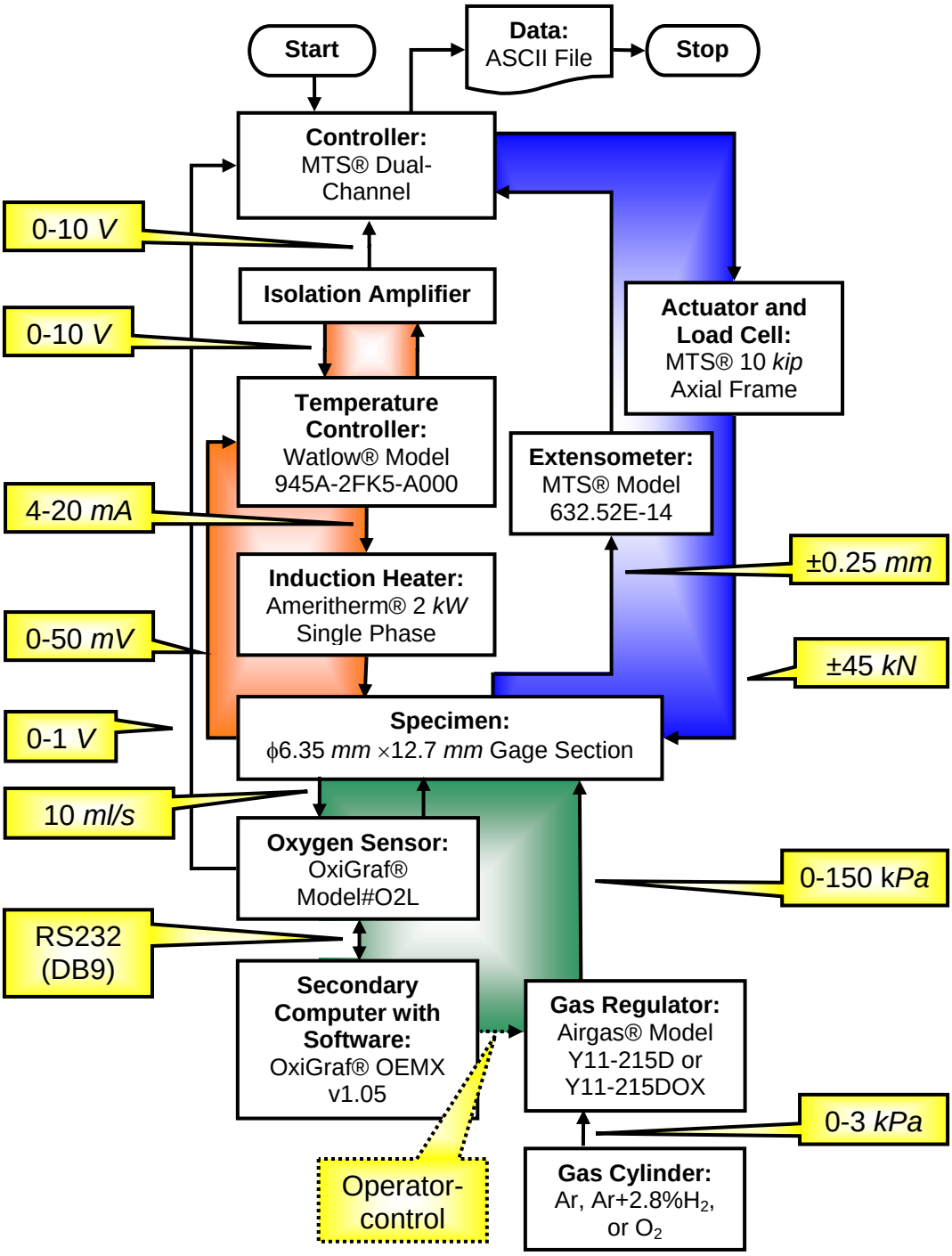


***Figure 3.16:*** *Components and respective signals transmitted in isothermal alternate environment testing.*

## *3.8 Metallography Procedure*

Specimens were examined using Light Optical Microscopy (LOM) and Scanning Electron Microscopy (SEM). The procedure used to prepare viewing samples from tested specimens consisted of a number of steps: sectioning, mounting, grinding, and polishing. Samples were sectioned using a diamond saw. Illustrations of the plane cuts are shown in Fig. 3.18. Although the plane with the maximum crack length is not known a priori, a general rule of thumb is to axially section the specimen in the midsection of the dominant surface crack, which at times could be visually observed. Typically, only two or three cuts were necessary to remove the desired samples from the gage section of the fatigue-tested specimen. Taking both the radial and axial sections allowed for a thorough overview of the sample to be made. For example, features such as cracks were observed in axial sections using microscopy.

A similar cutting procedure was applied for stress-free tested samples. Only one cut was needed to section samples from the disc-shaped oxidation specimens (Fig 3.18b).

After sectioning, samples were cold-mounted in an epoxy resin (Buehler EPO-KWICK). Mounted samples were ground and polished using a multi-step procedure. The procedure for grinding and polishing all of the samples is shown in Table 3.2. The samples were etched to expose the $\gamma'$ precipitate particles and the $\gamma$ matrix. The volumetric concentrations of etchant mixes that were used are listed in Table 3.3. There is no noticeable distinction between the effects of the two etchants used. The etchant is swabbed on the sample for 10 *s*. Afterwards, the specimens were immediately rinsed in water and dried with compressed air. In the event that the sample was over-etched, steps

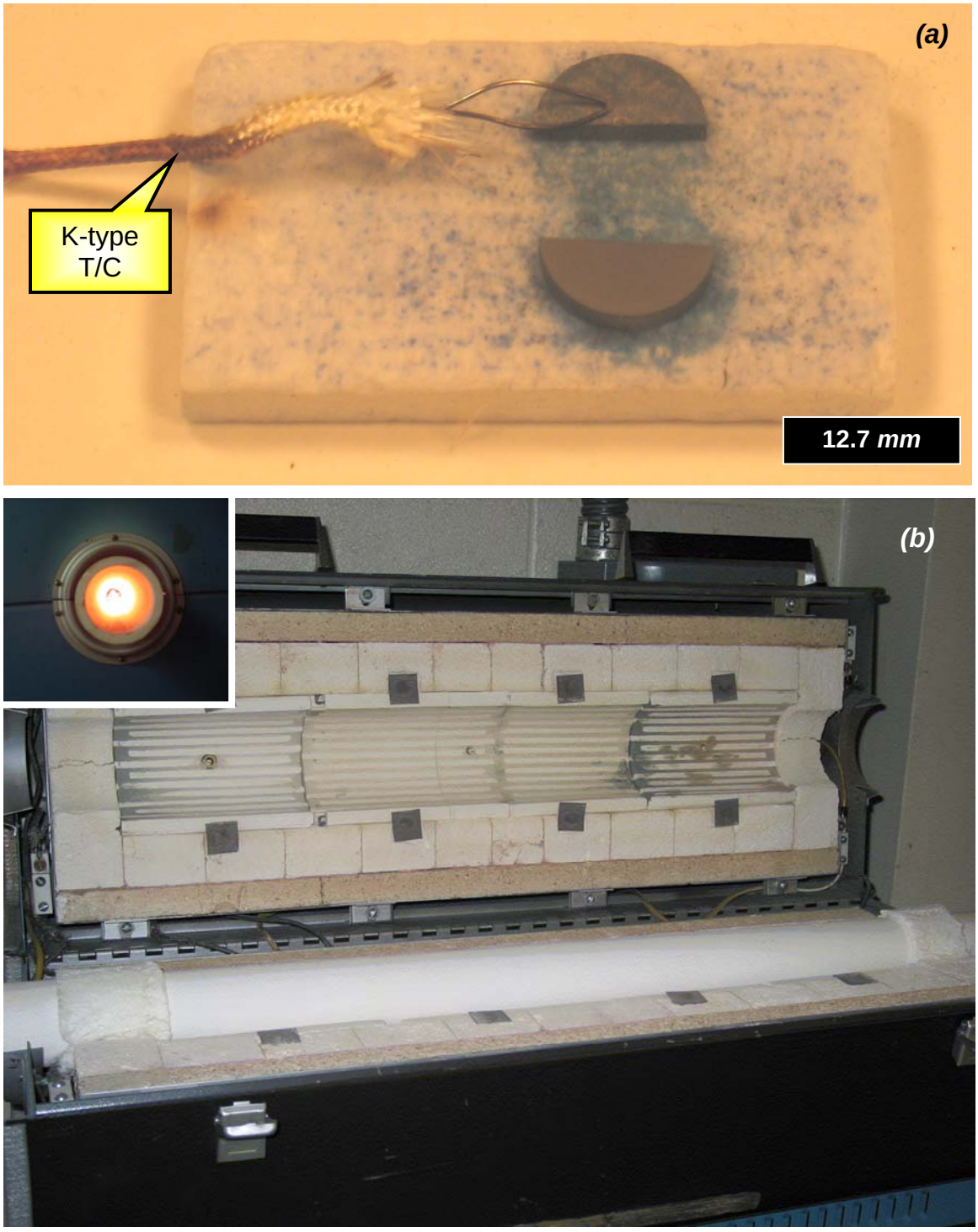


***Figure 3.17:*** *(a) Specimen seating on alumina float. (b) Three-zone tubular electric resistance furnace (Lindberg 240 V Model: 59744-A).*

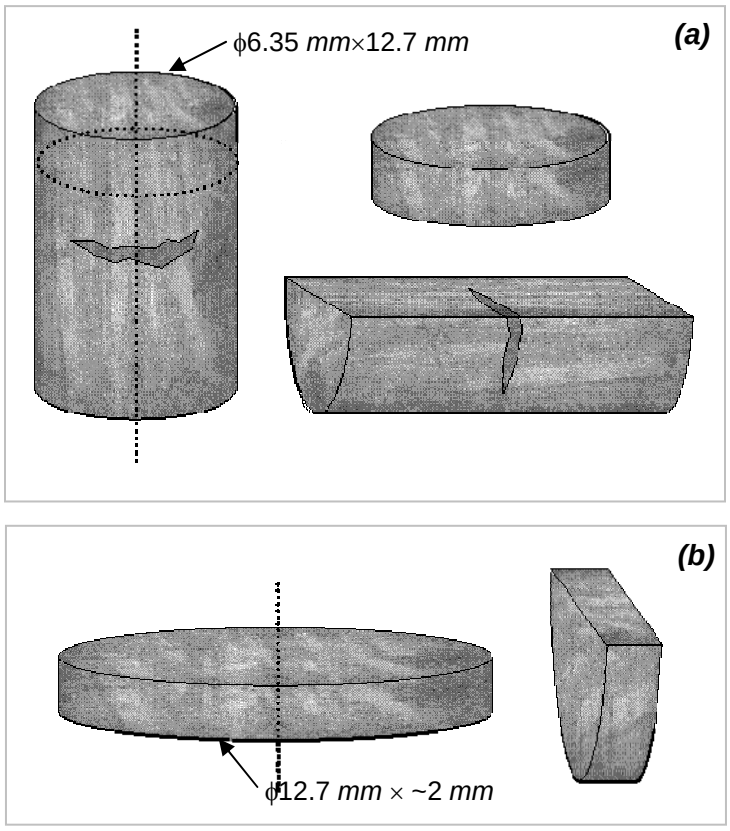


***Figure 3.18:*** *Sectioning convention for (a) fatigue and (b) oxidation specimens.*

3 and 4 in Table 3.2 were performed to remove a thin layer of material and then the etching procedure was then repeated.

An optical microscope was used to examine microstructural features (e.g. carbides, grain boundaries, and interdendritic regions), subsurface damage, and accumulated oxide layers of fatigue and unstressed samples of DS GTD-111. Because of the limited range of resolution of optical microscopy, objects smaller than 0.25 $\mu m$ (e.g. fine secondary $\gamma'$ precipitate particles) were difficult to distinguish even at the maximum optical magnification.

***Table 3.2:*** *Grinding and polishing steps for surface analysis of DS GTD-111*

| Step | Preparation Disc (Material) | Applied Force (N) | Suspension | Lubricant | Time (min) | Final Surface Finish (μm) |
|---|---|---|---|---|---|---|
| 1 (Coarse Grind) | MD Piano (Resin bonded diamond disc) | 35 | None | Water | 5 | 3 |
| 2 (Fine Grind) | MD Allegro (Composite disc) | 30 | $9\mu m$ DiaPro | None | 4 | 1 |
| 3 (Coarse Polish) | MD Mol (Woven wool) | 30 | DiaPro Mol | None | 4 | 0.25 |
| 4 (Fine Polish) | MD Chem (Porous synthetic) | 15 | OP-S Paste | Water | 2 | 0.04 |

***Table 3.3:*** Etchant mix used for DS GTD-111

| | Unnamed Etchant | Walker's Etchant |
|---|---|---|
| Chemicals (Formula) | Quantity | |
| Acetic Acid ($C_2H_4O_2$) | - | 20*mL* |
| Distilled Water ($H_2O$) | - | 50*mL* |
| Hydrochloric Acid (HCl) | - | 50*mL* |
| Hydroflouric (HF) | 4*mL* | 10*mL* |
| Iron Chloride ($FeCl_24H_2O$) | - | 15*g* |
| Lactic Acid ($C_3H_6O_3$) | 104*mL* | - |
| Nitric Acid ($HNO_3$) | 62*mL* | 30*mL* |
| Phosphoric Acid ($H_2PO_3$) | - | 10*mL* |

Scanning electron microscopy (SEM) was used to visually observe microstructural features that are too small to be clearly seen in an optical microscope. Prior to viewing, samples were made conductive by creating a bridge of carbon tape to the SEM holder. While using the SEM (JOEL® model JSM-840), the optimal accelerating voltage to obtain images of DS GTD-111 was $15kV$. A probe current between $1\times10^{-8}$ $A$ and $3\times10^{-8}$ $A$ was applied. Back-scattered electron images were obtained to more easily observe the contrast between matrix and precipitate phases.

# 4. EXPERIMENTAL RESULTS AND MICROSCOPY

Numerous experiments were conducted on specimens of both orientations of DS GTD-111 to characterize its thermal, environmental, and mechanical behavior. This chapter details the results for each of the types of experiments. Some data curves, specifically those generated from mechanical testing, are given in the Appendices. Experimental results are discussed as well as the description of microstructural observations.

The largest number of experiments in this study was conducted under isothermal LCF conditions. Of these experiments, the larger portion was conducted at 871°C (1600°F). Temperatures above this are of particular importance since the behavior of the material in both orientations undergoes a transition in its yield strength and oxidation behavior caused by microstructural instability. Above 871°C, inelastic deformation in DS GTD-111 is predominantly accommodated by quasi-cube slip within the matrix channels between adjacent precipitates. Below this temperature, deformation is accommodated by both slip mechanisms (i.e., octahedral and cube slip). Also, below this temperature there is a noticeable decrease is the material's tendency to develop surface oxides. For these reasons, 871°C (1600°F) is considered as a "benchmark" temperature.

## 4.1 Orientation Effects under Benchmark Conditions

Several strain-controlled isothermal fatigue tests were conducted at 871°C (1600°F) under continuous cycling (CC) conditions. A strain rate of 0.5%/s and strain ratio ($R_\varepsilon = \varepsilon_{min}/\varepsilon_{max}$) of -1 were maintained for these experiments. Tests were conducted using samples with both orientations. Strain- and life data for experiments on L- and T-oriented DS GTD-111 specimens are given in Tables 4.1 and 4.2, respectively. The last column of each table contains the figure numbers for the corresponding data curves (initial hysteresis loops and stress history) located in the Appendix. Based on the initial stabilized maximum tensile load, $P_{i,max}$, the load drop can be calculated (i.e., 90%$P_{i,max}$, 80%$P_{i,max}$, 50%$P_{i,max}$, 0%$P_{i,max}$). Using the stress history, the life can be determined for a particular load drop (e.g. $N$ at 90%$P_{i,max}$). The compared results of Tables 4.1 and 4.2 indicate that as the strain range is increased for each material orientation, the cycles to a particular percentage load drop decreased.

***Table 4.1:*** *Fatigue life of L-oriented DS GTD-111 at 871 °C under continuous cycling* [†]

| Total Strain Range, $\Delta\varepsilon$ (%) | Life, $N$ | | | | Specimen ID | Figure |
|---|---|---|---|---|---|---|
| | 90% | 80% | 50% | Fracture | | |
| 0.5 | 29159 | 29159 | 29159 | 29159 | L8-3 | A.14 |
| 0.8 | 3699 | 3699 | 3699 | 3699 | GTD-CC04 | A.3 |
| 0.9 | 867 | 987 | 1010 | 1054 | A27-L-F6 | A.38 |
| 1.0 | 315 | 1357 | 1409 | 1409 | GTD-CC05 | A.2 |
| 2.0 | 71 | 103 | 112 | 112 | B17-L-F5 | A.48 |
| 4.0 | 10 | 11 | 23 | 23 | L8-2A | A.10 |

[†] *All tests conducted with* $R_\varepsilon = -1$ *and* $\dot{\varepsilon} = 0.5\%/s$

***Table 4.2:*** *Fatigue life of T-oriented DS GTD-111 at 871 °C under continuous cycling*

| Total Strain Range, $\Delta\varepsilon$ (%) | Life, *N* | | | | Specimen ID | Figure |
|---|---|---|---|---|---|---|
| | 90% | 80% | 50% | Fracture | | |
| 0.5 | 16069 | 16069 | 16069 | 16069 | T8-2A | A.13 |
| 0.8 | 564 | 598 | 721 | 1091 | T8-5 | A.25 |
| 0.9 | 188 | 271 | 302 | 429 | B17-T-F2 | A.37 |
| 1.0 | 266 | 300 | 333 | 333 | T8-2 | A.17 |
| 2.0 | 28 | 28 | 28 | 28 | T8-1A | A.12 |
| 4.0 | 3 | 3 | 3 | 3 | T8-1 | A.11 |

† *All tests conducted with* $R_\varepsilon$ *= -1 and* $\dot{\varepsilon}$*= 0.5%/s*

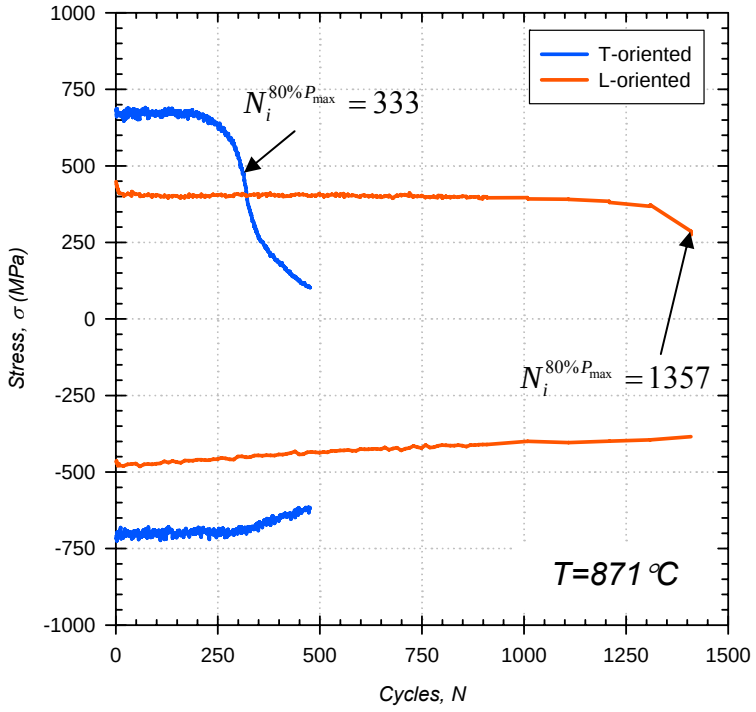


***Figure 4.1:*** *Stress histories for L and T-oriented DS GTD-111 at* $\Delta\varepsilon$*=1.0% and T=871°C (1600°F). For each case* $R_\varepsilon = -1$ *and* $\dot{\varepsilon} = 0.5\%/s$ .

The stress histories for L- and T-oriented DS GTD-111 subjected to a total (or mechanical) strain range ($\Delta\varepsilon$) of 1.0% are shown in Fig. 4.1. In this case, the fatigue life until fracture ($0\%P_{max}$) of the L-oriented specimen outlasted that of the T-oriented

specimen by nearly a factor of three. The discrepancy in the cyclic softening behavior of the two materials leading up to final failure is significant. While the L-oriented sample fractures suddenly, the T-oriented sample exhibits a gradual loss in load carrying capability. This gradual loss indicates that more than one crack may have initiated and failure was due to the propagation of the dominant one(s). This is plausible since T-oriented specimens contain numerous grain boundaries and weaker interdendritic channels transverse to the stress axis. These grain boundaries and interdendritic channels represent potential sites of crack initiation that are not present in L-oriented DS GTD-111. From Tables 4.1 and 4.2, it can be observed that the strain-controlled, strain lives of L-oriented specimens exceeded those of T-oriented samples by between a factor of 2.4 and 3.6.

Since the objective of the current investigation is to quantify the mechanisms of crack initiation, a minimum length scale of one grain must be considered. Allowing cracks longer than this scale to propagate may introduce unwanted variability in fatigue life estimates. Accordingly, each test was carried out until a crack having a desired length ($a_i$) between 0.50-2.00 *mm* (0.02-0.08 *in*) was initiated. This length is also very appropriate for crack formulation and early propagation investigations. These crack sizes are generally close to the lower detection limit of nondestructive evaluation (NDE) techniques used to maintain power generation components of Ni-base superalloys.

The estimated reduction in area due the presence of an initiated crack can be calculated based on the form of the crack: (1) a near-elliptical shape at the surface having a 2:1 aspect ratio, (2) a collection of short cracks spanning the outer boundary of the specimen, or (3) a collection of small subsurface microcracks or microvoids. In either

situation the area reduction could possibly range from 20 and 40%. Using the smaller end of this range, the load decrease is proportional to the area reduction, i.e.,

$$\frac{P_i}{P_0} = \frac{A_i}{A_0} = 0.20 \tag{4.1}$$

Thus the fatigue cycle in which the material exhibited a 20% drop in the maximum initial stabilized tensile load, denoted as $80\%P_{i,max,}$ was used as the criterion for defining crack "initiation" in the gage section of the specimen, i.e., $N = N_i$

A plot of $\Delta\varepsilon$ versus $N_i$ for the isothermal benchmark conditions of 871°C, $R_\varepsilon$ = -1, $\dot{\varepsilon} = 0.5\%/s$ under continuous cycling is shown in Fig. 4.2. Crack initiation lives of L-oriented material exceed those of the T-oriented material at 871° by a factor of 3.4.

The plastic component of the strain range, $\Delta\varepsilon_{pl}$, is determined as the difference between the mechanical strain range and the elastic component of the mechanical strain range, i.e.,

$$\Delta\varepsilon_{pl} = \Delta\varepsilon_m - \Delta\varepsilon_{el} = \Delta\varepsilon_m - \frac{\Delta\sigma}{E_i}, \tag{4.2}$$

where $\Delta\sigma$ is the stress range ($\sigma_{max}$ - $\sigma_{min}$), determined from stabilized stress history data. Table 4.3 contains the plastic and elastic strain ranges for each of the continuous cycling tests conducted at 871°C. The orientation of the material is given in the second-to-last column. The decomposed elastic and plastic-strain versus life curves are shown in Fig. 4.2. At high mechanical strain ranges ($\Delta\varepsilon_{el} + \Delta\varepsilon_{pl} \geq 0.01$), the plastic portion of strain

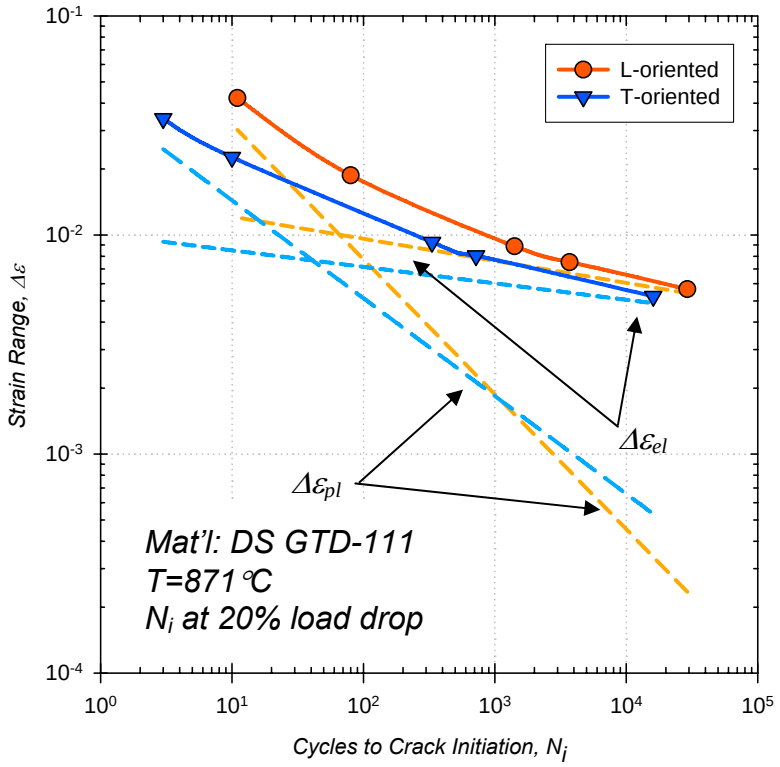


***Figure 4.2:*** *Strain-life curves of crack initiation lives of L and T-oriented DS GTD-111 at T=871°C (1600°F). For each case* $R_\varepsilon = -1$ *and* $\dot{\varepsilon} = 0.5\%/s$.

range is significantly higher than that obtained for low $\Delta\varepsilon_m$, and vice versa for low mechanical strain ranges. In the two cases for which $\Delta\varepsilon_{pl}$ is near the strain resolution of the extensometer, the value less than 0.01% is stated. In general, the crack initiation life, $N_i$, of each material orientation decreased with increasing $\Delta\varepsilon_{pl}$ or $\Delta\varepsilon_{el}$. The experimentally-measured crack initiation lives of both L- and T-oriented DS GTD-111 specimens follow the classical strain-life relation, i.e.,

$$\frac{\Delta\varepsilon_m}{2} = \frac{\sigma'_f}{E}\left(2N_i\right)^b + \varepsilon'_f\left(2N_i\right)^c, \tag{4.3}$$

***Table 4.3:*** *Crack Initiation life of L and T-oriented DS GTD-111 at 871 °C*

| Plastic Strain Range, $\Delta\varepsilon_{pl}$ (%) | Elastic Strain Range, $\Delta\varepsilon_{el}$ (%) | Crack Initation Life, $N_i$ | Specimen ID (Orientation) | Figure |
|---|---|---|---|---|
| < 0.01 | 0.50 | 29159 | L8-3 (L) | A.14 |
| 0.01 | 0.79 | 3699 | GTD-CC04 (L) | A.3 |
| 0.08 | 0.82 | 987 | A27-L-F6 (L) | A.38 |
| 0.03 | 0.97 | 1357 | GTD-CC05 (L) | A.2 |
| 0.80 | 1.20 | - | GTD-CC10 (L) | A.1 |
| 0.99 | 1.01 | 103 | B17-L-F5 | A.48 |
| 2.810 | 1.19 | 11 | L8-2A (L) | A.10 |
| < 0.01 | 0.50 | 16069 | T8-2A (T) | A.13 |
| 0.07 | 0.73 | 598 | T8-5 (T) | A.25 |
| 0.22 | 0.68 | 271 | B17-T-F2 (T) | A.37 |
| 0.22 | 0.78 | 300 | T8-2 (T) | A.17 |
| 1.46 | 0.54 | 28 | T8-1A (T) | A.12 |
| 2.87 | 1.13 | 3 | T8-1 (T) | A.11 |

† *All tests conducted with* $R_\varepsilon$ *= -1 and* $\dot{\varepsilon}$ *= 0.5%/s*

where $\sigma'_f$ is the fatigue strength coefficient, $E$ is the elastic modulus, $b$ is the fatigue strength exponent (also referred to as Basquin's exponent), $\varepsilon'_f$ is the fatigue ductility coefficient, and $c$ is the fatigue ductility exponent. The first term in Eq. (4.3) represents elastic-strain life relation, while the second term represents the plastic-strain life relation. To determine these material properties, which are listed in Table 4.4, power law regression analyses were used for both components. The transition crack initiation life, $N_i^{(t)}$, is defined as the life corresponding to $\Delta\varepsilon_{el} = \Delta\varepsilon_{pl}$. Using Eq. (4.3), the transition lives and mechanical strain ranges were determined as: $N_i^{(t)} = 65$, $\Delta\varepsilon_m$ = 1.0% (L-oriented), and $N_i^{(t)} = 38$, $\Delta\varepsilon_m$ = 0.7%, (T-oriented). These low transition life values are typical of higher strength alloys.

***Table 4.4:*** *Fatigue constants for DS GTD-111 at 871°C (1600°F) ($R_\varepsilon$=-1)*

| Orientation | Elastic | | | Plastic | |
|---|---|---|---|---|---|
| | E (GPa) (Msi) | $\sigma'_f$ (GPa) (Msi) | b | $\varepsilon'_f$ (m/m) | c |
| L | 96 | 2.74 | -0.10 | 0.17 | -0.62 |
| | 14 | 0.40 | | | |
| T | 153 | 2.92 | -0.08 | 0.06 | -0.46 |
| | 22 | 0.42 | | | |

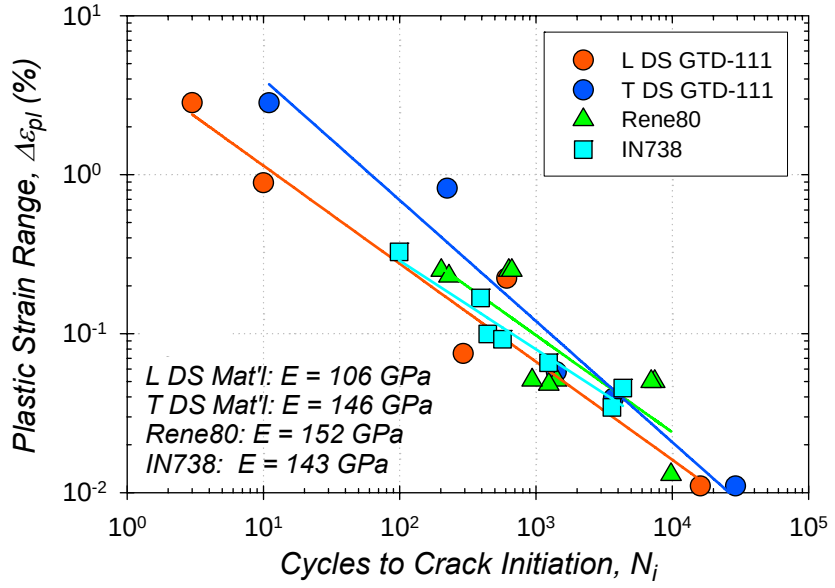


***Figure 4.3:*** *Comparison of plastic strain crack initiation lives of DS GTD-111 with PC Ni-base superalloys at 871°C (1600°F). For each case* $R_\varepsilon = -1$ *and* $\dot{\varepsilon} = 0.5\%/s$.

The plastic strain range versus crack initiation life curves of DS GTD-111 are compared for two polycrystalline Ni-base superalloys in Fig. 4.3. The close proximity of the data points between individual curves indicates that the difference in fatigue crack initiation lives of L and T orientations is mostly due to the elastic response of the material

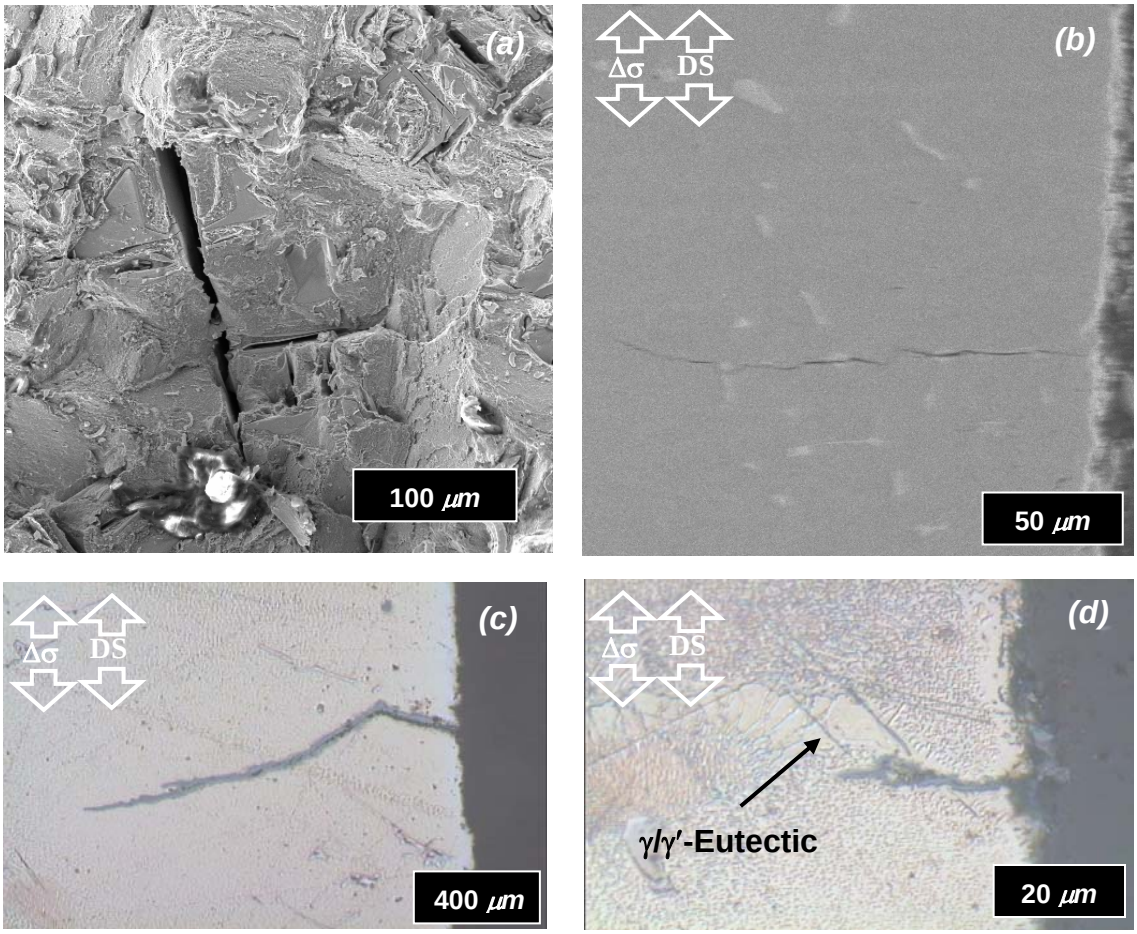


***Figure 4.4:*** *Strain range effect on crack initiation of L-oriented DS GTD-111 under (a,b) $\Delta\varepsilon$ = 0.5% and (c,d) $\Delta\varepsilon$ = 0.9%. For each case $R_\varepsilon$=-1, T=871°C, and $\dot{\varepsilon} = 0.5\%/s$. Images are of (a) fracture surface and (b-d) cross section of test samples.*

and not the inelastic properties. At the benchmark temperature, the elastic modulus of the T-oriented material exceeds that of L by a factor of 1.4.

Microscopic examination of fatigued specimens tested according to Table 4.3 reveals the underlying mechanisms responsible for damage in L- and T-oriented DS GTD-111 at 871°C. Microstructures of both materials tested at lower strain ranges and shown in Figs. 4.4 and 4.5 verify that the cracks form at the surface. For each case shown, $\Delta\varepsilon_{pl} < 0.10\%$. In this early stage of fracture, subsurface carbides influence the

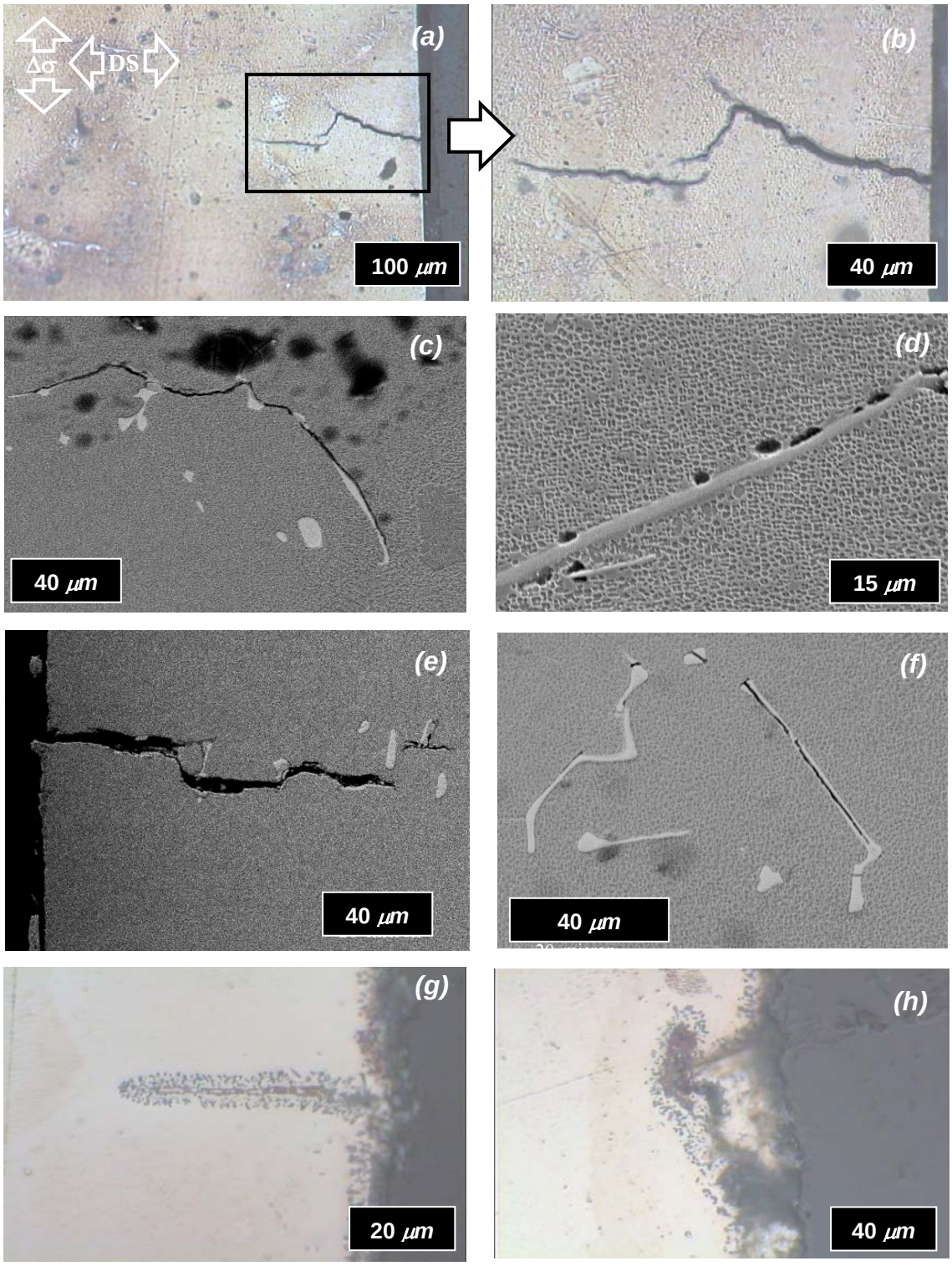


***Figure 4.5:*** *Strain range effect on crack initiation of T-oriented DS GTD-111 under (a-f) $\Delta\varepsilon$ = 0.5% and (g,h) $\Delta\varepsilon$ = 0.8%. For each case $R_\varepsilon$=-1, T=871°C, and $\dot{\varepsilon} = 0.5\%/s$.*

direction of propagation. This is evidenced by (1) the presence of carbides along the fracture surfaces and crack planes (Fig. 4.4a,b and Fig. 4.5e,h), and (2) the tortuous morphology of the fracture surfaces (Fig. 4.4c and Fig. 4.5a,b,e). Figure 4.4d shows a surface crack that was influenced by a eutectic of $\gamma/\gamma'$.

Inclusions that were not in the vicinity of the external specimen surface were also determined to be involved in the damage process by way of two separate mechanisms: (1) brittle cracking of carbides and (2) debonding at metal/carbide interfaces. Figure 4.5f shows a MC-type carbide inclusion that cracked internally. A collection of microcracks forming along the edge of carbides is shown in Fig. 4.5c,d. In either case, adjacent cracks coalesce and form large subsurface cracks transverse to the loading axis of the material. With increasing size, they lower the overall stress-carrying capability of the material and eventually coalesce with the external surface or cracks that have already been initiated at the surface. This could be the reason for the morphology of the cracks shown in Fig. 4.5b. These cracks are most likely connected on other viewing planes above or beneath the one illustrated.

Adjacent surface initiated cracks were typically separated by large distances on the order of a millimeter or more. Surface cracks that occurred in the gage section, consequently, were visually enumerable. It is evident that by decreasing the mechanical strain range from 4.0% to 0.5%, $N_i$ is increased; therefore, the total time at which a specimen is subjected to the elevated temperature environment is increased, accordingly. The samples shown in Figs. 4.4b and 4.5b were exposed to 871°C for 16.1 and 8.9 hours, respectively. Of the continuously cycled specimens fatigued at 871°C, those conducted at low mechanical strain ranges represent the most favorable opportunity for extensive

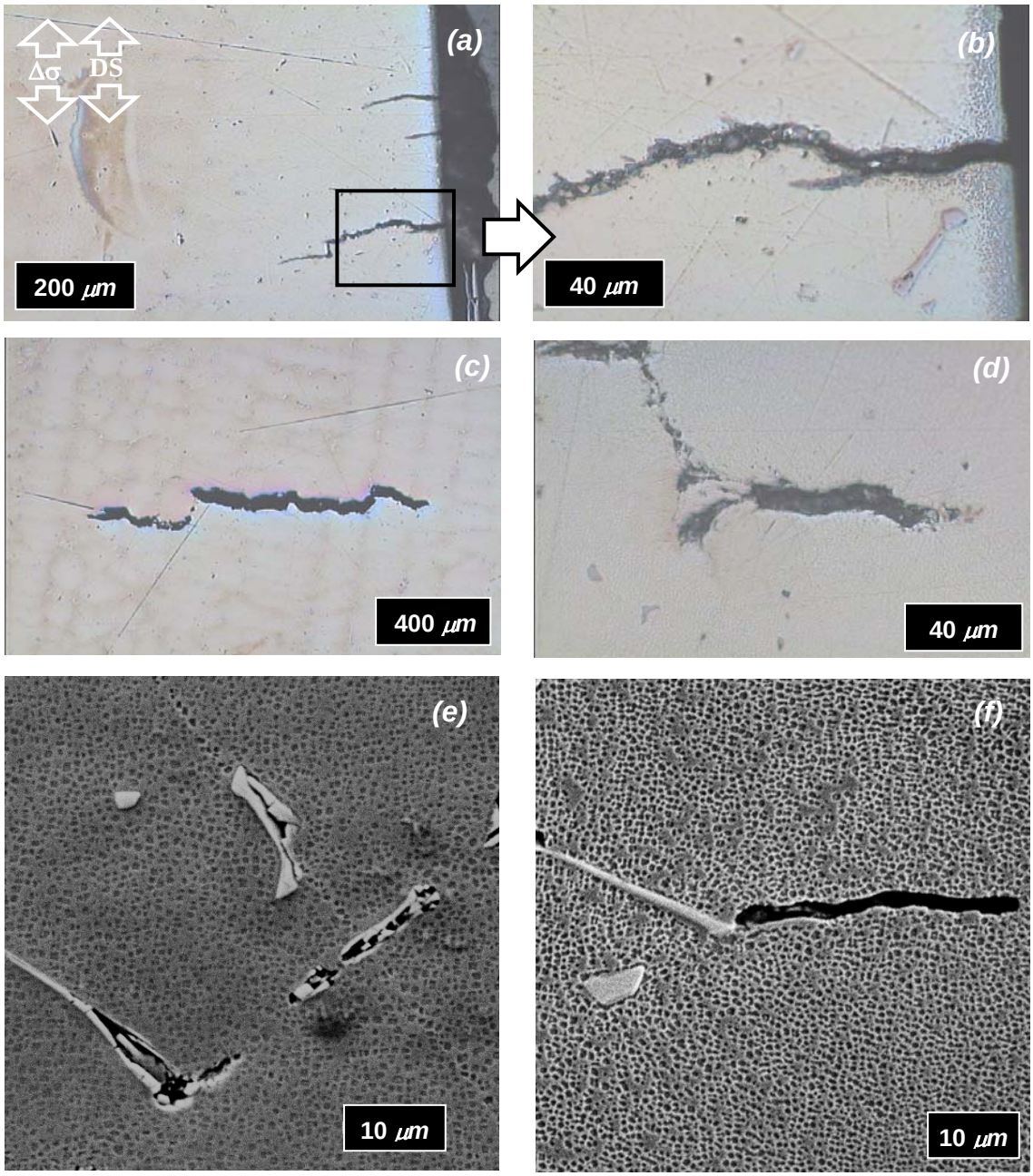


***Figure 4.6:*** *Strain range effect on crack initiation of L-oriented DS GTD-111 under (a-d) $\Delta\varepsilon$ = 2.0% and (e,f) $\Delta\varepsilon$ = 4.0%. For each case $R_\varepsilon$=-1, T=871℃, and $\dot{\varepsilon} = 0.5\%/s$.*

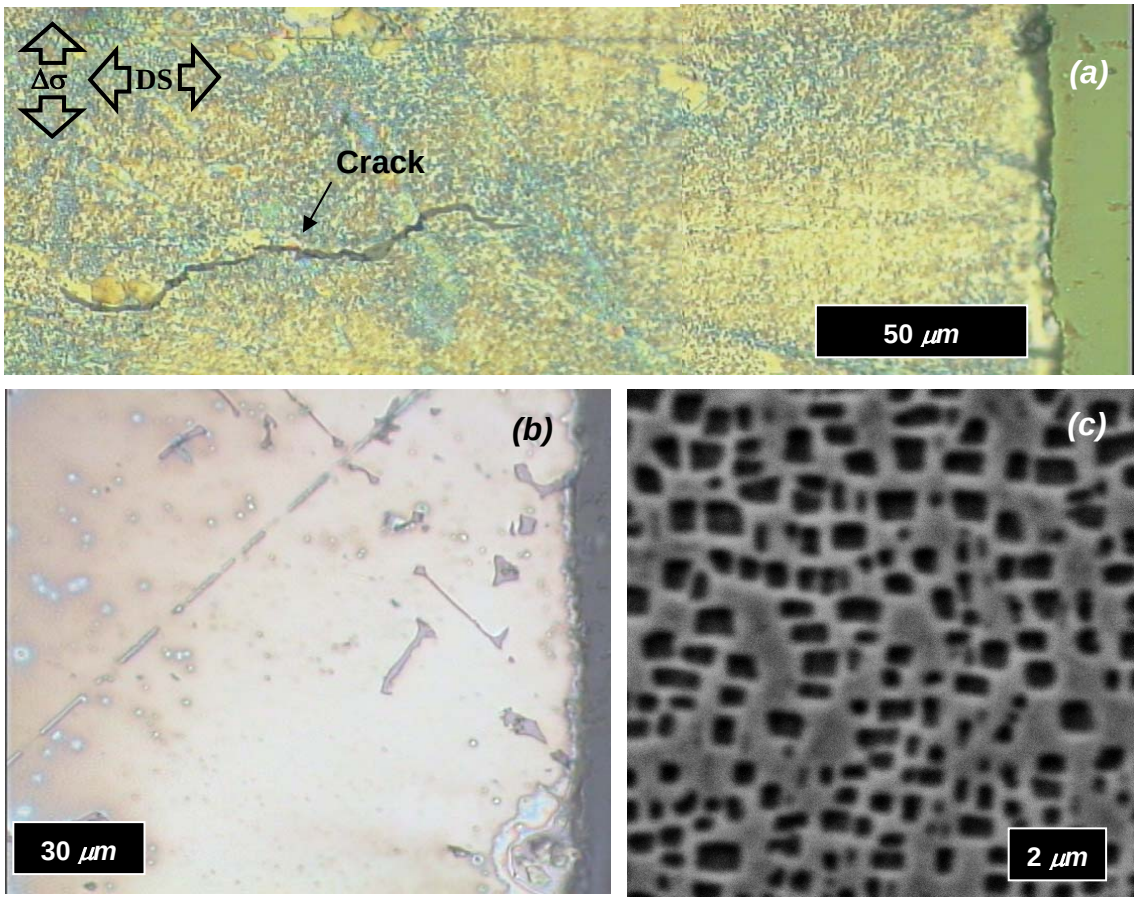


***Figure 4.7:*** *Strain range effect on crack initiation of T-oriented DS GTD-111 under (a) $\Delta\varepsilon$ = 0.9% and (b,c) $\Delta\varepsilon$ = 2.0%. For each case $R_\varepsilon$=-1, T=871°C, and $\dot{\varepsilon} = 0.5\%/s$.*

oxide penetration to occur. In these cases, and even those conducted at higher plastic strain ranges, only limited oxide-assisted surface cracking occurred.

Figures 4.6 and 4.7 show microstructures of L- and T-oriented specimens, respectively, cycled at $\Delta\varepsilon_{pl}$ > 0.22%. In each case subsurface cracking is facilitated by the presence of carbide inclusions and eutectics. Aided by the mismatch in elastic properties between the matrix and the carbides, shear stresses occurring at the metal/carbide interface contribute to the stress amplification. High stresses localize in and around the vicinity of the carbide, resulting in intense plastic deformation and slip banding. Depending on the orientation of the inclusion particle, these slip bands can cut

across the particle (as in Fig. 4.6e) or lead to microvoids at its interface (as in Fig. 4.6f). The linkage of microvoids leads to microcracks that further raise the local stress concentration. Aside from the damage that is localized at these inclusions, the microstructure of the specimen is virtually undisturbed. At very high plastic strain ranges, cracks formed at metal/carbide interfaces and carbides coalesce rapidly and cause material failure prior to significant contribution from surface oxidation. Precipitate phase particles maintain their cuboidal shape and distribution (as in Fig. 4.7c). For the variety of strain ranges considered, the oxidation penetration depth typically never exceeded 10 $\mu m$.

Based on the observation that both the final (a) surface-initiated and (b) subsurface-initiated fracture surfaces contained inclusion particles demonstrates that inclusion-assisted damage was the primary mechanism promoting crack initiation in L- and T-oriented DS GTD-111 at 871°C with $R_\varepsilon$ = -1, $\dot{\varepsilon} = 0.5\%/s$ under continuous cycling. Furthermore, at the lowest strain range considered, the limited presence of flat surface cracks indicated that oxidation played a minor role in crack initiation and early propagation. No observations can be made concerning mean stress effects and strain ratio effects since each of those variables was held constant for this series of experiments.

## *4.2 Mean Strain Effects*

Components seldom experience completely reversed loading; some mean stress or mean strain is usually present. The effect of mean strain was determined for L-oriented DS GTD-111 using a series of completely reversed ($R_\varepsilon$ = *-1)* and zero-to-tension ($R_\varepsilon$ = *0)* strain-controlled, low cycle fatigue tests at temperatures levels of 760°C and 871°C. The

results of each of these experiments are given in Table 4.5. At 871°C, the result of increasing $R_\varepsilon$ from -1 to 0 is a tensile shift of the strain range and thus an increase of the mean strain. Even though the strain range is unchanged, the result is higher peak tensile stresses. In cases where the plastic strain range was significant (i.e., $\Delta\varepsilon_{pl} > 0.10\%$), the material exhibits cyclic strain mean stress relaxation. The rate of decrease in mean stress progressively diminishes, typically within the first 100 reversals at $\Delta\varepsilon = 0.8\%$. The cyclic yield strength of the material does not change.

Due to the slight anisotropy of the tensile and compressive yield behavior of the material evident at temperatures less than or equal to 871°C, completely-reversed cases exhibit compressive mean stresses between 0 *MPa* and 100 *MPa* (14 *ksi*). As the strain ratio is increased to zero, however, the resulting mean stresses are typically tensile and the number of cycles to crack initiation is affected. Both $\sigma_m$ and $N_i$ were compared after the initial mean stress relaxation had occurred in each case. For example, at $\Delta\varepsilon = 0.8\%$, the difference in the mean stress for the two strain ratios considered was 48 *MPa* (6.96 *ksi*). This lead to a reduction of $N_i$ by a small factor of 1.23. At 760°C, the mean stress in the zero-to-tension case converged toward a tensile stress level that was 312 *MPa* (45 *ksi*) larger than the completely reversed case. The effect on the crack initiation life was a significant reduction by a factor of 2.5.

Strain-life and stress-life diagrams are used to distinguish the mean stress/strain effects on fatigue life. Figure 4.8 contains the strain (Fig. 4.8a) and stress ranges (Fig. 4.8b) versus crack initiation life diagrams for this series of experiments. Responses for both cases could be fit with the "$\Delta\varepsilon_m$-$N_i$" power law curves. Points corresponding to $R_\varepsilon = 0$ typically fall slightly beneath the "$R_\varepsilon$ = -1" curve, thus indicating that tensile mean

strain shortens crack initiation life. Since the material exhibits more cyclic mean stress relaxation at the higher temperature, the reduction of life was, therefore, less significant at the higher temperature.

***Table 4.5:*** *Comparison of mean strain effects of L-oriented DS GTD-111*

| Temperature (°C) | Temperature (°F) | Strain Ratio, $R_\varepsilon$ | Total Strain Range, $\Delta\varepsilon_m$ (%) | Plastic Strain Range, $\Delta\varepsilon_{pl}$ (%) | Elastic Strain Range, $\Delta\varepsilon_{el}$ (%) | Mean Stress, $\sigma_m$ (MPa) | Crack Initation Life, $N_i$ | Specimen ID (Orientation) | Figure |
|---|---|---|---|---|---|---|---|---|---|
| 760 | 760 | -1 | 0.8 | 0.04 | 0.76 | -2 | 19403 | B21-L-F3 (L) | A.47 |
| 760 | 1400 | -1 | 1.0 | 0.02 | 0.98 | -91 | 10224 | B17-L-F6 | A.50 |
| 760 | 1400 | -1 | 2.0 | 0.32 | 1.68 | 21 | 105 | L8-3A (L) | A.15 |
| 760 | 1400 | 0 | 1.0 | 0.07 | 0.93 | 221 | 4114 | B21-L-F2 (L) | A.46 |
| 871 | 1600 | -1 | 0.5 | ~ 0.01 | 0.5 | -42 | 29159 | L8-3 (L) | A.14 |
| 871 | 1600 | -1 | 0.8 | 0.01 | 0.79 | -18 | 3699 | GTD-CC04 (L) | A.3 |
| 871 | 1600 | -1 | 0.9 | 0.08 | 0.82 | -49 | 987 | A27-L-F6 (L) | A.38 |
| 871 | 1600 | -1 | 1.0 | 0.03 | 0.97 | -34 | 1357 | GTD-CC05 (L) | A.2 |
| 871 | 1600 | -1 | 2.0 | 0.99 | 1 | 0 | 103 | B17-L-F5 | A.48 |
| 871 | 1600 | 0 | 0.8 | 0.05 | 0.75 | 30 | 2990 | A27-L-F12 (L) | A.40 |
| 871 | 1600 | 0 | 1.2 | 0.32 | 0.88 | -6 | 454 | B21-L-F1 (L) | A.44 |

*All tests conducted at* $\dot{\varepsilon}$ *= 0.5%/s*

Mean stress has a weak effect of on life. The Goodman correlation was used to determine the equivalent completely reversed stress, $\sigma_{ar}$, for each of the tests. The $\sigma_{ar}$ - $N_i$ diagram (Fig. 4.8b) indicates that the Goodman relation over-corrects the data. Life correlates better with $\Delta\varepsilon_m$.

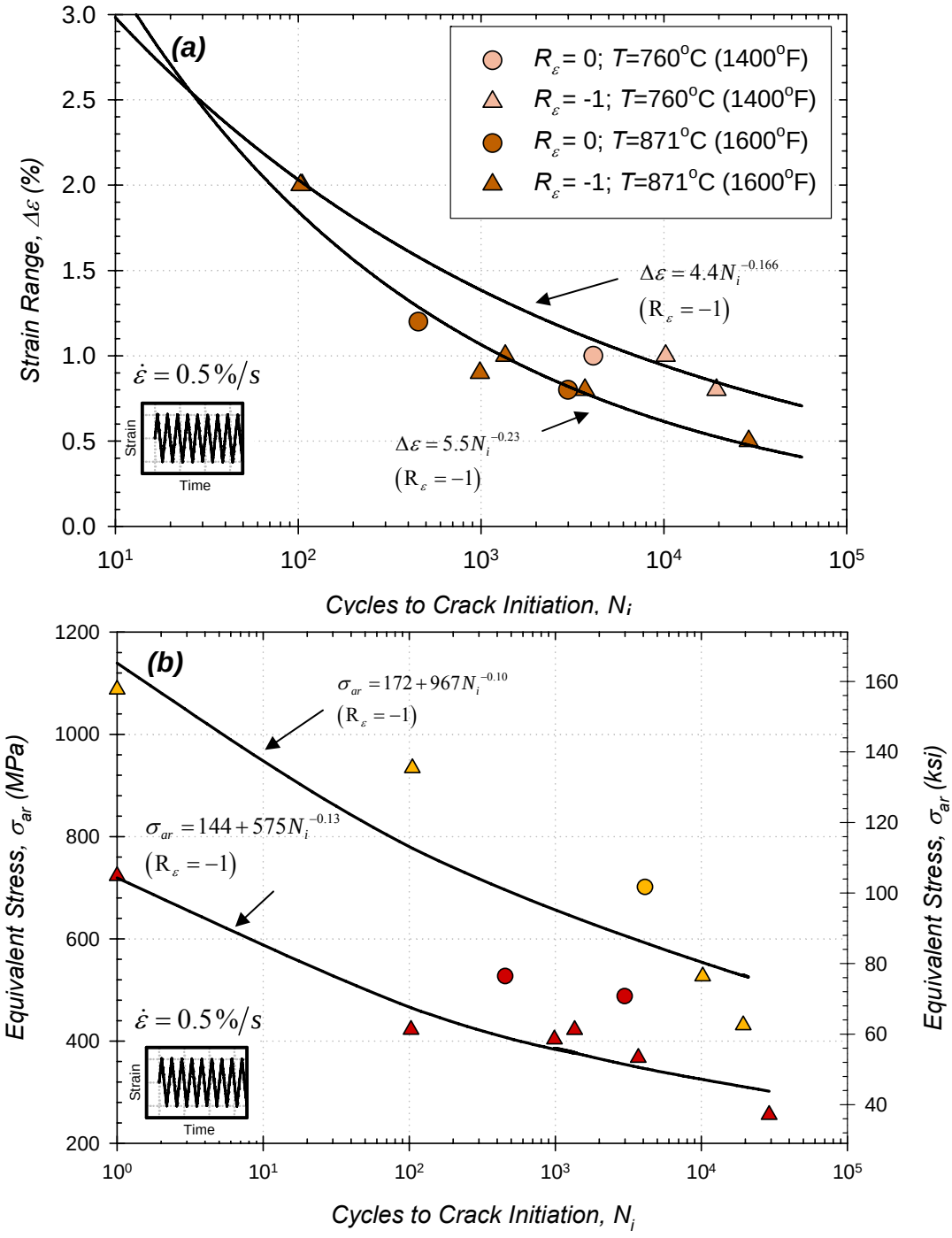


***Figure 4.8:*** *Mean strain effects on crack initiation life of L-oriented DS GTD-111 with $\dot{\varepsilon} = 0.5\%/s$. (a) Strain range versus life diagram and (b) equivalent completely-reversed stress versus life diagram.*

***Table 4.6:*** *Comparison of strain rate dependence of DS GTD-111.*

| Temperature (°C) | Temperature (°F) | Strain Rate (%/s) | Total Strain Range, $\Delta\varepsilon_m$ (%) | Plastic Strain Range, $\Delta\varepsilon_{pl}$ (%) | Elastic Strain Range, $\Delta\varepsilon_{el}$ (%) | Crack Initation Life, $N_i$ | Specimen ID (Orientation) | Figure |
|---|---|---|---|---|---|---|---|---|
| 982 | 1800 | 0.01 | 1.0 | 0.48 | 0.52 | 169 | A27-L-F13 (L) | A.42 |
| 982 | 1800 | 0.5 | 0.8 | 0.27 | 0.53 | 912 | L8-9A (L) | A.36 |
| 982 | 1800 | 0.5 | 1.0 | 0.43 | 0.57 | 562 | L8-4A (L) | A.19 |
| 982 | 1800 | 0.5 | 1.0 | 0.35 | 0.65 | 509 | L8-8A (L) | A.34 |
| 982 | 1800 | 0.5 | 2.0 | 1.19 | 0.81 | 112 | L8-8 (L) | A.35 |
| 982 | 1800 | 0.01 | 1.0 | 0.55 | 0.45 | 52 | A27-T-F2 (T) | A.43 |
| 982 | 1800 | 0.5 | 0.8 | 0.27 | 0.53 | 219 | T8-4 (T) | A.24 |
| 982 | 1800 | 0.5 | 1.0 | 0.42 | 0.58 | 207 | T8-3A (T) | A.18 |

*All tests conducted with $R_\varepsilon$ = -1*

If the damage mechanisms that lead to crack are unchanged, then increasing the test temperature beyond 871°C will most likely lead to a closer proximity of lives of samples fatigued at $R_\varepsilon = 0$ and -1. Conversely, lowering the temperature beyond 760°C will increase strain ratio effects. Figure 4.9 shows that an L-oriented sample fatigue-tested from zero-to-tension exhibits the same modes of damage as a completed-reversed sample. Crack initiation occurred by way of formation of cracking at inclusion particles. The fracture path is tortuous and exhibits a very thin oxide layer.

## *4.3 Frequency Effects*

The effect of strain rate, $\dot{\varepsilon}$, was investigated for L- and T-oriented DS GTD-111 using a series of isothermal tests conducted at 982°C. Two strain rates were considered, $\dot{\varepsilon} = 0.50\%/s$ and $\dot{\varepsilon} = 0.01\%/s$, corresponding to cycle times of 4*s* and 180*s*,

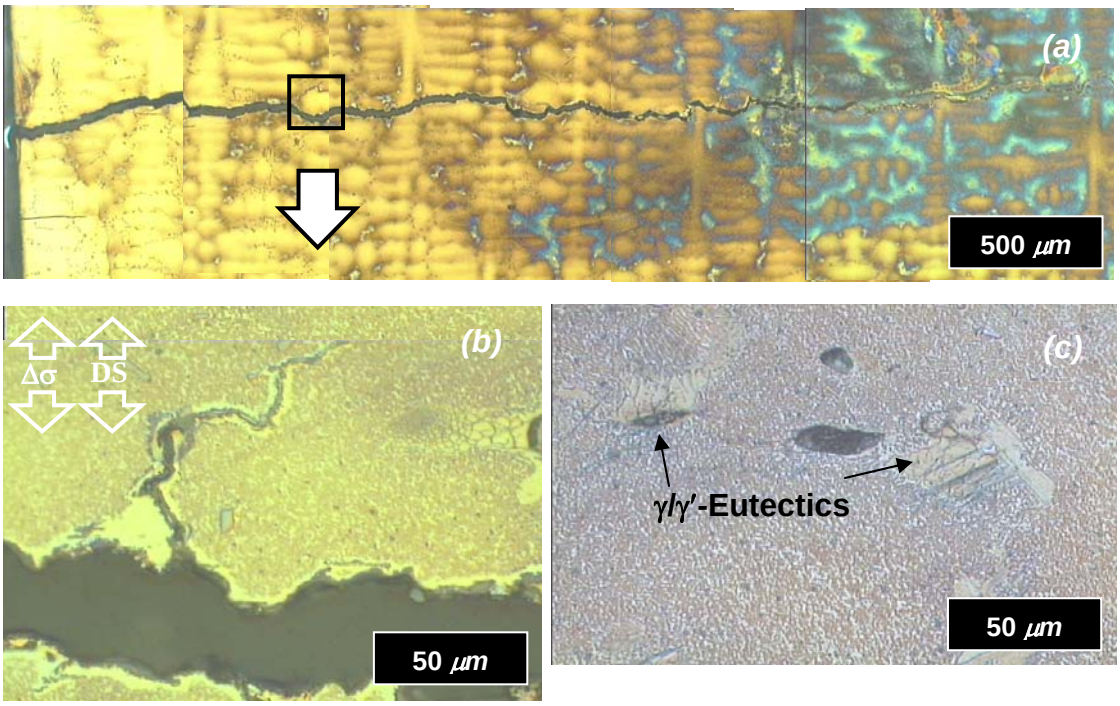


***Figure 4.9:*** *Crack initiation of L-oriented DS GTD-111 under $\Delta\varepsilon$ = 0.80%, $R_\varepsilon$ = 0, T=871°C, and $\dot{\varepsilon} = 0.5\%/s$. Images are of (a) the main crack, (b) a branched crack from the main crack, and (c) microcrack nucleation at eutectics.*

respectively. The temperature 982°C was used so that the effects of surface oxidation would be more significant than the effect at the baseline temperature of 871°C. The results of these experiments are given in Table 4.6.

Increasing the cycle time from 4 *s* to 180 *s* causes DS GTD-111 to exhibit additional inelastic deformation when tested at the same $\Delta\varepsilon_m$. The slower strain rate facilitates time-dependent generation and motion of dislocations along cube slip systems that are active in dual-phase Ni-base superalloys above 871°C. Damage in the forms of slip bands and microcracks near carbides accommodate lower flow stress during cycling. As shown in Fig. 4.10, the stress range is significantly decreased at the lower strain rate.

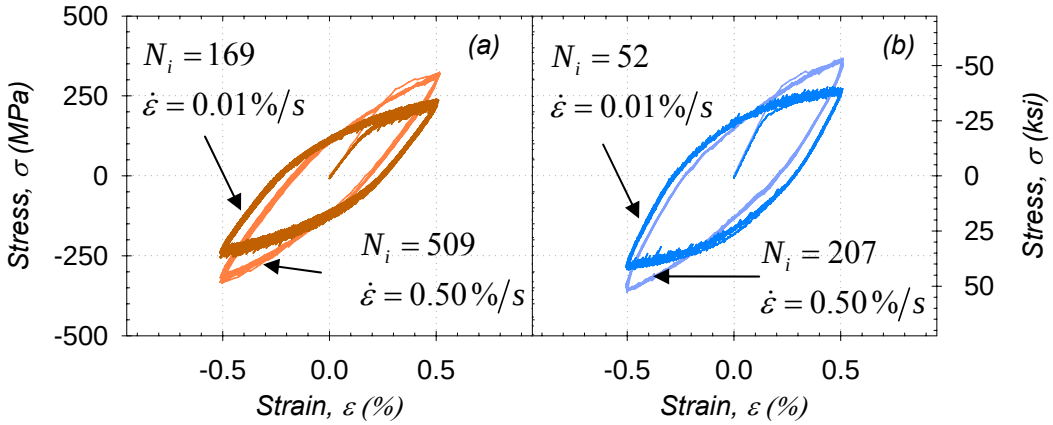


***Figure 4.10:*** *Initial hysteresis loops of (a) L-oriented and (b) T-oriented DS GTD-111 subjected to dissimilar strain rates with $R_\varepsilon$=-1 and T=982°C.*

Accordingly, the proportion of cyclic elastic strain range decreases and cyclic plastic strain increases. The elastic modulus, as expected, remains unchanged for the two rates.

The $\Delta\varepsilon$-$N_i$ curves for fast and slow strain rates are compared in Figure 4.11. It is observed that for either orientation, an increase of 25% in the plastic strain range corresponds to a significant reduction in crack initiation life. It should be noted that life data from the slow strain rate tests does not correlate well with $\Delta\varepsilon_{pl}$-$N_i$ curves of fast strain rate experiments either. This indicates that there is a crack initiation mechanism in addition to the inclusion-assisted crack initiation mechanism that lowers the service life of the material.

Figures 4.12 and 4.13 show the microstructures of fatigue-tested L- and T-oriented DS GTD-111, respectively, under the slow strain rates considered. In the L-oriented sample, the condition of the specimen is similar to that obtained from high strain rate experiments. The main difference is that more subsurface voids at inclusions and eutectics are present. The thickness of the accumulated oxidation layer is similar. In the

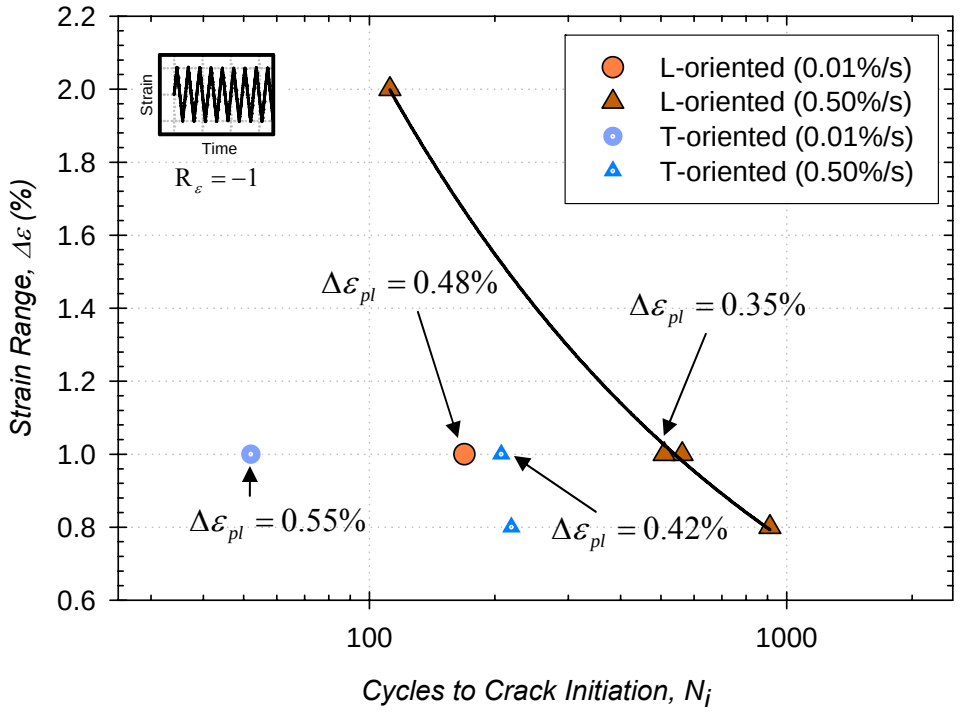


***Figure 4.11:*** *Strain rate effects on the crack initiation life of L- and T-oriented DS GTD-111 with $R_\varepsilon$=-1.*

slowly-cycled T-oriented sample, the crack formed and propagated along a grain boundary. As shown in Fig. 4.13, the crack arrested once it reached a grain boundary.

At the slow strain rate, there was only slight preferential oxidation of near-surface inclusions. Comparatively, at the higher strain rate of 0.5%/s, even carbides in the vicinity of the surface are more likely to participate in the crack incubation and early propagation process. This is illustrated in Fig. 4.14. Under slow strain rates, subsurface eutectics and carbides are favorable sites for crack initiation and coalescence.

## *4.4 Temperature Effects*

Continuous cycling (CC), mechanical strain-controlled tests were conducted at temperatures above and below the benchmark temperature (871°C), with $\Delta\varepsilon_m$ ranging

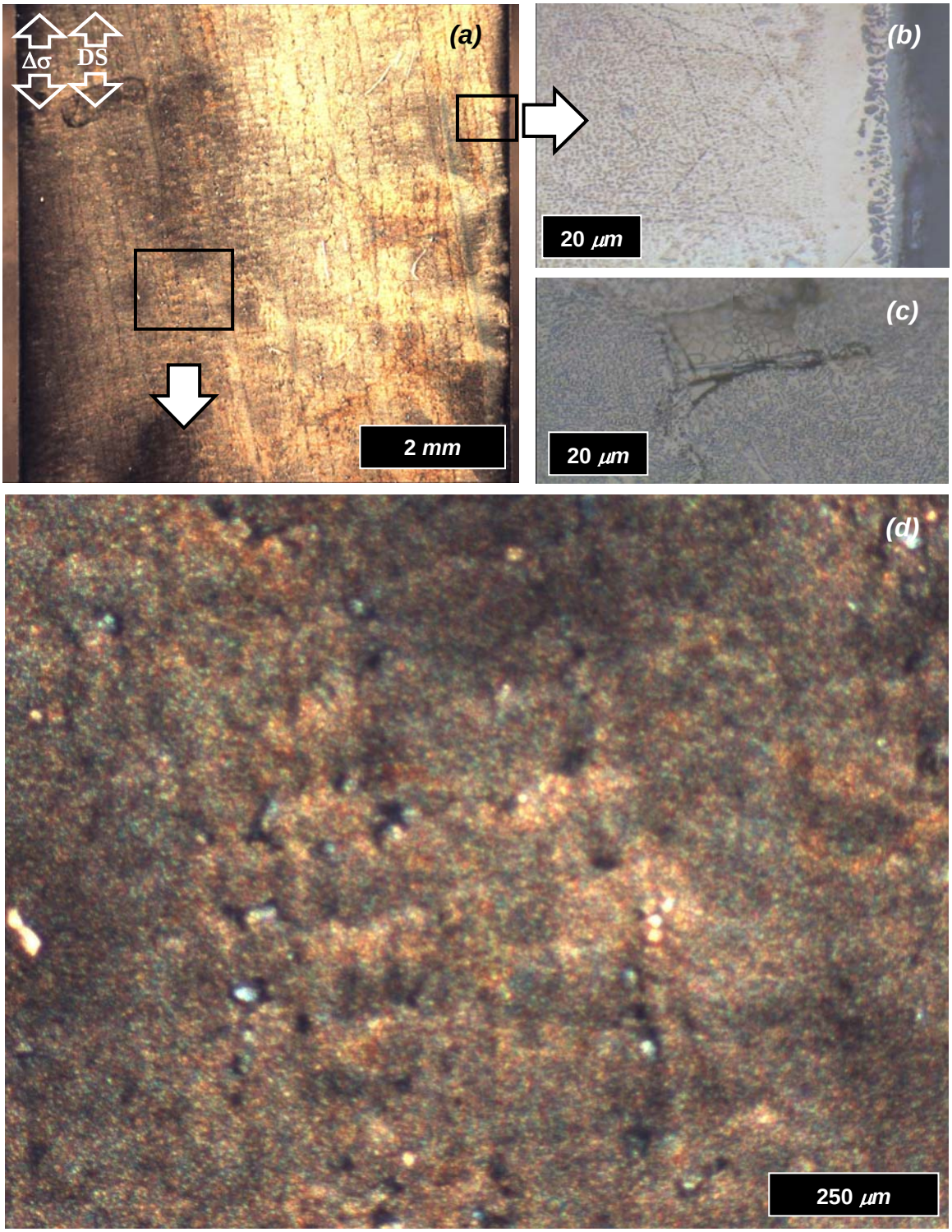


***Figure 4.12:*** *Crack initiation of continuously cycled L-oriented DS GTD-111 under* $\dot{\varepsilon} = 0.01\%/s$, $R_\varepsilon$*=-1,* $\Delta\varepsilon$*=1.0% and T=982°C. Images are of the (a) entire specimen cross section, (b) expanded view of surface oxidation, (c) microcrack nucleation at a eutectic, and (d) expanded view of microcracking at dendritic cores.*

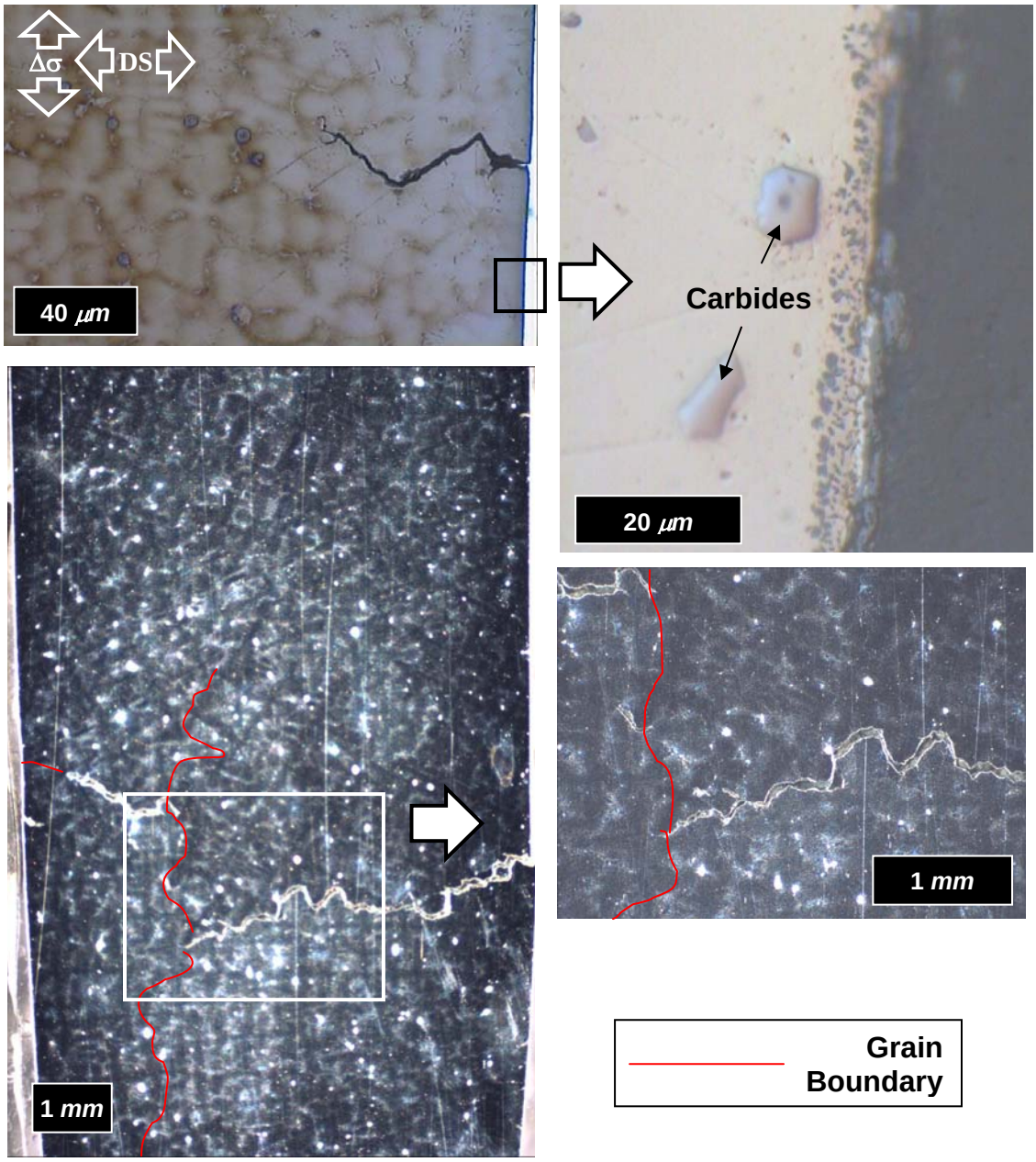


***Figure 4.13:*** *Effect of strain rate on crack initiation life of continuously cycled T-oriented DS GTD-111 under* $\dot{\varepsilon} = 0.01\%/s$. *For this case* $R_\varepsilon$*=-1 and T=982°C.*

from 0.5% to 2.0%. The isothermal temperatures ranged from 427°C (800°F) to 1038°C (1900°F) for the L-oriented material and 649°C (1200°F) to 1038°C for the T-oriented material. The crack initiation lives and decomposed plastic and elastic strain ranges from

these experiments at 871°C on L- and T-oriented DS GTD-111 are listed in Tables 4.7 and 4.8, respectively.

***Table 4.7:*** *Crack Initiation life of L-oriented DS GTD-111 at various temperatures*

| Temperature (°C) | Temperature (°F) | Total Strain Range, $\Delta\varepsilon_m$ (%) | Plastic Strain Range, $\Delta\varepsilon_{pl}$ (%) | Elastic Strain Range, $\Delta\varepsilon_{el}$ (%) | Crack Initation Life, $N_i$ | Specimen ID (Orientation) | Figure |
|---|---|---|---|---|---|---|---|
| 427 | 800 | 2.0 | 0.55 | 1.45 | 30 | L8-4 (L) | A.16 |
| 649 | 1200 | 1.0 | 0.09 | 0.91 | 14915 | A27-L-F10 (L) | A.52 |
| 649 | 1200 | 1.5 | 0.05 | 1.45 | 394 | A27-L-F5 (L) | A.51 |
| 760 | 1400 | 0.8 | 0.04 | 0.76 | 19403 | B21-L-F3 (L) | A.47 |
| 760 | 1400 | 1.0 | 0.02 | 0.98 | 10224 | B17-L-F6 | A.50 |
| 760 | 1400 | 2.0 | 0.32 | 1.68 | 105 | L8-3A (L) | A.15 |
| 871 | 1600 | 0.5 | < 0.01 | 0.50 | 29159 | L8-3 (L) | A.14 |
| 871 | 1600 | 0.8 | 0.01 | 0.79 | 3699 | GTD-CC04 (L) | A.3 |
| 871 | 1600 | 0.9 | 0.08 | 0.82 | 987 | A27-L-F6 (L) | A.38 |
| 871 | 1600 | 1.0 | 0.03 | 0.97 | 1357 | GTD-CC05 (L) | A.2 |
| 871 | 1600 | 2.0 | 0.80 | 1.20 | - | GTD-CC10 (L) | A.1 |
| 871 | 1600 | 2.0 | 0.99 | 1.01 | 103 | B17-L-F5 (L) | A.48 |
| 871 | 1600 | 4.0 | 2.81 | 1.19 | 11 | L8-2A (L) | A.10 |
| 982 | 1800 | 0.8 | 0.27 | 0.53 | 912 | L8-9A (L) | A.36 |
| 982 | 1800 | 1.0 | 0.35 | 0.65 | 509 | L8-8A (L) | A.34 |
| 982 | 1800 | 1.0 | 0.43 | 0.57 | 562 | L8-4A (L) | A.19 |
| 982 | 1800 | 2.0 | 1.19 | 0.81 | 112 | L8-8 (L) | A.35 |
| 1038 | 1900 | 1.0 | 0.45 | 0.55 | 539 | L8-7A (L) | A.29 |

*All tests conducted with $R_\varepsilon$ = -1 and $\dot{\varepsilon}$ = 0.5%/s*

There is no change in the dominant damage mechanism contributing to crack initiation in samples tested at or above the benchmark temperature under continuous cycling conditions. Figures 4.4c-d, 4.14a-c, and 4.15 indicate that inclusion-assisted

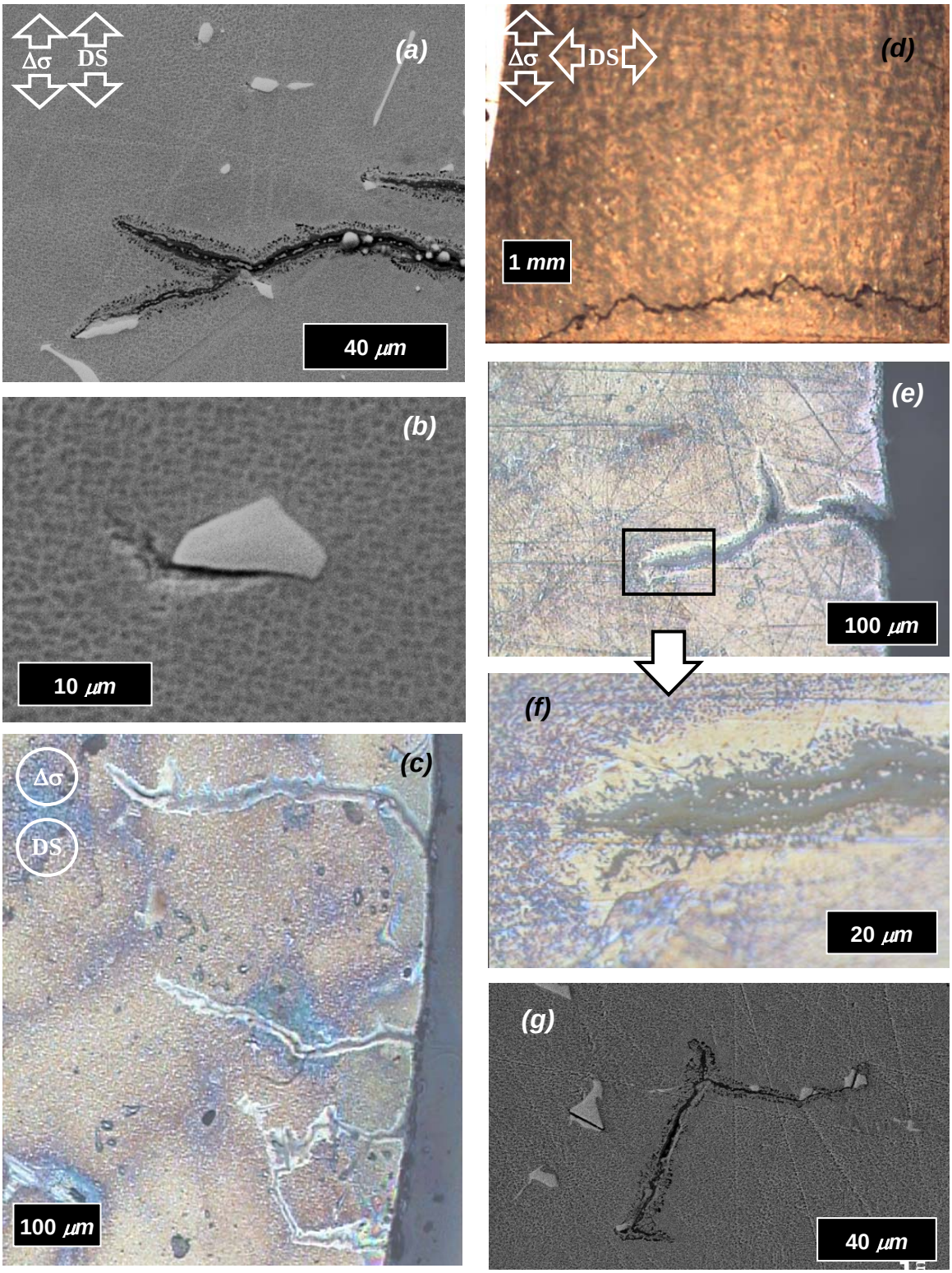


***Figure 4.14:*** *Crack initiation of continuously cycled (a-c) L and (d-g) T-oriented DS GTD-111 under $\dot{\varepsilon} = 0.5\%/s$, $R_\varepsilon$=-1, $\Delta\varepsilon$=1.0% and T=982℃. The loading and DS axes are transverse to the viewing plane for the case of image (c).*

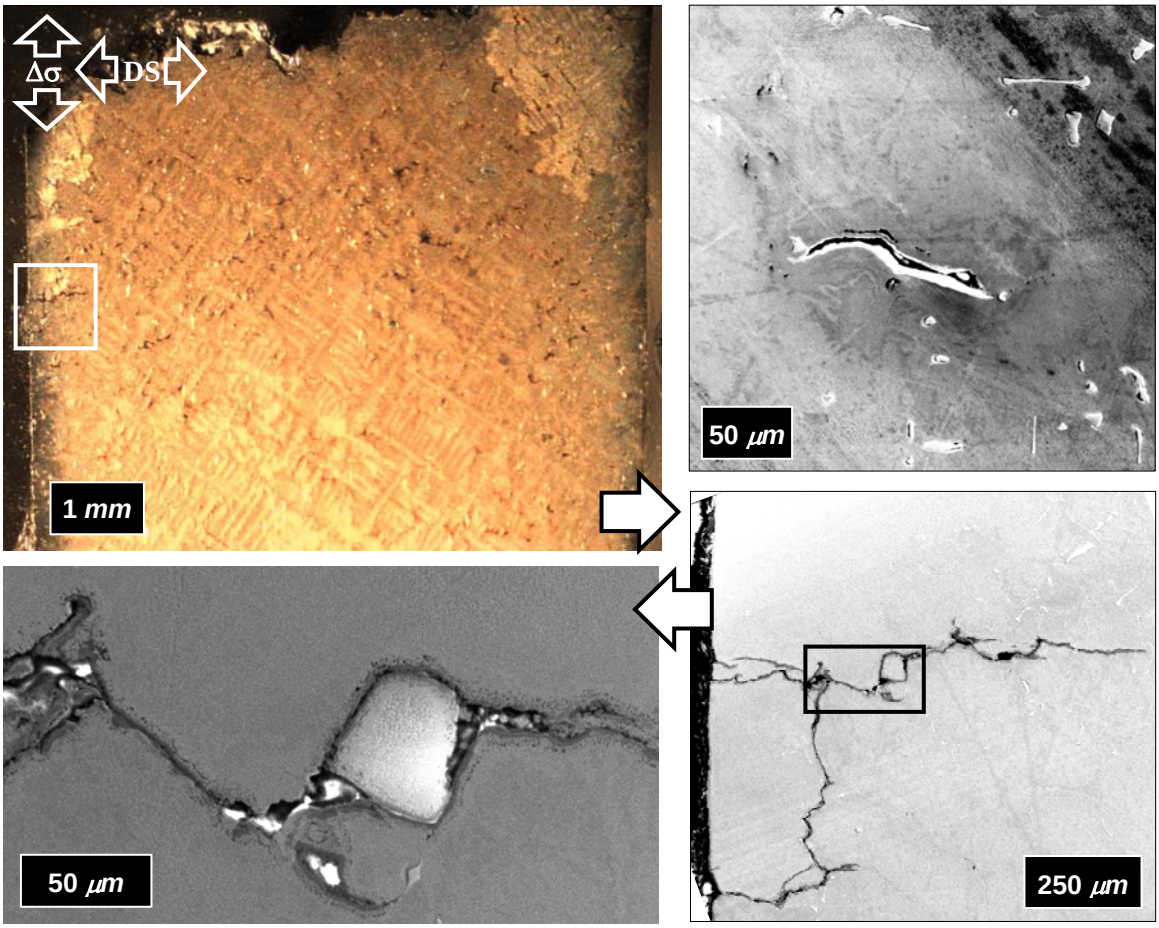


***Figure 4.15:*** *Strain-controlled low cycle fatigue of T-oriented DS GTD-111. For this case T=1038℃ and $\Delta\varepsilon$ = 1.0%.*

crack initiation is the key mechanism causing crack initiation in DS GTD-111. These samples were subjected to different temperatures, but otherwise similar testing conditions. In each case, cracks form at and beneath the external surface of the material. Carbides that were observed along the fracture surfaces participate in the crack initiation and early propagation processes.

At the higher temperatures there is some evidence of surface oxidation; however, since the plastic strain range accompanying high temperature tests can be substantial for even low strain range experiments, the role of oxidation is limited (Fig. 4.15). The cyclic

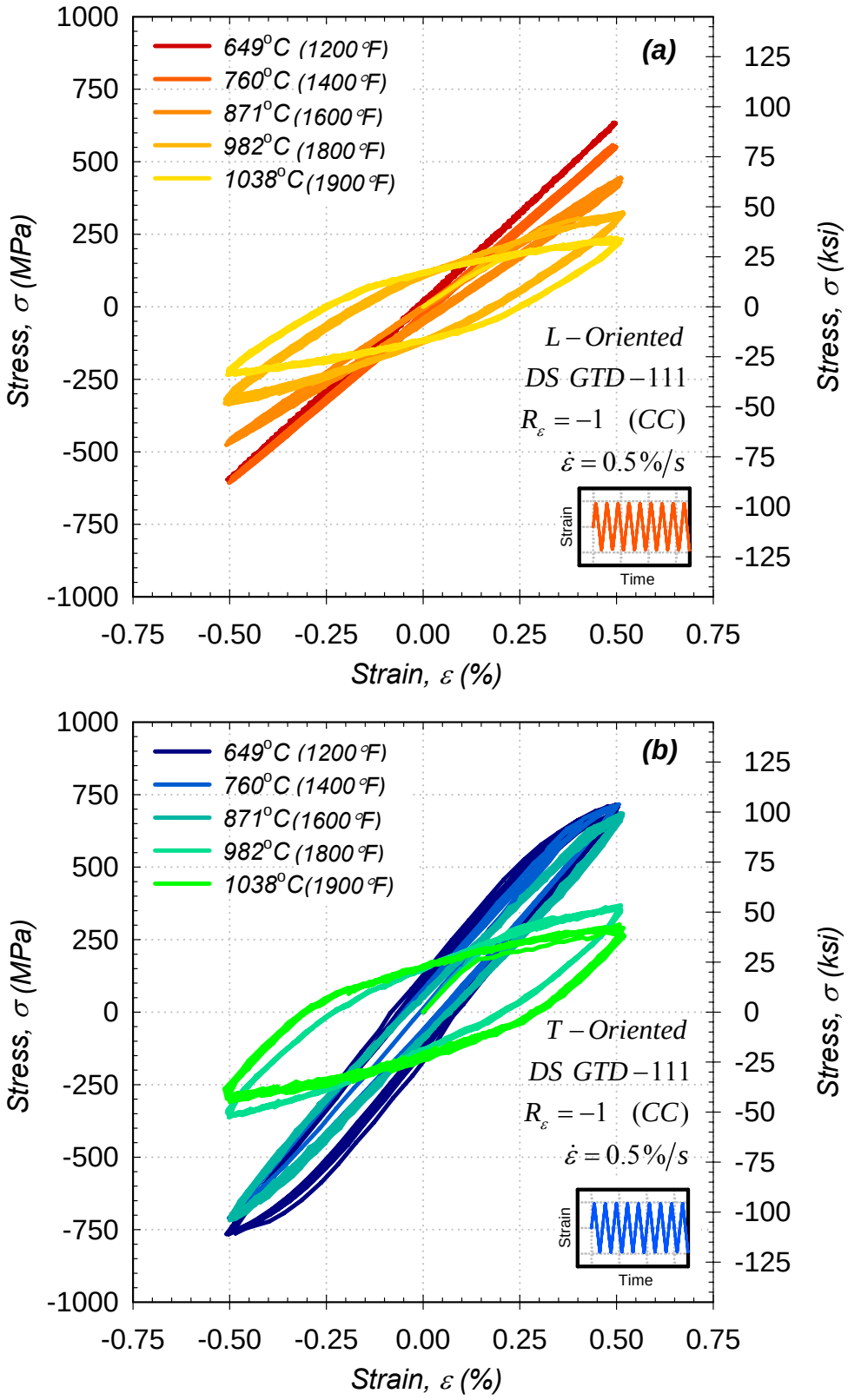


***Figure 4.16:*** *Comparison of initial stress responses of (a) L and (b) T-oriented DS GTD-111 under continuous cycle at* $\dot{\varepsilon} = 0.5\%/s$, $R_\varepsilon$ *= -1, and* $\Delta\varepsilon$ *= 1.0% at various temperatures.*

stress-strain responses for L- and T-oriented DS GTD-111 specimens fatigued at 1.0% mechanical strain range are shown in Figs. 4.16a and 4.16b, respectively. The decrease of the yield strength of the material with increasing temperature has the effect of increasing the cyclic plastic strain range for each orientation. The dominant crack initiation mechanism, even at elevated temperatures, is subsurface particle-assisted initiation.

For fatigue tests on L-oriented DS GTD-111 at various temperatures and at constant $\Delta\varepsilon$, the number of cycles needed to initiate a crack decreased with increasing temperature (Table 4.7). For example, cycling the mechanical strain range at 0.8%, and increasing the temperature from 760°C to 982°C caused the crack initiation life to decrease by a factor of 21. When cycling at 1.0%, increasing the temperature from 649° to 1038°C, caused $N_i$ to decrease by a factor of 27. Similar observations can be made from data from T-oriented DS GTD-111 specimens (Table 4.8). Increasing the temperature from 871°C to 982°C for $\Delta\varepsilon_m$ = 0.8%, resulted in a decrease of $N_i$ by a factor 2.7. Varying the temperature from 761°C to 1038°C at 1.0% caused the crack initiation life of the material to decrease by a factor of 7.4. Under CC loading with a constant strain rate (0.5%/s), the strain-life relations characterize the fatigue-dominance on crack initiation of DS GTD-111 under isothermal LCF testing.

***Table 4.8:*** *Crack Initiation life of T-oriented DS GTD-111 at various temperatures*

| Temperature (°C) | Temperature (°F) | Total Strain Range, $\Delta\varepsilon_m$ (%) | Plastic Strain Range, $\Delta\varepsilon_{pl}$ (%) | Elastic Strain Range, $\Delta\varepsilon_{el}$ (%) | Crack Initation Life, $N_i$ | Specimen ID (Orientation) | Figure |
|---|---|---|---|---|---|---|---|
| 649 | 1200 | 1.0 | 0.09 | 0.81 | 953 | A27-T-F1 | A.49 |
| 649 | 1200 | 1.2 | 0.35 | 0.85 | 194 | B18-T-F3 (T) | A.53 |
| 760 | 1400 | 1.0 | 0.15 | 0.85 | 1033 | A27-T-F3 (T) | A.45 |
| 871 | 1600 | 0.5 | < 0.01 | 0.50 | 16069 | T8-2A (T) | A.13 |
| 871 | 1600 | 0.8 | 0.07 | 0.73 | 598 | T8-5 (T) | A.25 |
| 871 | 1600 | 0.9 | 0.22 | 0.68 | 271 | B17-T-F2 (T) | A.37 |
| 871 | 1600 | 1.0 | 0.22 | 0.78 | 300 | T8-2 (T) | A.17 |
| 871 | 1600 | 2.0 | 1.46 | 0.54 | 28 | T8-1A (T) | A.12 |
| 871 | 1600 | 4.0 | 2.87 | 1.13 | 3 | T8-1 (T) | A.11 |
| 982 | 1800 | 0.8 | 0.27 | 0.53 | 219 | T8-4 (T) | A.24 |
| 982 | 1800 | 1.0 | 0.42 | 0.58 | 207 | T8-3A (T) | A.18 |
| 1038 | 1900 | 1.0 | 0.73 | 0.27 | 140 | T8-7 (T) | A.28 |

*All tests conducted with $R_\varepsilon$ = -1 and $\dot{\varepsilon}$ = 0.5%/s*

Strain range versus crack initiation life data are graphed in Fig. 4.17. Curves for L- and T-oriented DS GTD-111 specimen follow the 4-parameter power law relation used in the total strain life equation. Also included in the plots are data obtained from monotonic tensile tests on DS GTD-111 (Ibanez, 2003). Life data at all temperatures can be correlated with $\Delta\varepsilon$ at $R^2 > 0.9$ for each orientation, even considering the aforementioned differences in lives. Since the correlations hold for both long and short-lived tests, the influences of the other damage forms (e.g. environmental and creep) are, therefore, somewhat limited.

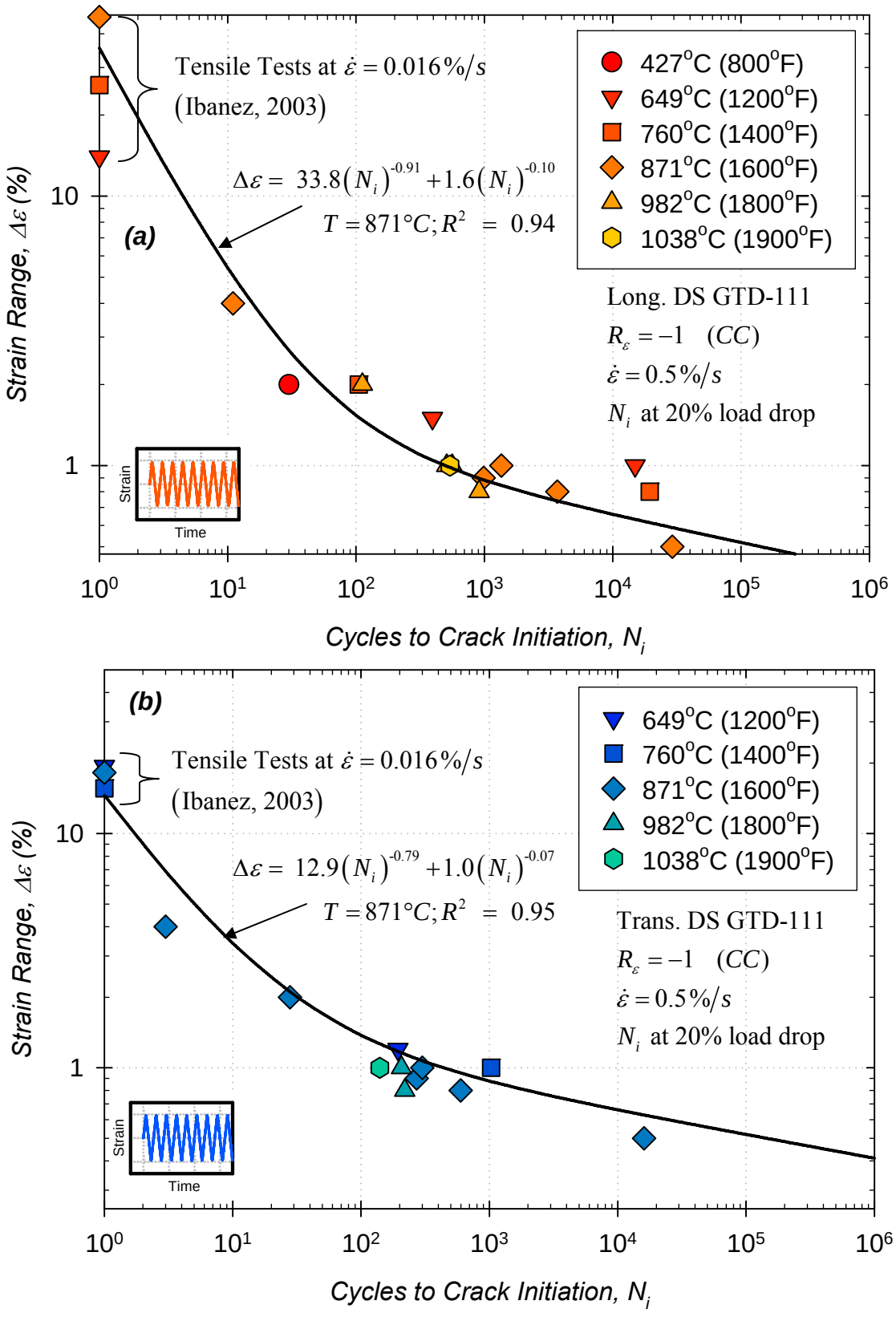


***Figure 4.17:*** *Temperature dependence of crack initiation life of (a) L and (b) T-oriented DS GTD-111 under continuous cycling conditions.*

***Table 4.9:*** *Crack initiation life of DS GTD-111 under isothermal creep-fatigue conditions*

| Temperature (°C) | Temperature (°F) | Hold Type | Hold Time, $t_h$ *(min)* | Total Strain Range, $\Delta\varepsilon_m$ *(%)* | Plastic Strain Range, $\Delta\varepsilon_{pl}$ *(%)* | Elastic Strain Range, $\Delta\varepsilon_{el}$ *(%)* | Crack Initation Life, $N_i$ | Specimen ID (Orientation) | Figure |
|---|---|---|---|---|---|---|---|---|---|
| 649 | 1200 | HC | 2 | 1.0 | 0.01 | 0.99 | 6768 | L8-6 (L) | A.32 |
| 871 | 1600 | HC | 2 | 0.8 | 0.12 | 0.68 | 678 | GTD-HC04 (L) | A.9 |
| 871 | 1600 | HC | 2 | 1.0 | 0.16 | 0.84 | >250 | GTD-HC05 (L) | A.7 |
| 871 | 1600 | HC | 2 | 2.0 | 0.68 | 1.32 | 49 | GTD-HC10 (L) | A.5 |
| 871 | 1600 | HC | 2 | 1.0 | 0.34 | 0.66 | 317 | B17-L-F4 (L) | A.55 |
| 871 | 1600 | HC | 10 | 1.0 | 0.34 | 0.66 | 213 | B17-L-F10 (L) | A.56 |
| 871 | 1600 | HT | 2 | 0.8 | 0.08 | 0.72 | ~248 | GTD-HT04 (L) | A.8 |
| 871 | 1600 | HT | 2 | 1.0 | 0.11 | 0.89 | 590 | GTD-HT05 (L) | A.6 |
| 871 | 1600 | HT | 2 | 2.0 | 0.69 | 1.31 | 84 | GTD-HT10 (L) | A.4 |
| 871 | 1600 | HT | 10 | 1.0 | 0.25 | 0.75 | 311 | B17-L-F12 (L) | A.60 |
| 982 | 1900 | HC | 2 | 0.5 | 0.05 | 0.45 | 1537 | L8-6A (L) | A.33 |
| 982 | 1900 | HC | 2 | 1.0 | 0.37 | 0.63 | 406 | L8-5A (L) | A.23 |
| 982 | 1800 | HT | 2 | 1.0 | 0.31 | 0.69 | 331 | L8-5 (L) | A.21 |
| 1038 | 1900 | HC | 2 | 1.0 | 0.46 | 0.54 | 464 | L8-7 (L) | A.30 |
| 1038 | 1900 | HC | 10 | 1.0 | 0.66 | 0.34 | ~479 | B17-L-F9 (L) | A.54 |
| 1038 | 1900 | HC | 10 | 1.0 | 0.58 | 0.42 | 481 | B17-L-F13 (L) | A.61 |
| 1038 | 1900 | HT | 10 | 1.0 | 0.54 | 0.46 | 181 | B17-L-F11 (L) | A.59 |
| 1038 | 1900 | HT | 2 | 1.0 | 0.52 | 0.48 | 175 | B17-L-F14 (L) | A.62 |
| 871 | 1600 | HC | 2 | 1.0 | 0.35 | 0.65 | 87 | T8-6A (T) | A.27 |
| 871 | 1600 | HT | 2 | 1.0 | 0.32 | 0.68 | 150 | T8-5A (T) | A.26 |
| 982 | 1800 | HC | 2 | 1.0 | 0.42 | 0.58 | 115 | T8-3 (T) | A.22 |
| 982 | 1800 | HT | 2 | 1.0 | 0.38 | 0.62 | 47 | T8-4A (T) | A.20 |
| 1038 | 1900 | HC | 2 | 1.0 | 0.50 | 0.50 | 152 | T8-7A (T) | A.31 |
| 1038 | 1900 | HC | 10 | 1.0 | 0.73 | 0.27 | 98 | T8-6 (T) | A.57 |
| 1038 | 1900 | HT | 10 | 1.0 | 0.53 | 0.47 | 21 | T8-9A (T) | A.58 |

*All tests conducted with* $R_\varepsilon$ *= -1 and* $\dot{\varepsilon}$ *= 0.5%/s*

## *4.5 Dwell Effects*

Cyclic experiments were carried out under strain-controlled, creep-fatigue loading conditions to investigate the time sensitive behavior of other damage mechanisms (e.g. surface oxidation and cracking at grain boundaries) on the overall crack initiation behavior of DS Ni-base superalloys. The life and hysteresis loops of these experiments are listed in Table 4.9. Two types of creep-fatigue experiments were conducted – those

with strain hold periods in compression (HC) or holds in tension (HT). The key variable in either type is the time length of the hold period, $t_h$. Either 2 *min* or 10 *min* times were applied. Here we denote hold times in tension and compression as $t_{ht}$ and $t_{hc}$, respectively. It should be noted that $t_h = 0$ corresponds to the special case of continuous cycling (CC). Because the specimens were loaded under strain-control, stresses in the material relaxed over the dwell period. Whenever possible, comparisons of (1) fatigue-tested microstructure, (2) crack initiation life, or (3) hysteresis loops were conducted for CC experiments conducted with $R_\varepsilon = -1$ and $\dot{\varepsilon} = 0.5\%/s$.

*Creep-Fatigue Effects at 871 ℃*

The initial hysteresis loops and stress-time histories of L-oriented DS GTD-111 under HC and HT creep-fatigue are illustrated in Fig. 4.18a,c and 4.18b,d, respectively. During the compressive (or tensile) hold periods, the strain level of -0.5% (or 0.5% for the HT case) is held constant for the desired $t_h$. Additional viscoplastic deformation occurs during this dwell period and the stress is relaxed toward a constant value. In either case, the majority of the stress relaxation occurs during the initial one-fourth of the hold period. For HT cases there is a slightly compressive mean stress; whereas for HC cases the mean stress is slightly tensile. The shape of the hysteresis loop typically converges by the $10^{th}$ cycle.

There is a crossover in the mechanism of crack initiation for cycling under CC, HC, and HT conditions. Figure 4.19 illustrates strain range versus life results for L- and T-oriented DS GTD-111 exposed to isothermal conditions ranging from 871°C to 1038°C. As expected when mechanical strain range increases, crack initiation life

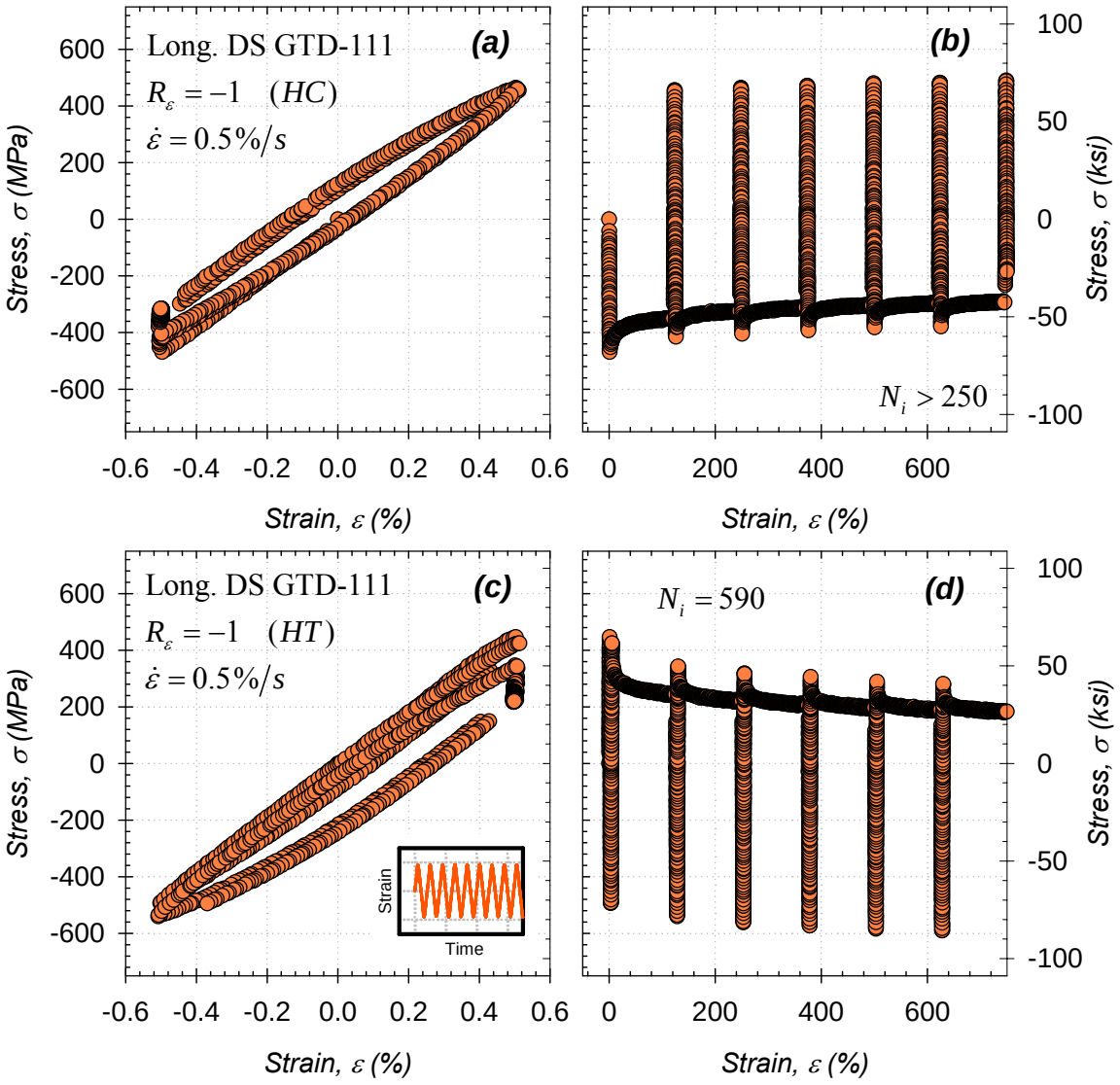


***Figure 4.18:*** *Initial (a,c) stress versus strain responses and (b,d) stress histories of L-oriented DS GTD-111 under creep-fatigue cycling subjected to 871°C, $\Delta\varepsilon$=1.0%, $R_\varepsilon$=-1, $\dot{\varepsilon} = 0.5\%/s$, and (a, b) $t_h$ = 2 min in compression, and (c, d) $t_h$ = 2 min in tension.*

decreases for either creep-fatigue case (HC or HT). For a given set of experimental conditions ($T$, $R_\varepsilon$, $\Delta\varepsilon$, and $\dot{\varepsilon}$) the plastic strain ranges of HC and HT cases were larger than those from CC conditions, and the crack initiation lives were shorter. As shown in Fig. 4.19a, the interpolated $\Delta\varepsilon$-$N_i$ curves for either HC or HT cases lie exist entirely

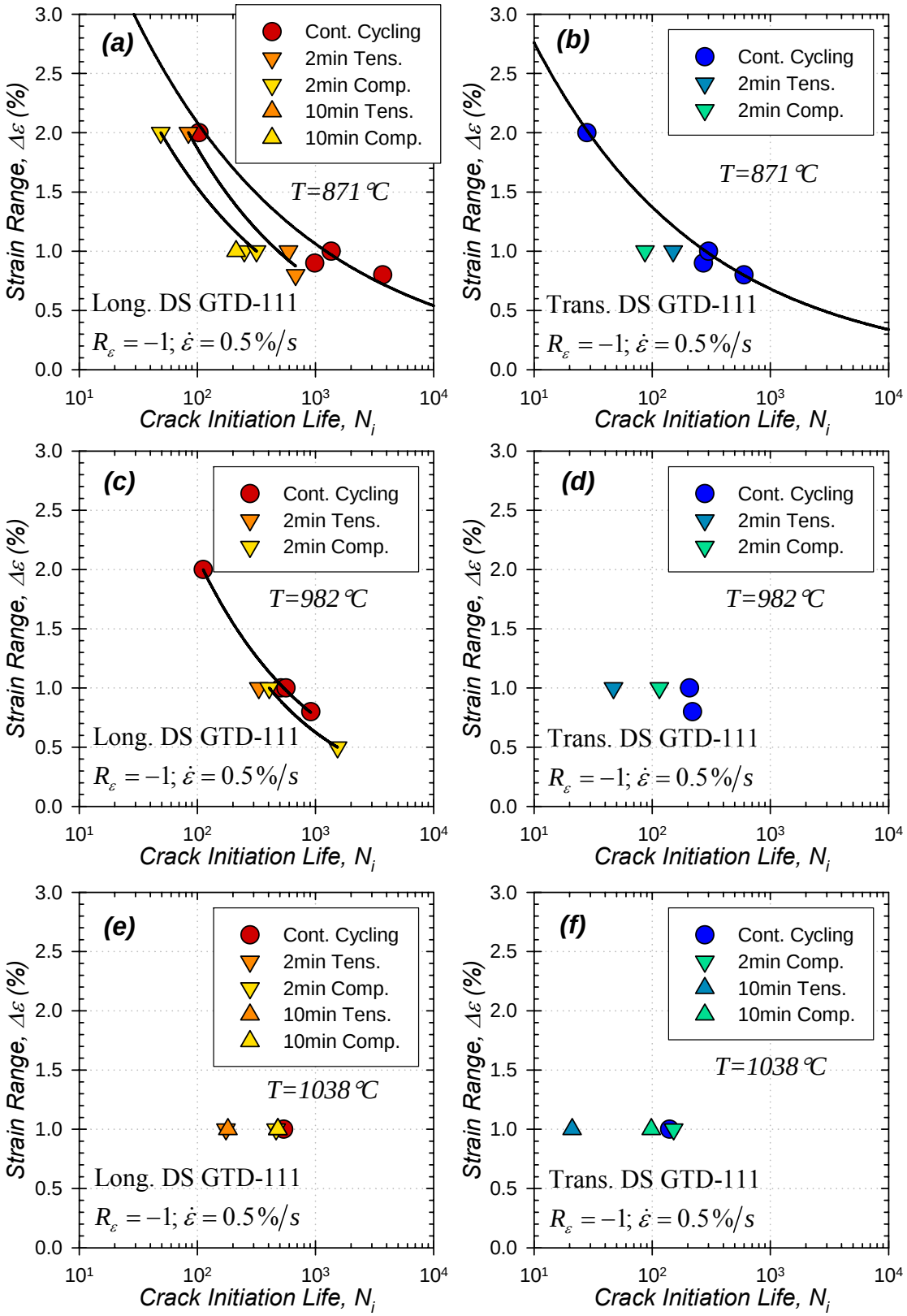


***Figure 4.19:*** *Crack initiation lives of (a, c, e) L-oriented and (b, d, f) and T-oriented DS GTD-111 under continuous and creep-fatigue cycling. For each case $R_\varepsilon$=-1 and $\dot{\varepsilon} = 0.5\%/s$.*

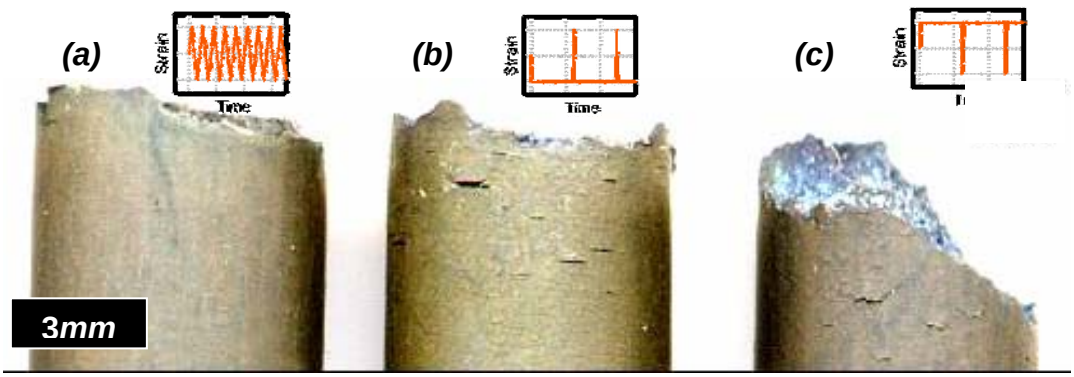


***Figure 4.20:*** *Effect of cycle type on fracture profile of L-oriented DS GTD-111 with $\Delta\varepsilon$ = 0.8%, $R_\varepsilon$=-1, $\dot{\varepsilon} = 0.5\%/s$, and 871°C (1600°F).*

beneath CC strain-life curves for the L-oriented material. By incorporating hold times, $N_i$ was shortened irrespective of the hold type, hold time, temperature, or material orientation. Visually comparing the profiles of samples of L-oriented fatigue-tested material indicates the presence(s) of additional mechanisms that hasten crack formation and early growth. Crack initiation lives under HT outlast those under HC by nearly a factor of two for either grain orientation at 871°C. As shown in Fig. 4.20, with $\Delta\varepsilon$ = 0.8% and CC the material has limited surface cracking. Under creep-fatigue conditions, both HT and HC cycled specimens contain numerous surface cracks. Surface cracks in the HC-tested case occur often and are aligned transverse to the stress axis, whereas cracks in the HT-tested material are tortuous and the surface crack density of lower.

*Effect of Hold Type*

Differences in the influences of the damage mechanisms are illustrated in Figs. 4.21 and 4.22. Crack initiation under creep-fatigue cycling with compressive dwells (Fig. 2.21) is facilitated by the ingression of surface oxides. For these testing conditions, at

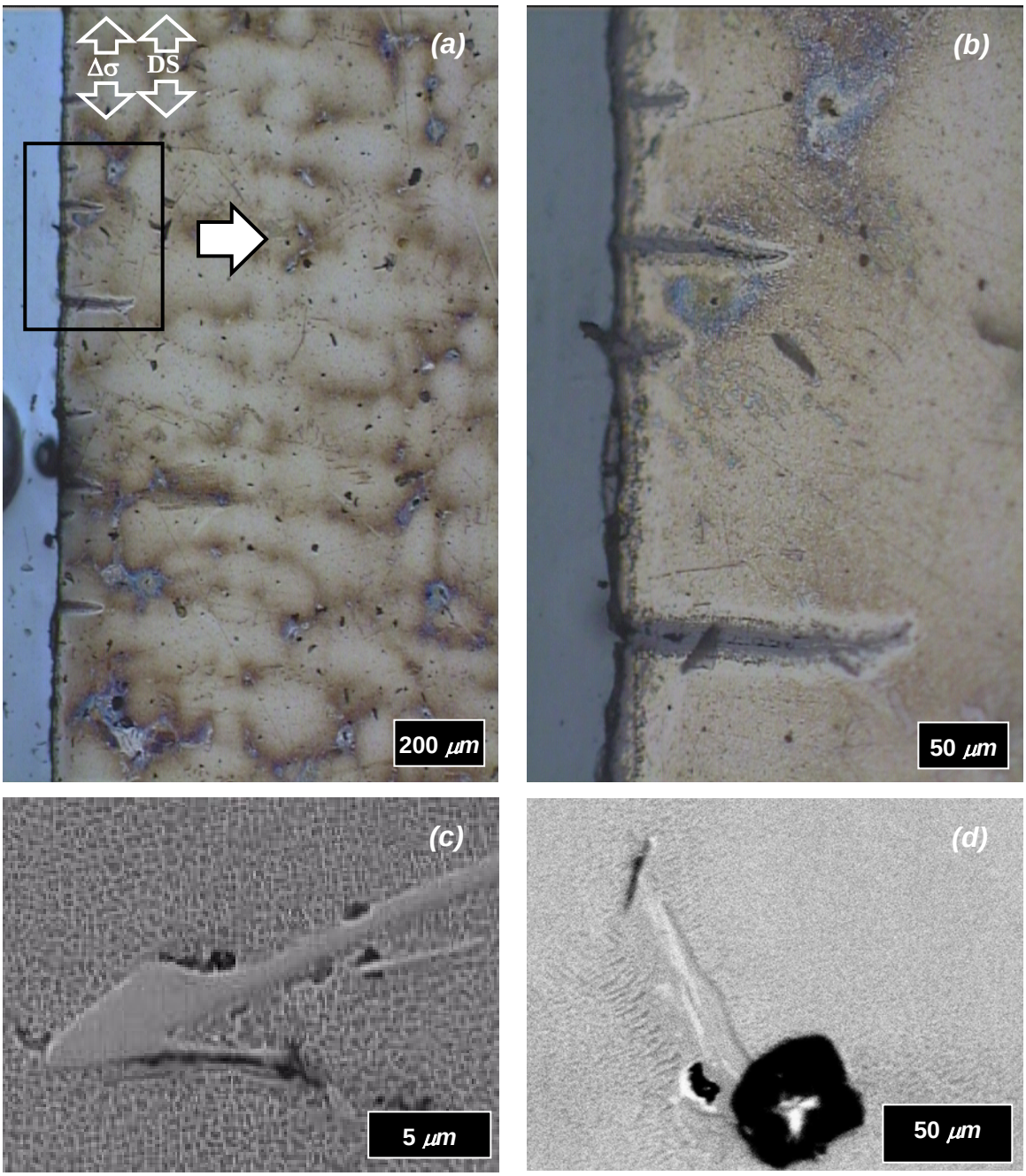


***Figure 4.21:*** *Crack initiation of creep-fatigue tested L-oriented DS GTD-111 under* $\dot{\varepsilon} = 0.5\%/s$, $R_\varepsilon$*=-1,* $\Delta\varepsilon$*=1.0% and T=982°C. For this case* $t_h$ *= 2 min in compression (Specimen ID: L8-5A).*

least 97% of the total crack initiation life of the specimen is spent in compression. During cyclic reversals, the typically brittle accumulated oxide layer fractures in tension and exposes underlying virgin material. Once this newly-oxidized material fractures, the process repeats. The result is the formation of a series of oxide spikes that propagate transverse to the direction of the applied load, as shown in Fig. 4.21a,b. The accumulated oxidation layer at the exposed surface or the fracture surface consists of several distinct layers. The outer layer is a homogeneous mixture of Ti- and Cr-rich oxides, while the inner layer is Al-rich and is intermingled with matrix material. Separating the oxide layers from the unaffected metal is a matrix layer denuded of primary precipitate particles. Limited microcrack growth also occurred under these conditions (Fig. 4.21c,d).

The morphologies of initiated cracks shown in the various micrographs can slightly vary for polishing planes above and below the viewing plane. Analogously, the morphologies of the accumulated oxides may slightly differ among a series of adjacent viewing planes.

The HT-tested sample displays a different mechanism dominating the crack initiation process, as shown in Fig. 4.22. Subsurface carbides were the main cause of crack initiation. Microcracks propagated in a nearly a straight line by coalescing with adjacent microcracks; however, the random nature of the carbide networks and their morphologies lead to non-planar cracks. In nearly all cases the carbides themselves did not fracture. The formation of oxidized surface cracks, also contributed to the damage process under these conditions (Fig. 4.22a,e); however, their nonlinear profile indicates that the initiation and early propagation is controlled by the participation of inclusions and other contaminants found in the interdendritic regions. Relative to the HC case, the

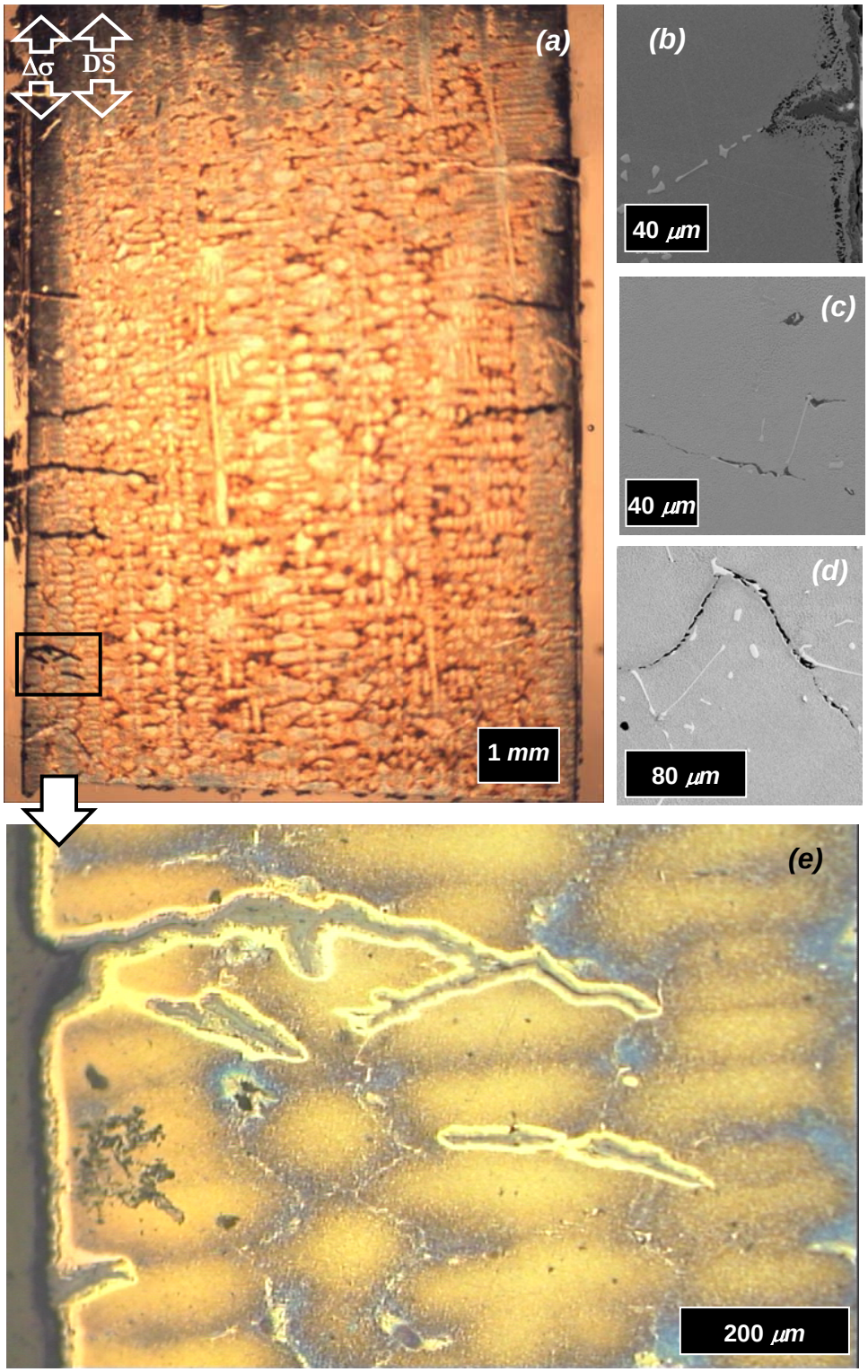


***Figure 4.22:*** *Crack initiation of creep-fatigue tested L-oriented DS GTD-111 under* $\dot{\varepsilon} = 0.5\%/s$, $R_\varepsilon$*=-1,* $\Delta\varepsilon$*=1.0% and T=982°C. For this case* $t_h$ *= 2 min in tension (Specimen ID: L8-5).*

HT-tested L-oriented profiles more closely resembles CC cases (Fig. 4.14) even though the lives differ. The key differences between the CC-tested and HT-tested profiles are related to features of the surface crack. The depth of the oxide and precipitate-free zone in the HT-tested case is nearly four times that of the CC-tested case. The depths of the cracks in the HT cases are also longer than those of the CC cases, by a factor of about two.

The HT-tested, T-oriented sample contains no visibly significant contribution from either crack initiation mechanism, as shown in Fig. 4.23; however, the rough fracture surface indicates the participation of inclusions in the crack formation process. No intergranular crack initiation was observed. At this high temperature, the lives of HC and CC-tested specimen outlasted those of HT cases.

For experiments conducted at a lower $\Delta\varepsilon$, $\Delta\varepsilon_{pl}$ decreases and $N_i$ increases. Damage mechanisms dominant in CC fatigue testing (e.g. cracks at inclusions) are expected to diminish in influence. As a result, the formation of oxide spikes is expected to increase. Figure 4.24 displays the sample microstructure of an L-oriented specimen tested under HC creep-fatigue conditions identical to those in Fig. 4.21 ($\dot{\varepsilon} = 0.5\%/s$, $R_\varepsilon$ = -1, $\Delta\varepsilon$ = 1.0%, and $T$ = 982°C) except for that $\Delta\varepsilon$ was lowered to 0.5%. As a consequence of the differing test conditions (i.e., $\Delta\varepsilon_{pl}$ = 0.37% for $\Delta\varepsilon$ = 1.0%, and $\Delta\varepsilon_{pl}$ = 0.05% for $\Delta\varepsilon$ = 0.5%), the nature of the crack initiation mechanisms vary. There are twice as many surface cracks present in the lower strain range case (Fig. 4.24a). There was some evidence of microcrack or microvoid nucleation at inclusion particles at the higher strain range case; however, this was not apparent at the lower strain range. The fatigue crack initiation lives of the two samples differed by a factor of 3.8 (Fig. 4.19c).

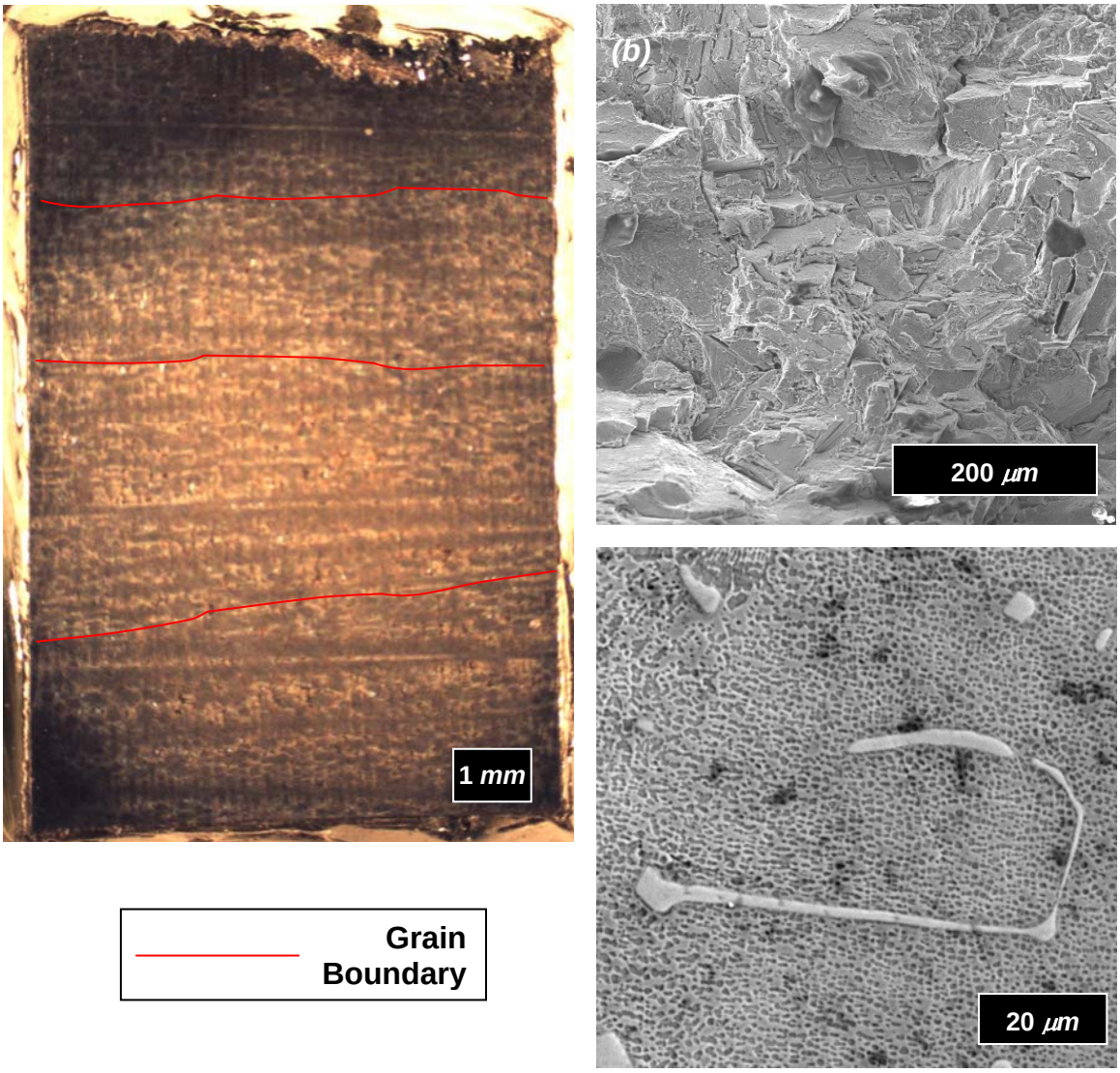


***Figure 4.23:*** *Crack initiation of creep-fatigue tested T-oriented DS GTD-111 under* $\dot{\varepsilon} = 0.5\%/s$, $R_\varepsilon$*=-1,* $\Delta\varepsilon$*=1.0% and T=982°C. For this case* $t_h$ *= 2 min in tension (Specimen ID: T8-4A).*

Because of the life difference, the lower strained sample was exposed to 982°C for a total of 52 *hr* (2.2 days). Precipitate particles began to coarsen into raft-like shapes parallel to the stress axis under these conditions, as shown in Fig. 4.24c. There was no evidence of this in the high strain range case.

*Controlling the Oxide-Fatigue Damage Mechanism*

The sustained oxidation-fatigue damage exhibited in Fig. 4.24 is not unique to the combination of temperature, strain range, strain ratio, and strain rate applied. Either the balance of several damage mechanisms or the dominance of a single mechanism can be attained under other conditions. For example, the occurrence of surface cracks in Fig. 4.25 was obtained at 871°C. In order for this to occur, the mechanical strain range had to be increased to 1.0%. Various aspects about the surface cracks show resemblance for the two cases (Figs. 4.24 and 4.25): (a) typical crack length, (b) shape of the crack, and (c) distance between adjacent cracks. Precipitate particle rafting occurred along the loading axis at 871°C (Fig. 4.25c). It should be noted that particle coarsening undoubtedly affects the ductility and the strength of the material, and it was not readily observed in continuous cycled LCF experiments.

It was determined that for the same temperature the presence of surface cracking is decreased by increasing the strain range. Comparing Figs. 4.25 and 4.26, the surface cracking mechanism decreases in importance as the strain range is increased. Surface cracks still appeared, and microcrack formation at inclusions and eutectics were promoted at higher strain range. The density of surface cracks was also lower as temperature decreased at the same strain range (Fig. 4.27). Increasing the strain range still maintains the result of lowering the number of cycles needed to cause crack initiation (Fig. 4.19a).

At 1.0% strain range, it was observed that oxide spiking became more prominent with a decrease in the ambient temperature from 982°C to 871°C (Figs. 4.21 and 4.25,

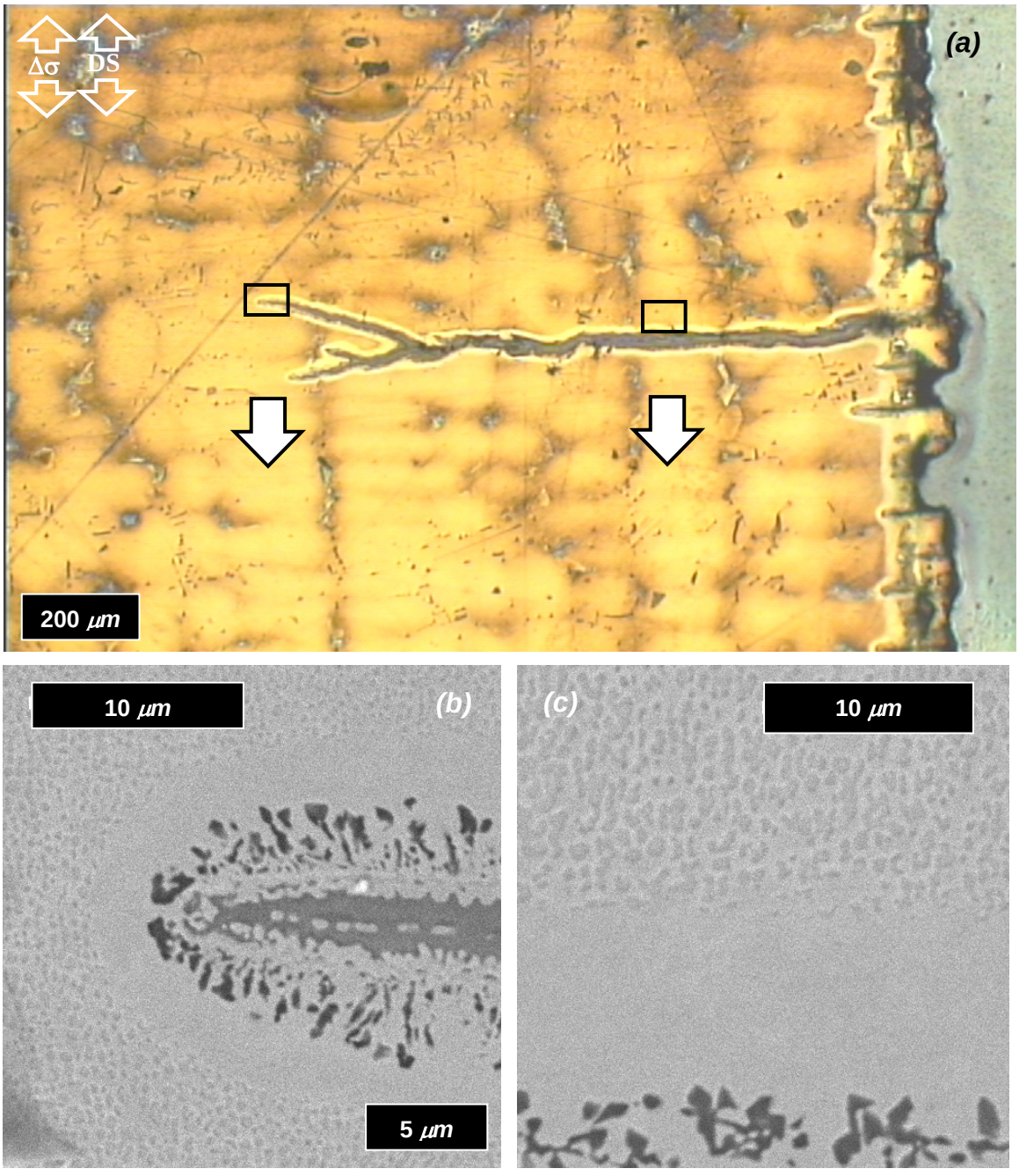


***Figure 4.24:*** *Crack initiation of creep-fatigue tested L-oriented DS GTD-111 under* $\dot{\varepsilon} = 0.5\%/s$, $R_\varepsilon$*=-1,* $\Delta\varepsilon$*=0.5% and T=982°C. For this case* $t_h$ *= 2 min in compression (Specimen ID: L8-6A).*

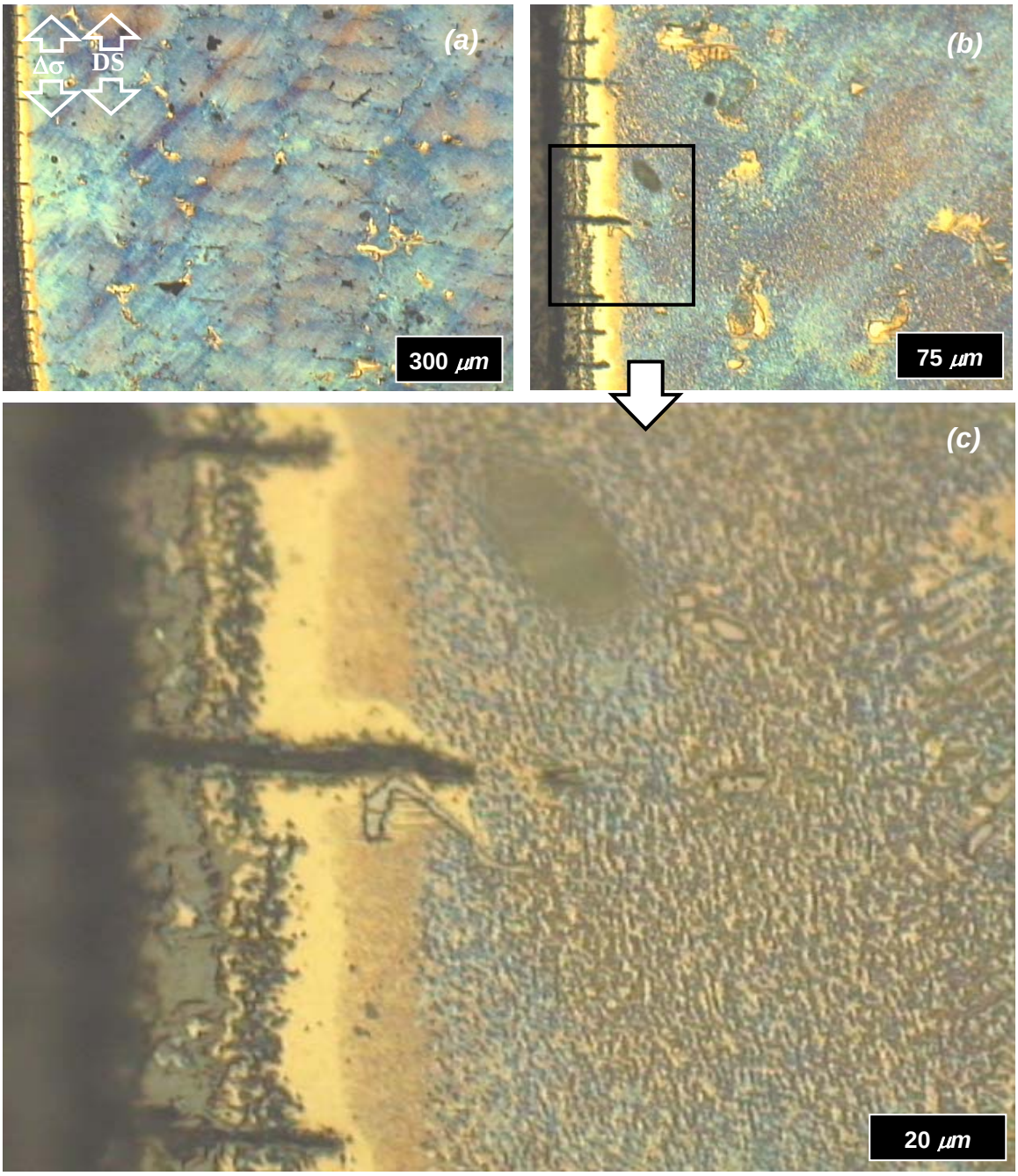


***Figure 4.25:*** *Crack initiation of creep-fatigue tested L-oriented DS GTD-111 under* $\dot{\varepsilon} = 0.5\%/s$, $R_\varepsilon$=-1, $\Delta\varepsilon$=1.0% *and T=871°C. For this case* $t_h$ *= 2 min in compression (Specimen ID: GTD-HC04).*

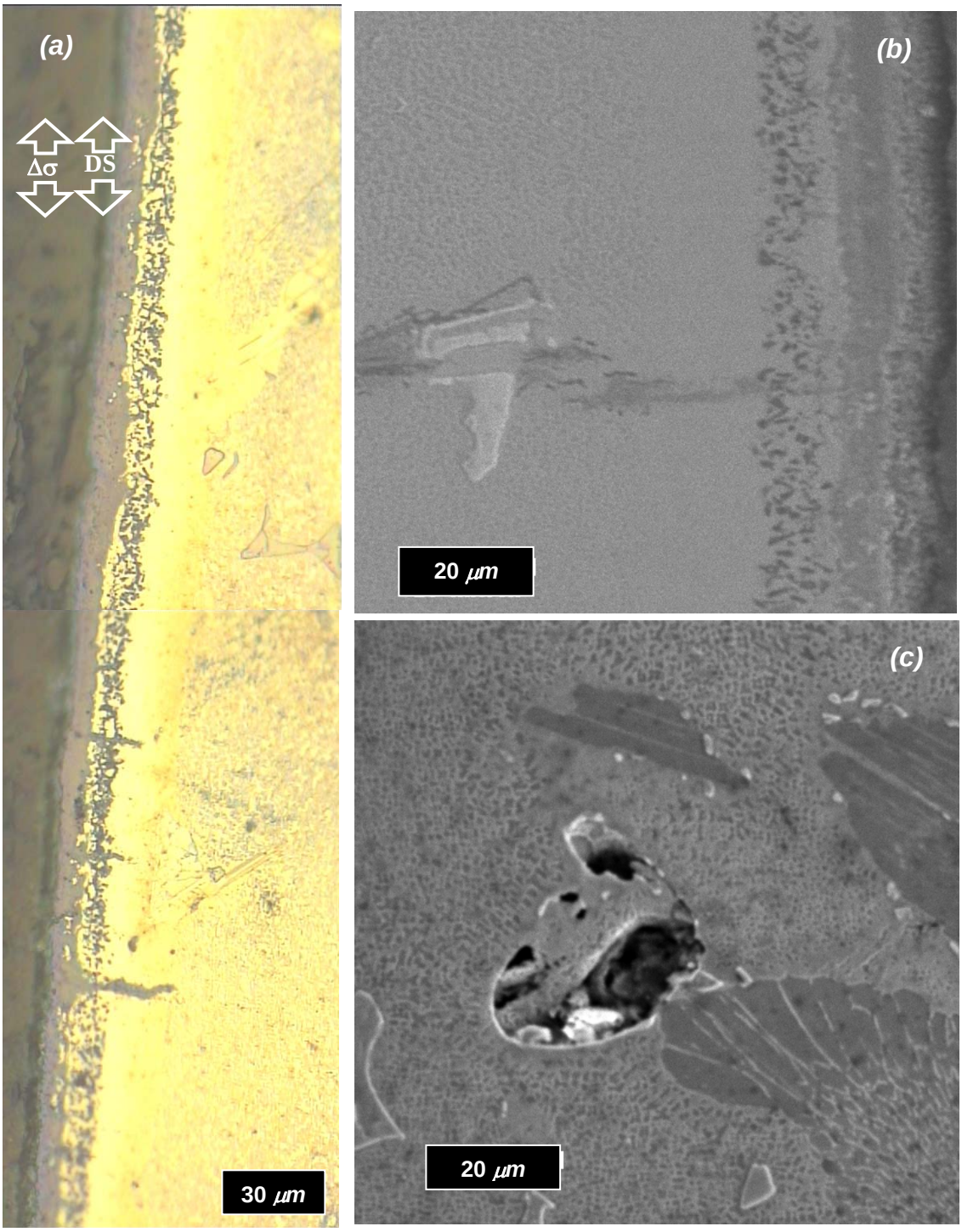


***Figure 4.26:*** *Crack initiation of creep-fatigue tested L-oriented DS GTD-111 under* $\dot{\varepsilon} = 0.5\%/s$, $R_\varepsilon$=-1, $\Delta\varepsilon$=2.0% *and T=871°C. For this case* $t_h$ *= 2 min in compression (Specimen ID: GTD-HC10 (L)).*

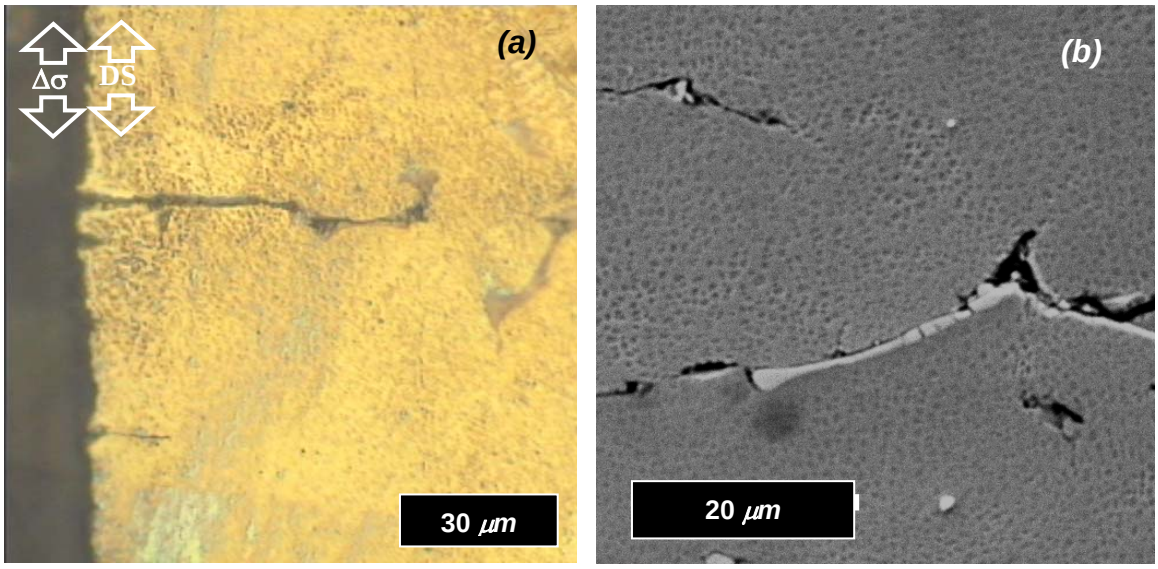


***Figure 4.27:*** *Crack initiation of creep-fatigue tested L-oriented DS GTD-111 under* $\dot{\varepsilon} = 0.5\%/s$, $R_\varepsilon$*=-1,* $\Delta\varepsilon$*=1.0% and T=649°C. For this case* $t_h$ *= 2 min in compression (Specimen ID: L8-6).*

respectively); however, decreasing the temperature to 649°C led to very limited surface cracking. Even though the sample shown in Fig. 4.27 was cycled for 233 *hr* (9.7 days), at this low temperature there was not enough thermodynamic driving force to promote surface diffusion processes. The damage mechanisms of (a) microcracking at subsurface inclusions and (b) cracking of inclusions were still observed at this loading condition (Fig. 4.27b). This resulted in slightly tortuous cracks occurring at and beneath the surface of the material.

*Effect of Increased Dwell Time*

As the length of the dwell period was increased, the creep-fatigue test resembled the strain-controlled, stress relaxation test. Similar to load-controlled, creep deformation tests, these experiments isolate the time-dependent inelastic behavior of the material. As such, applying longer dwell times emphasizes creep-related damage mechanisms.

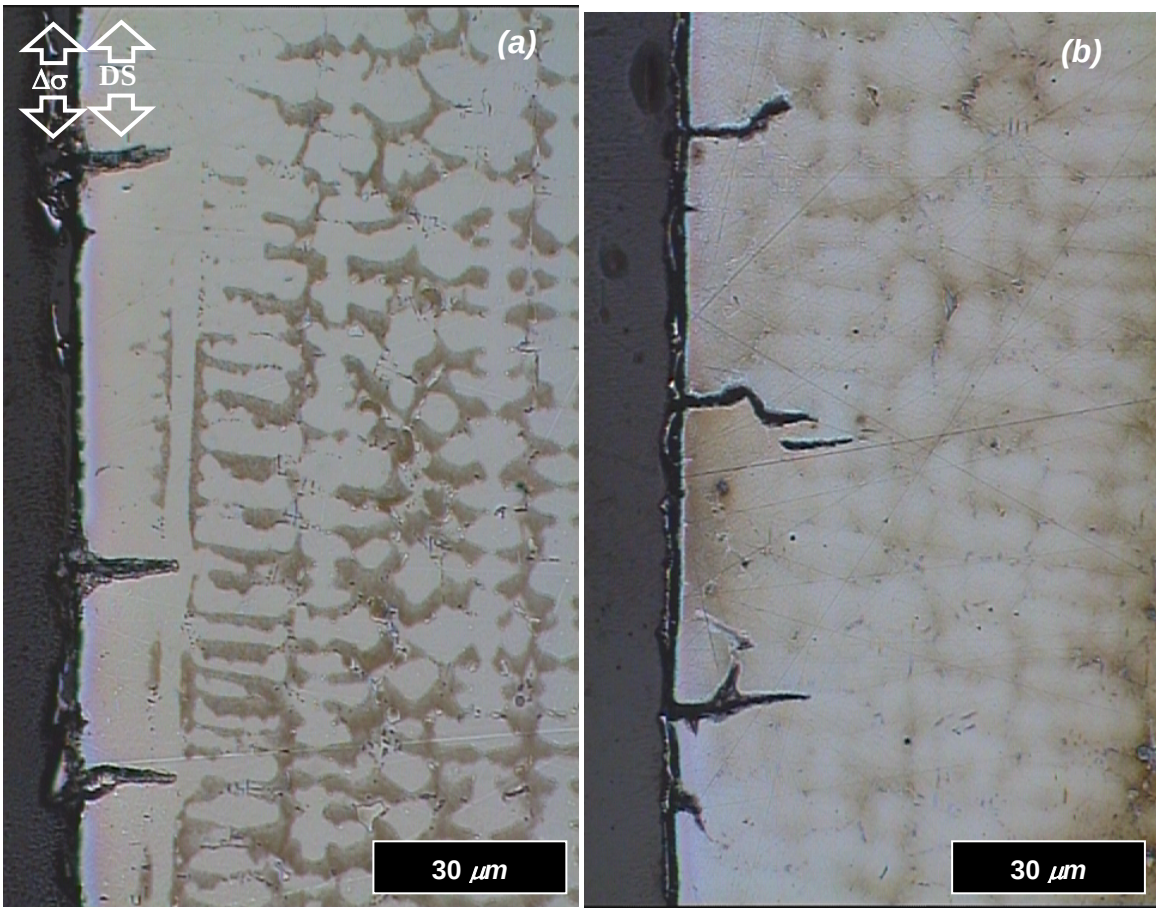


***Figure 4.28:*** *Crack initiation of creep-fatigue tested L-oriented DS GTD-111 under* $\dot{\varepsilon} = 0.5\%/s$, $R_\varepsilon$*=-1,* $\Delta\varepsilon$*=1.0% and T=871°C. For each case* $t_h$ *= 10 min in (a) compression and (b) tension.*

Several creep-fatigue experiments were conducted with hold times of 10 *min*. At the strain range level of 1.0%, which was used for all cases, the push-pull portion of the fatigue cycle accounts for 0.66% of the total cycle time. At 871°C, the surfaces of L-oriented DS GTD-111 with shorter dwell periods are similar to those obtained when cycled under either HC or HT at shorter dwell periods. The microstructures shown in Figs. 4.28a and 4.28b were identically tested with the exception that the former was subjected to compressive dwells and the latter was subjected to tensile dwells. The distribution and depths of surface cracks are similar for the two cases. The main

difference between the two samples is that the surface cracks from the HT-tested sample are more tortuous than those of the HC-tested case. This is an indication of the influence on subsurface features on crack formation and early propagation found in L-oriented DS GTD-111 when cycled under nominally tensile conditions. In compression, crack incubation and early crack propagation are oxidation-assisted. At this combination of temperature and strain range, increasing $t_h$ has the effect of decreaing the crack initiation lives of L- and T-oriented material, as shown in Table 4.10 and 4.11, respectively.

***Table 4.10:*** *Life ($N_i$) of L-oriented DS GTD-111 at $\Delta\varepsilon_m$=1.0%*

| Temperature | | Strain-Controlled Dwells | | | | |
|---|---|---|---|---|---|---|
| | | Compressive | | Cont. Cycling | Tensile | |
| (°C) | (°F) | 10min | 2min | | 2min | 10min |
| 649 | 1200 | - | 6768 | 14915 | - | - |
| 760 | 1400 | - | - | 10224 | - | - |
| 871 | 1600 | 213 | 317 | 1357 | 590 | 311 |
| 982 | 1800 | - | 406 | 535 | 331 | - |
| 1038 | 1900 | 481 | 464 | 539 | 175 | 181 |

***Table 4.11:*** *Life ($N_i$) of T-oriented DS GTD-111 at $\Delta\varepsilon_m$=1.0%*

| Temperature | | Strain-Controlled Dwells | | | | |
|---|---|---|---|---|---|---|
| | | Compressive Hold | | Cont. Cycling | Tensile Hold | |
| (°C) | (°F) | 10min | 2min | | 2min | 10min |
| 649 | 1200 | - | - | 963 | - | - |
| 760 | 1400 | - | - | 1033 | - | - |
| 871 | 1600 | - | 87 | 300 | 150 | - |
| 982 | 1800 | - | 115 | 207 | 47 | - |
| 1038 | 1900 | 98 | 152 | 140 | - | 21 |

Although the increase in $t_h$ had no effect on the plastic strain ranges determined for the 2 *min* and 10 *min* cases, as listed in Table 4.9, the life of sample tested with $t_h$ = 2 *min* had a slightly longer crack initiation life (by a factor of 1.49) than $t_h$ = 2 *min* cases. For 2 *min* and 10 *min* HC cases, Figures 4.25b and 4.28a show a reduction in the surface crack density with increased $t_h$.

Under HC with increasing temperature (from 871°C to 1038°C), there is a slight decrease in the number of observed surface cracks. This is evident when comparing the profiles of L-oriented DS GTD-111 in Figs. 4.28a and 4.29a. The total strain range was identical for the two cases; consequently, the increase in temperature caused the cyclic $\Delta\varepsilon_{pl}$ to increase by a factor of 1.7. The spiking mechanism was therefore heavily dependent on the plastic strain range, dwell time, and temperature. Additionally, subsurface precipitate particles rafted (Fig. 4.29c) along the stress axis of the material.

Long term creep-fatigue tests were also conducted for the transverse orientation. The distribution of surface cracks of the T-oriented material is generally analogous to L-oriented samples. Figure 4.30 illustrates a cross-section of the creep-fatigued sample tested at 1038°C with 10 *min* compressive dwell periods. The distribution of the surface cracks shown in Fig. 4.30a is similar to that observed in the L-oriented sample subjected to identical conditions (Fig. 4.29a). For both cases, two or three surface cracks tend to initiate per 1 *mm* of length along the specimen axis in the gage section. The main difference between the two orientations is that the depths of the surface cracks in the L-oriented sample are longer. This is attributed to the fact that the cyclic plastic strain range for the T-oriented sample is slightly larger. Thus, each cycle there is a larger contribution of damage induced at subsurface inclusions.

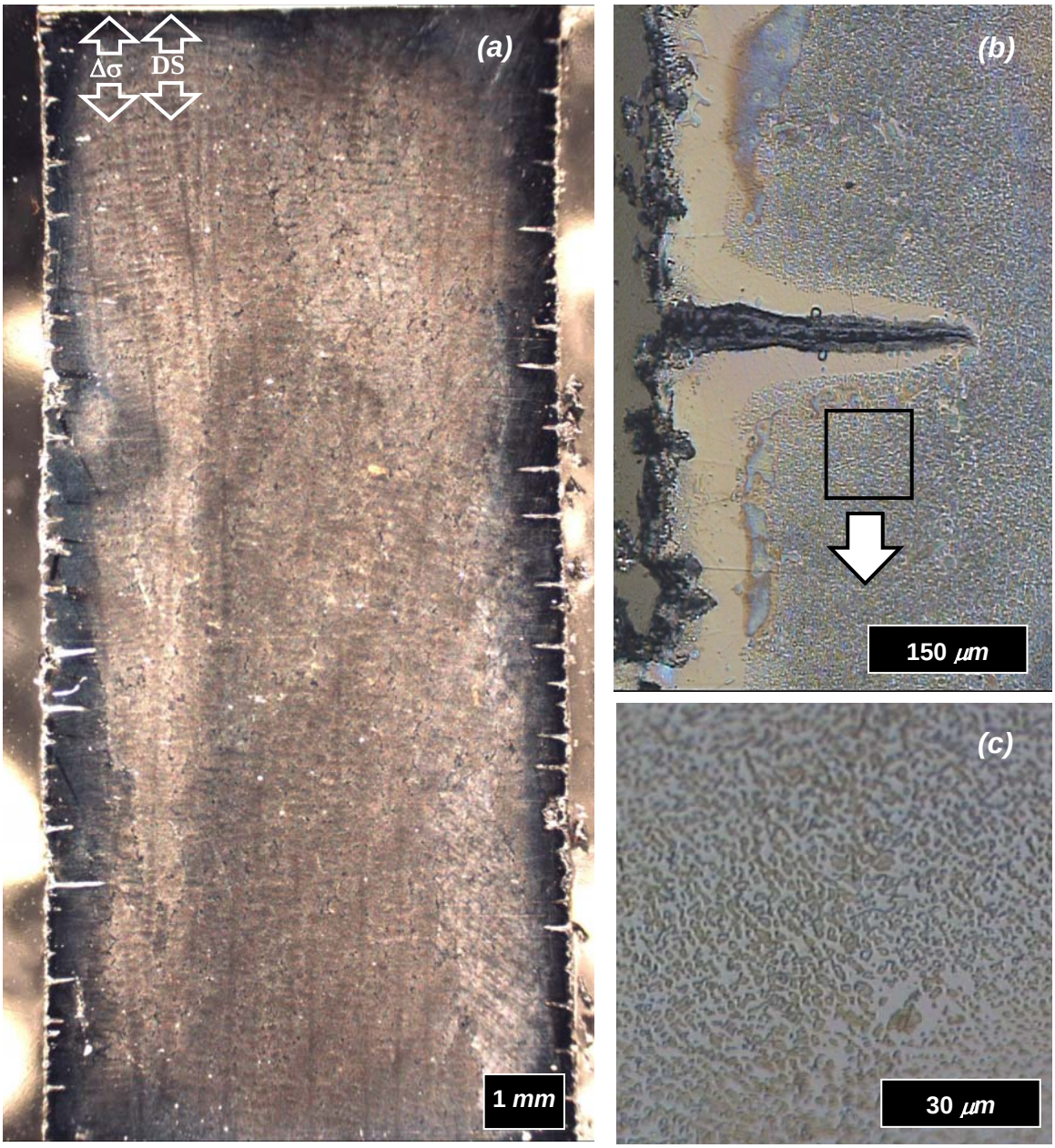


***Figure 4.29:*** *Crack initiation of creep-fatigue tested L-oriented DS GTD-111 under* $\dot{\varepsilon} = 0.5\%/s$, $R_\varepsilon$*=-1,* $\Delta\varepsilon$*=1.0% and T=1038°C. For this case* $t_h$ *= 10 min in compression.*

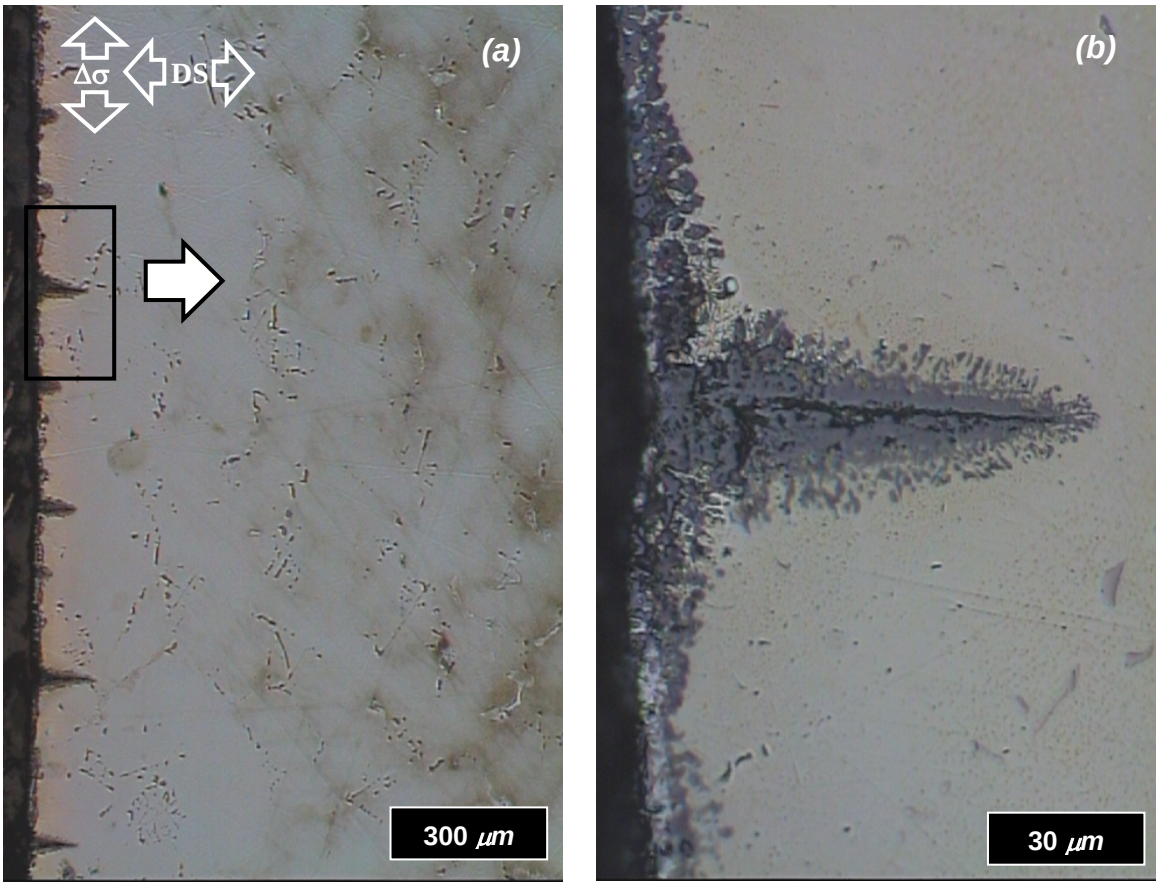


***Figure 4.30:*** *Crack initiation of creep-fatigue cycled T-oriented DS GTD-111 under $\dot{\varepsilon} = 0.5\%/s$, $R_\varepsilon$=-1, $\Delta\varepsilon$=1.0% and T=1038°C. For this case $t_h$ = 10 min in compression.*

Long term creep-fatigue testing with tensile dwells emphasizes traditional creep related damage mechanisms not evident in HC testing. Figures 4.31 and 4.32 emphasize crack initiation occurring at L- and T-oriented grain boundaries, respectively. The tortured grain boundaries in these materials were mimicked by the crack path. The high temperature caused some oxidation to occur at the exterior of the specimens. Under these tensile creep-fatigue conditions, the surface crack will either (a) propagate to the interdendritic regions (Fig. 4.31a) or (b) cause a stress concentration that will hasten the formation of subsurface voids and microcracks (Fig. 4.32a). Both grain boundary cracks

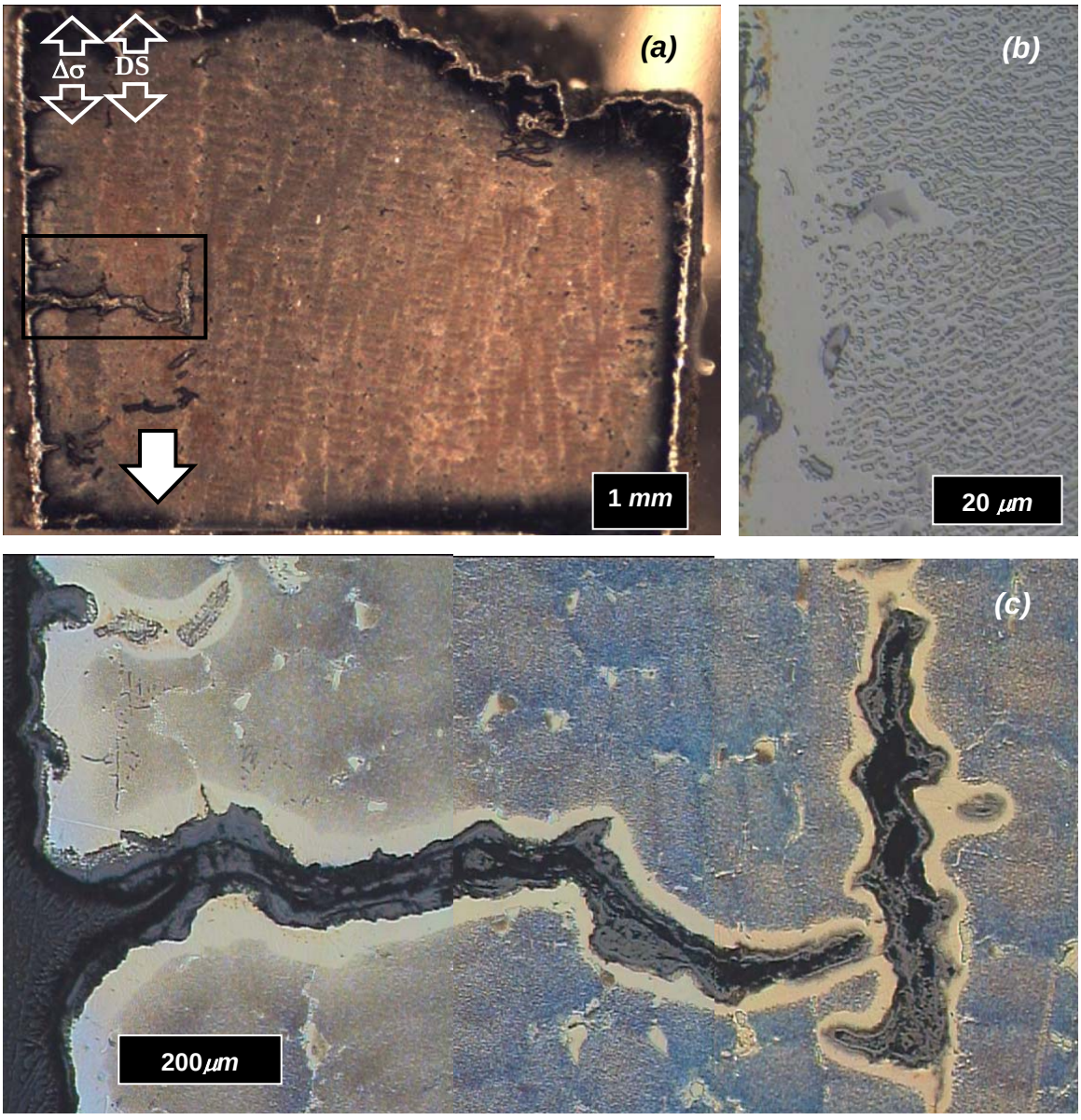


***Figure 4.31:*** *Crack initiation of creep-fatigue tested L-oriented DS GTD-111 under $\dot{\varepsilon} = 0.5\%/s$, $R_\varepsilon$=-1, $\Delta\varepsilon$=1.0% and T=1038℃. For this case $t_h$ = 10 min in tension.*

occurred near the surface and exhibit oxide layers that are very uniform. The reduction of life caused by introducing a tensile hold time at high temperature is more drastic for the T-oriented case. For example, at temperature of 1038°C and strain range of 1.0% under HT, L and T samples exhibited a difference in lives by a factor 8.6. The difference

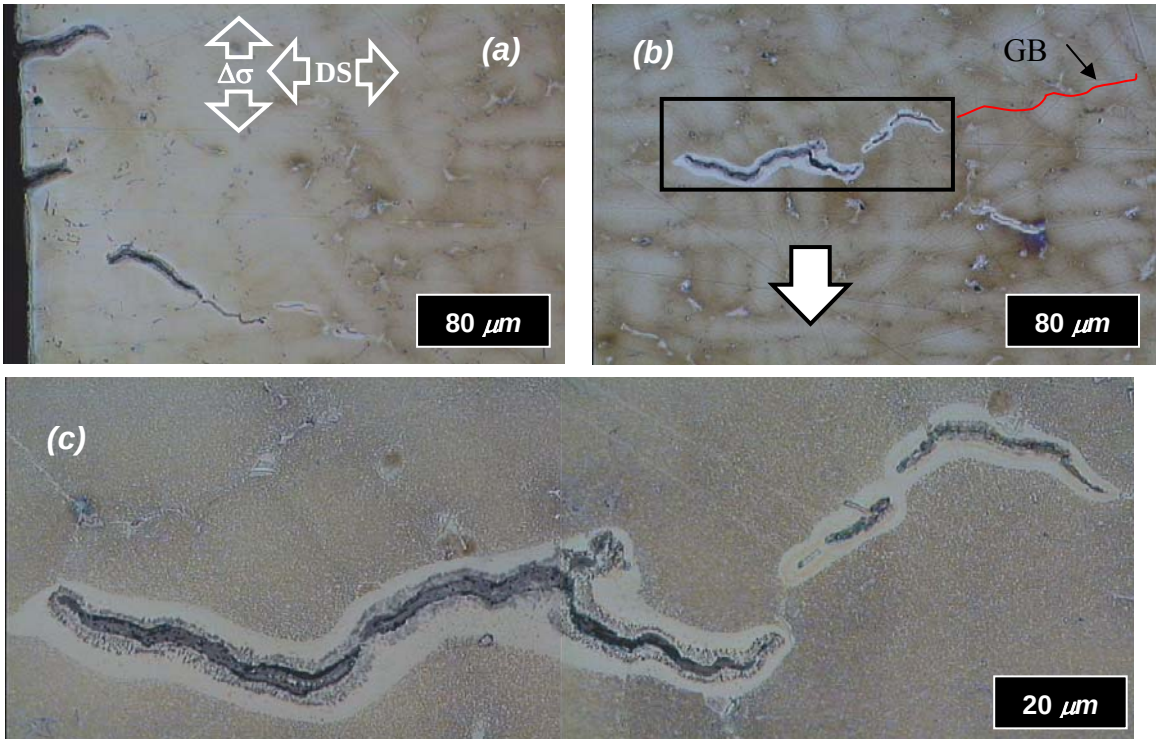


***Figure 4.32:*** *Crack initiation of creep-fatigue cycled T-oriented DS GTD-111 under* $\dot{\varepsilon} = 0.5\%/s$, $R_\varepsilon$*=-1,* $\Delta\varepsilon$*=1.0% and T=1038°C. For this case* $t_h$ *= 10 min in tension.*

was only 3.9 for CC under the same $\Delta\varepsilon$-$T$ combination. The larger quantity of grain boundaries present in the T-oriented case implies increased potential sites for crack initiation. Subsurface precipitate particles rafted (Fig. 4.31b) normal to the stress axis of the material.

*Effect of Dwell Time and Type on Crack Initiation Life*

The crack initiation lives of DS GTD-111 are influenced by dwell time. Dwell time/type and temperature results for $N_i$ of L and T-oriented are summarized in Tables 4.10 and 4.11, respectively. Important trends in the life results are as follows:

1) **Orientation:** Based on $\Delta\varepsilon_m$, the lives of L-oriented samples typically outlasted those of T-oriented samples. The lives of the materials are most similar when nominally fatigue-like conditions exist. Alternatively, the lives differ most dissimilar when tensile creep-like conditions prevail.
2) **Hold Time/Type:** Increased hold time in compression results in a lower density of cracking (more distance between adjacent cracks), but a shorter life. Increased hold time in tension results in a shorter life (more like creep conditions). Decreased hold time in tension or compression generally leads to a longer life (more life pure fatigue conditions). With increasing temperature, $N_i$ under HC quickly converge to $N_i$ under CC.
3) **Strain Range:** Decreasing the strain range at a temperature at or above 871°C shortens the crack initiation life (creates the most detrimental oxidizing conditions). When subjected to high strain ranges, DS GTD-111 samples have lives controlled by fatigue dominant mechanisms.
4) **Temperature:** Hold times do not have any effect on cycling at low temperatures (failure is controlled by plastic strain range). Increased temperature for the same hold time in compression leads to a longer life. Increased temperature for the same hold time in tension leads to a shorter life. Hold time in tension has shorter life than hold time in compression if the temperature is above 982°C (e.g. as to elicit creep conditions more rapidly).

## 4.6 Creep Deformation and Rupture

In order to understand the limitations of damage in DS Ni-base superalloys when fatigue damage is minimal, creep deformation and rupture experiments were conducted on DS GTD-111 (Ibanez, 2003). Using the rupture data and observations from microscopy, crack initiation estimates were obtained for cases when microstructural damage mechanisms related to creep dominate. Creep deformation histories and rupture data based on a variety of combinations of temperature and tensile stress used in this series of experiments are plotted in Appendix D. In each case there is a negligible amount of primary creep, and about of third of the total life in exhausted during steady state creep. The remaining portion is spent in tertiary creep.

***Table 4.12:*** *Creep data from rupture experiments on DS GTD-111*

| Temperature (°C) | Temperature (°F) | *Stress*, $\sigma$ (MPa) | *0.3% Strain (hr)* | *0.5% Strain (hr)* | *1.0% Strain (hr)* | *Rupture Time*, $t_r$ (hr) | Rupture Strain, $\varepsilon_f$ (%) | Specimen ID (Orientation) | Figure |
|---|---|---|---|---|---|---|---|---|---|
| 760 | 1400 | 414 | 17 | 123 | 745 | 5627 | 16 | L1-2A (L) | D.1 |
| 760 | 1400 | 552 | 2 | 14 | 115 | 685 | 10 | L5-11A (L) | D.1 |
| 760 | 1400 | 614 | 6 | 17 | 30 | 117 | 10 | L2-1A (L) | D.1 |
| 649 | 1200 | 896 | 22 | 51 | 118 | 466 | 6 | L503 (L) | D.1 |
| 760 | 1400 | 614 | 3 | 8 | 35 | 244 | 12 | L5-8 (L) | D.1 |
| 815 | 1500 | 455 | 4 | 18 | 64 | 321.5 | 22 | L5-5A (L) | D.2 |
| 871 | 1600 | 207 | 516 | 814 | 1454 | 4291 | 11 | L5-4 (L) | D.2 |
| 871 | 1600 | 242 | 21 | 29 | 97 | 495 | 12 | L3-1A (L) | D.2 |
| 871 | 1600 | 242 | 148 | 295 | 620 | 2149 | 19 | L5-5 (L) | D.2 |
| 871 | 1600 | 290 | 8 | 16 | 37 | 355 | 14 | L1-2 (L) | D.2 |
| 871 | 1600 | 290 | 19 | 62 | 162 | 673 | 12 | L5-6A (L) | D.2 |
| 871 | 1600 | 379.5 | 1 | 4 | 28 | 28 | 14 | L5-11 (L) | D.2 |
| 982 | 1800 | 124 | 83 | 174 | 365 | 822 | 18 | L5-4A (L) | D.3 |
| 982 | 1800 | 145 | 24 | 44 | 108 | 302 | 9 | L5-9A (L) | D.3 |
| 760 | 1400 | 414 | 800 | 1544 | 3125 | 5346 | 2 | T5-2 (T) | D.1 |
| 760 | 1400 | 517.5 | 2 | 10 | 132 | 375 | 7 | T5-9 (T) | D.1 |
| 760 | 1400 | 614 | 1 | 2 | 16 | 43 | 2 | T5-4A (T) | D.1 |
| 815 | 1500 | 455 | 4 | 18 | 51 | 127 | 5 | T5-4 (T) | D.2 |
| 871 | 1600 | 207 | 313 | 866 | 1836 | 2594 | 2 | T5-7A (T) | D.2 |
| 871 | 1600 | 242 | 100 | 192 | 373 | 980 | 13 | T5-3 (T) | D.2 |
| 871 | 1600 | 290 | 42 | 112 | 276 | 484 | 2 | T5-2A (T) | D.2 |

Creep rupture data for these experiments are summarized in Table 4.12. The first digit of the Specimen ID represents the batch from which the specimens were machined. The numbers 1 through 3 indicate Batch 1 while digits between 5 and 11 correspond to Batch 2. Specimens from Batch 1 consistently have shorter creep lives at the same stress level in comparison to those from Batch 2. This is due to the material processing route as described in Chapter 3.

Regardless of batch number, comparing tests performed at identical $\sigma$ and $T$ conditions, but different orientations, indicates that at high $\sigma$ and low $T$ levels, the time to rupture, $t_r$, in the L orientation is only 1.4 times longer than the rupture life of T-oriented cases. As conditions transition to low $\sigma$ and high $T$ levels, however, this factor increases by two orders of magnitude. The Larson-Miller Parameter shows this trend (Fig. 2.19).

Generally, the most creep-ductile regions at the surfaces are those that intersect dendritic boundaries. Because these regions contain a smaller volume fraction of hardening precipitate particles and a high content of oxide-formers, inelastic deformation accumulates there more rapidly. Microvoid nucleation in these areas rapidly advances to void coalesce and then to the formation of microcracks. This is also the case for fatigue cracks. Although some cracks have been observed to nucleate in the interior of the material, the vast majority of cracks in the material begin nearby if not directly on the surface. Figure 4.33 shows L and T-oriented creep-tested samples from different batches that exhibit this crack initiation behavior. In both cases cracks follow a tortuous path which is controlled by the location of the interfaces of dendritic cores. The rapid

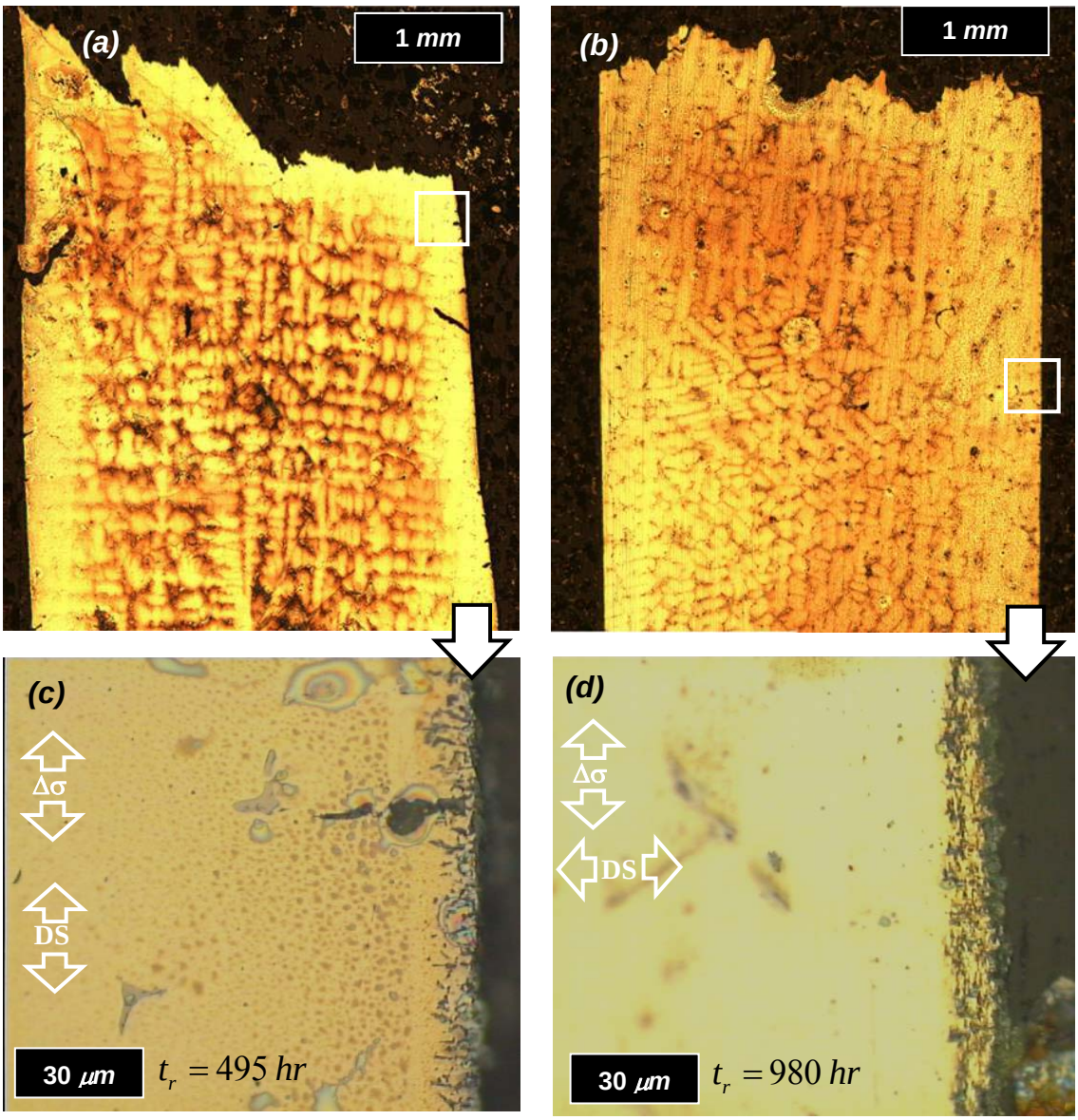


***Figure 4.33:*** *Creep deformation and rupture of (a, c) L-oriented and (b, d) T-oriented DS GTD-111. For each case T=871°C and σ = 242 MPa (Specimen IDs: L3-1A and T5-3).*

propagation of longer cracks shield the growth of neighboring cracks. As such, in nearly all cases one dominant crack is responsible for the final rupture of the specimen.

Although surfaces of creep specimens oxidize at the high temperature after long exposure times, the presence of surface layers are irrelevant under static conditions.

Cumulative oxide layers having a depth between 10 and 15 $\mu m$ penetrated the surfaces of samples shown in Figs. 4.33c and 4.33d subjected to 495 *hr* and 980 *hr*, respectively. Increasing the tensile stress from 242 *MPa* (35 *ksi*) to 380 *MPa* (55 *ksi*) leads to no significant diminishment of the extent of surface crack formation. The $t_r$ for this particular experiment was approximately 28 *hr*; accordingly, as such the cumulative surface oxides were thin, as illustrated in Fig. 4.34.

The characteristic of surface cracking is also very similar to that observed under creep-fatigue conditions accompanied by very long tensile dwells. The cracked samples found on Figs. 4.28b and 4.33 show periodically-spaced, tortuous surface cracks. The crept sample was subjected to 380 *MPa* and ruptured after approximately 54 *hr*, while the creep-fatigue-tested sample was subjected to $\sigma_{max}$ = 304 *MPa* that relaxed to 247 *MPa* by the end of the cycle. The sample was removed from loading after 52 *hr*.

Although increasing the temperature and decreasing the applied tensile load increases the rupture life of the material, even much thicker surface grown oxides have minimal influence of surface cracking. For example, Fig. 4.35 illustrates that surface oxides formed on L-oriented DS GTD-111 exposed to 982°C displayed no preferential behavior to assist in the growth of cracks located near the surface where voids have developed. Precipitate particle rafting was also observed in this specimen.

In nearly all cases, fracture surfaces follow interdendritic channels. The presence of large particles at the surfaces indicates that carbides participate in the link-up of cracks. For example, samples tested between 760°C and 871°C with stresses between 289 and 614 *MPa* have interdendritic fracture surfaces dense with Cr-rich carbides. At

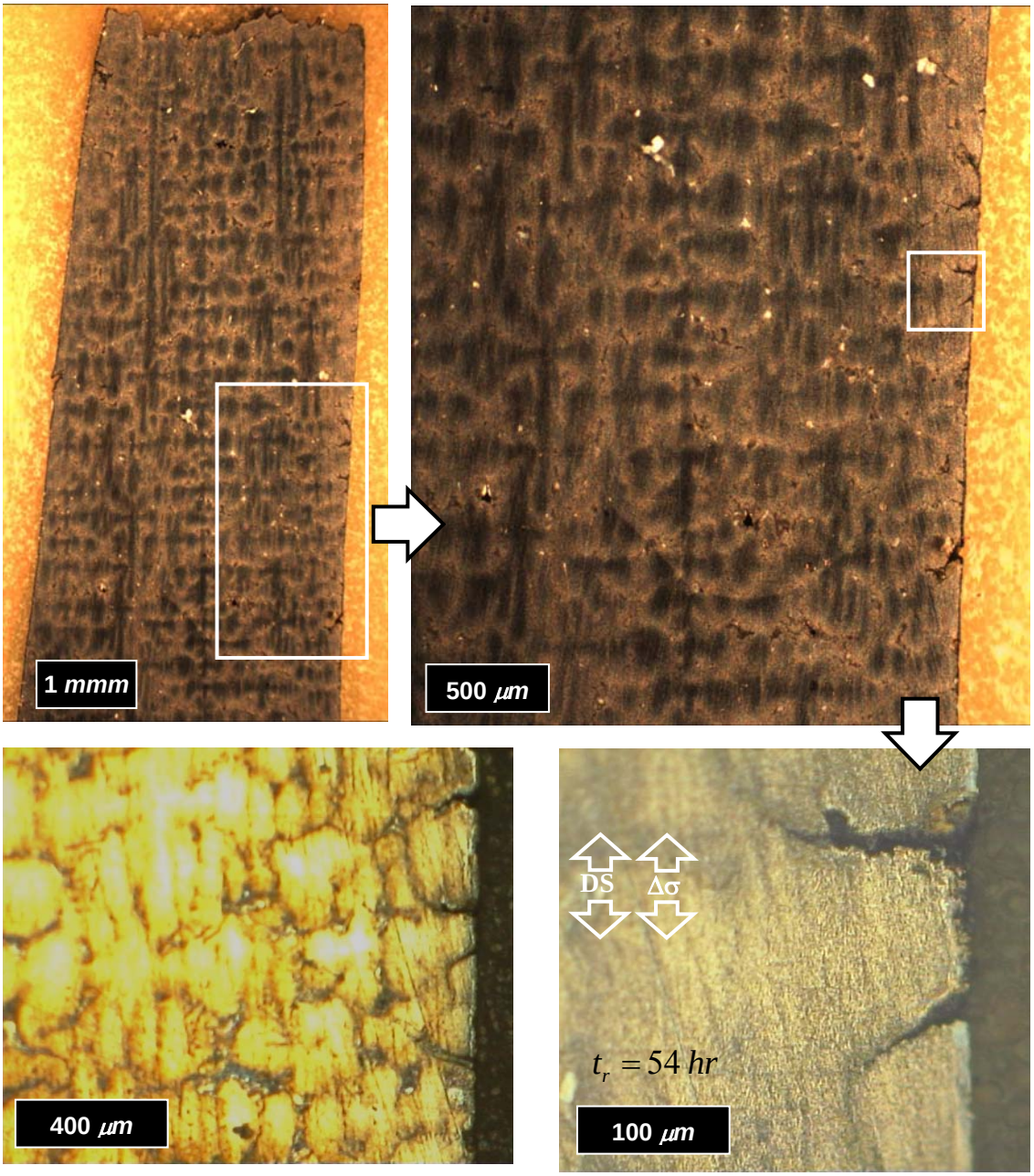


***Figure 4.34:*** *Creep deformation and rupture of L-oriented DS GTD-111. For this case T=871℃ and $\sigma$ = 380 MPa (Specimen ID L5-10).*

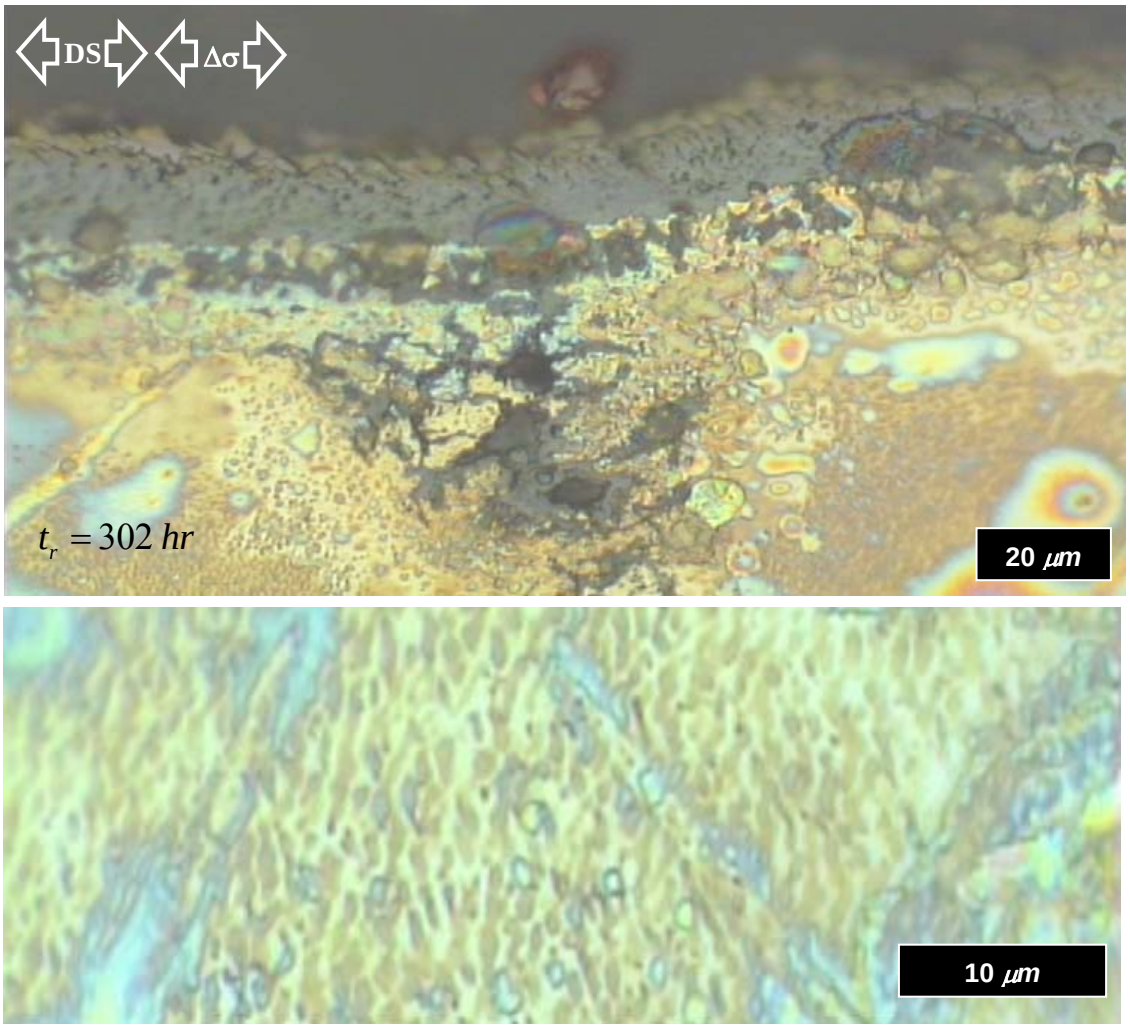


***Figure 4.35:*** *Oxidation and rafting of creep-tested L-oriented DS GTD-111. For this case T=982℃ and $\sigma$ = 145 MPa (Specimen ID: L5-9A).*

high temperatures, the fracture surfaces contain a large amount of dimples and cracks, an indication of higher creep ductility.

## *4.7 Non-Isothermal Effects*

Both L- and T-oriented DS GTD-111 specimens have been subjected to thermomechanical fatigue (TMF) cycling. Each of the results is listed in Table 4.13. In a typical TMF experiment, temperature was continuously cycled between 538°C and

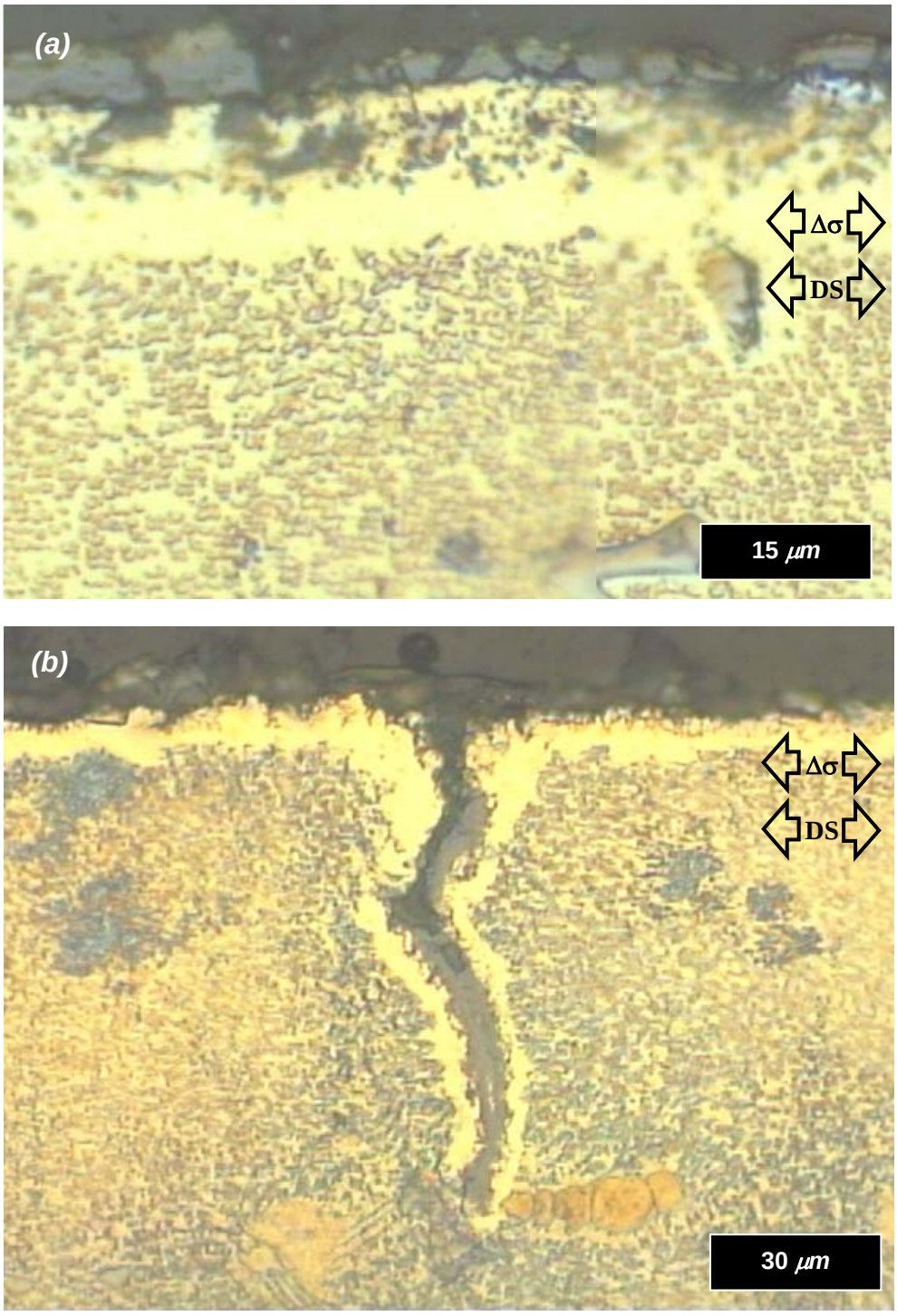


***Figure 4.36:*** *Oxide (a) spallation and (b) spiking observed in L-oriented DS GTD-111 resulting from (a) in-phase TMF cycling with $\Delta\varepsilon$=1.0%, $T_{max}$=1038°C, and (b) out-of-phase TMF cycling with $\Delta\varepsilon$=0.5%, $T_{max}$=927°C. For each case, $R_\varepsilon$=-1, $T_{min}$=538°C, and $t_{tc} = 180\ s$.*

927°C (at 538°C to 1038°C in two cases), and the cycle period was 180 *s*. Completely reversed mechanical strain ranges of 0.5% or 1.0% were either in-phase (IP) ($\phi = 0°$) or out-of-phase (OP) ($\phi = 0°$) with the thermal strain cycles. The coefficient of thermal expansion (CTE) of oxidized material is $9\times10^{-6}$/°C, which is nearly 75% of that for the base material. Oxide scales grown on the metal during maximum tensile conditions of fatigue reversals experience the largest compressive and shear stresses at the minimum strain level. Superimposing a compressive stress with a temperature drop, such as the case in IP TMF cycling, results in uneven thermal strain distribution across the oxide/metal interface, which accelerates the accumulation of oxide spallation. Adhesive oxide scales, like those grown on DS GTD-111 are prone to developing shear cracks that cause wedging. A typical spalled surface is shown in Fig. 4.36a.

***Table 4.13:*** *Crack initiation life of DS GTD-111 under TMF conditions ($R_\varepsilon$=-1)*

| Min. Temp. | | Max. Temp. | | Phase Shift (°) | Mechanical Strain Range, $\Delta\varepsilon_m$ *(%)* | Plastic Strain Range, $\Delta\varepsilon_{pl}$ *(%)* | Elastic Strain Range, $\Delta\varepsilon_{el}$ *(%)* | Thermal Strain Range, $\Delta\varepsilon_{el}$ *(%)* | Crack Initation Life, $N_i$ | Specimen ID (Orientation) | Figure |
|---|---|---|---|---|---|---|---|---|---|---|---|
| (°C) | (°F) | (°C) | (°F) | | | | | | | | |
| 538 | 1000 | 927 | 1700 | 180 | 1.00 | 0.19 | 0.81 | 0.53 | 148 | L8-11A (L) | B.3 |
| 538 | 1000 | 927 | 1700 | 180 | 0.50 | 0.02 | 0.48 | 0.61 | 1270 | L8-10A (L) | B.2 |
| 538 | 1000 | 1038 | 1900 | 0 | 1.00 | 0.13 | 0.87 | 0.53 | 58 | L8-9 (L) | B.1 |
| 538 | 1000 | 927 | 1700 | 180 | 1.00 | 0.44 | 0.56 | 0.53 | 17 | T8-10 (T) | B.4 |
| 538 | 1000 | 927 | 1700 | 180 | 0.50 | 0.20 | 0.30 | 0.53 | 173 | T8-10A (T) | B.5 |
| 788 | 1450 | 1038 | 1900 | 180 | 0.47 | 0.08 | 0.39 | 0.47 | 591 | B17-T-F2 (T) | B.7 |
| 538 | 1000 | 1038 | 1900 | 180 | 0.84 | 0.24 | 0.60 | 0.84 | 17 | B17-T-F3 (T) | B.6 |

Whereas the oxide spalling mechanism is a consequence of shear cracking and wedging, oxidation spiking (Fig. 4.36b) results from oxide formation under compressive conditions at high temperatures. Such is the case with OP TMF cycling. The oxidized material fractures upon cyclic reversals, much like isothermal continuously cycled cases.

The stress response of DS GTD-111 under TMF is plotted with respect to the mechanical component of strain for each test case in Figs. 4.37a and 4.37b. Since both the modulus and the yield strength of the material are temperature dependent, the stresses required to achieve the maximum and minimum strains are not equal. The consequence is positive mean stresses for OP cycling, and negative mean stresses for IP cycling. Increasing the mechanical strain range caused an increase in the fraction of plastic to total mechanical strain amplitude for both L and T cases. Mechanical strain-life curves for DS GTD-111 under TMF are shorter than those under LCF (Fig. 4.37c), due primarily to the additional microstructural mechanisms activated in the presence of non-isothermal cycling (e.g. oxide spiking for OP cases and spallation for IP cases), as well as increased cycle time that cause subsurface damage in IP cases.

## *4.8 Pre-Exposure Effects*

The most noticeable effects of exposing Ni-base superalloys to high temperature conditions, either with or without pre-loading, can be categorized as those affecting either the surface or the subsurface of the material. When DS GTD-111 is exposed to 982°C for 100 *hr* in static laboratory air, for example, an oxide layer measuring approximately 11 $\mu m$ forms on the surface. Once the material is subjected to mechanical loading, oxide spallation occurs (Fig. 4.38). The presence of the oxide layer prior to fatigue cycling alters the diffusion and damage processes near the surface and influences the mechanisms of crack initiation of the material.

The effect of prior exposure on crack initiation life of L- and T-oriented DS GTD-111 was investigated using a standard pre-exposure time, $t_{pre} = 100\ hr$, and temperature,

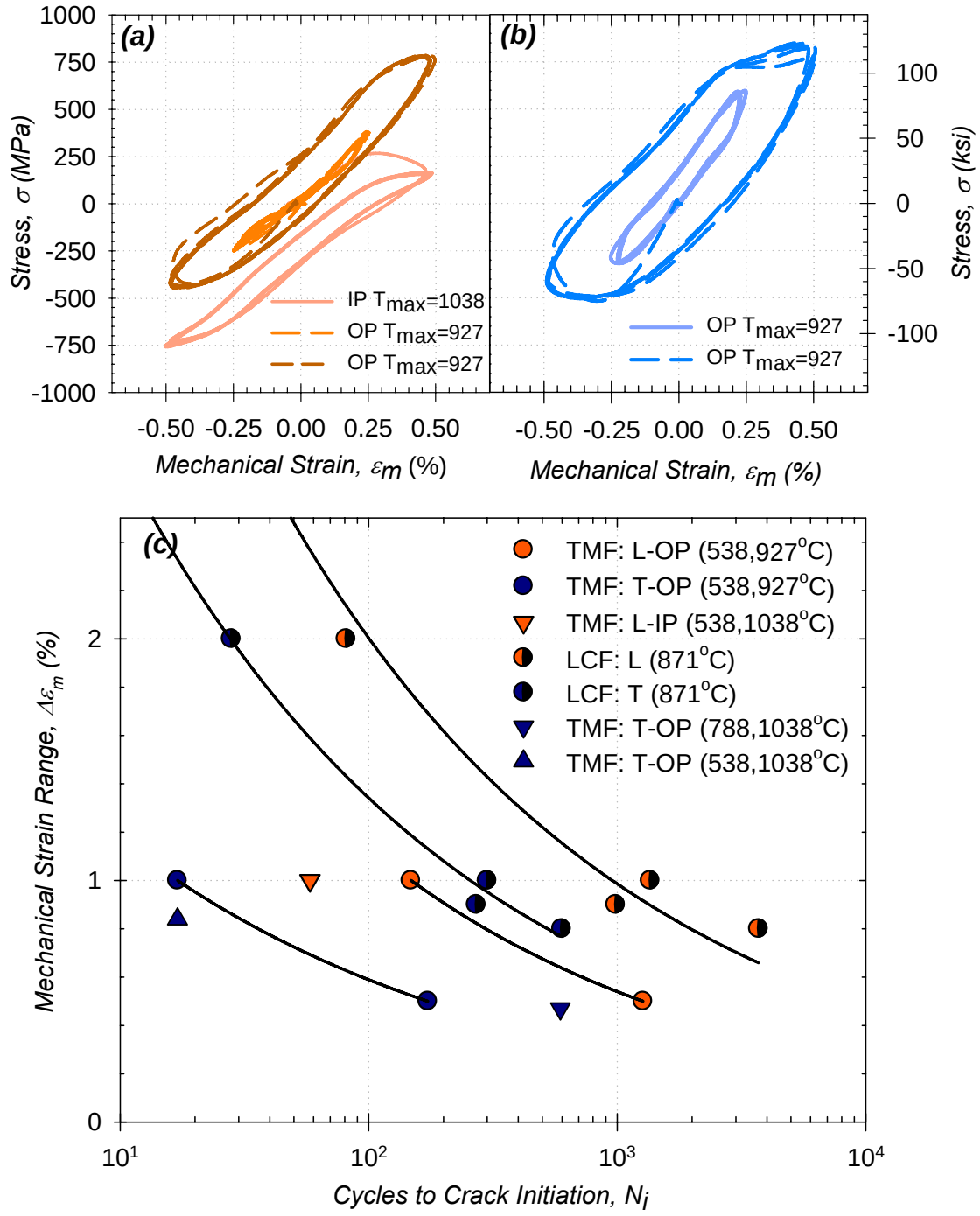


***Figure 4.37:*** *(a, b) Comparison of initial stress-mechanical strain responses of TMF cycled (a) L and (b) T DS GTD-111 with $T_{min}$=538ºC. (c) Comparison of mechanical strain crack initiation lives. For each case $R_\varepsilon$=-1. In two cases $T_{max}$=1038ºC.*

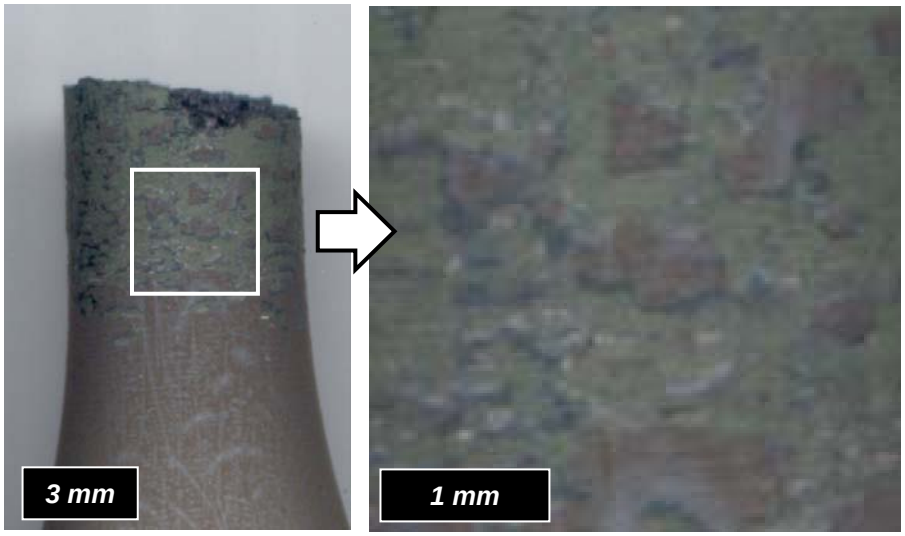


***Figure 4.38:*** *Oxide spallation after LCF cycling of a compressively pre-crept (982°C, $t_{pre}$=100 hr, 0 MPa, air) L-oriented DS GTD-111 specimen.*

$T_{pre} = 982°C$. While most specimens where pre-exposed in static air, two specimens where exposed to wet $H_2S$ that simulated the gasified operating environment of DS GTD-111 turbine blades. Additionally, while most specimens were pre-exposed under no load, several were subjected to static pre-loads of either $\pm 100\ MPa$. Afterwards, each sample was continuous fatigue cycling according to the test configurations listed in Table 4.14. A temperature of 871°C, with $R_\varepsilon$=*-1* and $\dot{\varepsilon} = 0.5\%/s$ was applied for all cases. The stress-strain histories for each of the tests are given in Appendix C.

Pre-exposing DS GTD-111 in either air or $H_2S$ alters the surface of the material, as shown in Fig. 4.39. The crack initiation behavior of the material is not only influenced by the cumulative oxide layer, but also the γ′-depleted zone. The presence of the oxide layer, in locations where it has not spalled, protects the material from further oxidation.

Nickel-base superalloys are known to passivate in this manner (Trexler and Sanders, 2002). Also during fatigue cycling, the ductile γ′-depleted zone (i.e., essentially a matrix layer containing fine $Ni_3Al$ particles), forms wide cracks that arrest at the virgin material. At room temperature, the γ′-depleted zone was found to have a Vickers hardness that was less than that of the unaffected material (Park et al., 2000). The stress concentrations at these early-formed crack tips initiate the oxide spiking damage mechanism. Under identical LCF conditions without prior exposure, the oxide spiking damage mechanism does not occur in DS GTD-111. Pre-exposing the material in the $H_2S$ environment led to deeper ingress of both layers compared to the air-exposed case. In both cases shown in Fig. 4.39, surface-initiated cracking was the dominant cause of damage. Multiple hairline cracks emanated from early-formed matrix cracks and extended into the bulk of the material. Very little oxidation formed on the fracture surface in either case since the cracks advanced quickly and the fatigue temperature was low. Since surface degradation was more aggressive in the $H_2S$-exposed case, the cracks in the matrix layer are longer.

In a previous study involving pre-exposure (Antolovich et al., 1980), it was demonstrated that removing both oxide and matrix layers via machining prior to high temperature fatigue cycling eliminated the life reduction effect for René 80 (Fig. 2.18). To characterize the individual roles of the surface layers, the oxide layer of an air-exposed DS GTD-111 sample was hand-polished to a depth of approximately 20 $\mu m$ and subsequently fatigue-tested. The polishing completely removed the oxide layer, and the γ′-depleted zone was left intact. It was determined that the spacing between surface cracks in the air-exposed and air-exposed polished cases were comparable. The crack initiation life of the polished sample was also comparable to that of the unpolished

***Table 4.14:*** *Crack initiation life of pre-exposed DS GTD-111 (For each case $t_{pre}$=100hr)*

| ***Pre-Exposure*** | | | | ***Fatigue Test*** | | | | | | | | |
|---|---|---|---|---|---|---|---|---|---|---|---|---|
| Temperature (°C) | Temperature (°F) | Environ-ment | Load (MPa) | Temperature (°C) | Temperature (°F) | Environ-ment | Total Strain Range, $\Delta\varepsilon_m$ (%) | Plastic Strain Range, $\Delta\varepsilon_{pl}$ (%) | Elastic Strain Range, $\Delta\varepsilon_{el}$ (%) | Crack Initation Life, $N_i$ | Specimen ID (Orientation) | Figure |
| 982 | 1800 | Air | 100 | 871 | 1600 | Air | 0.80 | 0.22 | 0.58 | 167 | A27-L-F1 (L) | C.1,C.2 |
| 982 | 1800 | Air | 100 | Creep deformation too large | | | | | | | A27-L-F2 | C.1 |
| 982 | 1800 | Air | -100 | 871 | 1600 | Air | 0.80 | < 0.01 | 0.80 | 1857 | A27-L-F8 (L) | C.1,C.3 |
| 982 | 1800 | Air | -100 | Specimen buckled under compression | | | | | | | L8-12A (L) | C.1 |
| 982 | 1800 | Air | -100 | Specimen buckled under compression | | | | | | | A27-L-F11 | C.1 |
| No Pre-Exposure | | | | 871 | 1600 | Air | 0.50 | < 0.01 | 0.50 | 29159 | L8-3 (L) | A.14 |
| 982 | 1800 | Air | 0 | 871 | 1600 | Air | 0.50 | 0.05 | 0.45 | 4250 | B18-L-F6 (L) | C.8 |
| No Pre-Exposure | | | | 871 | 1600 | Air | 0.80 | 0.01 | 0.79 | 3699 | GTD-CC04 (L) | A.3 |
| 982 | 1800 | Air | 0 | 871 | 1600 | Air | 0.80 | < 0.01 | 0.80 | 1958 | B17-L-F3 (L) | C.4 |
| 982 | 1800 | Wet $H_2S$ | 0 | 871 | 1600 | Air | 0.80 | 0.23 | 0.57 | 979 | A27-L-F15 (L) | C.5 |
| 982 | 1800 | Air/Polished | 0 | 871 | 1600 | Air | 0.80 | 0.03 | 0.77 | 1601 | L8-12 (L) | C.7 |
| No Pre-Exposure | | | | 871 | 1600 | Air | 0.50 | < 0.01 | 0.50 | 16069 | T8-2A (T) | A.13 |
| 982 | 1800 | Air | 0 | 871 | 1600 | Air | 0.50 | 0.04 | 0.46 | 548 | B17-T-F5 (T) | C.9 |
| No Pre-Exposure | | | | 871 | 1600 | Air | 0.80 | 0.07 | 0.73 | 598 | T8-5 (T) | A.25 |
| 982 | 1800 | Air | 0 | 871 | 1600 | Air | 0.80 | 0.16 | 0.64 | 221 | A27-T-F5 (T) | C.10 |
| 982 | 1800 | Wet $H_2S$ | 0 | 871 | 1600 | Air | 0.80 | 0.11 | 0.69 | 84 | A27-T-F4 (T) | C.6 |

specimen, as shown in Table 4.14. These two experiments along with the observation from the prior study by Antolovich and coworkers (Antolovich et al., 1980) implies that the presence of the γ′-depleted zone developed via prior exposure has a significant effect on the subsequent fatigue life.

In each case of this series of experiments, crack initiation life was reduced by pre-exposure. Microscopy was conducted to characterize the underlying mechanisms responsible for the reduction in mechanical strain life of the pre-loaded cases. Figure 4.40 compares the microstructures of the two pre-crept and fatigued samples to that of a sample that was pre-crept in tension, but not subjected to any fatigue cycling whatsoever. Common to the surface of each material is the accumulated oxidation layer. Oxides spalled from the majority of the surface area of the case pre-crept in compression (Fig. 4.40c). For the two cases pre-crept in tension (Fig. 4.40a,b), numerous microcracks were found beneath the surface of both the un-cycled and cycled cases. Upon fatigue cycling,

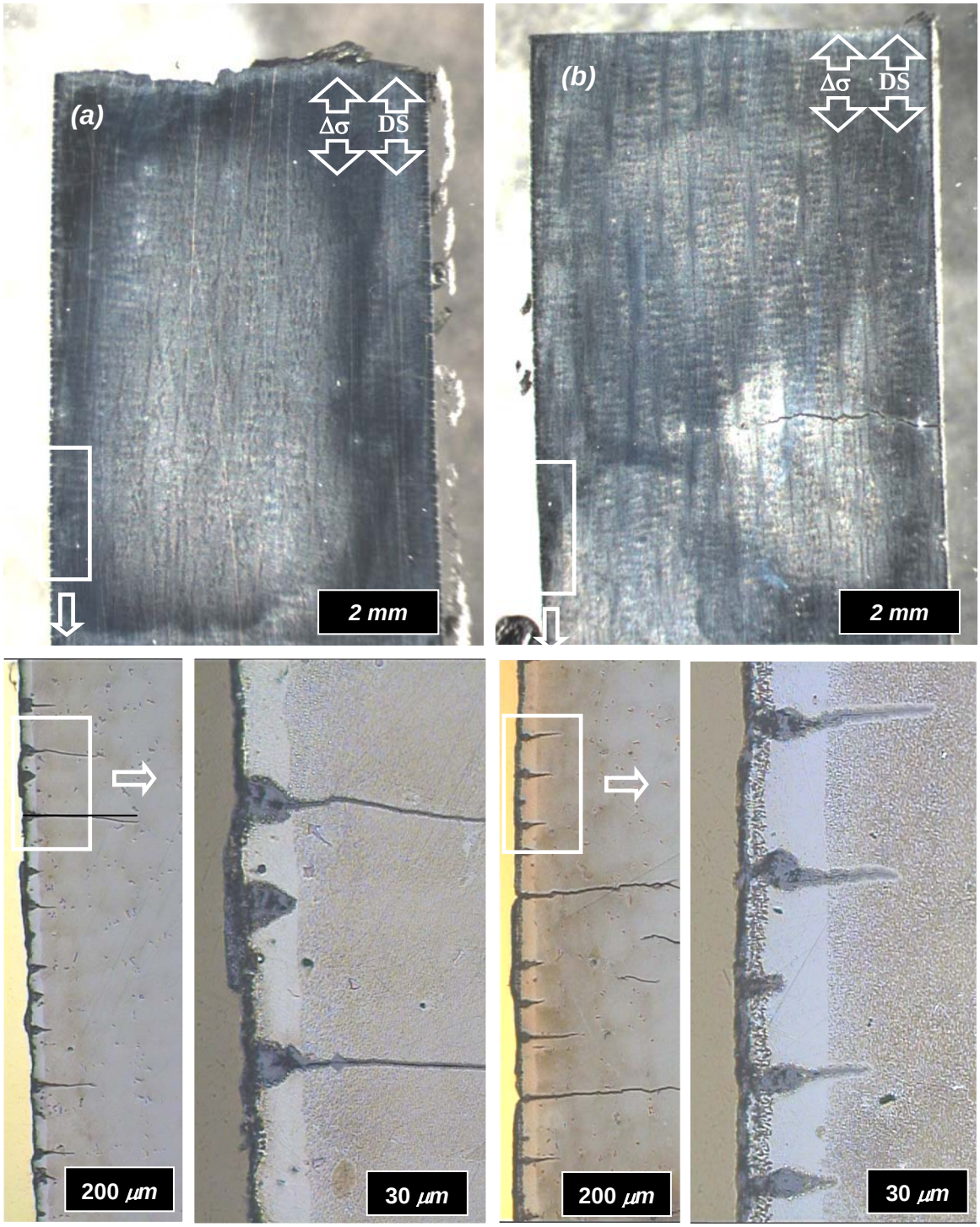


***Figure 4.39:*** *Comparison of microstructures of (a) air and (b) $H_2S$-exposed L-oriented DS GTD-111. Pre-exposure conditions: 982℃, 100 hr, 0 MPa. Fatigue cycling conditions: $\Delta\varepsilon$=0.8% 871℃, and $\dot{\varepsilon} = 0.5\%/s$.*

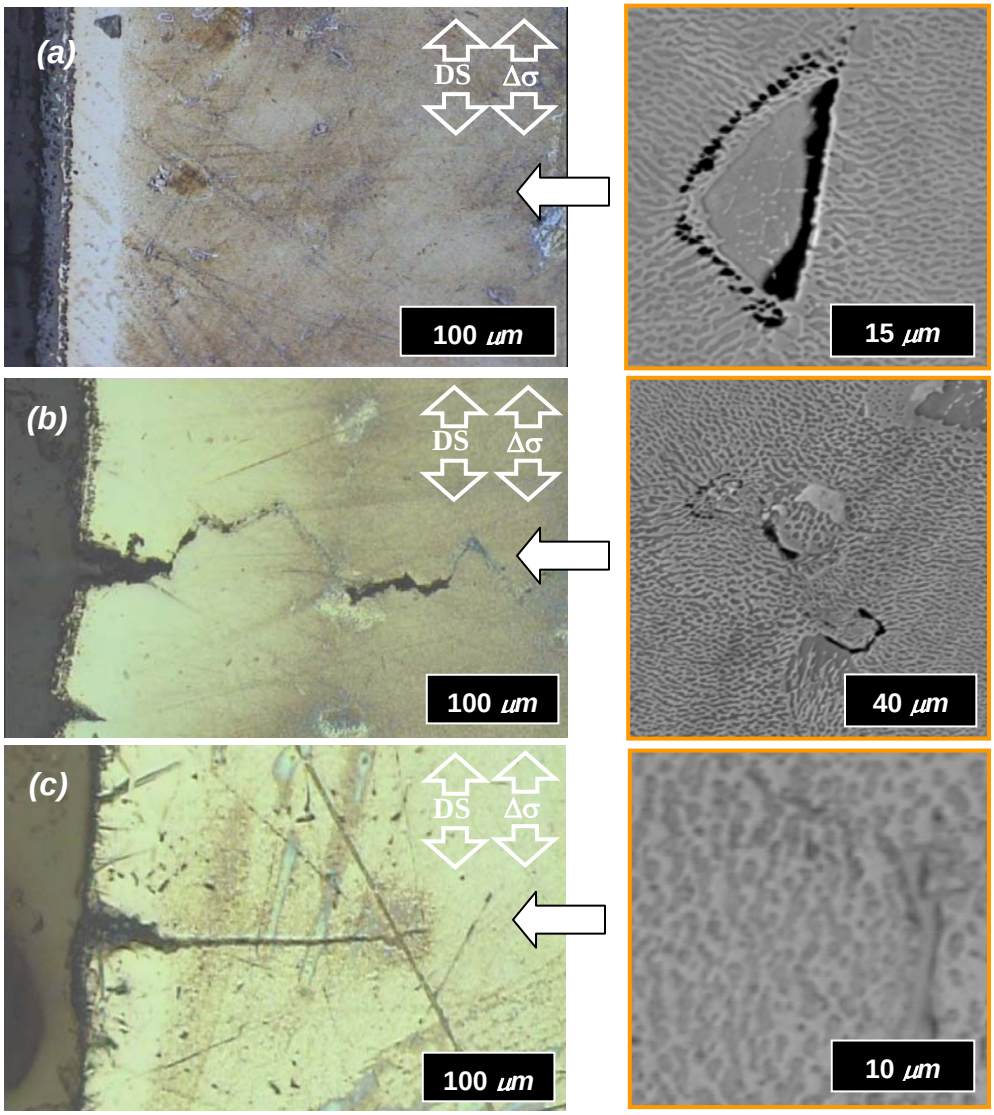


***Figure 4.40:*** *Pre-exposure effects on crack initiation behavior of L-oriented DS GTD-111 in static air under (a) pre-exposure only (100 hr, 982℃, 100 MPa), (b) pre-exposure (100 hr, 982℃, 100 MPa) and fatigue ($\Delta\varepsilon$=0.5% and 871℃), and (c) pre-exposure (100 hr, 982℃, -100 MPa) and fatigue ($\Delta\varepsilon$=0.8% and 871℃).*

cracks emanating from the surface coalesced with those initiated at the subsurface, thus creating a non-planar fracture path. These subsurface cracks do not form in the compressively pre-crept case; therefore, the crack initiation behavior is much like that of the pre-heated/unloaded cases.

In each of the pre-crept cases rafting occurred. These raft-shaped particles measure five times the original length of the cuboidal precipitate particles. Transmission electron microscopy (TEM) is needed to precisely determine the effect of rafting on the deformation behavior of the material, and is left for future study.

The alteration of the mechanical properties of DS GTD-111 depends on the pre-exposure conditions. The effect of pre-exposure on the elastic modulus of the material is compared with unexposed cases in Fig. 4.41. Values for $E$ were obtained from the initial loading cycle. Pre-creeping L-oriented DS GTD-111 in tension lowers $E$ by approximately 24%. Other forms of pre-exposure have marginal effects on the modulus of either L- (Fig. 4.41a) or T-oriented (Fig. 4.41a) DS GTD-111. The effect of pre-exposure on the initial cyclic stress strain response of L-oriented DS GTD-111 is compared with its unexposed response in Fig. 4.42. Air-exposed materials subjected to either 0 *MPa* or -100 *MPa* exhibit virtually no alteration of yield properties. Conversely, the materials pre-exposed in either tension or $H_2S$ have lower yield strengths.

The effect of pre-exposure on the reduction of the crack initiation lives of DS GTD-111 is a direct consequence of the degraded material and its mechanical properties. Figure 4.43 shows the effect of pre-exposure on life. Of all of the unloaded cases considered with $\Delta\varepsilon = 0.8\%$, pre-exposing the material in air has the least detrimental effect on life. Increasing the aggressive nature of the pre-exposure environment from air

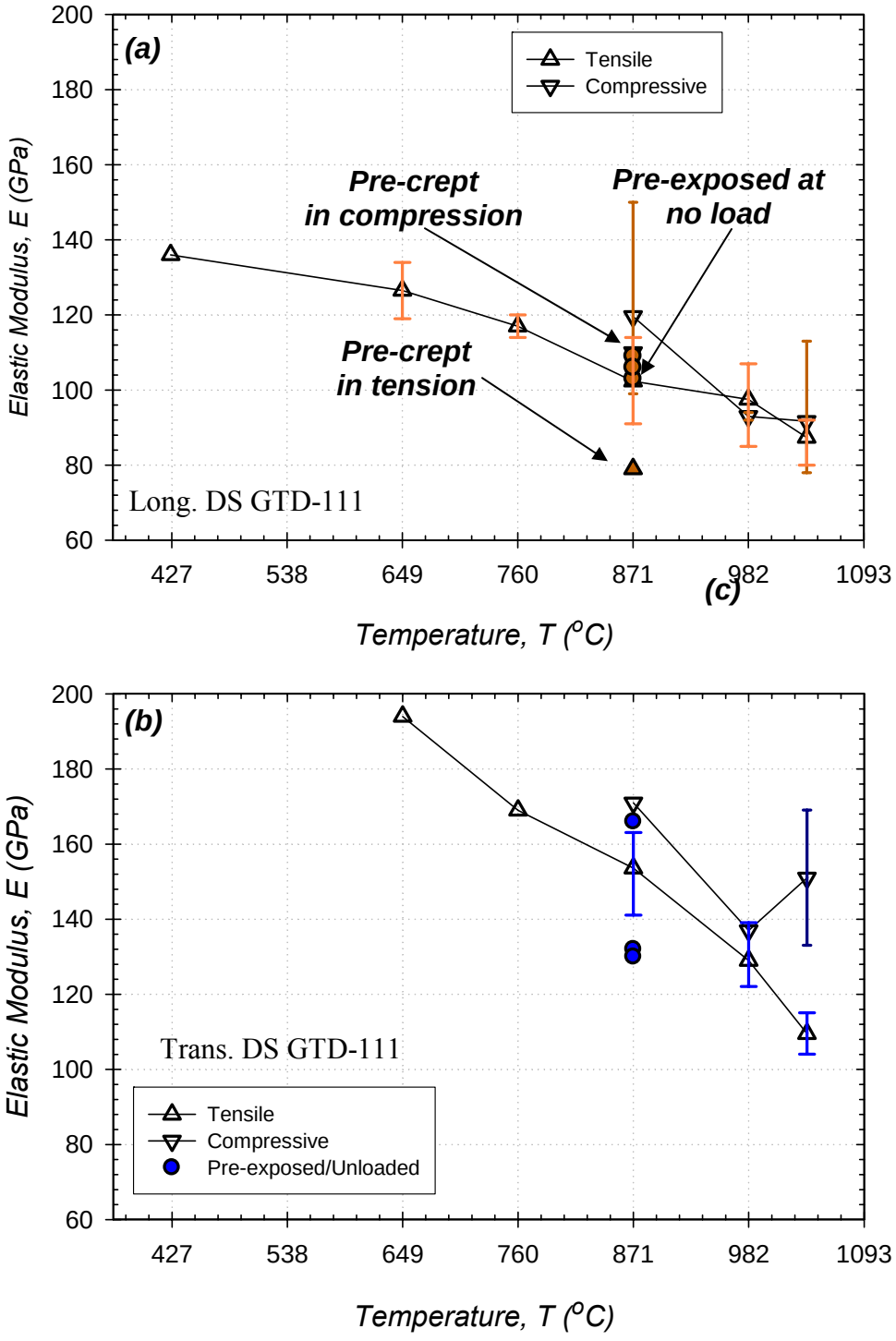


***Figure 4.41:*** *Elastic modulii of (a) L- and (b) T-oriented DS GTD-111 measured during initial cycle. For every case $R_\varepsilon$=-1, $\dot{\varepsilon} = 0.5\%/s$. For pre-exposed/crept cases $t_{pre}$=100 hr and $T_{pre}$=982°C (1800°F) in air.*

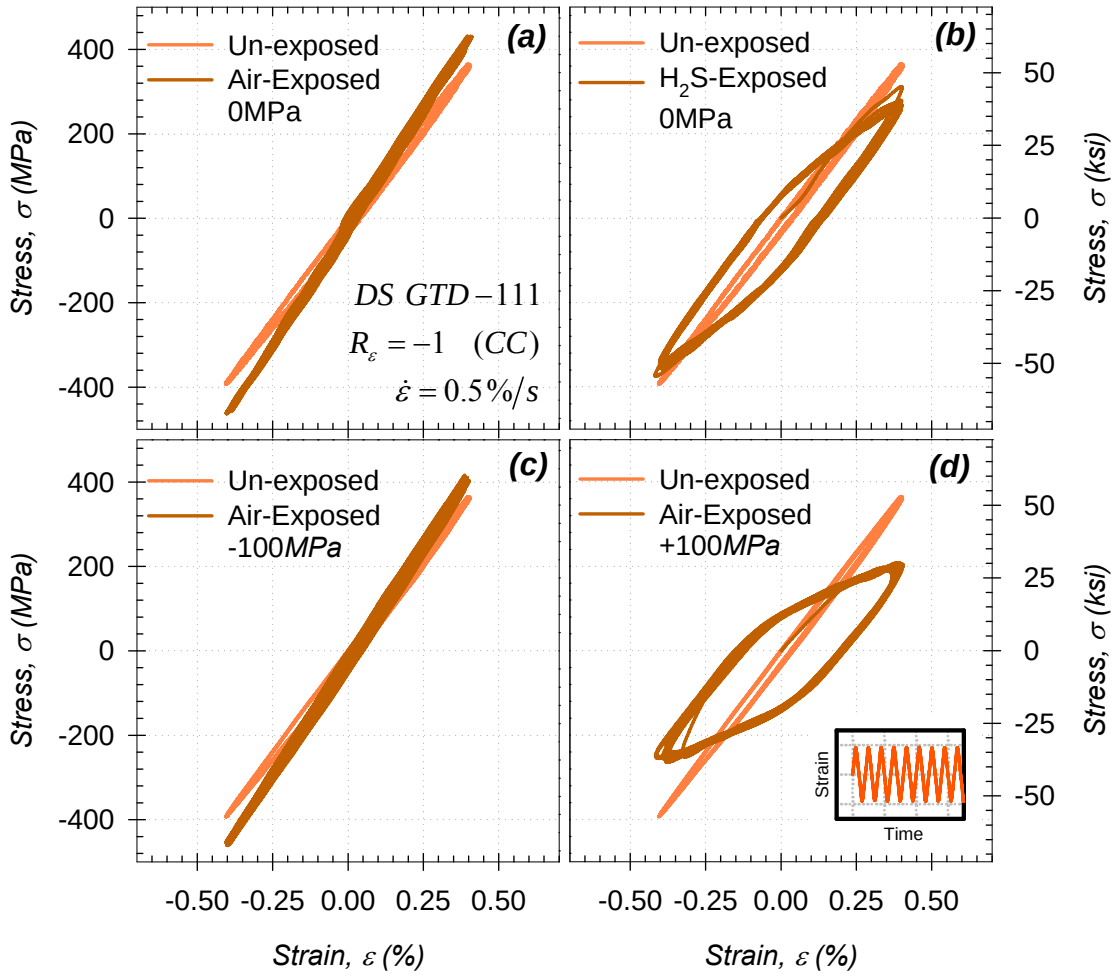


***Figure 4.42:*** *Pre-exposure effects on initial hysteresis loops of L-oriented DS GTD-111 under continuous cycling conditions with* $R_\varepsilon = -1, \dot{\varepsilon} = 0.5\%/s$, *and 871°C (1600°F): (a,b) pre-heated without pre-load and (c,d) pre-heated and pre-loaded. For each pre-exposed case T=982°C (1800°F) and* $t_{pre}$*=100 hr.*

to $H_2S$ had the effect of increasing the oxide penetration which further decreased life. These reductions were exhibited by both the L- and T-oriented specimens.

Pre-exposing the L-oriented material to either 0 *MPa* or -100 *MPa* in air had approximately an identical effect, i.e., a factor of two reduction in life. Formation of subsurface cracks caused by tensile creep, however, severely lowered the crack initiation

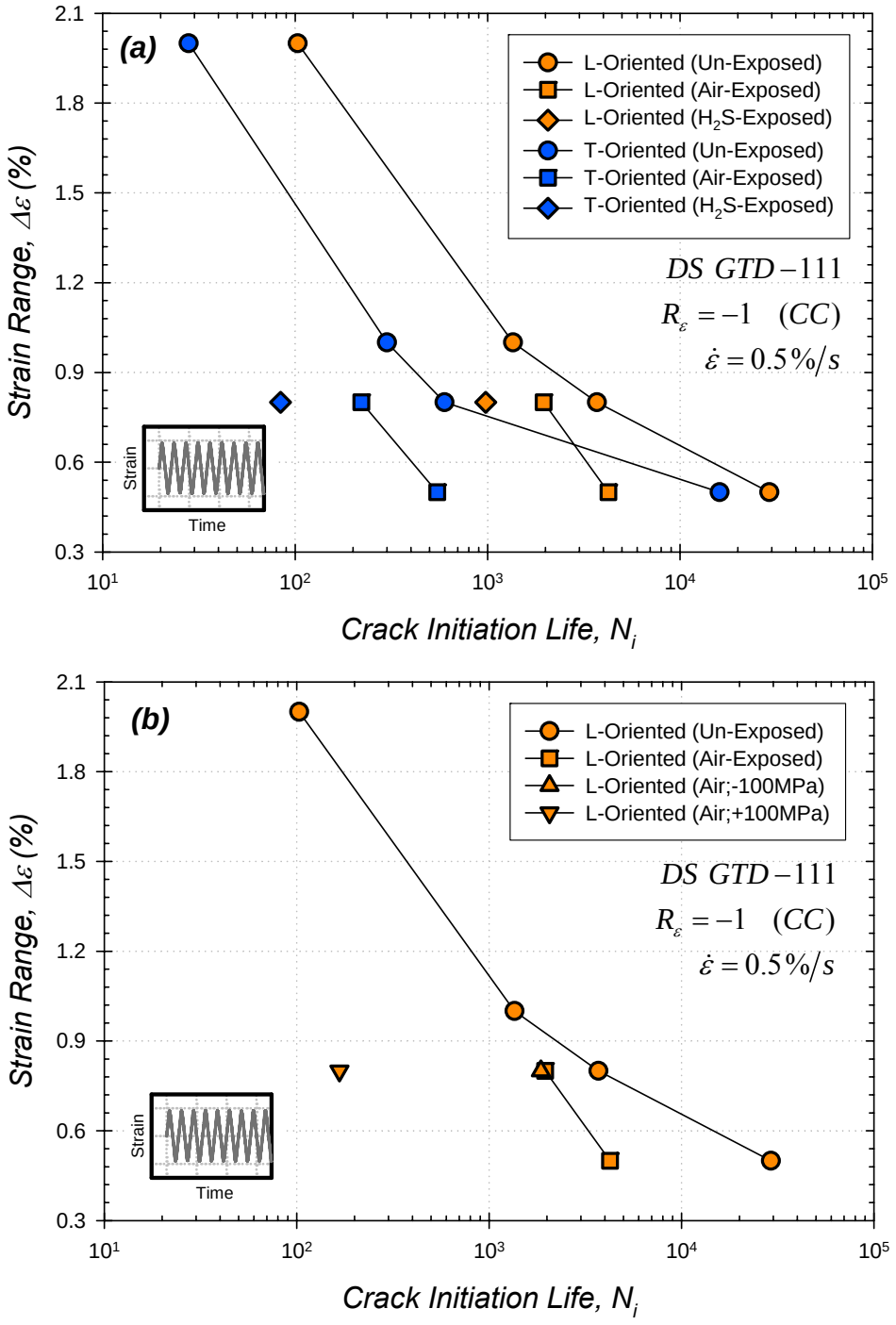


***Figure 4.43:*** *Effect of pre-exposure (a) environment and (b) load on LCF crack initiation life of L- and T-oriented DS GTD-111 under continuous cycling conditions with $R_\varepsilon$=-1, $\dot{\varepsilon} = 0.5\%/s$, and 871°C (1600°F). For each pre-exposed case T=982°C (1800°F) and $t_{pre}$=100 hr.*

life of the material compared to those samples not subjected to prior exposure whatsoever.

## 4.9 Effect of Environment

Several fatigue experiments were carried out in environments rich in or depleted of oxygen. A listing of the experimental results, is comparing results from tests conducted in air, is given in Table 4.15. The volume fraction of oxygen, $F_{O_2}$, sampled from the chamber is also tabulated. In Ar-rich cases, $F_{O_2}$ was nearly 2%, while tests conducted in pure oxygen had $F_{O_2}$ of 98%. It was determined that $F_{O_2}$ influences the crack initiation mechanism occurring in DS GTD-111 and its crack initiation life. Figure 4.44 illustrates the effect. At 871°C, the semi-inert environment limits the formation of surface oxides that would lead to oxide spiking in air ($F_{O_2} = 20\%$), as shown in Fig. 4.44a,b. Although the small amount of oxygen present in the Ar-rich environment lead to the formation of a very thin ($L_{ox} = 9\ \mu m$) oxide layer, the crack initiation mechanism was influenced by subsurface features (Fig. 4.44c).

In air, increasing the strain range from 0.8% to 1.0% both increases the plastic strain range and decreases the number of cracks present at the surface. The cracks at the higher strain range appear tortuous and the oxide layer formed at the surface is thinner. As such, the effect of subsurface inclusions on crack initiation has increased (Fig. 4.44d). An experiment conducted in Ar, but having the otherwise similar conditions, shows an increase in the density of non-planar surface cracks (Fig. 4.54e). Since the density of cracks at the surface of the air-tested specimen is slightly higher than that formed on the

Ar-tested sample, the oxide spiking damage mechanism still assists crack initiation at this higher strain range. One semi-inert experiment was carried out at 1038°C (1900°F). Compared to the air-tested case (Fig. 4.44f), the Ar-tested case (Fig. 4.44g) exhibited a slightly reduced amount of oxide formation at the surface.

***Table 4.15:*** *Comparison of environmental effect of DS GTD-111 ($R_\varepsilon$ = -1 and $\dot{\varepsilon}$ = 0.5%/s).*

| Temperature (°C) | Temperature (°F) | Gas Type | Oxygen Fraction, $F_{O2}$ | Hold Type (Time) | Total Strain Range, $\Delta\varepsilon_m$ (%) | Plastic Strain Range, $\Delta\varepsilon_{pl}$ (%) | Elastic Strain Range, $\Delta\varepsilon_{el}$ (%) | Crack Initation Life, $N_i$ | Specimen ID (Orientation) | Figure |
|---|---|---|---|---|---|---|---|---|---|---|
| 871 | 1600 | Air | 0.21 | HC (2 min) | 0.80 | 0.12 | 0.68 | 678 | GTD-HC04 (L) | A.9 |
| 871 | 1600 | Argon | 0.02 | HC (2 min) | 0.80 | 0.03 | 0.77 | 782 | B17-L-F1 (L) | C.13 |
| 871 | 1600 | Air | 0.21 | HC (2 min) | 1.00 | 0.34 | 0.66 | 317 | B17-L-F4 (L) | A.55 |
| 871 | 1600 | Argon | 0.02 | HC (2 min) | 1.00 | 0.14 | 0.86 | 510 | B18-L-F3 (L) | C.14 |
| 871 | 1600 | Air | 0.21 | None | 0.90 | 0.08 | 0.82 | 987 | A27-L-F6 (L) | A.38 |
| 871 | 1600 | $O_2$ | 0.91 | None | 0.90 | 0.09 | 0.81 | 2179 | B17-L-F7 (L) | C.11 |
| 1038 | 1900 | Air | 0.21 | HC (2 min) | 1.00 | 0.50 | 0.50 | 152 | T8-7A (T) | A.31 |
| 1038 | 1900 | Ar+2.8%$H_2$ | 0.05 | HC (2 min) | 1.00 | 0.35 | 0.65 | 132 | T8-8A (T) | C.12 |

Decreasing the quantity of the diffusing species present in the environment limits the environmental-fatigue crack initiation mechanism and thus increases the crack initiation life of the test material. As shown in Fig. 4.45, Ar-tested DS GTD-111 samples exhibit longer lives than those tested in air, by a factor of 1.4 for a given $\Delta\varepsilon_m$. This strain-life curve approaches that of the continuously-cycled cases which serve as an upper bound on life since they are not influenced by environment. It can therefore be assumed that further decreasing the presence of oxygen in the environment (e.g. by means of vacuum testing) would further increase the crack initiation life of the material.

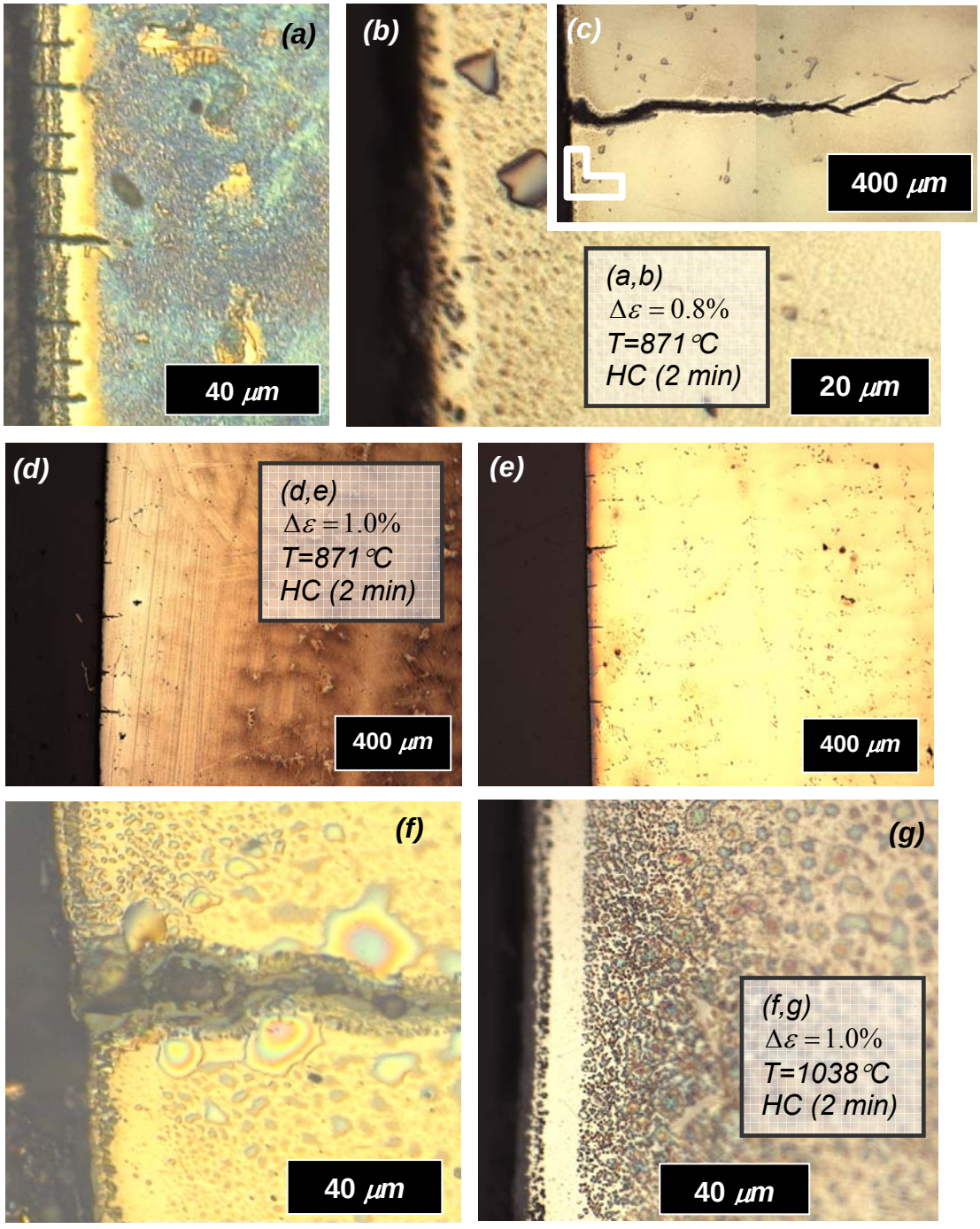


***Figure 4.44:*** *Effect of environment on damage mechanisms leading to crack initiation of (a-e) L- and (f,g) T-oriented DS GTD-111. For each case* $\dot{\varepsilon} = 0.5\%$*, (a,d,f) air, and (b,c,e,g) argon-rich environment.*

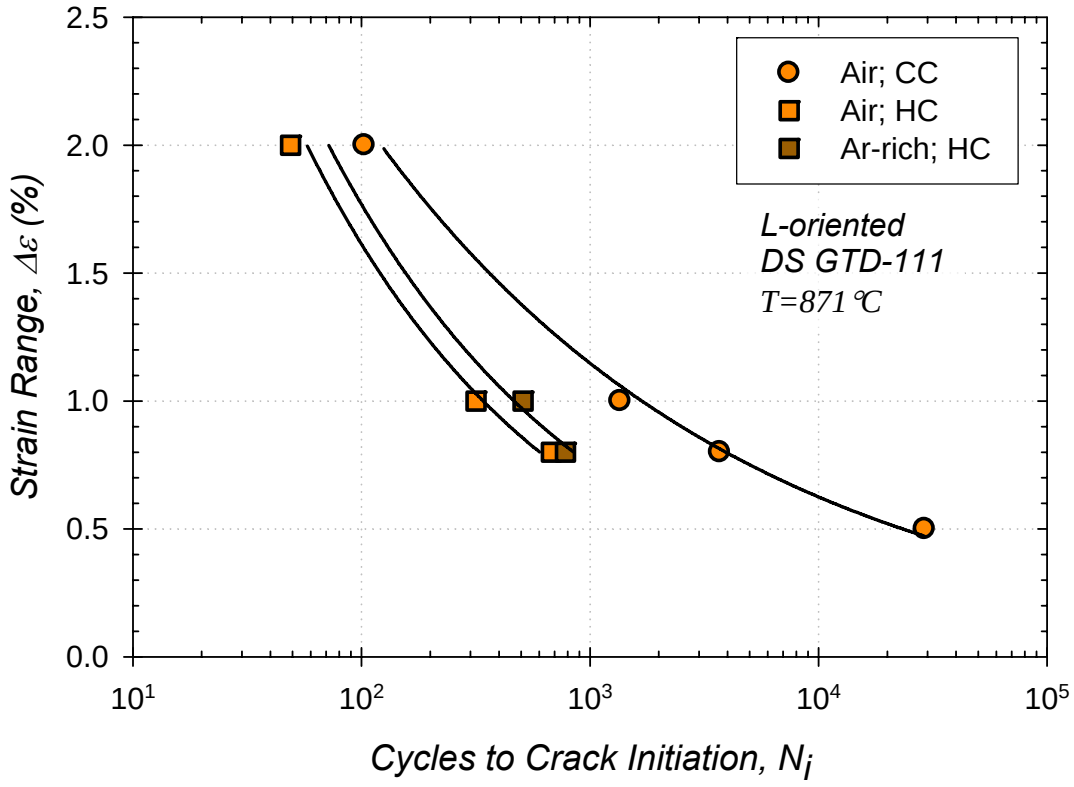


***Figure 4.45:*** *Effect of environment on crack initiation of L-oriented DS GTD-111 at 871℃ and* $\dot{\varepsilon} = 0.5\%/s$.

## *4.10 Stress-Free Surface Corrosion*

In order to characterize the stress-assisted environmental damage mechanisms occurring in DS superalloys, the stress-free corrosion kinetics of the material must be characterized. Isothermal stress-free heating tests were conducted on DS GTD-111 in two environments: air and $H_2S$.

*Stress-Free Oxidation*

Specimen discs were heated to temperatures between 871°C (1600°F) and 1093°C (2000°F) in static laboratory air. The exposure times ranged from 1 *hr* to 1000 *hr*. After experiments were completed, sets of samples were prepared for microscopy and

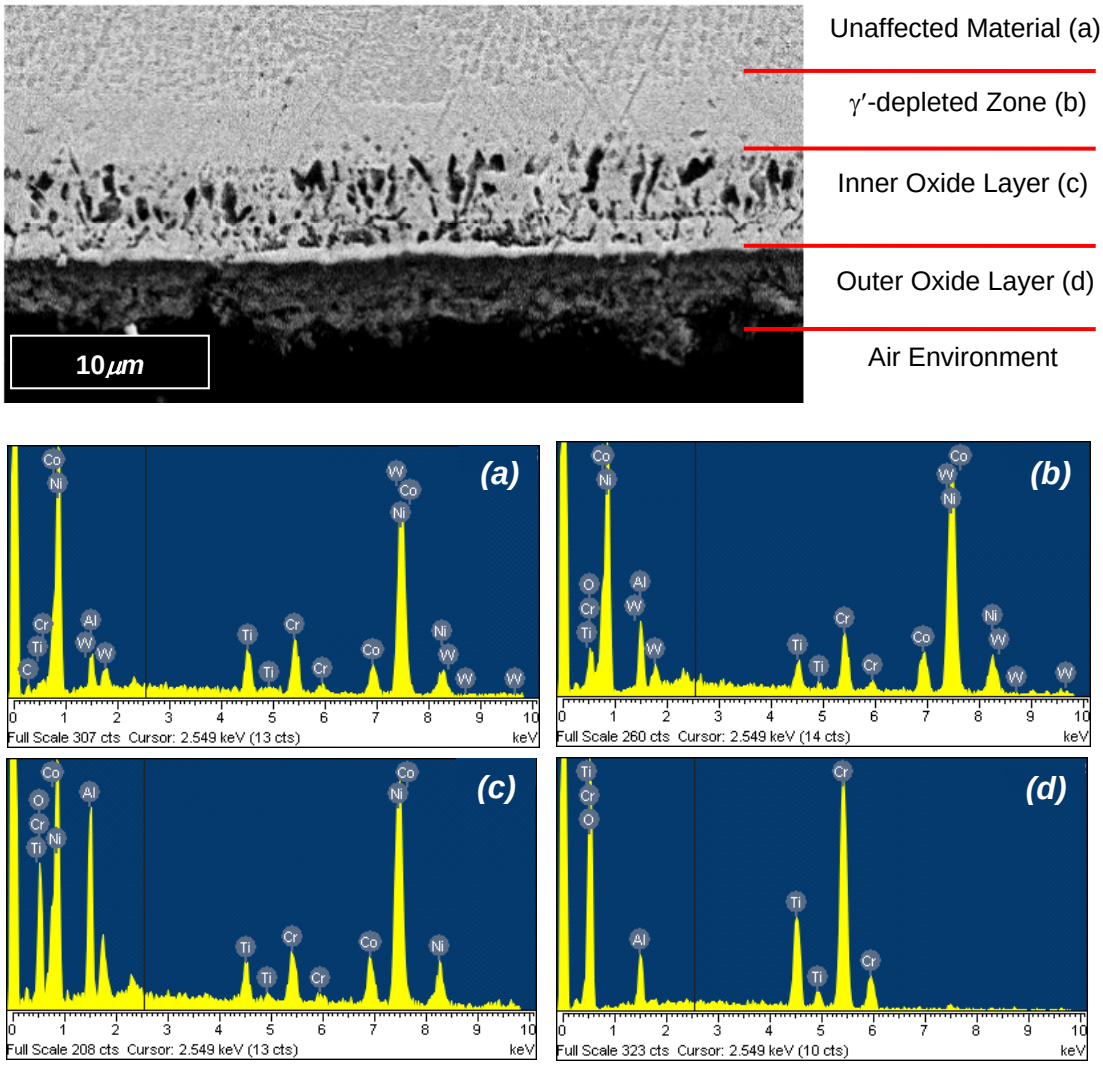


***Figure 4.46:*** *Surface oxidation in unstressed DS GTD-111 exposed to 982℃ for 312 hr and spectrum for each location.*

spectrometry. Based on the inspections, DS GTD-111 surfaces contain three distinct layers resulting from long term exposure to high temperature. An Energy Dispersive Spectrometer (EDS) was used in conjunction with an SEM to analyze the chemical composition of each layer, as shown in Figure 4.46. The two outer layers are surface oxides while the layer separating the oxides from the unaffected material is the γ′-

depleted zone. Table 4.16 contains the composition (weight and atomic percentages) of the major components in each of these layers and the unaffected material.

***Table 4.16:*** *Composition of surface layers in DS GTD-111*

| Chemical | Unaffected Material (A) | | $\gamma'$-depleted Zone (B) | | Inner Oxide Layer (C) | | Outer Oxide Layer (D) | |
|---|---|---|---|---|---|---|---|---|
| | Weight (%) | Atomic (%) | Weight (%) | Atomic (%) | Weight (%) | Atomic (%) | Weight (%) | Atomic (%) |
| C | 6.3 | 23.9 | - | - | - | - | - | - |
| Al | 3.8 | 6.4 | 6.0 | 11.1 | 12.9 | 17.7 | 3.7 | 3.6 |
| Ti | 5.2 | 4.9 | 2.7 | 2.8 | 2.9 | 2.2 | 11.1 | 6.1 |
| Cr | 8.6 | 7.5 | 7.4 | 7.1 | 5.4 | 3.8 | 43.8 | 22.2 |
| Co | 8.2 | 6.3 | 10.0 | 8.4 | 8.4 | 5.3 | - | - |
| Ni | 65.3 | 50.4 | 65.6 | 55.4 | 54.4 | 34.2 | - | - |
| W | 2.6 | 0.7 | 3.7 | 1.0 | - | - | - | - |
| O | - | - | 4.6 | 14.2 | 16.0 | 36.8 | 41.5 | 68.2 |

The weight composition of the unaffected material is the same as the composition of the as-cast material with the exception that the level of Cr has decreased. Chromium quickly diffuses from interdendritic areas to the surface. Oxygen does not reach the unaffected material. Oxygen is present, however, in the adjacent precipitate-free matrix layer. As expected, the oxygen content increases in proximity to the external surface. It accounts for slightly over 40% of the weight near the surface layer and 16% of the inner layer. The morphology of the two surfaces layers is distinct. While the outer layer has the form of a homogeneous oxidized material, the inner layer is a composite of matrix and oxidized material. Compared to the as-cast material, the outer oxide layer has three times the amount of Cr and twice the amount of Ti. The Al content in this layer is minimal. This outer layer is an oxide primarily composed of chromia/titania ($Cr2O_3/Ti_2O_3$). The inner oxide layer is composed of a non-continuous layer of alumina oxide ($Al_2O_3$). The alumina particles first appear as randomly-spaced polygons having lengths less than 0.1 $\mu m$ and coalesce into finger-like shapes measuring less than 1 $\mu m$

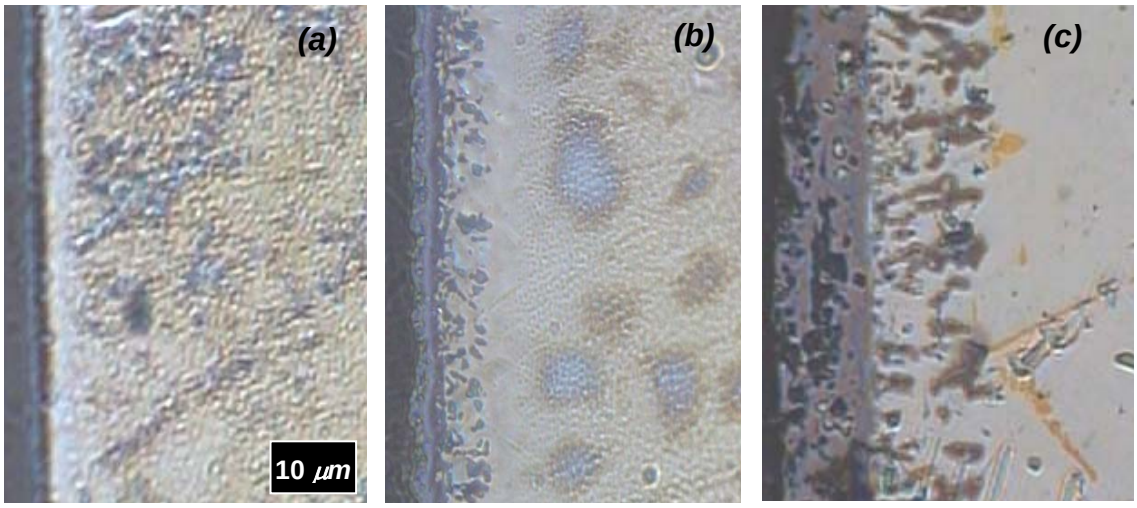


***Figure 4.47:*** *Surface oxidation of unstressed DS GTD-111. Specimens were exposed in air to 927ºC for (a) 3.2 hr, (b) 31.6 hr, and (c) 316 hr.*

wide and 3 $\mu m$ long. Compared to all other locations, the highest level of Al content is in the precipitate free zone and in the inner Al-rich layer.

Images of the surface layers as a function of time at constant temperature are shown in Figs. 4.47 and 4.48, and as a function of temperature after 31.6 *hr* of exposure in Fig. 4.49. After 3.2 *hr* of exposure, the Cr/Ti-rich layer is already present. The alumina layer is not readily present after the initial exposure. By 31.6 *hr*, Al atoms have diffused from $Ni_3Al$ precipitate particles, as evidenced by the thin precipitate particle depletion zone. These atoms traverse a short distance, and as the reaction proceeds, alumina particles react with available oxygen to form larger alumina particles. These alumina particles grow within the depleted zone with further exposure. Based on the aspect ratio of the typical particle at the final exposure time, the vertical expansion rate of the particles is less than the horizontal growth rate. Plainly stated, they elongate quicker than they widen. There was no preferential oxide growth at grain boundaries or

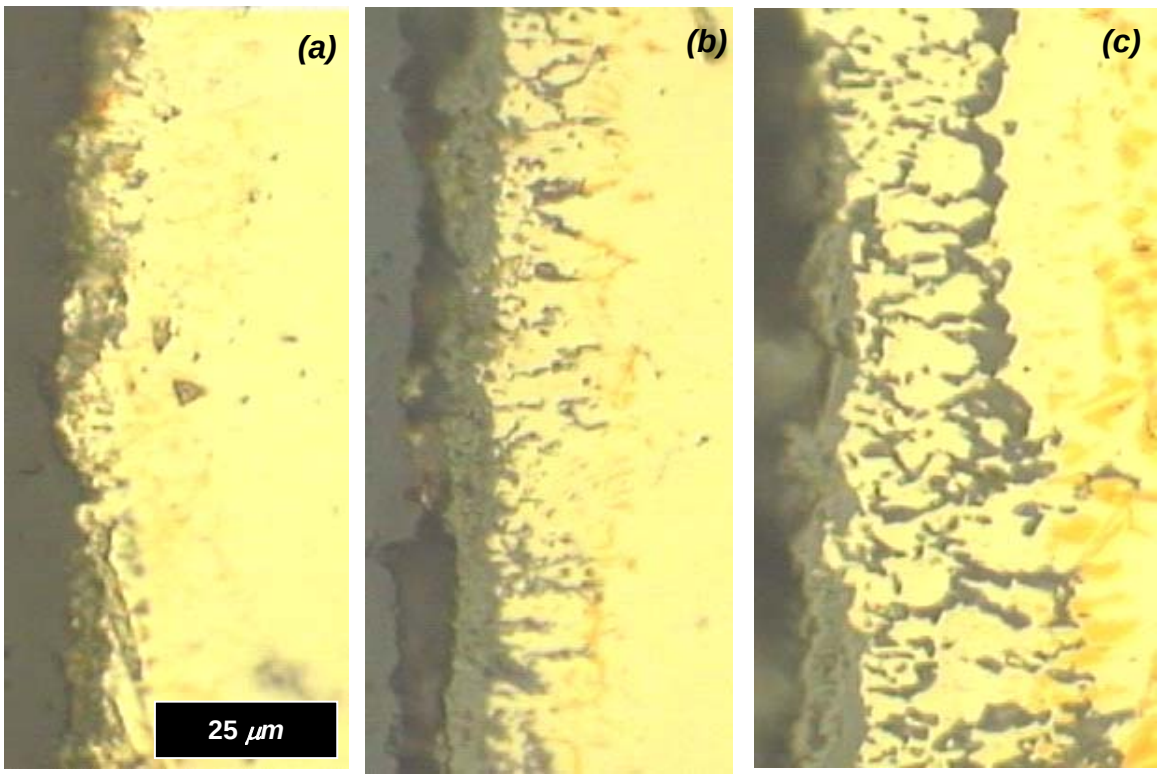


***Figure 4.48:*** *Surface oxidation of unstressed DS GTD-111. Specimens were exposed to 1038ºC in air for (a) 3.2 hr, (b) 31.6 hr, and (c) 316 hr.*

interdendritic regions; therefore, under stress-free conditions, the underlying microstructure does not influence oxidation behavior.

Specimens subjected to longer exposure times at constant temperature displayed an increased depth of oxide formation, as shown in Fig. 4.47. Additionally, increasing the temperature at a constant exposure time had the effect of increasing the penetration depth of the surface layers, as shown in Fig. 4.48. Although the ingression rates increased for both cases, the characteristic of formation of the layers remained unchanged. For each case, the accumulated thickness of the Al/Ti/Cr scale was initially very thin. As oxidation continued, the inner and outer layers became distinguishable. The thickness of the Al-rich layer typically exceeded that of the Cr/Ti-rich layer. Depths

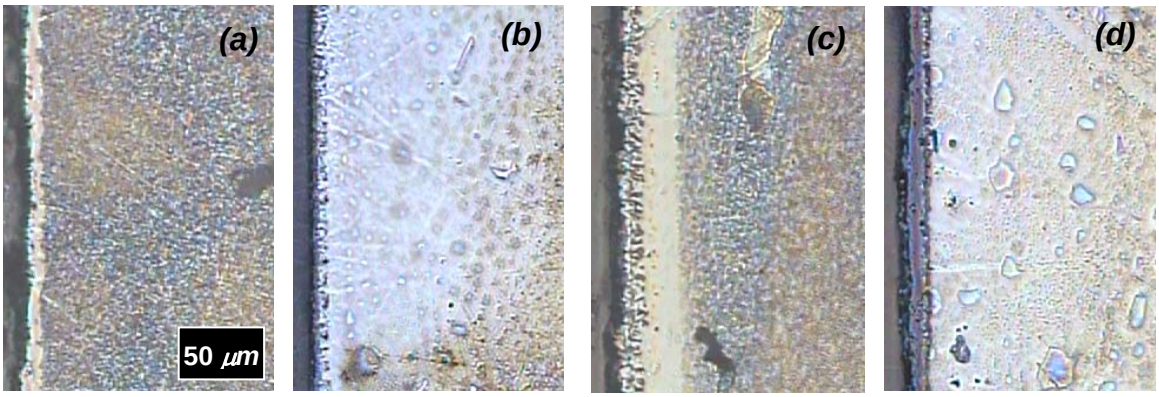


***Figure 4.49:*** *Surface oxidation of unstressed DS GTD-111. Specimens were exposed for 31.6 hr in air to (a) 871ºC, (b) 927ºC, (c) 1038ºC, and (d) 1093ºC.*

of the cumulative oxide layer, $L_{OX}$, and the γ′-depleted layer depth, $L_{GPD}$, were taken from multiple locations of micrographed samples. Reported values, listed in Table 4.17 and plotted in Fig. 4.50, are the maxima of several direct measurements of the respective unstressed sample. The γ′-depleted layer depth, $L_{GPD}$, was generally larger than the depth of the cumulative oxide layer, $L_{OX}$. Data in Fig. 4.50 are interpolated by best-fit two-parameter power laws.

Spallation of the outer oxide layer was often observed. After completion of each experiment the specimens were cooled to room temperature. The thermal contraction that occurs during this process lead to some buckling of the outer oxide layer at the surface. The oxide particles that were once unstressed at the test temperature are self-impinging as the substrate material converges to RT. Under the surface stresses, the particles buckle. This was easily observed in experiments conducted at or above 1038°C exposed for a duration of 316 *hr* or more. This spallation was noted by a fine powdery residue on the alumina float and by a "popping" sound during cooling. This spallation is

***Table 4.17:*** *Oxidation and γ′-depletion in DS GTD-111 in air*

| Temperature | | Exposure Time, *t* (*hr*) | Surface Depths | | Specimen ID |
|---|---|---|---|---|---|
| °C | °F | | $L_{OX}$ (*μm*) | $L_{GPD}$ (*μm*) | |
| 871 | 1600 | 1 | 1 | 5 | L16-1 |
| 871 | 1600 | 3 | 2 | 7 | L16-2 |
| 871 | 1600 | 10 | 3 | 7 | L16-3 |
| 871 | 1600 | 32 | 4 | 8 | L16-4 |
| 871 | 1600 | 100 | 4 | 9 | L16-5 |
| 871 | 1600 | 314 | 5 | 10 | L16-6 |
| 871 | 1600 | 1006 | 6 | 12 | L16-7 |
| 927 | 1700 | 1 | 2 | 5 | L17-1 |
| 927 | 1700 | 3 | 3 | 8 | L17-2 |
| 927 | 1700 | 10 | 6 | 9 | L17-3 |
| 927 | 1700 | 32 | 9 | 10 | L17-4 |
| 927 | 1700 | 100 | 11 | 12 | L17-5 |
| 927 | 1700 | 316 | 17 | 15 | L17-6 |
| 927 | 1700 | 1000 | 17 | 17 | L17-7 |
| 982 | 1800 | 1 | 3 | 7 | L18-1 |
| 982 | 1800 | 3 | 7 | 10 | L18-2 |
| 982 | 1800 | 10 | 8 | 13 | L18-3 |
| 982 | 1800 | 32 | 13 | 15 | L18-4 |
| 982 | 1800 | 100 | 17 | 16 | L18-5 |
| 982 | 1800 | 314 | 21 | 20 | L18-6 |
| 982 | 1800 | 1006 | 24 | 29 | L18-7 |
| 1038 | 1900 | 1 | 4 | 5 | L19-1 |
| 1038 | 1900 | 3 | 9 | 10 | L19-2 |
| 1038 | 1900 | 10 | 11 | 12 | L19-3 |
| 1038 | 1900 | 32 | 18 | 21 | L19-4 |
| 1038 | 1900 | 100 | 19 | 33 | L19-5 |
| 1038 | 1900 | 316 | 29 | 37 | L19-6 |
| 1038 | 1900 | 1182 | 40 | 46 | L19-7 |
| 1093 | 2000 | 1 | 5 | 8 | L20-1 |
| 1093 | 2000 | 3 | 8 | 11 | L20-2 |
| 1093 | 2000 | 10 | 12 | 14 | L20-3 |
| 1093 | 2000 | 32 | 20 | 20 | L20-4 |
| 1093 | 2000 | 100 | 24 | 32 | L20-5 |
| 1093 | 2000 | 316 | 33 | 42 | L20-6 |
| 1093 | 2000 | 1000 | 44 | 53 | L20-7 |

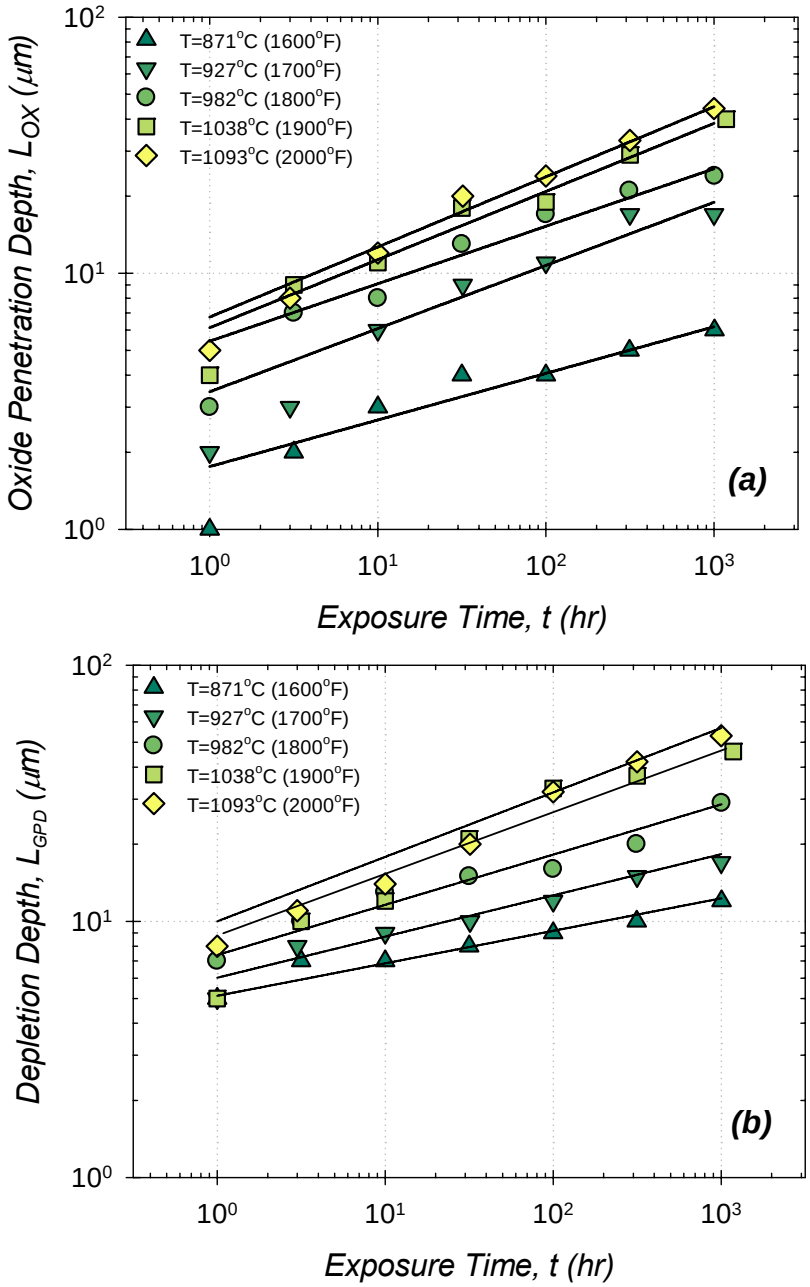


***Figure 4.50:*** *(a) Oxidation ingression and (b) precipitate particle depletion of DS GTD-111 between 1 hr and 1000 hr.*

one possible source of error that can lead to underestimated measurements of the oxide depth especially towards the end of the data series at higher temperatures.

Oxidation accumulation was correlated using the expression

$$L_{OX} = \alpha_{OX}\Theta_{OX}\left(T\right)t^{m_{OX}} . \tag{4.4}$$

A similar model was also used to describe the growth of the γ′ depleted layer, i.e.,

$$L_{GPD} = \alpha_{GPD}\Theta_{GPD}\left(T\right)t^{m_{GPD}} . \tag{4.5}$$

In Eqs. (4.4) and (4.5), the temperature dependence of the diffusivity is expressed via the Arrhenius forms for $\Theta_{OX}\left(T\right)$ and $\Theta_{GPD}\left(T\right)$, i.e.,

$$\begin{aligned} \Theta_{OX} &= \theta_{OX}\exp\left(-\frac{Q_{OX}}{RT}\right) \\ \Theta_{GPD} &= \theta_{GPD}\exp\left(-\frac{Q_{GPD}}{RT}\right) \end{aligned}, \tag{4.6}$$

where $\theta_{OX}$ and $\theta_{GPD}$ are material properties, $Q_{OX}$ *and* $Q_{GPD}$ are activation energies (minimum energiesy needed), $T$ is the material temperature measured in degrees Kelvin, and $R$ is the universal gas constant (8.314 *J/mol-K*). The activation energies of the two diffusion processes were determined by plotting the normalized scale depth versus the inverse temperature and interpolating the data with modified forms of Eqs. (4.4) and (4.5) , as shown in Fig. 4.51. The constants $\alpha_{OX}$ and $\alpha_{GPD}$ were each defined to be 1 $\mu m$. Regression analyses were used to determine the remaining constants listed in Table 4.18. Compared to data generated in other studies [Mar-M247: $Q_{OX}$ = 175.9 *kJ/mol*, $Q_{OX}$ = 163.3 *kJ/mol*, $m$ = 0.5 (Boismier and Sehitoglu, 1990b), René 80: $Q_{OX}$ = 40.2 *kJ/mol*, $m$ = 0.5 (Anotolovich, 1981a)], DS GTD-111 is more resistant to oxidation since oxide

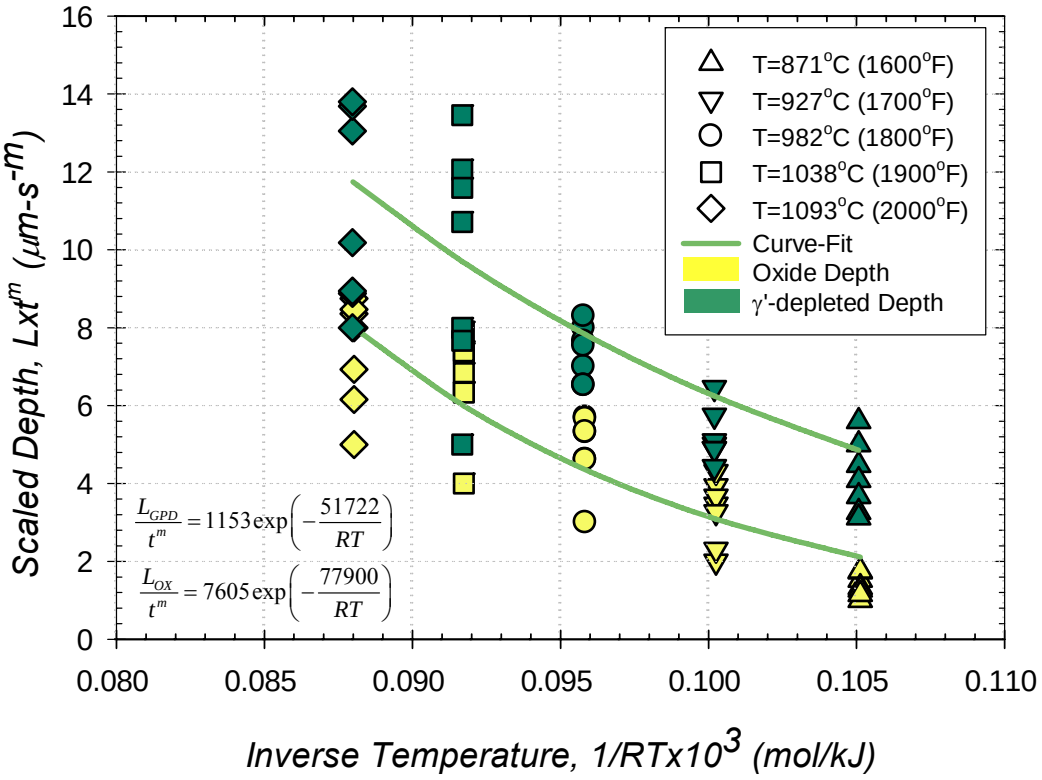


***Figure 4.51:*** *Temperature-dependent oxidation ingression and precipitate particle depletion of DS GTD-111 between 1 hr and 1000 hr.*

accumulation occurs less rapidly.

Correlations were made with the depth equations and compared with experimental measurements in Fig. 4.52. Nearly all of the data points fall within error bands that are placed within a factor of two of the experimental measurements.

***Table 4.18:*** *Unstressed oxidation, γ'-depletion, and sulphidation constants for DS GTD-111*

| Model | $\alpha$ (mm) | $\theta$ (hr-m) | Q (kJ/mol) | m |
|---|---|---|---|---|
| Oxidation | 1 | 7603 | 77.9 | 0.24 |
| GPD | 1 | 1153 | 51.7 | 0.20 |
| Sulphidation | 1 | 7603 | 66.9 | 0.33 |

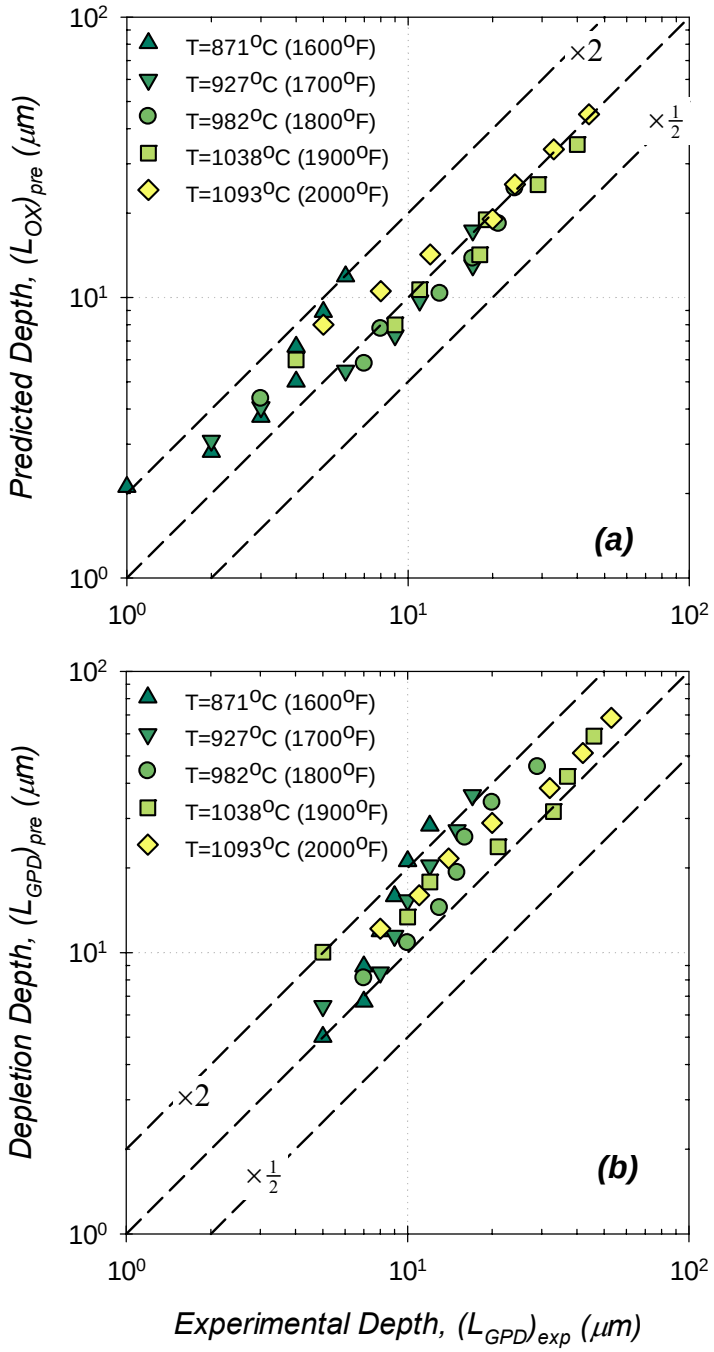


***Figure 4.52:*** *Comparison of correlated modeling of (a) oxidation ingression and (b) precipitate particle depletion of DS GTD-111 between 871°C and 1093°C.*

*Stress-Free Sulphidation*

Turbine blades are typically subjected to atmospheric conditions that are drastically more corrosive than static laboratory air. One example is the syngas (synthesis gas) produced from the Integrated Gasification Combined Cycle (IGCC), which is an efficient and clean approach to fossil fuel combustion. This environment consists of gases of varying composition that are generated in coal gasification. Syngas consists primarily of carbon monoxide and hydrogen. It also contains sulfur compounds which are reactive with the turbine blade material. Several samples of DS GTD-111 were exposed to $H_2S$ in order to compare the kinetics of sulphidation to oxidation (Gordon et al., 2005). Two types of tests were conducted. In the first experiment one specimen was exposed to 100 *ppm* $H_2S$ mixed in $N_2$ for 100 *hr* at 982°C. A thermogravimetric analysis was conducted in the second type. Isothermal tests were carried out using a vertical tube furnace in which samples were hung using a Pt wire. The samples were held at two test temperatures for times ranging from 1 to 14 *hr* in dry gas with a composition of 100 *ppm* $H_2S$ mixed in $N_2$.

The high temperature exposure of the material to the simulated syngas environment leads to the transformation of surface layers in the same manner as oxidation does. Multiple layers (e.g. two oxide layers and a matrix layer) occurred at the surface of each specimen, as shown in Fig. 4.53. The surface layers accumulated as a result of exposure in the simulated service environment (i.e., $H_2S$) are 1.7 times thicker than that occurring with exposure in air; both were exposed to 982°C at 100 *hr*. This suggests that GTD-111 DS is less resistant to sulfur attack than oxygen penetration.

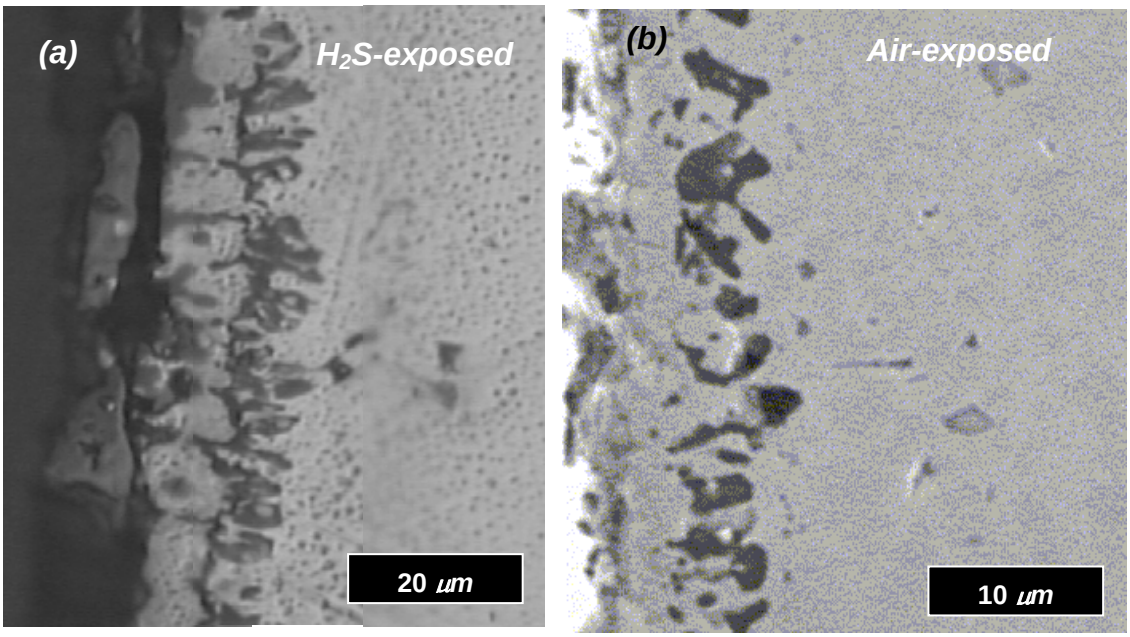


***Figure 4.53:*** *Surface corrosion of DS GTD-111 resulting from exposure to (a) $H_2S$ at 982ºC for 100 hr and (b) air at 982ºC for 100 hr.*

The amount of mass gain is significant and the corresponding sulfide scale is easily detectable. Correlation between mass gained and penetration depth can be made using the squared mass gain, $\Delta m^2$. The $\Delta m^2$-histories of DS GTD-111 in the syngas environment, shown in Fig. 4.54, can be interpolated with a two-parameter power law, i.e.,

$$\Delta m^2 = \alpha_S \Theta_S t^{m_s} \tag{4.7}$$

where the constant $\alpha_S$ is with units of $g^2$, $\Theta_S$ is the rate coefficient, and $m_s$ is the rate exponent. For the two temperatures considered (760°C and 1038°C), the mass gained at

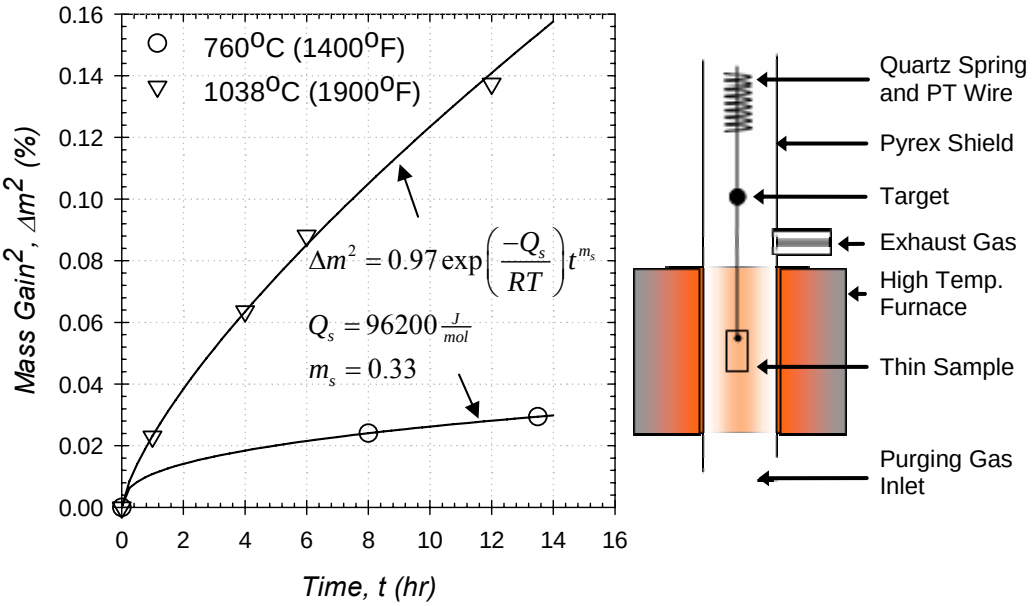


***Figure 4.54:*** *Mass gain histories of DS GTD-111 during thermogravimetric analysis (TGA). For each case the TGA measuring system (schematic of fundamental components shown at right) contained isothermal 100 ppm $H_2S$ gas.*

the higher temperature is greater, as is expected. The activation energy, $Q_s$, of the reaction can be estimated using a semi-log plot of the rate constant versus $(RT)^{-1}$, i.e.,

$$\Theta_S = \theta_S \exp\left(\frac{-Q_S}{RT}\right) \tag{4.8}$$

Here $Q_s$ is approximately as 66.9 *kJ/mol*, which is lower than that determined for the oxidation reactions. The remaining constants from Eq. (4.8) are listed in Table 4.18.

## 4.11 Stress-Assisted Surface Corrosion

The testing conditions under which a specimen is cycled effects the morphology of the oxide layer enclosing the crack tip. In creep-fatigue experiments with compressive dwell periods, for example, the oxide layer at the crack tip is considerably thicker for experiments with 10 *min* holds compared to those with 2 *min* holds. Figures 4.55a and 4.55b illustrate this observation at $\Delta\varepsilon = 1.0\%$, $T$ = 871°C (1600°F) and $\dot{\varepsilon}_m = 0.5\%/s$. Increasing the dwell time increases the opportunity for oxygen to embrittle the virgin material at the crack tip. Decreasing the mechanical strain range has the effect of decreasing the stress intensity at the crack tip and slows the rate of cyclic crack propagation. This also results in a thicker oxide layer surrounding the crack tip. This phenomenon is illustrated for the case in which $\Delta\varepsilon_m$ is varied from 1.0% to 0.5% (Figs 4.55a and 4.55c).

The measured thickness of the oxide layer extending ahead of the crack tip into the material, $\overline{h}_f$, occurring in the most highly oxidized samples is listed in Table 4.19 and plotted in Fig. 4.56. Generally, DS GTD-111 samples that were pre-exposed to high temperature at no load displayed small $\overline{h}_f$ compared to unexposed cases. The reason for this difference is that pre-exposure introduced oxygen to a volume of material near the surface. This changed the microstructure and the mechanical properties of the material near the surface.

Analogous to the creep-fatigue case, decreasing the mechanical strain range increased $\overline{h}_f$. Samples that were subjected to creep-fatigue cycling with long compressive dwell periods resulted in high $\overline{h}_f$.

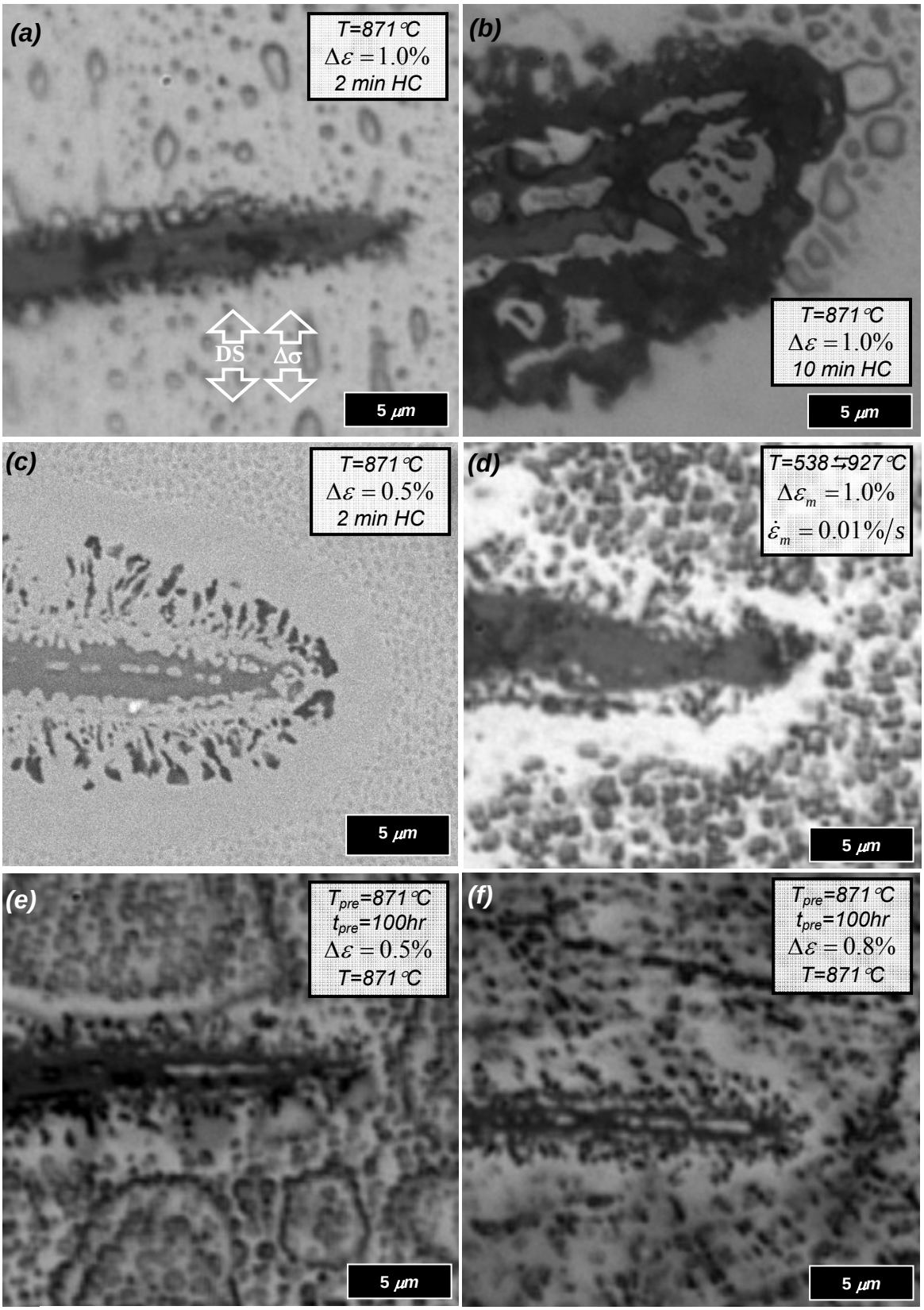


***Figure 4.55:*** *Oxide ingression under (a,c) 2 min HC, (b) 10 min HC, (d) TMF-OP, (e,f) pre-exposure in air followed by LCF. For each isothermal case* $\dot{\varepsilon} = 0.5\%/s$.

***Table 4.19:*** *Critical oxide rupture thickness.*

| Test Type | Temperature (°C) | Temperature (°F) | Test Details | Mech. Strain Range, $\Delta\varepsilon_m$ (%) | Rupture Thickness, $\hat{h}_f$ (μm) | Specimen ID (Orientation) | Figure |
|---|---|---|---|---|---|---|---|
| LCF | 871 | 1600 | Air; CC | 0.8 | 3.3 | T8-5 (T) | A.25 |
| Creep-Fatigue (CF) | 871 | 1600 | HC 2min | 0.8 | 3.47 | GTD-HC04 (L) | A.9 |
| | 871 | 1600 | HC 2min | 1.0 | 5.49 | B17-L-F4 (L) | A.55 |
| | 871 | 1600 | HC 2min | 2.0 | 2.09 | GTD-HC10 (L) | A.5 |
| | 982 | 1900 | HC 2min | 0.5 | 7.69 | L8-6A (L) | A.33 |
| | 982 | 1900 | HC 2min | 1.0 | 9.89 | L8-5A (L) | A.23 |
| | 1038 | 1900 | HC 2min | 1.0 | 7.25 | T8-7A (T) | A.31 |
| | 871 | 1600 | HC 10min | 1.0 | 13.19 | B17-L-F10 (L) | A.56 |
| | 1038 | 1900 | HC 10min | 1.0 | 11.04 | B17-L-F13 (L) | A.61 |
| | 1038 | 1900 | HC 10min | 1.0 | 15.38 | B17-L-F9 (L) | A.54 |
| TMF | 538 ⇆ 1038 | 1000 ⇆ 1900 | In-Phase | 1.0 | 11.76 | L8-9 (L) | B.1 |
| | 538 ⇆ 927 | 1000 ⇆ 1700 | Out-of-Phase | 1.0 | 1.76 | L8-11A (L) | B.3 |
| Pre-Exposed, LCF | 871 | 1600 | Pre-heated in air | 0.5 | 2.94 | B18-L-F6 (L) | C.8 |
| | 871 | 1600 | Pre-heated in air | 0.8 | 1.65 | B17-L-F3 (L) | C.4 |
| | 871 | 1600 | Pre-heated in $H_2S$ | 0.8 | 2.75 | A27-L-F15 (L) | C.5 |

Measurements from TMF-tested DS GTD-111 samples were also taken. The measured $\bar{h}_f$ from the sample subjected to OP cycling (Fig. 4.55d) was greatly exceeded by those subjected to creep- fatigue conditions. Since oxide spiking formation was not observed in IP cycled TMF cases, $\bar{h}_f$ was measured as the penetration depth of spalled oxide particles at the surface of the specimen (Fig. 4.36a). Depth measure for IP cases greatly exceeded $\bar{h}_f$ from TMF-OP cases. A correlation model for $\bar{h}_f$ that includes the effects of compressive dwell periods is presented in Chapter 6.

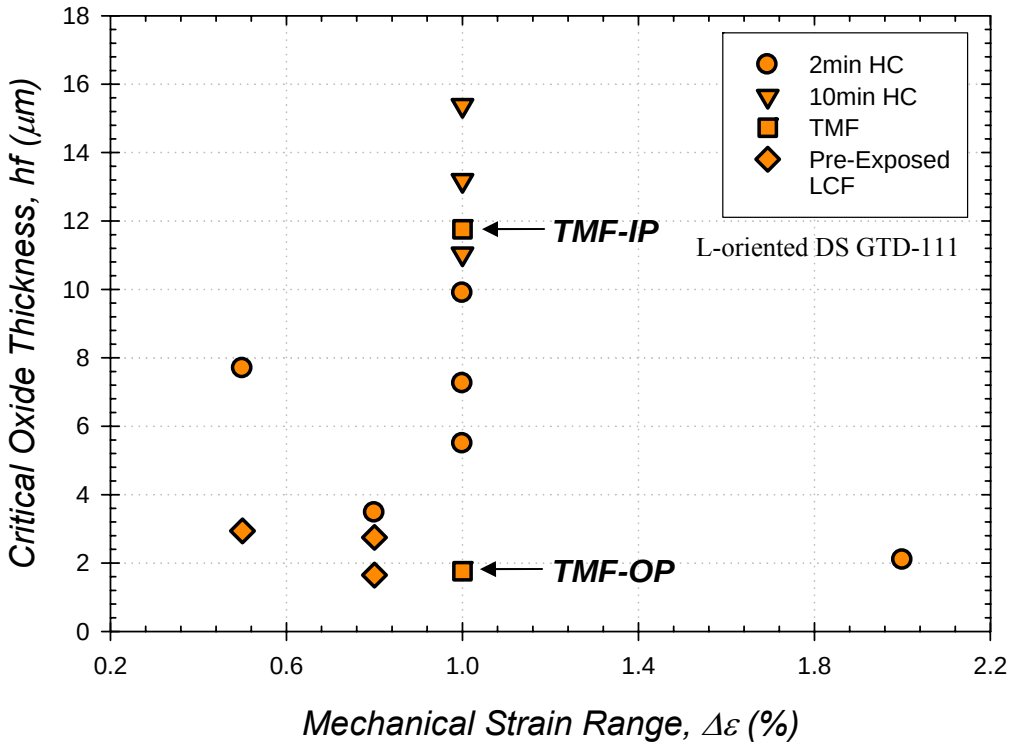


***Figure 4.56:*** *Oxide ingression under (a,c) 2 min HC, (b) 10 min HC, (d) TMF-OP, (e,f) pre-exposure in air followed by LCF. For each isothermal case* $\dot{\varepsilon} = 0.5\%/s$.

# 5. NUMERICAL SIMULATION

## *5.1 Motivation*

A variety of data from both L- and T-oriented directionally-solidified (DS) GTD-111 materials are necessary to make predictions of crack initiation lives of the material under conditions representative of those of in-service turbine blades. As described in Chapter 4, over one hundred mechanical experiments were conducted on DS GTD-111. Test conditions ranged from isothermal fatigue, creep-fatigue (fatigue with dwells), creep deformation, and thermomechanical (non-isothermal) fatigue as needed to either emphasize or limit the desired contribution of particular microstructural damage mechanisms on crack initiation. Crack initiation, as well as the mechanisms that manifest it, depend highly on the deformation response. Further diversifying the combinations of test variables (e.g. temperature, strain range, strain ratio) and their levels would improve the range of the experimental observations and feasibly expand the capability of any prediction model. It is unrealistic, however, to conduct experiments involving all test variations due to limited amounts of available material, machining resources, and simply the cost and time involved to conduct each test.

Since it is impractical to conduct a full factorial of experiments under every possible combination of loading, temperature, etc., the response must be predicted with an accurate constitutive model calibrated to a full set of loading parameters and then correlated using experimental lives and damage mechanisms using the simulated

response. It is necessary to use the simulated response in life correlations since small differences between the simulated and experimental responses can magnify the error on predicted life.

Using the constitutive model developed by Shenoy and others (2005), a parametric study was performed to obtain the finite element (FE) response of the materials. A total of nearly six hundred simulations were conducted for each of the types of mechanical tests and tabulated for ease of use in the damage modeling. These tabulated results were particularly useful in the development stage of the damage modules.

The content and organization of the remaining sections of this chapter are as follows. First the constitutive model formulation and its implementation in finite element modeling is detailed. The uniaxial cyclic deformation response for DS GTD-111 is determined and compared with several experiments. Finally, some observations are made from the simulated data.

## *5.2 Implementation and Parameter Estimation*

Using the anisotropic elastic and crystal plasticity framework reviewed in Chapter 2, a constitutive model developed by Shenoy and coworkers (2005) has been implemented in ABAQUS/Analysis as a User-Defined Material Subroutine (UMAT) which was. This model has the capability to account for grain orientation (e.g. L and T) of DS GTD-111. The UMAT implemented by Shenoy was based upon the scheme developed by McGinty (2001). Linear elements were used in all cases. For each

integration point and at each time step increment, the UMAT updates the following: stresses, internal state variables (ISVs), and the Jacobian matrix. The implementation details are given by Shenoy et al. (2005).

Modeling grains of L- and T-oriented DS GTD-111 required different finite element models. A single finite element per grain was used to determine the constants and the stress-strain behavior of DS GTD-111 subjected to cyclic loading. Both the L- and T-oriented materials were modeled with 8-noded three-dimensional, linear, solid elements designated as C3D8 by ABAQUS. The model was subjected to displacements on opposing ends which simulates uniaxial strain-controlled experiments. The L-oriented element was composed of one grain, however, the response of the material in the transverse orientation is an average response of material comprising 100 grains. The Taylor constraint for intergranular interactions is assumed in this averaging process, such that each grain within the T-oriented model is subjected to the same deformation gradient. The orientation of the grains relative to the stress axis can be described using the three parameters known as Euler angles, which are denoted by $(\phi,\theta,\psi)$. For the L-oriented case, the grain growth direction is aligned with the stress axis and $(\phi,\theta,\psi)=(0,0,0)$. For the T case, grains are aligned normal to the stress axis and $\phi$ values for each grain were random elements of $(0,2\pi)$. The remaining angles were set to 0.

Predictions for the off-axis cyclic responses were also obtained. For these cases, several columnar grains were modeled. The orientation angle, $\omega$, between the axis of the collection of grains and the stress axis was varied from 0° (L-oriented) to 90° (T-oriented). The Euler angles of the individual grains were randomly-oriented.

Determining material constants for DS GTD-111 requires a systematic procedure. First, certain physical parameters such as elastic properties and activation energies of thermally-activated diffusional processes are obtained from literature. For example, the activation energy is based on that obtained for PC GTD-111 (Daleo and Wilson, 1998). Although some parameters can be determined/refined graphically using trial and error approaches, the most robust and efficient technique is to use an optimization scheme to iteratively evaluate the model parameters. This approach integrates the constitutive model in order to simulate the actual loading histories.

The automated optimization scheme involves executing a simulation of an experiment (e.g. isothermal low cycle fatigue, creep-fatigue, creep deformation) using a set of parameters suggested by the optimization code. The outputted numerically correlated response is compared to the actual experimental response generating a value of an objective function defined on the basis of the norm of the error between the experimental and correlated stress responses, as shown in Fig. 5.1. The Epogy optimization code minimizes the error function by iteratively modifying the material parameters in each subsequent simulation. The total error is the sum of the equally-weighted errors for the cyclic and creep deformation data, i.e.,

$$Error_{total} = Error_{cyclic} + Error_{creep} \tag{5.1}$$

For uniaxial cyclic data, the error norm function is defined in terms of the stress response, i.e.,

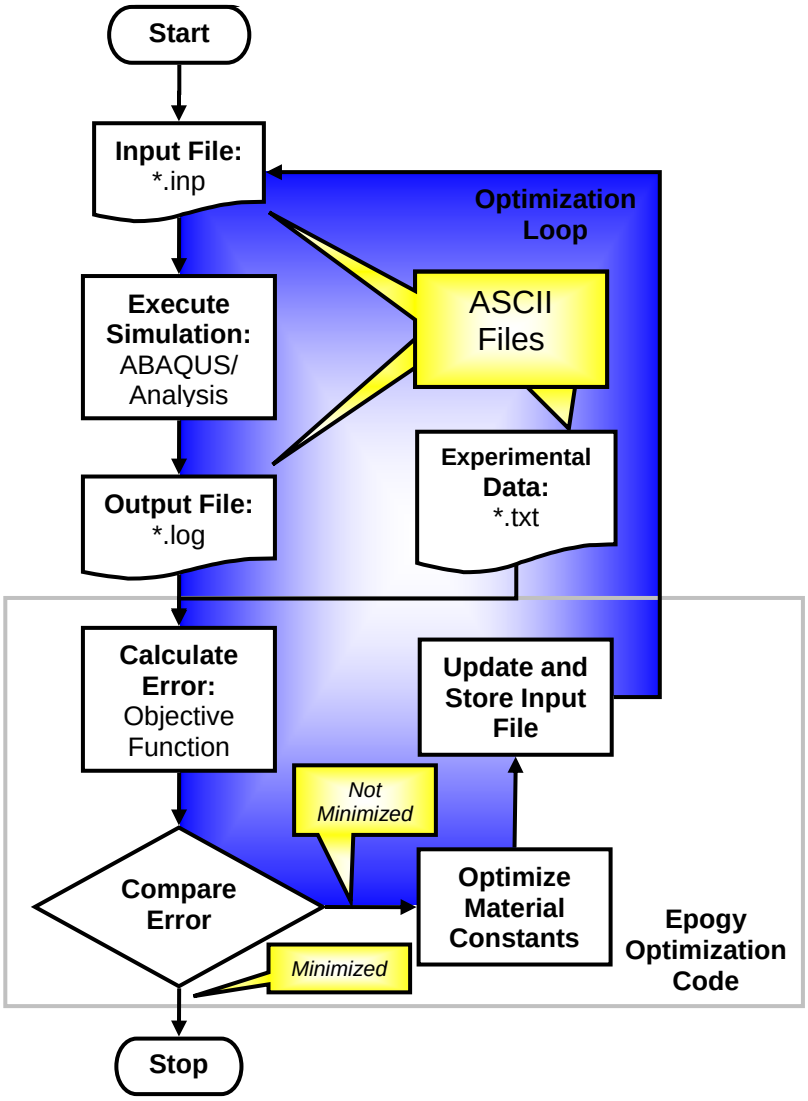


***Figure 5.1:*** *Processes used automated optimization of material constants used for finite element modeling of DS GTD-111.*

$$Error_{cyclic} = \sum_{i=1}^{n} \left( \sigma^{i}_{model} - \sigma^{i}_{exp} \right)^{2} W_{i} \quad . \tag{5.2}$$

For the $i^{th}$ of $n$ cyclic stress values, $\sigma^{i}_{model}$ is the stress predicted by the model, $\sigma^{i}_{exp}$ is the experimentally measured stress, and $W_i$ is a weighting parameter. The $W_i$-values depend

on the region in which the $i^{th}$ data point is a member. Less weight is placed on data from the elastic portions of the CSSC (i.e., $W_i = 0.8$), while more is placed on data from inelastic deformation (i.e., $W_i = 1.2$). Each of the weighing parameters were determined from a previous study (Shenoy et al., 2005).

An average weight is used (i.e., $W_i = 1.0$) during dwell periods in which slight stress relaxation occurs. Since some terms in the model are only active for long hold periods (e.g. static thermal recovery terms), a separate error function is required to fit data exhibiting creep deformation. To fit the response of experimental data containing substantial stress relaxation, such as cycling with long hold periods or creep deformation during secondary creep, the following error norm function is used:

$$Error_{creep} = \sum_{i}^{n} \left( \varepsilon_{model}^{i} - \varepsilon_{exp}^{i} \right)^2 E_{avg}^2 \ . \tag{5.3}$$

At the $i^{th}$ of $n$ instances, $\varepsilon_{model}^{i}$ and $\varepsilon_{\exp}^{i}$ are the predicted and experimentally-obtained strains, and $E_{avg}$ is the average value of the elastic modulus of DS GTD-111 in the specified L or T orientation at a particular temperature.

## *5.3 Simulations of Experiments*

A parametric study, consisting of nearly 600 simulations, was carried out under the following conditions and independent variables:

- Isothermal low cycle fatigue (LCF) at various temperatures – **Temperature, $T \in$ {649, 760, 871, 982, 1038°C}**; Total Strain Range, $\Delta\varepsilon \in$ {0.25, 0.50, 0.75, 1.00, 1.50, 2.00, 3.00, 4.00%}; Strain Ratio, $R_\varepsilon$ = -1; Temperature Range, $\Delta T$ = 0; and Strain Rate, $\dot{\varepsilon}$ = 0.50%/s.
- Isothermal LCF at various strain rates – Temperature, $T \in$ {649, 760, 871, 982, 1038°C}; Total Strain Range, $\Delta\varepsilon \in$ {0.50, 1.00, 2.00%}; Strain Ratio, $R_\varepsilon$ = -1; Temperature Range, $\Delta T$ = 0; and **Strain Rate, $\dot{\varepsilon} \in$ {0.01, 0.50, 25.00%/s}**.
- Isothermal low cycle fatigue (LCF) at various mean strains – Temperature, $T \in$ {760, 871°C}; Total Strain Range, $\Delta\varepsilon \in$ {0.25, 0.50, 0.75, 0.80, 1.00, 1.20, 1.50, 2.00, 3.00, 4.00%}; **Strain Ratio, $R_\varepsilon \in$ {0, -1, -∞}**; Range, $\Delta T$ = 0; and Strain Rate, $\dot{\varepsilon}$ = 0.50%/s.
- Isothermal creep-fatigue with various hold times – Temperature, $T \in$ {649, 760, 871, 982, 1038°C}; Total Strain Range, $\Delta\varepsilon \in$ {0.50, 1.00, 2.00%}; Strain Ratio, $R_\varepsilon$ = -1; Temperature Range, $\Delta T$ = 0; Strain Rate, $\dot{\varepsilon}$ = 0.50%/s; Hold Time, $t_h \in$ {2, 10, 50, 1250, 6250 *min*}; and Dwell Type ∈ {Tensile (HT), Compressive (HC)}.
- Thermomechanical fatigue (TMF) – **Temperature Range, $\Delta T \in$ {538 ⇆ 927, 538 ⇆ 1038°C}**; Mechanical Strain Range, $\Delta\varepsilon_m \in$ {0.25, 0.50, 1.00, 2.00, 4.00%}; Strain Ratio, $R_\varepsilon$ = -1; **Total Cycle Time, $t_{tc}$ = 3 *min*; and Phasing, $\phi \in$ {0° (In-Phase), 180° (Out-of-Phase)}**.
- Isothermal low cycle fatigue (LCF) at various orientations – Temperature, $T$ = 871°C; Total Strain Range, $\Delta\varepsilon$ = 2.00%; Strain Ratio, $R_\varepsilon$ = -1; Temperature

Range, $\Delta T$ = 0; Strain Rate, $\dot{\varepsilon}$ = 0.50%/s; **Orientations∈ {0° (L-oriented), 15°, 30°, 45°, 60°, 75°, 90° (T-Oriented)}**.

The plastic strain range, $\Delta\varepsilon_{pl}$, maximum stress, $\sigma_{max}$, stress range, $\Delta\sigma$, etc., were obtained from each stabilized hysteresis loop and are tabulated in Appendix E.

## *5.4 Comparison of FE Simulations and Experiments*

Comparison of experiments and numerical simulations are shown in Figs. 5.2-5.11. For the simulations at the benchmark temperature 871°C (1600°F) shown in Figs. 5.2 and 5.3, the simulated $E_i$ matched the modulus determined from experiments on both L- and T-oriented material. The most notable variation in the curves is the stress range for T-oriented DS GTD-111. For each case shown in Fig. 5.3, the minimum and maximum stresses obtained from the model underestimated those determined from experiments. This could be an indication that the constitutive and FE models do not capture some deformation phenomenon accurately at this particular temperature. In each of the figures (Fig. 5.3a-c), the modeled elastic modulus of 130 *MPa* (19 *ksi*) simulates an aggregate of many grains. Transversely-oriented samples of DS GTD-111 contain between three and ten grains; as such, the modulus measured from experiments at 871°C range between 141 *MPa* (20 *ksi*) (Fig. A.11) and 163 *MPa* (24 *ksi*) (Fig. A.37).

The effect of temperature on response is shown in Figs. 5.4 and 5.5. The effect of strain rate at 982°C is shown Fig. 5.6. The effect of mean strain is illustrated in Fig. 5.7. Since the constants are matched to the cyclic response, the initial loading is not captured as well.

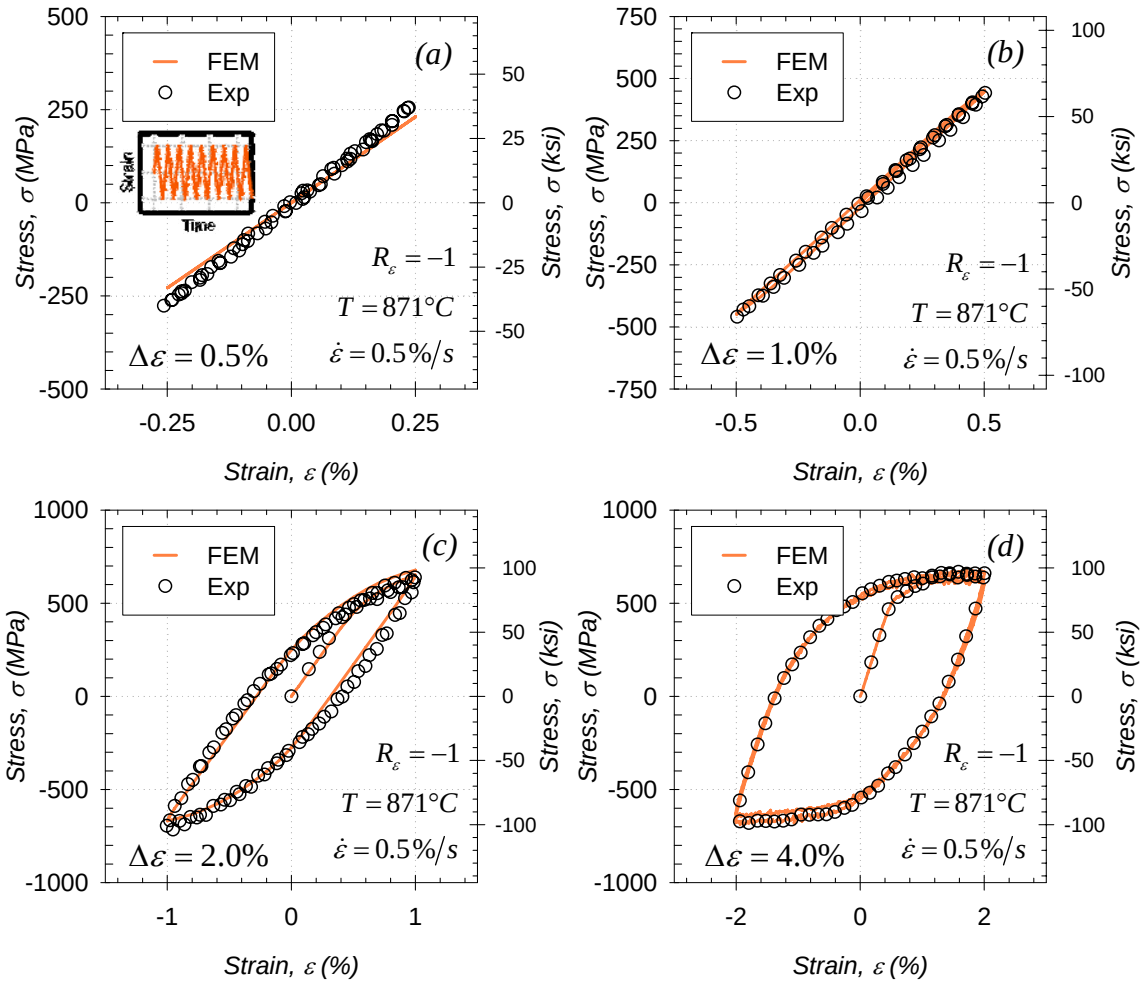


***Figure 5.2:*** *Simulated and actual experimental responses of L-oriented DS GTD-111 under isothermal LCF at (a) $\Delta\varepsilon$ = 0.5%, (b) $\Delta\varepsilon$ = 1.0%, (c) $\Delta\varepsilon$ = 2.0%, and (d) $\Delta\varepsilon$ = 4.0%. For each case $R_\varepsilon$=-1, $\dot{\varepsilon} = 0.5\%/s$, and 871°C (1600°F).*

The effect of creep-fatigue cycling is shown in Figs. 5.8 - 5.10. The constitutive model performs well in capturing both the push-pull and the stress relaxation portion of the saturated cyclic response. The modeled hysteresis achieved good agreement with experiments on both grain orientations (Fig 5.8), at increased temperatures (Fig. 5.9), and increased hold time or hold type (Fig. 5.10).

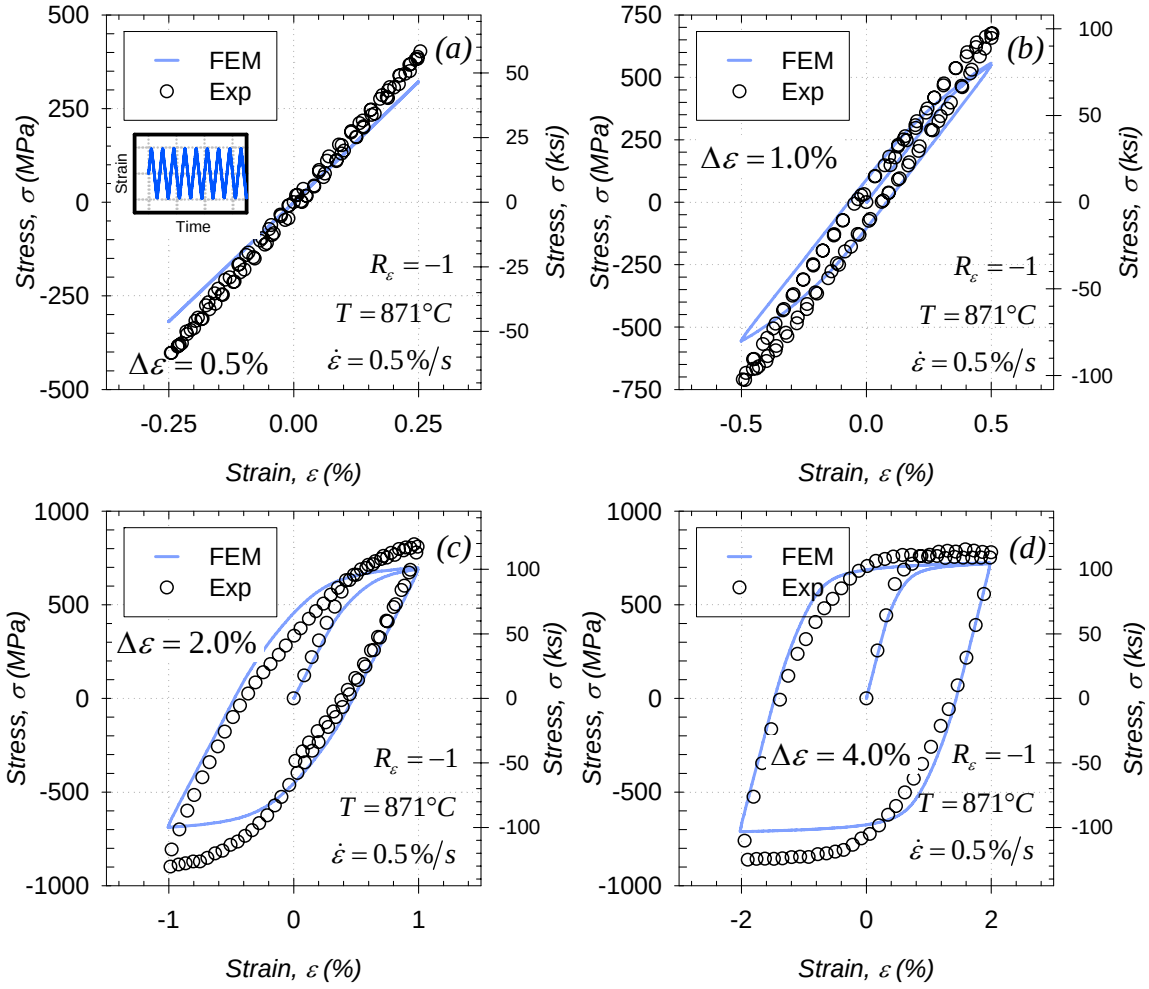


***Figure 5.3:*** *Simulated and actual experimental responses of T-oriented DS GTD-111 under isothermal LCF at (a) $\Delta\varepsilon$ = 0.5%, (b) $\Delta\varepsilon$ = 1.0%, (c) $\Delta\varepsilon$ = 2.0%, and (d) $\Delta\varepsilon$ = 4.0%. For each case $R_\varepsilon$=-1, $\dot{\varepsilon} = 0.5\%/s$, and 871 ℃ (1600 ℉).*

The response under OP TMF cycling are shown in Fig. 5.11. The constitutive model underestimates inelastic strain hysteresis exhibited in both L- (Fig. 5.11a) and T-oriented (Fig. 5.11c) cases. This is most likely an artifact of the slight mismatch in modeling the cyclic thermal strain versus temperature response. For each case the predicted and experimentally-measured $\sigma_{max}$ coinciding with the minimum temperature is within 2% error.

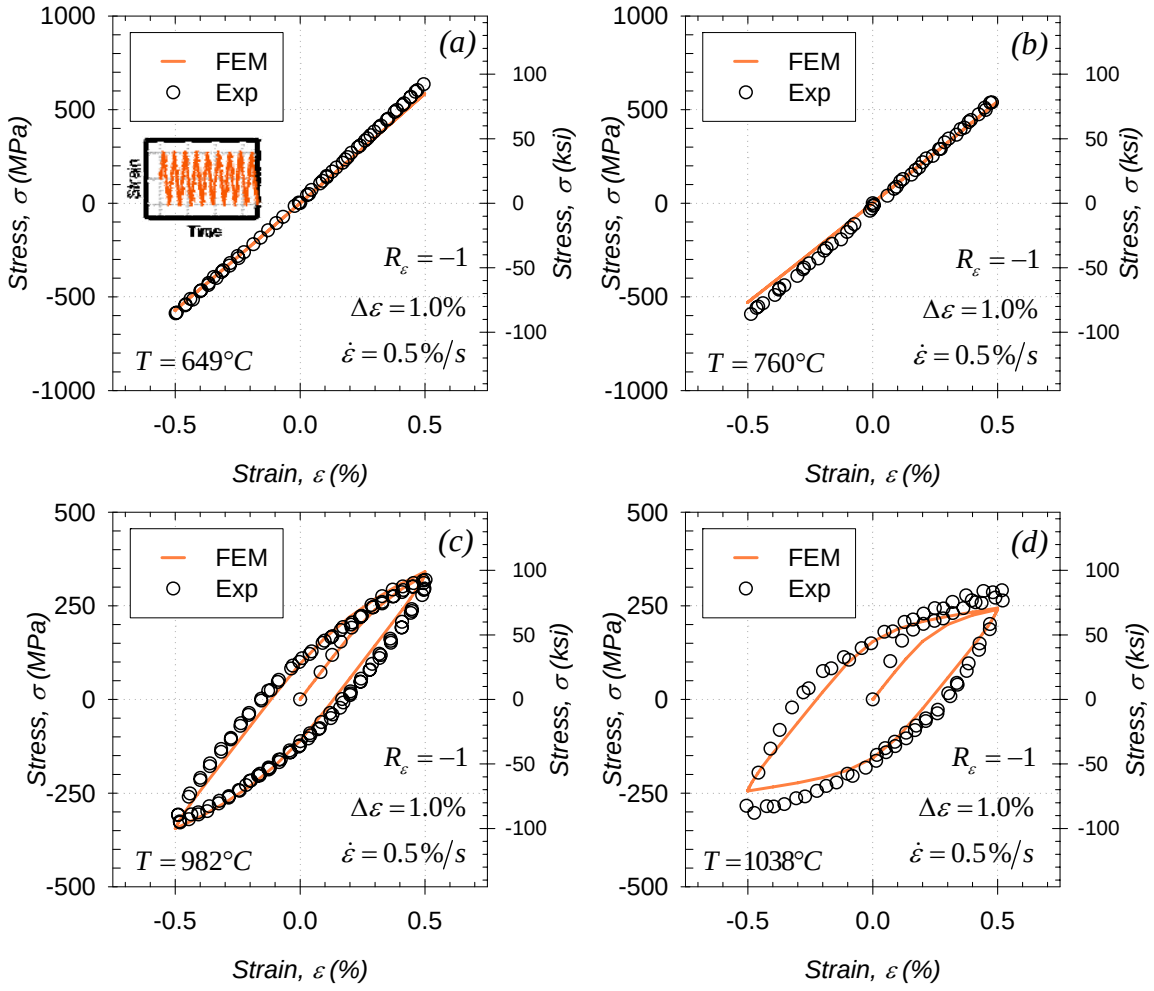


***Figure 5.4:*** *Simulated and actual experimental responses of L-oriented DS GTD-111 under isothermal LCF at (a) 649°C (1200°F), (b) 760°C (1400°F), (c) 982°C (1800°F), and (d) 1038°C (1900°F). For each case $R_\varepsilon$=-1, $\dot{\varepsilon} = 0.5\%/s$, and $\Delta\varepsilon$ = 1.0%.*

## 5.5 Trends in Simulated Experimental Responses

The results of numerical simulations of fatigue experiments on L- and T-oriented DS GTD-111 have been tabularized in Appendix E. Small subsets of the results are illustrated in Figs. 5.12 – 5.21. For continuous cycling cases involving L-oriented material, plastic strain range, $\Delta\varepsilon_{pl}$, is measured from the 1 grain that was modeled. No averaging is needed. For the T-oriented cases, however, $\Delta\varepsilon_{pl}$ is averaged over all of the

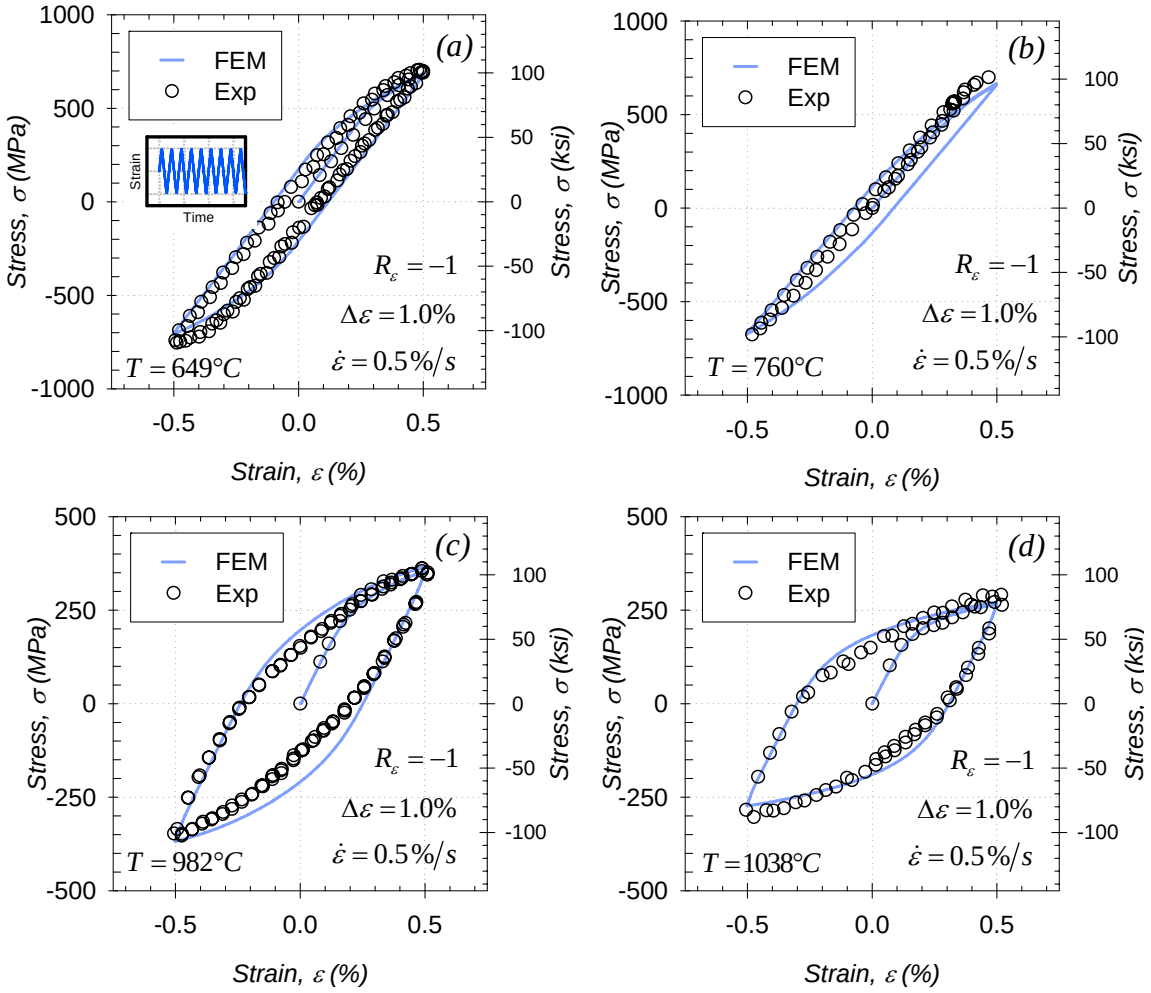


***Figure 5.5:*** *Simulated and actual experimental responses of T-oriented DS GTD-111 under isothermal LCF at (a) 649℃ (1200℉), (b) 760℃ (1400℉), (c) 982℃ (1800℉), and (d) 1038℃ (1900℉). For each case $R_\varepsilon$=-1, $\dot{\varepsilon} = 0.5\%/s$, and $\Delta\varepsilon$ = 1.0%.*

grains. In models involving creep-fatigue cycling, the same procedure is used with the exception that the plastic portion of strain range includes both time–independent and –dependent portions, e.g. $\Delta\varepsilon_{pl}$ and $\Delta\varepsilon_{cr}$, respectively, and is referred to as the inelastic strain range, denoted as $\Delta\varepsilon_{in}$.

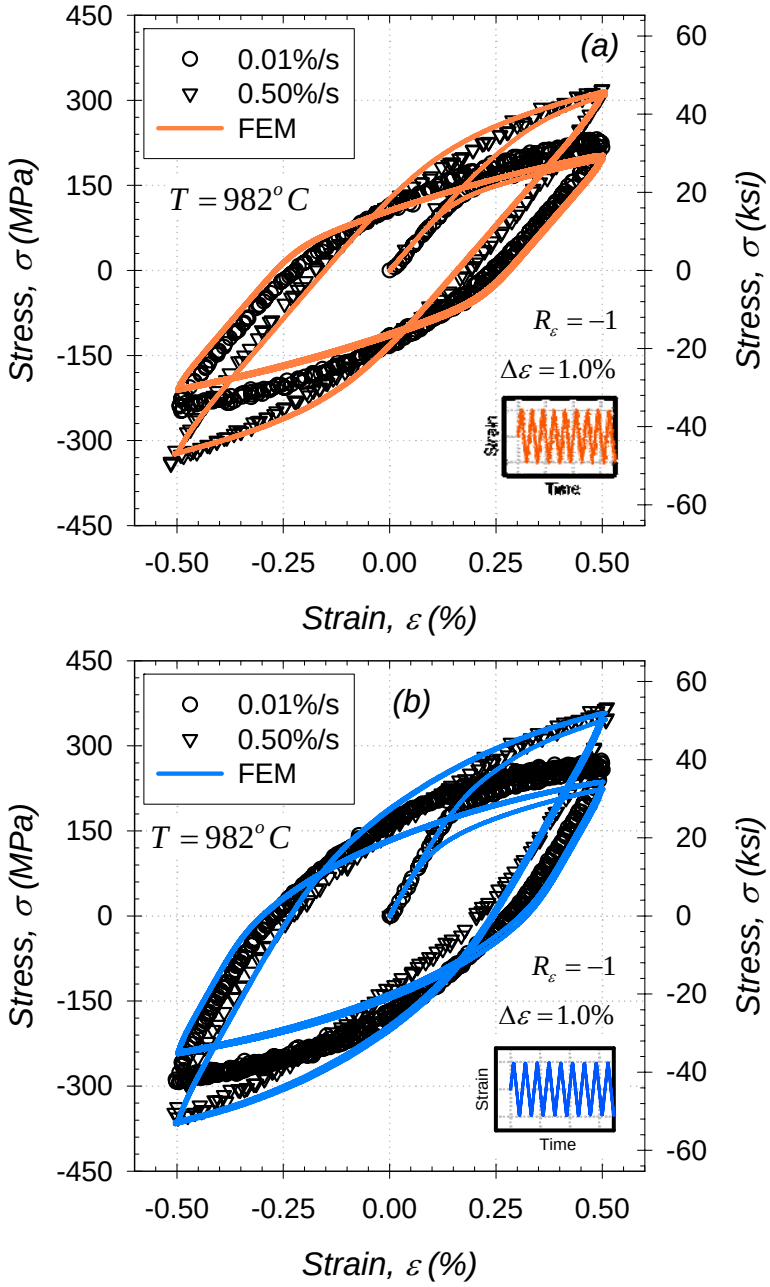


***Figure 5.6:*** *Simulated and actual experimental responses of DS GTD-111 under isothermal LCF in (a) L-orientation and (b) T-orientation at two strain rates. For each case 982℃ (1800℉), $R_\varepsilon$=-1, and $\Delta\varepsilon$ = 1.0%.*

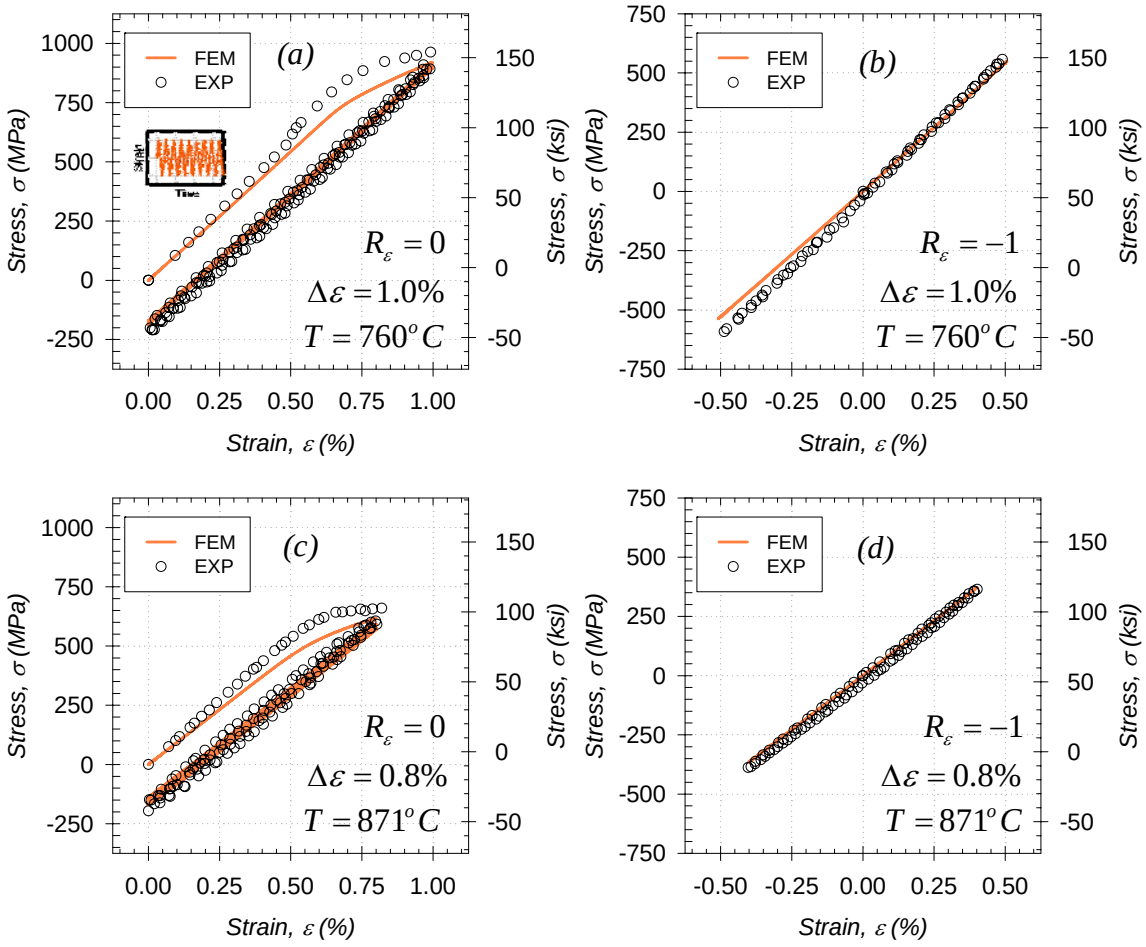


***Figure 5.7:*** *Simulated and actual experimental responses of L-oriented DS GTD-111 under isothermal LCF under (a, c) zero-to-tension cycling ($R_\varepsilon = 0$) and (b, d) completely-reversed cycling ($R_\varepsilon = -1$). For each case, $\dot{\varepsilon} = 0.5\%/s$.*

It should be noted that these simulations are based on the "batch" of DS GTD-111 material having specific attributes (i.e., grain size, precipitate particle size, SDAS) based on the manufacturing processes (i.e., heat treatment, chemical composition) used to develop specimen slabs. Observations from collections of the simulations are discussed next.

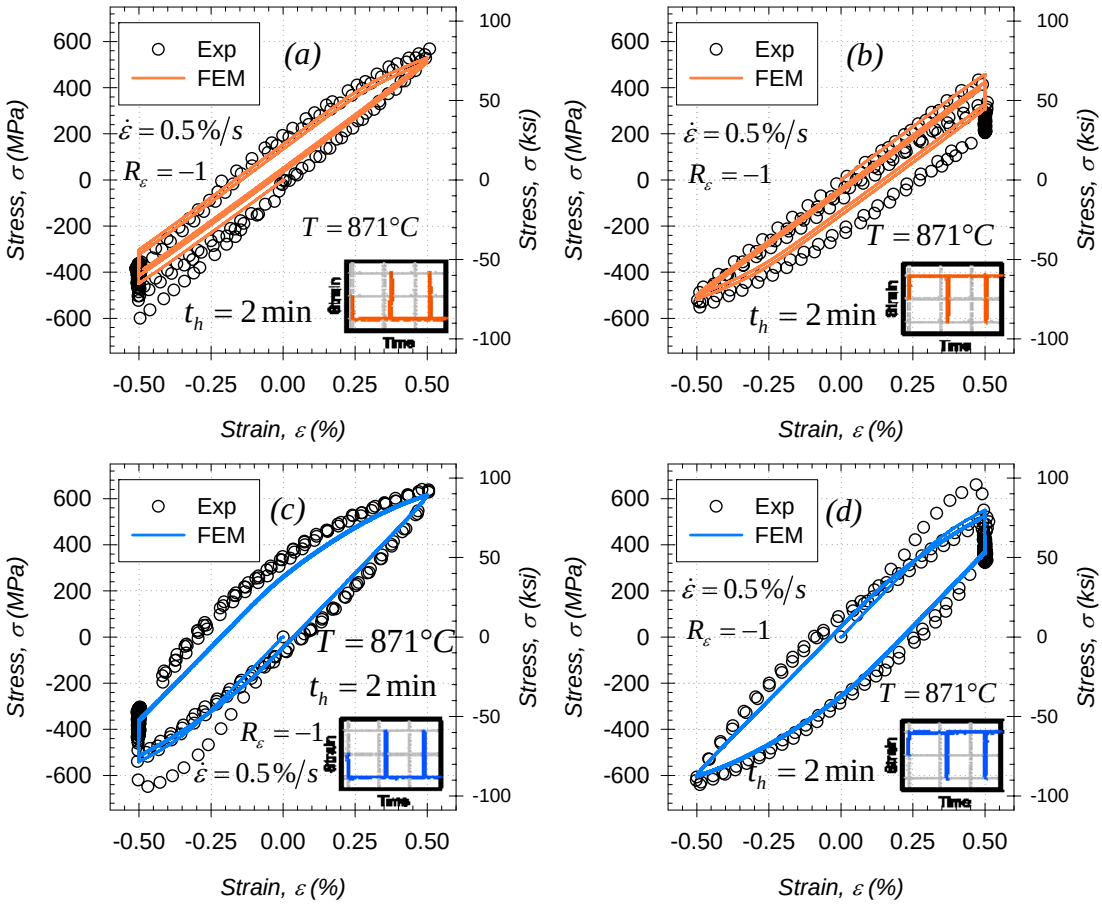


***Figure 5.8:*** *Simulated and actual experimental responses of (a, b) L-oriented and (c, d) T-oriented DS GTD-111 under isothermal creep-fatigue cycling at 871°C (1600°F). For each case* $R_\varepsilon = -1$, $t_h = 2\,\text{min}$, *and* $\dot{\varepsilon} = 0.5\%/s$.

*Isothermal Low Cycle Fatigue (LCF) at Various Temperatures*

The relationship between plastic strain range and total strain range is shown in Fig. 5.12. Symbols represent simulations and the interpolations were made using 3rd order polynomials. The effect of temperature on plastic strain range is also shown in Fig. 5.12. The minimum $\Delta\varepsilon_{pl}$, for constant $\Delta\varepsilon$, occur at 760°C (1400°F). Similar trends in isothermal LCF modeling were observed for $\sigma_{max}$ versus $\Delta\varepsilon$ and stress range $\Delta\sigma$ versus $\Delta\varepsilon$. For each specific combination of $T$ and $\Delta\varepsilon$, the $\Delta\varepsilon_{pl}$ versus $\Delta\varepsilon$ curve for L-oriented

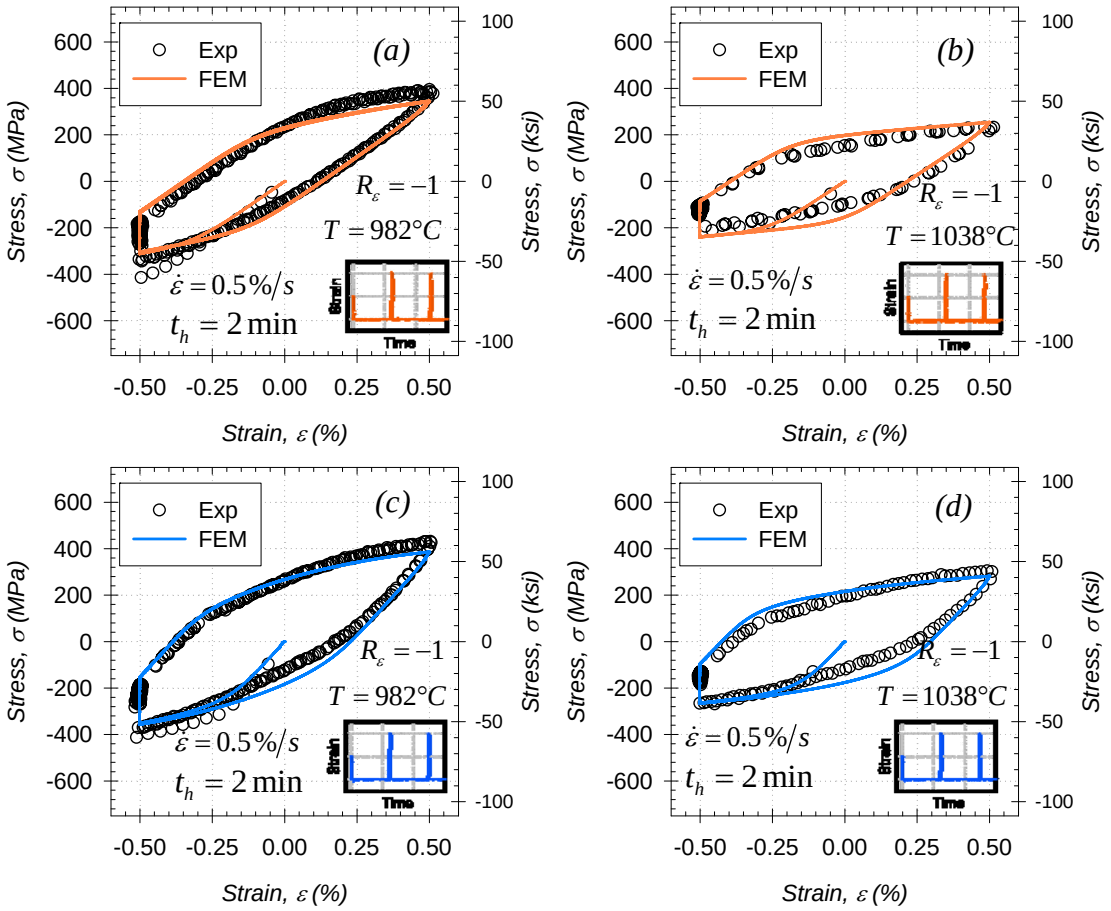


***Figure 5.9:*** *Simulated and actual experimental responses of (a, b) L-oriented and (c, d) T-oriented DS GTD-111 under isothermal creep-fatigue cycling at (a, c) 982°C (1800°F) and (b, d) 1038°C (1900°F). For each case* $R_\varepsilon = -1$, $t_h = 2\,\text{min}$, *and* $\dot{\varepsilon} = 0.5\%/s$.

DS GTD-111 fell below that of the T-oriented material because of the greater $\Delta\varepsilon_{el}$ contribution in the L-orientation material.

*Isothermal LCF at Various Strain Rates*

Increasing $\dot{\varepsilon}$ generally caused both $\sigma_{max}$ and $\Delta\sigma$ to increase. As a result, $\Delta\varepsilon_{pl}$ decreased with increasing $\dot{\varepsilon}$, shown in Fig. 5.13. This finding is attributed to the effect

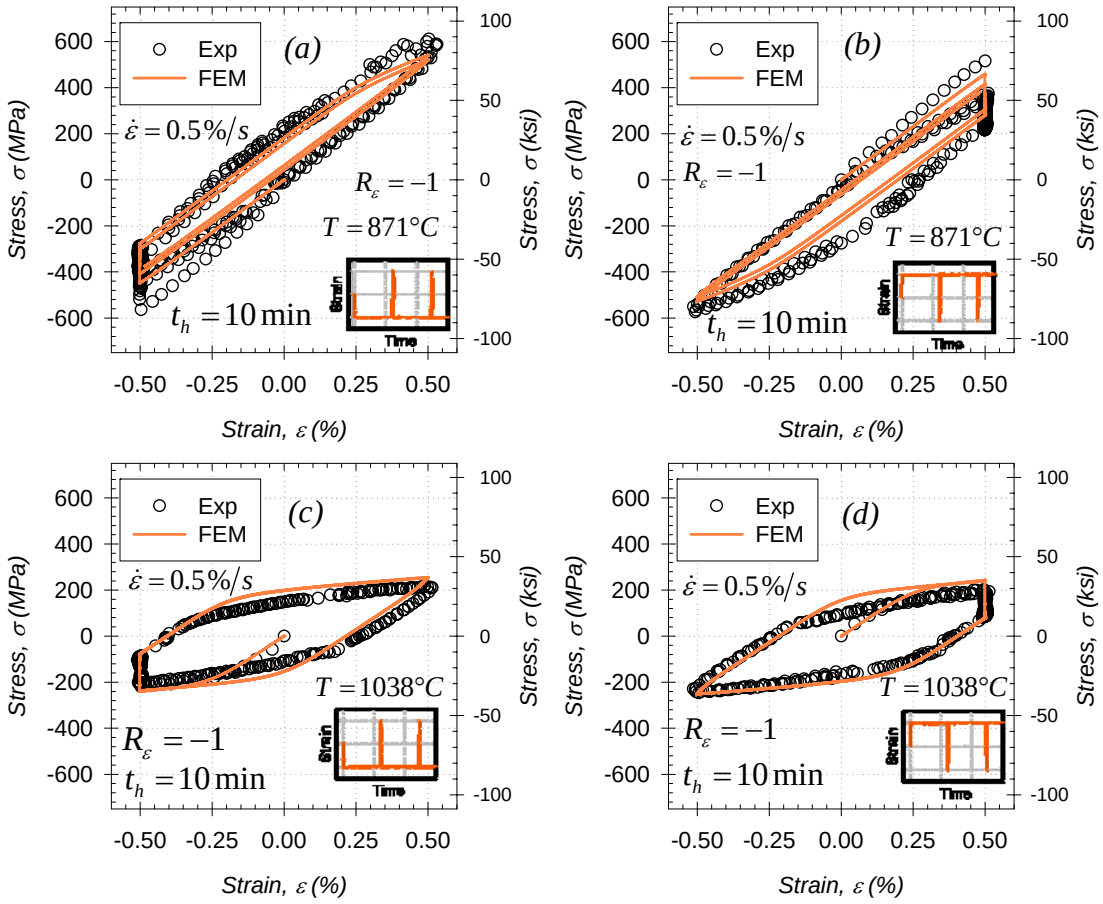


***Figure 5.10:*** *Simulated and actual experimental responses of L-oriented DS GTD-111 under isothermal creep-fatigue cycling at (a, b) 871°C (1600°F) and (c, d) 1038°C (1900°F). For each case* $R_\varepsilon = -1$, $t_h = 10\,\text{min}$, $\Delta\varepsilon = 1.0\%$, *and* $\dot{\varepsilon} = 0.5\%/s$.

of strain rate on response at 871°C and above. This was most evident at the lowest $\dot{\varepsilon}$ considered in which the most creep deformation was observed.

*Isothermal Low Cycle Fatigue (LCF) at Various Mean Strains*

The effect of mean strain on plastic strain is shown in Fig. 5.14. Regardless of the grain orientation (L or T) or temperature, strain ratio had a minimal impact on either $\Delta\varepsilon_{pl}$ or $\Delta\sigma$. Decreasing the $R_\varepsilon$ from 0 to -∞, caused $\Delta\varepsilon_{pl}$ to slightly increase for both

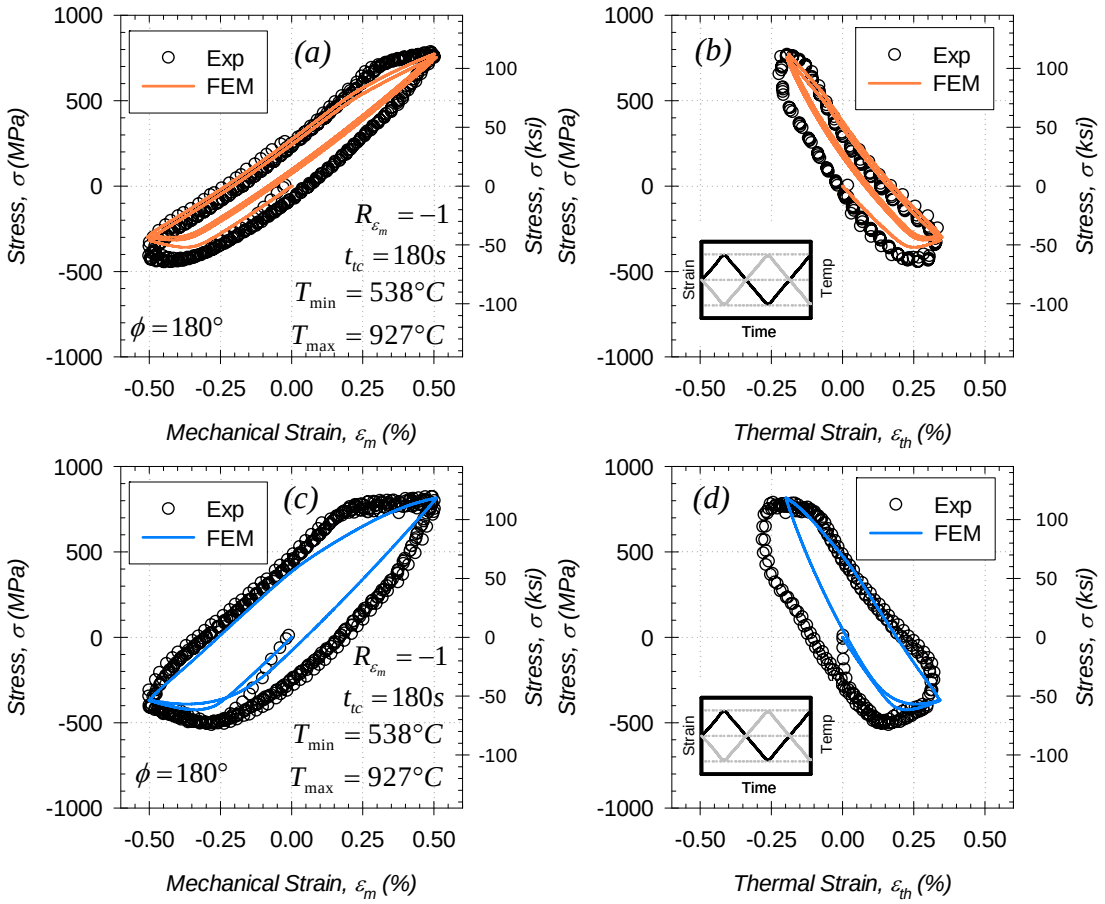


***Figure 5.11:*** *Simulated and actual experimental responses of (a, b) L-oriented and (c, d) T-oriented DS GTD-111 under thermomechanical fatigue cycling. For both cases* $R_{\varepsilon_m} = -1$, $t_{tc} = 180\,s$, *and* $\Delta\varepsilon_m = 1.0\%$, *and* $\Delta T = 389°C\,(700°F)$.

orientations, as shown in Fig. 5.14. This variation in the plastic component of the cyclic deformation is a direct consequence of the slight tension/compression asymmetry occurring at low temperatures. Even though both $\sigma_{min}$ and $\sigma_{max}$ decreased with decreasing strain ratio, $\Delta\sigma$ is nearly independent of $R_\varepsilon$ for various $T$-$\Delta\varepsilon$ combinations.

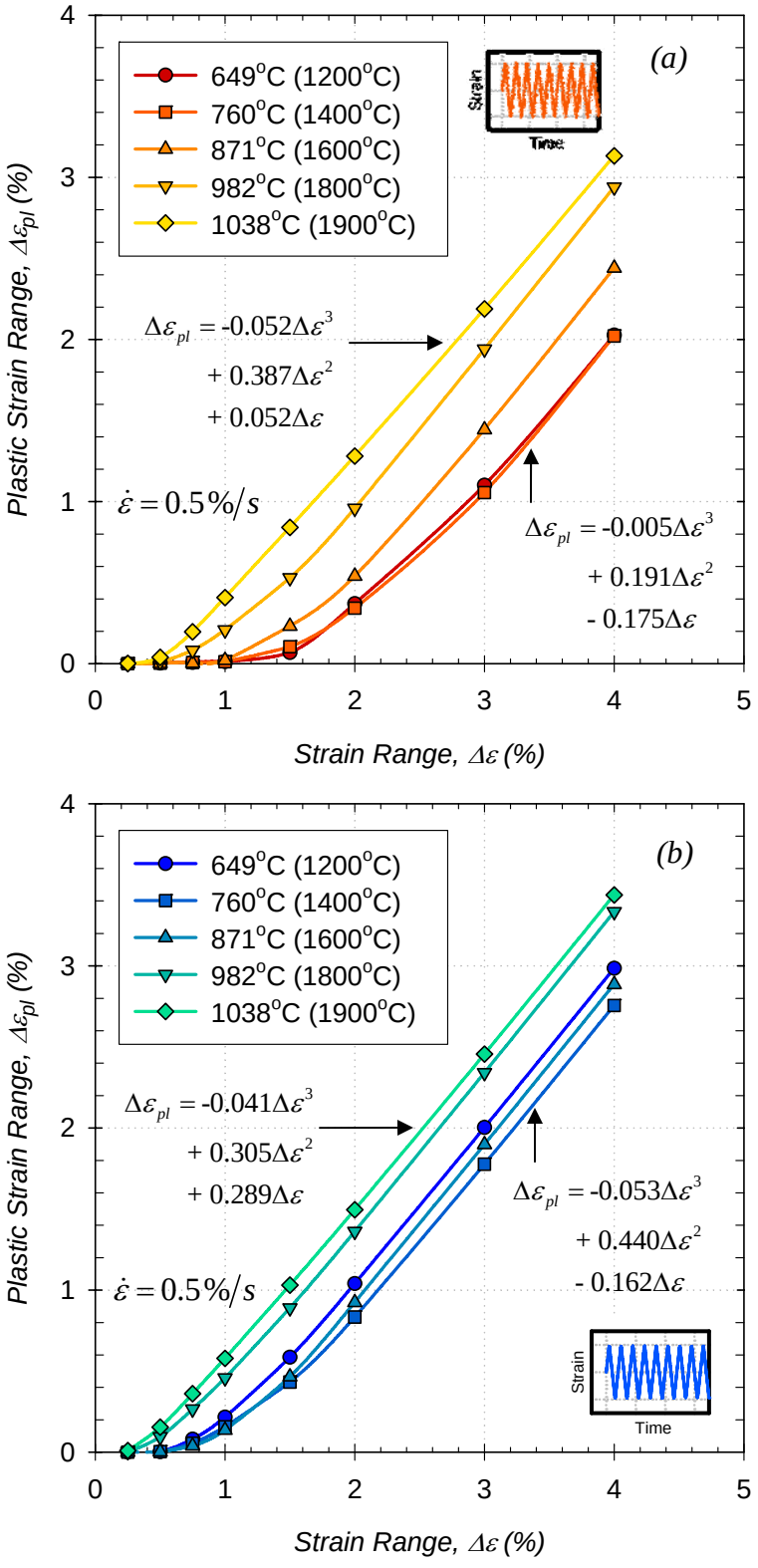


***Figure 5.12:*** *Simulated experimental responses of (a) L-oriented and (b) T-oriented DS GTD-111 under isothermal low cycle fatigue various temperatures. For each case* $R_\varepsilon = -1$ *and* $\dot{\varepsilon} = 0.5\%/s$.

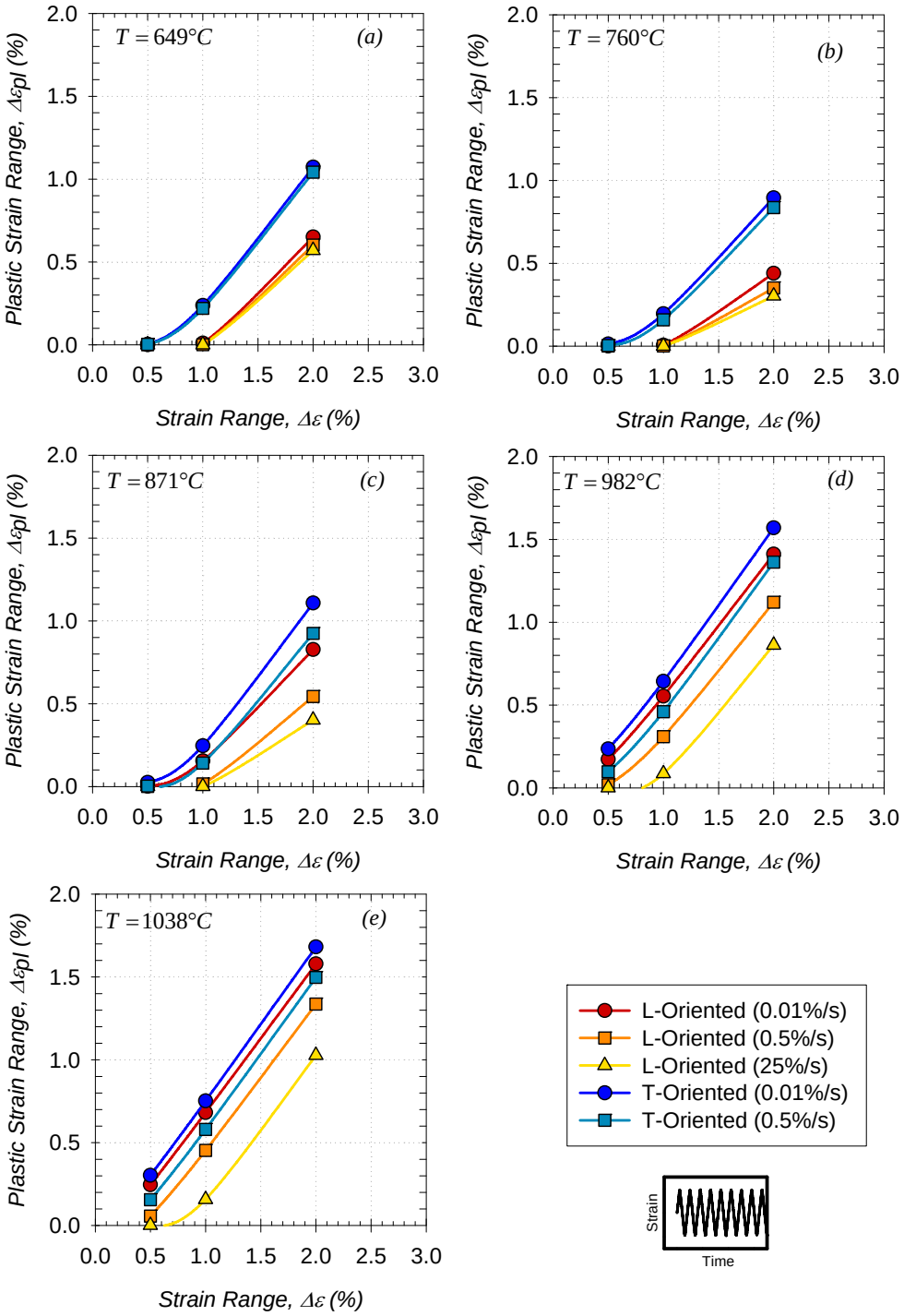


***Figure 5.13:*** *Simulated experimental responses of DS GTD-111 under isothermal low cycle fatigue at various strain rates and (a) 649℃ (1200℉), (b) 760℃ (1400℉), (c) 871℃ (1600℉), (d) 982℃ (1800℉) and (e) 1038℃ (1900℉). For each case* $R_\varepsilon = -1$.

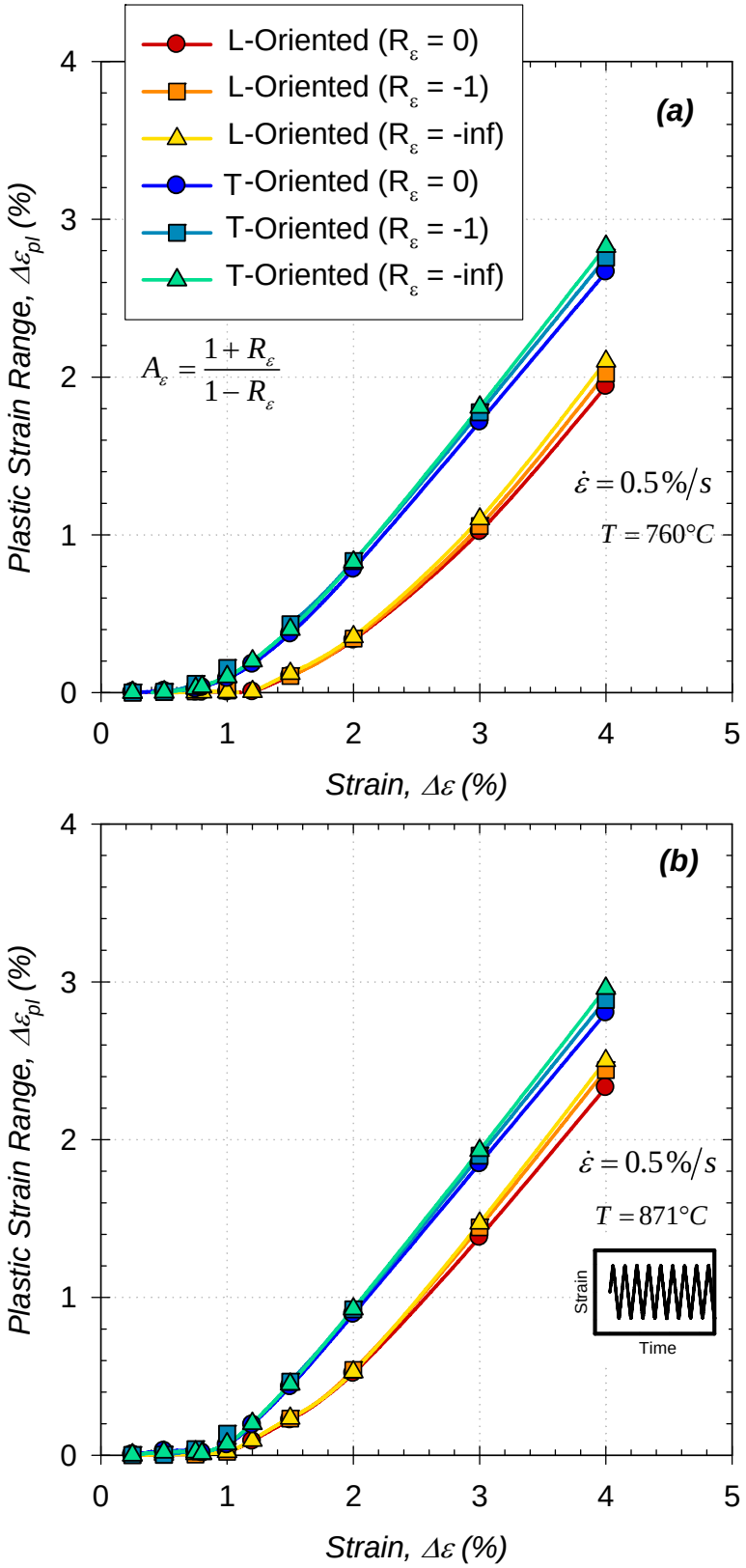


***Figure 5.14:*** *Simulated experimental responses of DS GTD-111 under isothermal low cycle fatigue at various mean strains and (a) 760℃ (1400℉) and (b) 871℃ (1600℉). For each case* $\dot{\varepsilon} = 0.5\%/s$.

*Isothermal Creep-Fatigue with Various Hold Times*

The $\Delta\varepsilon_{pl}$ calculated from hysteresis data was determined to be independent of hold type and hold types that are greater than or equal to two minutes. The results from four sets of conditions shown in Fig. 5.15, are virtually identical; therefore, hold time and type have very little effect on the hysteresis loops. For each grain orientation at a specific strain range and hold time/type pairing, the minimum $\Delta\varepsilon_{pl}$ occurred at 760°C (1400°F), since the maximum yield strength occurs near $T$ = 760°C.

During strain-controlled dwell periods, materials subjected to elevated temperatures undergo the early stages of creep. In strain holds, time-dependent deformation is manifested as stress relaxation. The stress at the end of a cyclic dwell period, $t_h$, is denoted as relaxed stress $\sigma_r$, and is repeated in Figs 5.16 through 5.20. The relaxed stress $\sigma_r$ converges to a steady state value when $t_h$ is increased. For example, the variation in $\sigma_r$ is negligible between hold times of 1250 *min* (0.87 *days*) and 6260 *min* (4.34 *days*). This finding occurs for either hold type (e.g. HC or HT)..

*Non-Isothermal Fatigue*

Results from simulations under IP and OP TMF cycling are shown in Figs. 5.21a and 5.21b, respectively. As with the previous cases, the $\Delta\varepsilon_{pl}$-$\Delta\varepsilon$ curve for the L-oriented material falls completely below that of the analogous T-oriented case. Increasing $T_{max}$ has the effect of lowering the yield strength in both IP and OP cases. Compared to the 538°C ⇆ 927°C case, 538°C ⇆ 1038°C cycled cases exhibit slightly larger plastic strain ranges.

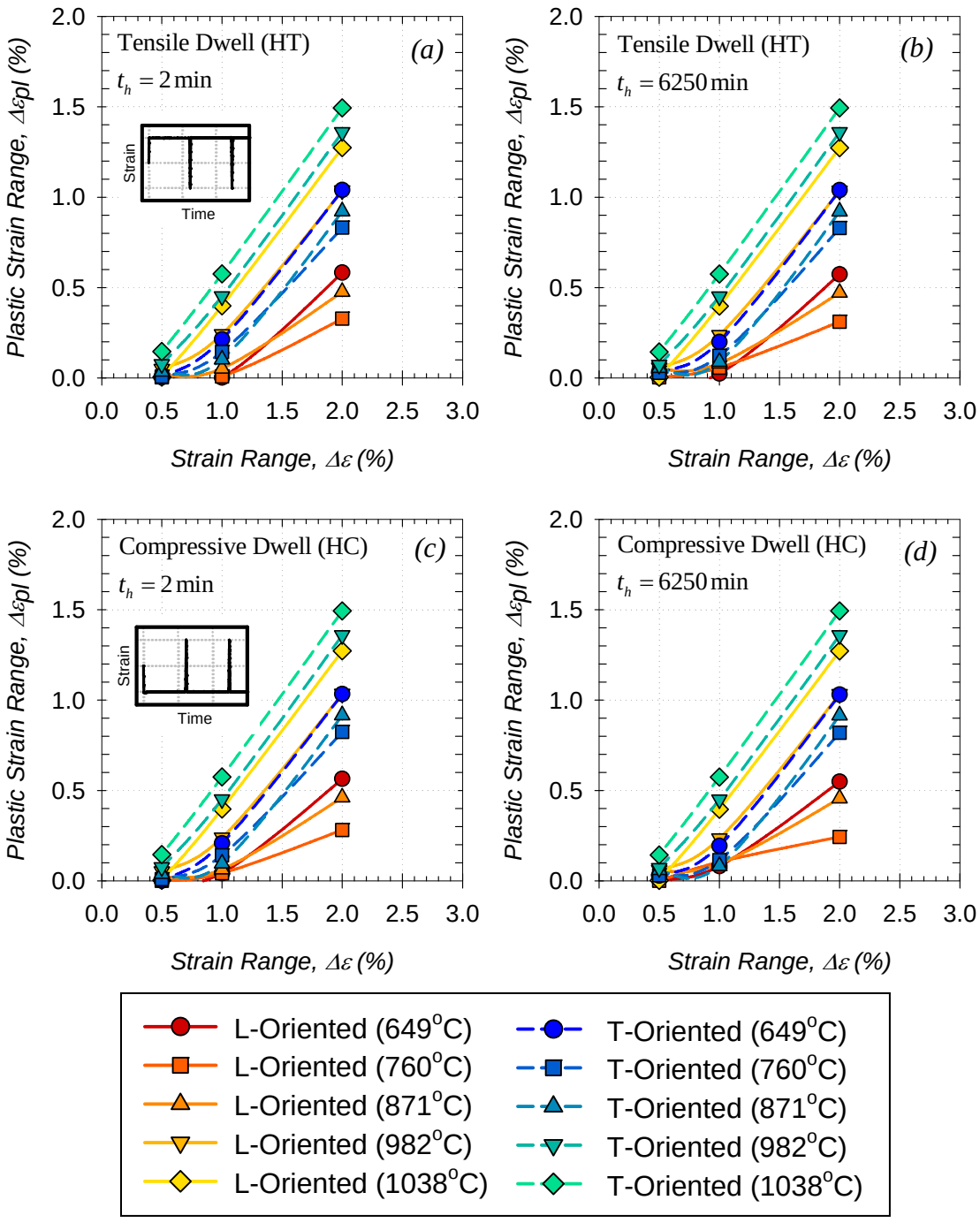


***Figure 5.15:*** *Simulated experimental responses of DS GTD-111 under isothermal creep-fatigue cycling at various temperatures and hold types (a) HT 2 min, (b) HT 6250 min, (c) HC 2 min, and (d) HC 6250 min. For each case* $R_\varepsilon = -1$.

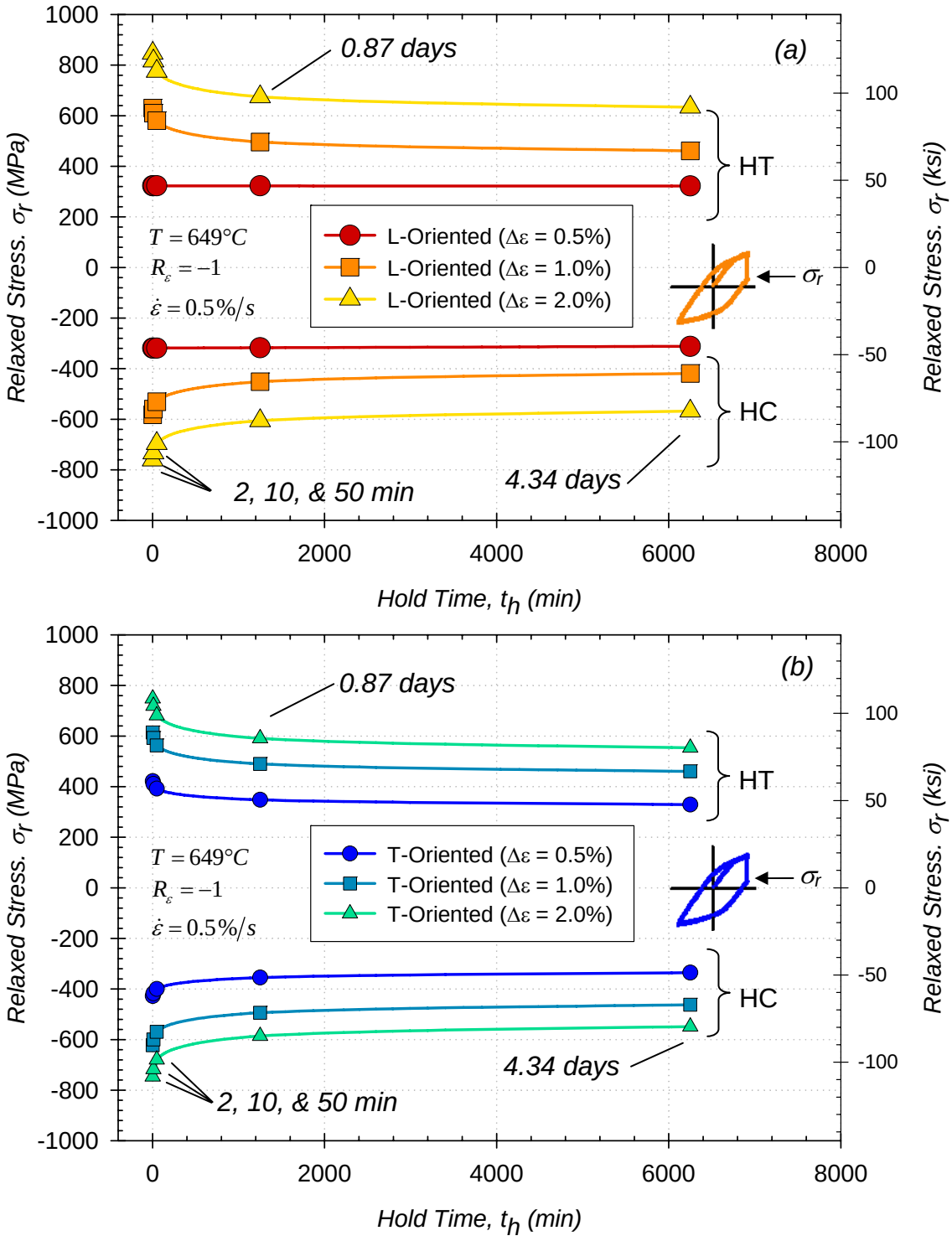


***Figure 5.16:*** *Simulated experimental responses of relaxed stress at the end of the dwell period of DS GTD-111 under creep-fatigue cycling at various hold times: (a) L-oriented and (b) T-oriented. For each case T=649℃ (1200℉),* $\dot{\varepsilon} = 0.5\%/s$*, and* $R_\varepsilon = -1$.

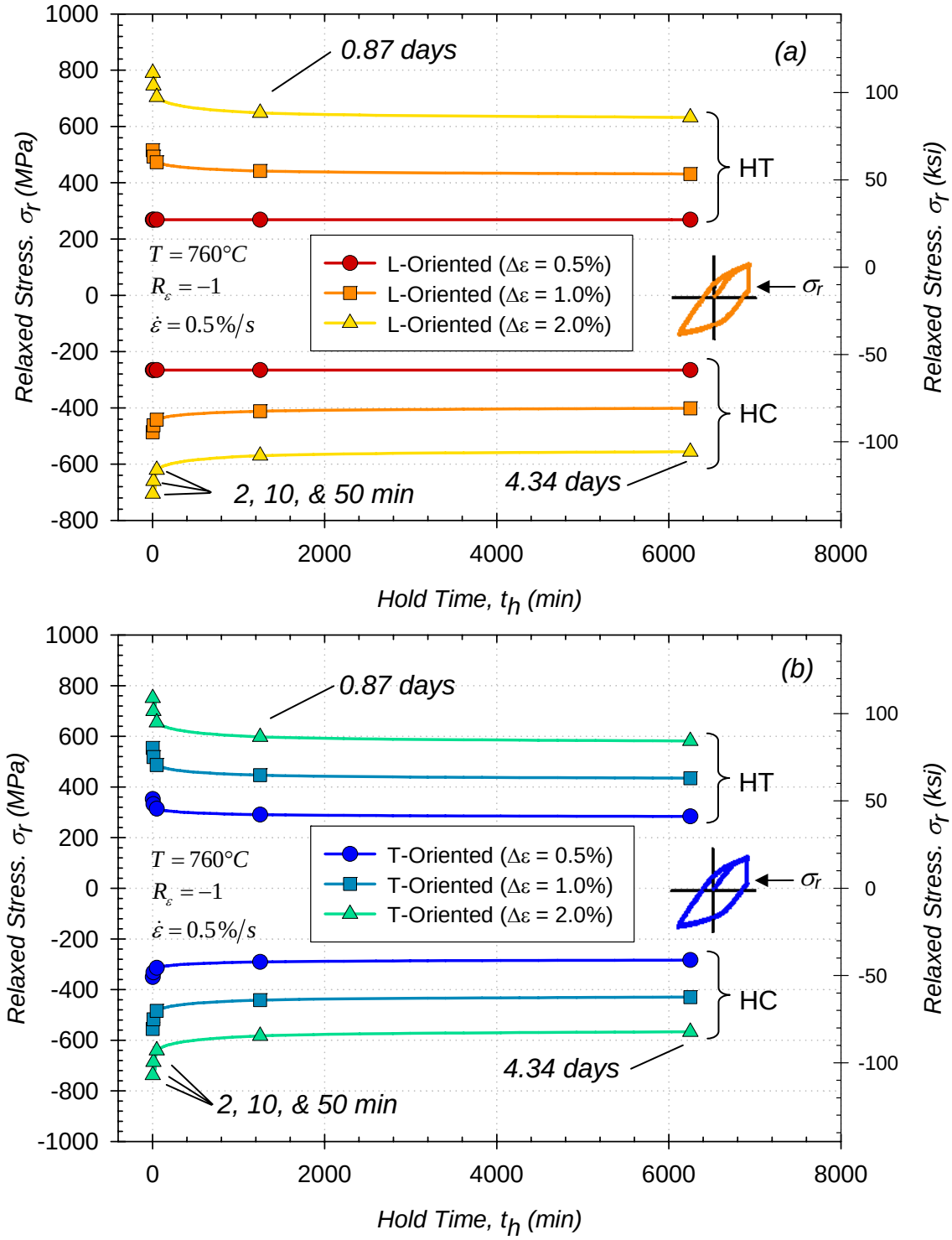


***Figure 5.17:*** *Simulated experimental responses of relaxed stress at the end of the dwell period of DS GTD-111 under creep-fatigue cycling at various hold times: (a) L-oriented and (b) T-oriented. For each case T=760℃ (1400℉),* $\dot{\varepsilon} = 0.5\%/s$, *and* $R_\varepsilon = -1$.

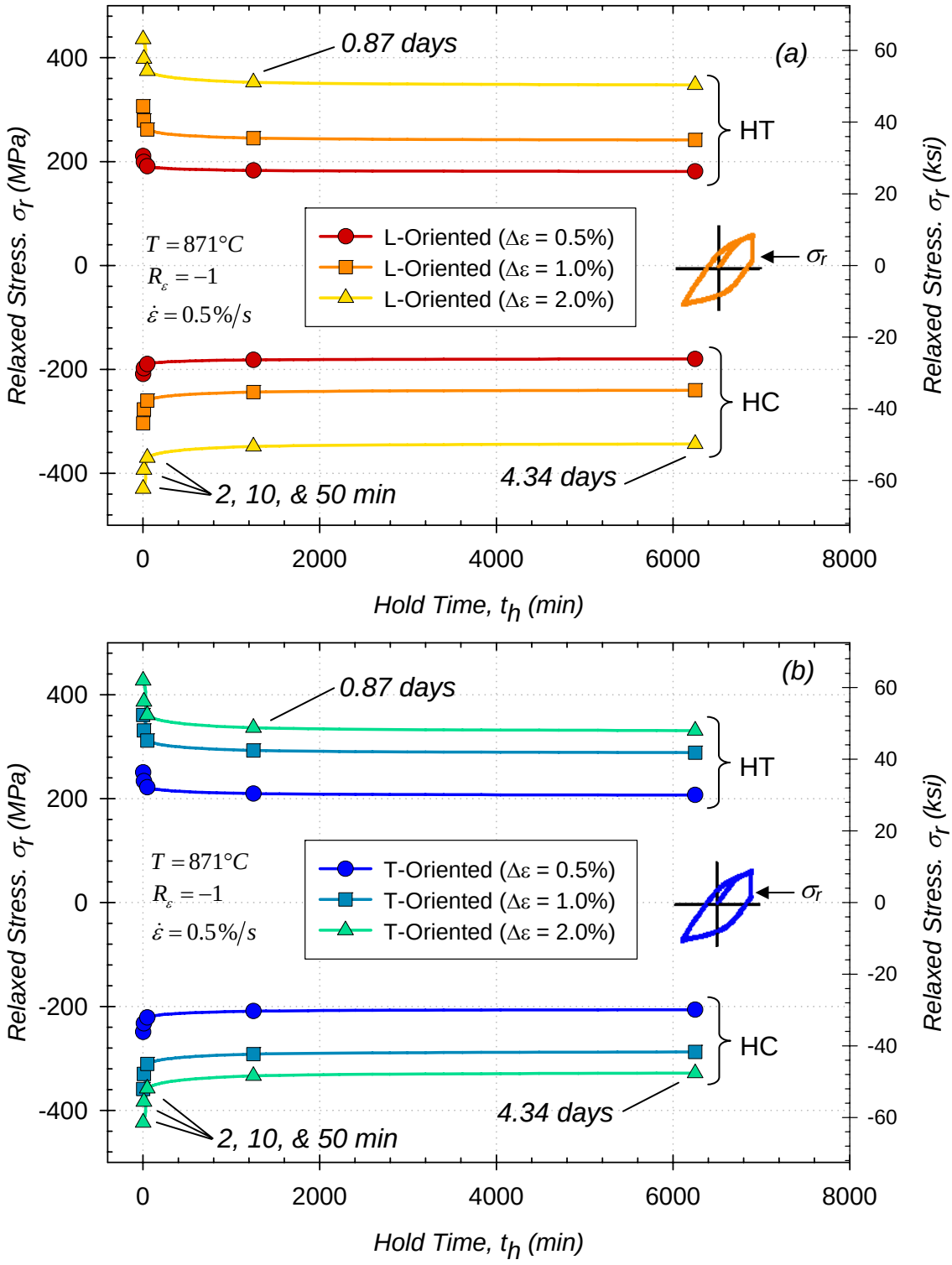


***Figure 5.18:*** *Simulated experimental responses of relaxed stress at the end of the dwell period of DS GTD-111 under creep-fatigue cycling at various hold times: (a) L-oriented and (b) T-oriented. For each case T=871℃ (1600℉),* $\dot{\varepsilon} = 0.5\%/s$, *and* $R_\varepsilon = -1$.

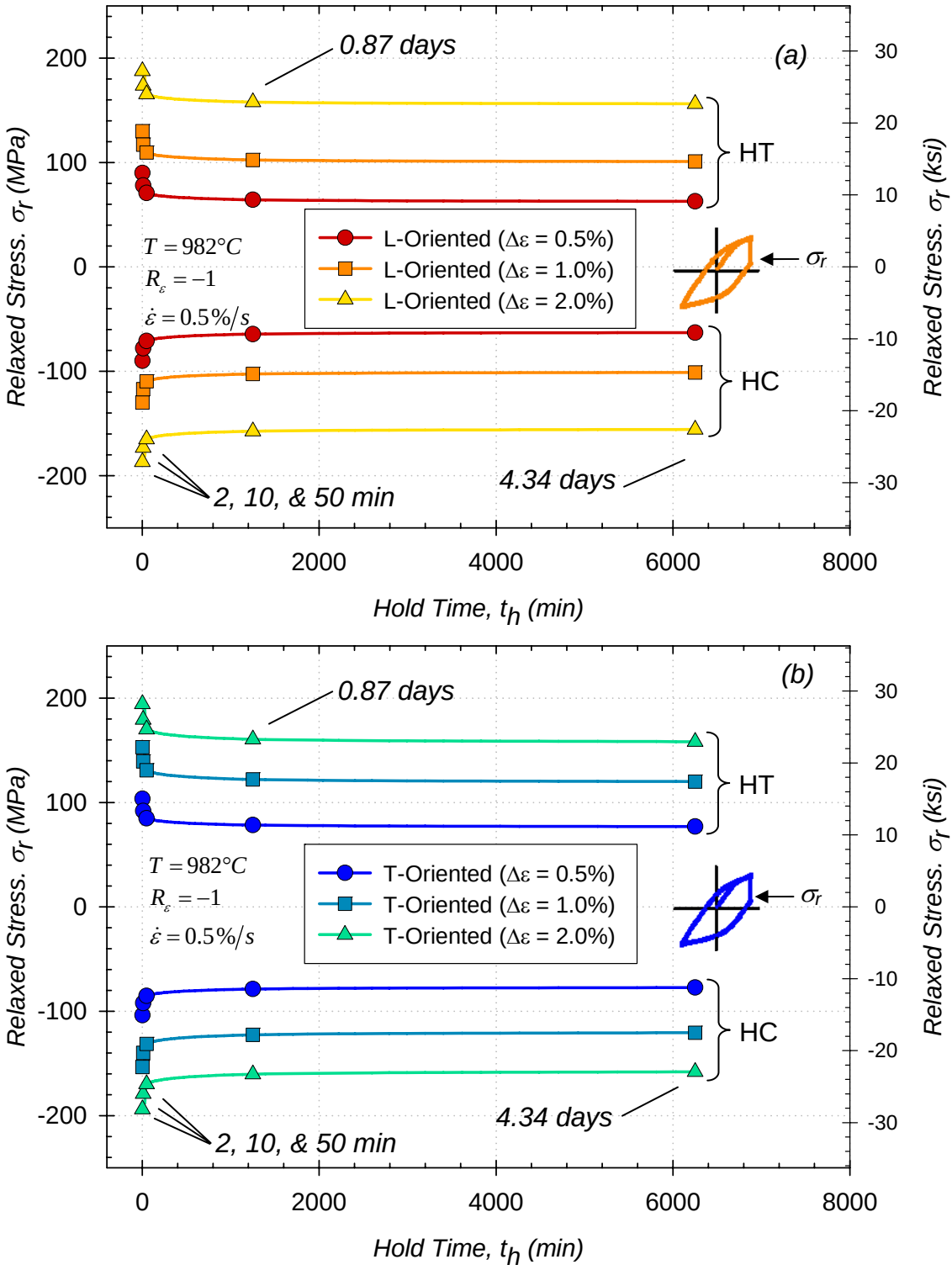


***Figure 5.19:*** *Simulated experimental responses of relaxed stress at the end of the dwell period of DS GTD-111 under creep-fatigue cycling at various hold times: (a) L-oriented and (b) T-oriented. For each case T=982℃ (1800℉),* $\dot{\varepsilon} = 0.5\%/s$, *and* $R_\varepsilon = -1$.

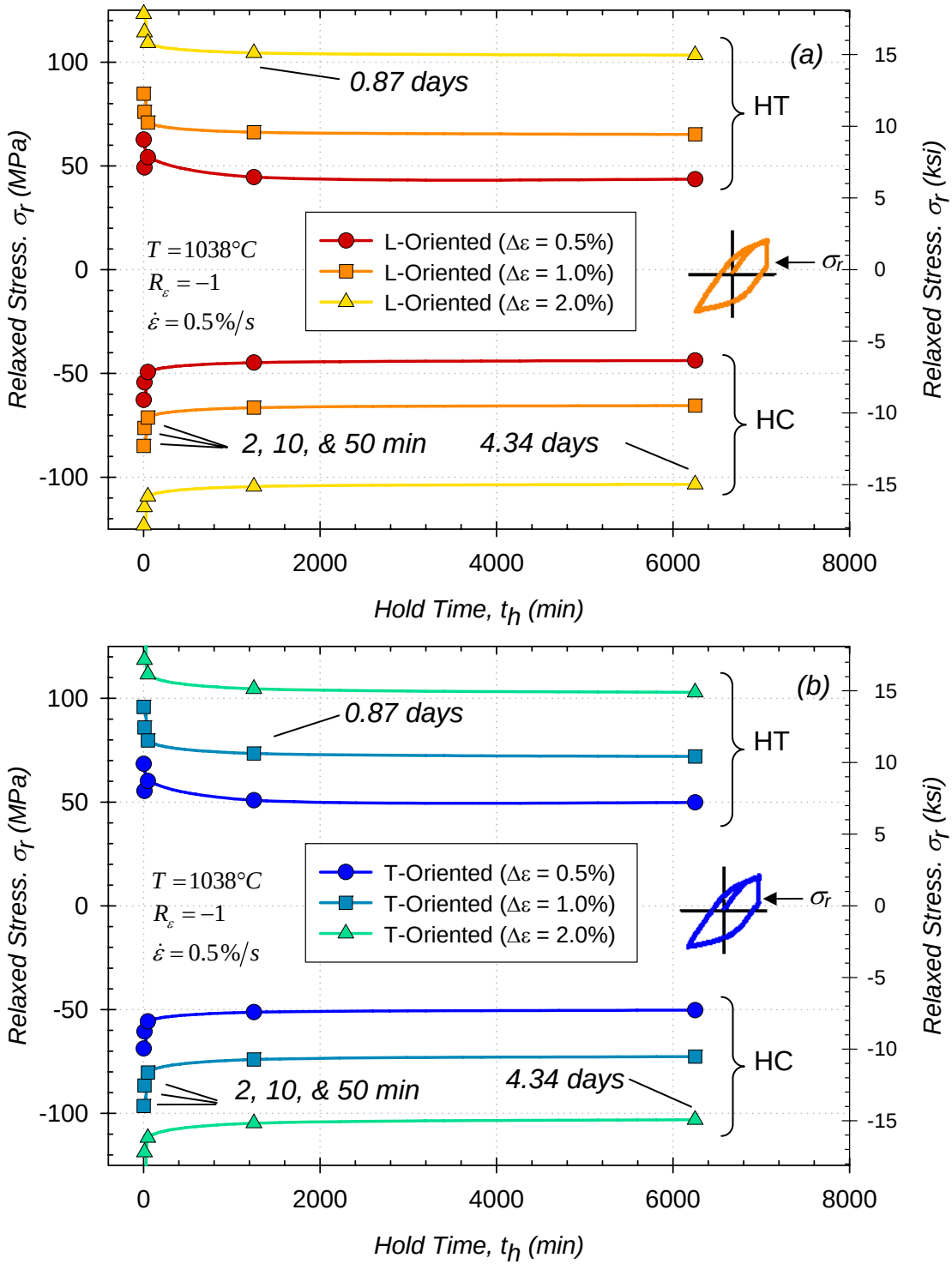


***Figure 5.20:*** *Simulated experimental responses of relaxed stress at the end of the dwell period of DS GTD-111 under creep-fatigue cycling at various hold times: (a) L-oriented and (b) T-oriented. For each case T=1038℃ (1900℉),* $\dot{\varepsilon} = 0.5\%/s$, *and* $R_\varepsilon = -1$.

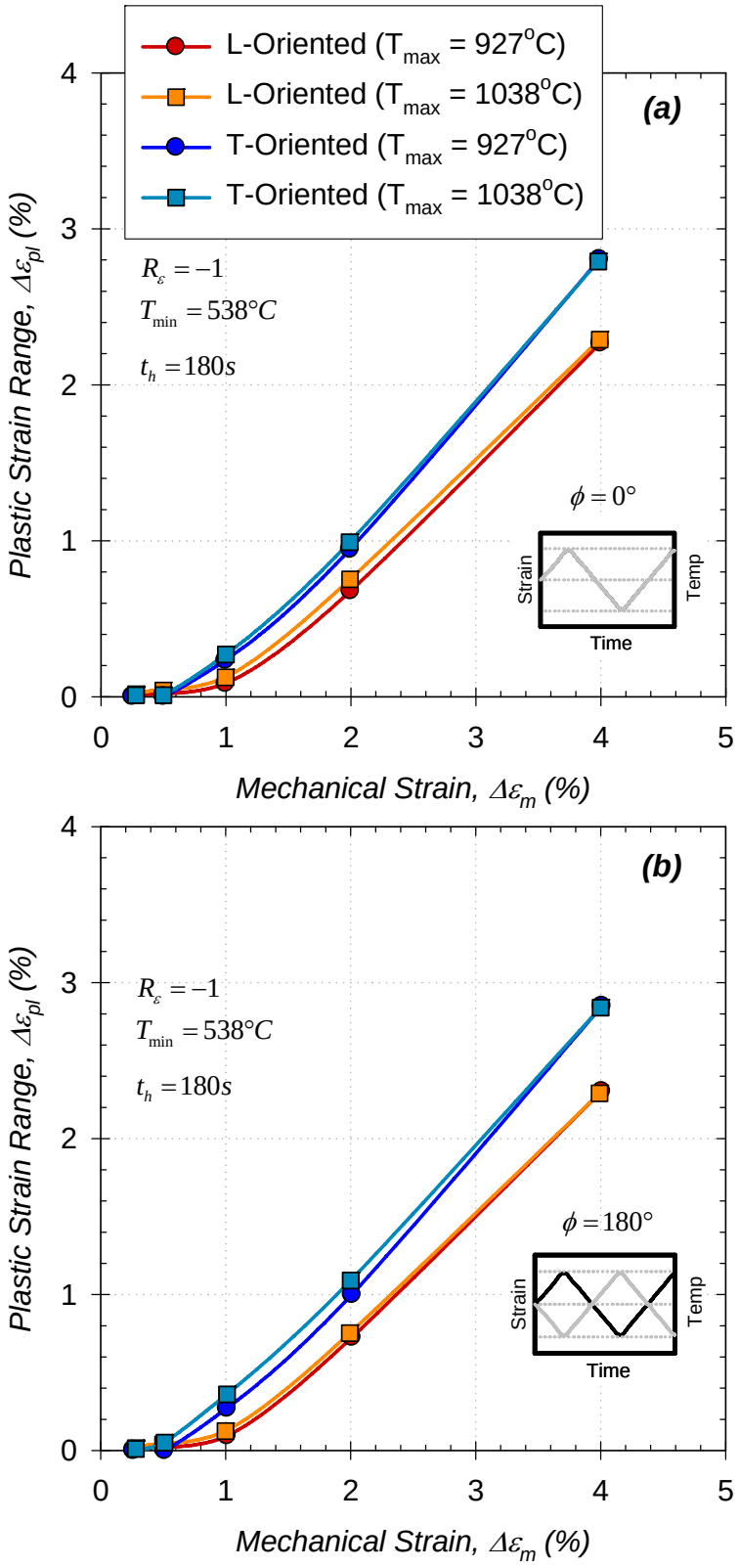


***Figure 5.21:*** *Simulated experimental responses of DS GTD-111 under thermomechanical (e.g. non-isothermal) fatigue (TMF) with (a) in-phase and (b) out-of-phase cycling.*

*Isothermal Fatigue at Intermediate Various Orientations*

Results from simulations of isothermal LCF at various orientations are shown in Fig. 5.22. At the modeled conditions (e.g. $T$=871°C, $\Delta\varepsilon_m$ = 2.0%, $\dot{\varepsilon} = 0.5\%/s$, and $R_{\varepsilon_m} = -1$) and range of orientations considered, both the yield and maximum stresses have peak values at $\omega = \pi/4$. The shape of the curves are nearly symmetric with respect to $\omega$. The deformation response of the material is captured in Fig. 5.22b. The peak values of both the predicted elastic modulus and plastic strain range occur at $\omega = \pi/4$. It should be noted that the values of each of the curves at the L- and T-oriented endpoints shown in Fig. 5.22 are identical to those determined via experiments conducted under analogous conditions (Table 4.3).

In the various types of experimental cases analyzed here, data could be represented with power law regression fits. In this manner, data between existing data points can be easily interpolated without additional finite element modeling. Even though both the discussion here and included illustrations are limited to $\sigma_r$ versus $\Delta\varepsilon$ for simulations having dwell periods and $\Delta\varepsilon_{pl}$ versus $\Delta\varepsilon$ data for all simulated experiments, relationships for $\sigma_m$-$\Delta\varepsilon$, $\sigma_{max}$-$\Delta\varepsilon$, and $\Delta\sigma$-$\Delta\varepsilon$ data can all be readily obtained from the Tables in Appendix E.

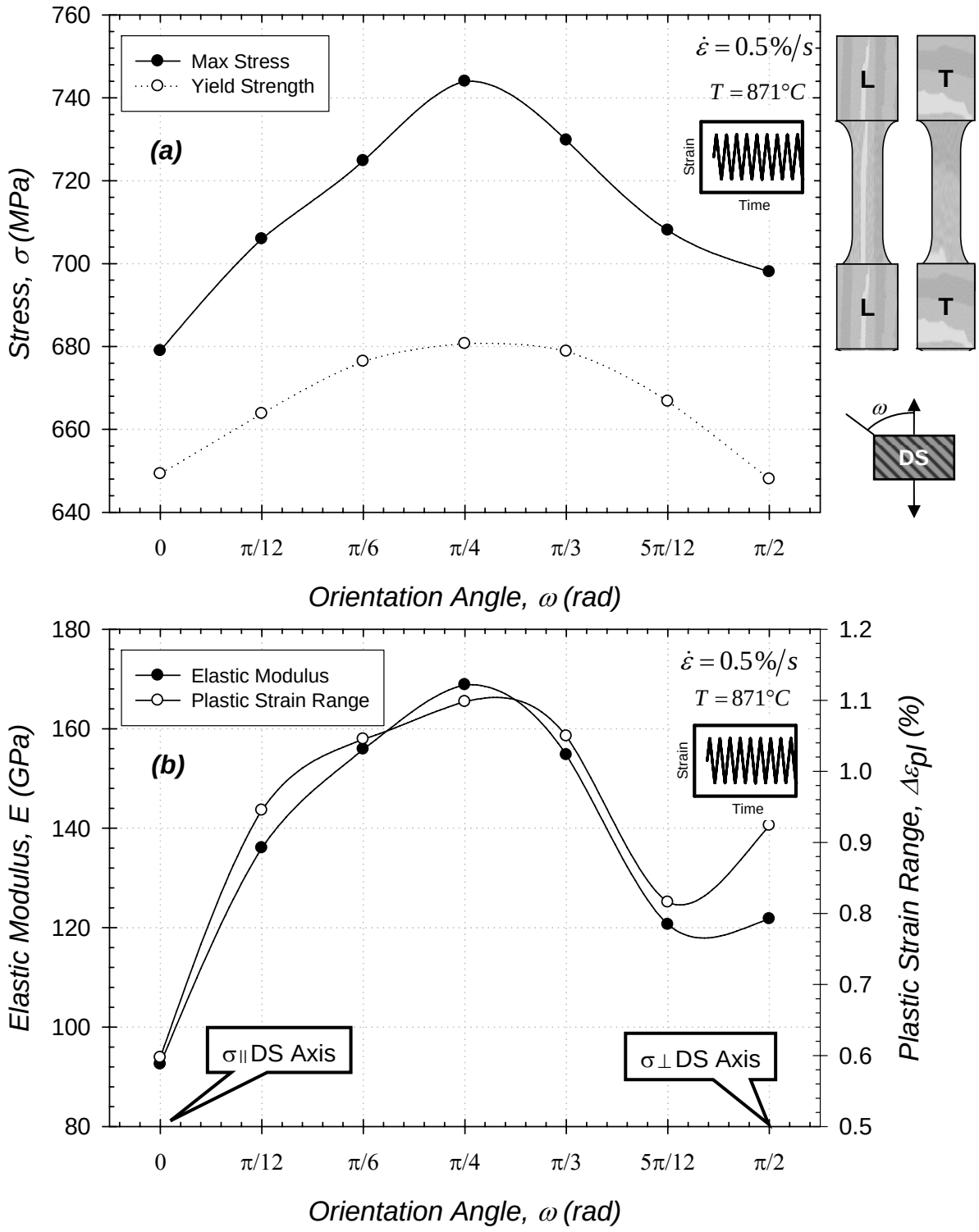


***Figure 5.22:*** *Predicted (a) stress and (b) elastic modulus and plastic strain range response of DS GTD-111 under isothermal low cycle fatigue (LCF) at various orientations. For each case* $R_{\varepsilon_m} = -1$, *and* $\Delta\varepsilon_m = 2.0\%$, $T = 871°C\left(1600°F\right)$, *and* $\dot{\varepsilon} = 0.5\%/s$.

# 6. CRACK INITIATION MODELING

## *6.1 Fatigue Damage*

Fatigue damage is represented by classical fatigue mechanisms that nominally operate at ambient or low temperatures. A primary example is cyclic dislocation slip that leads to crack initiation within the bulk of the material. Most of the experiments in this study were conducted under conditions for which damage caused by creep and oxidation may affect life (e.g. high temperatures, tensile or compressive dwell periods, non-isothermal conditions, etc.). The fatigue-life term, however, is assumed to be represented by the inelastic strain range, $\Delta\varepsilon_{in}$, and estimated from a strain-life relation, e.g.

$$N_i^{fat} = C_{in} f_{in}(\omega)\left(\Delta\varepsilon_{in}\right)^{d_{in}}, \tag{6.1}$$

where $C_{in}$, and $d_{in}$ are constants. The inelastic strain range is applied here since it accounts for both time-independent and time-dependent deformation. Orientation dependence is accounted for via the function $f_{in}$ in terms of the grain orientation, $\omega$, measured in radians. This function is normalized to unity for L-oriented cases (i.e., $f_{in}(\omega = 0) = 1$). The remaining material constants are listed in Table 6.1.

The constants in Eq. (6.1) are determined from mechanical strain range versus crack initiation life data of isothermal fatigue cycling at low temperatures (i.e., $T \le 871°C$) and higher stain rates (i.e., $\dot{\varepsilon} \ge 0.5\%/\text{s}$) at which little or no oxidation and

creep would occur. Using this subset of data for curve-fitting ensures that the module only accounts for fatigue damage. This group of test configurations is based on microscopically observed crack initiation in L (Figs. 4.4, 4.6, 4.9 and 4.20a) and T orientations (Figs. 4.5 and 4.7) that demonstrate fatigue-dominant damage (i.e., enhanced slip at defects). The boundaries of the test configurations leading to fatigue-dominant damage can be expressed in a damage mechanism map graphed in terms of temperature versus mechanical strain range. Each form of damage was introduced earlier (c.f. Section 2.7). Based on Fig. 6.1, fatigue damage dominates at high temperatures and high mechanical strain ranges. Oxidation spiking is only a factor at low mechanical strain ranges (below 1.0%) and high temperature (above 871°C). The transition between the two regions is estimated with a dotted line for each material. Equation (6.1) also captures the effect of time-dependent deformation when other mechanisms are not dominant.

***Table 6.1:*** *Constants used in fatigue strain-life term*

| $C_{in}$ | $f_{in}(\omega=0)$ | $f_{in}(\omega=\pi/2)$ | $d_{in}$ |
|---|---|---|---|
| 0.033 | 1.000 | 0.470 | -1.555 |

Simulated data were also useful in determining the bounds for fatigue dominance. Figure 5.14 demonstrates that time-dependent deformation is precluded from the modeled plastic strain range at low to intermediate temperatures (i.e., $T \leq 871°C$) and higher strain rates (i.e., $\dot{\varepsilon} \geq 0.5\%/\text{s}$).

In Fig. 6.2, strain-life curves for both L- and T-oriented DS GTD-111 are shown along with experimental data. The illustrated strain-life curves were fit to fatigue data at 649°C. To make life predictions at other temperature conditions, the inelastic cyclic

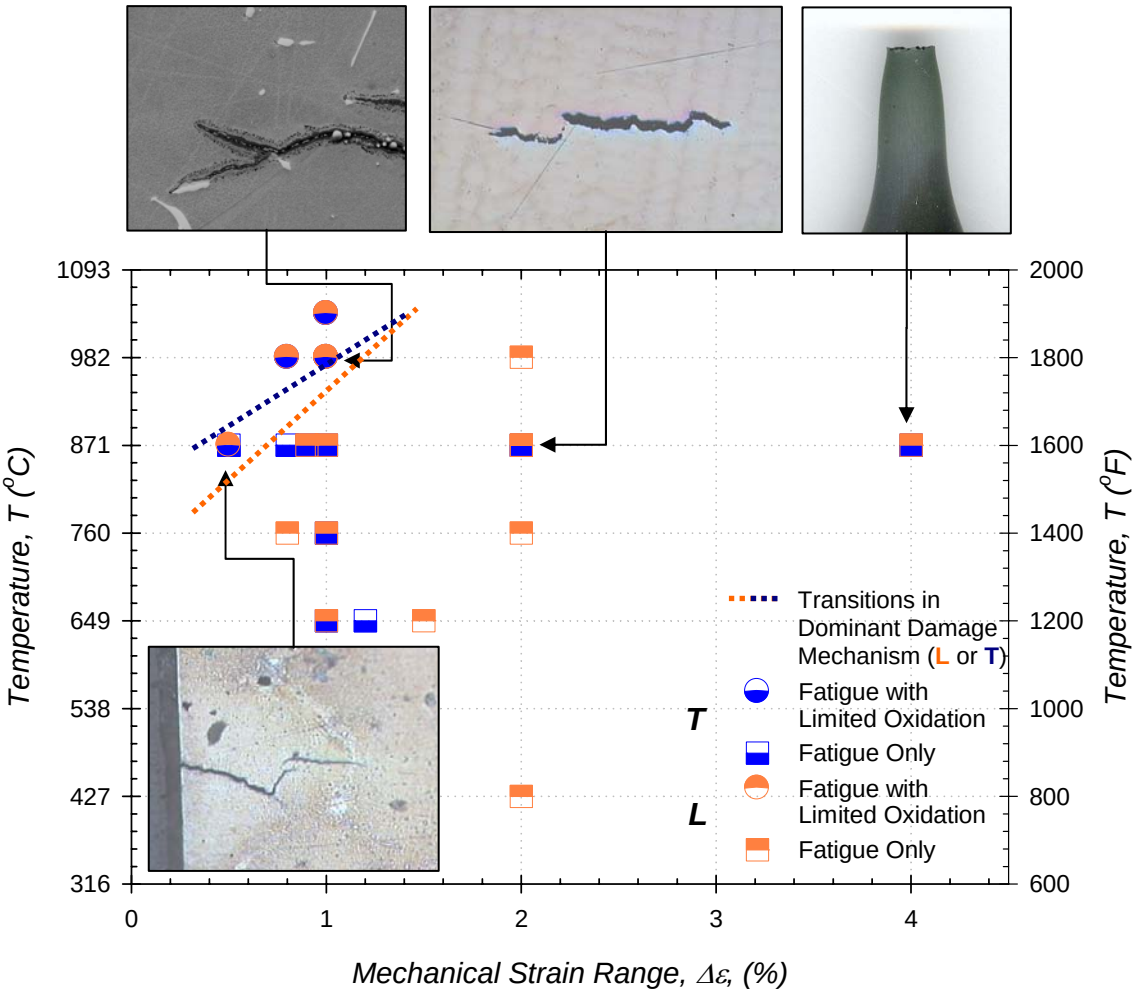


***Figure 6.1:*** *Damage mechanism map of crack initiation of isothermal, continuous cycled L- and T-oriented DS GTD-111. For each case,* $\dot{\varepsilon} \geq 0.5\%/\mathrm{s}$.

inelastic strain range at the corresponding temperature must be used. Crack initiation life correlations based solely on Eq. (6.1) and the constitutive response are compared with experimental results in Fig. 6.3. In situations where the crack initiation life is above $10^3$ cycles, $\Delta\varepsilon_{in}$ is typically small compared to $\Delta\varepsilon_m$. This indicates that other damage mechanisms are operative at longer crack initiation lives and that another parameter is needed to characterize $N_i$ to obtain a more accurate correlation.

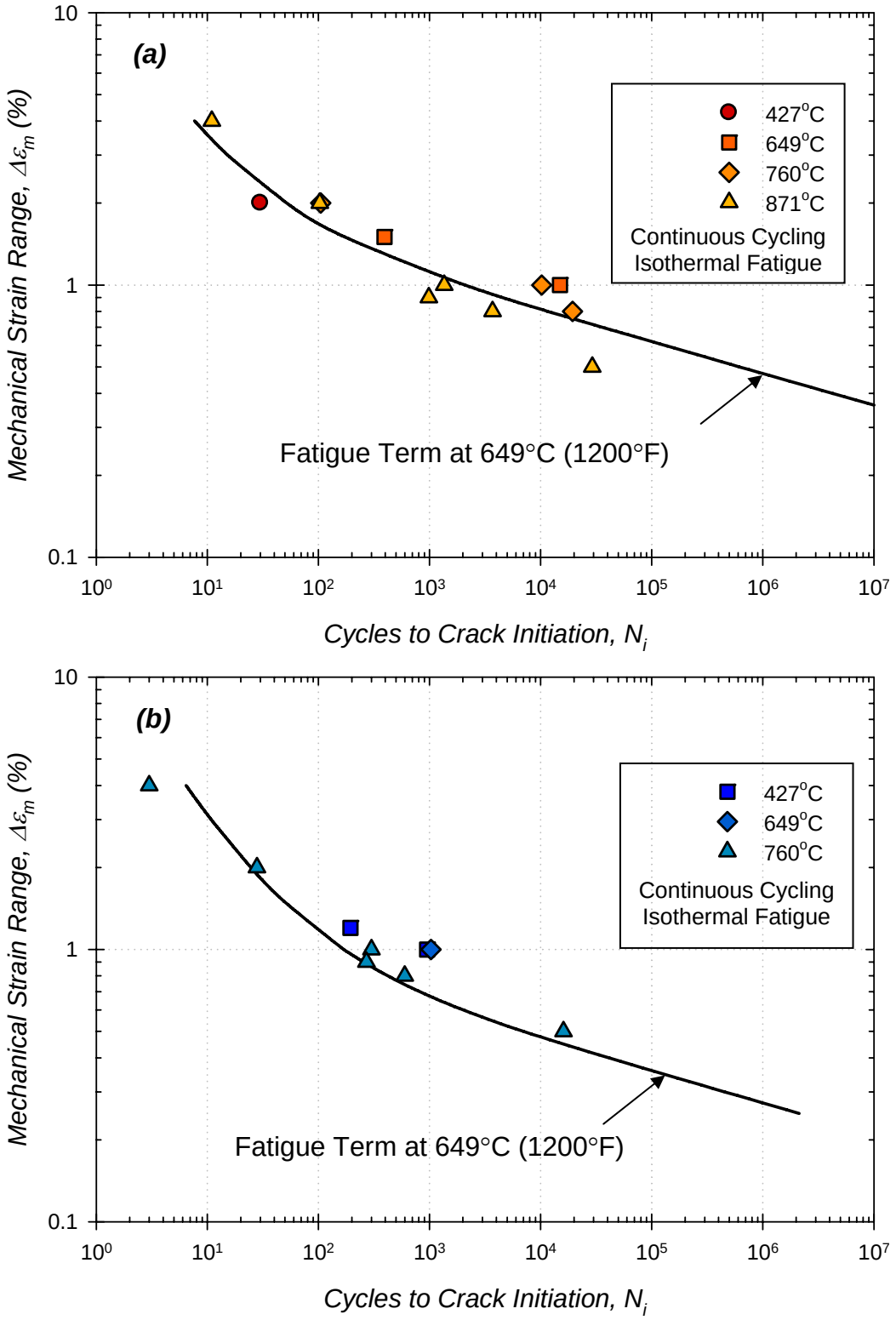


***Figure 6.2:*** *Low temperature strain-life curves for (a) L- and (b) T-oriented DS GTD-111 with test results which have lives governed by fatigue damage only, i.e., isothermal fatigue cycling in air at low temperatures (i.e.,* $T \le 871°C$*), high stain rates (i.e.,* $\dot{\varepsilon} \ge 0.5\%/\text{s}$*).*

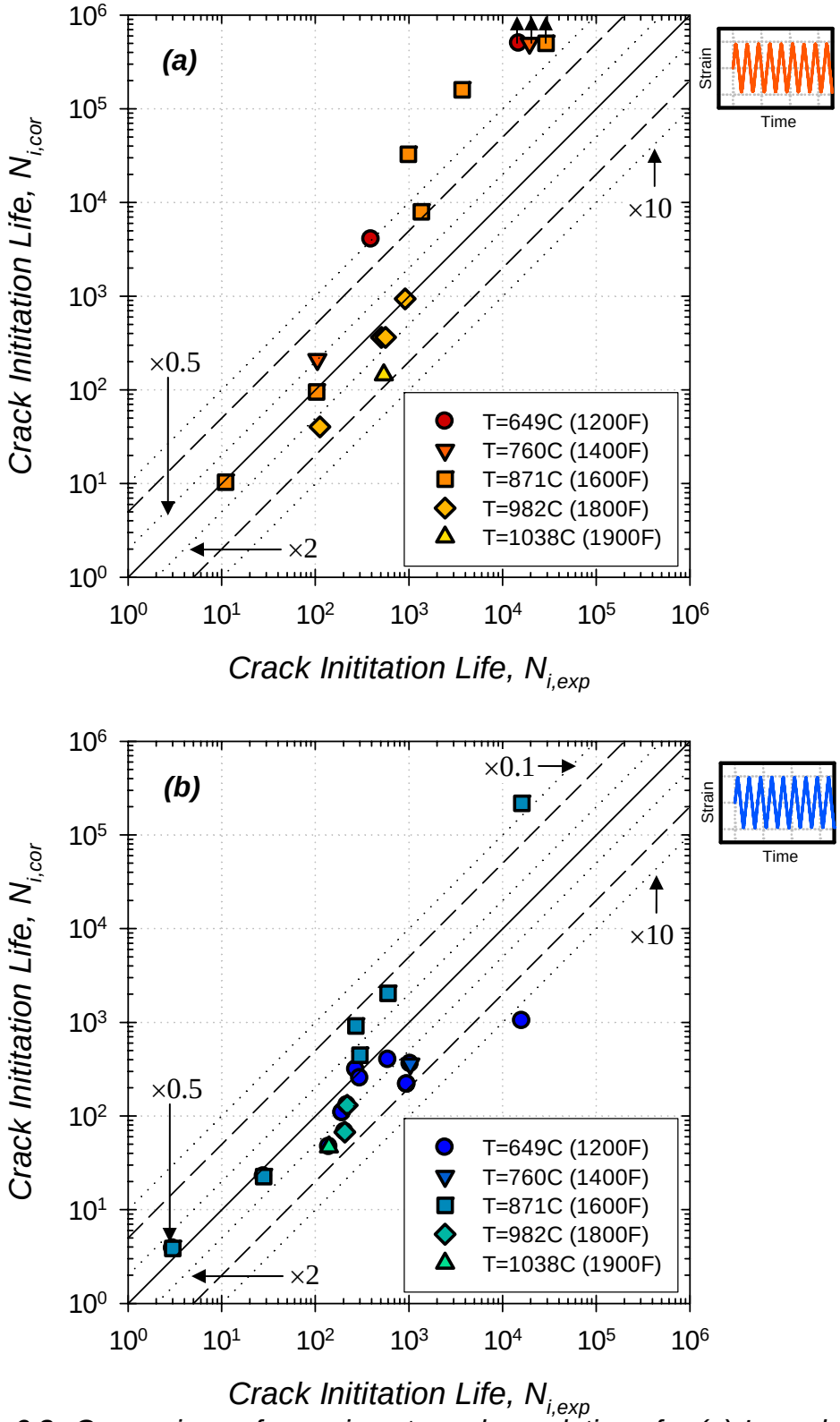


***Figure 6.3:*** *Comparison of experiments and correlations for (a) L- and (b) T-oriented DS GTD-111 under isothermal LCF conditions via fatigue damage module and constitutive response. For each case $R_\varepsilon$=-1, $\dot{\varepsilon}_{th} = 0$, and $\dot{\varepsilon} = 0.5\%/s$.*

The $\Delta\varepsilon_{in}$ responses for the two orientations at various combinations of $\Delta\varepsilon_m$ versus $T$ from Fig. 5.12 are shown as a contour plot in Fig. 6.4 a,b. Since the contours have been normalized by $\Delta\varepsilon_m$, the contour corresponding to 0.5 represents the crossover at which $\Delta\varepsilon_{in} = \Delta\varepsilon_{el}$. For both L- and T-oriented cases subjected to a constant mechanical strain range, the inelastic fraction of the mechanical strain range increases with increasing temperature. By way of the ratio between $\Delta\varepsilon_{in}\left(\omega = 0\right)$ and $\Delta\varepsilon_{in}\left(\omega = \frac{\pi}{2}\right)$, Fig. 6.4c compares the deformation response of the L- and T-oriented material for various combinations of $\Delta\varepsilon_m$ versus $T$. The materials are similar in terms of inelastic strain response when the temperature is above 871°C and when the mechanical strain range is above 2.0%. Using Eq. (6.1) and modeled $\Delta\varepsilon_{in}$ data, the critical damage parameter associated with the contribution of fatigue mechanisms is defined as the reciprocal of the crack initiation life, i.e.,

$$D^{fat} = \frac{1}{N_i^{fat}}. \tag{6.2}$$

The key to the fatigue damage modeling is a highly accurate time-dependent deformation model that accounts for orientation effects. With an accurate prediction of the deformation response, most crack initiation lives can be predicted.

All experiments in this study where conducted on specimens with grains in either the L or T orientation. Data for off-axis-oriented DS GTD-111 material is proprietary, and there is no way to explicitly determine the variation of $f_{in}$ without experimental data. In a previous study of crack initiation behavior of DS Ni-base superalloys Mar-M247LC

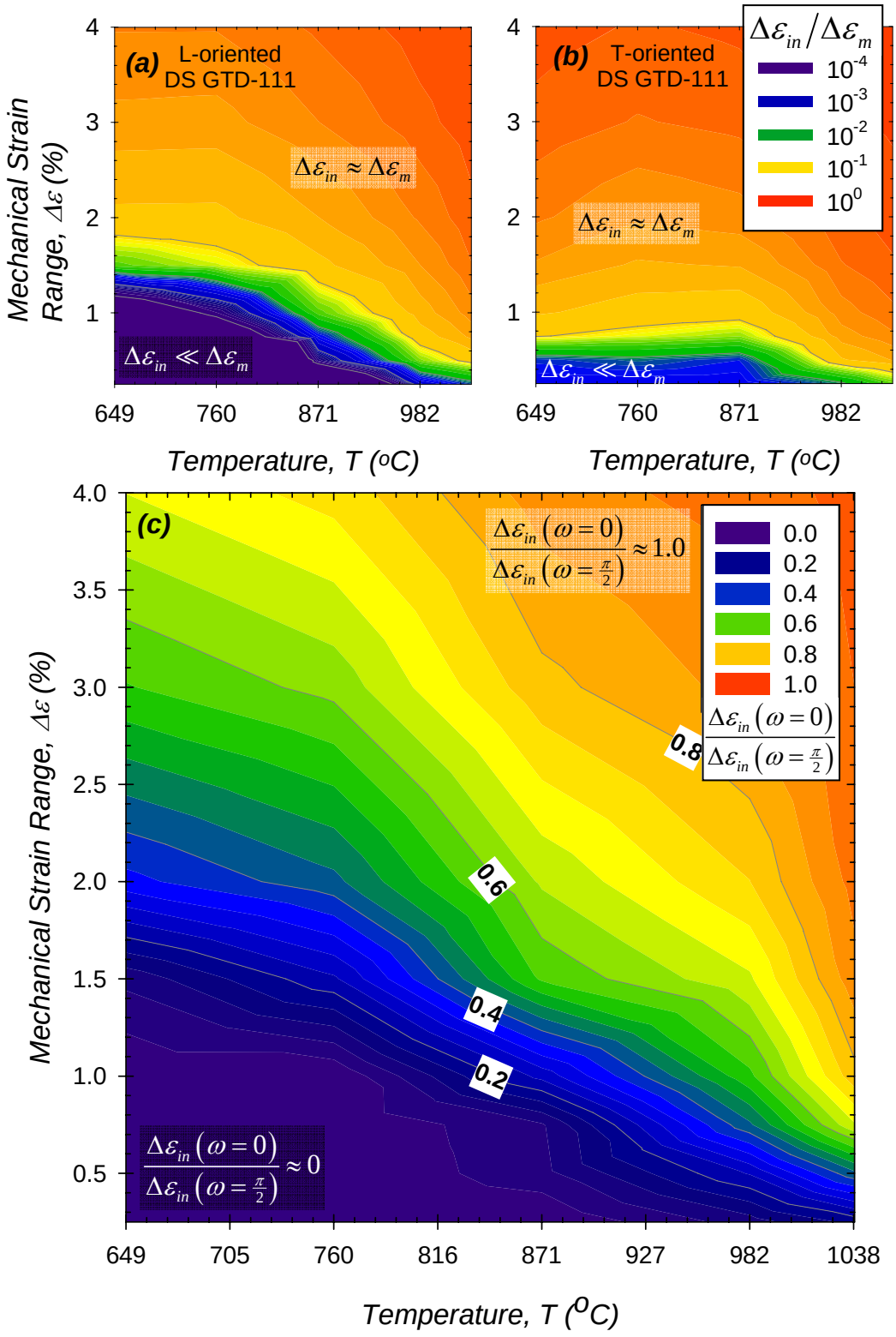


***Figure 6.4:*** *Inelastic fraction of the total cyclic strain range (e.g.* $\Delta\varepsilon_{in}/\Delta\varepsilon_m$*) for (a) L- and (b) T-oriented DS GTD-111 under continuous cycling. (c) Ratio of inelastic strain range of L- to T-oriented DS GTD-111. For each case* $\dot{\varepsilon} = 0.5\%/\text{s}$ *and* $\dot{\varepsilon}_{th} = 0$.

(Hasebe et al., 1992) found that fatigue crack initiation lives of 45°-oriented specimens were less than both L- and T-oriented data (Fig. 2.15b). This particular set of off-axis LCF life data was selected amongst other available data (i.e. Huron, 1986), since this data more closely resembles the benchmark data at 871°C and since it was determined for a similar load drop of 25%. Orientation dependence can be interpolated with a $5^{th}$ order polynomial to interpolate this existing crack initiation life data based numerical simulations of off-axis cyclic plastic strain range behavior of DS GTD-111 (Fig. 5.22b), i.e.,

$$f_{in}(\omega) = 1.28\omega^5 - 6.67\omega^4 + 11.71\omega^3 - 7.12\omega^2 + 1.0\,. \tag{6.3}$$

Here $\omega$ is the grain orientation measured in radians. The coefficients for this relation were curve-fit to satisfy the boundary condition at the L orientation, $f_{in}(\omega = 0) \equiv 1.0$. The condition at the T-orientation was determined by arithmetic elimination. Simplifying the quotient of Eq. (6.1) for the T-oriented case normalized by that for the L-oriented case gives

$$f_{in}\left(\omega = \tfrac{\pi}{2}\right) = \frac{N_i^{fat}\left(\omega = \frac{\pi}{2}\right)}{N_i^{fat}(\omega = 0)}\left[\frac{\Delta\varepsilon_{in}(\omega = 0)}{\Delta\varepsilon_{in}\left(\omega = \frac{\pi}{2}\right)}\right]^{d_{in}} \tag{6.4}$$

For the benchmark temperature of 871°C under continuous cycling at 2.0%, $f_{in}(\omega = \pi/2) = 0.47$, and fatigue damage facilitated crack initiation in both orientations

of DS GTD-111. The remaining conditions that were imposed were that the slopes at both the L, T, and 45° orientations be flat, i.e., $f'_{in}(\omega = 0) = f'_{in}(\omega = \frac{\pi}{4}) = f'_{in}(\omega = \frac{\pi}{2}) = 0$. This equation can only be verified with experimental crack initiation life results obtained for off-axis specimens of DS GTD-111 fatigued under isothermal, continuous cycling at low temperatures (i.e., $T \leq 871°C$) and high stain rates (i.e., $\dot{\varepsilon} \geq 0.5\%/\text{s}$). The variation of $f_{in}$ with respect to material orientation in show in Fig. 6.5a. Predictions of off-axis fatigue-dominant crack initiation using Eqs. (6.1) and (6.3) are shown in Fig. 6.5b. The model predictions that crack initiation life is lowest for the case where $\omega = \pi / 4$ (45°) which is similar to the crack initiation life results obtained for the off-axis specimen of the DS Ni-base superalloy Mar-M247LC (Hasebe et al., 1998), as shown in Fig. 2.15b.

Optical micrographs shown in Figs. 4.6c, 4.7a, and 4.9a demonstrate that crack initiation and early propagation in DS GTD-111 follows carbides that are most plentiful within interdendritic channels. As such, the secondary dendritic arm spacing (SDAS) (e.g. the distance between the centers of two adjacent secondary dendrite arms) is a microstructural measure that might be relevant to crack initiation life prediction. For example, the lead coefficients for the elastic and plastic components in Eq. (6.1) could be re-written as $C_{in} = g(SDAS)$. In this study, however, the variation of the SDAS between the three batches was not substantial enough to draw accurate observations of the influence of SDAS on crack initiation life of DS GTD-111.

In cases where other forms of damage accumulate, the formulation presented in Eqs. (6.1) - (6.3) fails to accurately predict life. Other damage modules will be presented in later sections to overcome this limitation.

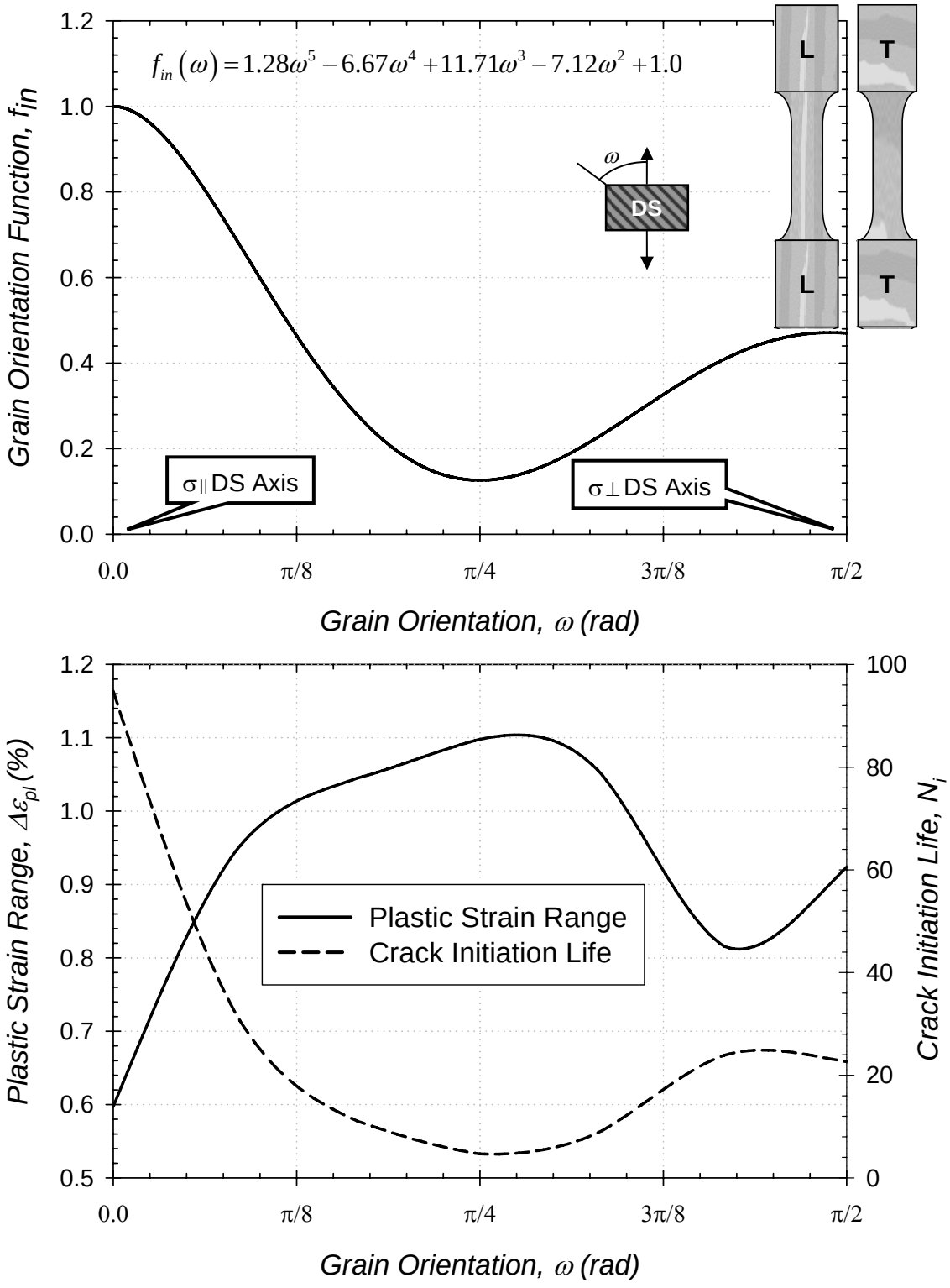


***Figure 6.5:*** *(a) Angular variation of $f_{in}$. (b) Plastic strain and crack initiation life estimates for off-axis cases of DS GTD-111 under continuous cycling at T=871°C, $\Delta\varepsilon_m = 2.0\%$, and $\dot{\varepsilon} = 0.5\%/s$*

### *6.2 Creep-Fatigue Damage*

Introducing periodic dwell periods during fatigue cycling establishes the opportunity for increased fatigue damage to occur beyond that manifested by continuous cycling conditions. The increased inelastic strain occurring under creep-fatigue conditions is an indicator of the presence of primary creep deformation associated with stress relaxation during dwell periods in either tension or compression. The stress reduction rate is very high at the beginning of the dwell period, and as time elapses under constant strain, the rate of stress relaxation reduces. During this period, the material dissipates energy via viscoplastic flow. Simulated hysteresis curves of DS GTD-111 with various strain hold periods are shown in Fig. 6.6. All of the curves with different dwell periods but otherwise identical conditions follow the same pattern; there is a relatively high stress relaxation rate at the beginning of the hold, then the relaxation rate continuously decreases. Regardless of the length of the strain hold period or its type, $t_{hc}$ or $t_{ht}$, the stress nearly saturates to the relaxed stress, termed $\sigma_r$, during the first few seconds of the dwell. Of course, $\sigma_r$ is a characteristic of creep and is strongly dependent on both strain range and temperature, which are the main fatigue parameters, as shown in Figs. 5.17-5.20. The deformation model predicts the slight increases of cyclic inelastic strain range with increasing hold time. It also shows that $\Delta\varepsilon_{in}$ saturates with increasing hold period for either HC or HT cases.

A damage mechanism map is used to associate creep-fatigue damage mechanisms with experimental conditions. For a given mechanical strain range, $\Delta\varepsilon_m = 1.0\%$, various types of damage were observed within a given temperature versus hold time graph, shown in Fig. 6.7. Each form of damage was introduced earlier (c.f. Section 2.7). When

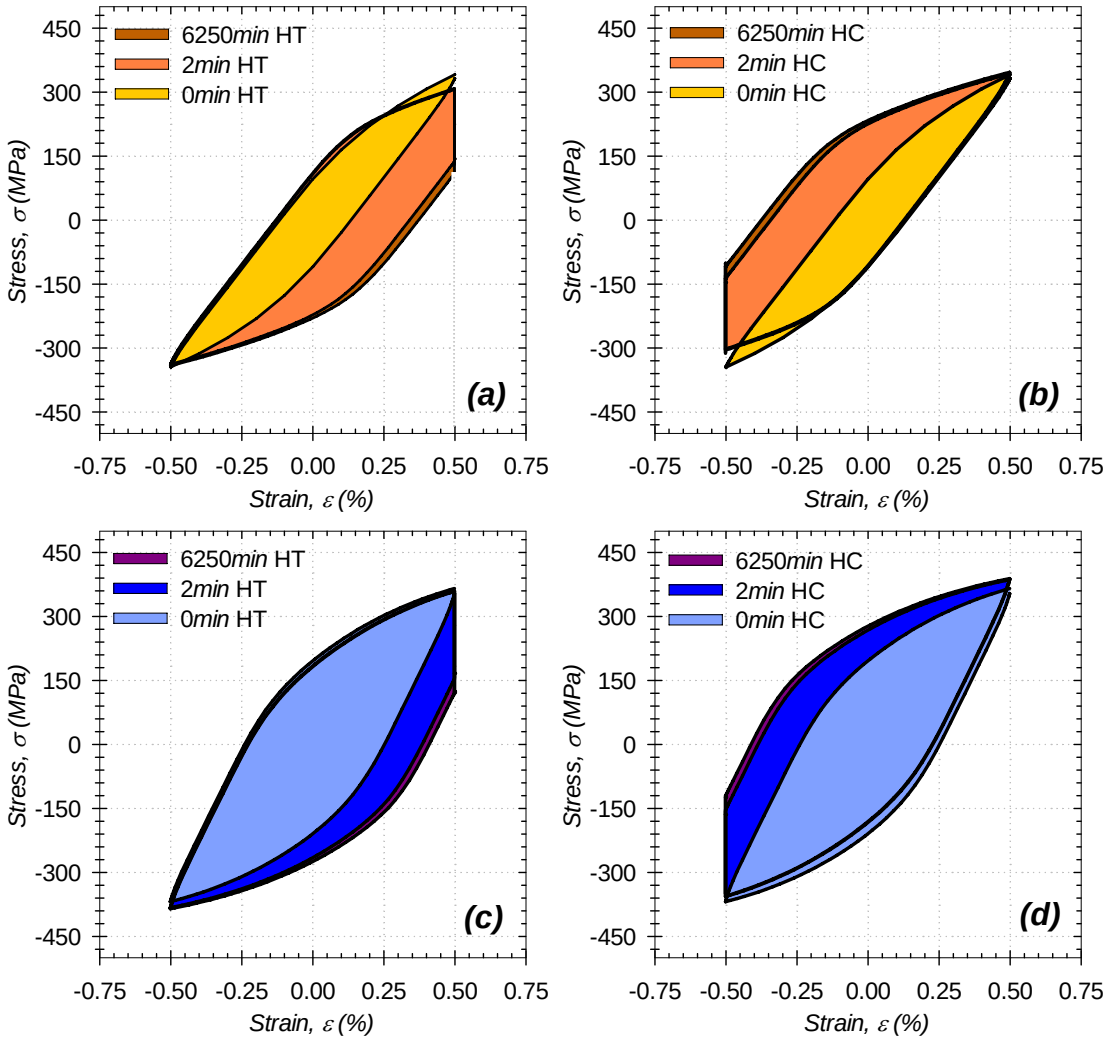


***Figure 6.6:*** *Stress-strain curves for (a, b) L- and (c, d) T-oriented DS GTD-111 under creep-fatigue cycling at 982°C, $\Delta\varepsilon_m = 1.0\%$, with long and short dwell periods in (a, c) tension and (b, d) compression.*

$\Delta\varepsilon_m = 1.0\%$, the damage mechanism leading to crack initiation depends on temperature, hold time, and hold type. For experiments with tensile hold periods at high temperature, the dominant mechanism causing crack initiation is enhanced slip at inclusions since they are plentiful along the fracture surface. Intense slip and deformation at carbide leads to crack nucleation at grain boundaries, dendrite cores, and interdendritic regions. Once

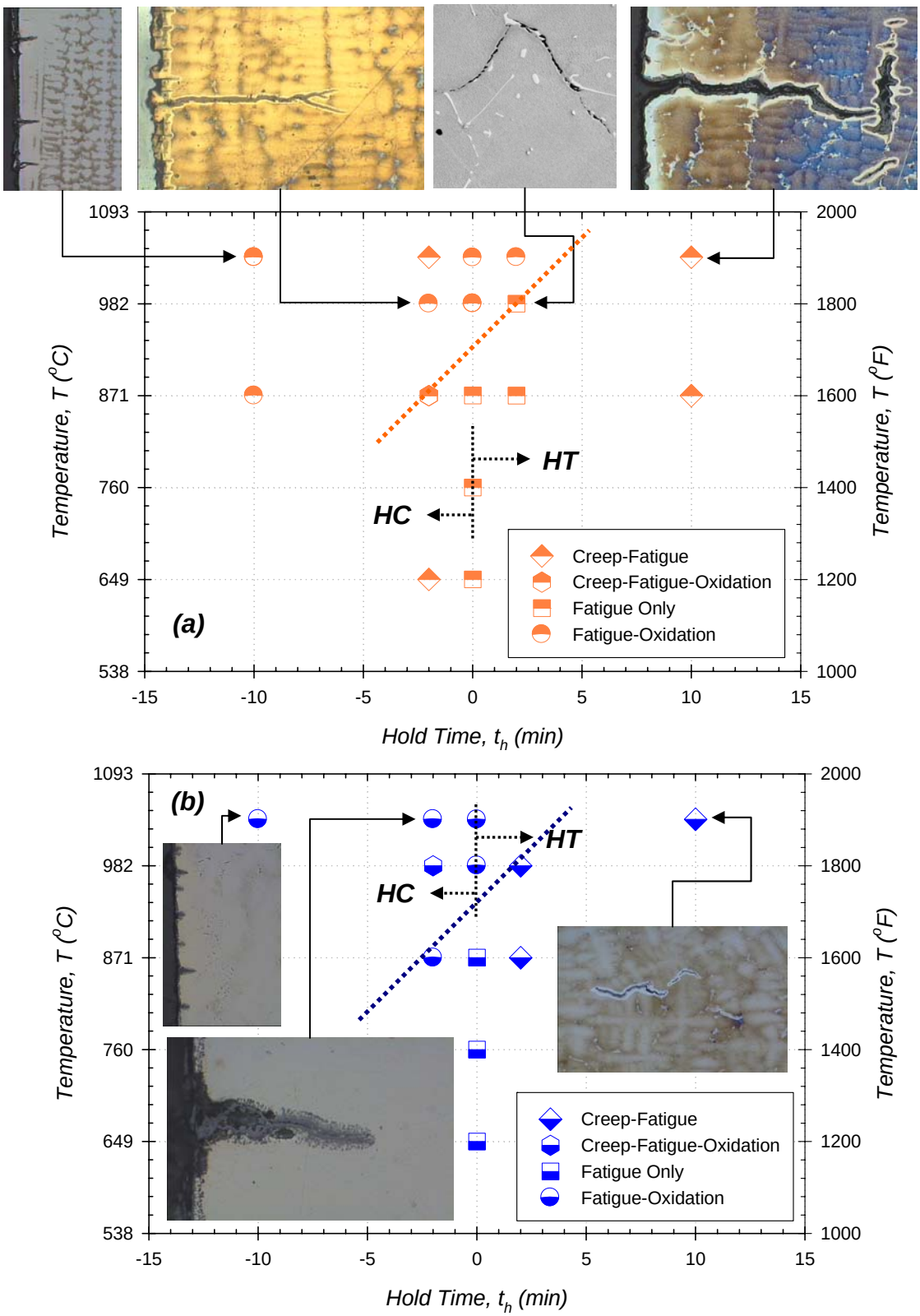


***Figure 6.7:*** *Damage mechanism map of crack initiation of isothermal, creep-fatigue cycled (a) L- and (b) T-oriented DS GTD-111. For each case,* $\Delta\varepsilon = 1.0\%$ *and* $\dot{\varepsilon} \geq 0.5\%/\text{s}$.

microcracks coalesce, they form longer cracks that connect adjacent inclusions. For 10 *min* hold times these cracks tend to follow interdendritic regions and GBs, similar to specimens subjected to pure creep conditions (Ibanez, 2003).

When the hold type changes from tensile to compressive, the damage mechanism also changes. Oxide spiking was observed in several cases; however, if the temperature is too high or too low, then an alternate damage mechanism dominates (Fig. 6.7). For example, if the temperature is too low (below 871°C), then oxidation will not as significant and the mechanism will be related to creep and fatigue; alternatively, if the test temperature is too high (for example above 1038°C), then the majority of the cyclic mechanical strain will be dominated by cyclic plastic strain, leading to fatigue dominant crack initiation.

The reduction of life when superimposing LCF conditions with short dwell periods (< 1 *hr*) can be modeled with the cyclic inelastic strain range since it is higher in these cases. Using the correlation model for fatigue damage (e.g. Eqs. (6.1) - (6.3)), crack initiation life for L- and T-oriented DS GTD-111 subjected to creep-fatigue conditions have been predicted according to Figs. 6.8 and 6.9, respectively. The variation of $N_i$ with hold type at temperatures less than or equal to 871°C is a direct consequence of the slight tension/compression asymmetry occurring at low temperatures. Hence the fatigue damage module coupled with the deformation model sufficiently captures creep-fatigue damage without further modification. The key reason why this is successful is the accurate prediction of the deformation response. This observation is also supported by Fig. 6.10 which compared the modeled and experimental crack initiation lives for various creep-fatigue conditions.

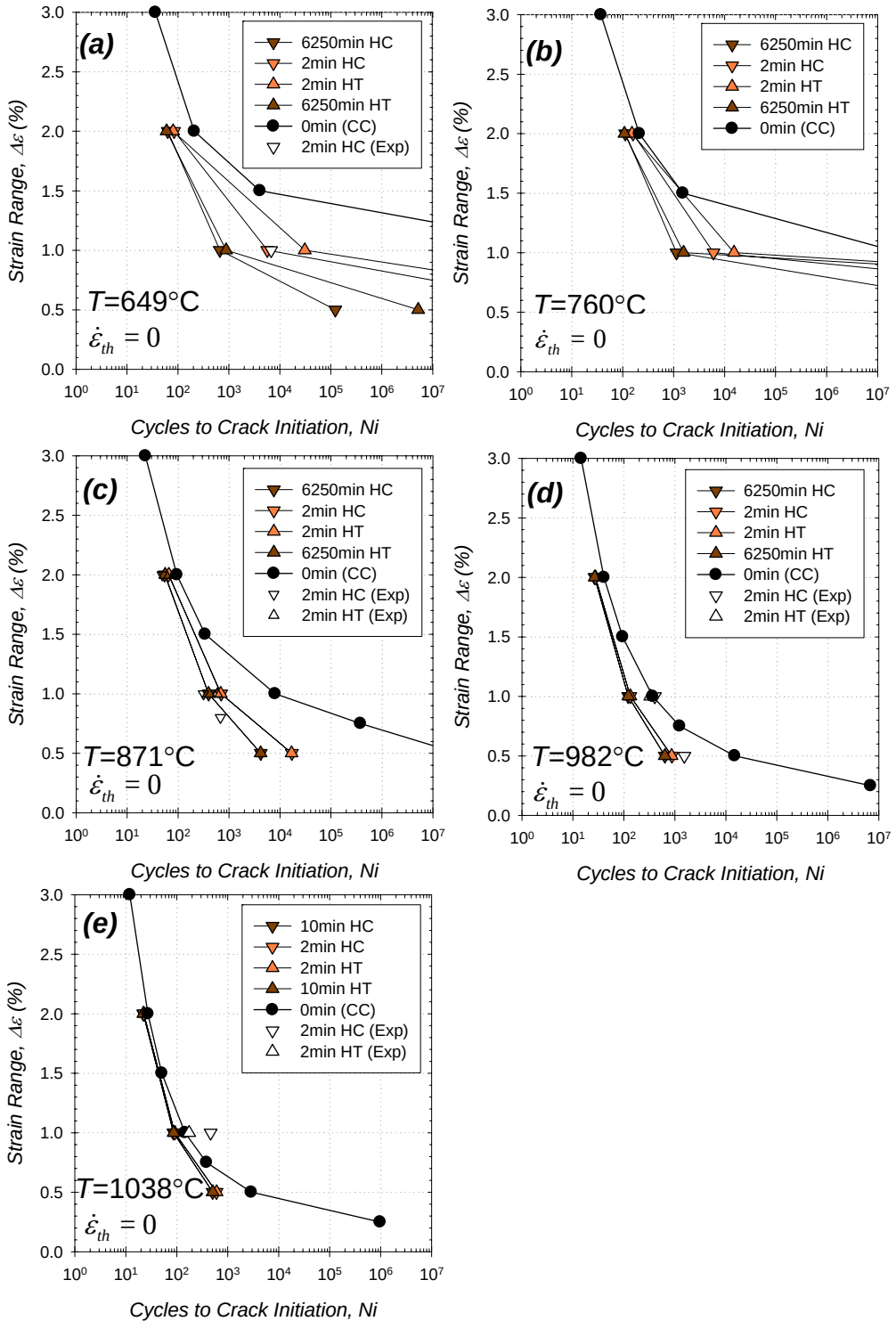


***Figure 6.8:*** *Correlations of total life based on L-oriented DS GTD-111 under LCF conditions at various creep-fatigue conditions modeled with fatigue damage module and constitutive response. For each case $R_\varepsilon$=-1.*

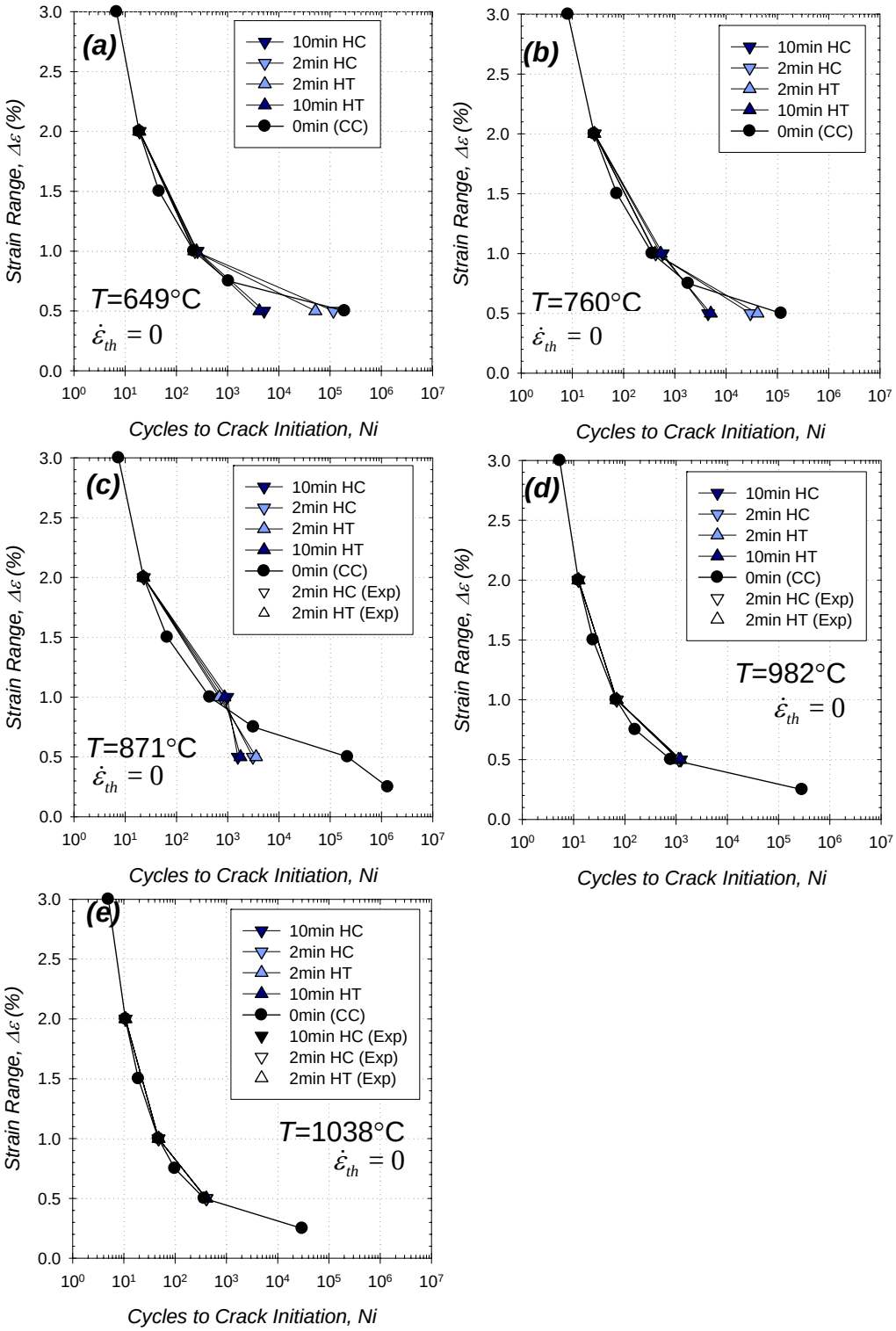


***Figure 6.9:*** *Correlations of total life based on T-oriented DS GTD-111 under LCF conditions at various creep-fatigue conditions modeled with fatigue damage module and constitutive response. For each case $R_\varepsilon$=-1.*

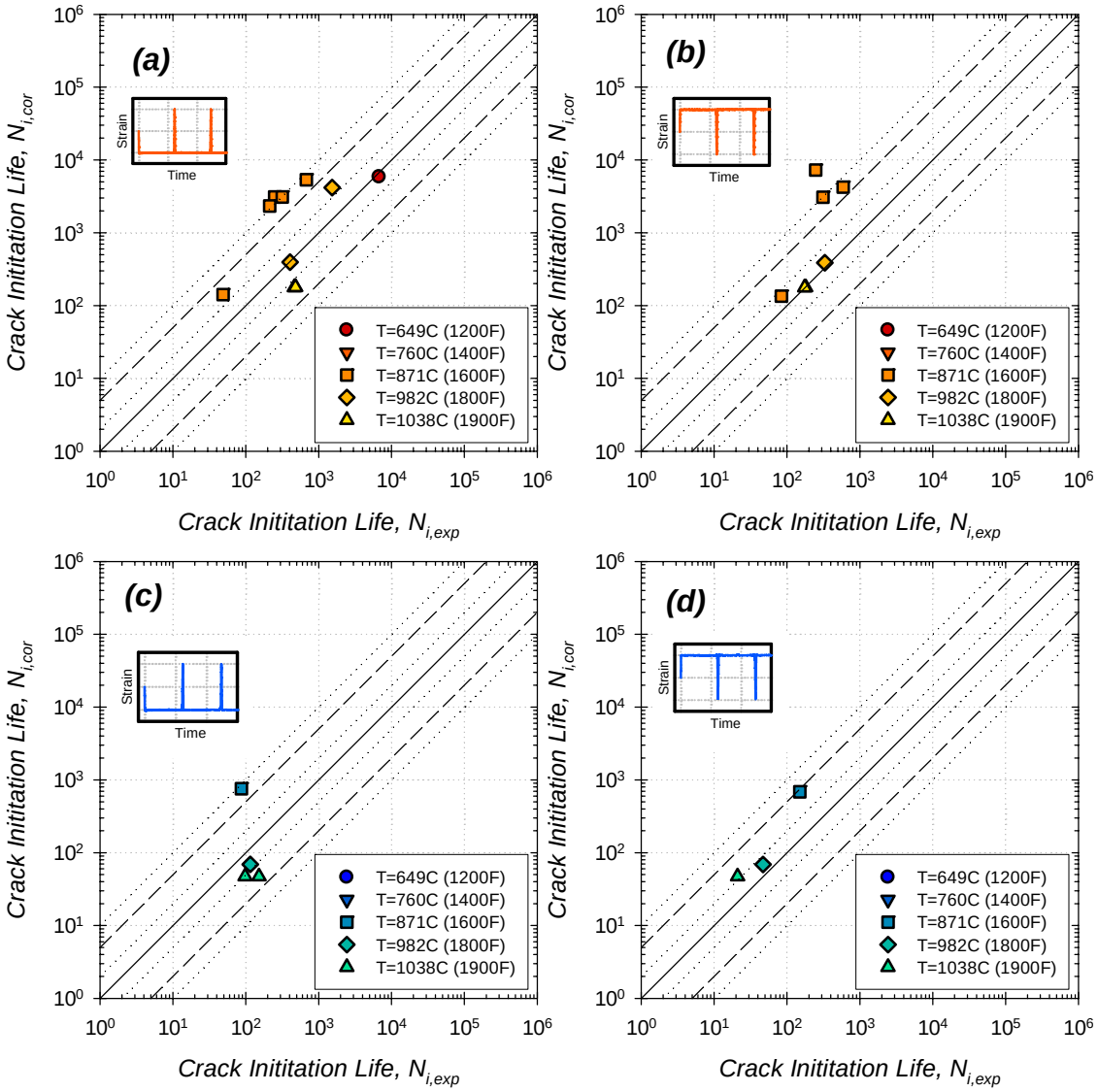


***Figure 6.10:*** *Comparison of experiments and correlations for (a, b) L- and (c,d) T-oriented DS GTD-111 under isothermal creep-fatigue conditions with (a,c) compressive and (b, d) tensile dwell periods modeled with fatigue damage module and constitutive response. For each case $R_\varepsilon$=-1, $\dot{\varepsilon}_{th} = 0$, and $\dot{\varepsilon} = 0.5\%/s$.*

### *6.3 Creep Damage*

The key ramification of increasing the fraction of hold time during cyclic creep-fatigue conditions is the transition of the damage contributions from being dominantly time dependent. Experimentally-tested samples accompanied by very long dwell times

and load-controlled conditions to rupture due to creep mechanisms (e.g. diffusional creep, grain boundary sliding, cavitation). In this manner, creep damage overshadows all other damage mechanisms. A separate damage module is needed to account for service conditions having high temperature, long tensile dwell periods, and low tensile stresses.

The expression for creep damage is based on the relationship between the Larson-Miller Parameter (LMP) and its relationship with applied stress for materials subjected to nominally creep conditions. For DS GTD-111, LMP at rupture is determined using Eq. 2.10. The term $C$ is a generic constant, and temperature is measured in $K$. This relation can be accurately curve-fit with a power law relationship with the uniaxially applied tensile stress, i.e.,

$$\frac{T\left(\log t_r + C\right)}{1000} = B\left(\sigma_{tens}\right)^{-k}. \tag{6.5}$$

Here $B$ and $k$ are regression constants. In order to customize this relationship to model the creep deformation and rupture behavior of the subject material, which exhibits anisotropic creep properties, the regression constants for each orientation, coefficients and exponents, namely $B_L$ , $k_L$, $B_T$, and $k_T$, must be determined. Regression analyses were conducted to determine the constants using existing creep deformation and rupture data for L- and T-oriented DS GTD-111 obtained by Ibanez (2003) (Appendix D).

Currently no experimental creep deformation or rupture data are available for off-axis (i.e., $\omega \in \left(0, \frac{\pi}{2}\right)$) DS GTD-111. Some off-axis creep rupture data is available for the DS superalloy Mar-M247 at 850°C (Ohno et al., 1992). The data indicate L-oriented

Mar-M247 rupture time exceed those from the T orientation. Compared to L- and T-oriented samples, $\frac{\pi}{6}$-oriented samples have the shortest creep rupture life at 850°C. For identical creep conditions and varying grain orientation, the data shown in Fig. 2.20 follow a 5$^{th}$ order polynomial, e.g.,

$$f_{cr}(\omega) = -0.14\omega^5 + 0.64\omega^4 - 0.95\omega^3 + 0.45\omega^2 + 1.0 \tag{6.6}$$

This formulation was defined to mimic the shape of the LMP results shown in Fig. 2.20. At the L-, T- and $\pi/6$-orientations, the curve is flat (e.g., $f'_{cr}(\omega = 0) = f'_{cr}(\omega = \frac{\pi}{2}) = f'_{cr}(\omega = \frac{\pi}{6}) = 0$). Along the primary stress axis, $f_{cr}(\omega = 0) \equiv 1.000$. The remaining constraints are as follows: $f_{cr}(\omega = \frac{\pi}{2}) = 0.970$ and $f_{cr}(\omega = \frac{\pi}{6}) = 1.027$. The angular variation function is designed so that small variations (e.g. $\pm 5°$) in the vicinity of the L orientation result in a negligible variation of *f*. Similarly, small variations in the grain orientation (e.g. $\pm 10°$) at the T orientation lead to negligible variations of *f*. The orientation model can be plotted with respect to grain orientation angle as shown in Fig. 6.11.

By isolating the creep rupture time in Eq.(6.5), the expression can be rewritten as

$$t_r = \Theta_{cr} \exp\left(\frac{1000 B_L f_{cr}(\sigma_{tens})^{-k_L}}{T}\right). \tag{6.7}$$

Replacing $1000B_L$ with $B'_L/R$ leads to

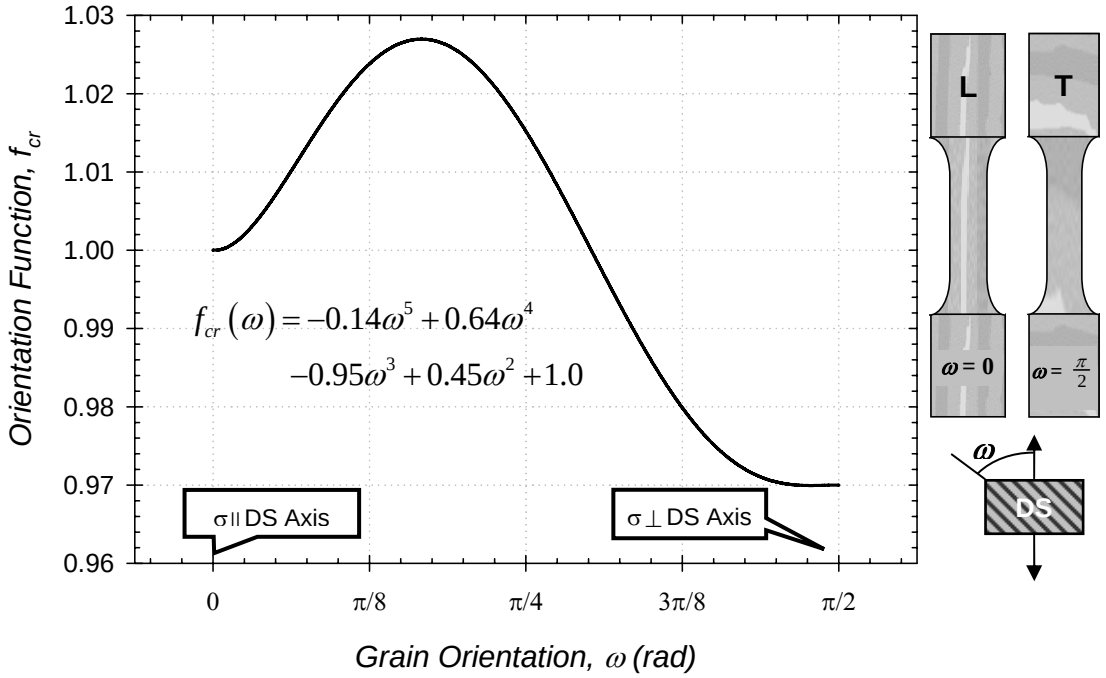


***Figure 6.11:*** *Angular variation of* $f_{cr}$.

$$t_r = \Theta_{cr} \exp\left( \frac{B'_L f_{cr} \left(\sigma_{tens}\right)^{-k_L}}{RT} \right). \tag{6.8}$$

Here, $\Theta_{cr}$ is a constant and it is listed along with the remaining material constants in Table 6.2. The units of $B'_L$ are $MPa^{k_L} mol / J$. With this formulation, it is assumed that a compressive dwell period does not contribute to creep rupture damage, which is consistent with experiments. Under compressive creep conditions at 982°C and −100 *MPa*, L-oriented DS GTD-111 does not reach the tertiary creep stage that it does at 100 *MPa* (Fig. C.1). Only tensile dwells contribute to this form of damage. When dominantly tensile creep-fatigue conditions are imposed, cracks initiated in DS GTD-111 should resemble samples shown in Figs. 4.31 - 4.34.

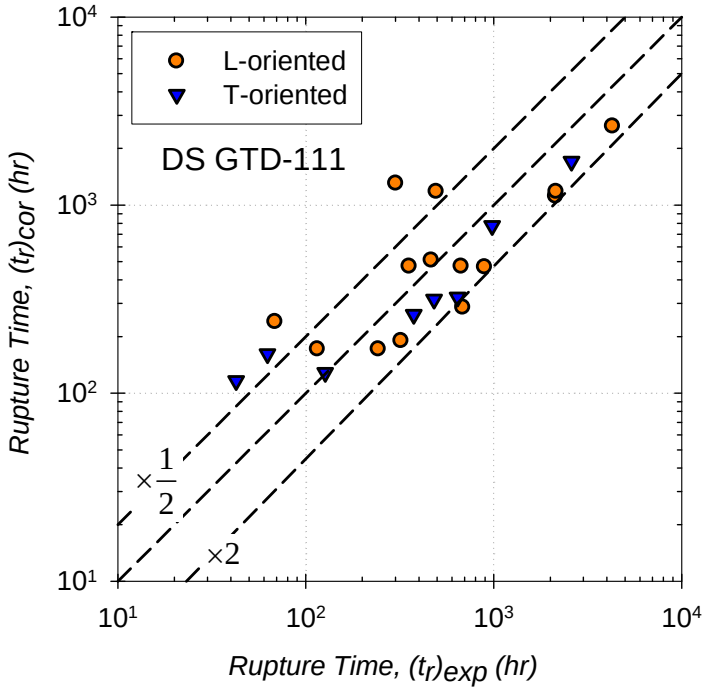


***Figure 6.12:*** *Comparison of rupture experiments and correlations for L- and T-oriented DS GTD-111 under isothermal creep conditions.*

***Table 6.2:*** *Constants used in creep damage term*

| $B'_L$ | $f_{cr}(\omega=0)$ | $f_{cr}(\omega=\pi/2)$ | $k_L$ | $\Theta_{cr}$ |
|---|---|---|---|---|
| 724814.52 | 1.000 | 0.970 | 0.189 | 2.06E-09 |

Similar to the LMP, Eq. (6.8) represents an upper bound on rupture life. Rupture time estimates were made by utilizing the stress and temperature conditions from creep rupture experiments on L- and T-oriented DS GTD-111 (Table 4.13). As shown in Fig. 6.12, Eq. (6.7) models creep rupture data of T-oriented DS GTD-111 with a correlation of $R^2 = 0.98$. The L-oriented material is fit with $R^2 = 0.73$. Approximately 73% of the data fits within the displayed error bands.

Estimates of creep damage that occurs during tensile dwells during strain-controlled cycling are made using the creep rupture time model [Eq. (6.7)]. In these instances, creep strain accumulates, simultaneously relieving elastic strains and relaxing the tensile stress. Equation (6.7) does not account for non-isothermal effects or evolution of material compliance due to creep. The creep damage associated with creep-fatigue cycling can be written as the ratio of the dwell time to the rupture time, i.e.,

$$D^{cr} = \frac{1}{N_i^{cr}} = \frac{t_{ht}}{t_r}. \tag{6.9}$$

The critical damage parameter corresponding to the number of cycles to cause creep rupture is its reciprocal, i.e.,

$$N_f^{cr} = \frac{\Theta_{cr}}{t_{ht}} \exp\left( \frac{B_L' f_{cr} \left( \sigma_{tens} \right)^{-k_L}}{RT} \right). \tag{6.10}$$

If the load carrying capability of the specimens had been checked periodically throughout the life of the creep experiment, it would have been possible to accurately determine the crack initiation life of the material under nominally creep conditions. This creep damage term assumes a decoupling of creep from fatigue when the dwell portion of the cycle dominates. The term is designed to behave according to the following requirements: (i) $\lim_{T \to RT} N_f^{cr} = \infty$ and (ii) $\lim_{\sigma_{tens} \to 0} N_f^{cr} = \infty$, and (iii) $\lim_{t_{ht} \to 0} N_f^{cr} \left( t_r = const \right) = \infty$. The contours illustrated in Fig. 6.13 express constant rupture life for a range of temperature versus

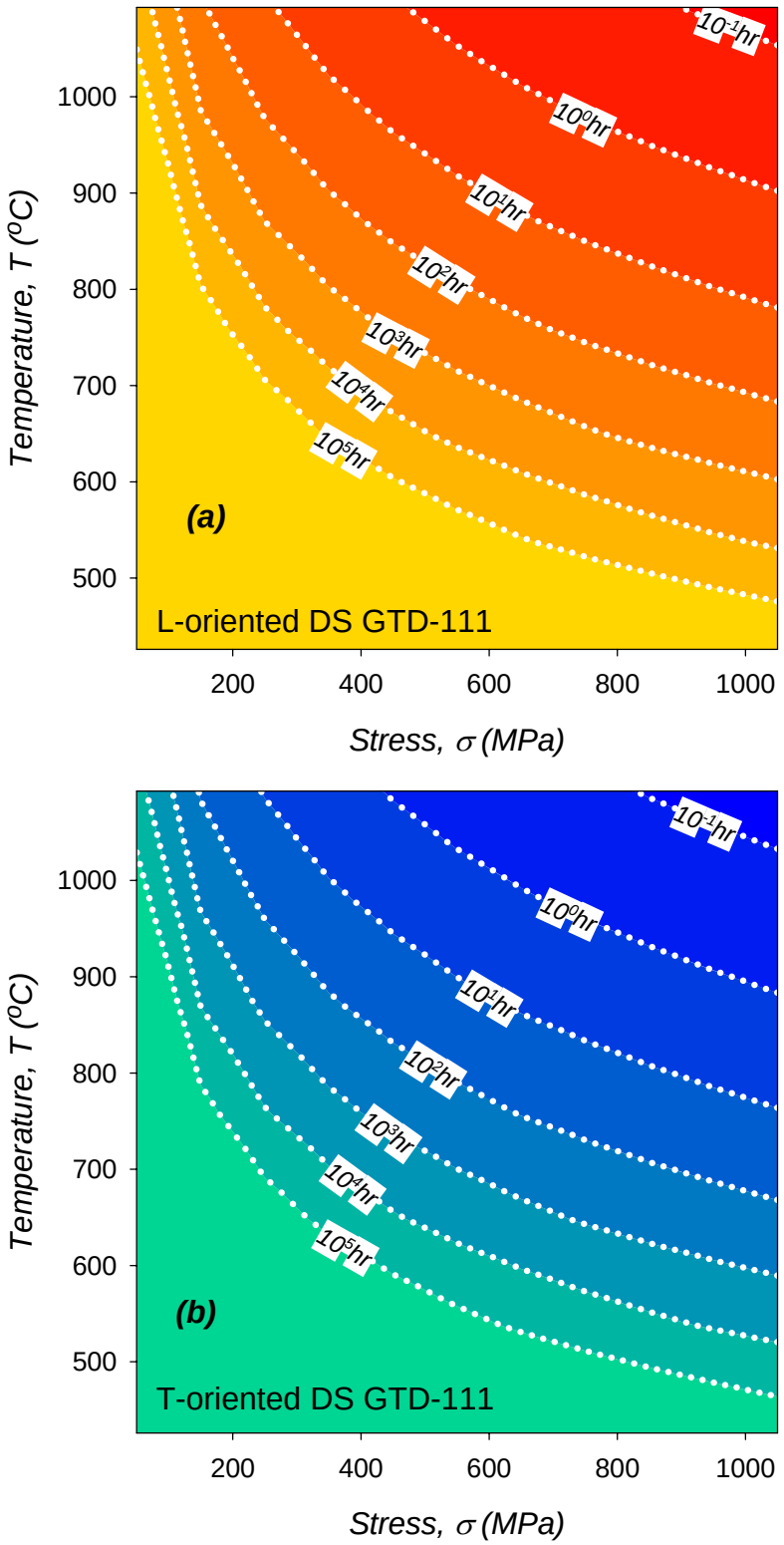


***Figure 6.13:*** *Correlated contours of* $N_f^{cr} \cdot \tau_h$ for (a) L- and (b) T-oriented under nominally creep conditions.

uniaxial stress conditions. At high temperatures and low stresses, the actual rupture times for the L- and T-oriented specimens are similar. In low temperature and high stress situations, however, viscous flow is less rapid and depends upon grain orientation. Although the trends in Fig. 6.13 are similar for the two distinct orientations, the rupture lives differ.

Each of these trends is reflected in the diagram; furthermore, the requirements (i)-(ii) are satisfied. Equation (6.10) can be expressed as the product of separable functions, e.g.,

$$\frac{1}{N_f^{cr}} = \prod_{i=1}^{2} \xi_i^{cr} \tag{6.11}$$

where

$$\begin{aligned} \xi_1^{cr} &= \xi_1^{cr}\left(\text{Diffusion}\right) = \frac{t_{ht}}{\Theta_{cr}} \\ \xi_2^{cr} &= \xi_2^{cr}\left(\text{Stress and Orientation}\right) = \exp\left(-\frac{B_L' f_{cr}\left(\sigma_{tens}\right)^{-k_L}}{RT}\right) \end{aligned} \tag{6.12}$$

### *6.4 Environment-Fatigue Damage*

Coupled environmental-fatigue damage is the most complex of the physically-based damage modules. It was demonstrated through experimentation that this form of damage exhibited by DS GTD-111 occurs in the same manner as other large grain Ni-

base superalloys (Antolovich et al., 1980a; Reuchet and Rémy, 1983; Sehitoglu and Boismier, 1990a; Rémy et al., 2000; Koster et al., 2002). This type of damage is most dominant in two situations: (1) during compressive creep-fatigue testing when the temperature is above 871°C (1600°F), and (b) during out-of-phase (OP) TMF cycling. In both cases the cyclic plastic strain range had to be small compared to the elastic strain range, i.e., $\Delta\varepsilon_{pl} \ll \Delta\varepsilon_{el}$.

Coupled environmental-fatigue damage was manifested in the form of repeated rupture of oxide intrusions that form oxide spikes on the specimen surface. Because the oxide spikes expose virgin material, the growth kinetics of fresh metallic material at the crack tip must be applied in an iterative manner, as shown in Fig. 6.14. As a consequence, the growth kinetics of oxide spikes are parameterized not only by the oxidation ingression (e.g., temperature, time, oxygen content), but also on the total mechanical strain range, the mechanical strain rate, and the phasing between the thermal and mechanical strain rate. A general model for the effective oxide growth rate per unit cycle of an oxide spike in a Ni-base superalloy has been given by applying the chain rule (Boismier and Sehitoglu, 1990b), i.e.,

$$\frac{dh}{dN} = \frac{dh}{dt}\frac{dt}{dN}, \tag{6.13}$$

where $h$ is the depth of the oxide spike. Here $dt/dN$ is the cycle period, $t_{cc}$, i.e.,

$$\frac{dh}{dN} = \frac{dh}{dt}t_{cc}. \tag{6.14}$$

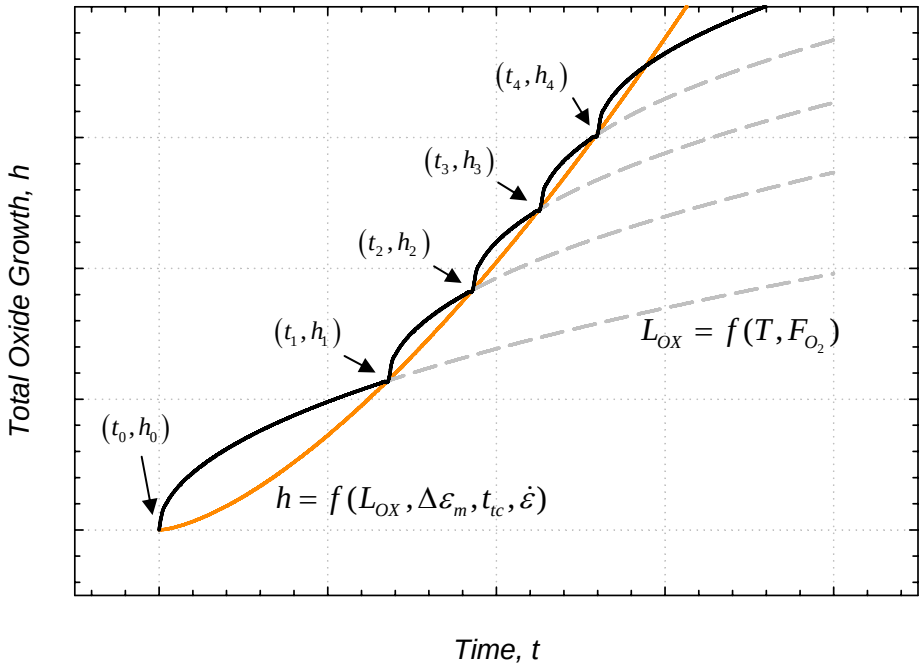


***Figure 6.14:*** *Kinetics of cyclic oxide growth and repeated rupture occurring in DS GTD-111 under TMF and creep-fatigue conditions.*

The locus of points at which the oxide ruptures and exposes new material is parameterized by a 2-parameter power law relation (Fig. 6.14). While the stress-free oxidation growth of DS GTD-111 has a power law decreasing relation with time (e.g., the exponent, *m*, is between zero and unity, Table 4.18), the effective oxide growth kinetics follows a power law increasing relation, e.g.,

$$h = g \cdot (t_{tc})^{\beta}, \tag{6.15}$$

where the exponent, $\beta$, is greater than unity. The function, *g*, is a separable function of the oxidation kinetics (e.g. temperature and environment) and rupture kinetics (e.g.

mechanical strain range, strain rate, and thermomechanical phasing) of the oxidized material, e.g.,

$$g = B_{ox} \frac{\Theta_{OX}\left(T, F_{O_2}\right)}{h_f\left(\Delta\varepsilon_m, \dot{\varepsilon}, \Phi^{OX}\right)}, \tag{6.16}$$

where $B_{ox}$ is a constant.

Based on the stress-free corrosion experiments, the parameterizing term for oxide growth, $\Theta_{OX}$, follows the Arrhenian diffusion law, i.e.,

$$L_{OX} \propto \Theta_{OX}\left(T\right) t^m = \theta_{OX} \exp\left(-\frac{Q_{OX}}{RT}\right) t^m, \tag{6.17}$$

These experiments performed using DS GTD-111 were useful in determining that the coefficient for surface layer growth kinetics depends on the concentration of the diffusing species in the atmosphere, i.e.

$$\theta_{OX} = f\left(F_{O_2}\right), \tag{6.18}$$

In static lab air, $F_{O_2} = 0.21$ and $\theta_{OX,air} = 30203\ \mu m \cdot hr^{-m}$. In the Ar-rich environment, $F_{O_2} = 0.02$ and $\theta_{OX,Ar-rich} = 23425\ \mu m \cdot hr^{-m}$. Decreasing the oxygen content in the

atmosphere, therefore, must require $\theta_{OX}$ to converge to 0 (i.e., in a vacuum environment with $F_{O_2} = 0$, $\theta_{OX,vac}$ must be 0). Curve-fitting these points yields the relationship

$$\theta_{OX} = \theta_{OX,0}\left(F_{O_2}\right)^{\theta_{OX,1}} = 35752\left(F_{O_2}\right)^{0.1081}, \tag{6.19}$$

where $\theta_{OX,0}$ and $\theta_{OX,1}$ are constants. It should be noted that in the simulated IGCC environment, $\theta_{S,IGCC} = 66924\ \mu m \cdot hr^{-m}$.

An expression for the repeated rupture of the oxide spike tip, which involves strain range, $\Delta\varepsilon_m$, and rate, $\dot{\varepsilon}$, thermal-mechanical strain rate phasing, $\Phi_{OX}$, for continuous cycling cases, was established in previous studies (Neu and Sehitoglu, 1989b; Sehitoglu and Neu, 1990b), i.e.,

$$\overline{h}_f = \frac{\delta_0}{\left(\Delta\varepsilon_{mech}\right)^2 \Phi_{OX} \dot{\varepsilon}^a} \tag{6.20}$$

where $\delta_0$, and *a* are constants. The phasing term is given as

$$\Phi_{OX} = \exp\left[-\frac{1}{2}\left(\frac{\frac{\dot{\varepsilon}_{th}}{\dot{\varepsilon}_m}+1}{\xi_{OX}}\right)^2\right] \tag{6.21}$$

where $\xi_{ox}$ is a parameter that is a measure of the amount of damage associated with the different phasing types. Equation (6.20) does not account for other types of load histories, namely creep-fatigue cycling and pre-exposure conditions, in which the coupled environmental-fatigue damage mechanism was found to operate.

*Effect of Compressive Dwell Period*

The critical oxide rupture thickness relation was extended to DS GTD-111 based on direct measurements from fatigue tested sampled that displayed an environmental damage mechanism, shown in Fig. 4.56., i.e.,

$$\overline{h}_f = \frac{\delta_{cc} + t_{hc}\delta_{hc}}{\left(\Delta\varepsilon_m\right)^b \Phi_{cc}^{env} \dot{\varepsilon}^a}. \tag{6.22}$$

Here $\delta_{cc}$, $\delta_{hc}$, $a$, and $b$ are constants and $t_{hc}$ is the hold period measured in seconds. Although $\overline{h}_f$ increases with increasing $t_{hc}$, Eq. (6.22) does not completely capture the effect of compressive dwell periods on life. Crack initiation life data (Tables 4.9 – 4.11) and corroborating microscopy indicate that the growth rate of oxide spikes increased with increasing $t_{hc}$; $N_i$ was also reached more rapidly with increasing $t_{hc}$. The compressive dwell periods effect on crack initiation life must be taken into account.

The growth of an oxide spike must be less than that occurring during push-pull reversals since compressive conditions exist at the tip of the oxide spike during the compressive hold. Modeling this phenomenon cannot be carried out by summing the cyclic and hold periods (e.g., $t_{cc} + t_{hc}$). Since the conditions during which oxide growth

occurs are compressive, the oxides are stress free at the peak compressive stress. This makes the magnitude of the strain range more effective (i.e., peak tensile stress in oxide will be higher in HC cases compared to CC cases). An appropriate formulation that incorporates $t_{hc}$ as a modifier of the elapsed time the specimen is subjected to the fatigue portion of cycling, $t_{pp}$, is given as

$$h = g\left[t_{pp}\sqrt{\tau_{hc}t_{hc}+1}\right]^{\beta}. \tag{6.23}$$

The term $t_{pp}$ is the total time that the sample is subjected to fatigue portion of cycling (i.e., $t_{pp} = Nt_{cc}$). Here $h$ is the oxide spike length, and $\tau_{hc}$ is defined as a parameter that captures the sensitivity of the material to oxide spiking during compressive dwell periods. Clearly, as $t_{hc}$ approaches 0, the cyclic oxide growth rate converges to that occurring during CC conditions. Alternatively with increasing $t_{hc}$ the rate increases rapidly, as shown in Fig. 6.15. Experiments indicated that DS GTD-111 oxidation is not substantial enough to display the oxide spiking mechanism under CC conditions. Other damage mechanisms dominate before this environmental mechanism becomes a factor. As such, increasing the dwell period brings out the environmental mechanism that would otherwise not be involved.

Differentiating Eq. (6.23) with respect to time $t_{pp}$ and substituting the results into Eq. (6.14) yields,

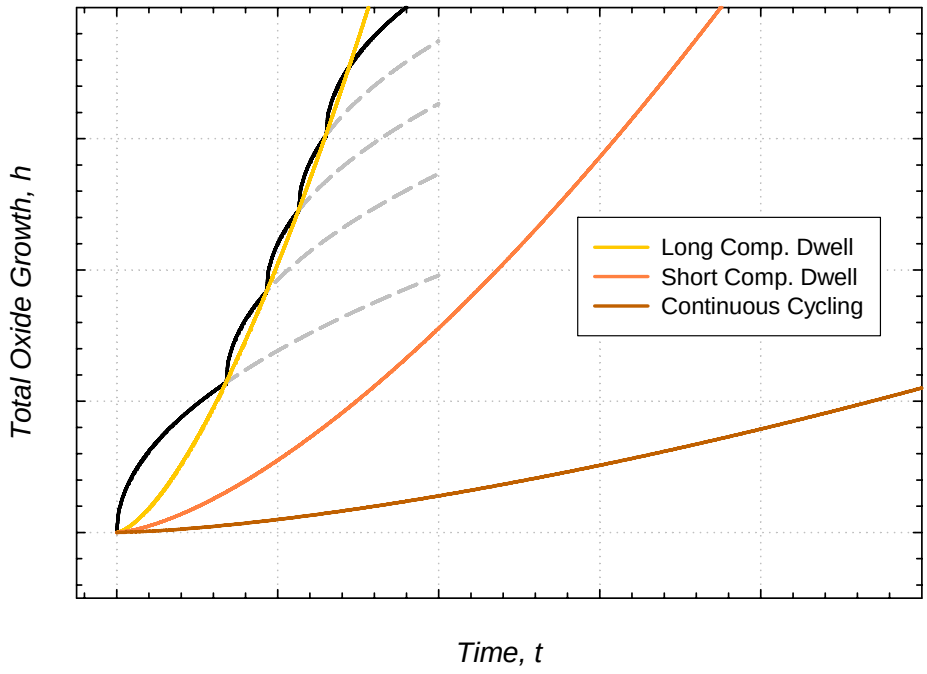


***Figure 6.15:*** *Kinetics of cyclic oxide growth and repeated rupture occurring in DS GTD-111 under creep-fatigue conditions.*

$$\frac{dh}{dN} = g\beta \exp\left(\frac{t_{hc}}{\tau_{hc}}\right)\left[t_{pp}\sqrt{\tau_{hc}t_{hc}+1}\right]^{\beta-1} t_{cc} \tag{6.24}$$

It should be noted that both $t_{hc}$ and $t_{cc}$ are assumed to be constant. This relation assumes that the hold period remains constant with respect to time. Substituting Eq. (6.16) into Eq. (6.24) gives

$$\frac{dh}{dN} = B\frac{\Theta_{OX}\left(\Delta\varepsilon_m\right)^b \Phi_{cc}^{env}\dot{\varepsilon}^a}{\delta_{cc}+t_{hc}\delta_{hc}}\beta\left[\sqrt{\tau_{hc}t_{hc}+1}\right]^{\beta} t_{cc}\left(t_{pp}\right)^{\beta-1} \tag{6.25}$$

The total uniaxial cycle time $t_{pp}$ (e.g. push-pull portion only) can be expressed as expressed in terms of the cycle period and the number of cycles, i.e.,

$$\frac{dh}{dN} = B\frac{\Theta_{OX}\left(\Delta\varepsilon_m\right)^b \Phi_{cc}^{env}\dot{\varepsilon}^a}{\delta_{cc}+t_{hc}\delta_{hc}}\beta\left[\sqrt{\tau_{hc}t_{hc}+1}\right]^{\beta} t_{cc}\left(t_{cc}N\right)^{\beta-1} \tag{6.26}$$

Furthermore, the cycle time can be written as the ratio of strain range to strain rate, which gives

$$\frac{dh}{dN} = B\frac{\Theta_{OX}\left(\Delta\varepsilon_m\right)^b \Phi_{cc}^{env}\dot{\varepsilon}^a}{\delta_{cc}+t_{hc}\delta_{hc}}\beta\left[\sqrt{\tau_{hc}t_{hc}+1}\right]^{\beta}\left(\frac{2\Delta\varepsilon_m}{\dot{\varepsilon}}\right)^{\beta}\left(N\right)^{\beta-1} \tag{6.27}$$

Integration yields

$$\frac{1}{N_i^{env}} = B\left[\frac{\Theta_{OX}\left(\Delta\varepsilon_m\right)^b \Phi_{cc}^{env}\dot{\varepsilon}^a}{h_{cr}\left(\delta_{cc}+t_{hc}\delta_{hc}\right)}\right]^{\frac{1}{\beta}}\left[\sqrt{\tau_{hc}t_{hc}+1}\right]\left(\frac{2\Delta\varepsilon_m}{\dot{\varepsilon}}\right), \tag{6.28}$$

where $h_{cr}$ is the critical oxide spike length at which the crack is sufficiently long enough to grow quickly by fatigue damage which is assumed to comprise a small fraction of life. This term describes the surface condition of the material at crack initiation. To reduce the number of constants involved, $\delta_{cc}$ and 2 are factored out and $2B\left(\delta_{cc}\right)^{-\frac{1}{\beta}}$ is replaced by $B_{env}$, and $\delta_{hc}/\delta_{cc}$ is replaced by $\delta'_{hc}$. Simplification gives

$$\frac{1}{N_i^{env}} = B_{env}\left[\frac{\Theta_{OX}\Phi_{cc}^{env}\dot{\varepsilon}^{a-\beta}\left(\Delta\varepsilon_m\right)^{b+\beta}}{h_{cr}\left(1+t_{hc}\delta'_{hc}\right)}\right]^{\frac{1}{\beta}}\left[\sqrt{\tau_{hc}t_{hc}+1}\right]. \tag{6.29}$$

Temperature and environment are incorporated in Eq. (6.29) via Eqs. (6.17), (6.19), and (6.21).

*Effect of Pre-Exposure at Zero Applied Stress*

Subjecting DS GTD-111 to unstressed high temperature exposure in either laboratory air or simulated IGCC environments prior to fatigue cycling resulted in the development surface layers (Fig. 4.39). Upon cycling, cracks initiating from the surface propagated through the oxide layer and γ′-depleted zone rapidly. After this initial period, continued crack growth occurred by way of the oxide spiking mechanism. Compared to un-exposed samples as in Fig. 4.43 and Table 4.14, pre-developed oxide layers severely shortened the crack initiation lives of fatigue specimens by giving the cyclic oxide growth and rupture kinetics an early introduction to the surface of the material. This "head start" can be represented graphically in terms of cyclic oxide rupture, as in Fig. 6.16. Instead of initiating from the origin, the oxide's growth and cyclic rupture kinetics begin where the pre-exposure ends, i.e. $\left(t_{pre}, h_{pre,ox}+h_{pre,GPD}\right)$. Here $t_{pre}$ is the pre-exposure time and $h_{pre,ox}$ and $h_{pre,GPD}$ are the thicknesses of the oxide layer and γ′-depleted zone after pre-exposure, respectively, i.e.,

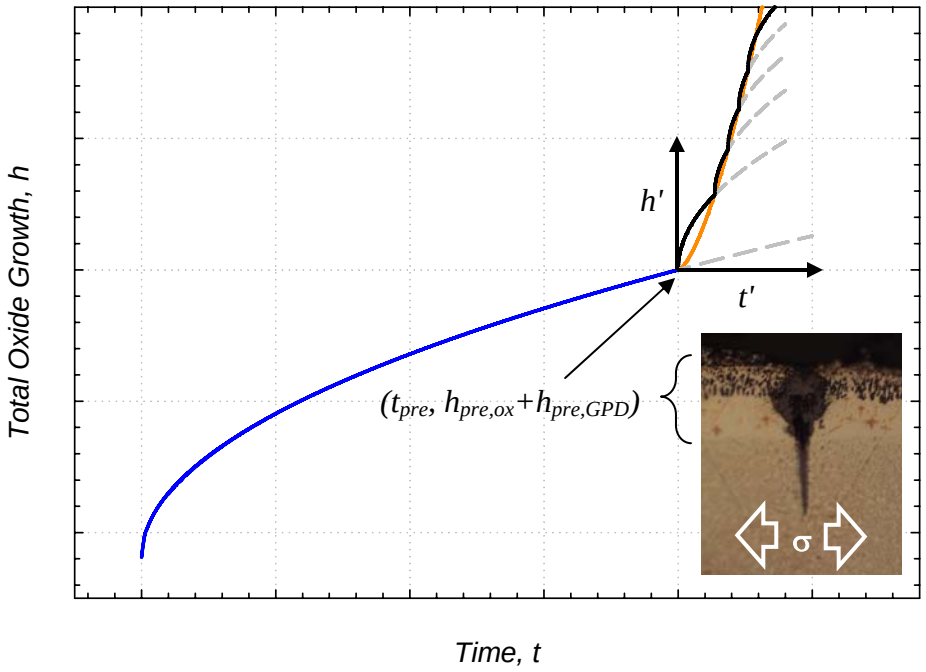


***Figure 6.16:*** *Kinetics of cyclic oxide growth for pre-exposed and subsequently fatigue cycled DS GTD-111.*

$$h_{pre,ox} = \Theta_{ox}\left(T_{pre}, F_{O_2,pre}\right)\left(t_{pre}\right)^m$$
$$h_{pre,GPD} = \Theta_{GPD}\left(T_{pre}, F_{O_2,pre}\right)\left(t_{pre}\right)^m \qquad (6.30)$$

Here the subscript "*pre*" on $T_{pre}$ and $t_{pre}$ denotes the temperature and length of the pre-exposure period, respectively. Based on the stress-free oxidation study, a good approximation for the summed surface layer depths developed by high temperature pre-exposure is

$$2h_{pre} \approx h_{pre,ox} + h_{pre,GPD}\,. \qquad (6.31)$$

Consequently, Eq. (6.23) is re-written as

$$\left(h-2h_{pre}\right)=g\left[\left(t_{pp}-t_{pre}\right)\sqrt{\tau_{hc}t_{hc}+1}\right]^{\beta} \tag{6.32}$$

This relation assumes that growth kinetics during cycling and repeated rupture is merely shifted and not scaled by the pre-exposure. For unexposed cases, Eq. (6.29) assumes that the initial and final crack sizes are 0 and $h_{cr}$, respectively. For pre-exposed cases, the initial and final crack sizes are $2h_{pre}$ and $h_{cr}$, respectively. The analytical procedure used to obtain Eq. (6.29) can be repeated to include the pre-exposure condition that, upon substitution, yields

$$\frac{1}{N_i^{env}}=B_{env}\left[\frac{\Theta_{OX}\Phi_{cc}^{env}\dot{\varepsilon}^{a-\beta}\left(\Delta\varepsilon_m\right)^{b+\beta}}{\left(h_{cr}-2h_{pre}\right)\left(1+t_{hc}\delta'_{hc}\right)}\right]^{\frac{1}{\beta}}\sqrt{\tau_{hc}t_{hc}+1}\,. \tag{6.33}$$

It is assumed here that $h_{cr}>2h_{pre}$ in all cases. For cases where $h_{cr}\le 2h_{pre}$, the condition of the surface after pre-exposure is assumed to be extensively corroded.

Coupled environmental-fatigue damage is most dominant in cases having small plastic strain ranges. To account for orientation, $f_{el}\left(\omega\right)$ is designed to have a similar shape $f_{in}\left(\omega\right)$ in Eq. (6.1) can be used, i.e.,

$$f_{el}\left(\omega\right)=1.97\omega^5-9.25\omega^4+14.89\omega^3-8.52\omega^2+1.0\,. \tag{6.34}$$

which gives

$$\frac{1}{N_i^{env}} = B_{env}\left[\, f_{el}\left(\omega\right)\right]^{-1}\left[\frac{\Theta_{OX}\Phi_{cc}^{env}\dot{\varepsilon}^{a-\beta}\left(\Delta\varepsilon_m\right)^{b+\beta}}{\left(h_{cr}-2h_{pre}\right)\left(1+t_{hc}\delta'_{hc}\right)}\right]^{\frac{1}{\beta}}\sqrt{\tau_{hc}t_{hc}+1}\,. \tag{6.35}$$

Here $f_{el}\left(\omega=0\right)\equiv 1.0$ and the slopes at both the L and T orientations are designed to be flat, i.e., $f'_{el}\left(\omega=0\right)= f'_{el}\left(\omega=\frac{\pi}{4}\right)= f'_{el}\left(\omega=\frac{\pi}{2}\right)=0$. The remaining coefficient in Eq. (6.34) was determined by comparing the lives of L- and T-oriented DS GTD-111 subjected to similar conditions in which the coupled environmental-fatigue mechanism is dominant. For example, imposing the condition of air-pre-exposure with subsequent cycling at 0.8% leads $f_{el}\left(\omega=\frac{\pi}{2}\right)$ after systematic elimination, e.g.,

$$f_{el}\left(\omega=\tfrac{\pi}{2}\right)=\frac{N_i^{env}\left(\omega=\frac{\pi}{2}\right)f_{el}\left(\omega=0\right)}{N_i^{env}\left(\omega=0\right)}=\frac{\left(221\right)\left(1.0\right)}{\left(1958\right)}=0.11 \tag{6.36}$$

Equation (6.33) can be assumed as the product of separable effects, i.e.,

$$\frac{1}{N_i^{env}}=\prod_{i=0}^{6}\xi_i^{env}\,. \tag{6.37}$$

where

$$
\begin{aligned}
\xi_0^{env} &= const = B_{env} \\
\xi_1^{env} &= \xi_1^{env}\left(\text{Orientation}\right) = \left[\, f_{el}\left(\omega\right)\right]^{-1} \\
\xi_2^{env} &= \xi_2^{env}\left(\text{LCF}\right) = \left(\dot{\varepsilon}^{a-\beta}\left(\Delta\varepsilon_m\right)^{b+\beta}\right)^{\frac{1}{\beta}} \\
\xi_3^{env} &= \xi_3^{env}\left(\text{TMF}\right) = \left(\Phi_{cc}^{env}\right)^{\frac{1}{\beta}} \\
\xi_4^{env} &= \xi_4^{env}\left(\text{Creep-Fatigue}\right) = \left(1+t_{hc}\delta'_{hc}\right)^{\frac{-1}{\beta}}\sqrt{\tau_{hc}t_{hc}+1} \\
\xi_5^{env} &= \xi_5^{env}\left(\text{Diffusion}\right) = \left(\Theta_{ox}\right)^{\frac{1}{\beta}} \\
\xi_6^{env} &= \xi_6^{env}\left(\text{Surface Condition}\right) = \left(h_{cr}-2h_{pre}\right)^{\frac{-1}{\beta}}
\end{aligned}
\tag{6.38}
$$

The exponents $b$ and $\beta$ in Eq. were fixed according to a prior study on Ni-base superalloys (Boismier and Sehitolgu, 1990b). The constants corresponding to the diffusion function, $\xi_5^{env}$, were determined from stress-free corrosion data. The remaining constants for this module were fine tuned using an optimization tool built into Microsoft Excel® (Newton search algorithm). All of the constants for this damage term are listed in Table 6.3.

***Table 6.3:*** *Constants used in environmental-fatigue damage term*

| $B_{env}$ ($\mu m^{-1/\beta}$-$s^{1-a/\beta}$) | $f_{el}(\omega=0)$ | $f_{el}(\omega=\pi/2)$ | $\theta_{ox,1}$ | $\theta_{ox,2}$ |
|---|---|---|---|---|
| 863.4 | 1.000 | 0.58 | 35752 | 0.11 |
| $Q_{ox}$ (J-mol$^{-1}$) | $\xi_{ox}$ | $a$ | $\beta$ | $b$ |
| 96200 | 0.32 | 0.75 | 1.5 | 1.5 |
| $h_{cr}$ ($\mu m$) | $\delta'_{hc}$ ($s^{-1}$) | $\tau_{hc}$ ($s^{-1}$) | | |
| 43.5 | 0.00398 | 0.441 | | |

Crack initiation life correlations were made using the environmental-fatigue damage term. The creep-fatigue damage function in Eq. (6.38) allows the model to

capture the steep reduction in $N_i$ that occurs due to oxide spiking caused by compressive holds at 871°C as shown in Fig. 6.17a. It should be noted that as $t_h$ is decreased to 0, the model overestimates $N_i$ that was obtained from CC LCF experimentation because environment-fatigue damage is no longer the dominant mechanism; however, as $\Delta\varepsilon_m$ is reduced under otherwise identical conditions, $N_i^{env}$ more closely resembles $N_i$. The same observation can be if $T$ is increased to 982°C (Fig. 6.17b).

The surface condition function in Eq. (6.38) allows the model to capture the reduction of life due to pre-exposure, as shown in Fig. 6.18a. This factor incorporates the stress-free corrosion kinetics of the material to model the degradation at the surface caused by high temperature pre-exposure to either air or the simulated IGCC environment. The model captures the experimental observation that the IGCC pre-exposure is more detrimental to crack initiation life than pre-exposure in air. Orientation is also captured in Eq. (6.38), as shown in (Fig. 6.18b).

When the concentration of the diffusing species in the atmosphere surrounding a specimen is decreased, $N_i$ was shown to increase. Using the cyclic oxide growth and rupture model that is built into the diffusion function of Eq. (6.38), the model characterizes the increase of life induced by eliminating the majority of oxygen from the vicinity of the specimen (Fig. 6.19).

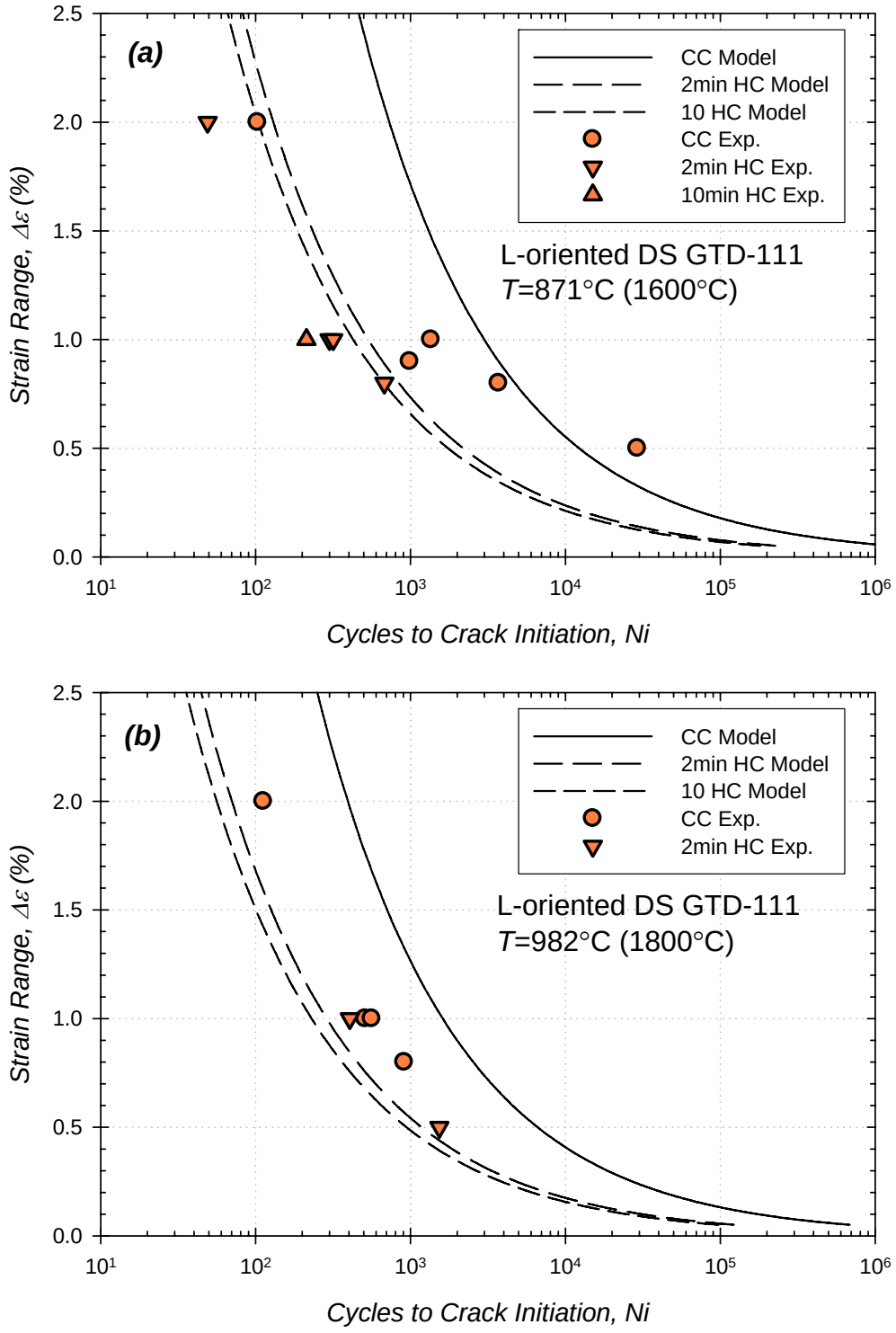


***Figure 6.17:*** *Correlations of crack initiation life using environmental-fatigue damage module based of L-oriented DS GTD-111 under LCF and creep-fatigue conditions. For each case (a) T=871℃, (b) T=982℃ , $R_\varepsilon$=-1, and $\dot{\varepsilon} = 0.5\%/s$.*

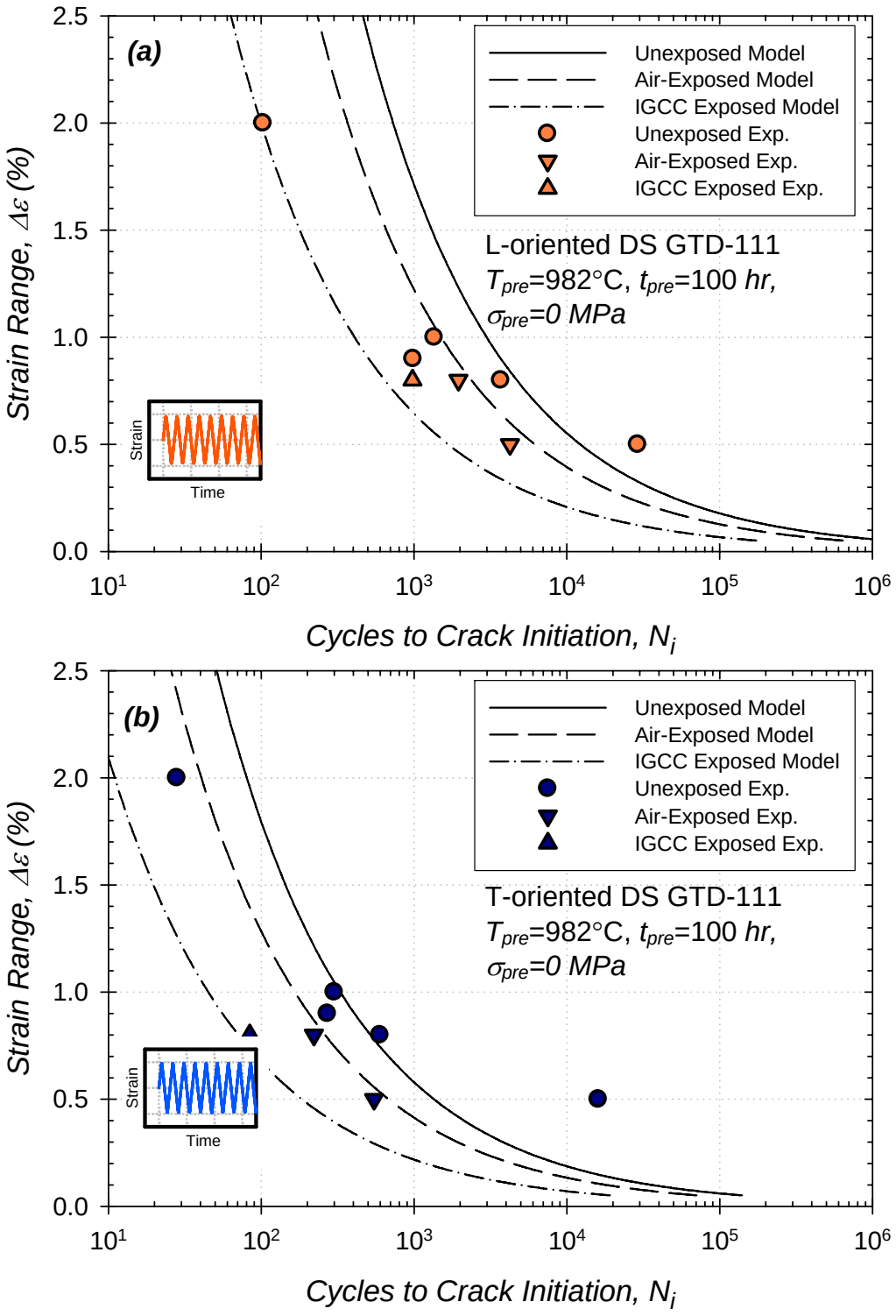


***Figure 6.18:*** *Correlations of crack initiation life using environmental-fatigue damage module based on pre-exposed and un-exposed (a) L- and (b) T-oriented DS GTD-111 under LCF and creep-fatigue conditions. For each case T=871℃, $R_\varepsilon$=-1, and* $\dot{\varepsilon} = 0.5\%/s$.

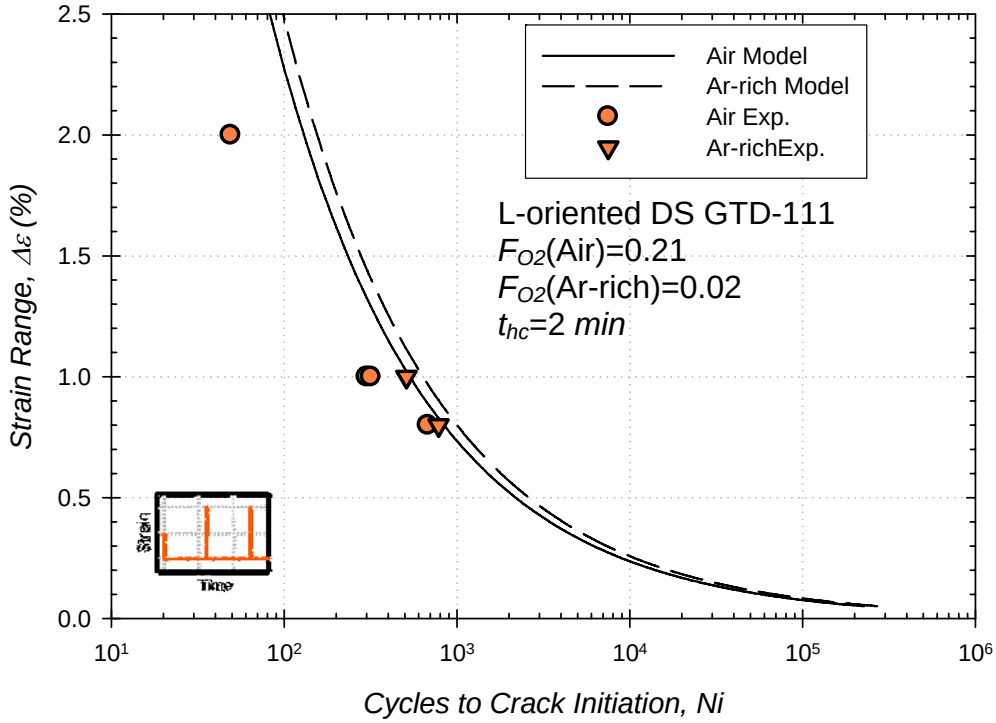


***Figure 6.19:*** *Correlations of crack initiation life using environmental-fatigue damage module based on L-oriented DS GTD-111 under creep-fatigue and creep-fatigue conditions in air and semi-inert environment. For each case T=871℃, $R_\varepsilon$=-1, and* $\dot{\varepsilon} = 0.5\%/s$.

### *6.5 Predictions of Total Crack Initiation Life*

Predictions of total life of DS GTD-111 are made from combining the damage modules into a damage mechanism formulation. There are two alternatives that are used to make calculations. Dominant damage is determined using contribution from only the most prominent damage form, e.g.,

$$\left.\frac{1}{N_i}\right|_{dom} = \max\left\{\frac{1}{N_i^{fat}}, \frac{1}{N_i^{cr}}, \frac{1}{N_i^{env}}\right\}. \tag{6.39}$$

Cumulative damage is predicted based on the summed contribution of all active mechanisms, e.g.,

$$\left.\frac{1}{N_i}\right|_{cum} = \frac{1}{N_i^{fat}} + \frac{1}{N_i^{cr}} + \frac{1}{N_i^{env}} \tag{6.40}$$

Crack initiation life predictions were made for L-oriented DS GTD-111 using both techniques (Eq. (6.39) and (6.40)) in Fig. 6.20. Both methods yield approximately identical results when damage caused by one mechanism exceeds all other active mechanisms by one or more orders of magnitude. When the damage contributions are comparable, Eq. (6.40) is the more conservative of the two methods since $2N_i\big|_{cum} \approx N_i\big|_{dom}$. Another important characteristic of the two methods is that the crossover in dominant damage mechanism is easier to distinguish graphically due to the "bump" in the curve. These inflections are needed to determine the discrete boundaries of damage mechanism maps. The locus of points that define the boundaries are determined mathematically as the set of conditions (e.g. temperature, environment, mechanical strain range, etc.) resulting in the equality of two or more of the individual damage contributions, i.e.,

$$\frac{1}{N_i^{(j)}} = \frac{1}{N_i^{(k)}} \tag{6.41}$$

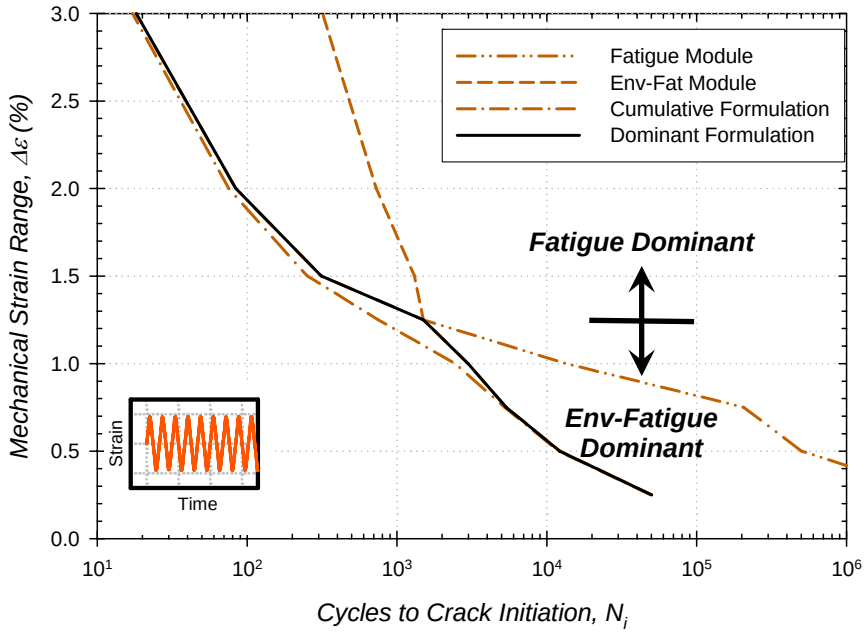


***Figure 6.20:*** *Generic comparison of total damage formulations with two operative damage forms.*

where $j,k = fat,cr,env$ and $j \neq k$. For this reason, predictions of total life are made using Eq. (6.39). All calculations were carried out in an Excel spreadsheet using deformation data contained in Chapter 5.

*Crack Initiation Life Under Isothermal Low Cycle Fatigue Conditions*

Predictions of total crack initiation life defined by percentage load drop were made for L- and T-oriented DS GTD-111 subjected to a variety of completely-reversed, LCF strain-controlled conditions. Along with the more prominent test variables (temperature and mechanical strain range), pre-exposures, and environments were considered. In each case, however, isothermal $\left(\dot{\varepsilon}_{th} = 0\right)$ and continuous cycling $\left(t_{ht} = t_{hc} = 0\right)$ conditions were assumed.

The fatigue damage mechanism is dominant for nearly all of $\Delta\varepsilon$-$T$ combinations that were considered. The coupled environmental-fatigue mechanism only dominates when the plastic strain range is below 0.5% and the temperature is in the range of 760°C and 982°C. Above 982°C the plastic portion of the cyclic mechanical strain range is high causing fatigue damage to dominate. The usage of both damage modules allows a good correlation for the experimental data, as shown in Fig. 6.21. Constant temperature strain versus life data used in Fig. 6.21 was reorganized as contours of constant life for couples of temperature and strain range, as shown in Fig. 6.22. Borders have been superimposed to demarcate the regions of dominant damage. These boundaries correspond to the inflection points of curves in Fig. 6.21. Each was derived from mathematically interpolating from $N_i^{fat} / N_i^{env}$ contours. The contours are shown for L- (Fig. 6.22a) and T-oriented (Fig. 6.22b) cases such that $N_i^{fat} / N_i^{env} = 1$.

It should be noted that in Fig. 6.22 and other similar plots that the coupled environmental-fatigue damage mechanism is predicted to dominate at low temperatures (below 871°C) where oxidation is minimal. This is one limitation of the form of the model which does not account for high cycle fatigue (HCF) effects which are modeled with the elastic portion of the mechanical strain range. Additional fatigue experiments at low temperatures and low strain ranges (below 0.5%) would be needed to precisely determine the dominant damage mechanism(s).

The damage mechanism map corresponding to the isothermal LCF behavior of unexposed L- and T-oriented DS GTD-111 with $R_\varepsilon$=*-1* and $\dot{\varepsilon} = 0.5\%/s$, shown in Fig. 6.1, indicates that the experimentally-observed transition between fatigue-dominant and environmental-fatigue dominant crack initiation behavior is dependent of the

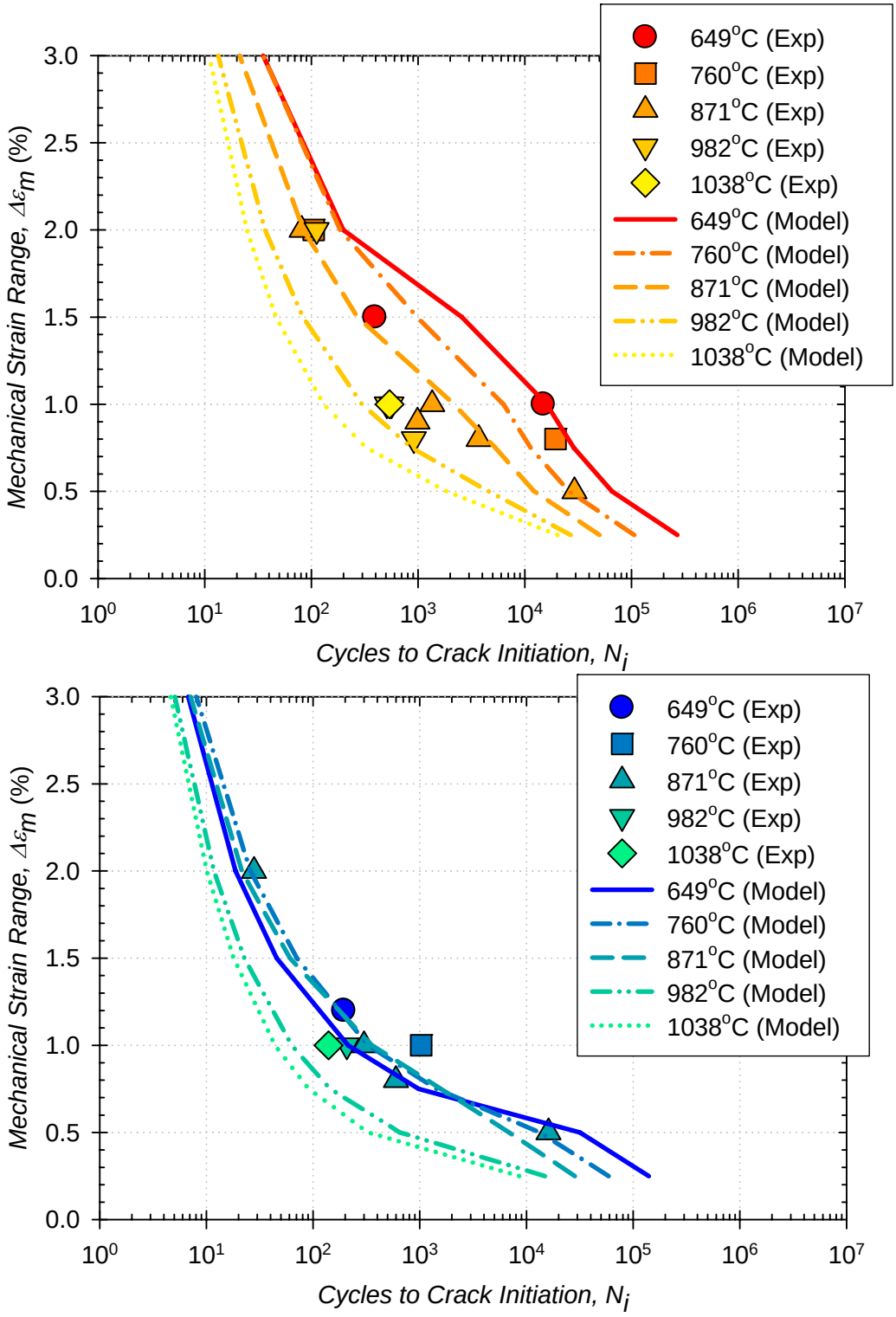


***Figure 6.21:*** *Correlations of total life based on (a) L- and (b) T-oriented DS GTD-111 under LCF conditions. For each case $R_\varepsilon$=-1, and* $\dot{\varepsilon} = 0.5\%/s$ *.*

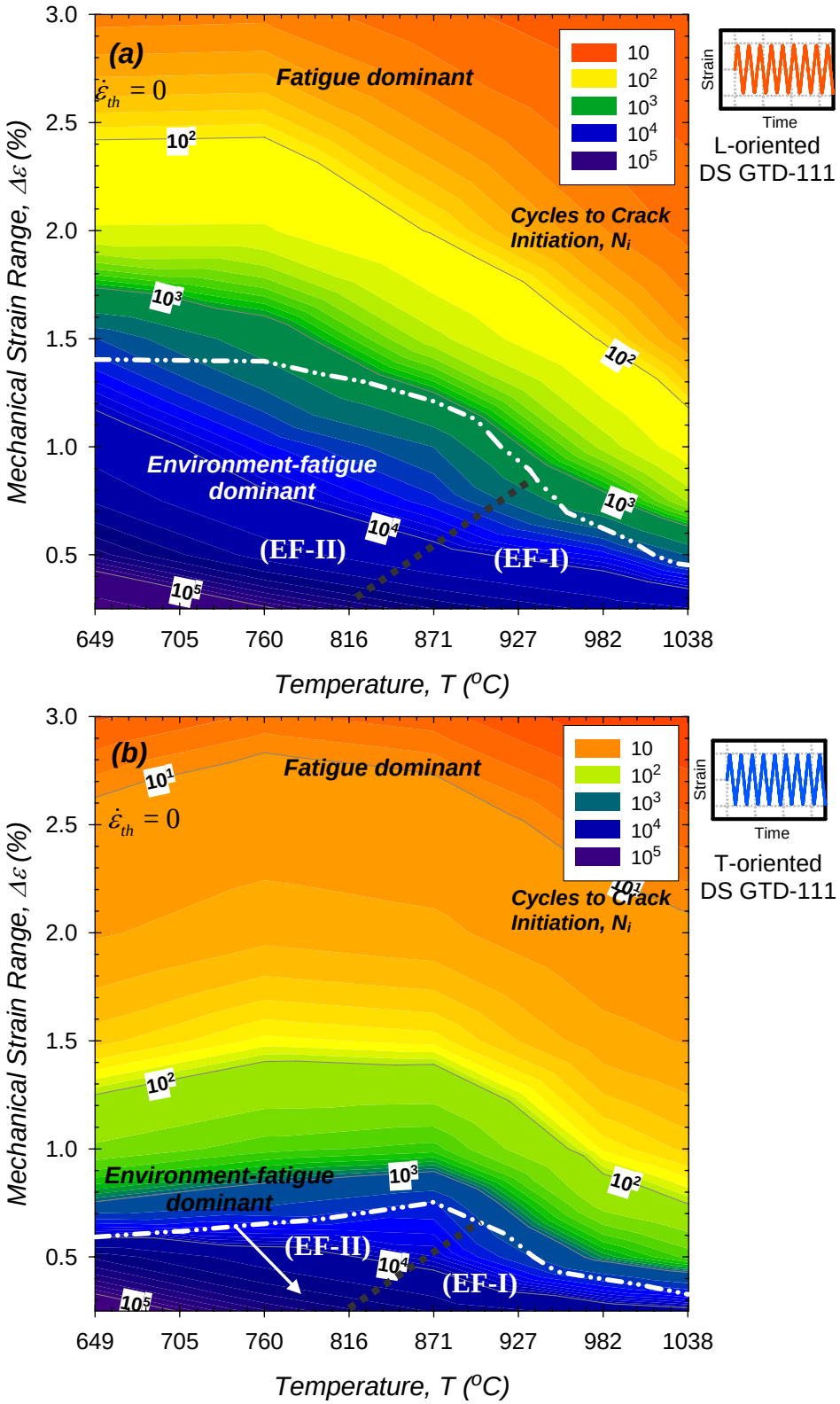


***Figure 6.22:*** *Predictions of total life based of (a) L- and (b) T-oriented DS GTD-111 under continuous cycling conditions. For each case* $R_\varepsilon$*=-1,* $\dot{\varepsilon}_{th} = 0$*, and* $\dot{\varepsilon} = 0.5\%/s$*.*

combination of $\Delta\varepsilon_m$ and $T$. For example, below 871°C for any level of $\Delta\varepsilon_m$, oxide spiking was not observed as a contributor to crack initiation. The transition contour shown in Fig. 6.1 is super-imposed in Fig. 6.22 to segment the region in which total crack initiation life is correlated with environmental-fatigue dominant term. The sub-region "EF-I" is the region in which oxide spiking was observed, and "EF-II" is the region where oxide spiking was not observed; however, crack initiation life in "EF-II" is likely to be sensitive to microstructural discontinuities (i.e., inclusion size, morphology, distribution) coupled with elevated stress due to geometric stress concentrations. With a higher resolution of a LCF data at combinations of $\Delta\varepsilon_m$ and $T$ in the vicinity of the damage mechanism transition in Fig. 6.1, a well-defined transition curve separating "EF-I" and "EF-II" can be developed.

All predictions to this point thus far were based on unexposed DS GTD-111 cycled in laboratory air. Comparisons of the predicted lives of the material tested in air are compared with those tested in for the "semi-inert" environment in Fig. 6.23. Reducing the oxygen content in the atmosphere increases the life of both orientations of the material (Fig. 6.23) by a slight factor.

Pre-exposure effects on predicted life are shown in Fig. 6.24. In each of the pre-exposed cases shown, the pre-heating conditions were carried out in at 982°C. Various combinations of environment and pre-exposure times were applied. For each case the material was subsequently cycled at 871°C. For the L-oriented material, pre-exposure has an effect on life when the material is cycled below $\Delta\varepsilon$ = 1.6%. This threshold exists at $\Delta\varepsilon$ = 1.1% for the T-oriented material. Amongst air and the simulated IGCC pre-exposures, the latter has the most damaging effect on life. Decreasing the duration at

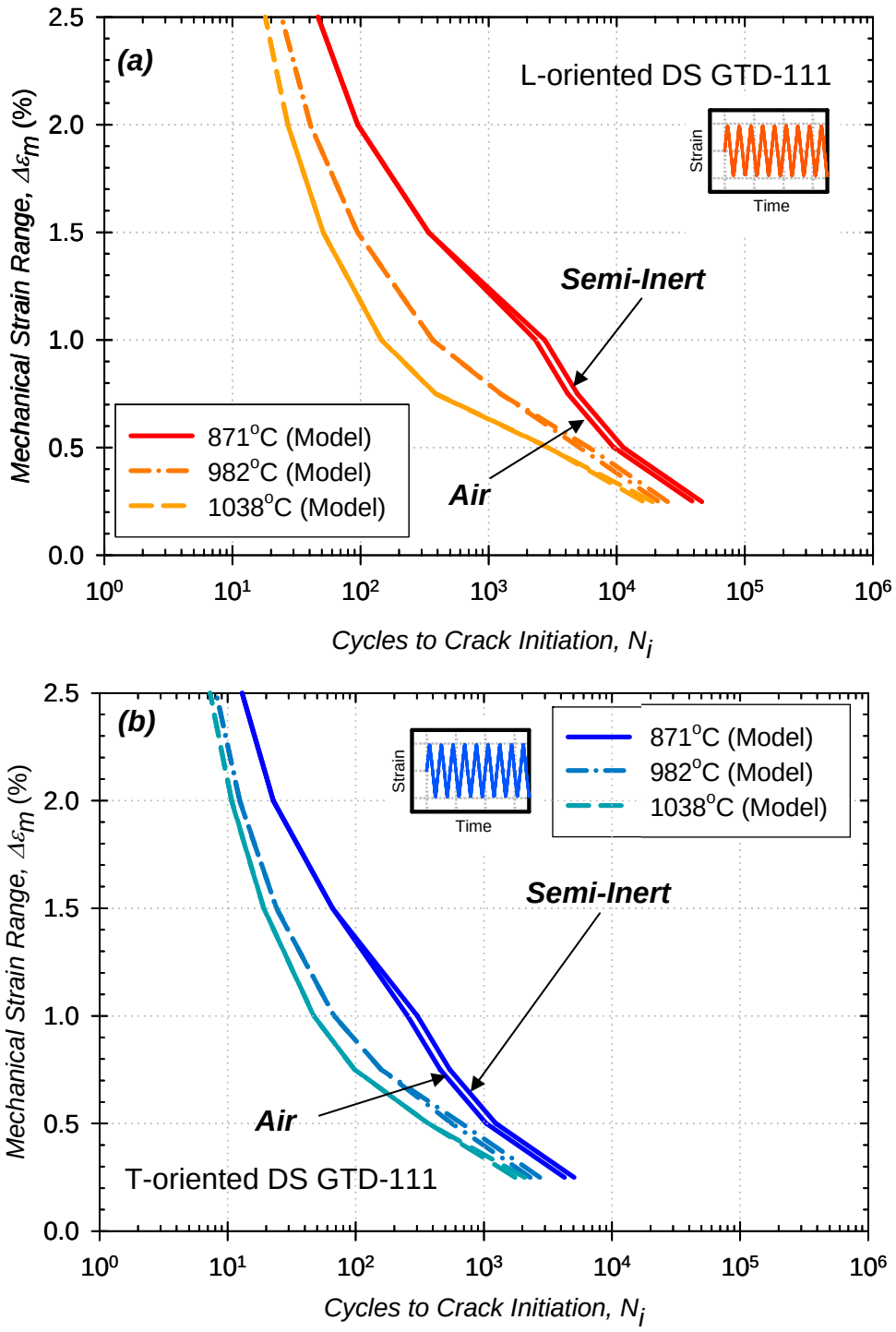


***Figure 6.23:*** *Predictions of total life based on (a) L- and (b) T-oriented DS GTD-111 under LCF conditions in air* $\left(F_{O_2}=0.21\right)$ *and semi-inert* $\left(F_{O_2}=0.02\right)$ *environment. For each case* $R_\varepsilon$*=-1, and* $\dot{\varepsilon}=0.5\%/s$.

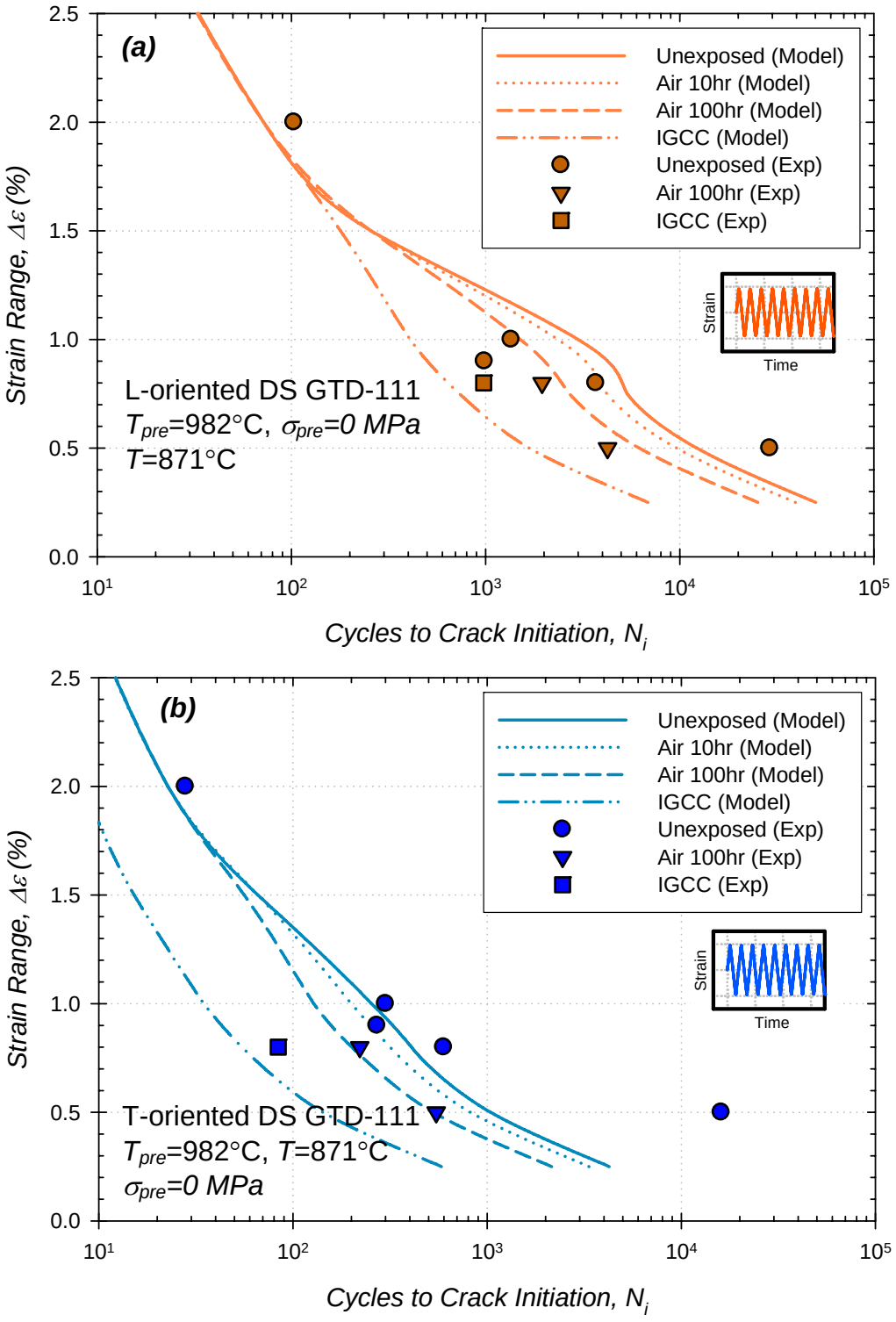


***Figure 6.24:*** *Correlations of total life based on pre-exposed (a) L and (b) T-oriented DS GTD-111 under LCF conditions in air. For each case $R_\varepsilon$=-1, and $\dot{\varepsilon} = 0.5\%/s$.*

which a specimen is pre-exposed in air has the effect of increasing the predicted life. The upper bound on predicted life under any type on pre-exposure is the life of the unexposed material.

The damage boundary interpolation technique was also applied to analyze both "pre-exposed" and "semi-inert environment" cycled cases, as shown in Fig. 6.25. The predicted transitions from fatigue to environment-fatigue damage for both the L- and T-oriented material are affected the most by long term pre-exposure to the simulated IGCC environment. The shapes of the contours do not change greatly for the air-exposed and unexposed cases. Compared to the L-oriented material, however, predicted contours for the T-oriented material occur at lower mechanical strain ranges for constant temperature. For identical fatigue conditions, DS Ni-base are designed to exhibit material properties facilitating higher fatigue strength along the primary stress axis compared to that of the transverse axis. This is a consequence of the lower elastic modulus and high yield strength along the L orientation.

*Crack Initiation Life Under Isothermal-Creep Fatigue Conditions*

Total life predictions were made for the subject material cycled under isothermal creep-fatigue conditions. Although dwell periods ranging from 2 *min* (0.03 *hr)* to $3.75\times10^5$ *min* (6250 *hr*) were simulated, only short dwell periods are shown in Figs. 6.26 and 6.27. For either material, the model predicts nearly identical lives at any temperature level with a mechanical strain range of 2.0%. Fatigue damage dominants at high strain ranges irrespective of the hold time or type. As the strain range is decreased to 1.0%, there is a transition in the dominant mechanism that causes crack initiation in the L-

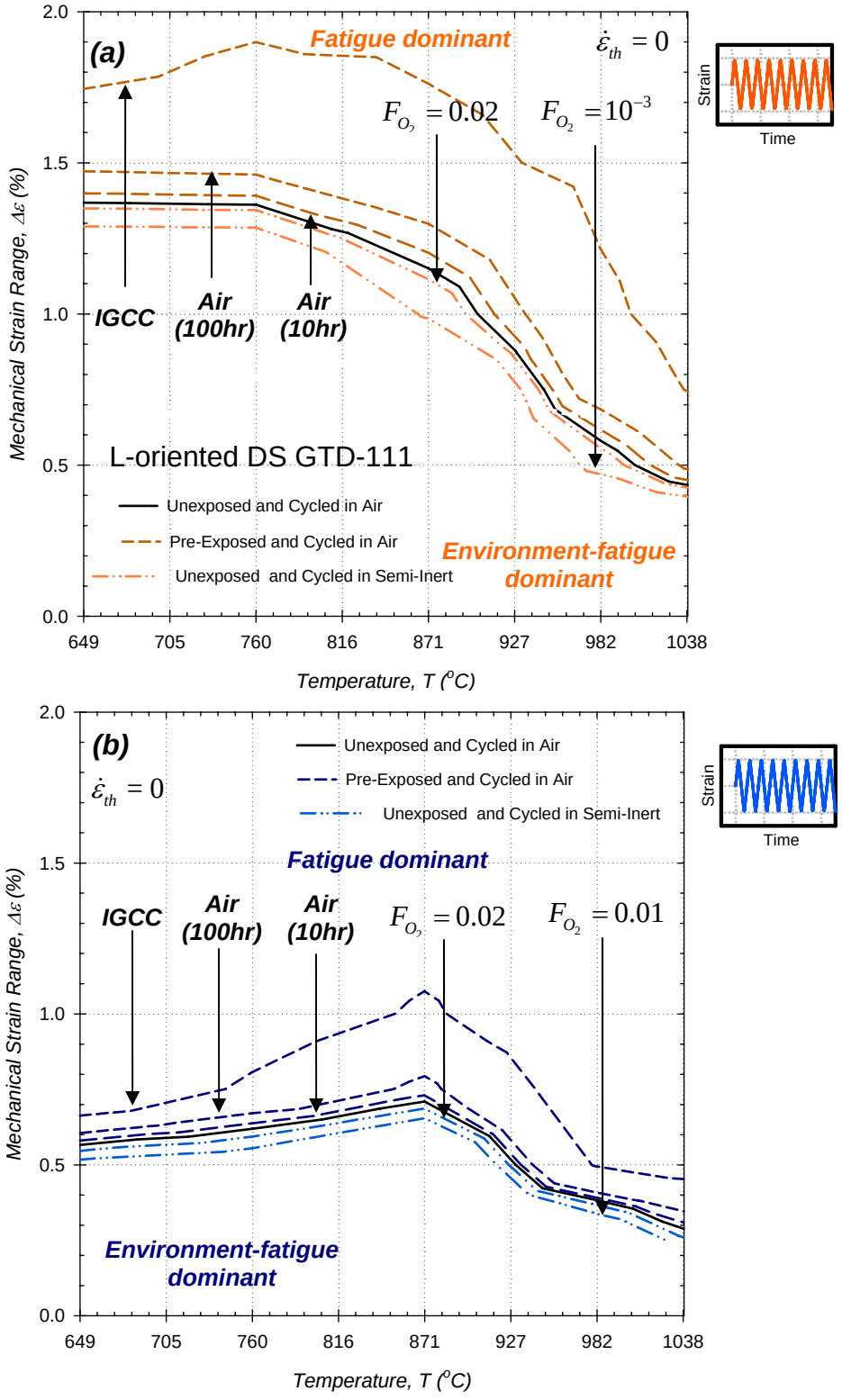


***Figure 6.25:*** *Predictions of transition in dominant damage mechanism based of (a) L and (b) T-oriented DS GTD-111 under continuous cycling conditions. For each case* $R_\varepsilon$*=-1,* $\dot{\varepsilon}_{th} = 0$*, and* $\dot{\varepsilon} = 0.5\%/s$*.*

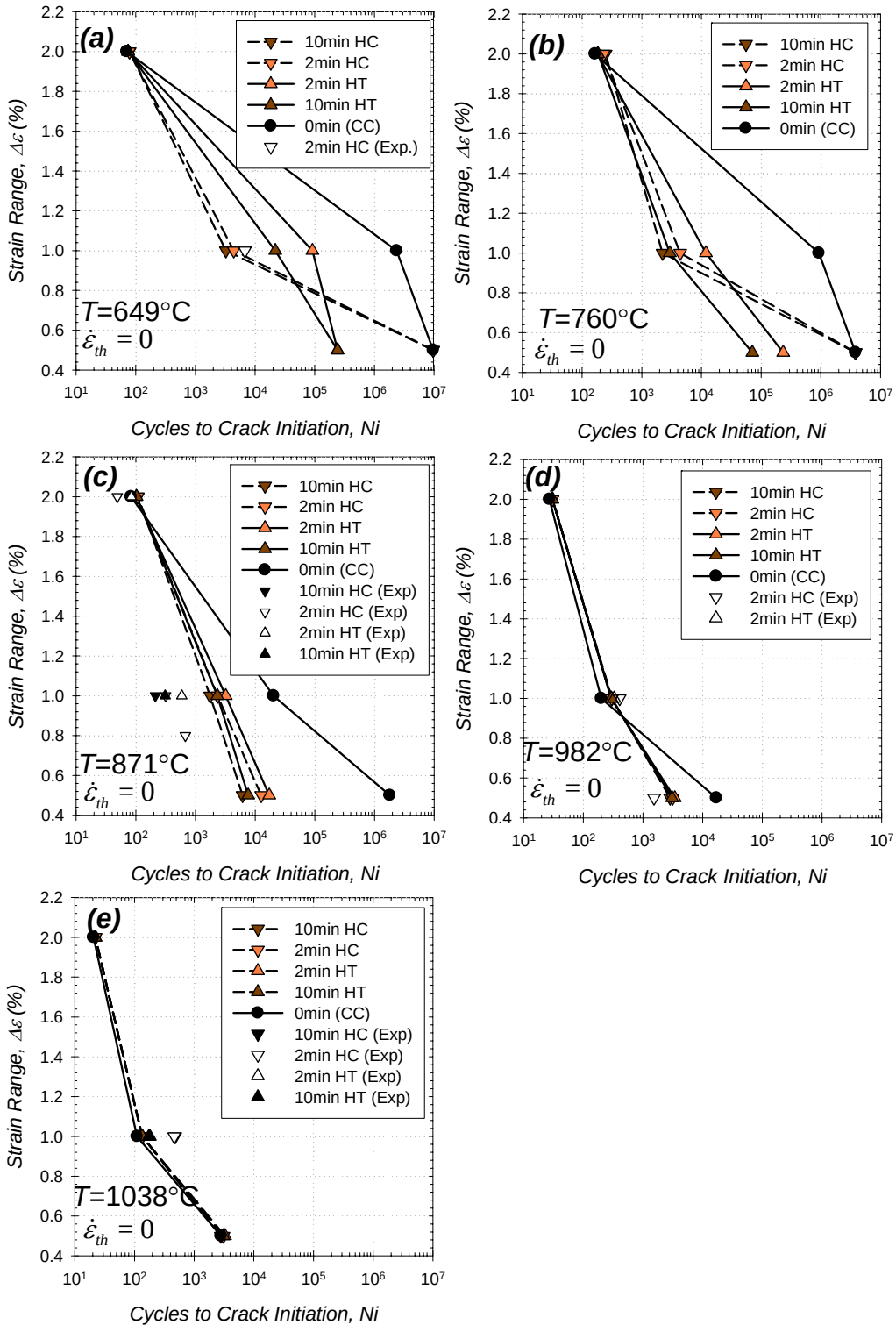


***Figure 6.26:*** *Correlations of total life based on L-oriented DS GTD-111 under creep-fatigue conditions at various strain rates. For each case $R_{\varepsilon}$=-1.*

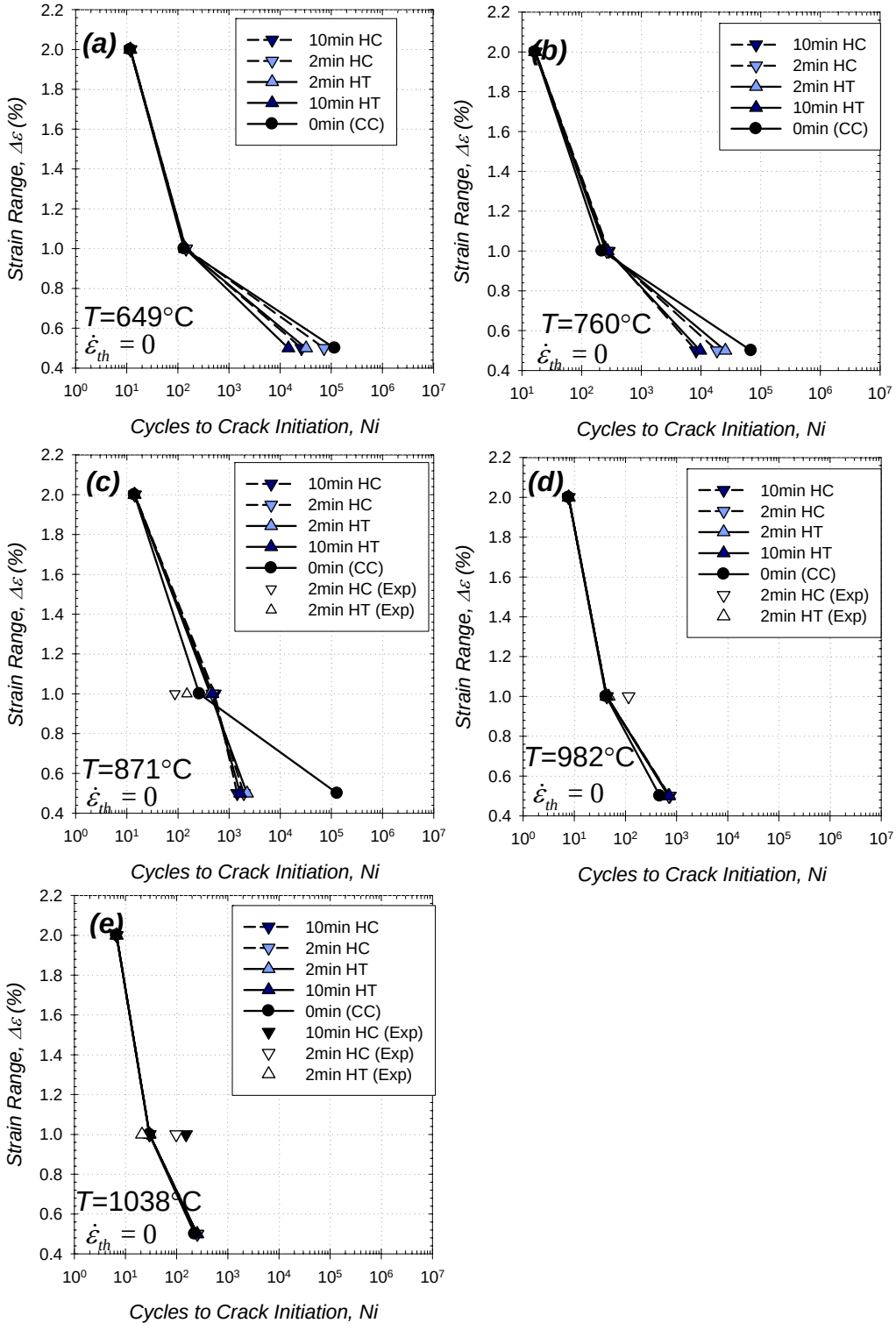


***Figure 6.27:*** *Correlations of total life based on T -oriented DS GTD-111 under creep-fatigue conditions at various strain rates. For each case* $R_\varepsilon$*=-1.*

oriented material at and below 871°C. This phenomenon only occurs in the T-oriented material at a strain range of 0.5%.

Dominant damage mechanism boundaries have been super-imposed over total crack initiation life contours for both the L- and T-oriented material, as shown in Fig. 6.28 and 6.29. The damage boundaries correspond to either such that $N_i^{fat} / N_i^{cr} = 1$ or such that $N_i^{fat} / N_i^{env} = 1$. Compression creep-fatigue cases are shown on the left, while HT cases are on the right. Abscissas on both planes are log-scaled, and predictions along the center-line correspond to CC conditions having a pseudo hold time of 0.003 *min* ($5.3\times10^{-5}$ *hr*). At the small strain range of 0.5%, all forms of damage mechanisms are present in the ranges of temperature versus hold time. Depending on the temperature level, creep mechanisms dominate at dwell periods above an hour. In L-oriented DS GTD-111, the environmental-fatigue mechanism is active during compressive dwells at low temperatures. The fatigue mechanism dominates at high temperature, and it also separates the creep and coupled environmental-fatigue damage regimes. Because the plastic strains are typically larger in the T-oriented cases, crack initiation is controlled by fatigue mechanisms at more $t_h$-$T$ combinations that in L-oriented cases.

As the strain range is increased from 0.5% (Fig. 6.28a) to 1.0% (Fig. 6.29a) to 2.0% (Fig. 6.29b) in the L-oriented cases, the dominance of environmental-fatigue damage is eliminated. Even with the increases in mechanical strain range, creep damage is still operative at long tensile dwell periods. The model predicts that at these higher strain ranges, $N_i$ in T-oriented DS GTD-111 is dominated by fatigue damage.

The identical analysis procedure used to segment the "environmental-fatigue dominant" damage region in Fig. 6.22 was repeated for Fig. 6.28. These transition

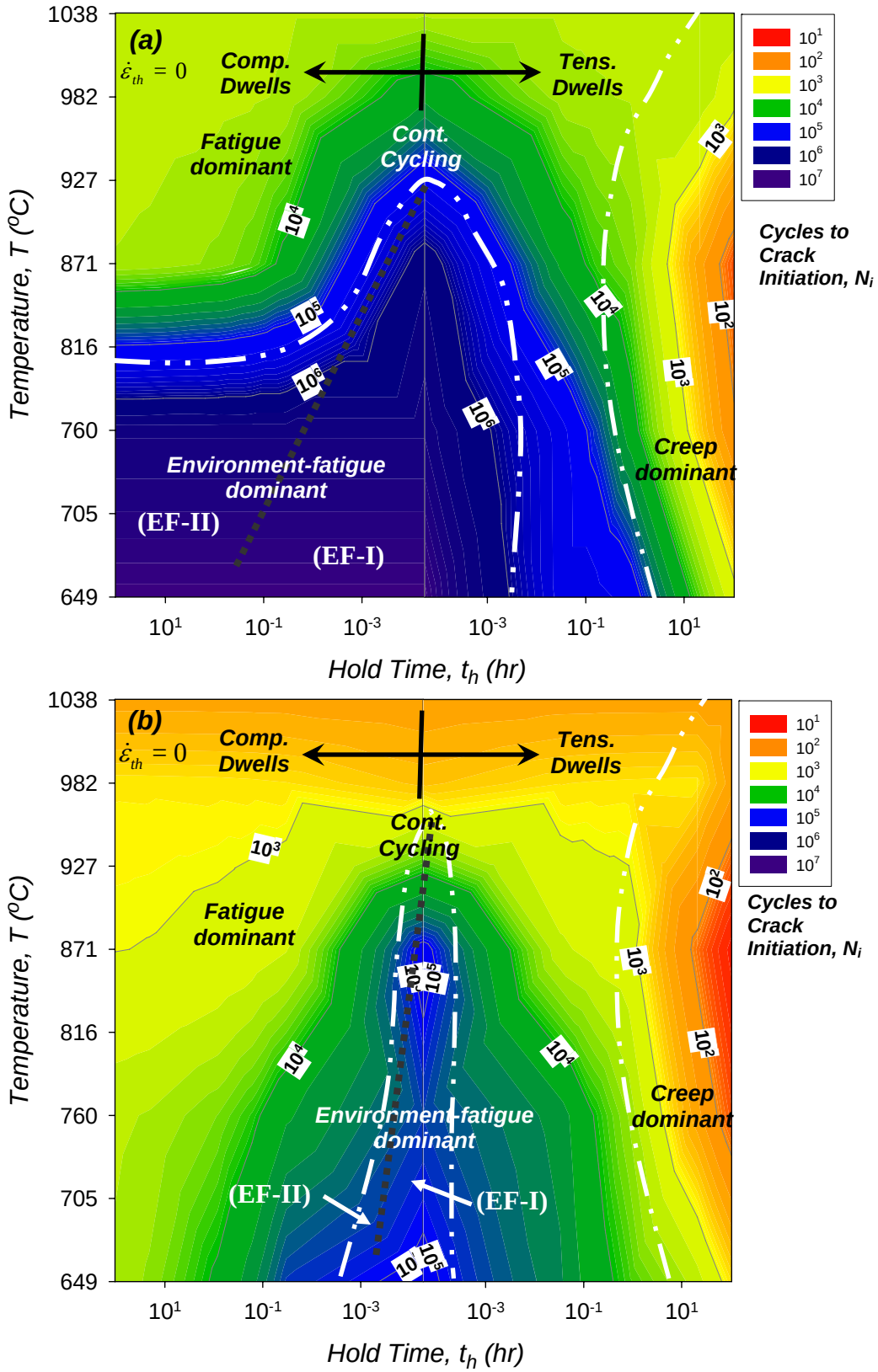


***Figure 6.28:*** *Predictions of total life based of (a) L- and (b) T-oriented DS GTD-111 under creep-fatigue conditions. For each case* $\Delta\varepsilon = 0.5\%$ $R_\varepsilon$*=-1,* $\dot{\varepsilon}_{th} = 0$*, and* $\dot{\varepsilon} = 0.5\%/s$*.*

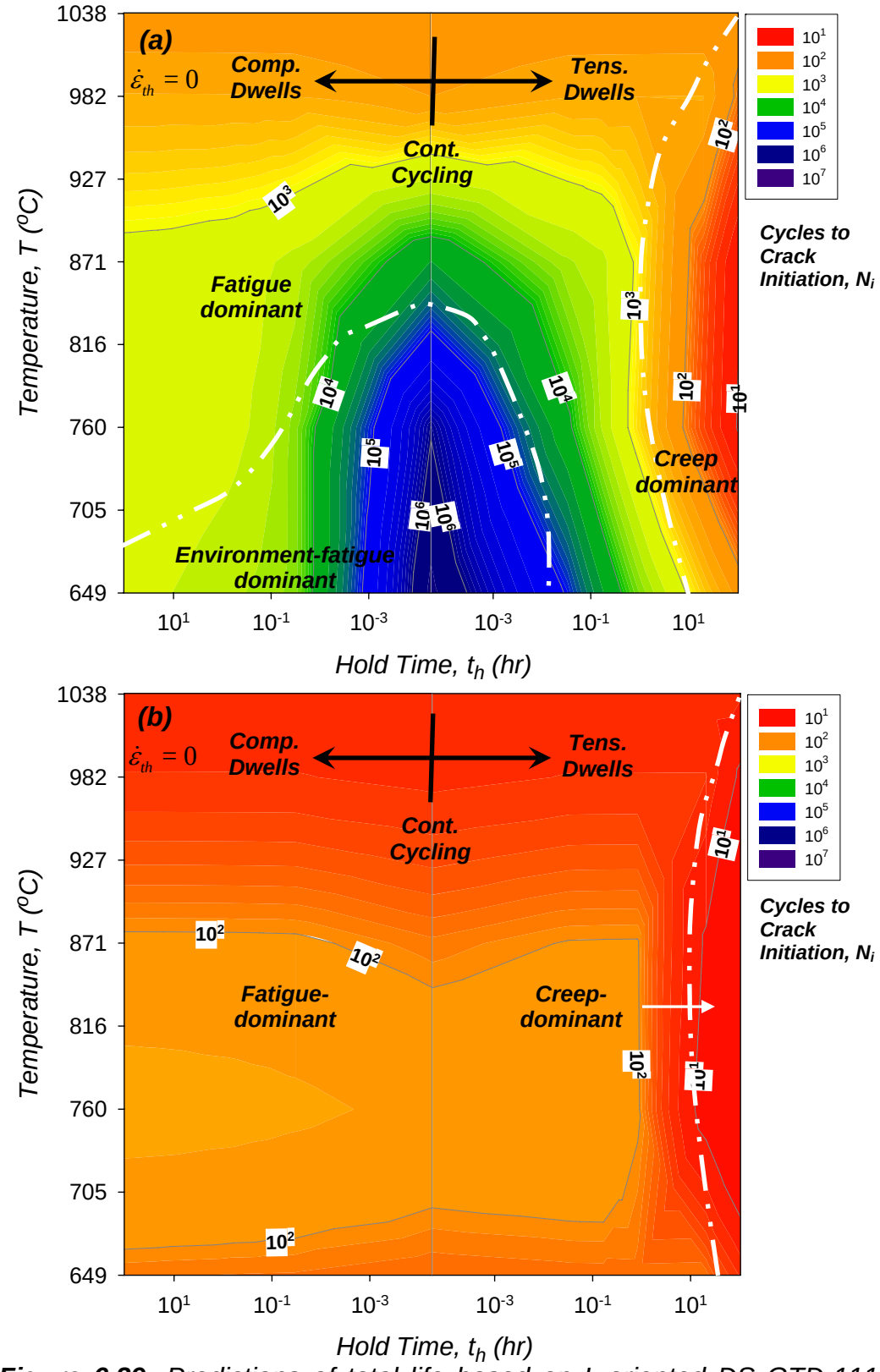


***Figure 6.29:*** *Predictions of total life based on L-oriented DS GTD-111 under creep-fatigue conditions with (a)* $\Delta\varepsilon = 1.0\%$ *and (b)* $\Delta\varepsilon = 2.0\%$*. For each case* $\Delta\varepsilon = 0.5\%$ *$R_\varepsilon$=-1,* $\dot{\varepsilon}_{th} = 0$*, and* $\dot{\varepsilon} = 0.5\%/s$*.*

contours were experimentally-obtained from the fatigue damage mechanism maps shown in Fig. 6.7.

*Crack Initiation Life Under Thermomechanical Fatigue Conditions*

Total life predictions based on DS GTD-111 were made for both in-phase and out-of-phase TMF conditions, as shown in Fig. 6.30. For a mechanical strain range of 1.0% with temperature cycling between $T_{min}$ = 538°C and $T_{max}$ = 927°C, both L- and T-oriented material are predicted to fail more rapidly in OP cycling compared to IP cycling. This trend is consistent if $T_{max}$ is increased to 1038°C; however, crack initiation occurs even fewer cycles. Generally, the L-oriented material withstands more cycles to crack initiation than T-oriented DS GTD-111.

Contours of constant crack initiation life are shown for both orientations of the DS material in Fig. 6.31. Deformation data from FEM simulations, which are listed in Appendix E.) were used to make the predictions. In each plot, the endpoints of the collection of thermal strain range, i.e., -0.70% and 0.70%, correspond to OP cycling with $T_{min}$ = 538°C and $T_{max}$ = 1038°C and IP cycling with $T_{min}$ = 538°C and $T_{max}$ = 1038°C. As such, the left half-planes of both plots correspond to the variation of $T_{max}$ from 1038°C to 538°C. The origin of the abscissa corresponds to the isothermal case. In the right-half planes, $T_{max}$ increases from 538°C to 1038°C.

Damage boundaries were interpolated between $(\Delta\varepsilon_{th}, \Delta\varepsilon_{m})$ points in which damage via fatigue transitioned from being more to less damaging than the environmental fatigue mechanisms (i.e., $N_i^{fat} / N_i^{env} = 1$). These contours of damage crossover are shown in Fig. 6.31. For the L-oriented material, the fatigue damage module is typically more

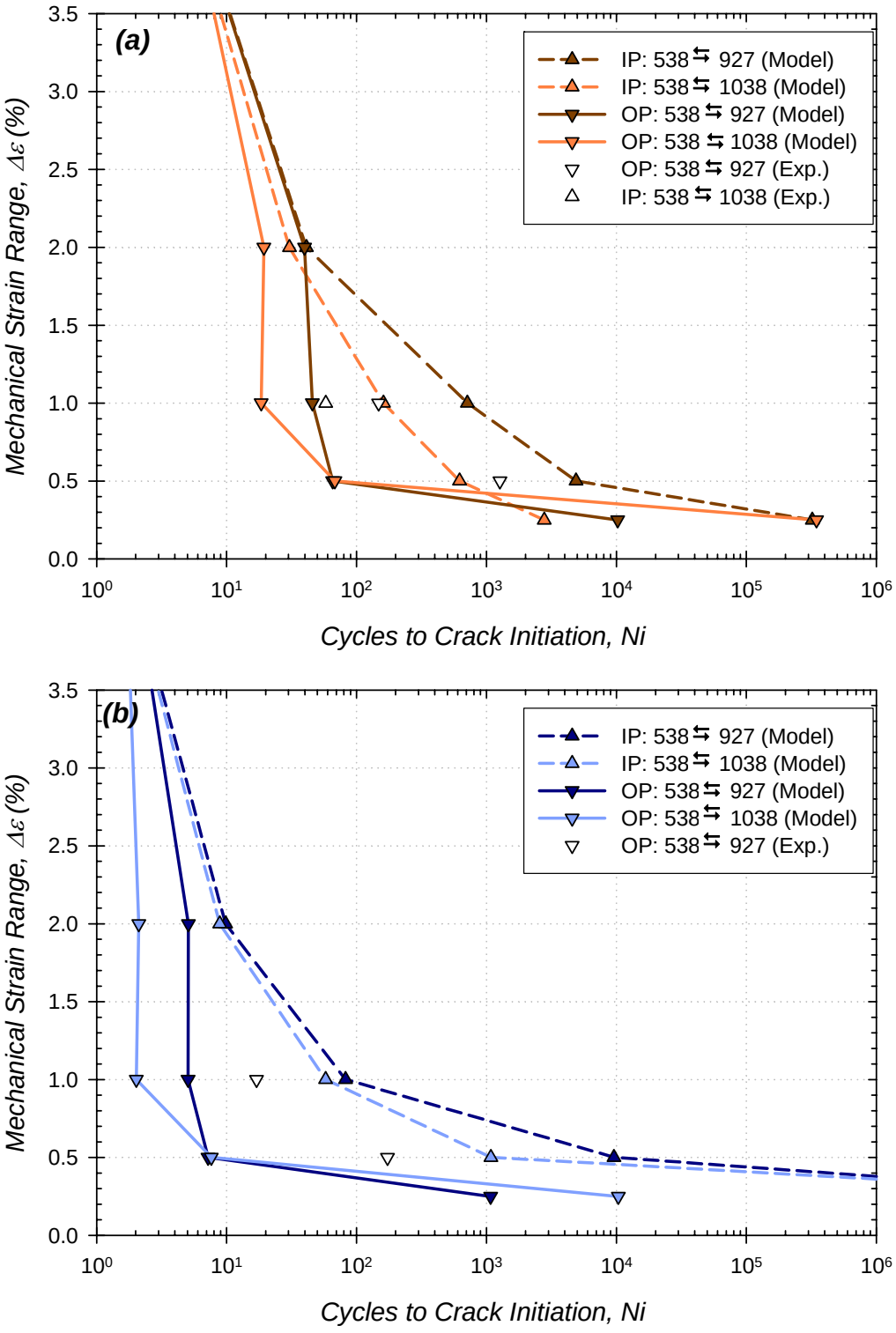


***Figure 6.30:*** *Correlations of total life based on (a) L- and (b) T-oriented DS GTD-111 under TMF conditions ($R_\varepsilon$=-1, $T_{min}$=538℃, $t_{tc} = 180\ s$, $\dot{\varepsilon}_m, \dot{\varepsilon}_{th} \neq const$ ).*

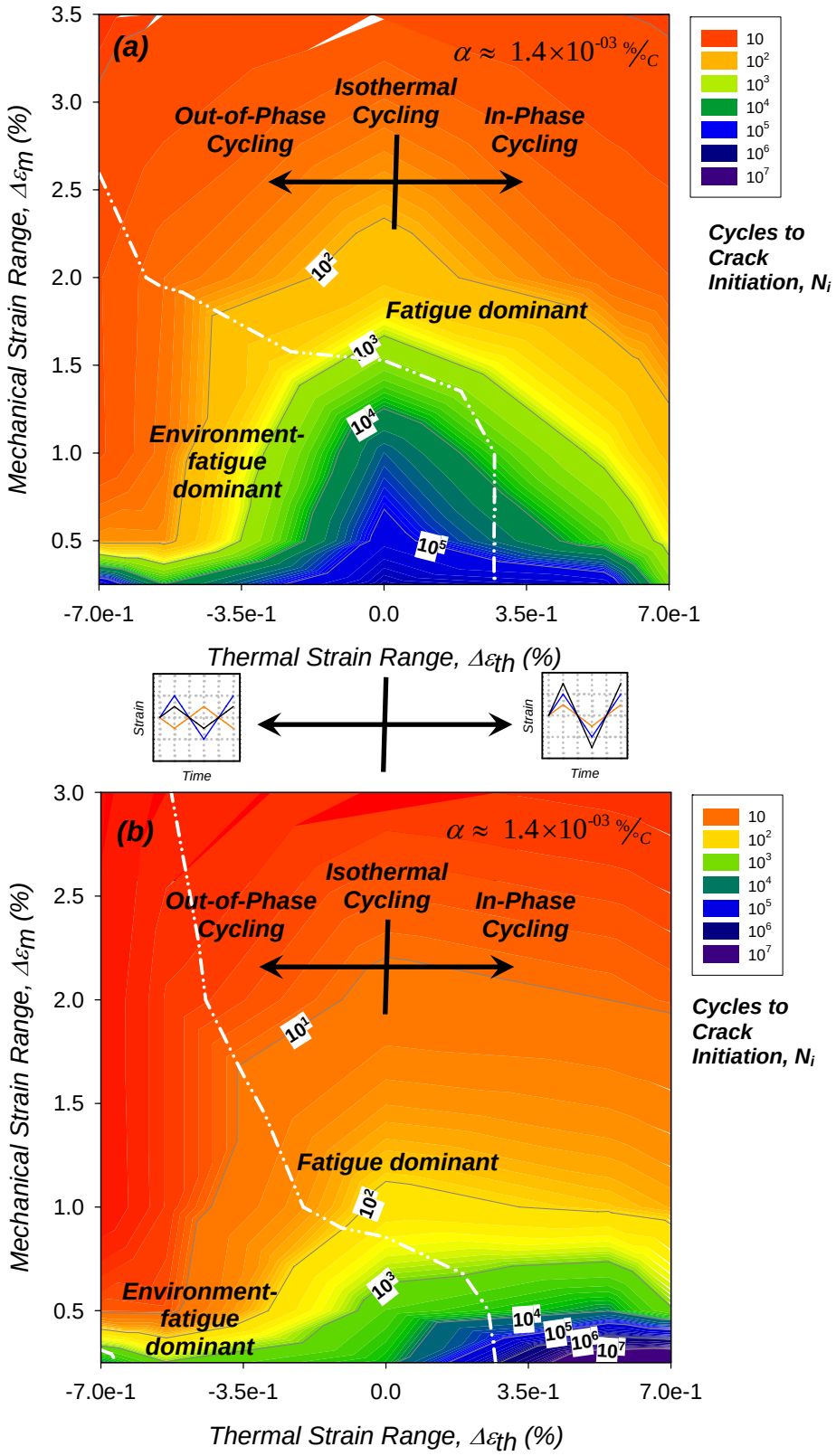


***Figure 6.31:*** *Predictions of total life based of (a) L- and (b) T-oriented DS GTD-111 under TMF conditions ($R_\varepsilon$=-1, $T_{min}$=538°C, $t_{tc} = 180\ s$, $\dot{\varepsilon}_m, \dot{\varepsilon}_{th} \neq const$ ).*

dominant for $\Delta\varepsilon_m$ above 2.0% under either phasing type and during IP cycling for $\Delta\varepsilon_{th}$ = 0.27%. The environmental-fatigue module is dominant elsewhere. For the T-oriented cases, fatigue damage generally dominates for $\Delta\varepsilon_m$ above 1.3% under either phasing type and during IP cycling for $\Delta\varepsilon_{th}$ = 0.16%.

### *6.6 Notes for Model Application*

The formulation presented in the previous sections is composed of modules that are associated with the various forms of damage that were observed to occur in DS GTD-111. The mathematical formulations of each damage module were used because they sufficiently correlated the types of microstructural damage observed in experiments. The fatigue damage module given in Eq. (6.1) is a modification of the Coffin-Manson Law. The creep damage module given in Eq. (6.12) was derived based on experimental observations of creep damage. The coupled environmental-fatigue module given in Eq. (6.38) was analytically derived based on the observations of repeated rupture of surface oxides under a variety of experimental conditions.

Crack initiation life correlations are compared with experiments in Figs. 6.32-6.35. With the exception of a small number of outliers, the model performs well for both L- and T-oriented DS GTD-111 under a variety of conditions including isothermal LCF (Fig. 6.32), isothermal creep-fatigue (Fig. 6.33), pre-exposed and subsequent isothermal LCF (Fig. 6.34), and TMF (Fig. 6.35). Figures 6.32 and 6.33 demonstrate the improvement of the correlations when using the minimum life formulation as opposed to correlations based solely on the formulation based on Eq. (6.1) and the constitutive response (Figs. 6.3 and 6.10).

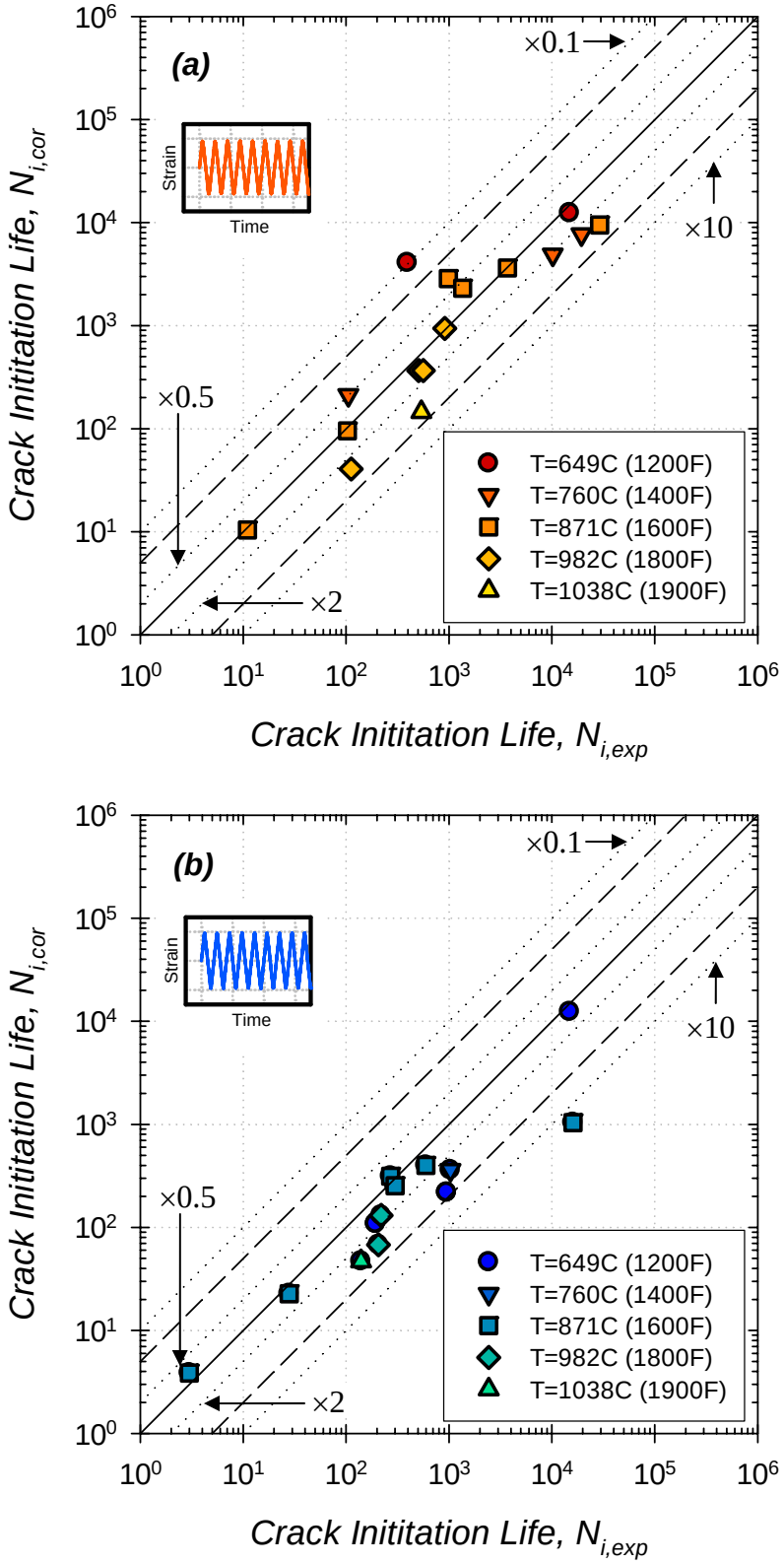


***Figure 6.32:*** *Comparison of experiments and correlations for (a) L- and (b) T-oriented DS GTD-111 under isothermal LCF conditions. For each case $R_\varepsilon$=-1, $\dot{\varepsilon}_{th} = 0$, and $\dot{\varepsilon} = 0.5\%/s$.*

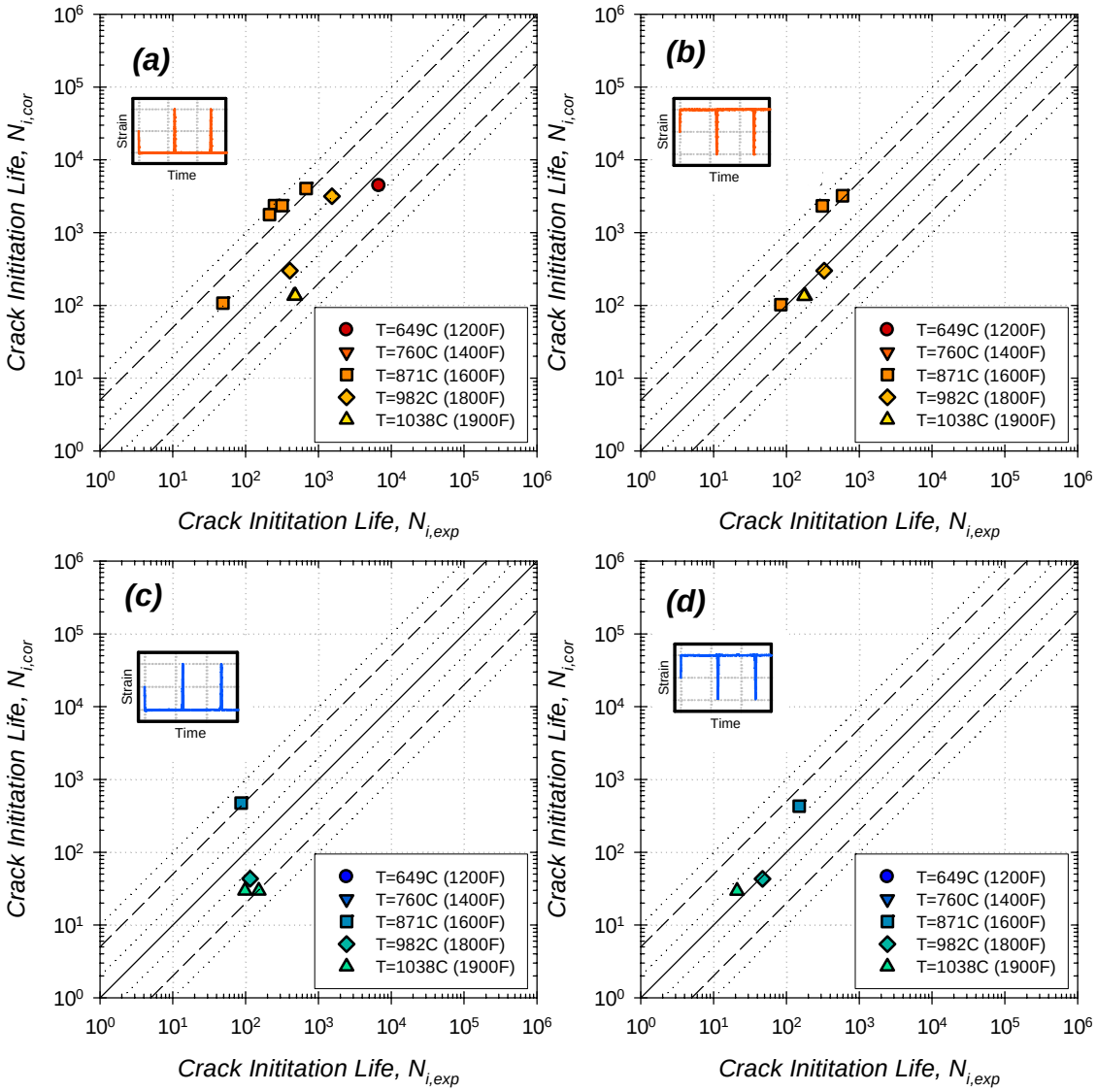


***Figure 6.33:*** *Comparison of experiments and correlations for (a, b) L- and (c,d) T-oriented DS GTD-111 under isothermal creep-fatigue conditions with (a,c) compressive and (b, d) tensile dwell periods. For each case $R_\varepsilon$=-1, $\dot{\varepsilon}_{th} = 0$, and $\dot{\varepsilon} = 0.5\%/s$.*

Under the assumption that the experimental $N_i$ data follow a Gaussian distribution, the best method for quantifying the correlation between the modeled and experimental data is the square of the Pearson product-moment correlation coefficient $R^2$. Since this measure is only meaningful for data sets containing three or more

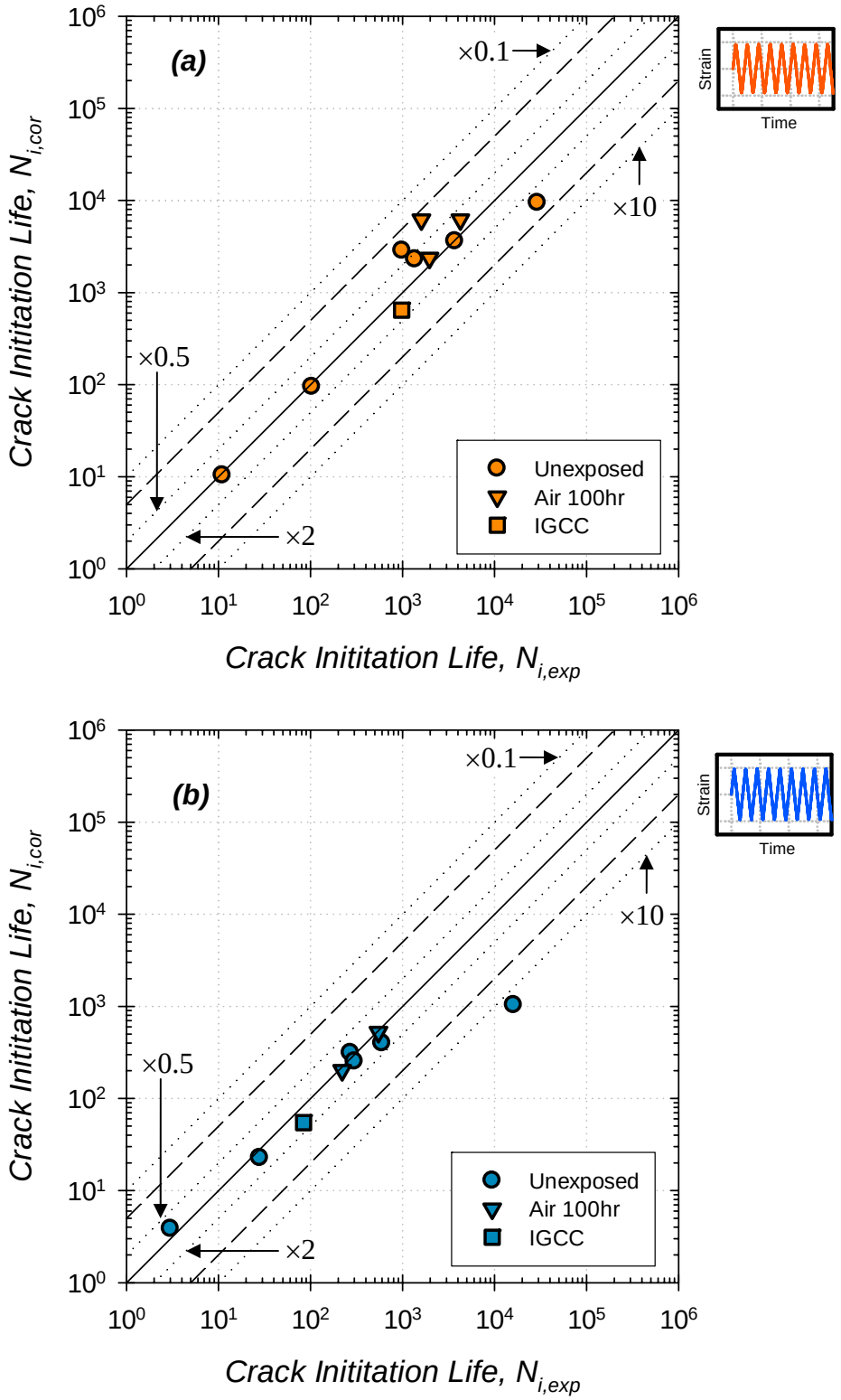


***Figure 6.34:*** *Comparison of experiments and correlations for (a) L- and (b) T-oriented DS GTD-111 under unexposed and pre-exposed isothermal LCF conditions. For each case* $R_\varepsilon$*=-1,* $\dot{\varepsilon}_{th} = 0$*, and* $\dot{\varepsilon} = 0.5\%/s$*.*

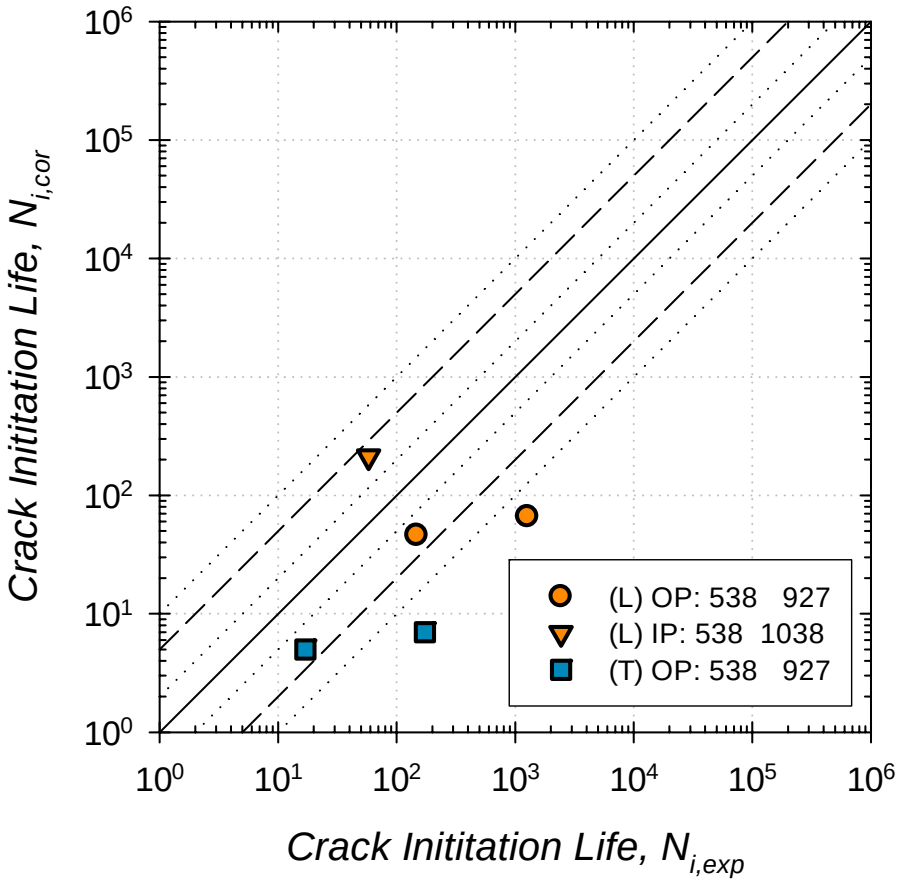


***Figure 6.35:*** *Comparison of experiments and correlations for L- and T-oriented DS GTD-111 under thermomechanical fatigue conditions. For each case $R_\varepsilon$=-1, $t_{tc} = 180\ s$, $\dot{\varepsilon}_m, \dot{\varepsilon}_{th} \neq const$.*

elements, $R^2$ was only determined for a limited number of experimental conditions, as shown in Table 6.4. The listed values demonstrate that the model performs well for many of the conditions. Based on the observation that the L-oriented data lay generally lies in closer proximity to the $N_{i,exp} = N_{i,cor}$ axes (Figs. 6.32-6.35), the model performs better for L-oriented DS GTD-111 than the T-oriented material.

It is reasonable that the form of this model can be used to make predictions of crack initiation life for other variations of DS Ni-base superalloys (e.g. DS Mar-M247, René80 DS); however, experimental results are needed to determine if the material constants listed in Tables 6.1 - 6.3 are appropriate. Additionally, since the L-oriented

material has mechanical properties that resemble single crystal (SC) materials, this model is also applicable to SC turbine blade materials.

***Table 6.4:*** *Performance of crack initiation life model for DS GTD-111 material*

| Experiment Type | Orientation | Temperature, $T$ (°C) | Temperature, $T$ (°F) | Pearson Product[†], $R^2$ |
|---|---|---|---|---|
| Low Cycle Fatigue (LCF) | L-oriented | 760 | 1400 | 0.99 |
| | L-oriented | 871 | 1600 | 0.89 |
| | L-oriented | 982 | 1800 | 0.94 |
| | T-oriented | 871 | 1600 | 0.85 |
| Compressive Creep-Fatigue (CF-HC)[‡] | L-oriented | 871 | 1600 | 0.91 |
| | L-oriented | 1038 | 1900 | 0.99 |
| Tensile Creep-Fatigue (CF-HT)[‡] | L-oriented | 871 | 1600 | 0.91 |

[†] *Only computed for experimental types with three or more sets of data points*

[‡] *Various hold times*

The mathematical formulation assumes the material had been subjected to no prior fatigue loading whatsoever. Except in cases containing pre-exposure in laboratory air or the simulated IGCC environment, the DS GTD-111 material did not initially contain any fatigue damage whatsoever. In order to capture damage evolution during fatigue cycling a damage-rate model that correlates a physically measurable quantity, such as microcrack propagation, would need to be developed. Correlations of crack initiation life and the dominant damage were made with the formulation under the

assumption that the material was subjected to unvarying thermal, mechanical, environmental conditions for the duration of loading (e.g. $d\Delta\varepsilon_m/dt = 0$, $dt_{hc}/dt = 0$, etc.). In order to capture the effects of variable loading conditions, a nonlinear damage model would need to be developed.

### *6.7 Summary of Modeling Capabilities*

To visualize the regimes under which the relevant mechanisms operate, the notion of damage mechanism mapping was applied. A variety of high temperature mechanical and thermal test types were conducted to identify and categorize the damage mechanisms occurring in DS GTD-111 under a wide range of test conditions. Dominant damage mechanisms were identified primarily by extensive post-test metallographic analysis. Damage mechanism maps were also useful in developing mathematical models of crack initiation, since the formulation of the model depends on the mechanism. A separate module was developed for each basic form of damage that was observed via microscopy.

*Orientation Effects*

The effect of orientation (e.g. L versus T) on crack initiation life was determined for DS GTD-111. Subjecting both the L- and T-oriented materials to sets of identical testing configurations allowed the discrepancy of deformation and damage responses to be determined. In all cases, $N_i$ for the L-orientated material exceeded that of the T-oriented material. This is primary due to the fact that under identical conditions the plastic portion of cyclic strain range exhibited by the T-oriented material generally exceeds that of the L-oriented material. This disparity in life is also due to the fact that

grain boundaries lying transverse to the primary stress axis are favorable locations of crack initiation due to their high content of carbides.

Based on literature (Wright and Anderson, 1980; Ohno, et al., 1992; Okada et al., 1998) describing the behavior of comparable DS Ni-base superalloys between the L and T orientations, $N_i$ correlations for DS GTD-111 were made via $f_{el}(\omega)$, $f_{cr}(\omega)$, and $f_{in}(\omega)$ that were designed to interpolate off-axis orientations of the material between L $(\omega = 0)$ and T $(\omega = \pi/2)$.

*Dwell Effects*

The sign of the dwell played a key role in determining the dominant damage mechanism. Tensile dwells (e.g. HC) promoted creep damage characterized by extensive subsurface cracking. Subsurface damage occurring at inclusions and at GBs indicated dominantly creep-induced damage. To model the effect of HT on life under creep-fatigue conditions, $\Theta_{cr} \exp\left( \frac{B'_L \tilde{q}(\omega, \sigma_{tens})^{-k_L}}{RT} \right)$ is a term that serves as the upper limit on the summation of the tensile hold periods. This term captures the effect of stress, temperature, and orientation that are all critical determinants of creep driving force and rupture time.

Alternatively, compressive dwells (e.g. HC) promoted an environment-fatigue mechanism characterized by multiple cracks forming on surface in the brittle oxide layers. The surface damage was caused by oxide spiking, which is widely-recognized as an indication of coupled environment-fatigue damage. In both cases, crack initiation lives were shortened relative to those obtained from CC tests but with otherwise identical

conditions. To model the effect of HC on life under compressive creep-fatigue conditions, the product $\left(1+t_{hc}\delta'_{hc}\right)^{\frac{-1}{\beta}}\sqrt{\tau_{hc}t_{hc}+1}$ was used. This form was selected since it is relevant to the cyclic oxide rupture term that models the oxide spiking mechanism, and since it does converges to 1 as the dwell period is reduced to 0.

*Environmental Effects*

Fatigue testing in a semi-inert gas environment was used to characterize the effect of environment on crack initiation of DS GTD-111. To do so, a semi-closed gas chamber was designed and fabricated to enclose a cycling specimen in a non-corrosive environment at high temperature. Decreasing oxygen from the vicinity of the specimen, by flooding the chamber with Ar, prevented the oxide spiking mechanism from occurring under testing conditions in which it rapidly occurs in the presence of static air. In its place, fatigue damage dominated, and the crossover in mechanisms resulted in an increase of crack initiation life. This effect on life as captured using an Arrhenian diffusion term (e.g. $\theta_{OX,0}\left(F_{O_2}\right)^{\theta_{OX,1}}$) written as a function of oxygen fraction, $F_{O_2}$. Several stress-free exposures at elevated temperature were carried out to establish this relation.

*Pre-Exposure Effects*

The effects of prior exposure on crack initiation behavior of DS GTD-111 were investigated by pre-exposing specimens to high temperature either in unloaded or sustained loading conditions.. For the unloaded and compressively loaded cases, formation of the oxide and γ′-depleted layers allowed surface cracks to initiate very rapidly during subsequent fatigue cycling. Simulated IGCC environment (rich-in highly

corrosive sulphidizing contaminants) was more detrimental to the crack initiation life than the oxidizing environment. The most malevolent pre-exposure configuration was that in which a sample was subjected to a sustained tensile load at high temperature. During subsequent loading, cracks were nucleated by coalescence of microcracks that had formed near inclusion particles during the pre-exposure period. In either case, the damage mechanism responsible for crack initiation in the material was moderated by the pre-exposure condition.

The term $\left(h_{cr} - 2h_{pre}\right)^{\frac{-1}{\beta}}$ was developed to capture the effect of stress-free surface degradation on the reduction of $N_i$, when coupled environmental-fatigue damage dominates. Since $h_{pre}$ is a function of pre-exposure conditions, variables such temperature, time, and environment are included in the formulation.

*Application of Deformation Modeling*

An anisotropic elastic crystal viscoplasticity model developed by Shenoy and coworkers (Shenoy et al., 2005) was employed to characterize the deformation behavior of DS GTD-111. The constitutive model has been developed to account for many of the features (e.g., heterogeneous microstructure, crystallographic orientation) that are common to dual phase $L1_2$-structured Ni-base superalloys tending to have rather large crystallographic grains. Using this time-dependent, constitutive model allows calculation of the decomposed elastic and inelastic response. Under dominantly-fatigue conditions when creep and environmental damage mechanisms are weak, the accuracy of the model is critical for capturing damage and life. As a part of this study, deformation responses for both orientations of the material were determined for a variety of testing

configurations. The constitutive model captures the increase of the plastic strain range with the presence of dwell periods.

*Crack Initiation Modeling*

This physically-based formulation presents a framework that can be used to determine $N_i$ for other DS Ni-base superalloys under both isothermal and non-isothermal LCF. Crack initiation life correlations, based on the life models for each damage mechanism, were found to follow the experimental trends. The findings emerging from this work have implications for future development of DS Ni-base superalloys. Several possible avenues of investigation are discussed in Chapter 8.

# 7. CONCLUSIONS

In service conditions, cracks initiate in the Ni-base superalloy directionally-solidified (DS) GTD-111 by way of contributions from a variety of damage mechanisms that are not manifested in the identical manner as when cycled under classical isothermal fatigue testing. In order to develop a comprehensive crack initiation model that accurately accounts for variations in orientation, temperature, cyclic frequency, stress ratio, pre-exposure, firing gas composition, sustained-load hold times, and interactions resulting from complex load histories (i.e., high and low-cycle fatigue, creep-fatigue, thermal-mechanical fatigue, and environmental degradation), several series of thermal and mechanical experimentation were performed. A physically-based model was developed to determine the crack initiation behavior of DS GTD-111 under the wide range of conditions. The model consists of independent modules for each of the three damage mechanisms that have been observed: “fatigue” damage (microcrack nucleation at carbides within dendritic cores), “creep” damage (microvoid growth at inclusions near interdendritic channels and GBs), and “environmental-fatigue” damage (oxide spiking). These modules allow the model to capture the effects of orientation, dwell period, pre-exposure, environment, etc. Calculations are made using test configuration details (i.e., temperature, thermal and mechanical strain rate, strain ratio, strain range, etc.) and the deformation response provided from finite element modeling.

The outcomes of this research are as follows:

**(1) Characterized the dominant damage mechanisms.** Experiments were used simulate the material behavior under a variety of service conditions. Damage occurring to DS GTD-111 which is responsible for failure has been identified by conducting isothermal and non-isothermal fatigue tests, creep-fatigue tests, isothermal unstressed tests, and creep deformation tests. In general, temperatures that were considered ranged from 649ºC (12900ºF) to 1038ºC (1900ºF). Mechanical strain ranged from 0.5% to 4.0%. Strain rate and strain ration were typically held constant at $R_\varepsilon$=*-1*, and $\dot{\varepsilon} = 0.5\%/s$, respectively. The dominant damage mechanisms were due to fatigue damage (crack initiation at subsurface inclusions), coupled environmental-fatigue (surface oxide spiking), and creep (crack initiation at grain boundaries and interdendritic regions).

**(2) Developed a formulation that facilitates estimation of crack initiation behavior under both isothermal and non-isothermal LCF.** Microscopic analyses of samples of tested material were coupled with quantitative test data to develop fatigue damage maps and mathematical models of crack initiation behavior. The model development was supported by data from experiments that isolated the microstructural mechanisms of fatigue, coupled environmental-fatigue, and creep damage. The model consists of three independent modules corresponding to the three dominant damage mechanisms. Finite element simulations and a constitutive model were used to make predictions of the behavior of DS GTD-111.

**(3) Determined the influence of material orientation on crack initiation.** Since crack initiation experiments were carried out on L- and T-oriented DS GTD-111, the influence of material orientation was determined in orientations either longitudinal or transverse to

the DS axis. The observation that the crack initiation lives of L-oriented samples typically exceeded that of the T-oriented samples, is due to the fact that grain boundaries lying transverse to the primary stress axis are favorable locations of crack initiation due to their high content of carbides.

**(4) Defined the role of thermal/mechanical pre-exposure on crack initiation life.** Comparisons of unexposed and pre-exposed samples revealed that the type of pre-exposure influenced the dominant damage mechanism that led to crack initiation under subsequent fatigue cycling. The number of cycles necessary for crack initiation of pre-exposed samples was always less than that of unexposed samples.

# 8. RECOMMENDATIONS

Although it would be convenient to argue that the microstructural damage mechanisms responsible for crack initiation of as-cast, uniaxially-tested, DS GTD-111 conform to the current crack initiation model when applied at conditions well-outside of the range of this study, this may not be accurate. In order to broaden that characterization of this material, several avenues for future work are considered. Listed below are items that would advance the state of knowledge on the fatigue crack initiation behavior of directionally-solidified Ni-base superalloys.

*Determine Off-Axis and Multiaxial Behavior of DS Ni-base Superalloys*

Even though the primary axis of DS gas turbine blading materials is designed to be nearly-aligned with the stress axis, conditions can arise when crack initiation and early growth occur at skew orientations. Conducting creep, creep-fatigue, and TMF tests in the presence of multiaxial loading would lead to the characterization of grain orientation effects on crack initiation life. A multiaxial crack initiation model could be developed once there is more data available on mixed mode fracture and shearing forces acting on oxide spikes.

*Connect Creep Rupture and Crack Initiation of DS Ni-base Superalloys*

In the current investigation, rupture data and microscopy from creep deformation experiments were used to determine the limitations of fatigue-assisted crack initiation. The physically-based module introduced to predict creep damage can be more accurately descriptive of crack initiation if interrupted creep tests are conducted. In general, creep tests are conducted until complete rupture of the material; however, if a creep test is halted prior complete fracture, perhaps in the early stages between secondary and tertiary creep, then more accurate time estimates of to crack initiation life can be developed. Surface replication could be used to determine the evolution of the crack size relative to the overall deformation of the material.

*Connect Service Conditions with Testing Conditions*

A key aim of the current research was to characterize damage evolution in test conditions that simulate those found in actual service conditions. In so doing, DS GTD-111 was subjected to a variety of mechanical, thermal, and environmental conditions. Additional experimental configurations exist that could more precisely duplicate the exact service conditions are thus increase the accuracy of describing which damage and crack nucleation occur in DS GTD-111 and other Ni-base superalloys. These testing thrusts are as follows:

A. Use samples with surface protective coatings

B. Conduct fatigue experiments while simultaneously exposing to a sulfidizing environment

C. Use more realistic thermal and mechanical cycling histories for TMF experiments.

*Conduct High Cycle Fatigue (HCF) Experiments*

The current investigation emphasized LCF behavior of DS Ni-base superalloys. Load-control experiments conducted with negligible cyclic plastic strain ranges should be carried out to characterize the effects of orientation, temperature, hold time, hold type, and mean stress on HCF crack initiation life of both L- and T-oriented DS GTD-111. This corresponds to the EF-II region in Figs. 6.22 and 6.28. Stress-based models should be used to correlate crack initiation under these conditions. Drivers for crack initiation in this regime would be aspects of microstructural discontinuities (i.e., inclusion size, morphology, distribution) coupled with elevated stress due to geometric stress concentrations.

The results of these activities might prove useful to the IGT designers. Characterizing material behavior under these supplementary conditions would augment the characterization of damage mechanisms, and incorporating the results would expand the functionality of the model.

The numerical results of this investigation have shown promise in the ability of crystal plasticity to accurately deformation under high temperature, non-isothermal fatigue loading conditions. An obvious challenge would be modeling the inherent surface embrittlement that occurs under these conditions. In the current investigation it was not relevant to numerically connect oxidation to the degradation of material properties. As increased computational power and improved efficiency in post-

processing becomes available, however, the thrust to connect realistic microstructural evolution of the material to its macroscopic behavior will necessitate the inclusion of diffusion modeling. The UMAT subroutine applied here could be modified to include the couplings of chemical-mechanical interactions that promote oxidation near the surface. Information from new and existing experiments could be applied to characterize conditions for slip irreversibility due to the formation of oxides. The flow rule and corresponding internal state variable (ISV) evolution equations could be refined as needed.

# APPENDIX A

## ISOTHERMAL LOW CYCLE FATIGUE DATA
## (Chronologically ordered)

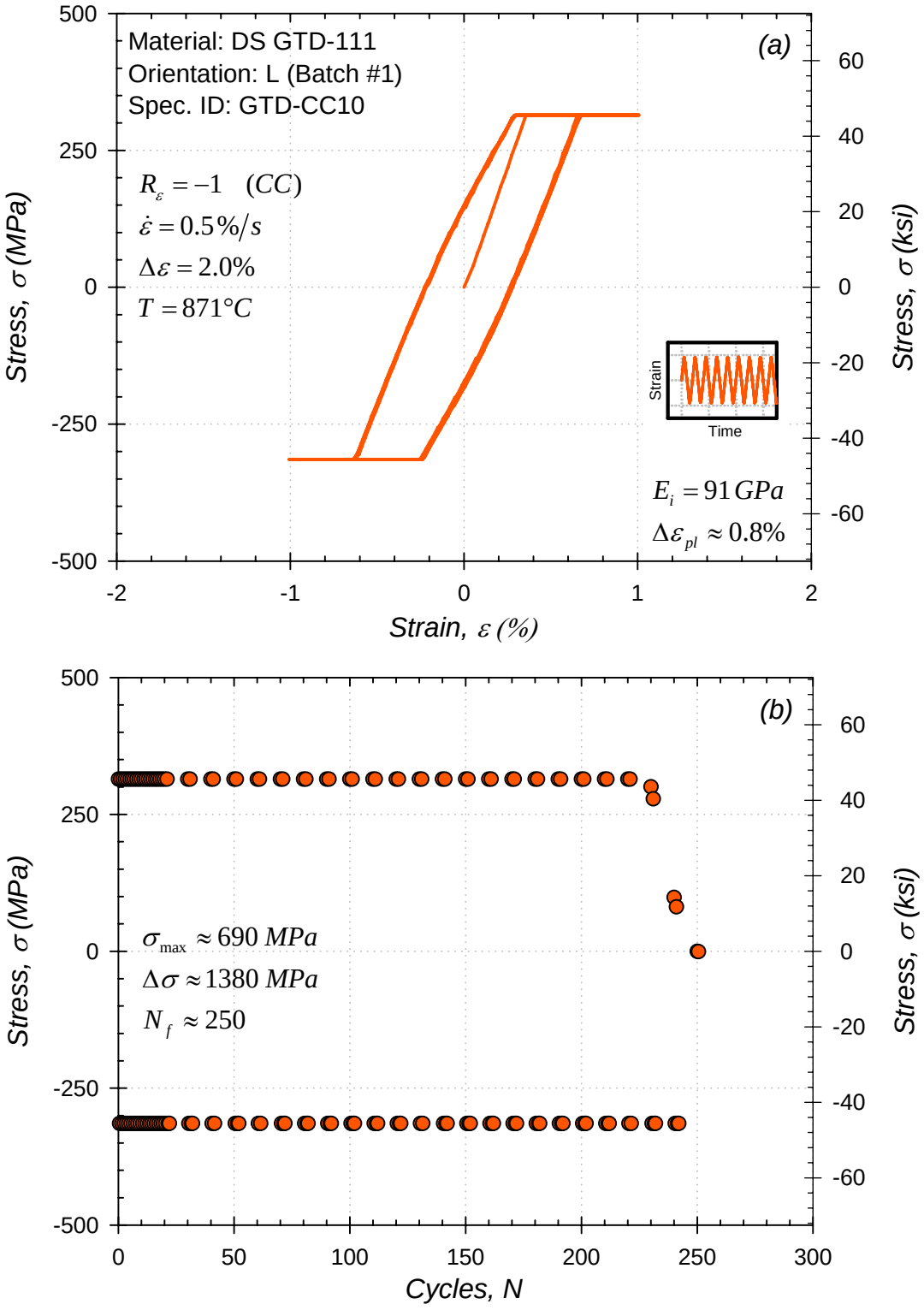


***Figure A.1:*** *(a) Initial stress-strain hysteresis loops and (b) stress history for low cycle fatigue test at 871°C [Note: load cell range set too low].*

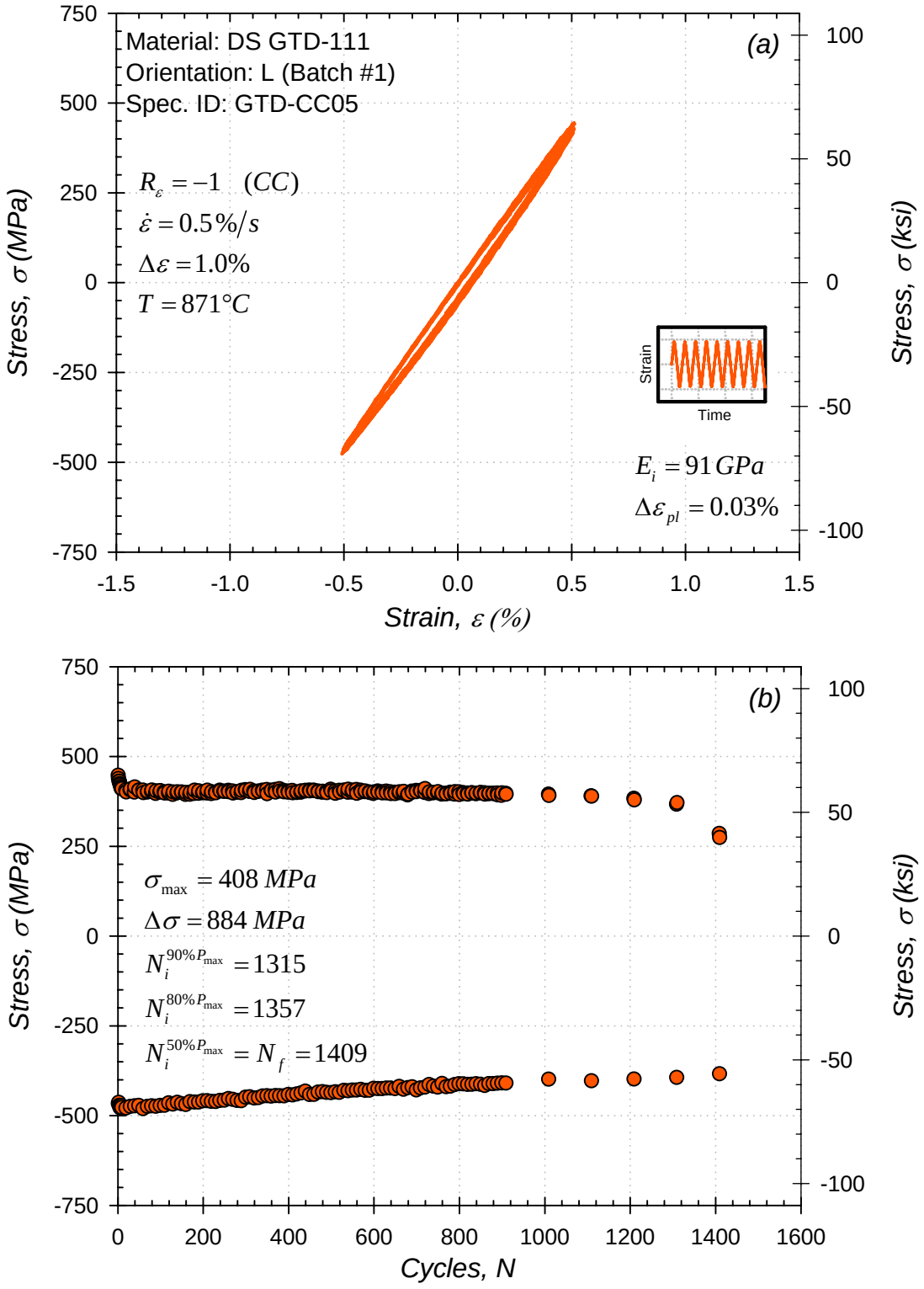


***Figure A.2:*** *(a) Initial stress-strain hysteresis loops and (b) stress history for low cycle fatigue test at 871°C.*

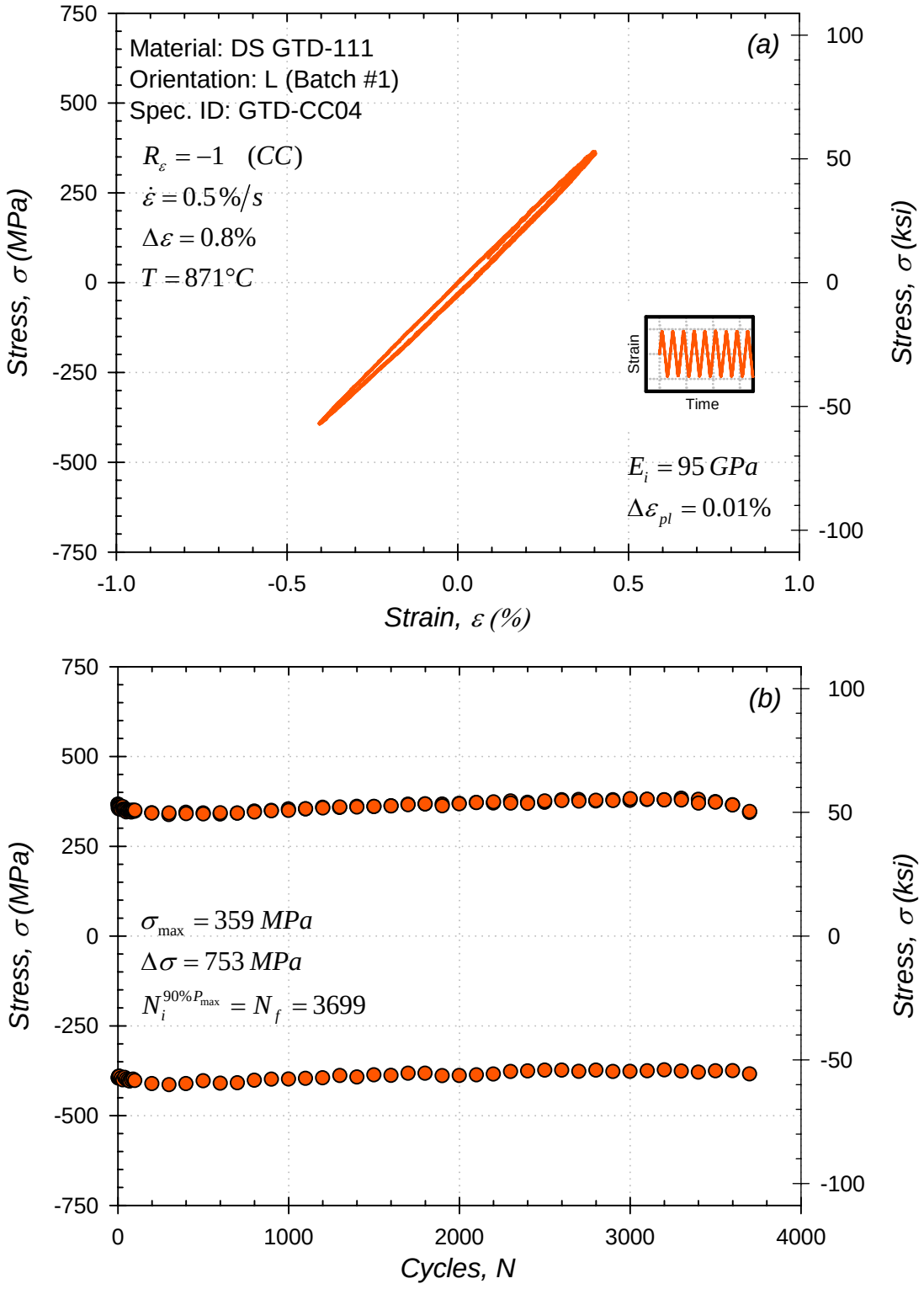


***Figure A.3:*** *(a) Initial stress-strain hysteresis loops and (b) stress history for low cycle fatigue test at 871°C.*

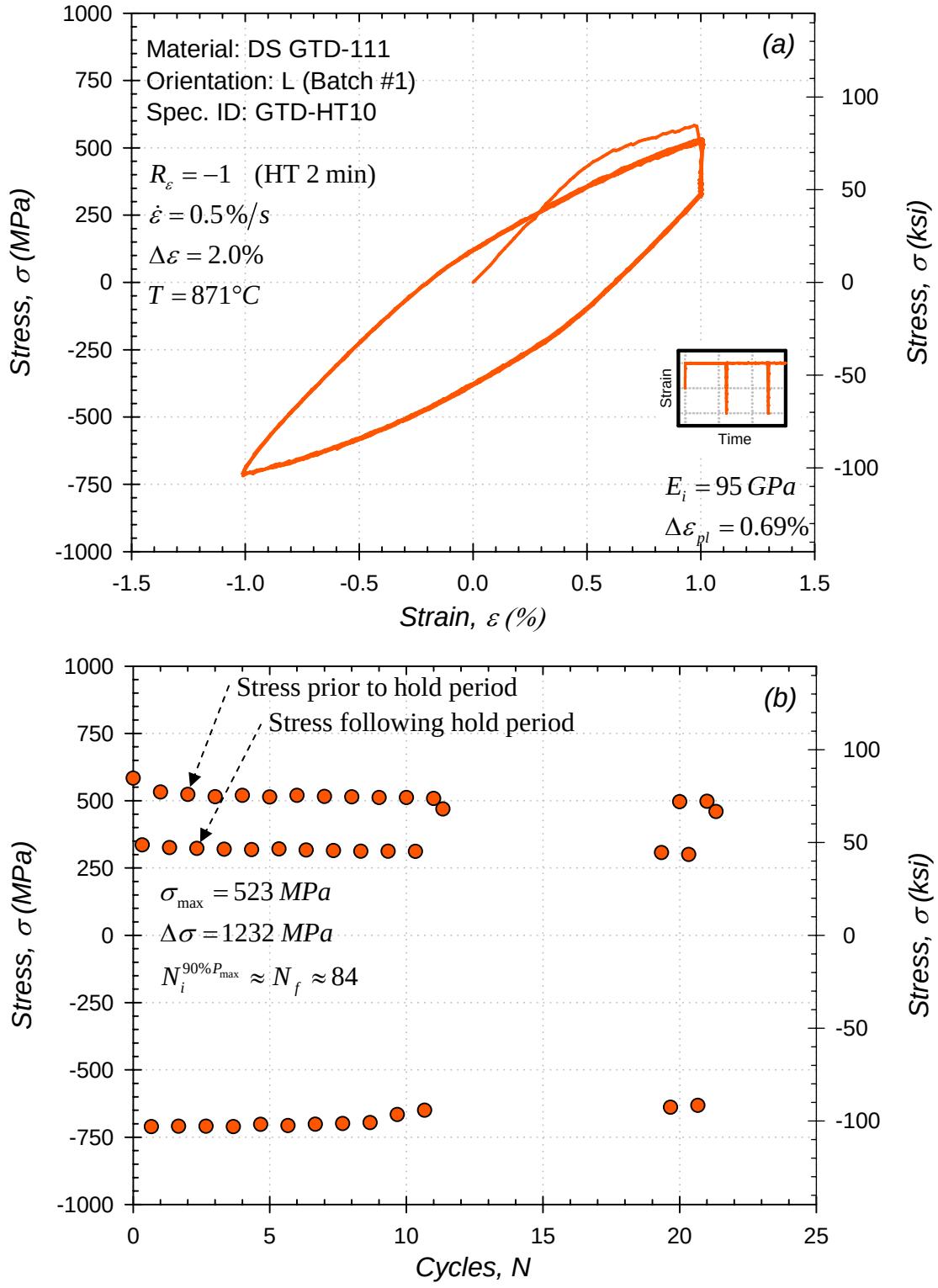


***Figure A.4:*** *(a) Initial stress-strain hysteresis loops and (b) stress history for low cycle fatigue test at 871°C.*

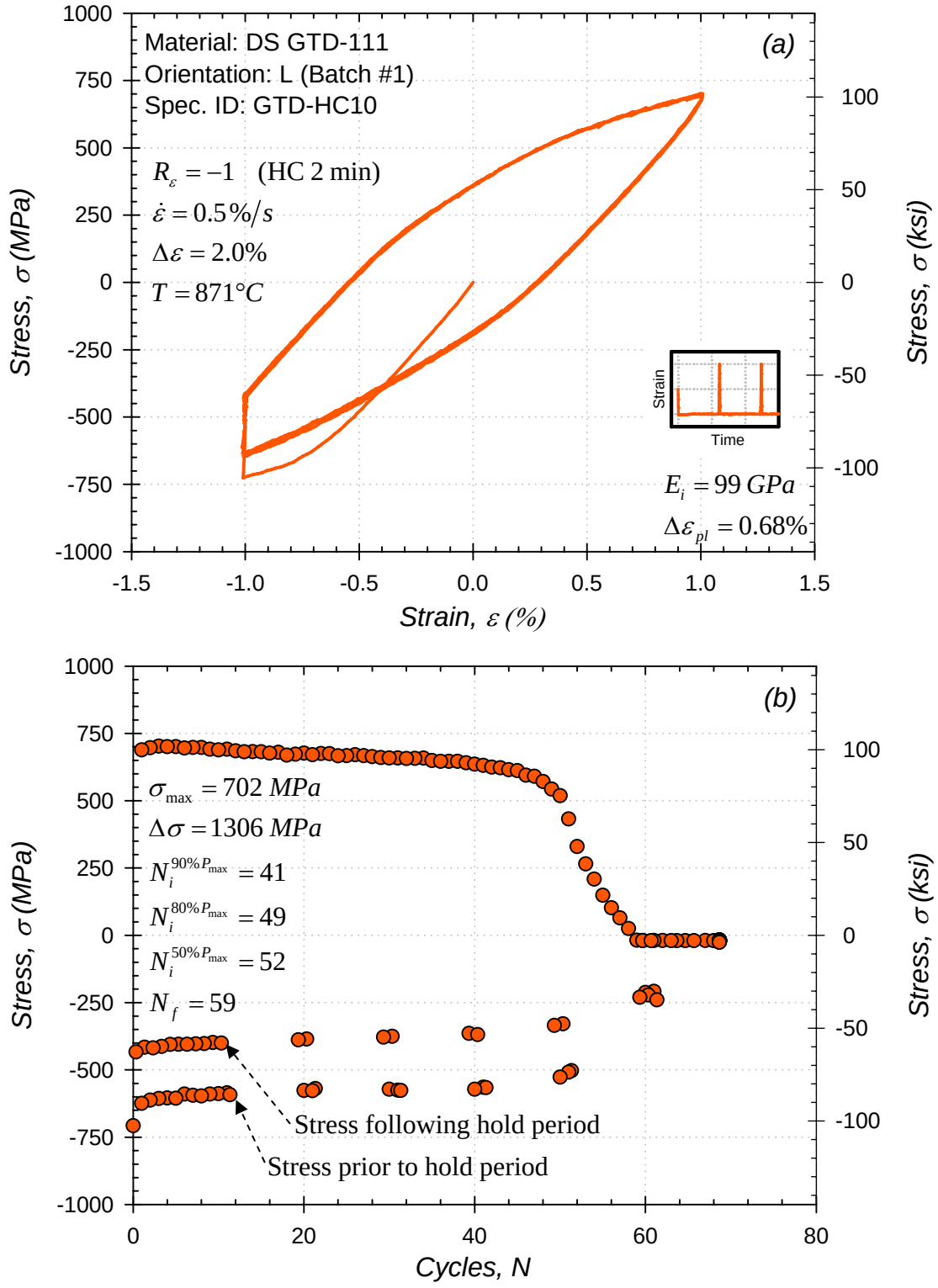


***Figure A.5:*** *(a) Initial stress-strain hysteresis loops and (b) stress history for low cycle fatigue test at 871°C.*

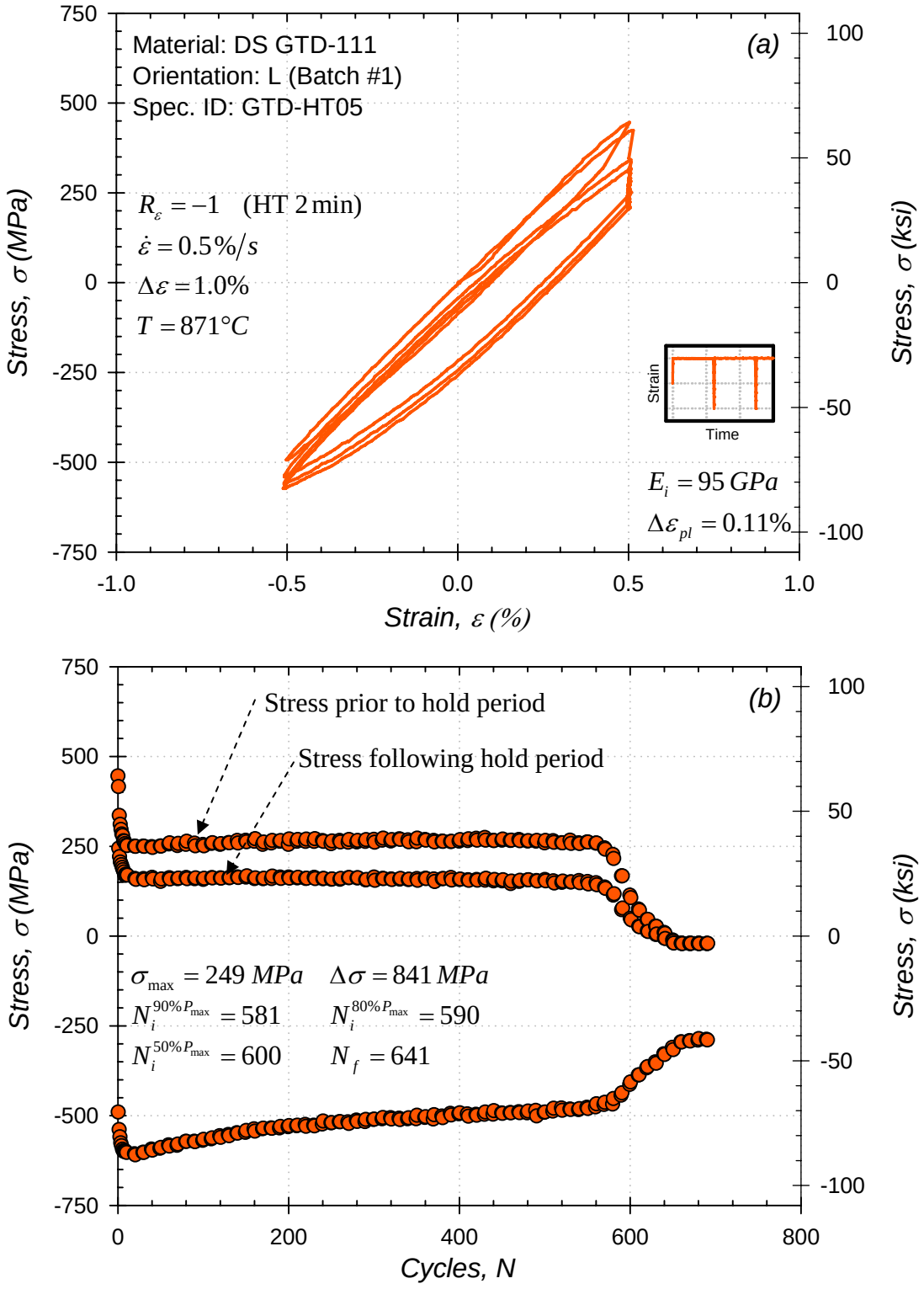


***Figure A.6:*** *(a) Initial stress-strain hysteresis loops and (b) stress history for low cycle fatigue test at 871°C.*

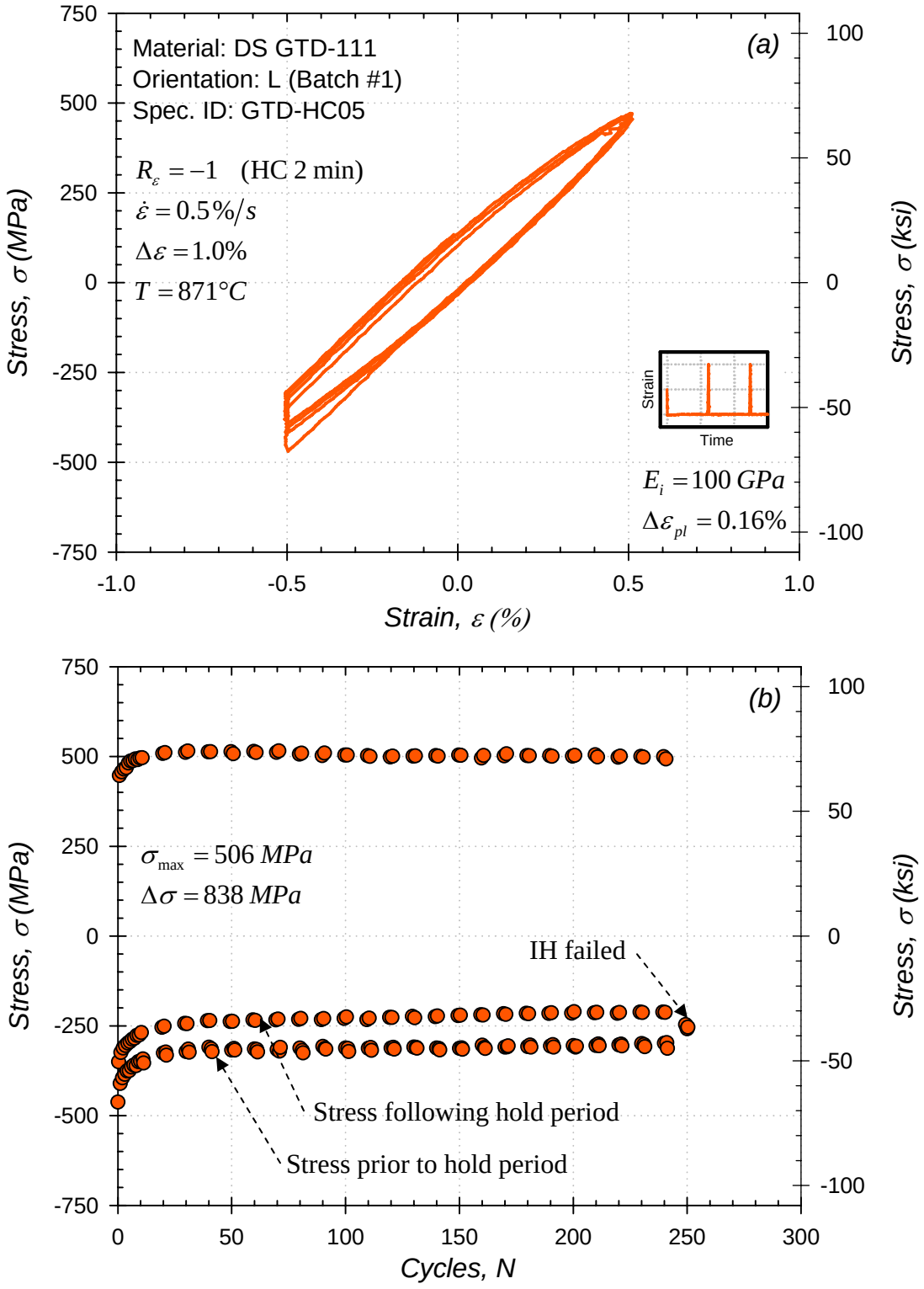


***Figure A.7:*** *(a) Initial stress-strain hysteresis loops and (b) stress history for low cycle fatigue test at 871°C.*

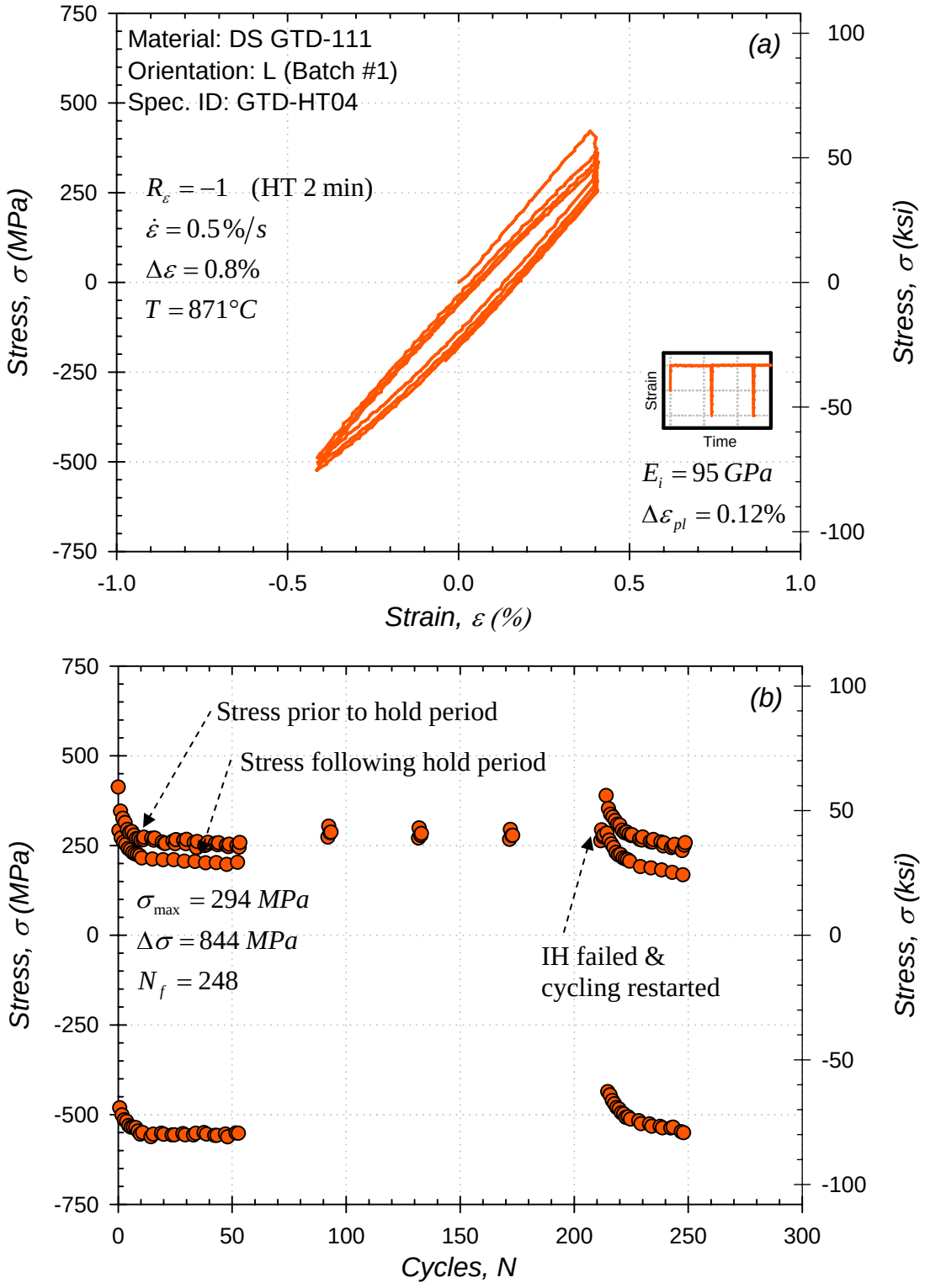


***Figure A.8:*** *(a) Initial stress-strain hysteresis loops and (b) stress history for low cycle fatigue test at 871°C.*

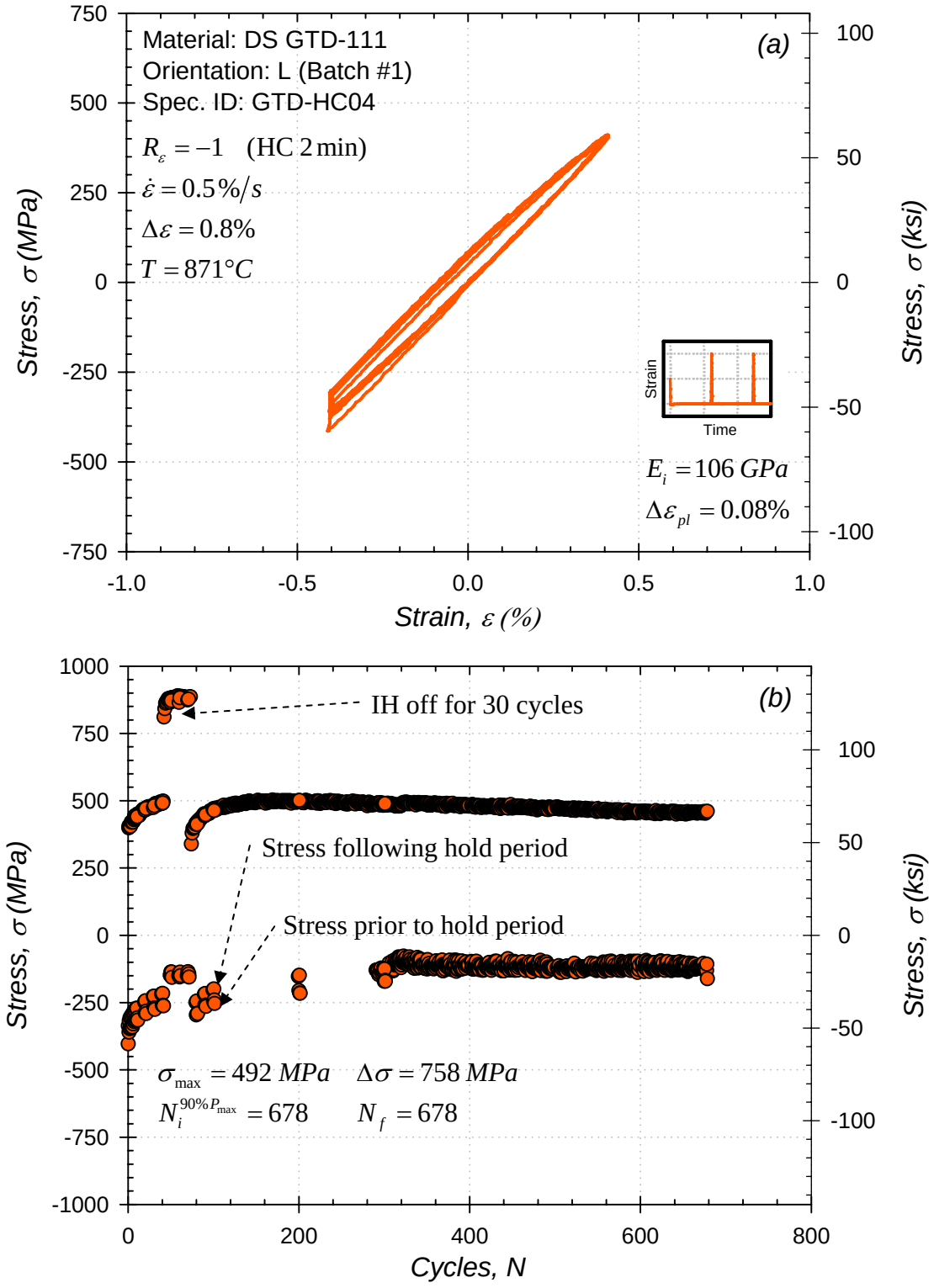


***Figure A.9:*** *(a) Initial stress-strain hysteresis loops and (b) stress history for low cycle fatigue test at 871°C.*

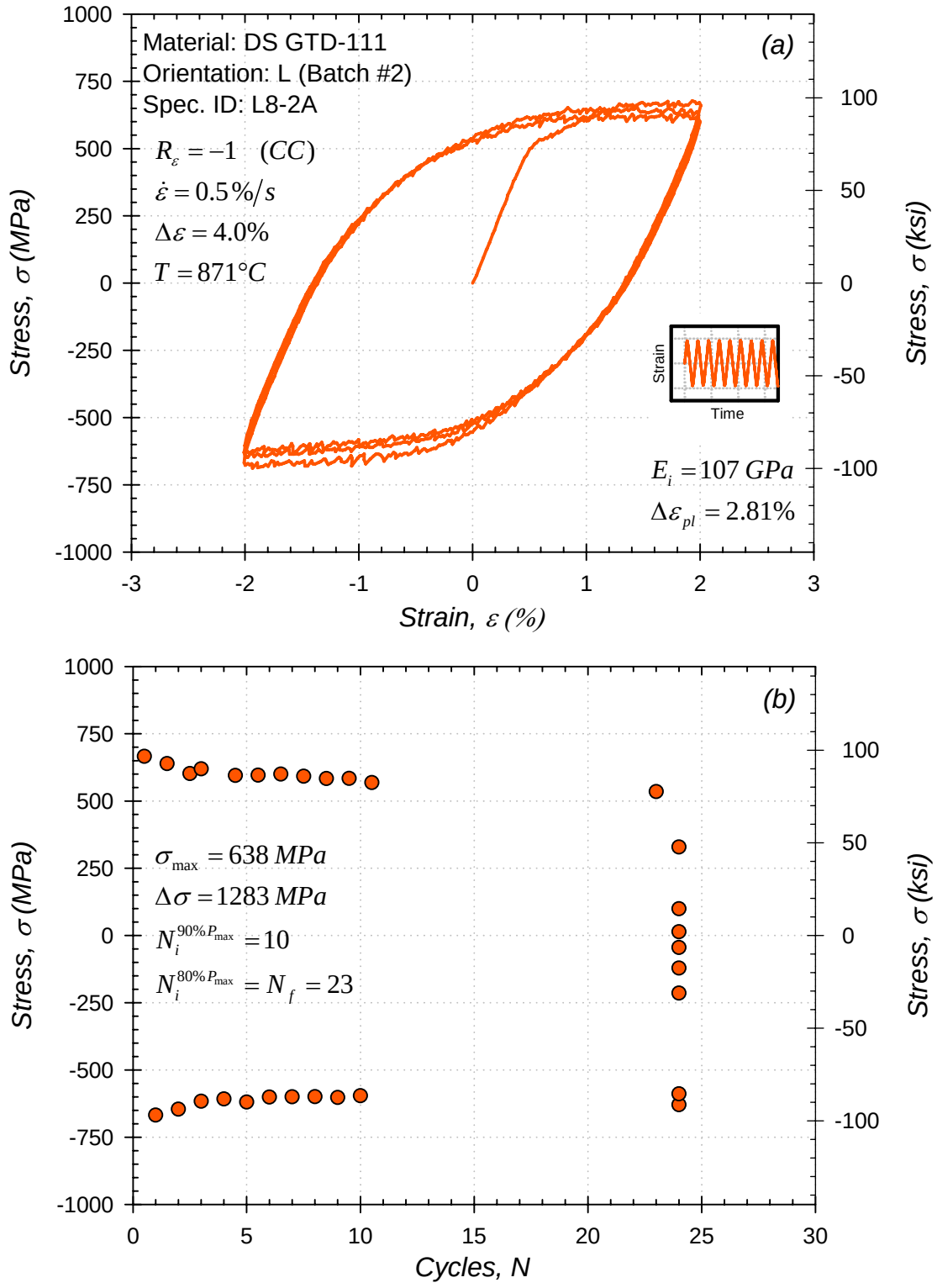


***Figure A.10:*** *(a) Initial stress-strain hysteresis loops and (b) stress history for low cycle fatigue test at 871°C.*

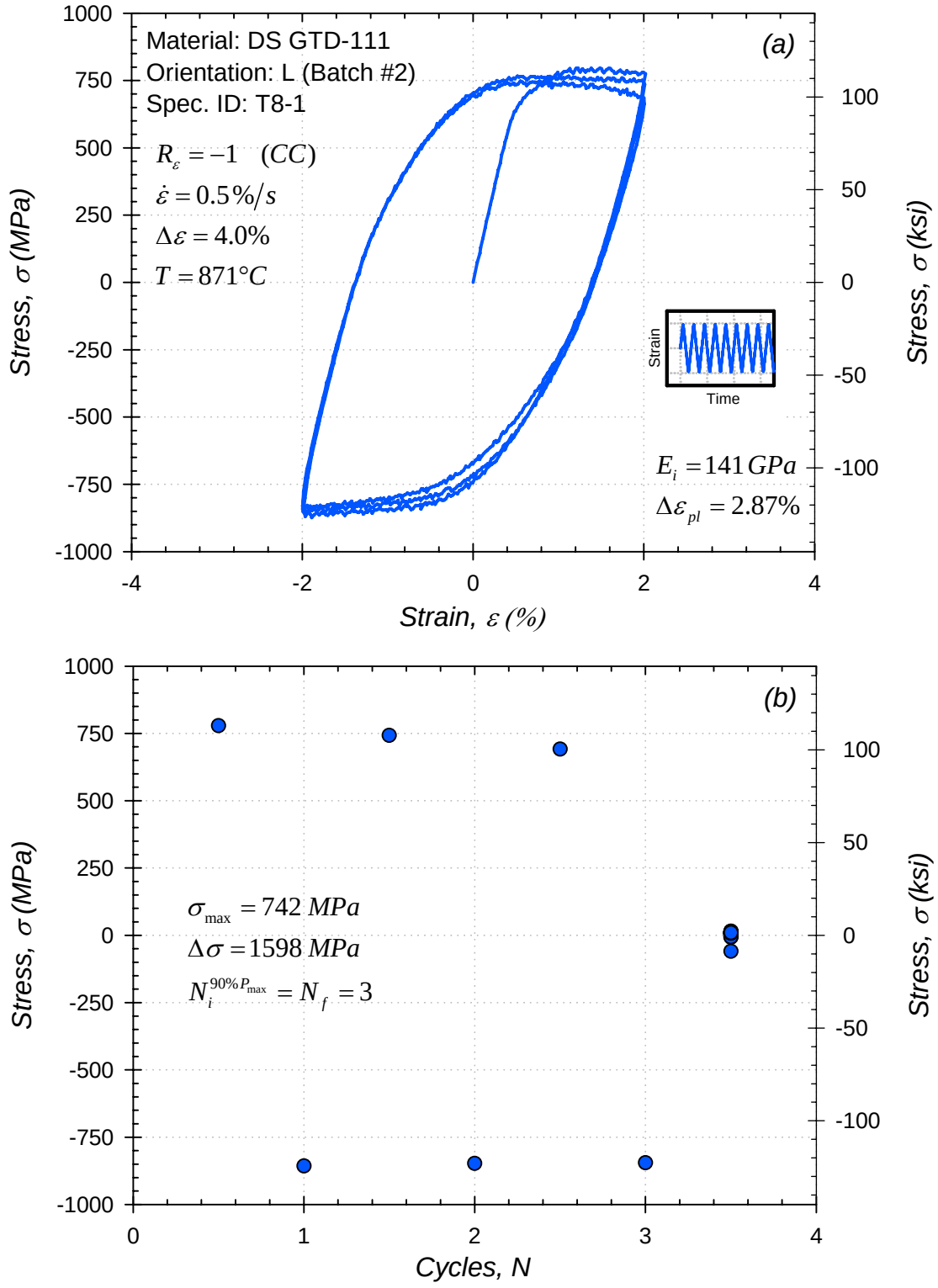


***Figure A.11:*** *(a) Initial stress-strain hysteresis loops and (b) stress history for low cycle fatigue test at 871°C.*

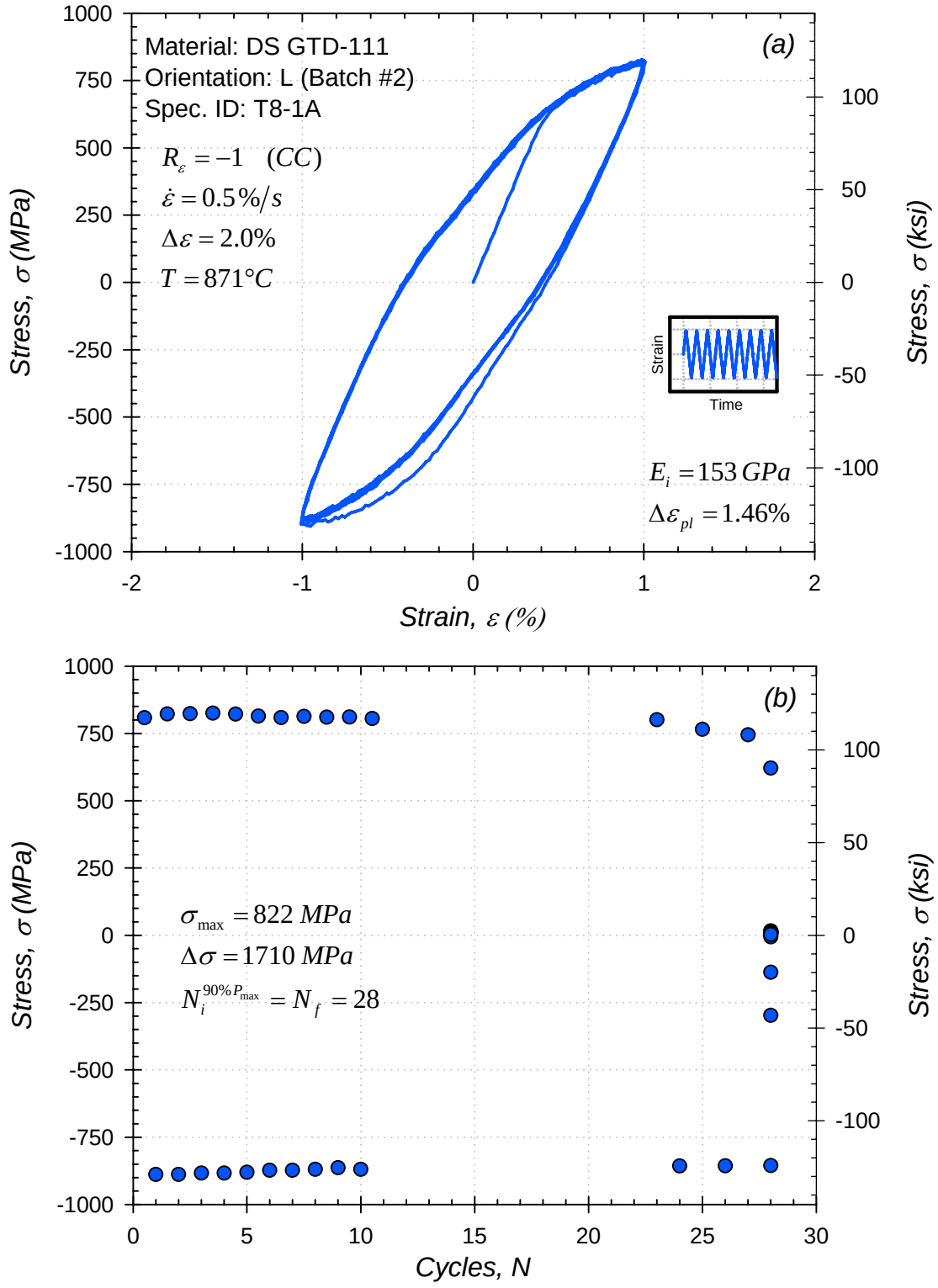


***Figure A.12:*** *(a) Initial stress-strain hysteresis loops and (b) stress history for low cycle fatigue test at 871°C.*

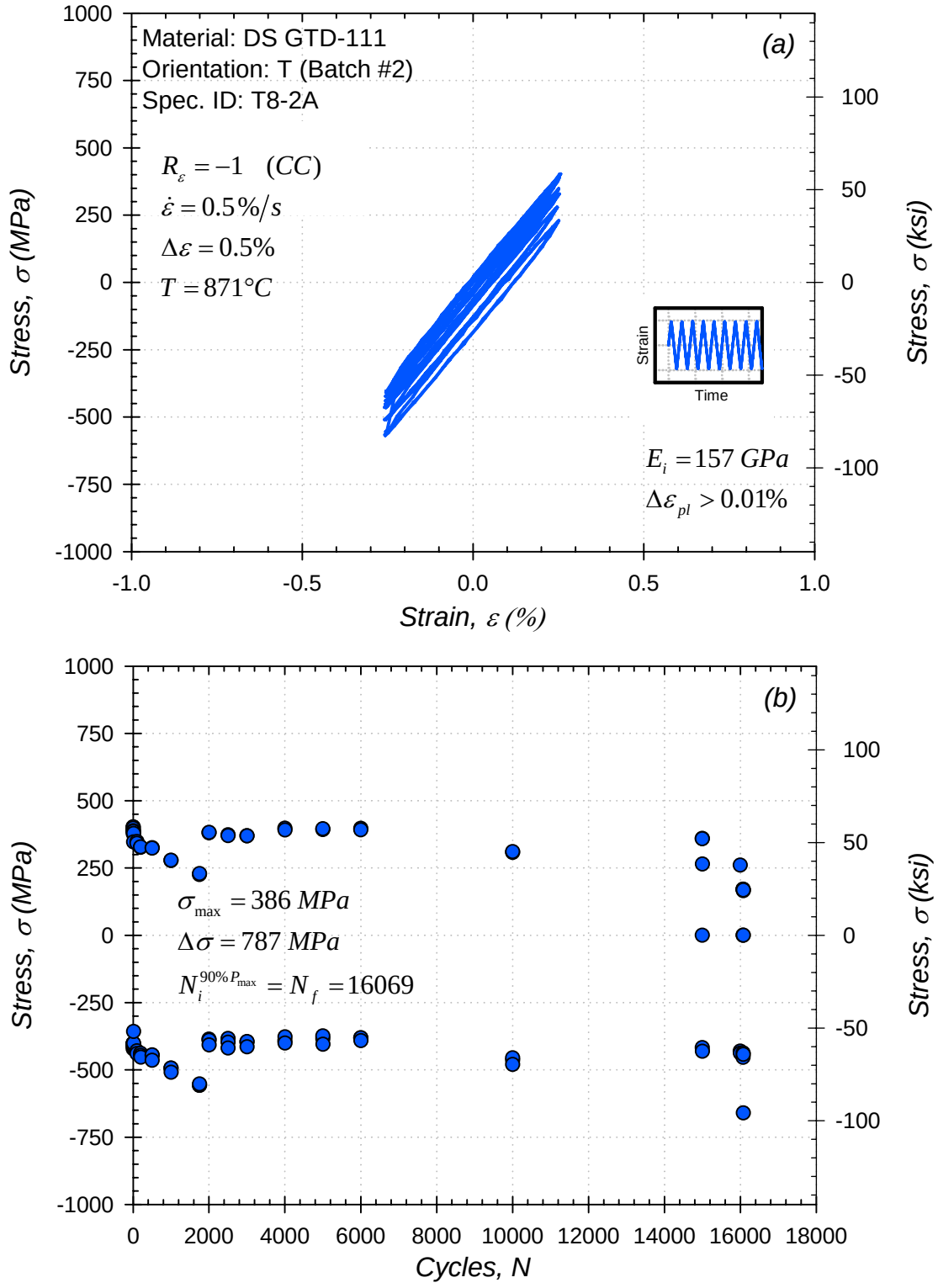


***Figure A.13:*** *(a) Initial stress-strain hysteresis loops and (b) stress history for low cycle fatigue test at 871°C.*

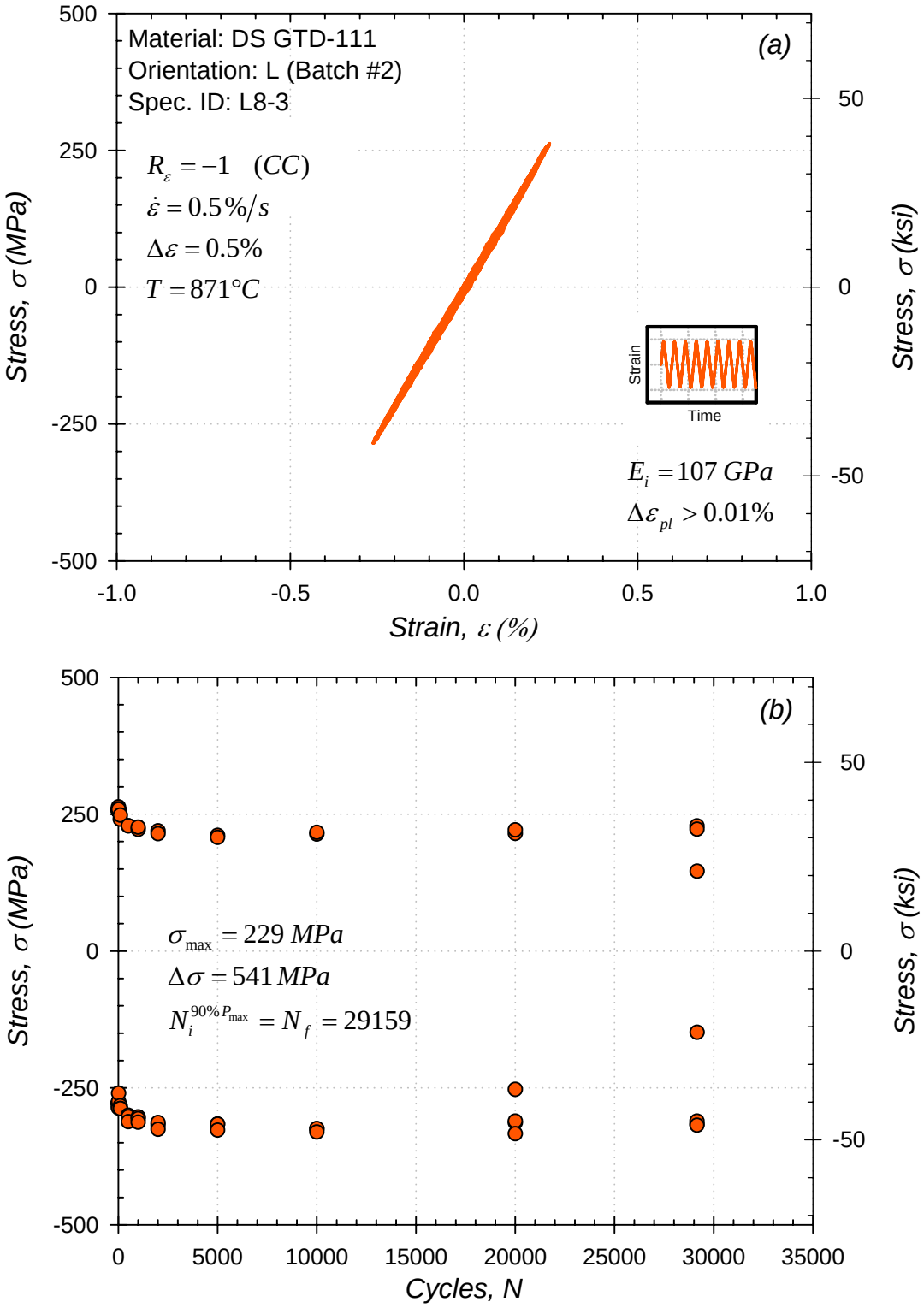


***Figure A.14:*** *(a) Initial stress-strain hysteresis loops and (b) stress history for low cycle fatigue test at 871°C.*

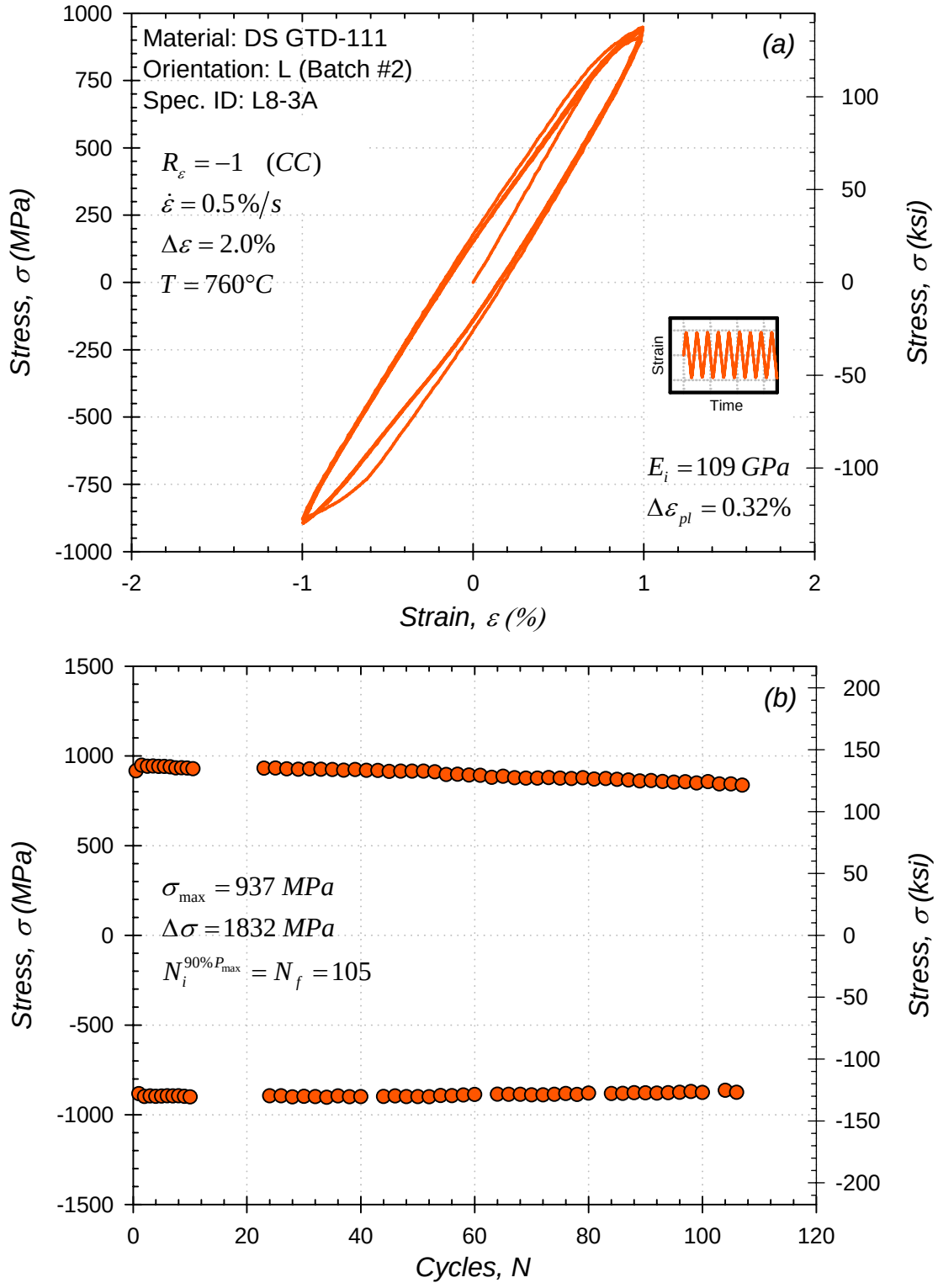


***Figure A.15:*** *(a) Initial stress-strain hysteresis loops and (b) stress history for low cycle fatigue test at 871°C.*

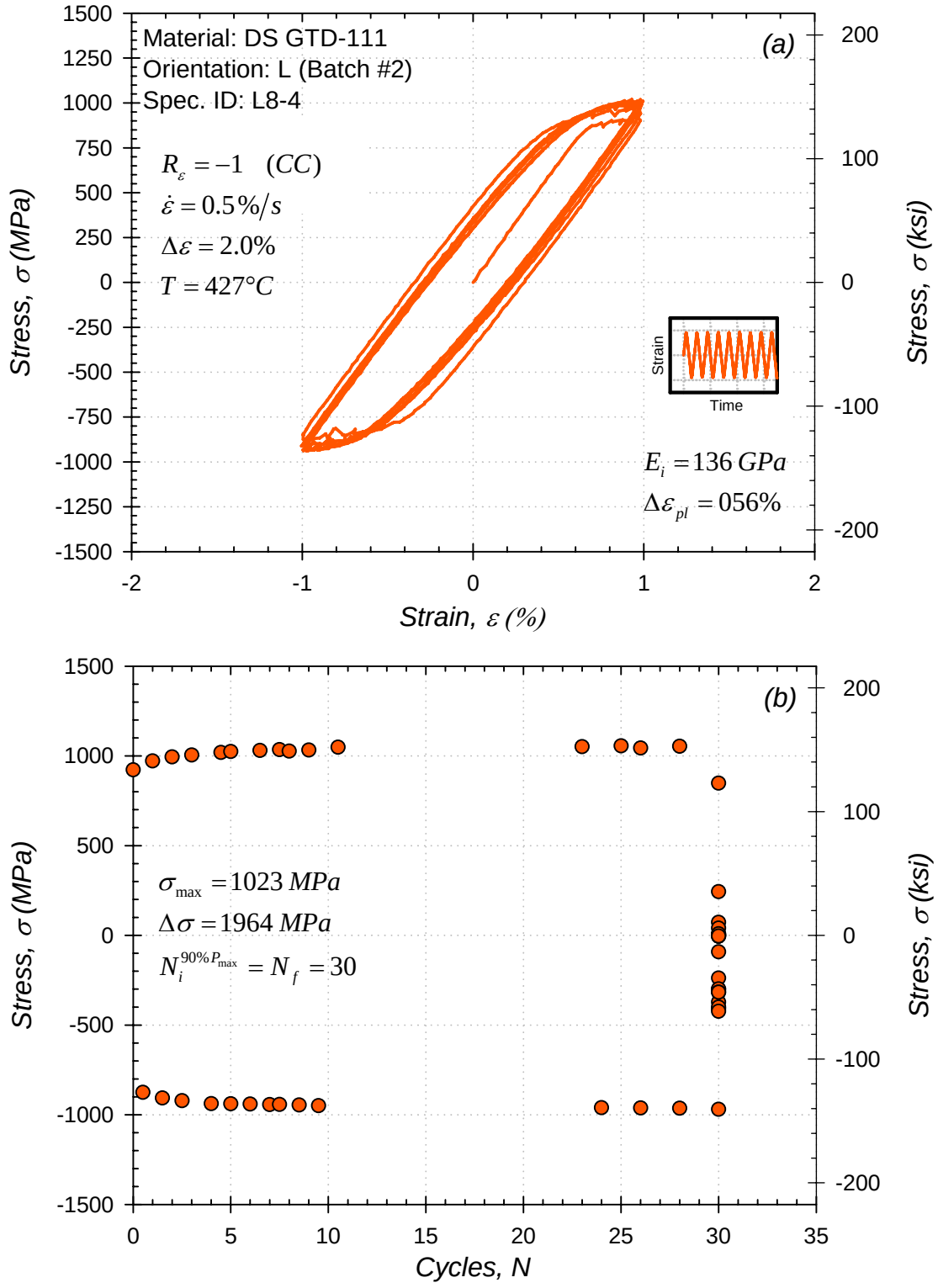


***Figure A.16:*** *(a) Initial stress-strain hysteresis loops and (b) stress history for low cycle fatigue test at 426°C.*

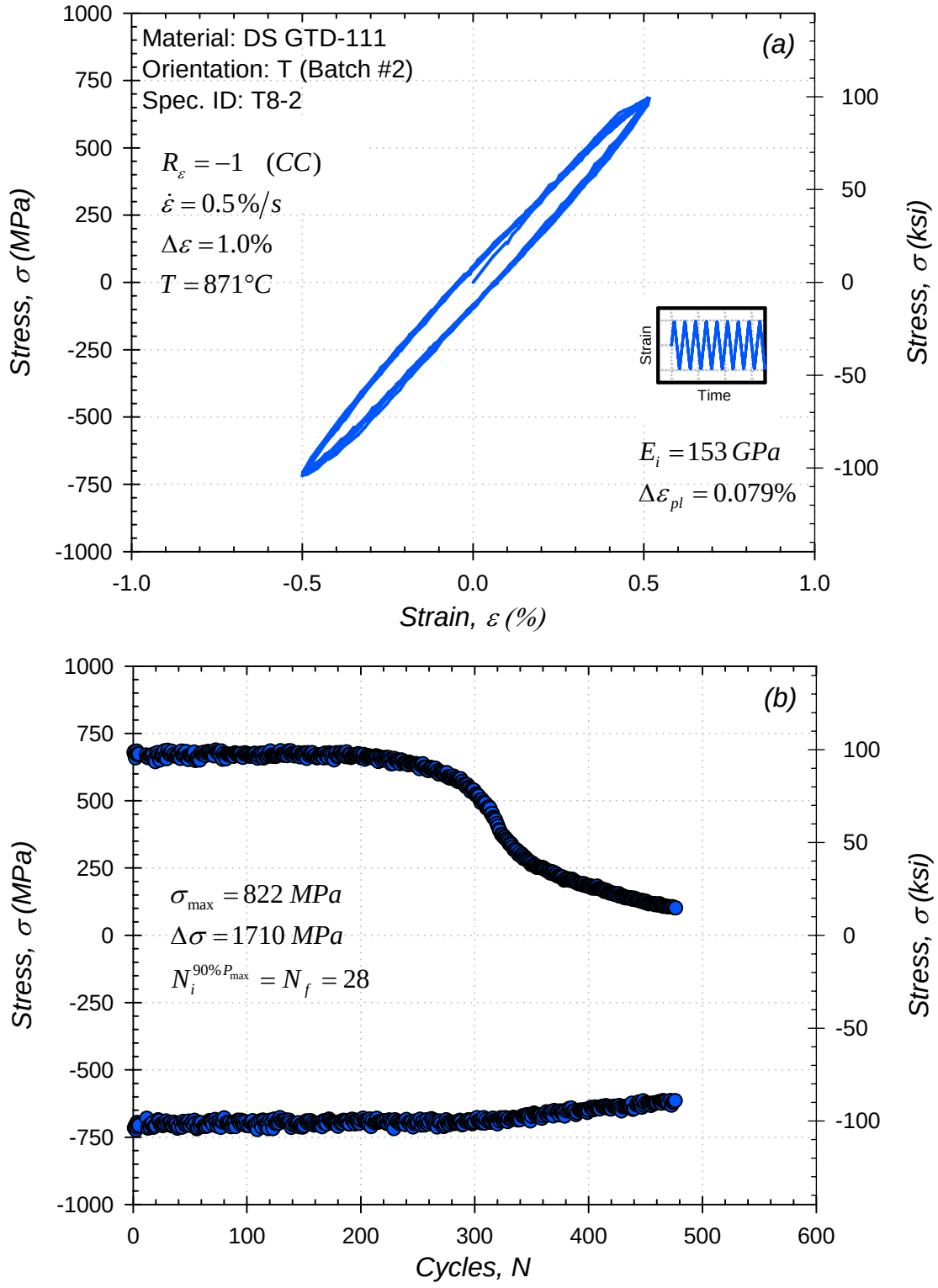


***Figure A.17:*** *(a) Initial stress-strain hysteresis loops and (b) stress history for low cycle fatigue test at 871°C.*

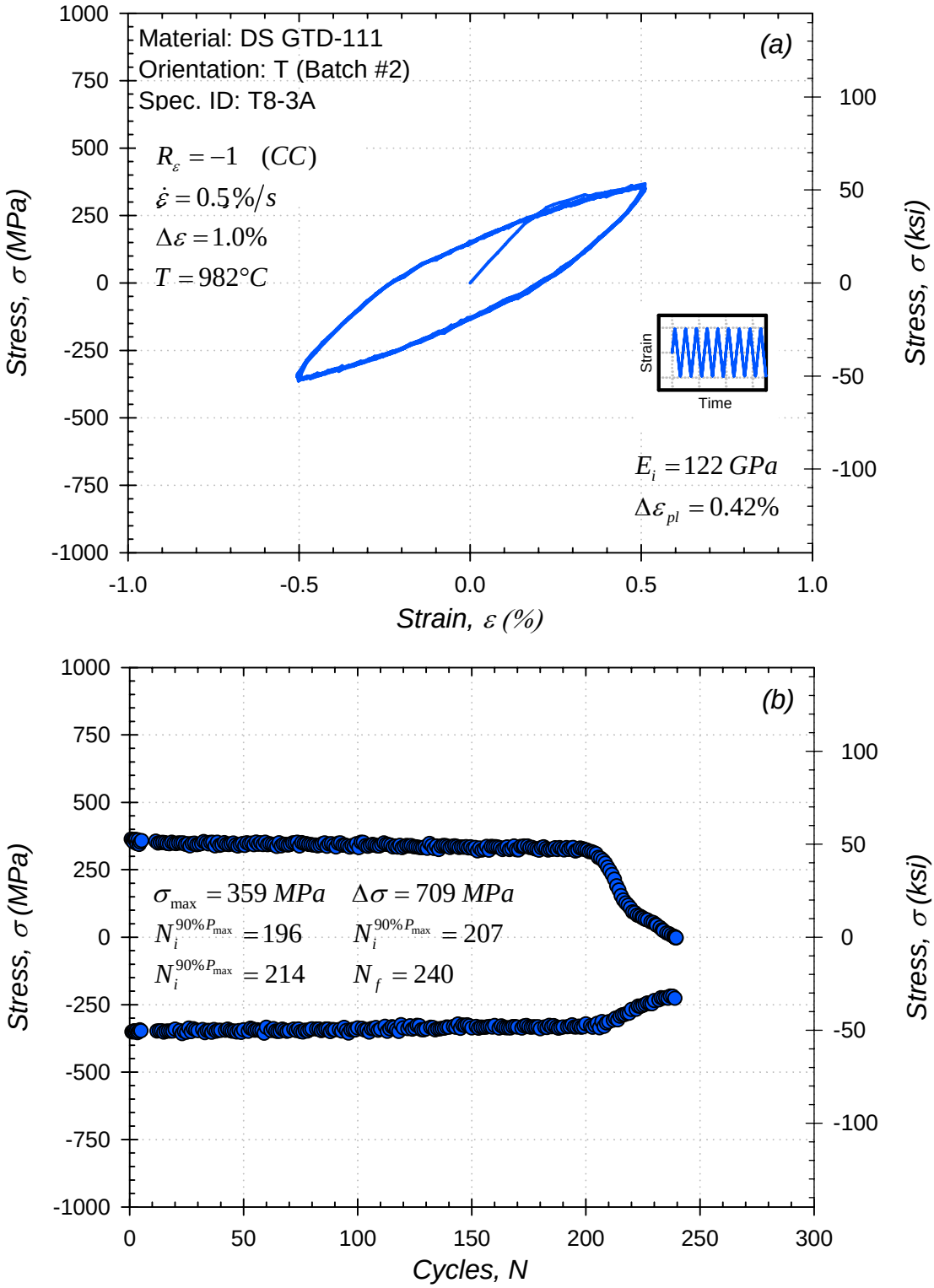


***Figure A.18:*** *(a) Initial stress-strain hysteresis loops and (b) stress history for low cycle fatigue test at 982°C.*

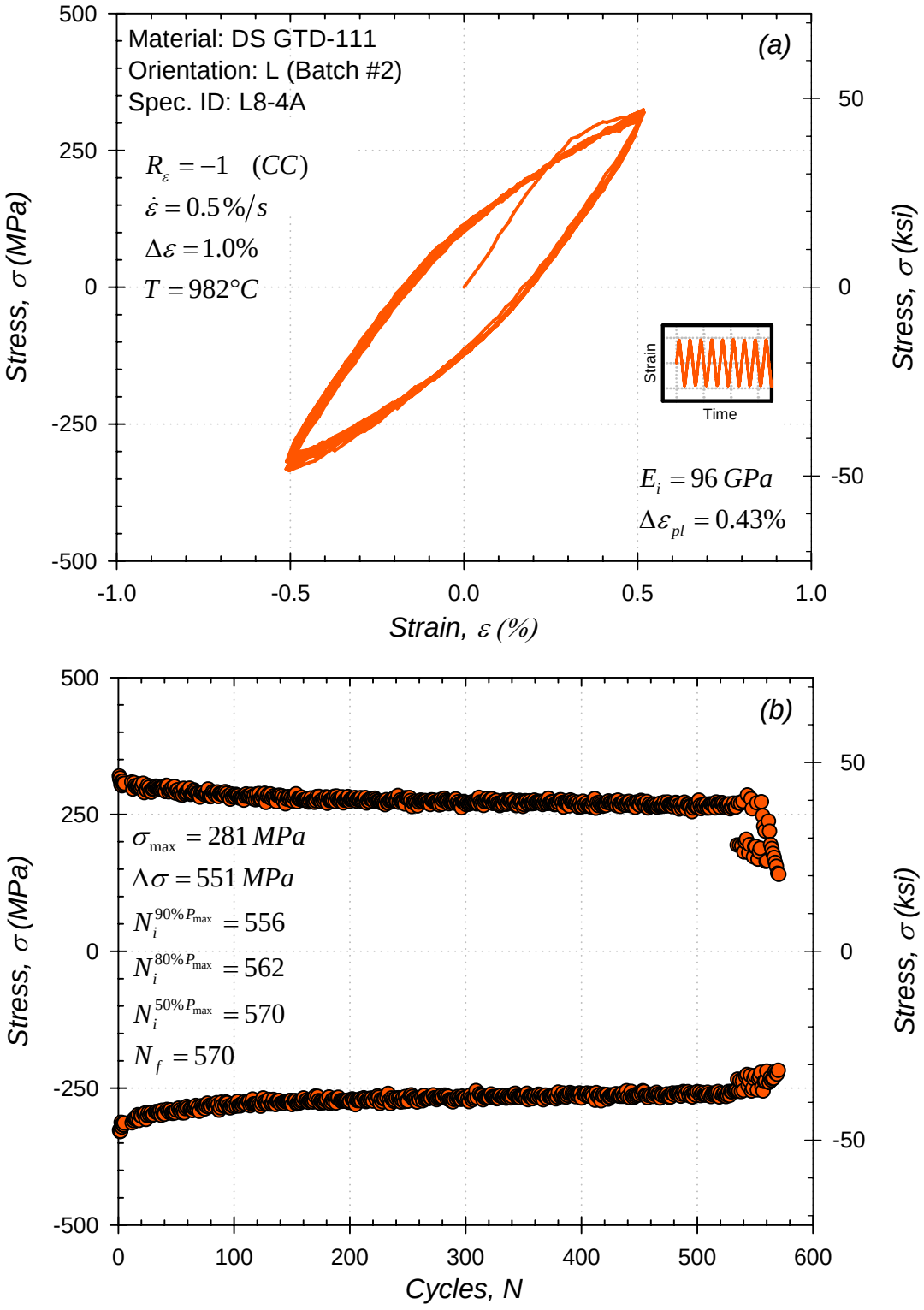


***Figure A.19:*** *(a) Initial stress-strain hysteresis loops and (b) stress history for low cycle fatigue test at 982°C.*

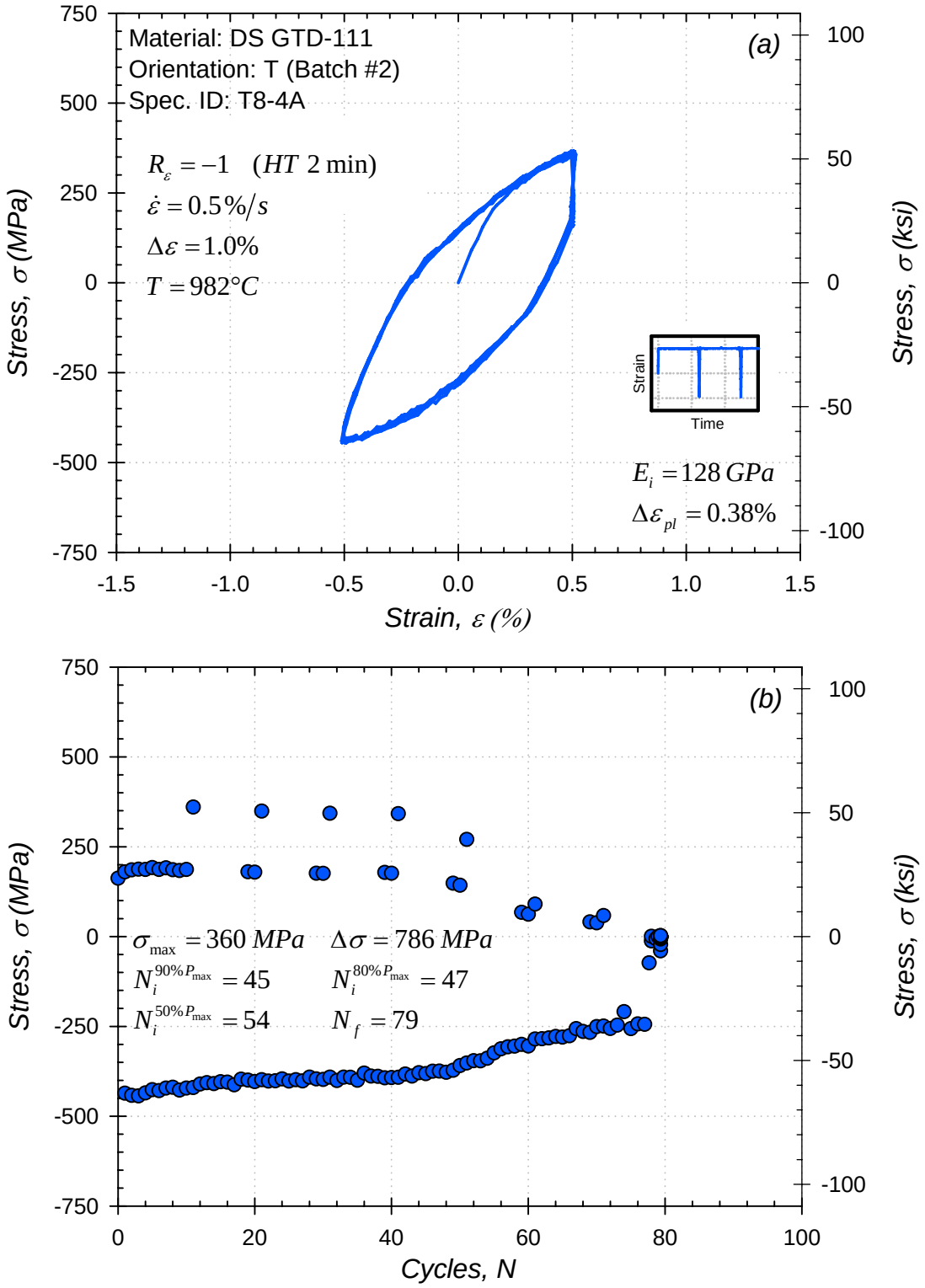


***Figure A.20:*** *(a) Initial stress-strain hysteresis loops and (b) stress history for low cycle fatigue test at 982°C.*

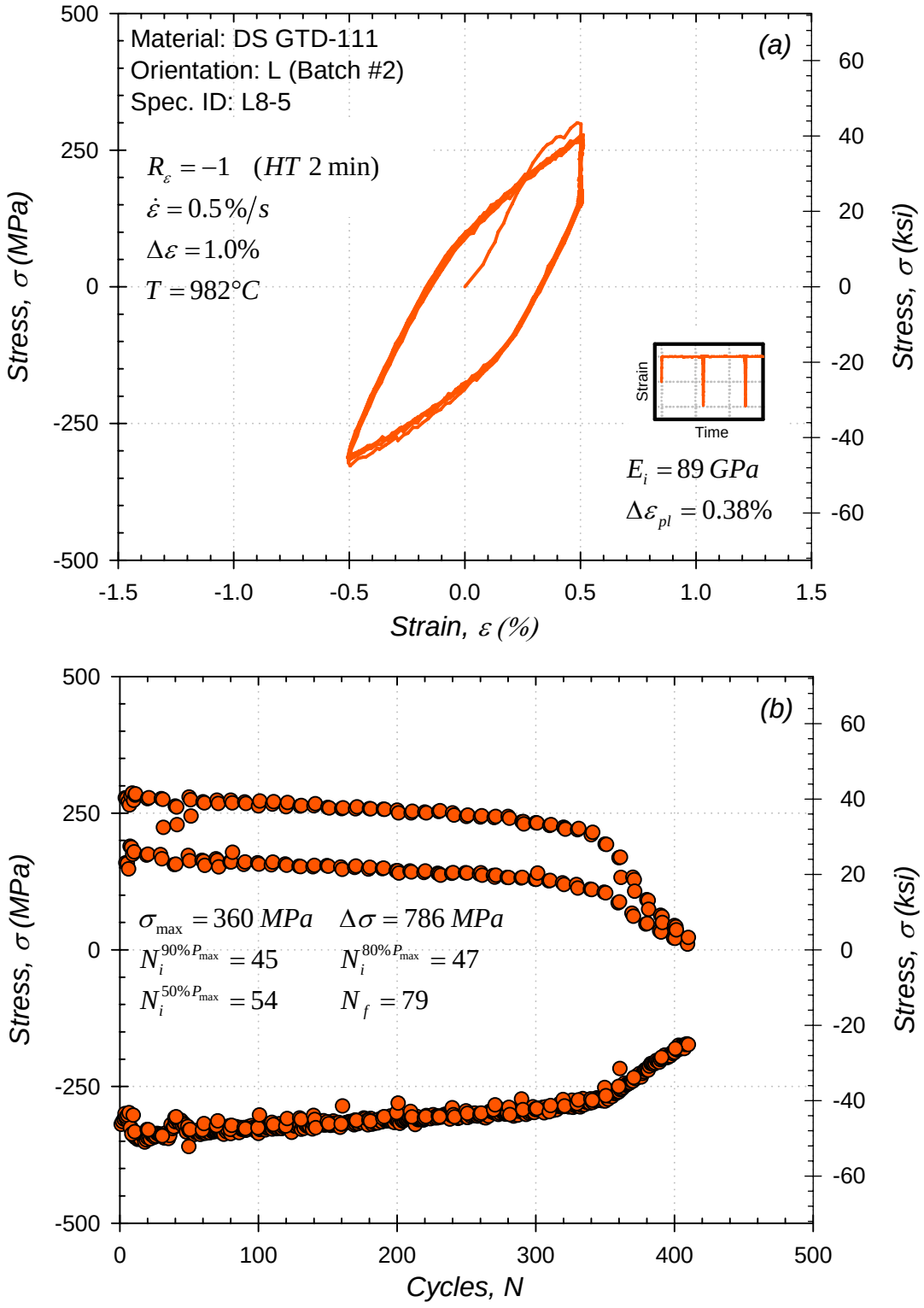


***Figure A.21:*** *(a) Initial stress-strain hysteresis loops and (b) stress history for low cycle fatigue test at 982°C.*

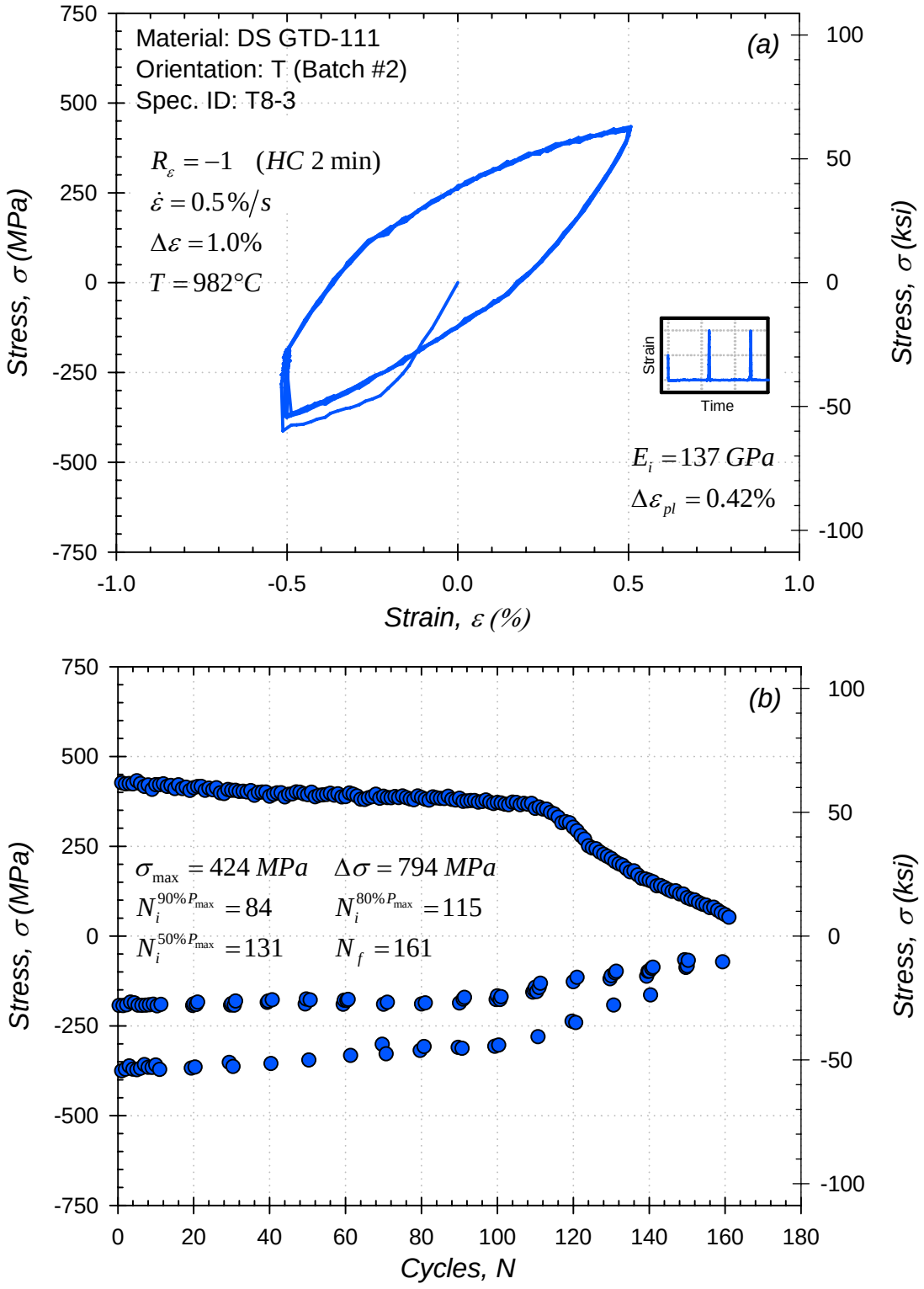


***Figure A.22:*** *(a) Initial stress-strain hysteresis loops and (b) stress history for low cycle fatigue test at 982°C.*

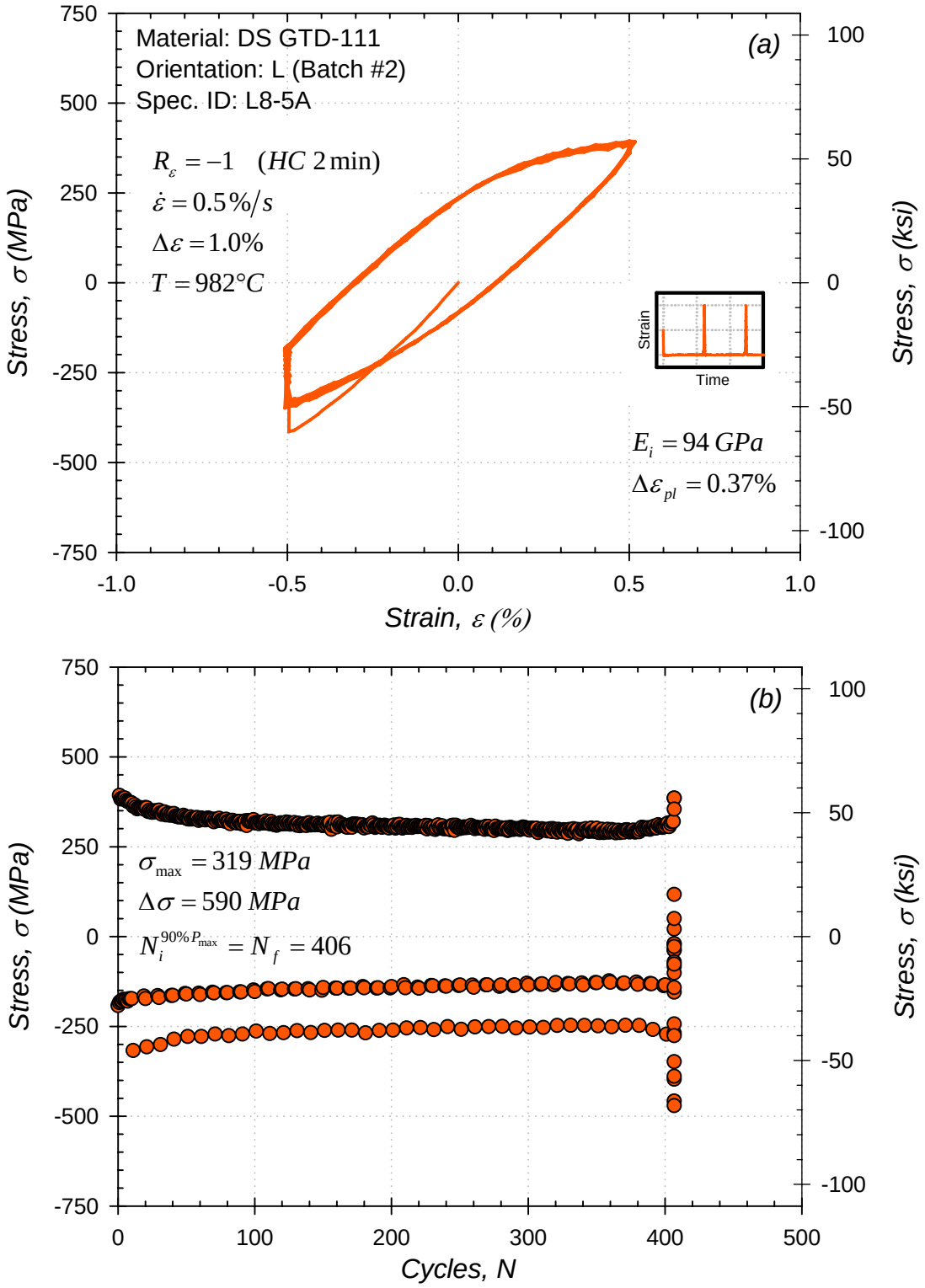


***Figure A.23:*** *(a) Initial stress-strain hysteresis loops and (b) stress history for low cycle fatigue test at 982°C.*

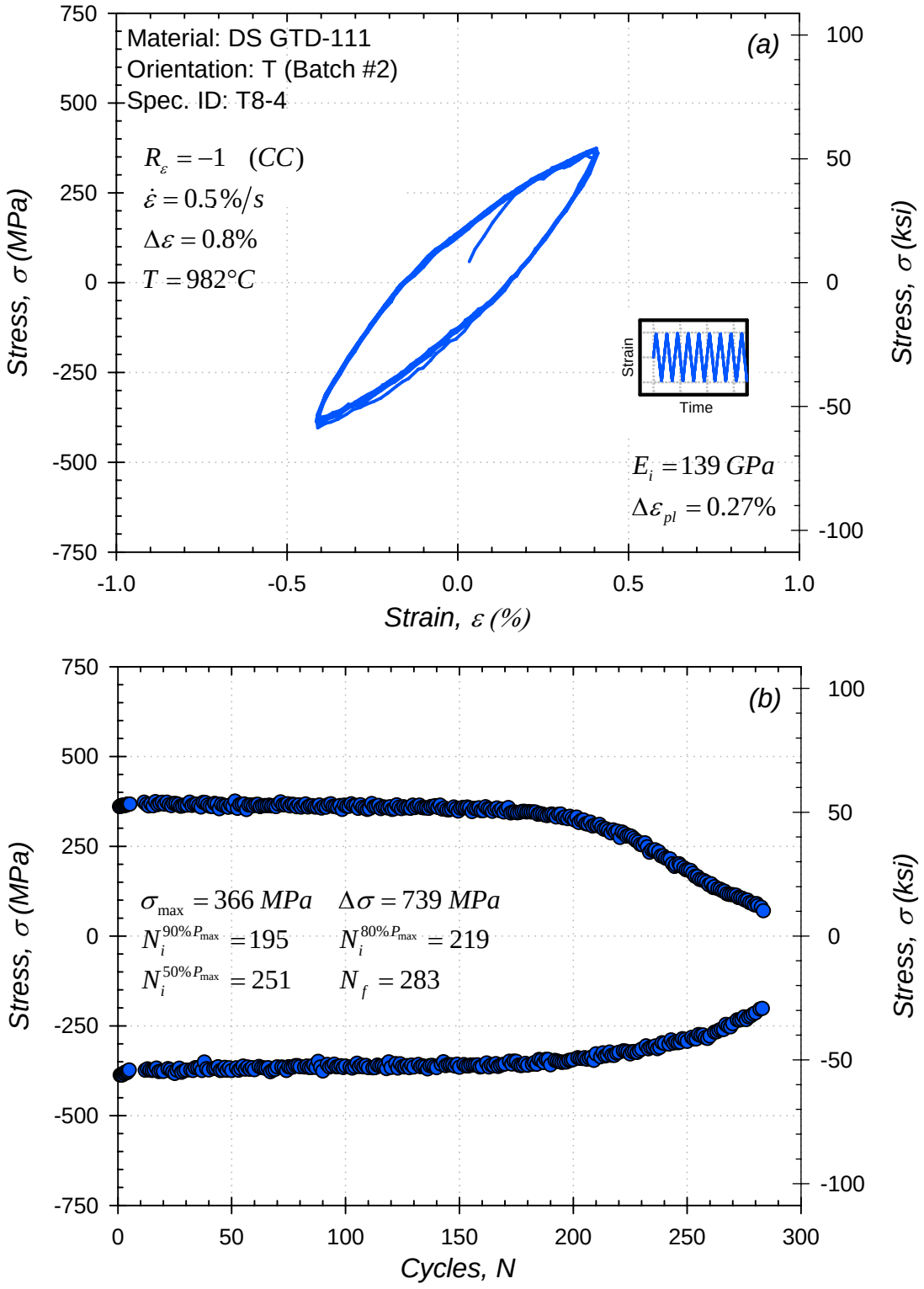


***Figure A.24:*** *(a) Initial stress-strain hysteresis loops and (b) stress history for low cycle fatigue test at 982°C.*

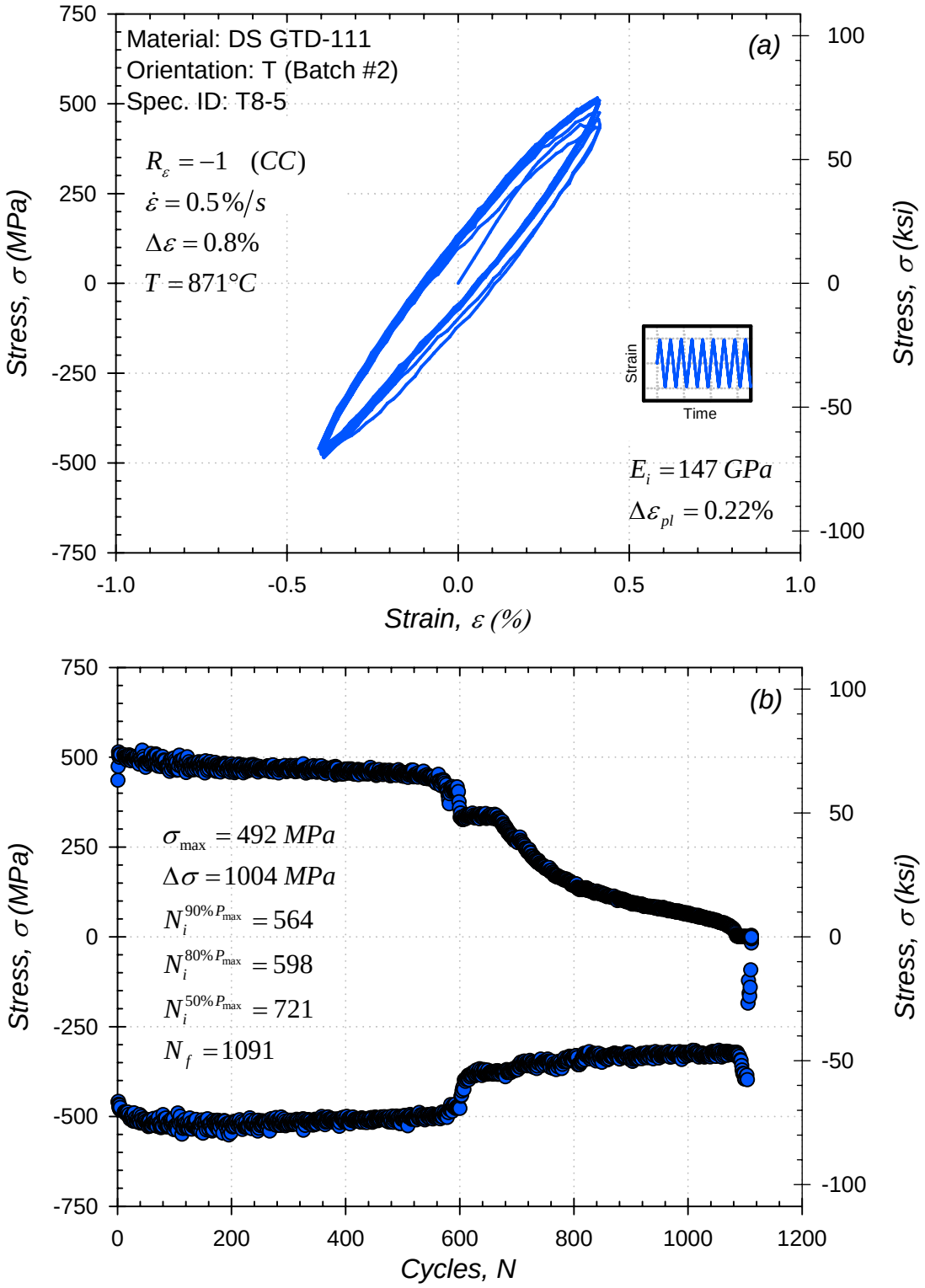


***Figure A.25:*** *(a) Initial stress-strain hysteresis loops and (b) stress history for low cycle fatigue test at 871°C.*

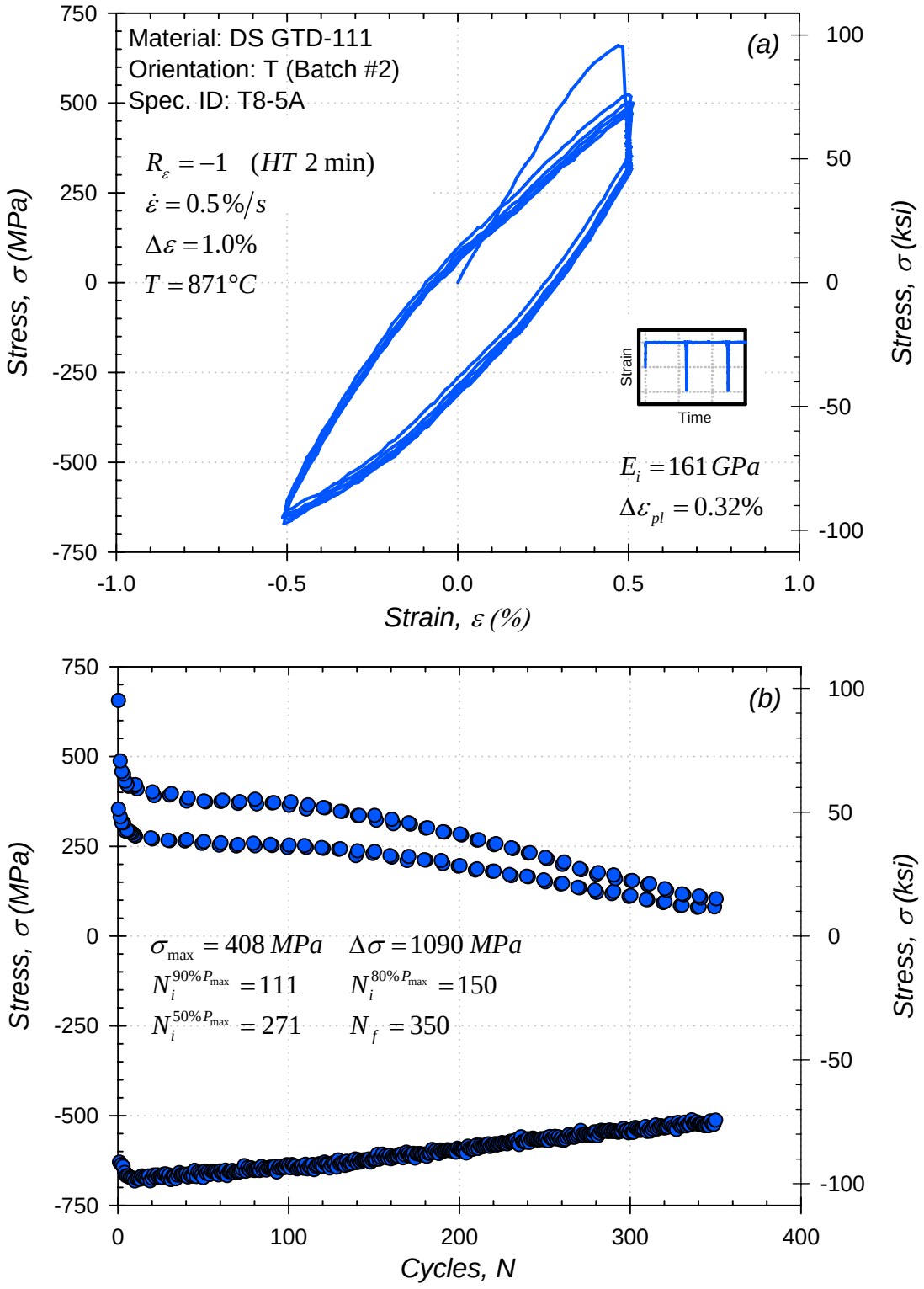


***Figure A.26:*** *(a) Initial stress-strain hysteresis loops and (b) stress history for low cycle fatigue test at 871°C.*

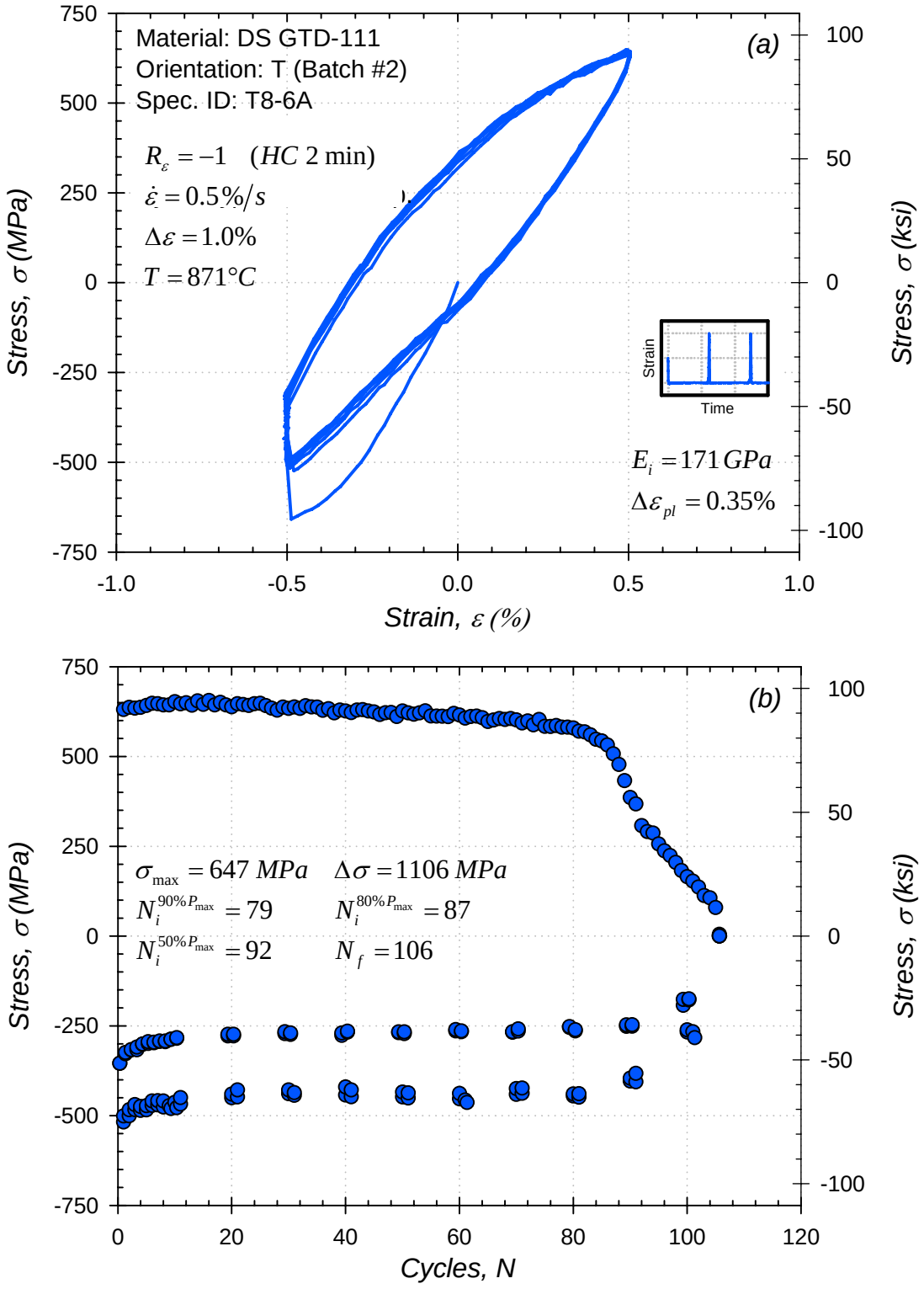


***Figure A.27:*** *(a) Initial stress-strain hysteresis loops and (b) stress history for low cycle fatigue test at 871C.*

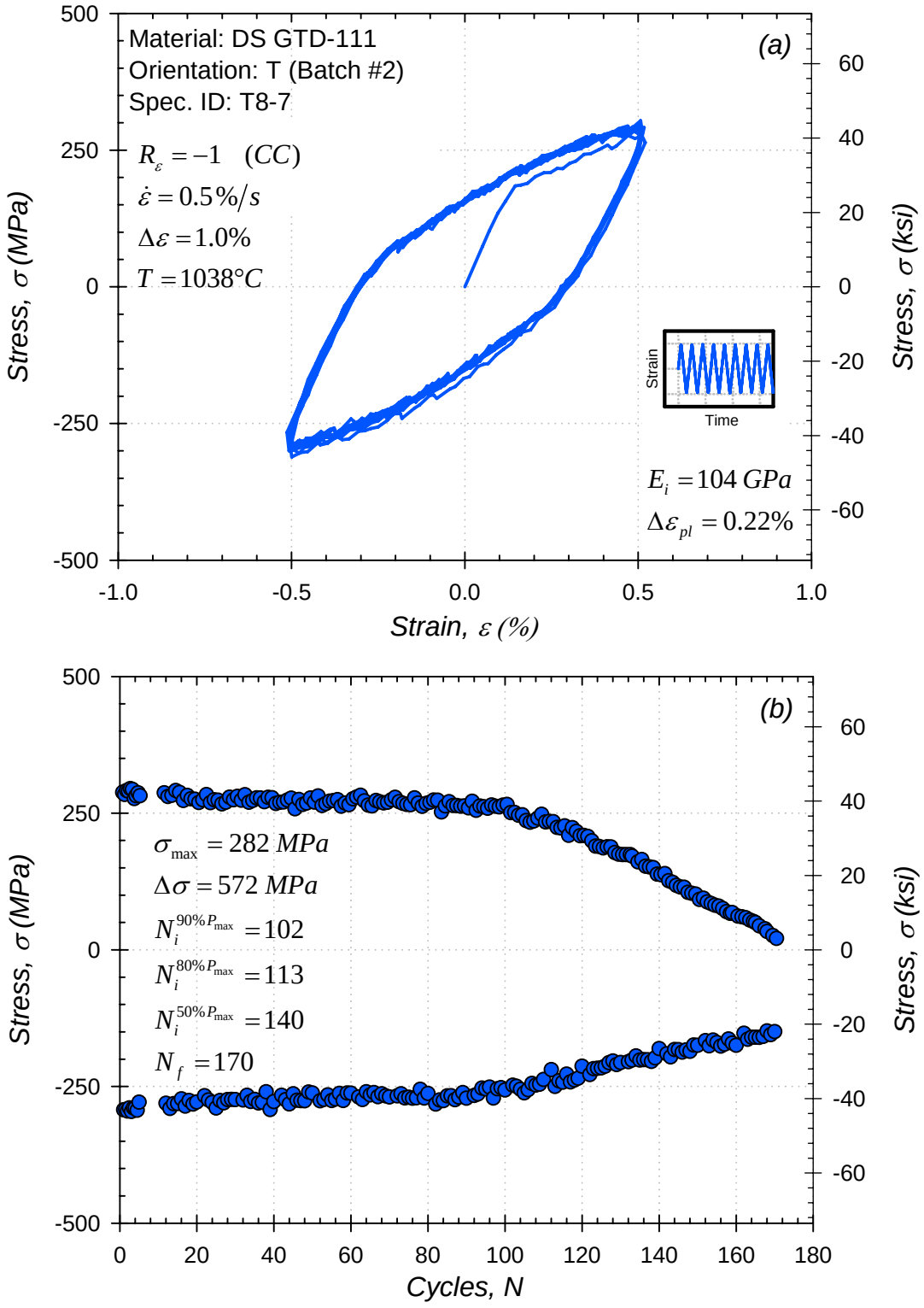


***Figure A.28:*** *(a) Initial stress-strain hysteresis loops and (b) stress history for low cycle fatigue test at 1038°C.*

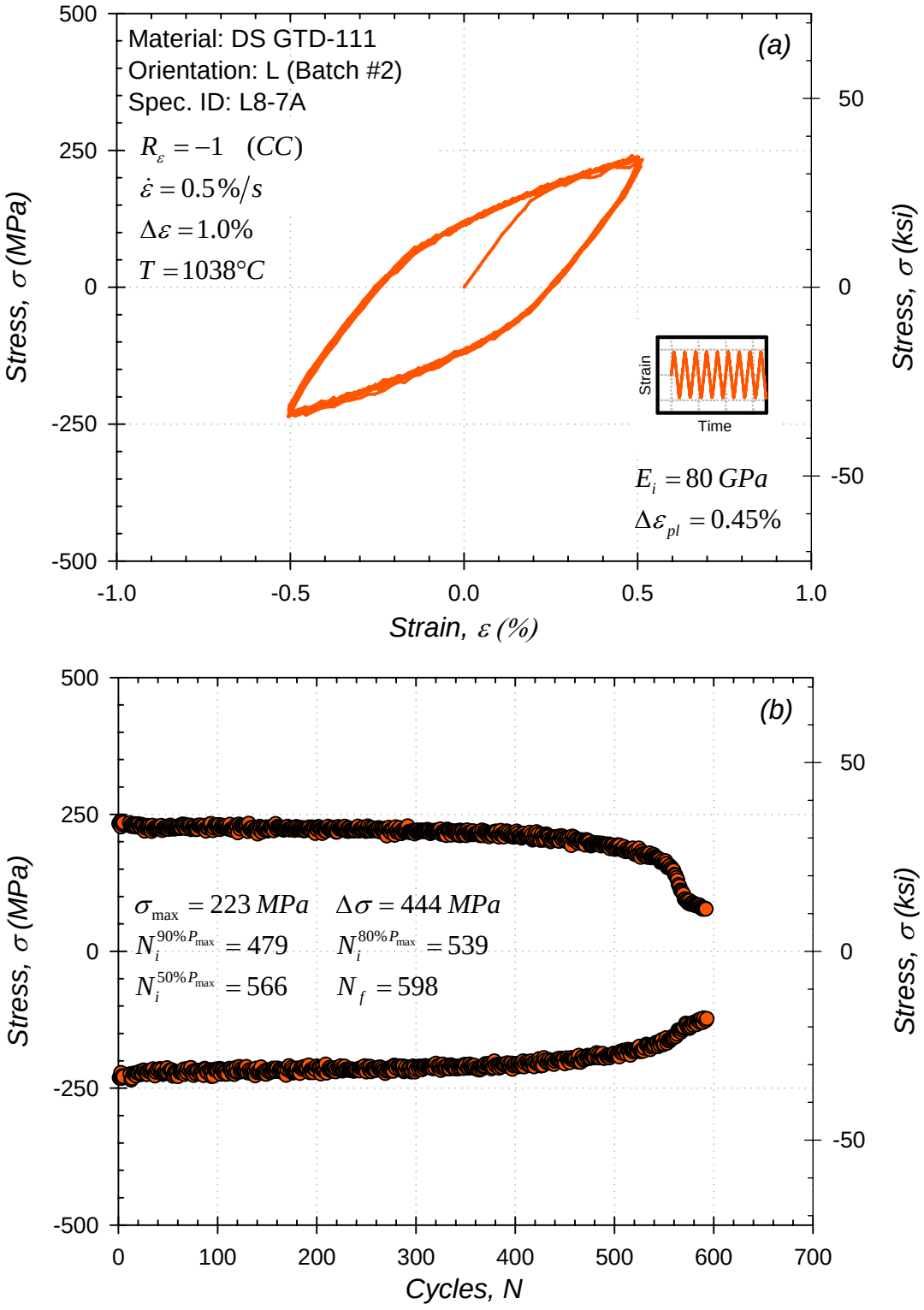


***Figure A.29:*** *(a) Initial stress-strain hysteresis loops and (b) stress history for low cycle fatigue test at 1038°C.*

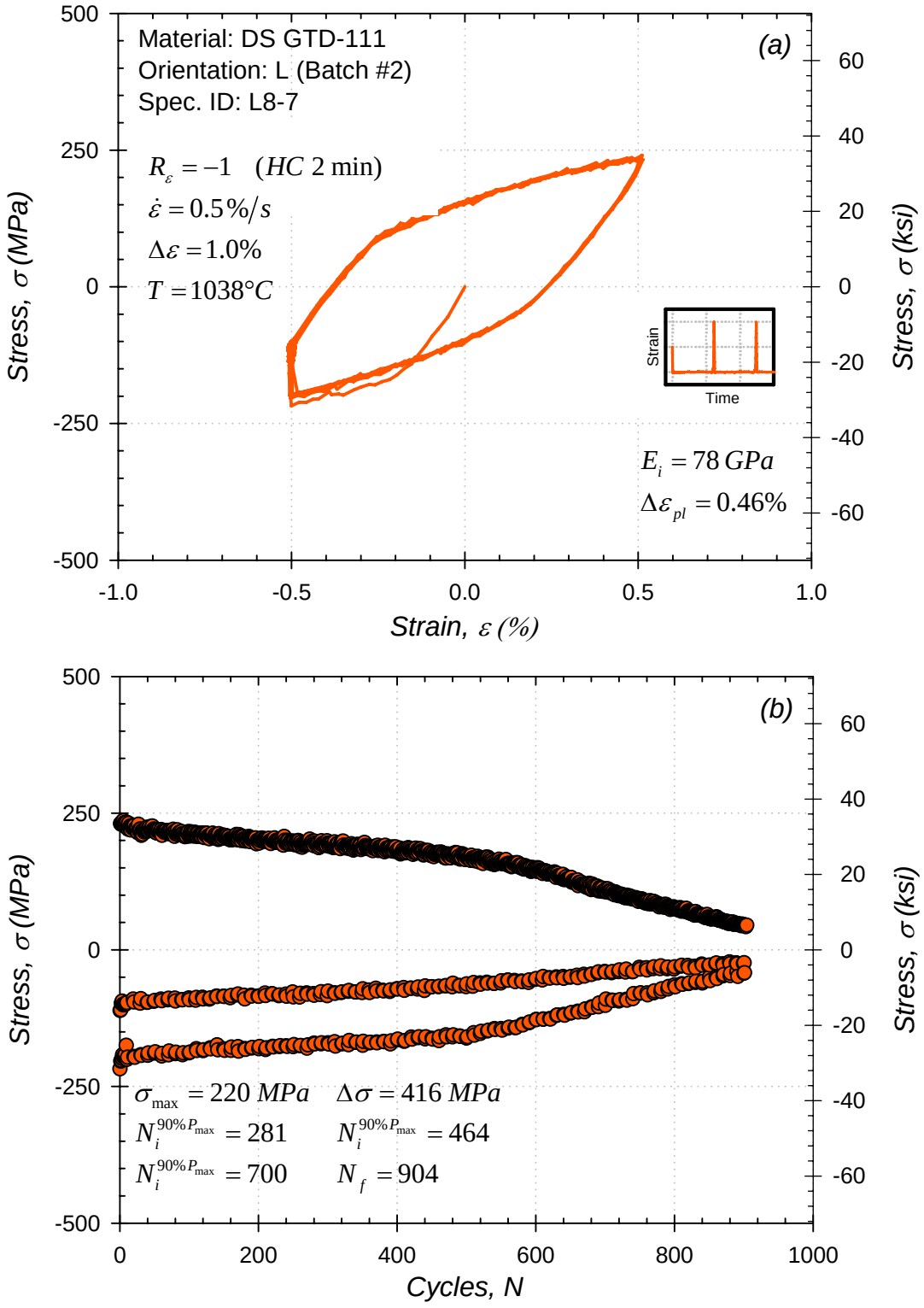


***Figure A.30:*** *(a) Initial stress-strain hysteresis loops and (b) stress history for low cycle fatigue test at 1038°C.*

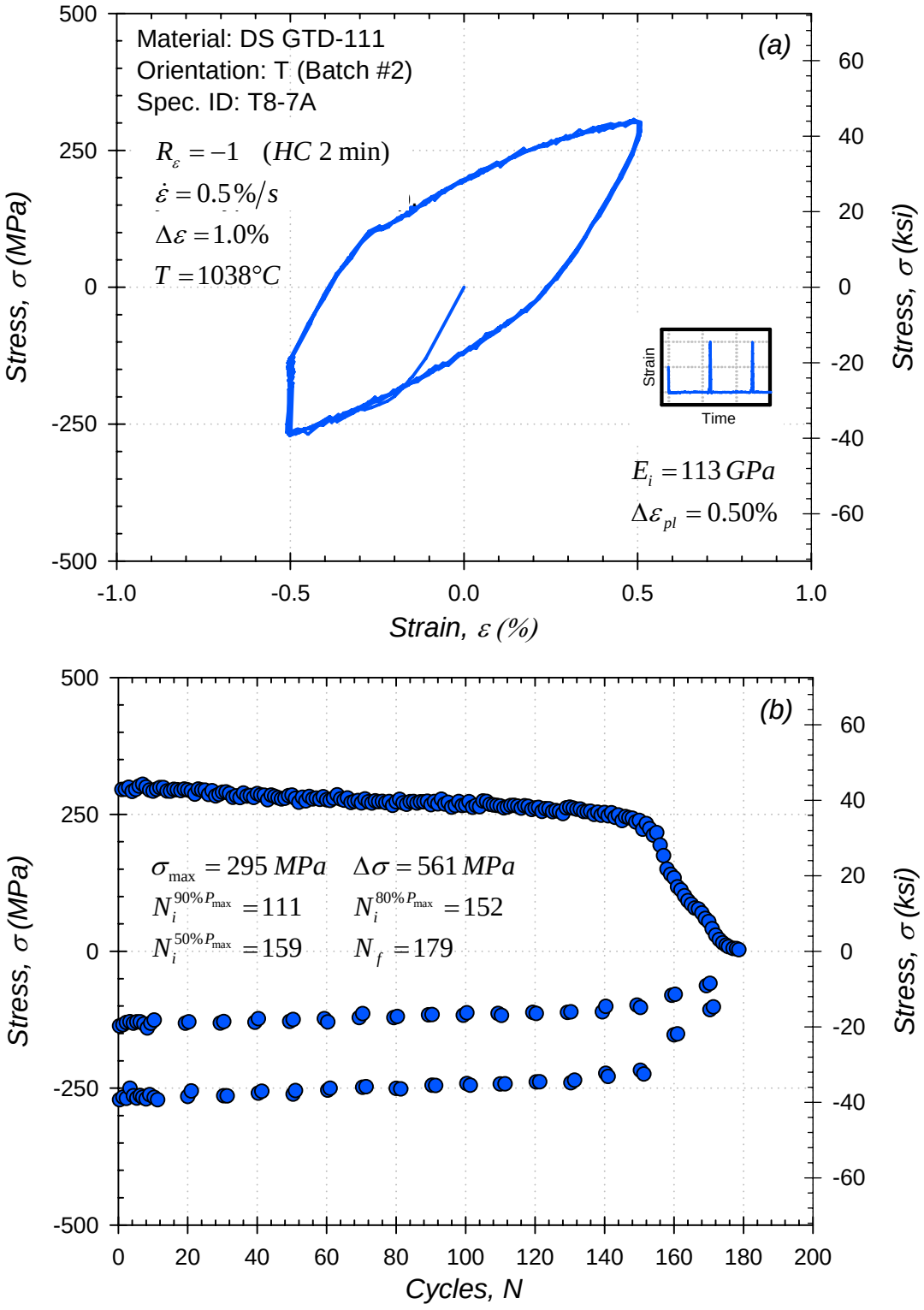


***Figure A.31:*** *(a) Initial stress-strain hysteresis loops and (b) stress history for low cycle fatigue test at 1038°C.*

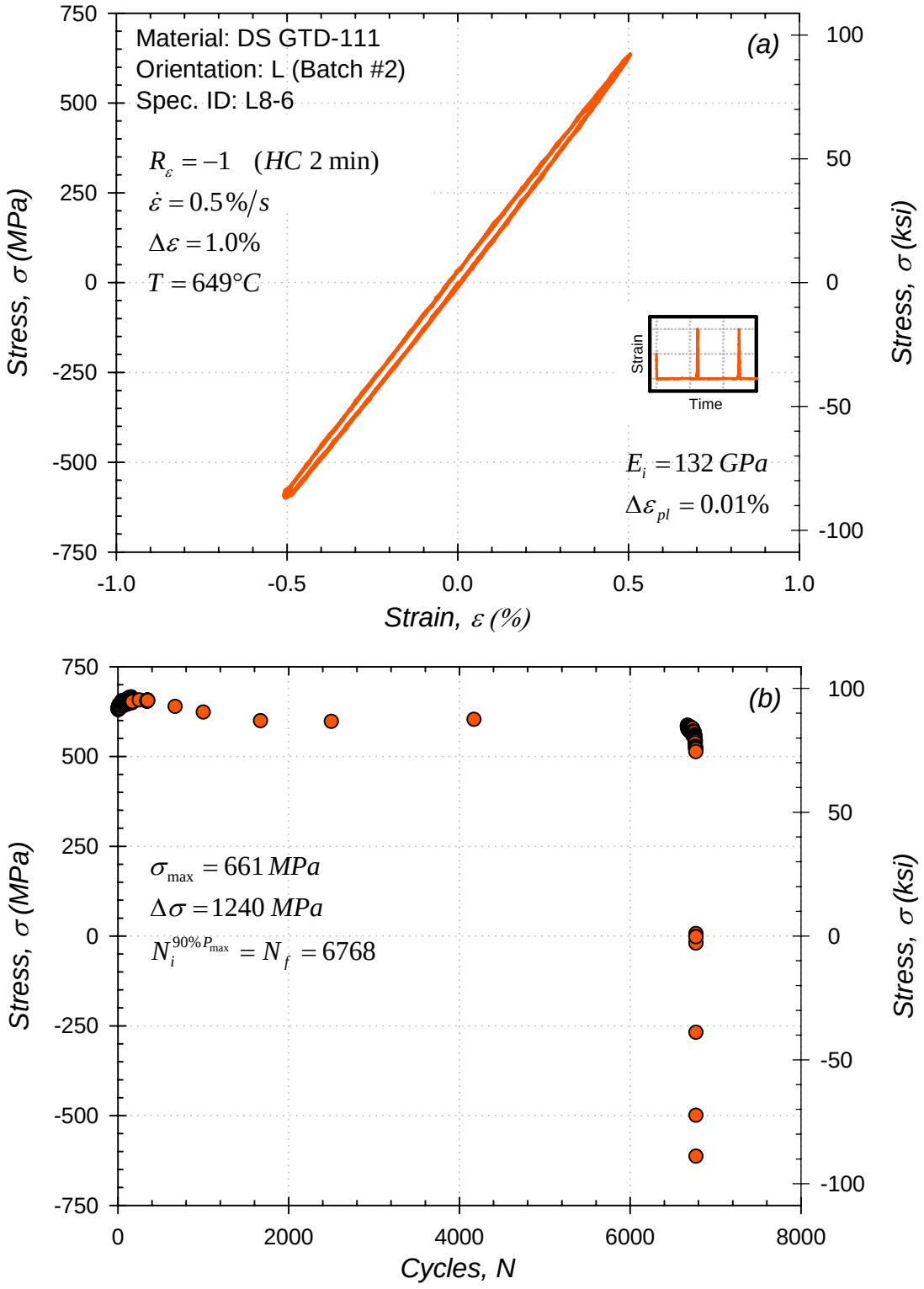


***Figure A.32:*** *(a) Initial stress-strain hysteresis loops and (b) stress history for low cycle fatigue test at 649°C.*

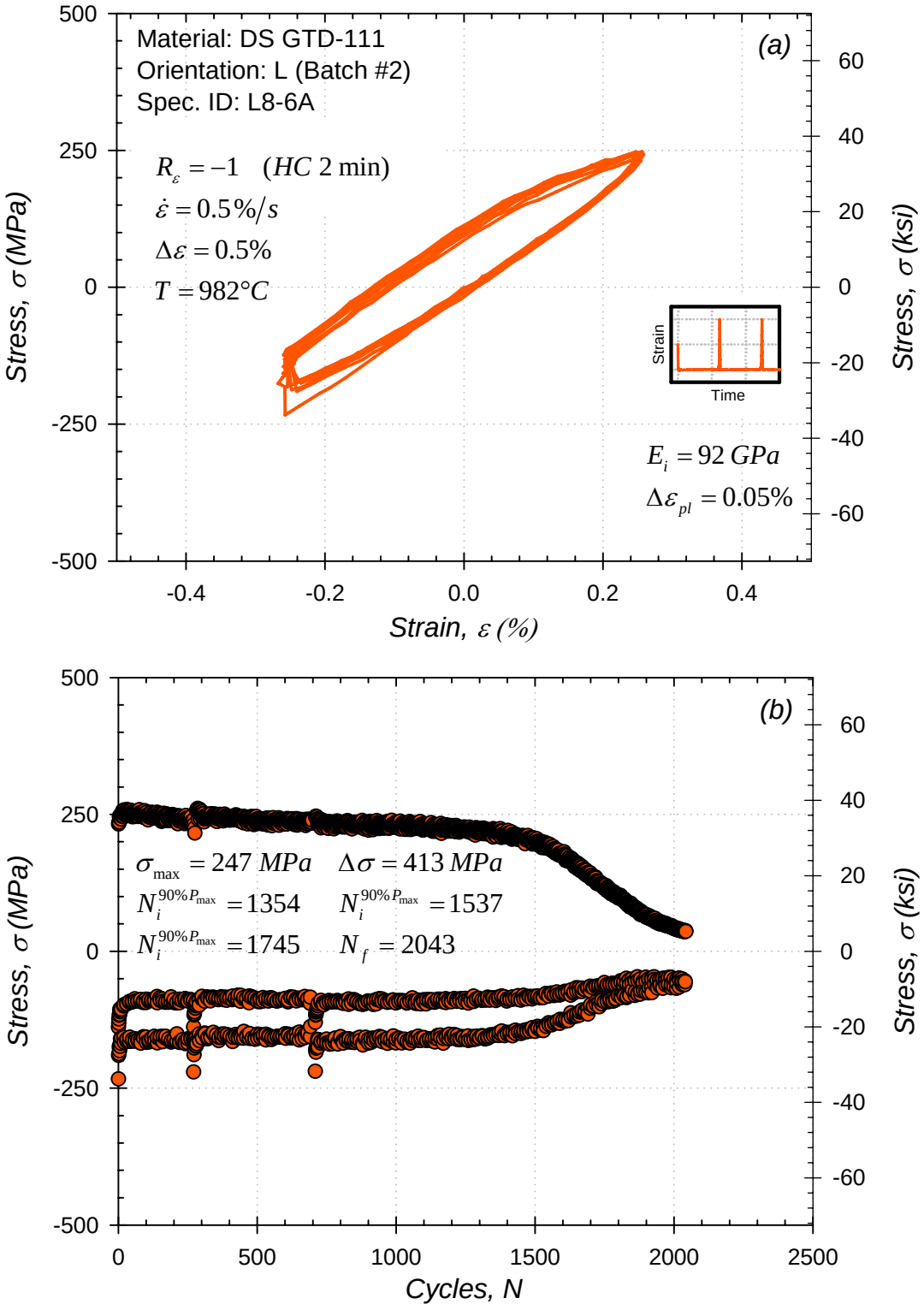


***Figure A.33:*** *(a) Initial stress-strain hysteresis loops and (b) stress history for low cycle fatigue test at 982°C.*

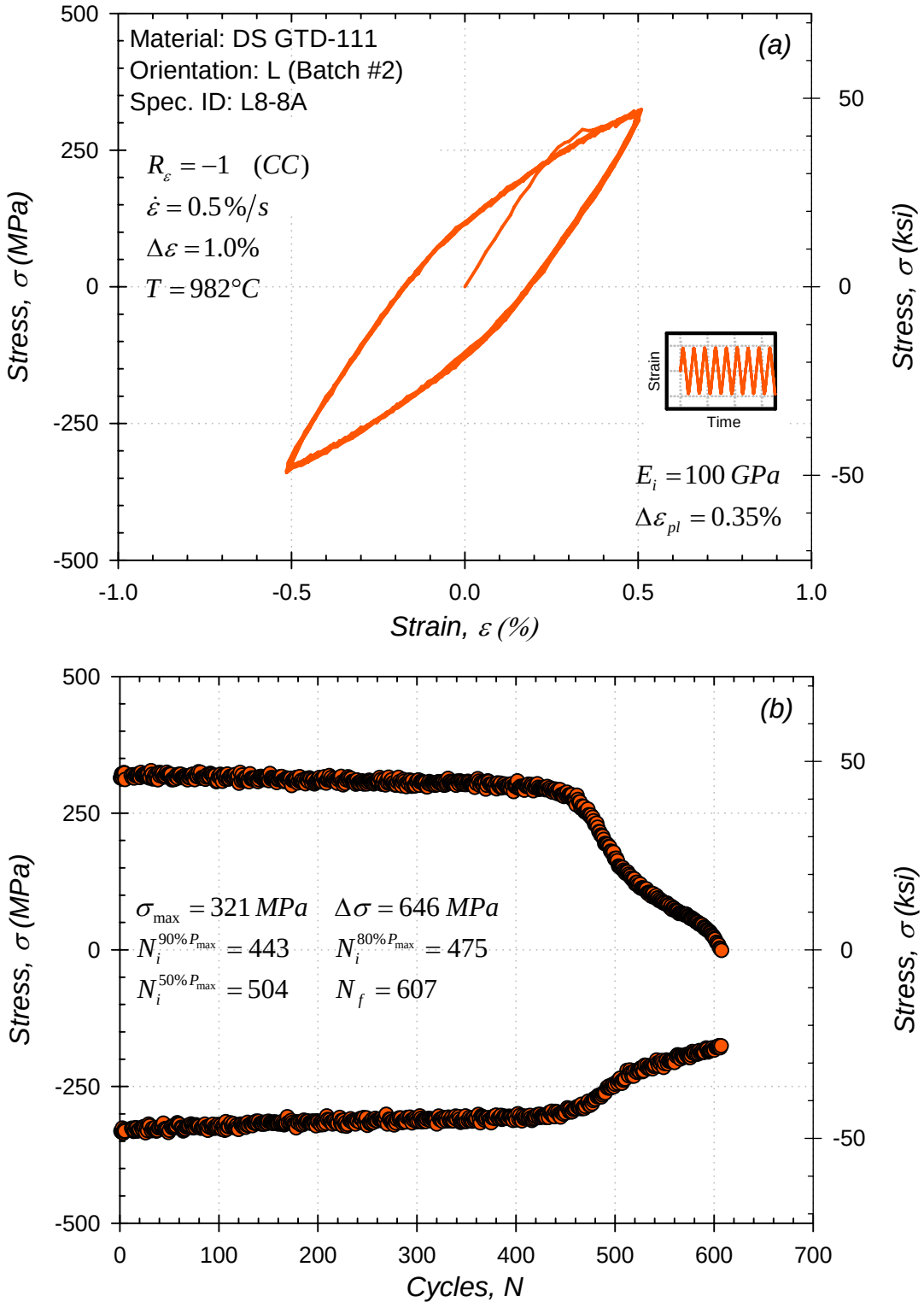


***Figure A.34:*** *(a) Initial stress-strain hysteresis loops and (b) stress history for low cycle fatigue test at 982°C.*

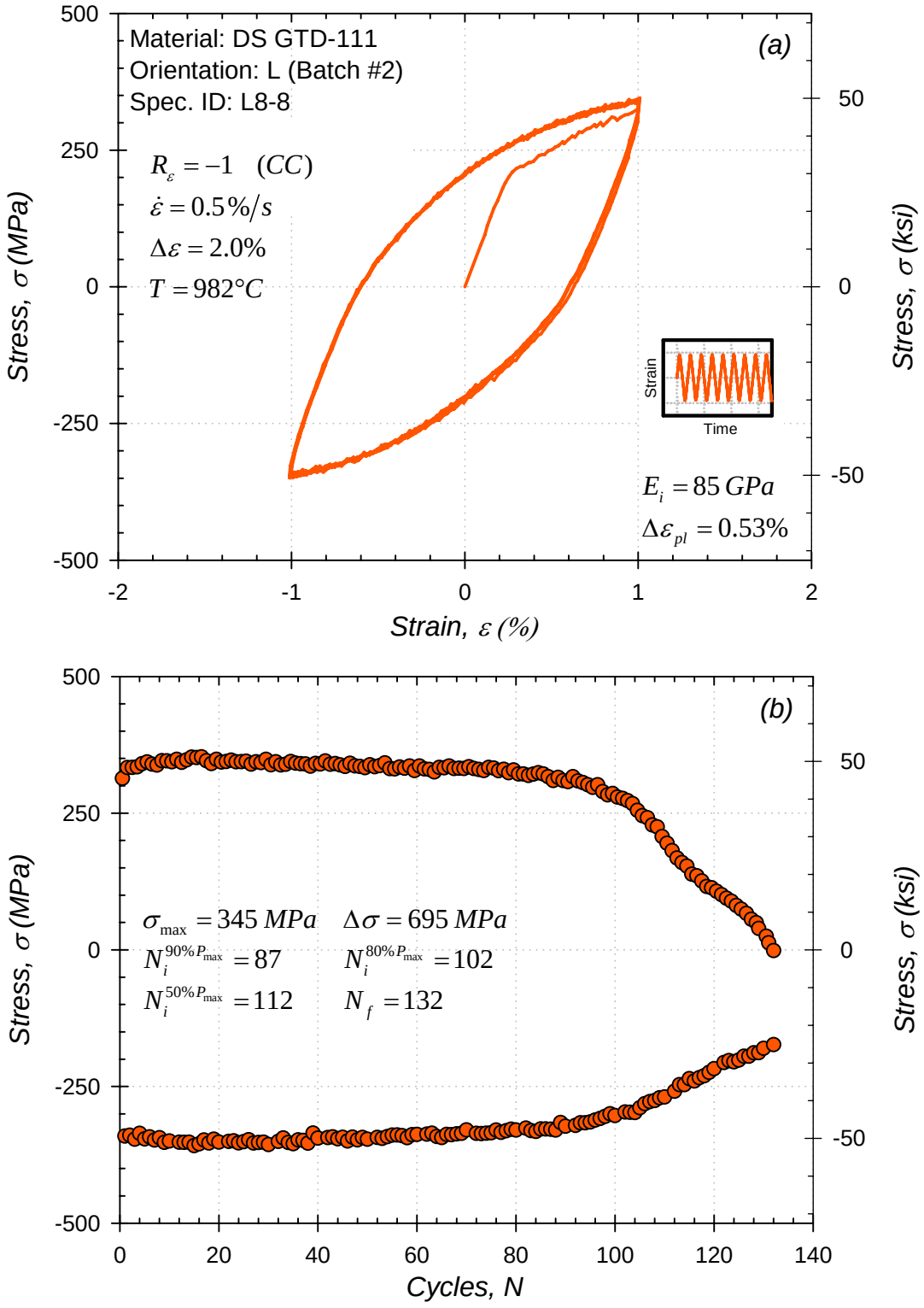


***Figure A.35:*** *(a) Initial stress-strain hysteresis loops and (b) stress history for low cycle fatigue test at 982°C.*

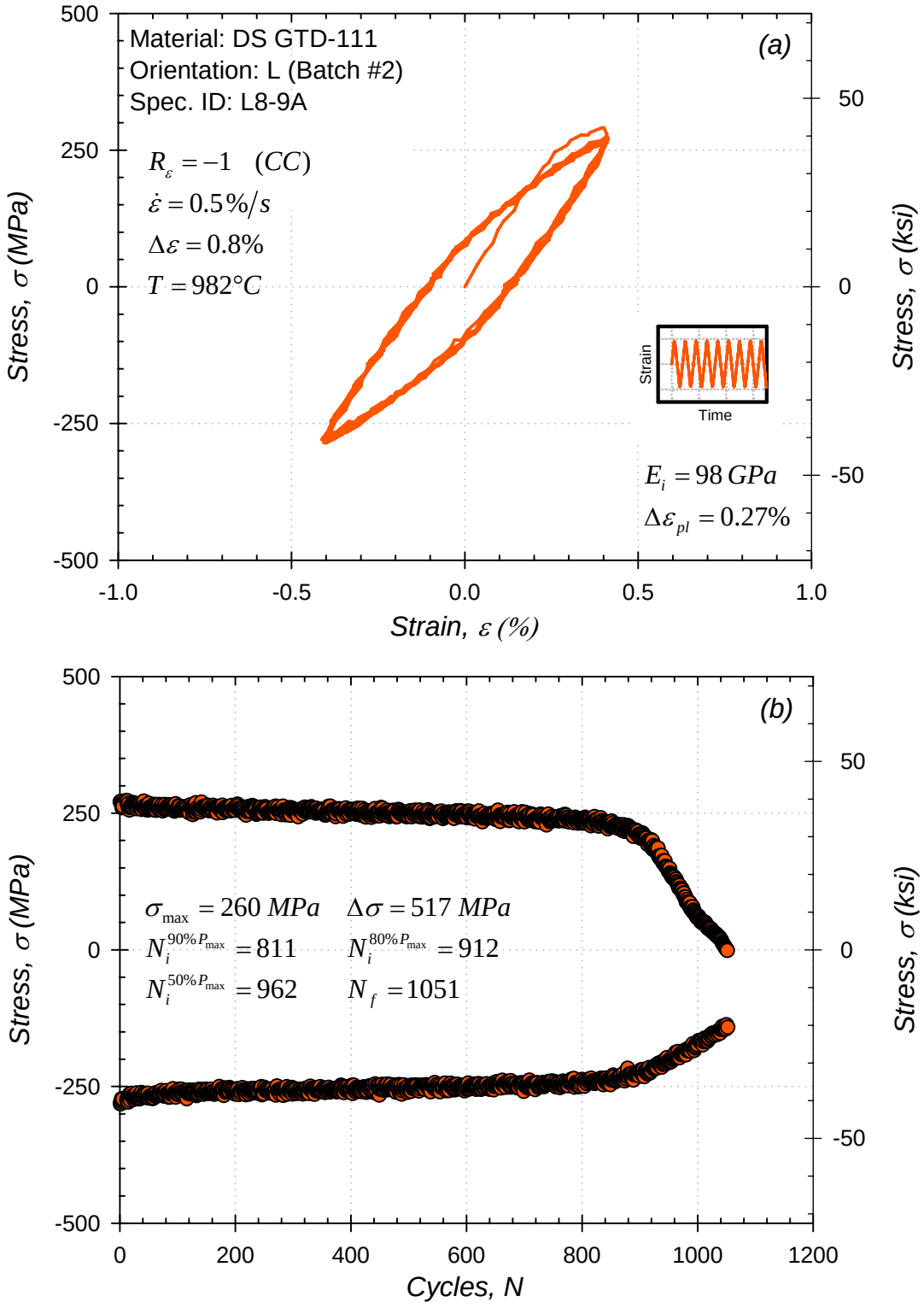


***Figure A.36:*** *(a) Initial stress-strain hysteresis loops and (b) stress history for low cycle fatigue test at 982°C.*

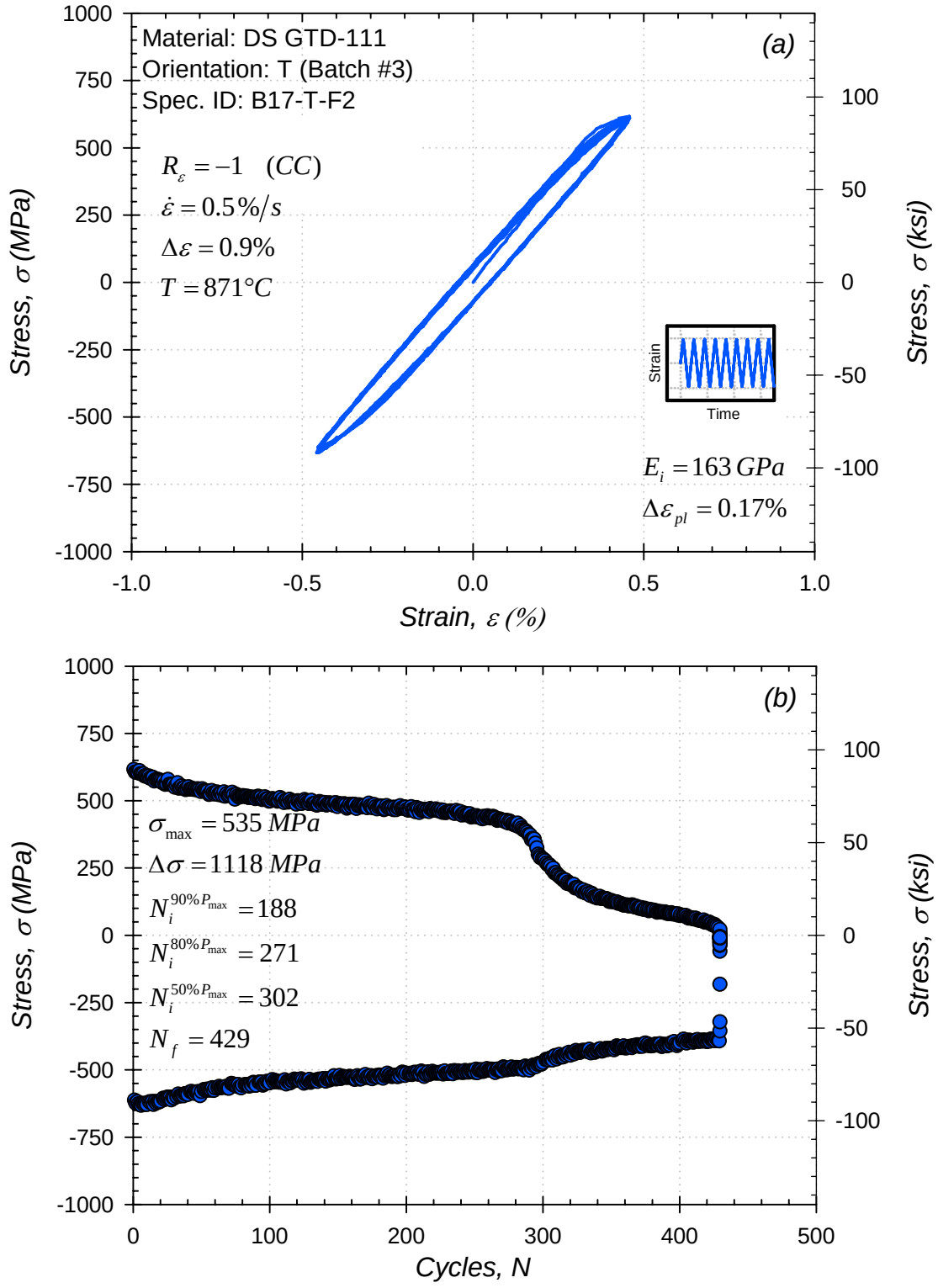


***Figure A.37:*** *(a) Initial stress-strain hysteresis loops and (b) stress history for low cycle fatigue test at 871°C.*

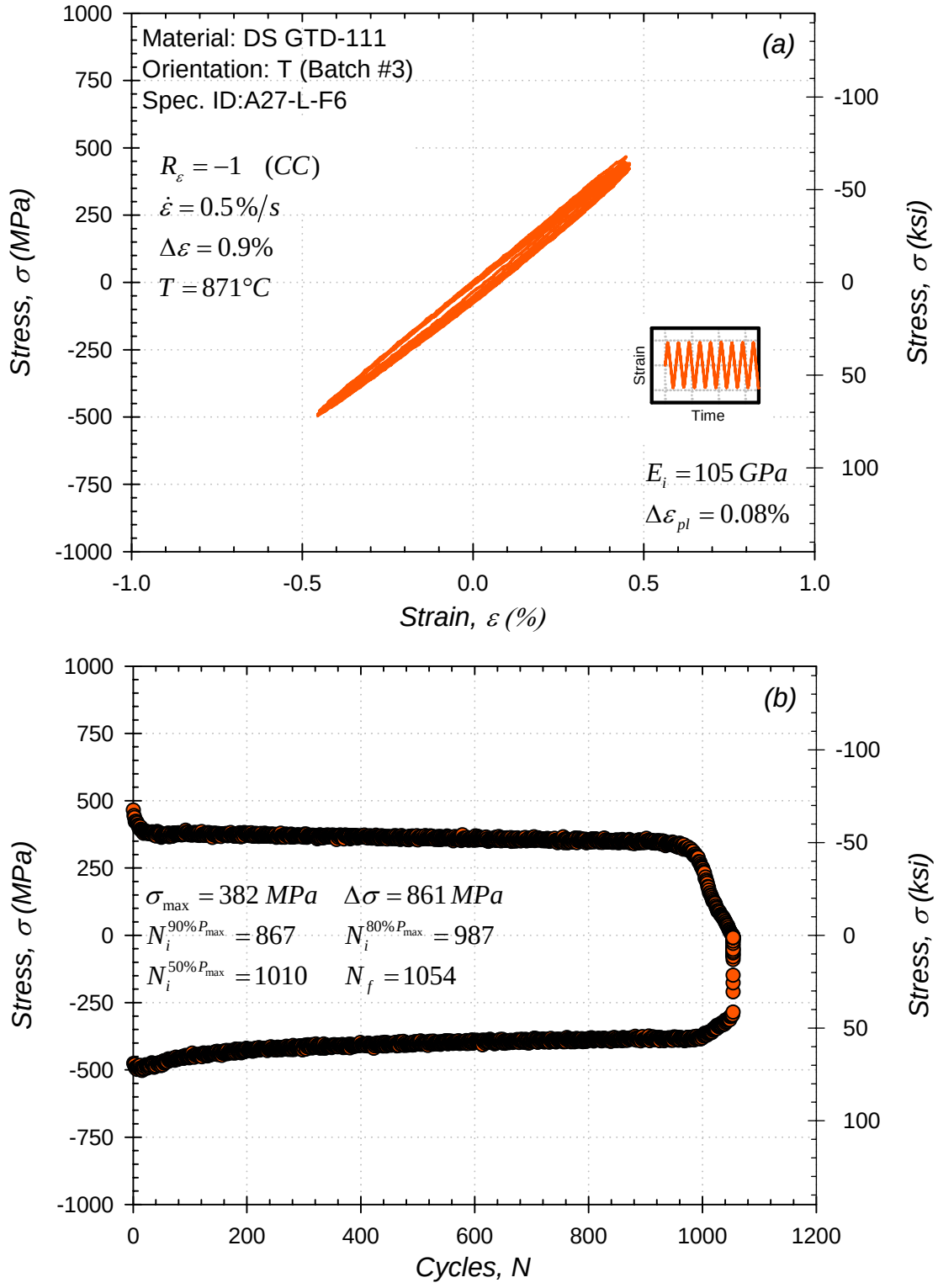


***Figure A.38:*** *(a) Initial stress-strain hysteresis loops and (b) stress history for low cycle fatigue test at 871°C.*

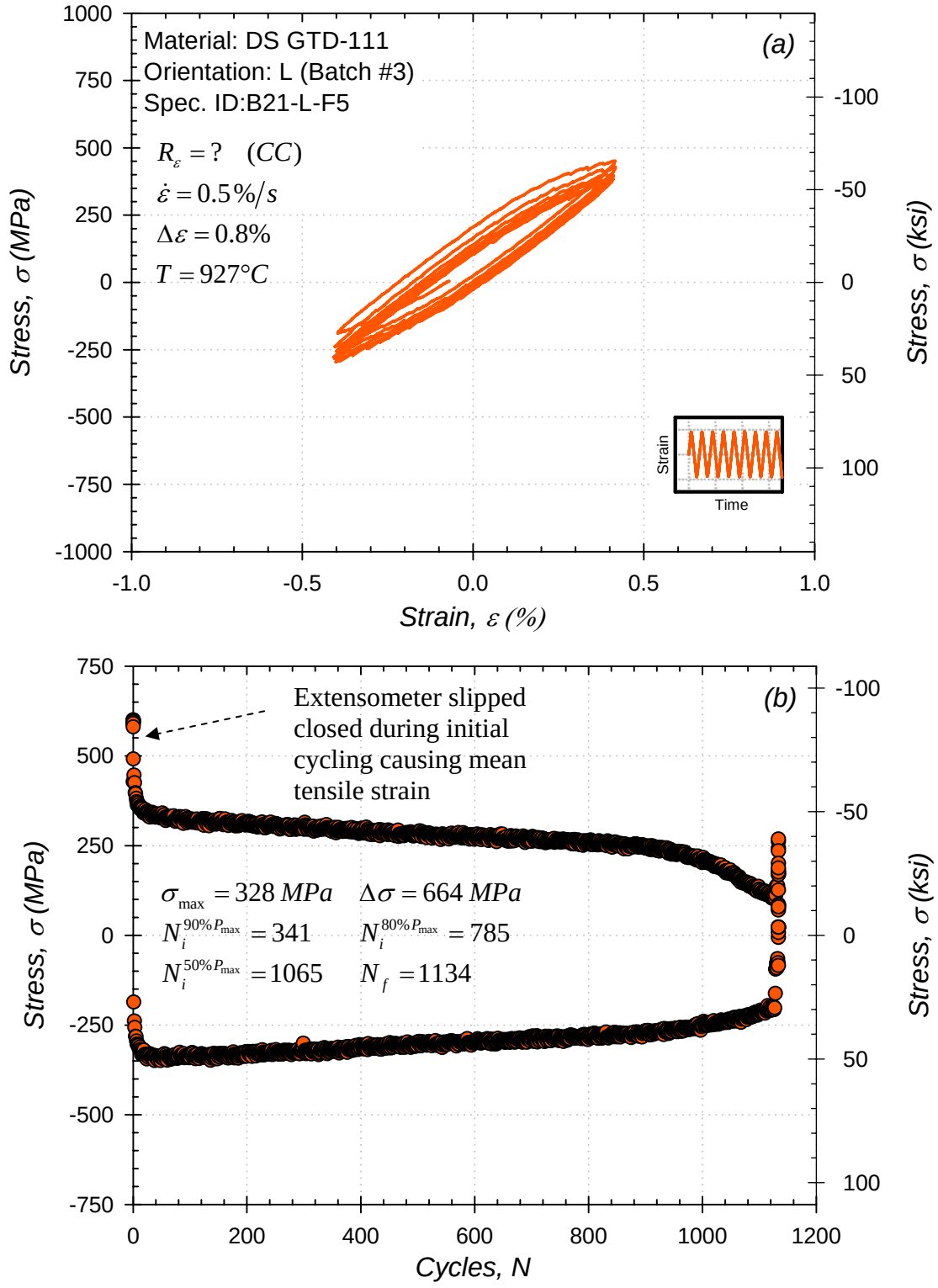


***Figure A.39:*** *(a) Initial stress-strain hysteresis loops and (b) stress history for low cycle fatigue test at 927°C.*

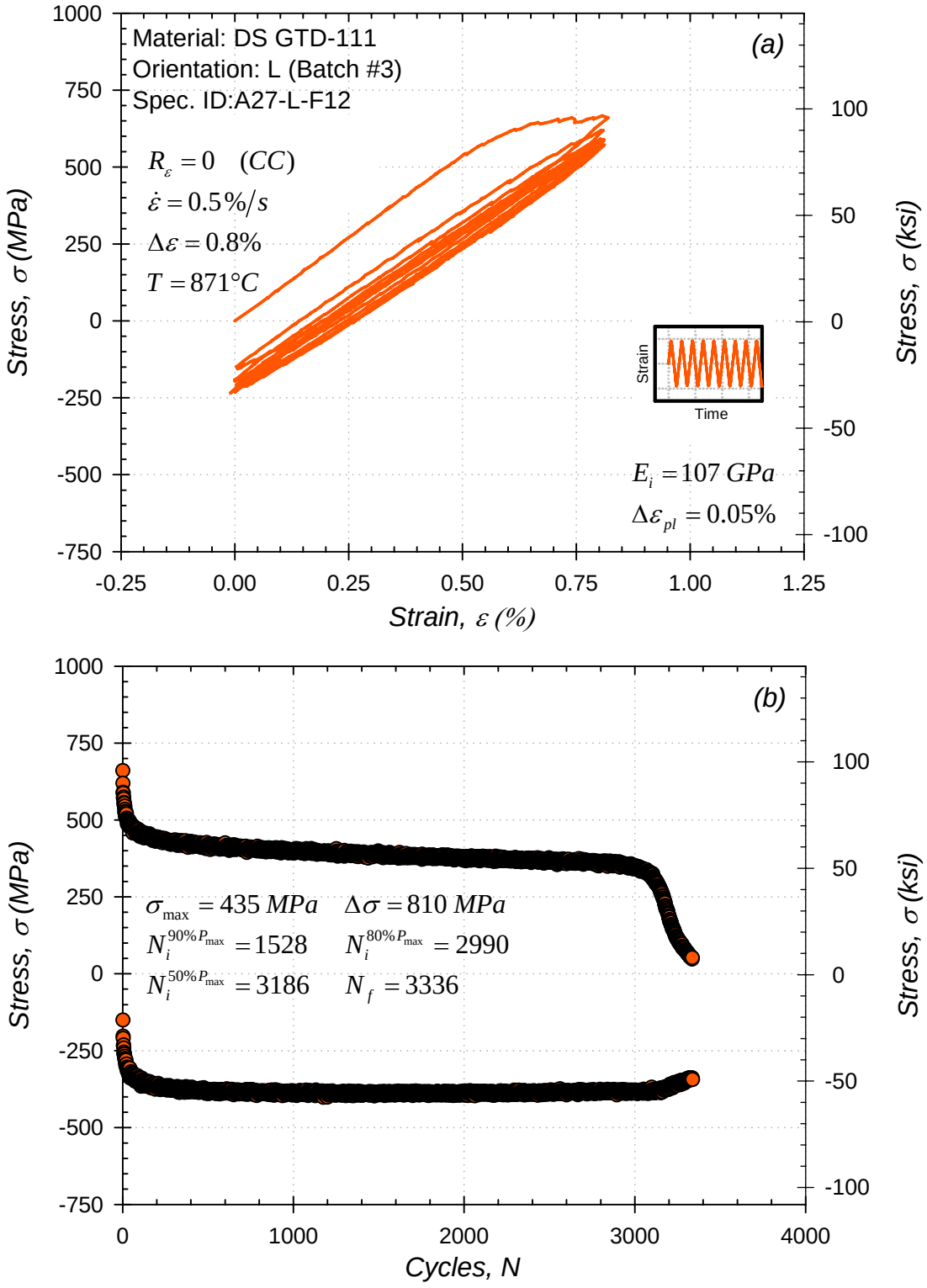


***Figure A.40:*** *(a) Initial stress-strain hysteresis loops and (b) stress history for low cycle fatigue test at 871°C.*

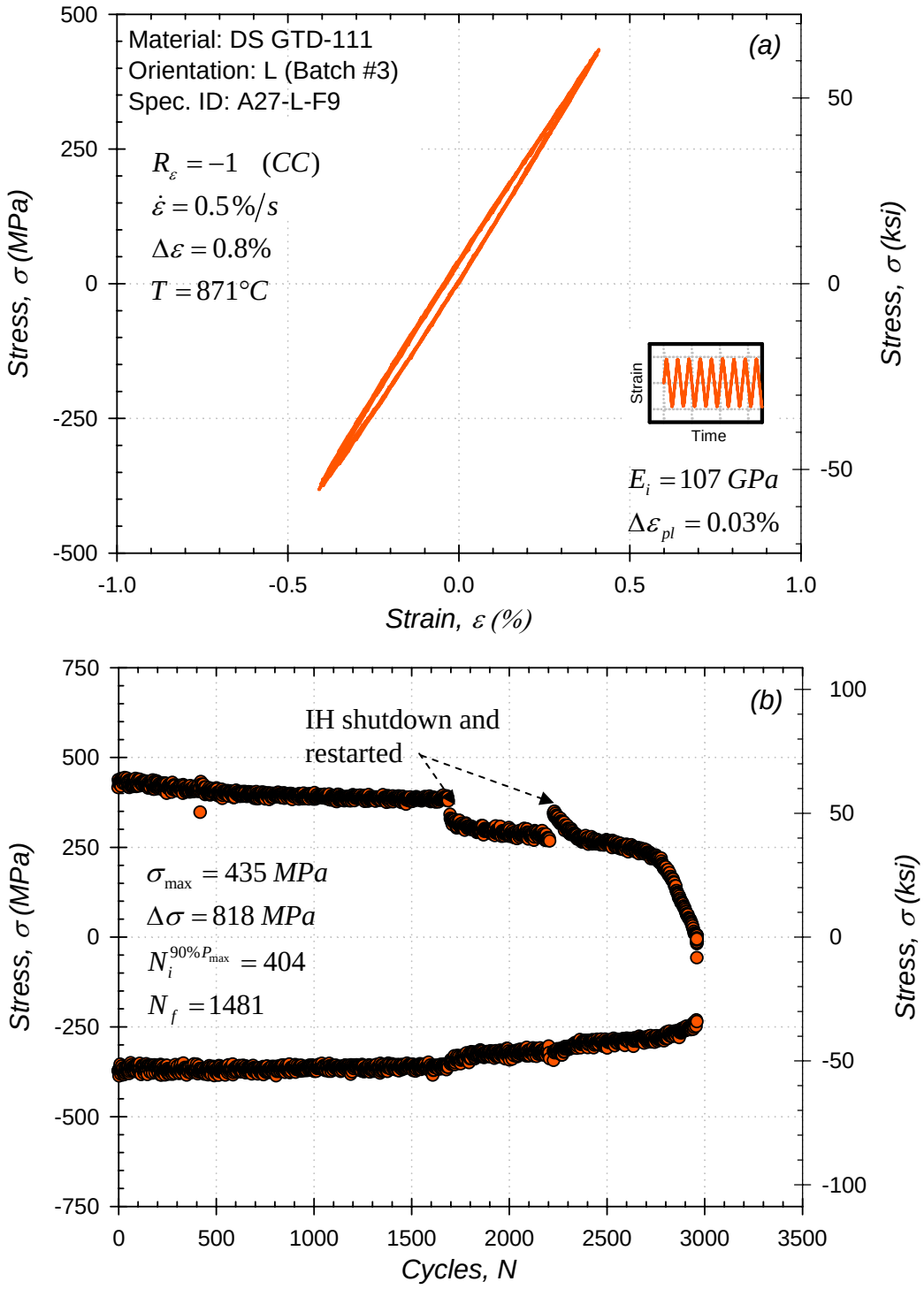


***Figure A.41:*** *(a) Initial stress-strain hysteresis loops and (b) stress history for low cycle fatigue test at 871°C.*

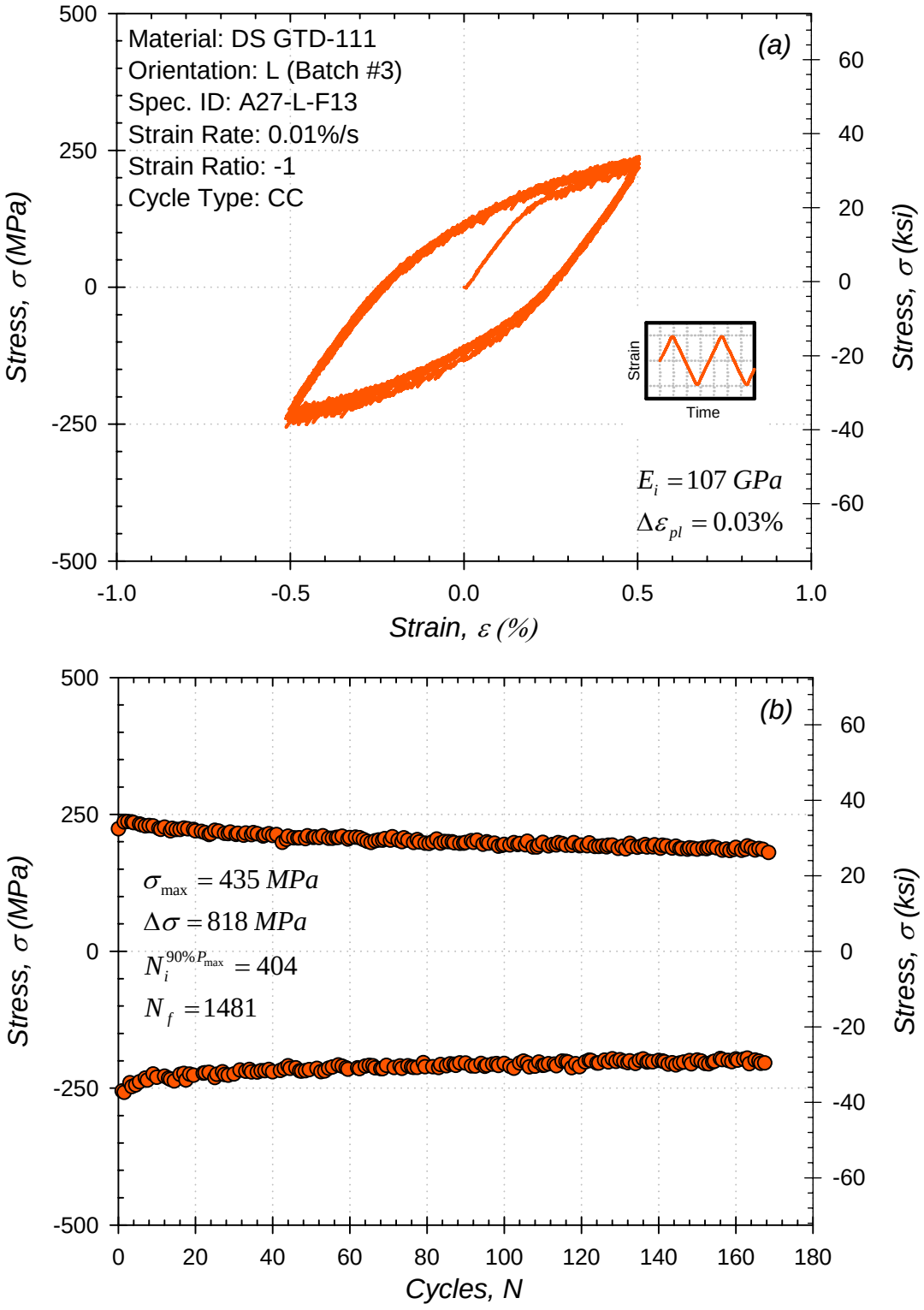


***Figure A.42:*** *(a) Initial stress-strain hysteresis loops and (b) stress history for low cycle fatigue test at 982°C.*

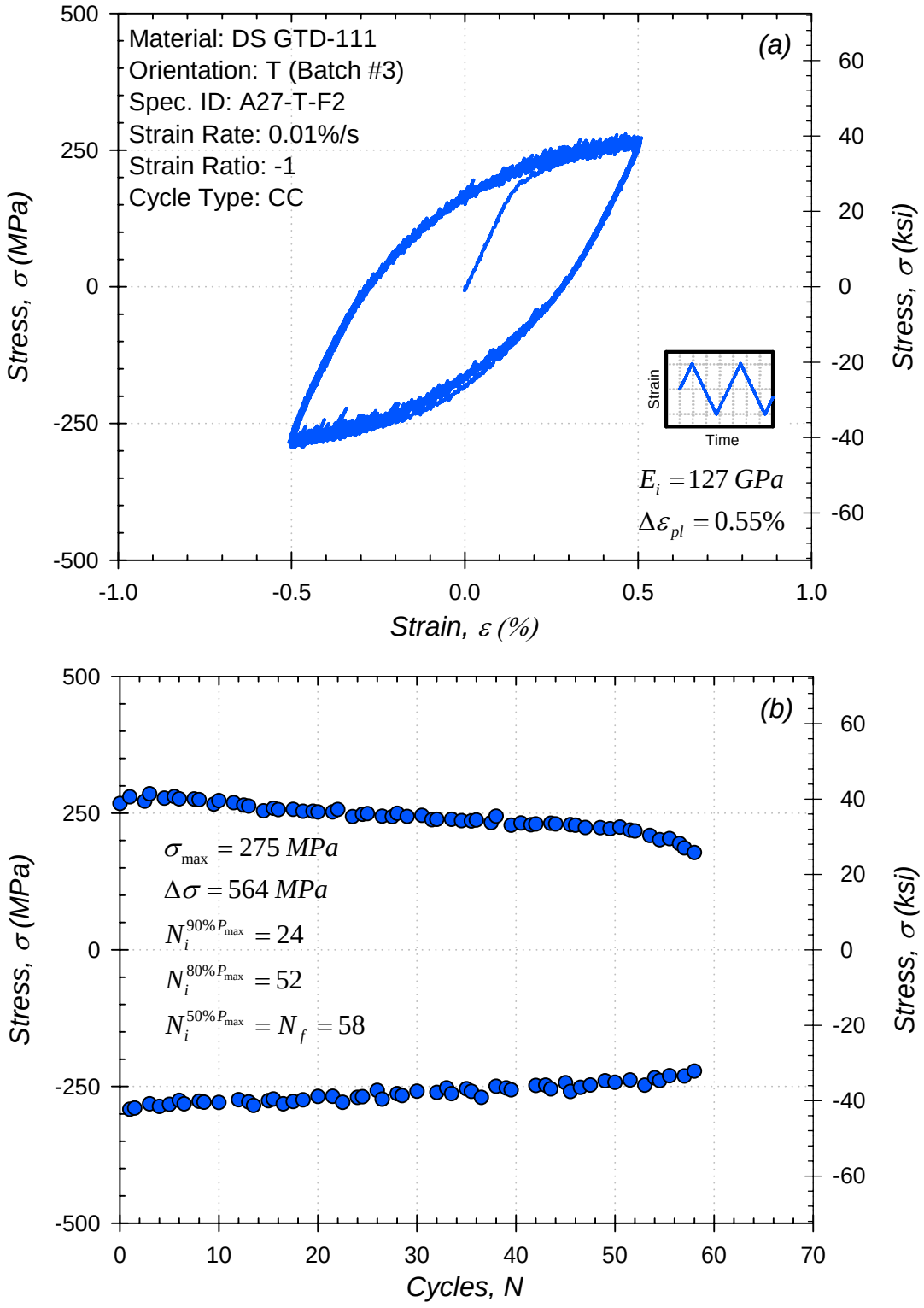


***Figure A.43:*** *(a) Initial stress-strain hysteresis loops and (b) stress history for low cycle fatigue test at 982°C.*

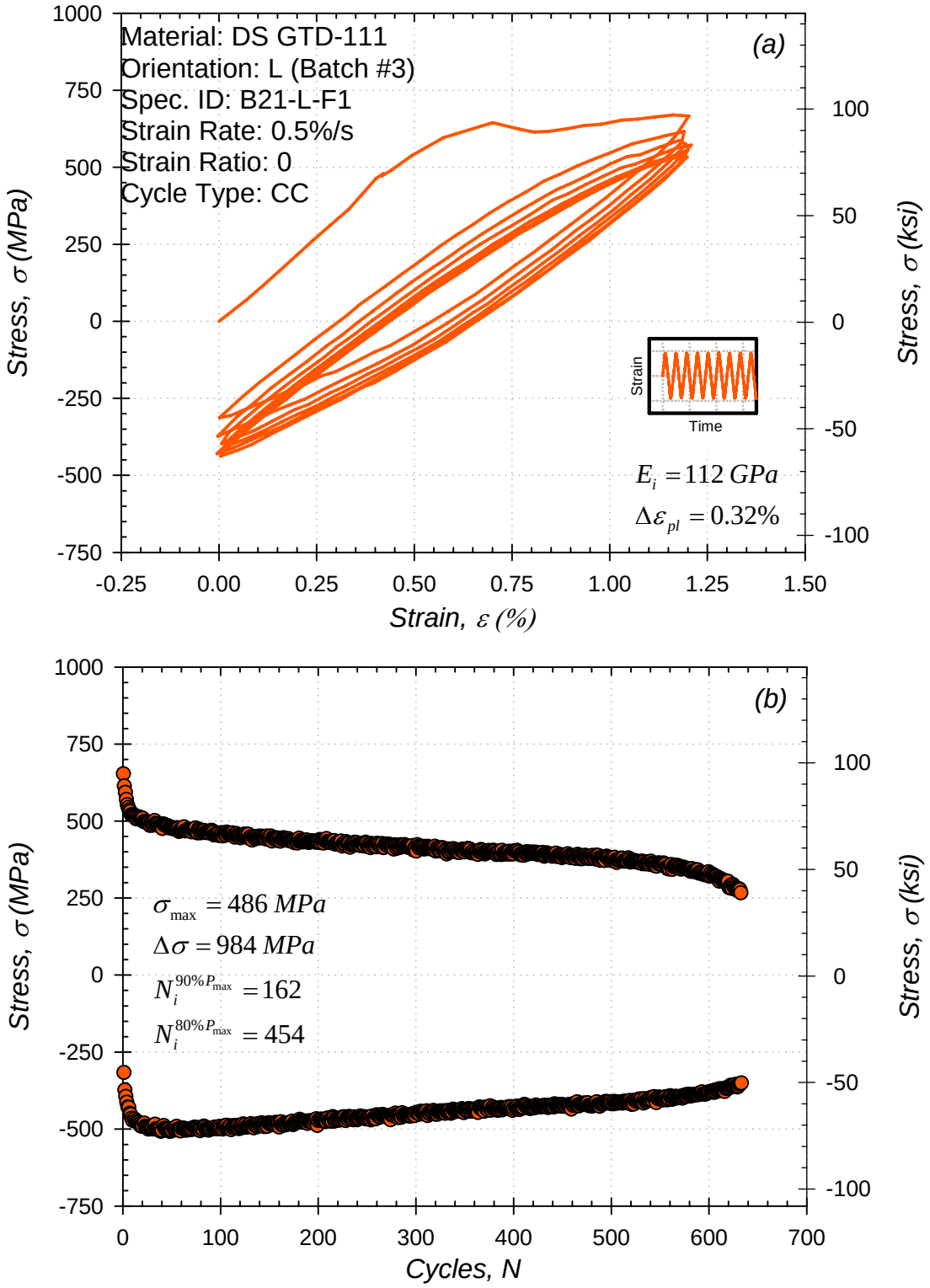


***Figure A.44:*** *(a) Initial stress-strain hysteresis loops and (b) stress history for low cycle fatigue test at 871°C.*

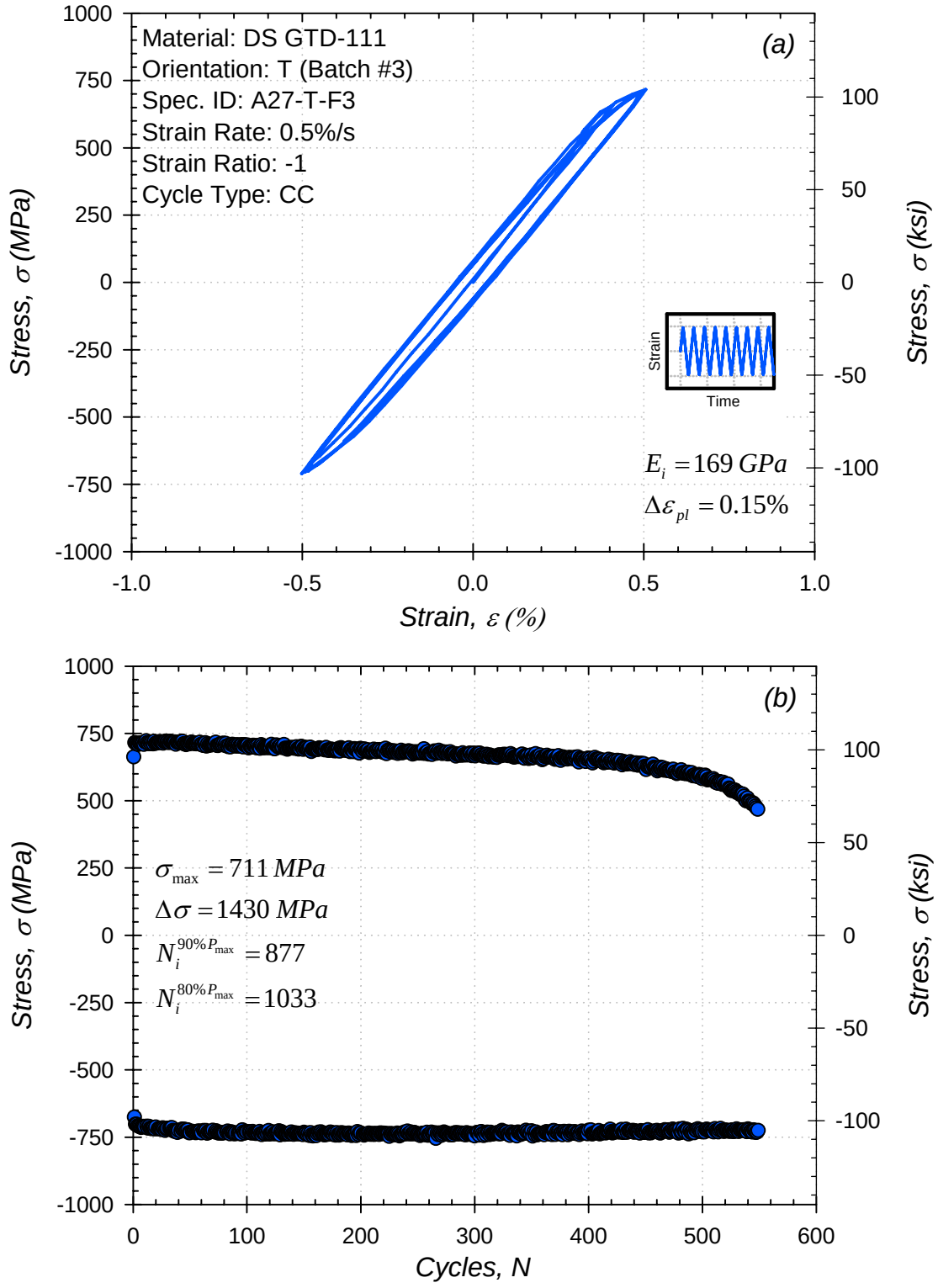


***Figure A.45:*** *(a) Initial stress-strain hysteresis loops and (b) stress history for low cycle fatigue test at 760°C.*

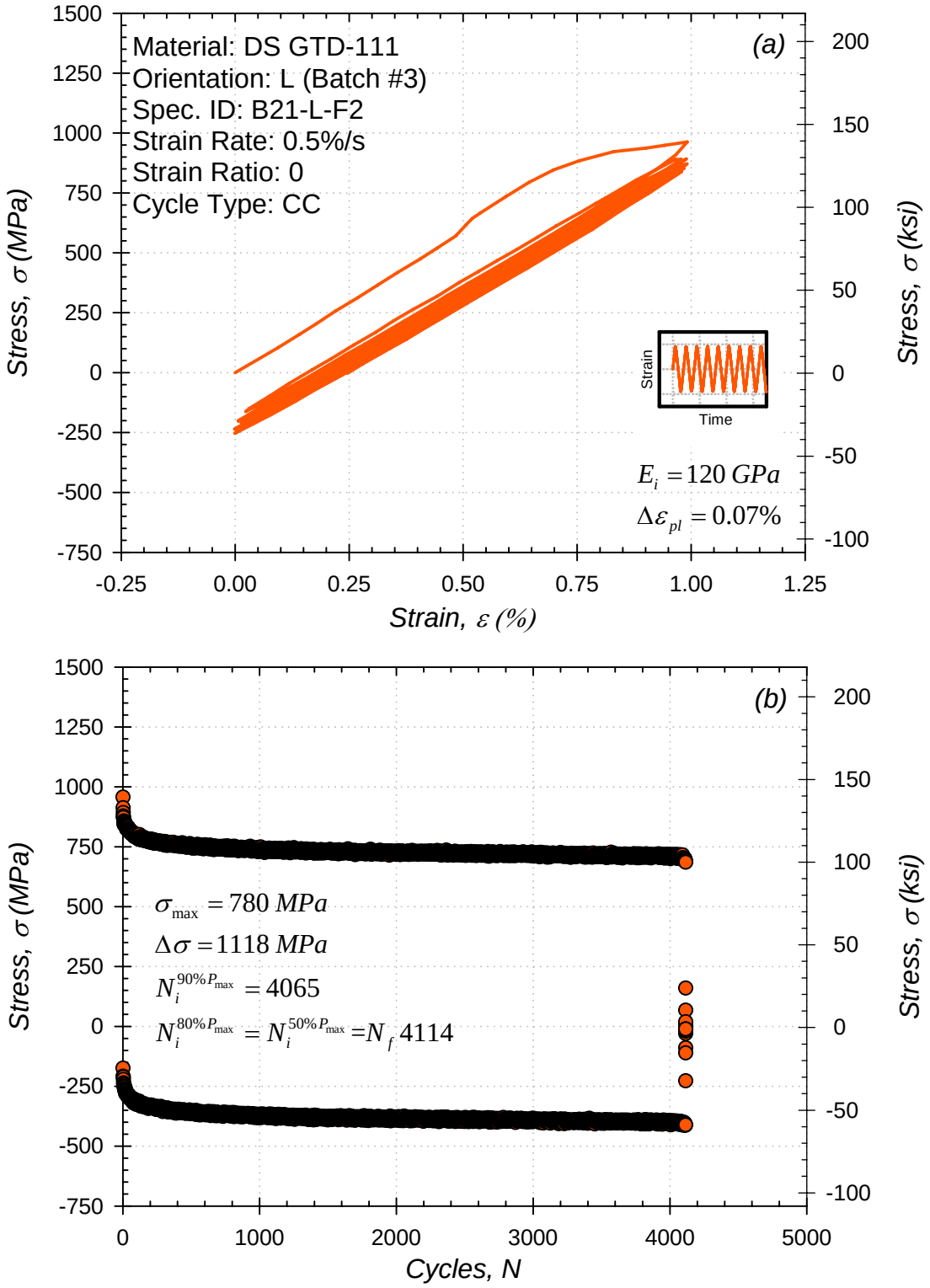


***Figure A.46:*** *(a) Initial stress-strain hysteresis loops and (b) stress history for low cycle fatigue test at 760°C.*

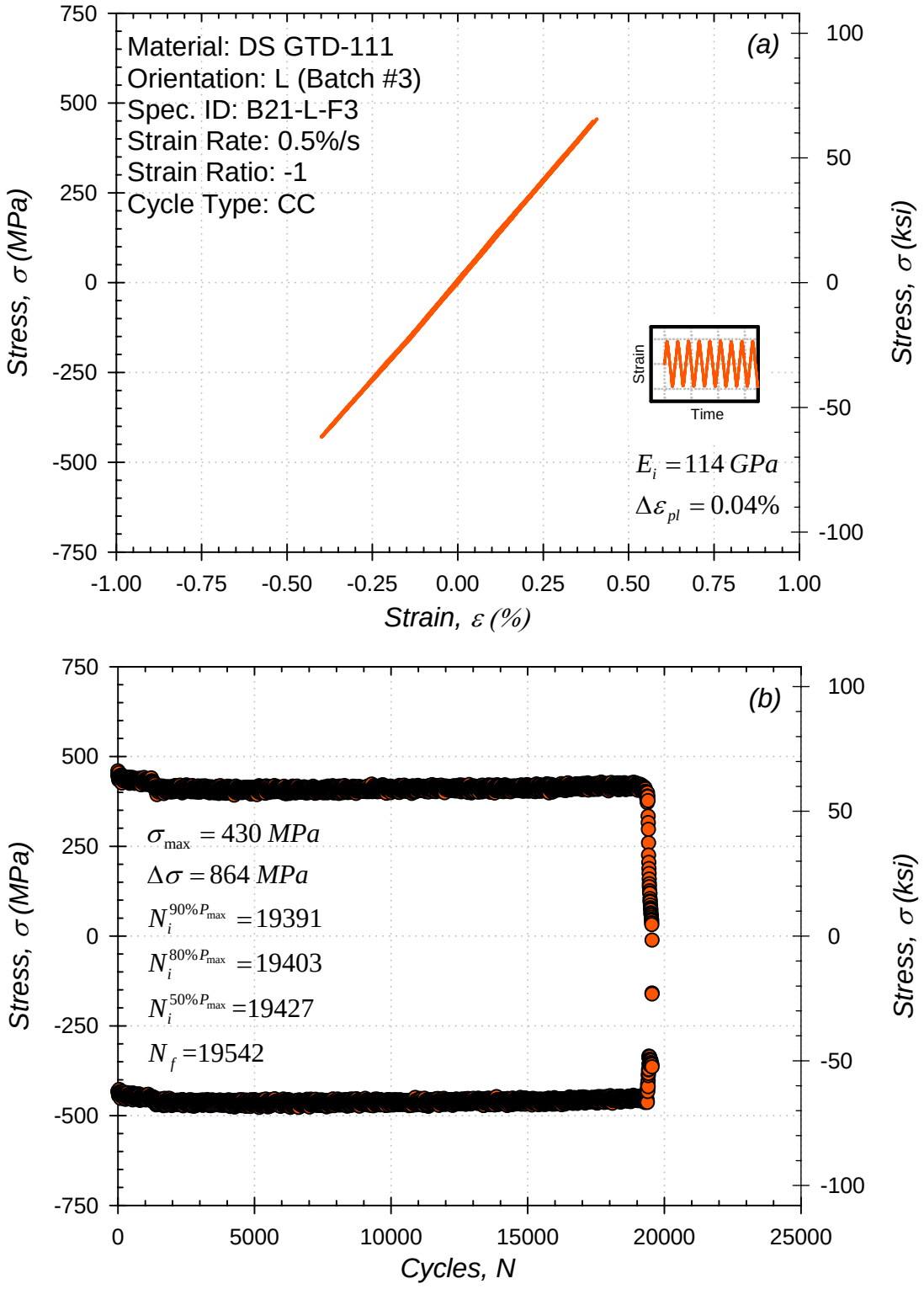


***Figure A.47:*** *(a) Initial stress-strain hysteresis loops and (b) stress history for low cycle fatigue test at 760°C.*

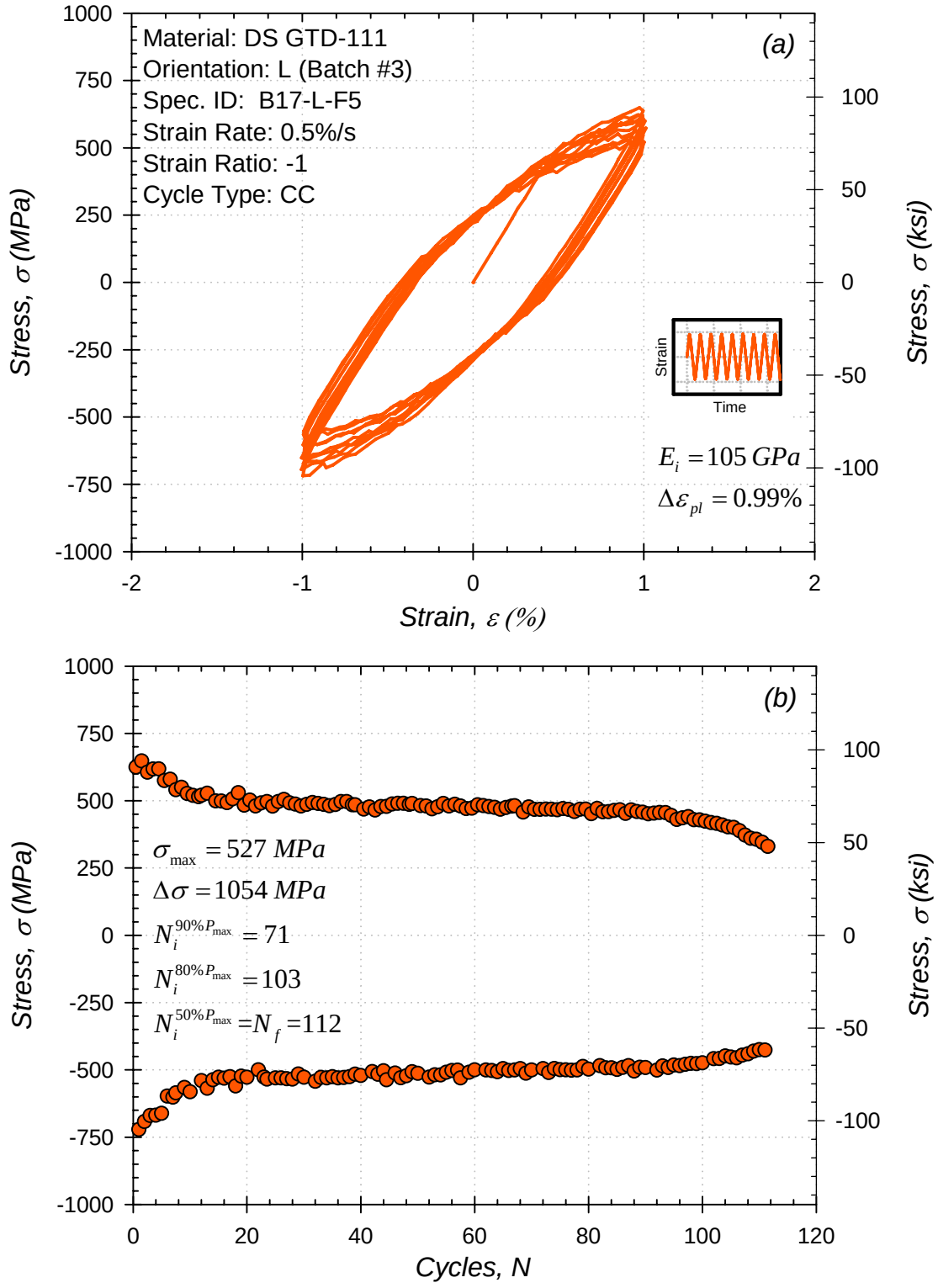


***Figure A.48:*** *(a) Initial stress-strain hysteresis loops and (b) stress history for low cycle fatigue test at 871°C.*

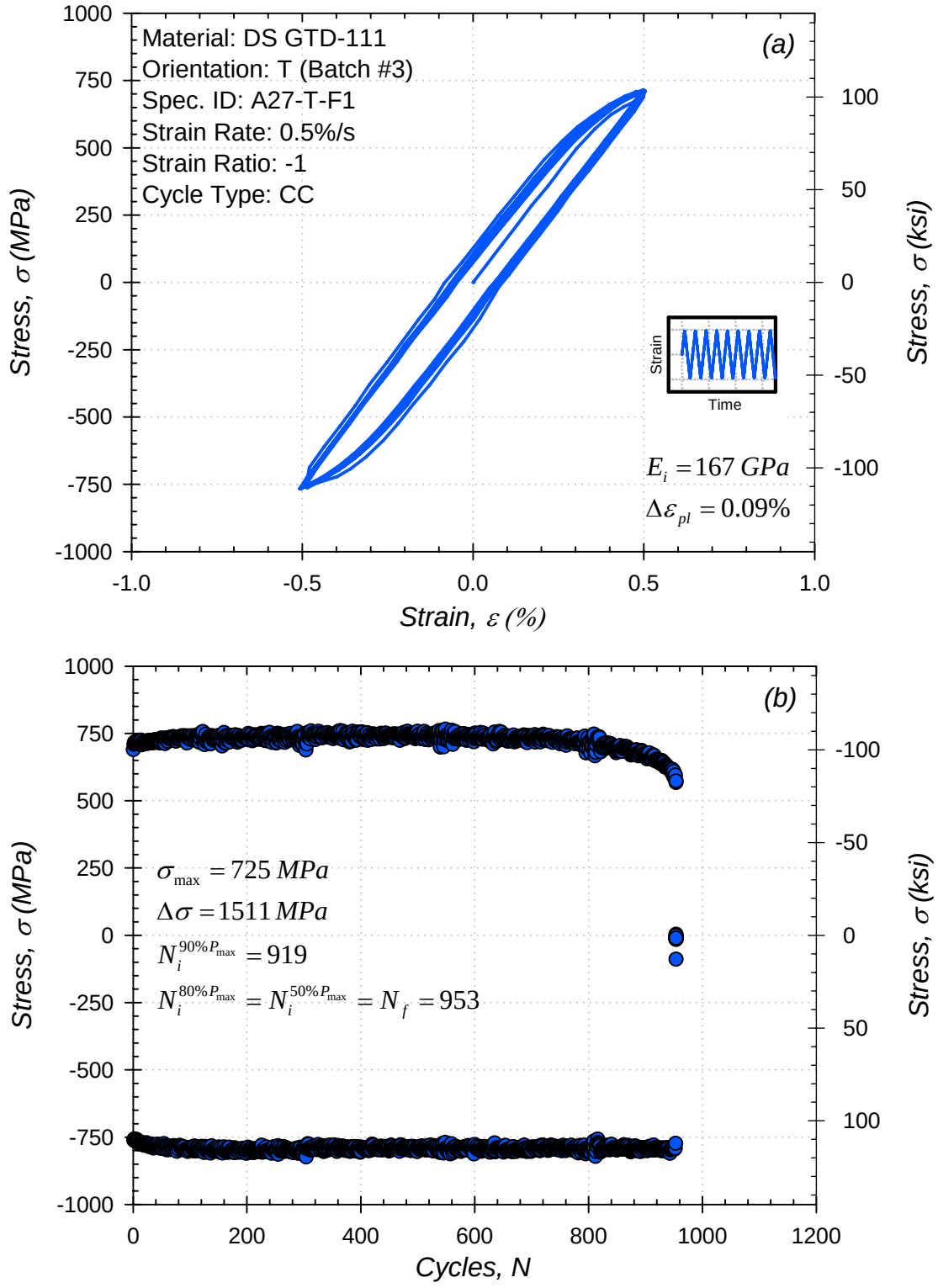


***Figure A.49:*** *(a) Initial stress-strain hysteresis loops and (b) stress history for low cycle fatigue test at 649°C.*

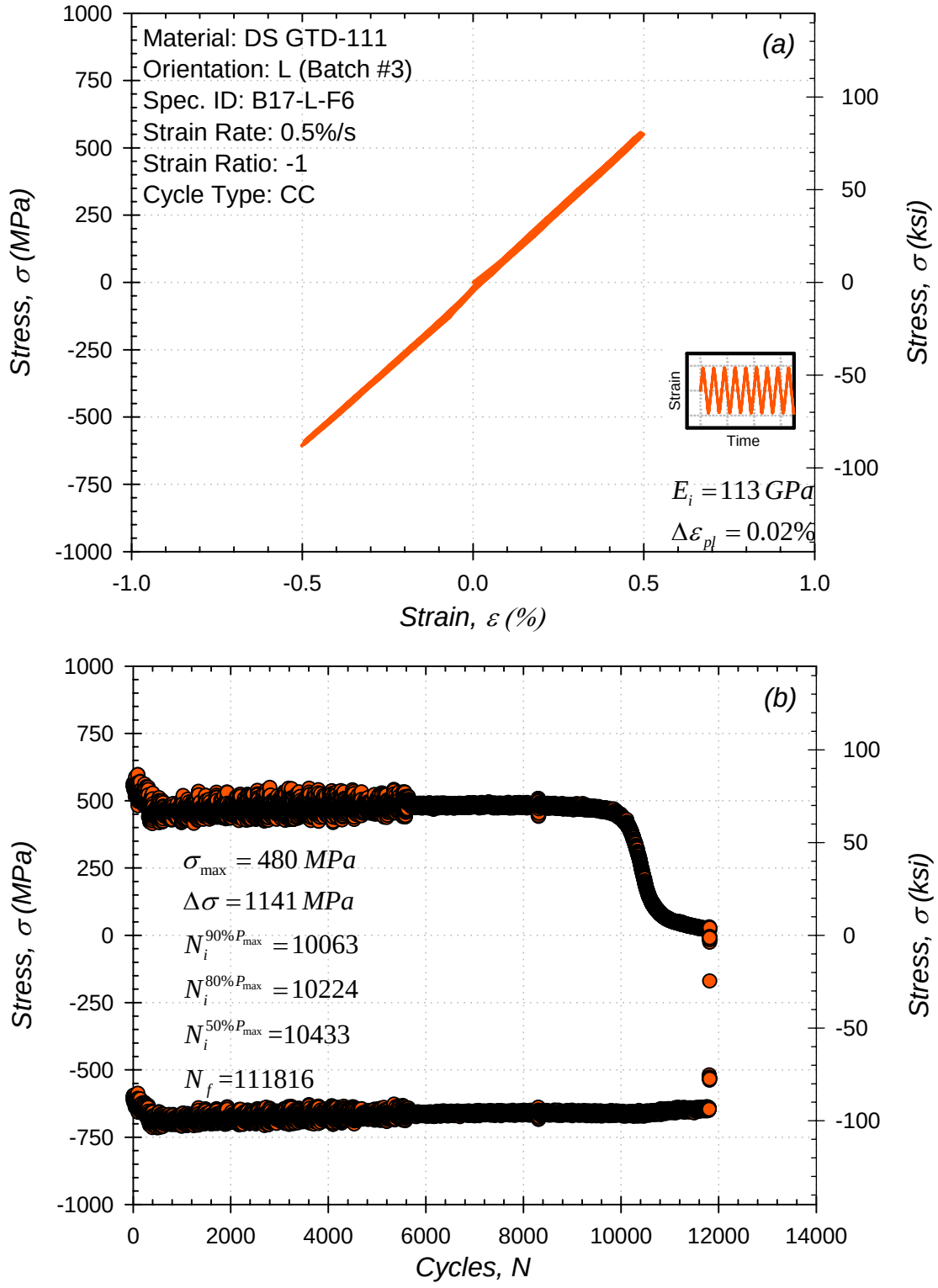


***Figure A.50:*** *(a) Initial stress-strain hysteresis loops and (b) stress history for low cycle fatigue test at 760°C.*

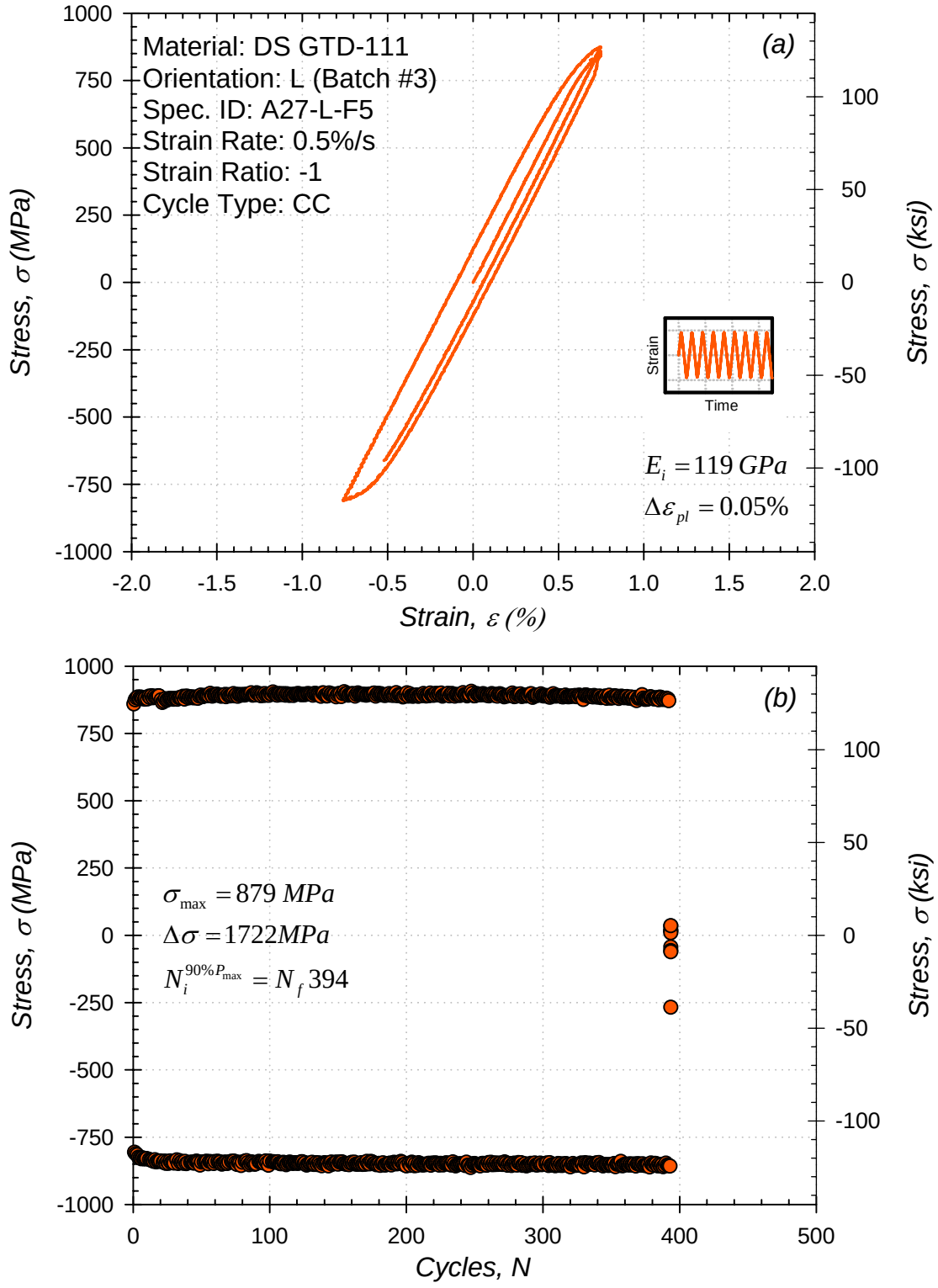


***Figure A.51:*** *(a) Initial stress-strain hysteresis loops and (b) stress history for low cycle fatigue test at 649°C.*

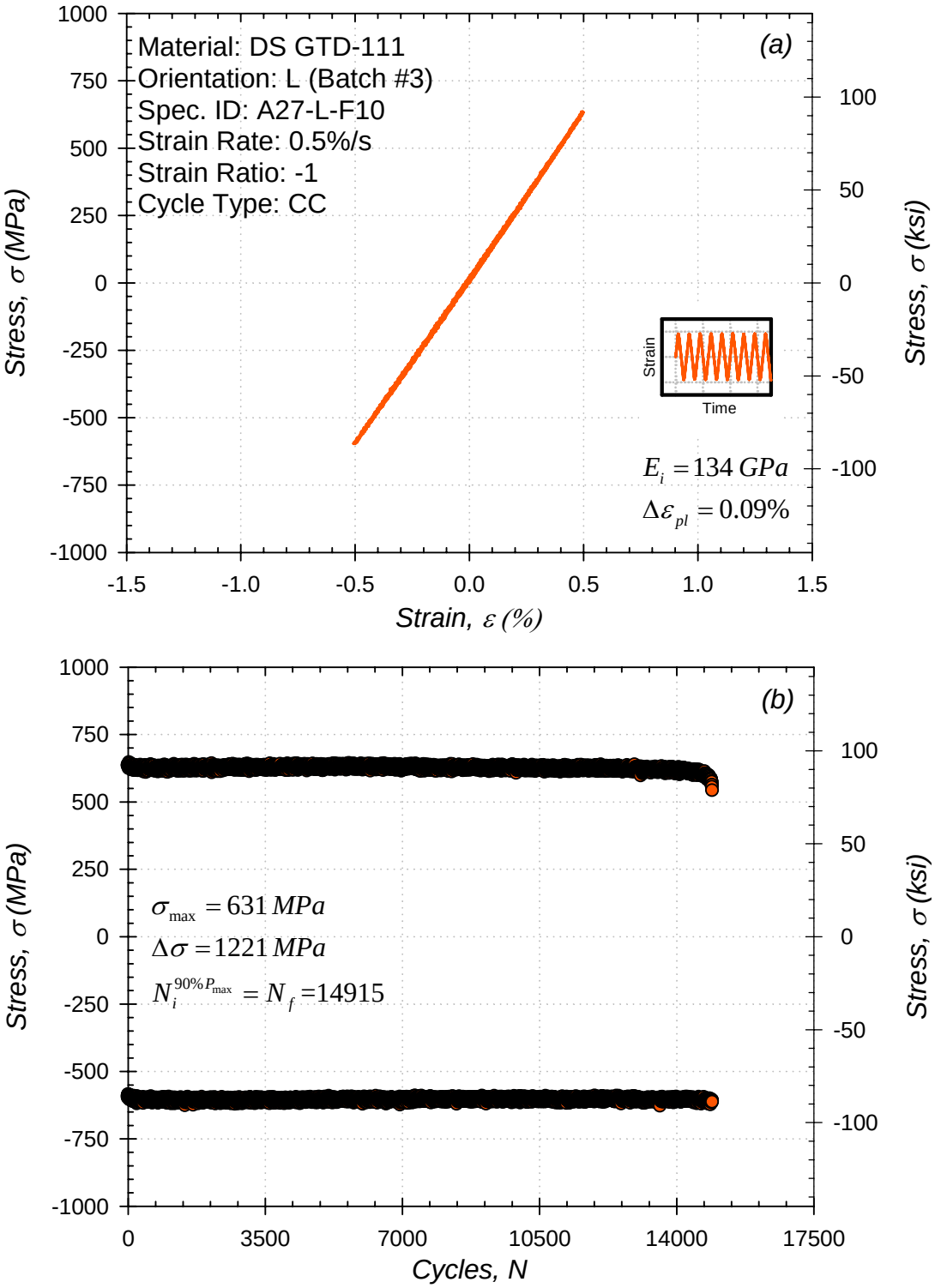


***Figure A.52:*** *(a) Initial stress-strain hysteresis loops and (b) stress history for low cycle fatigue test at 649°C.*

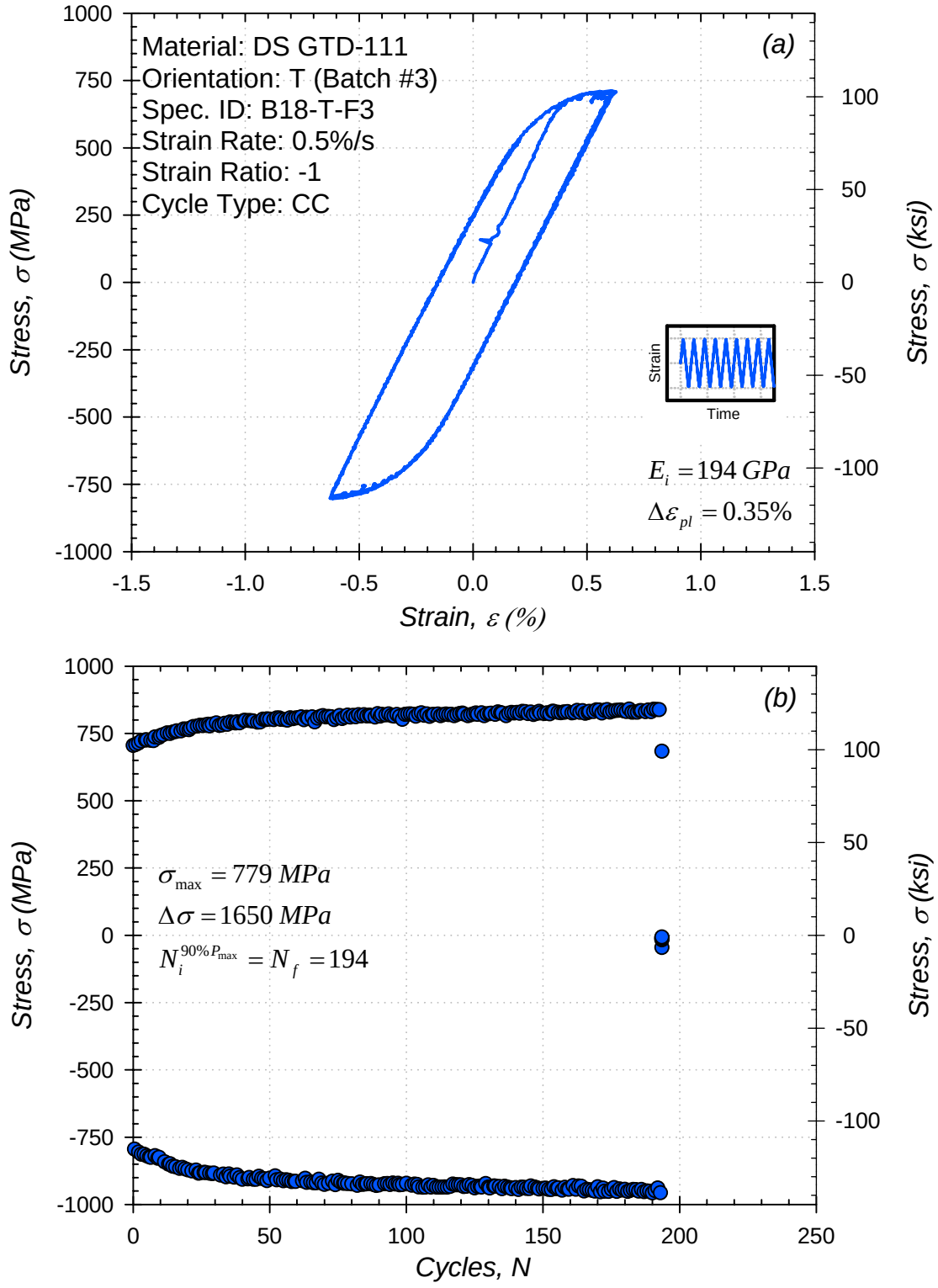


***Figure A.53:*** *(a) Initial stress-strain hysteresis loops and (b) stress history for low cycle fatigue test at 649°C.*

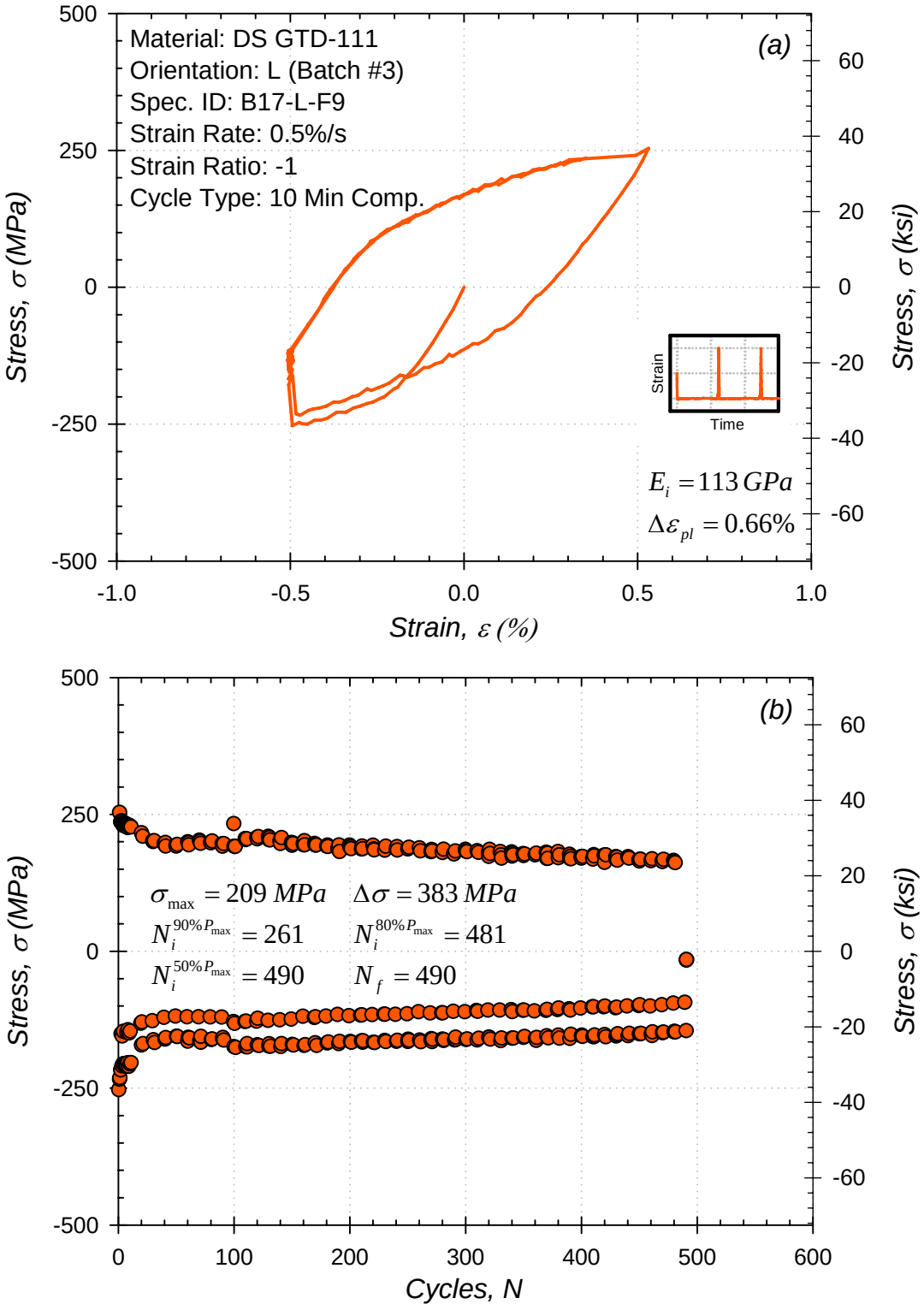


***Figure A.54:*** *(a) Initial stress-strain hysteresis loops and (b) stress history for low cycle fatigue test at 1038°C.*

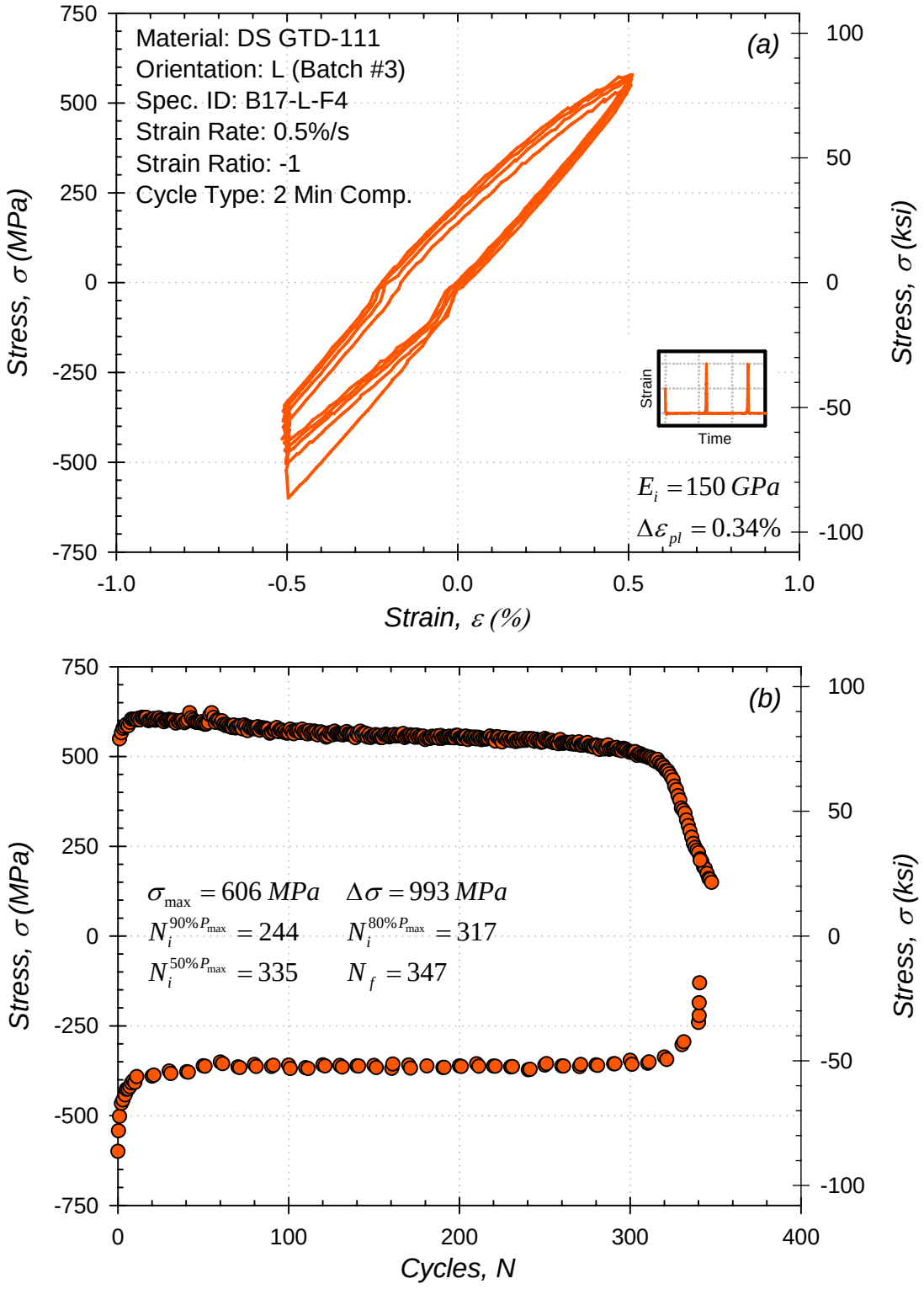


***Figure A.55:*** *(a) Initial stress-strain hysteresis loops and (b) stress history for low cycle fatigue test at 871°C.*

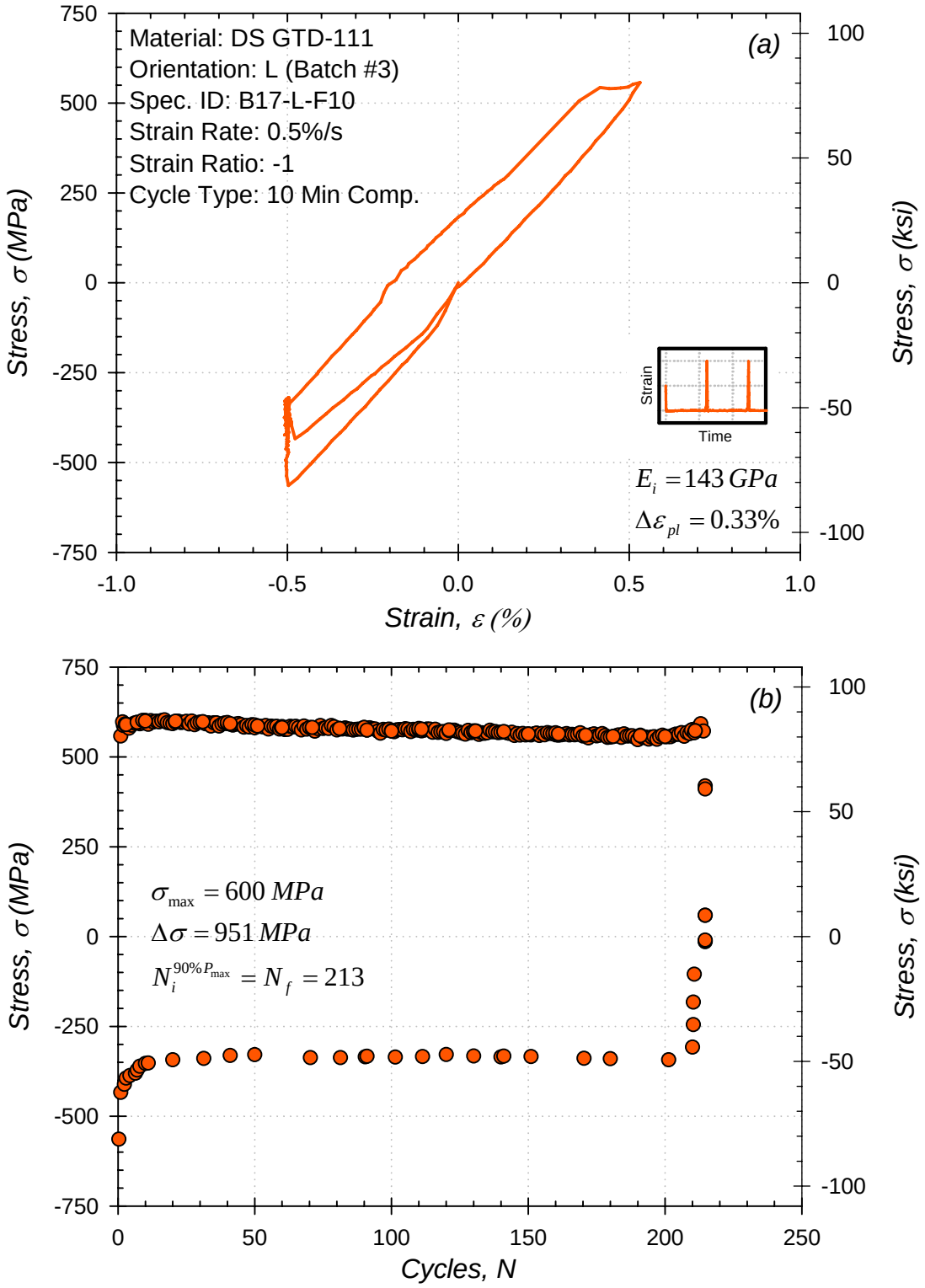


***Figure A.56:*** *(a) Initial stress-strain hysteresis loops and (b) stress history for low cycle fatigue test at 871°C.*

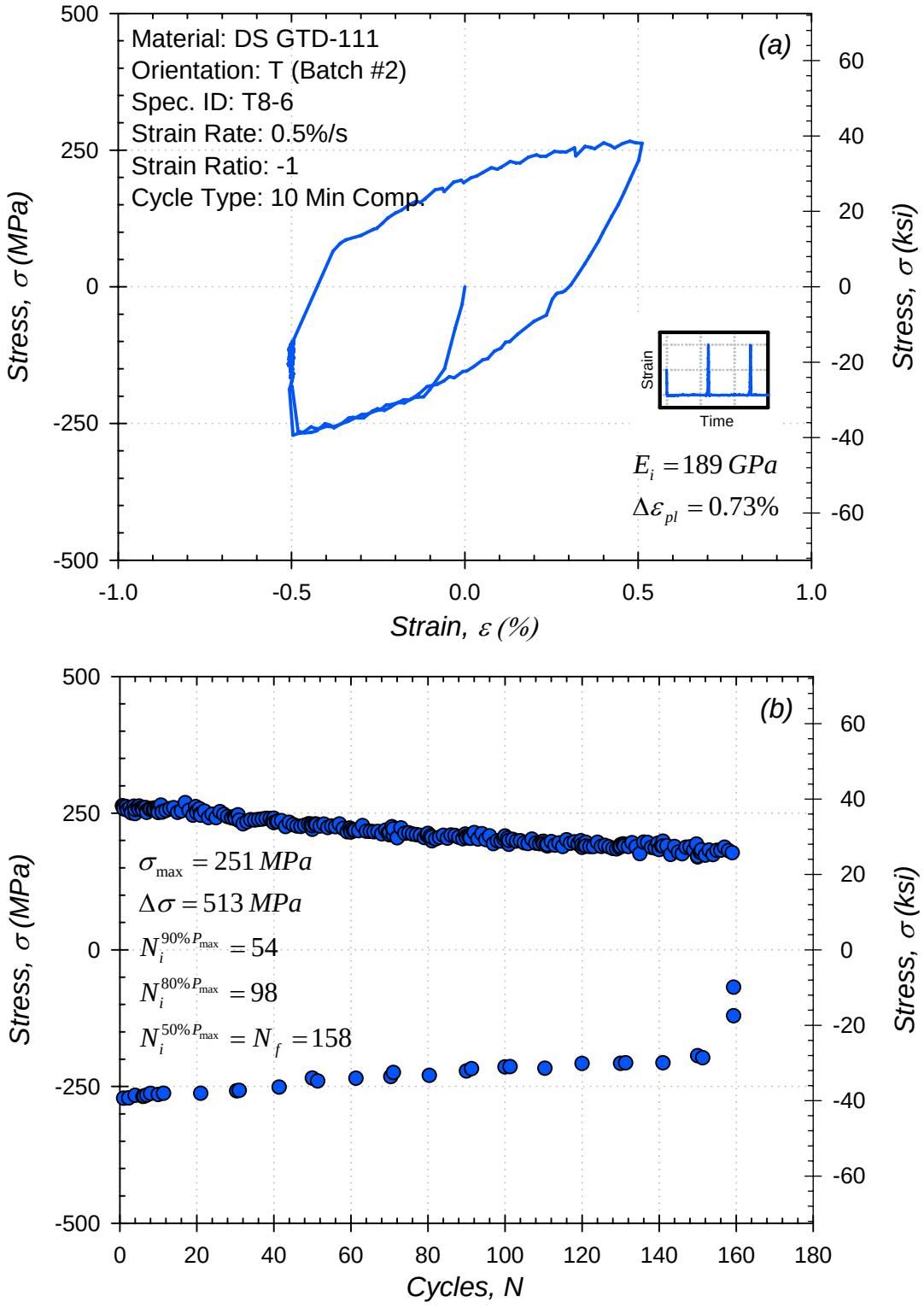


***Figure A.57:*** *(a) Initial stress-strain hysteresis loops and (b) stress history for low cycle fatigue test at 1038°C.*

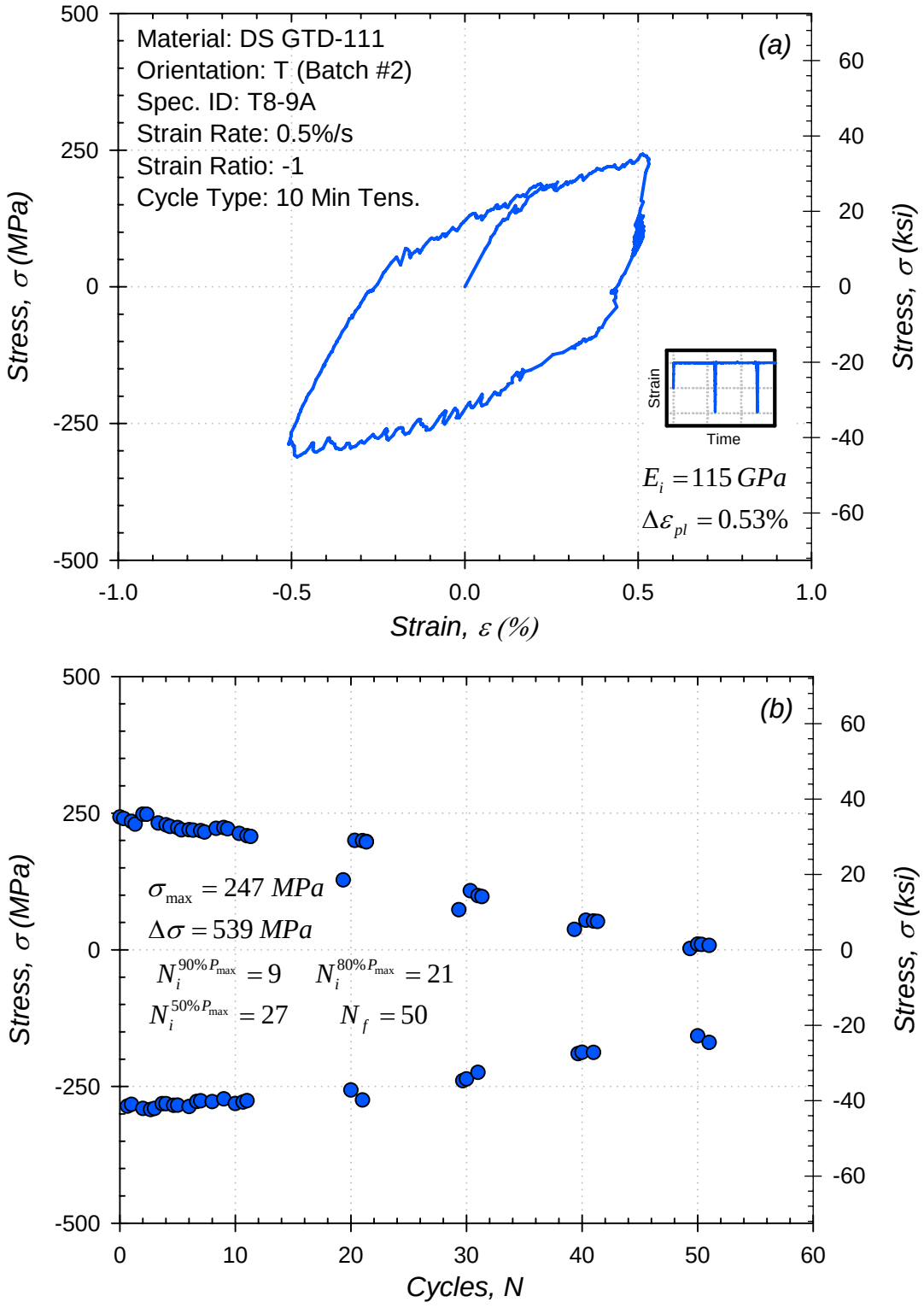


***Figure A.58:*** *(a) Initial stress-strain hysteresis loops and (b) stress history for low cycle fatigue test at 1038°C.*

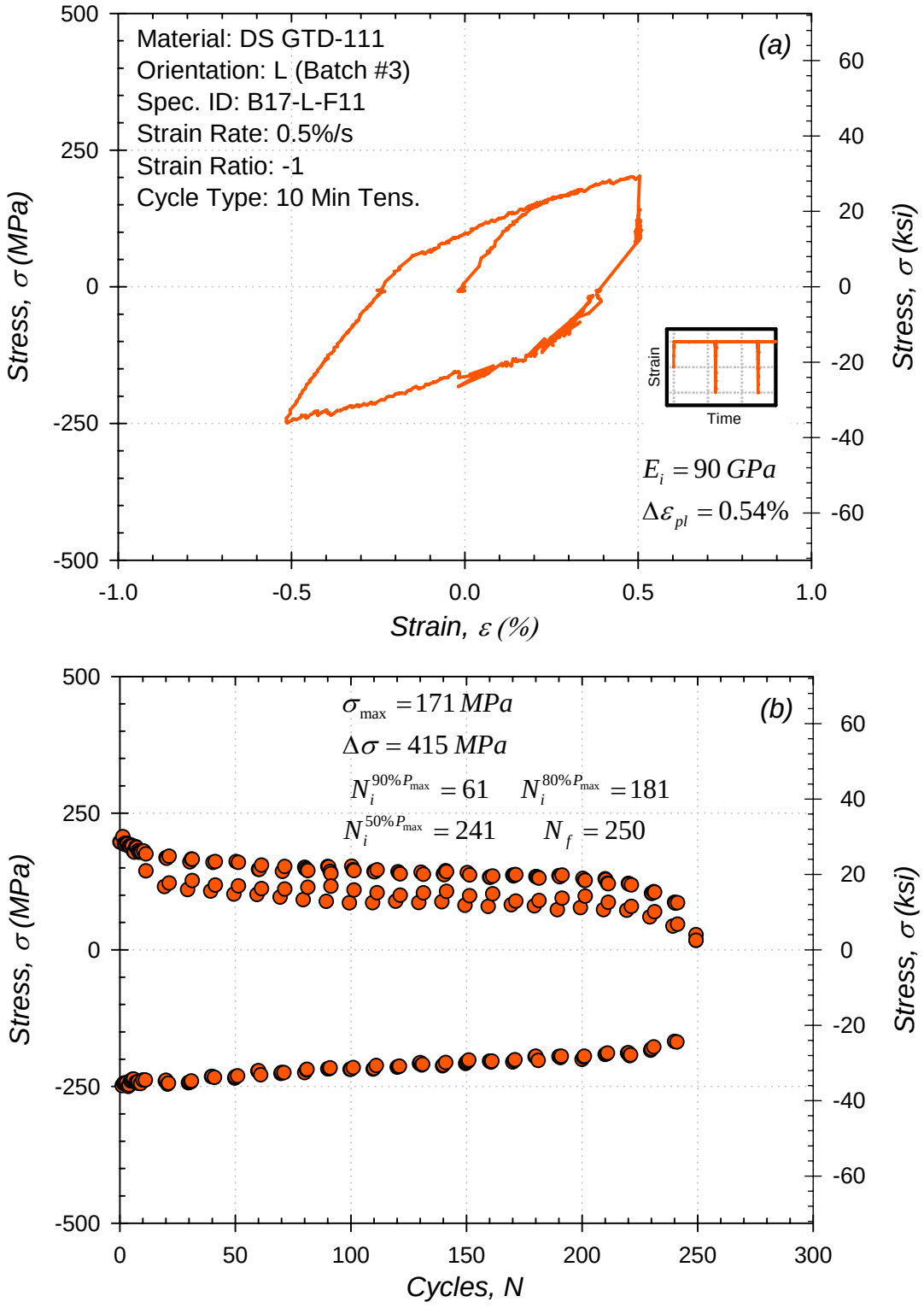


***Figure A.59:*** *(a) Initial stress-strain hysteresis loops and (b) stress history for low cycle fatigue test at 1038°C.*

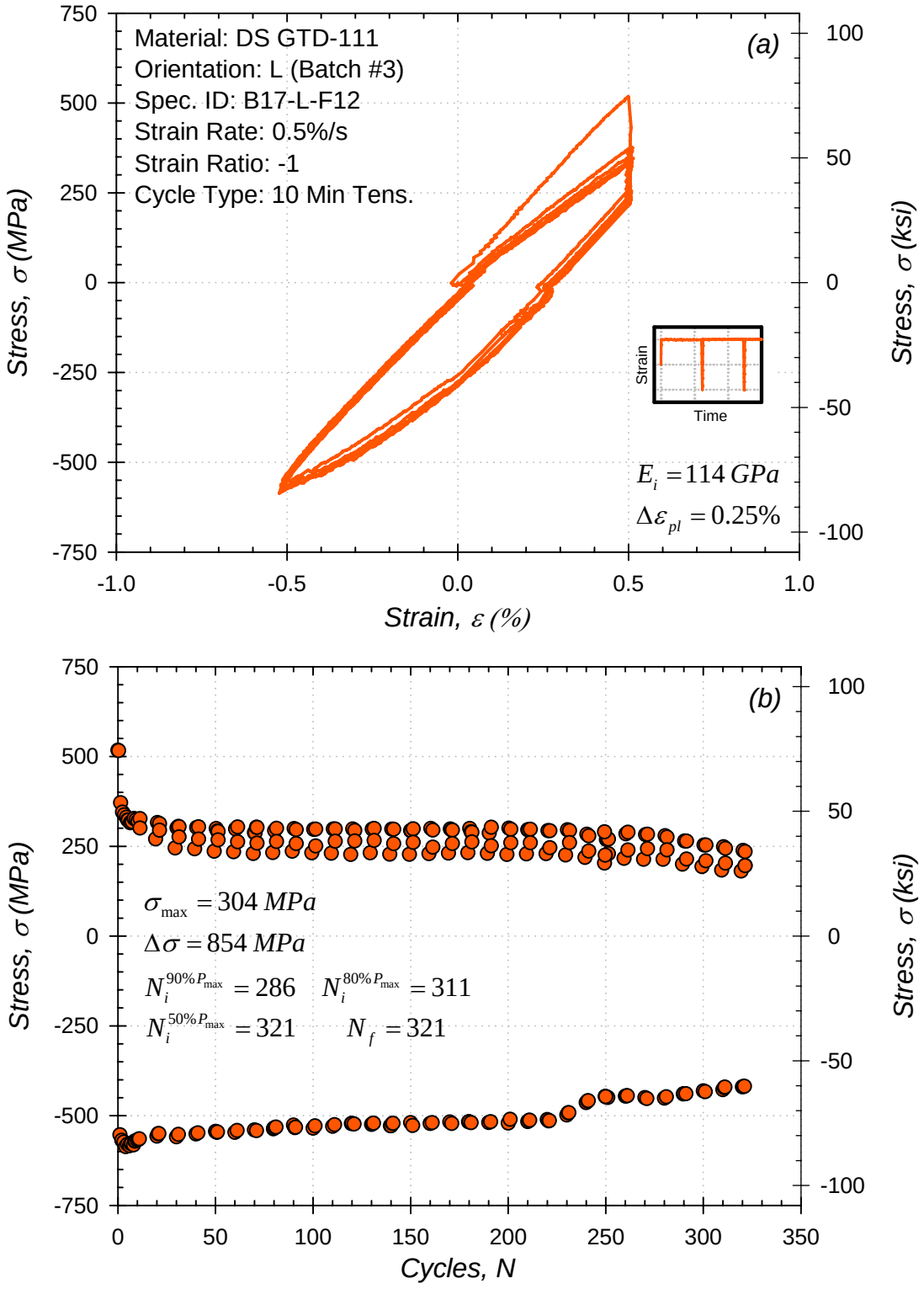


***Figure A.60:*** *(a) Initial stress-strain hysteresis loops and (b) stress history for low cycle fatigue test at 871°C.*

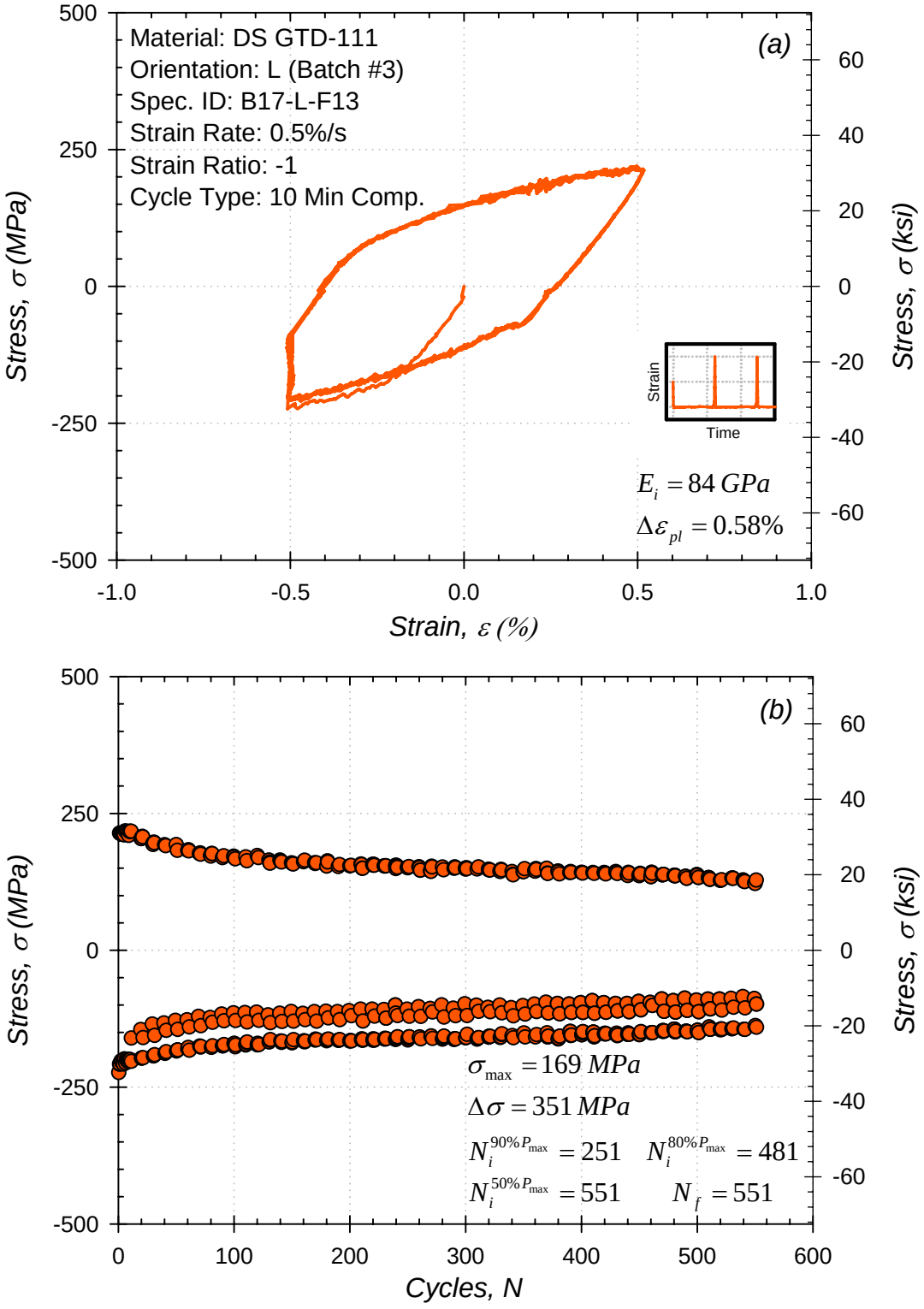


***Figure A.61:*** *(a) Initial stress-strain hysteresis loops and (b) stress history for low cycle fatigue test at 1038°C.*

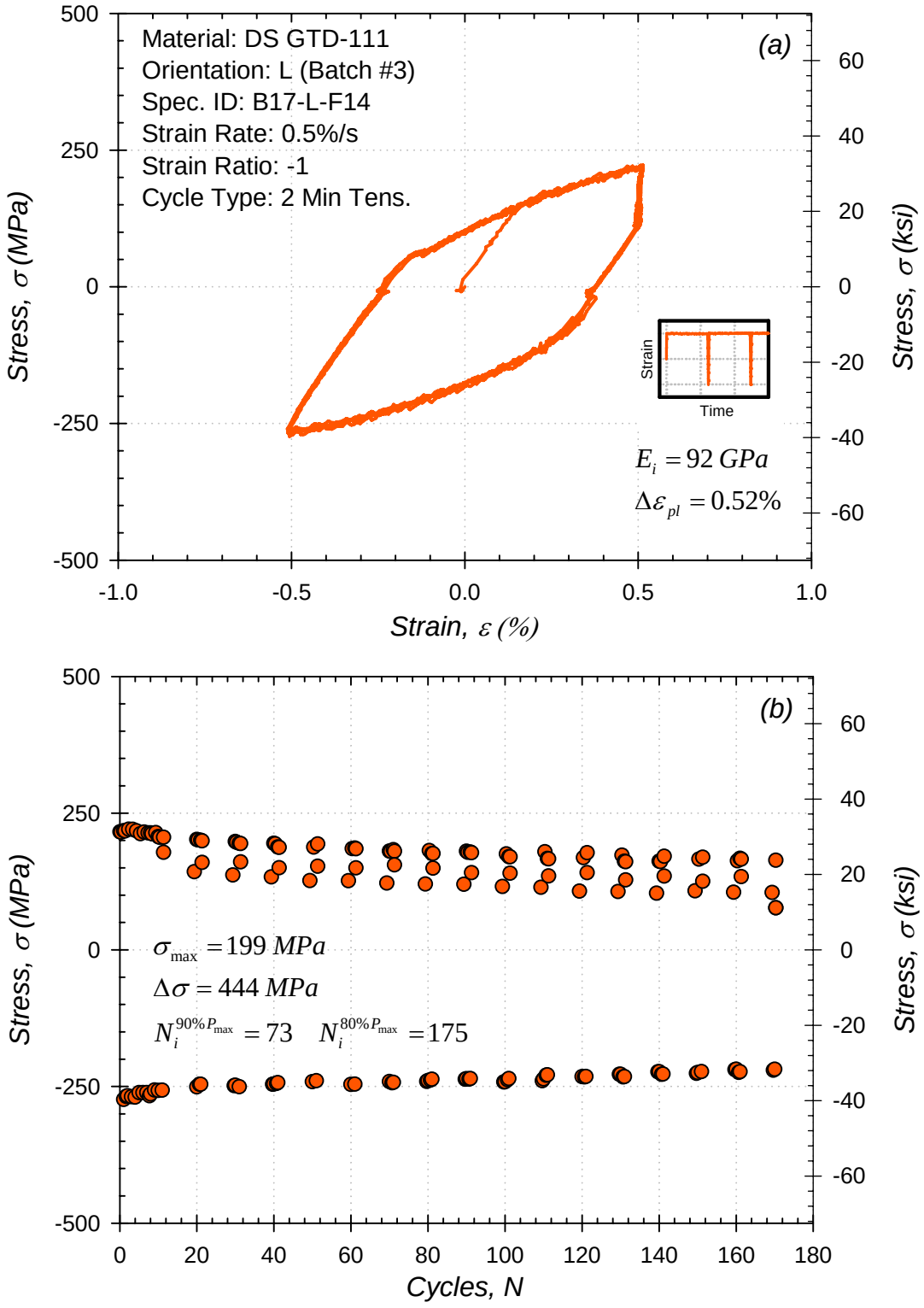


***Figure A.62:*** *(a) Initial stress-strain hysteresis loops and (b) stress history for low cycle fatigue test at 1038°C.*

# APPENDIX B

## THERMOMECHANICAL FATIGUE TEST CURVES
(Chronologically Ordered)

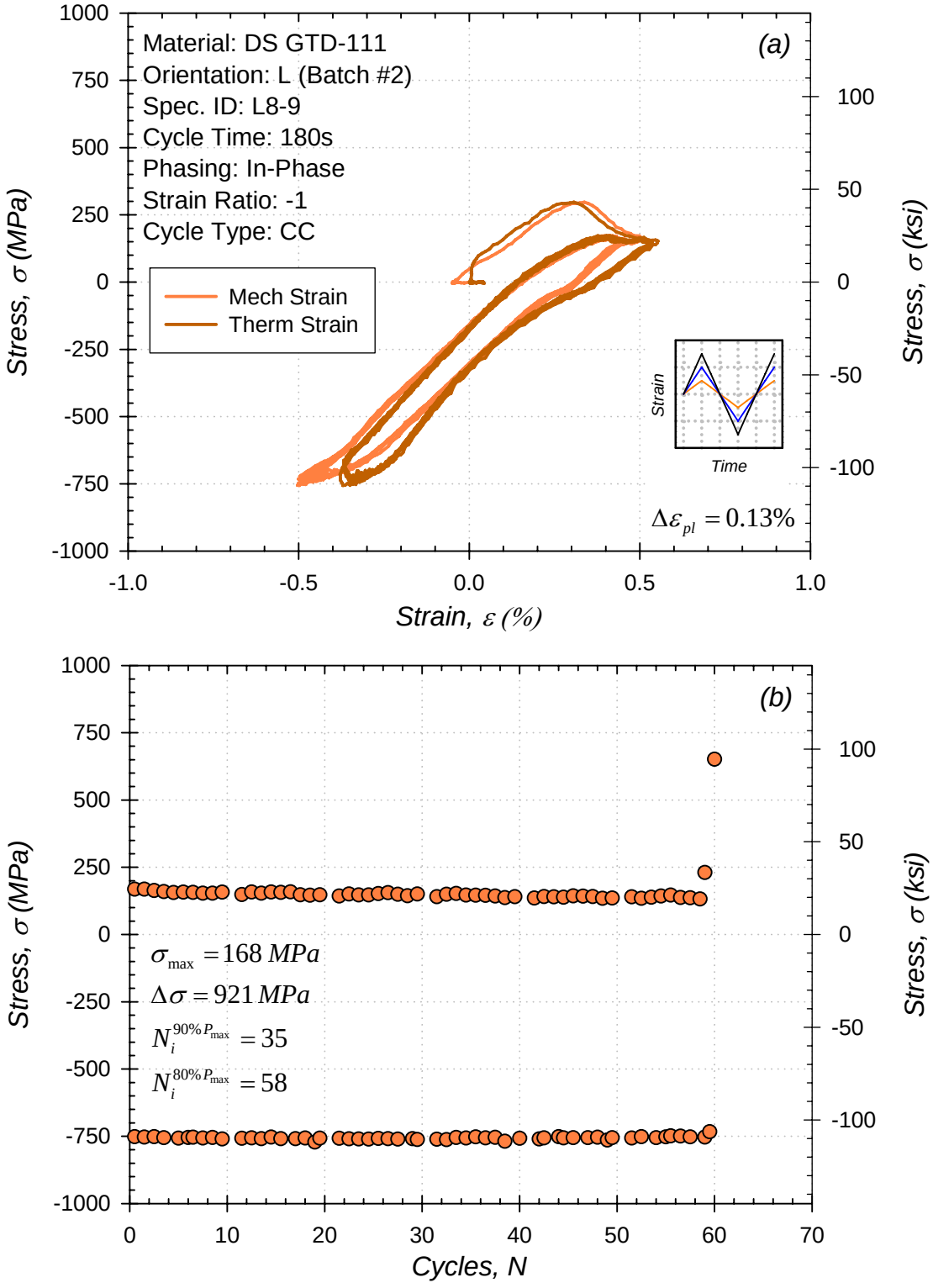


***Figure B.1:*** *(a) Initial stress-strain hysteresis loops and (b) stress history for TMF test with $T_{min}$ = 538°C and $T_{max}$ = 1038C.*

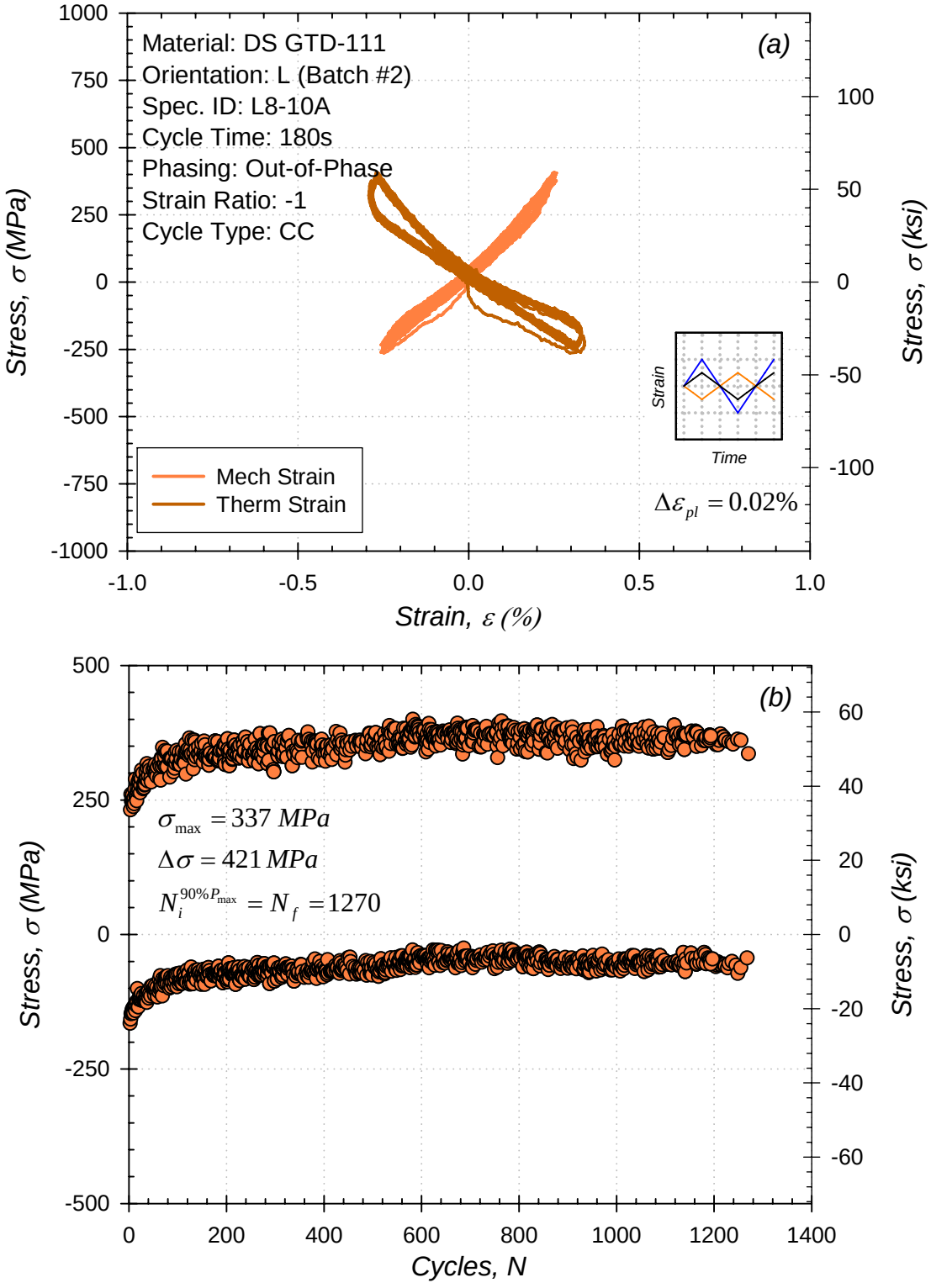


***Figure B.2:*** *(a) Initial stress-strain hysteresis loops and (b) stress history for TMF test with $T_{min}$ = 538°C and $T_{max}$ = 927°C.*

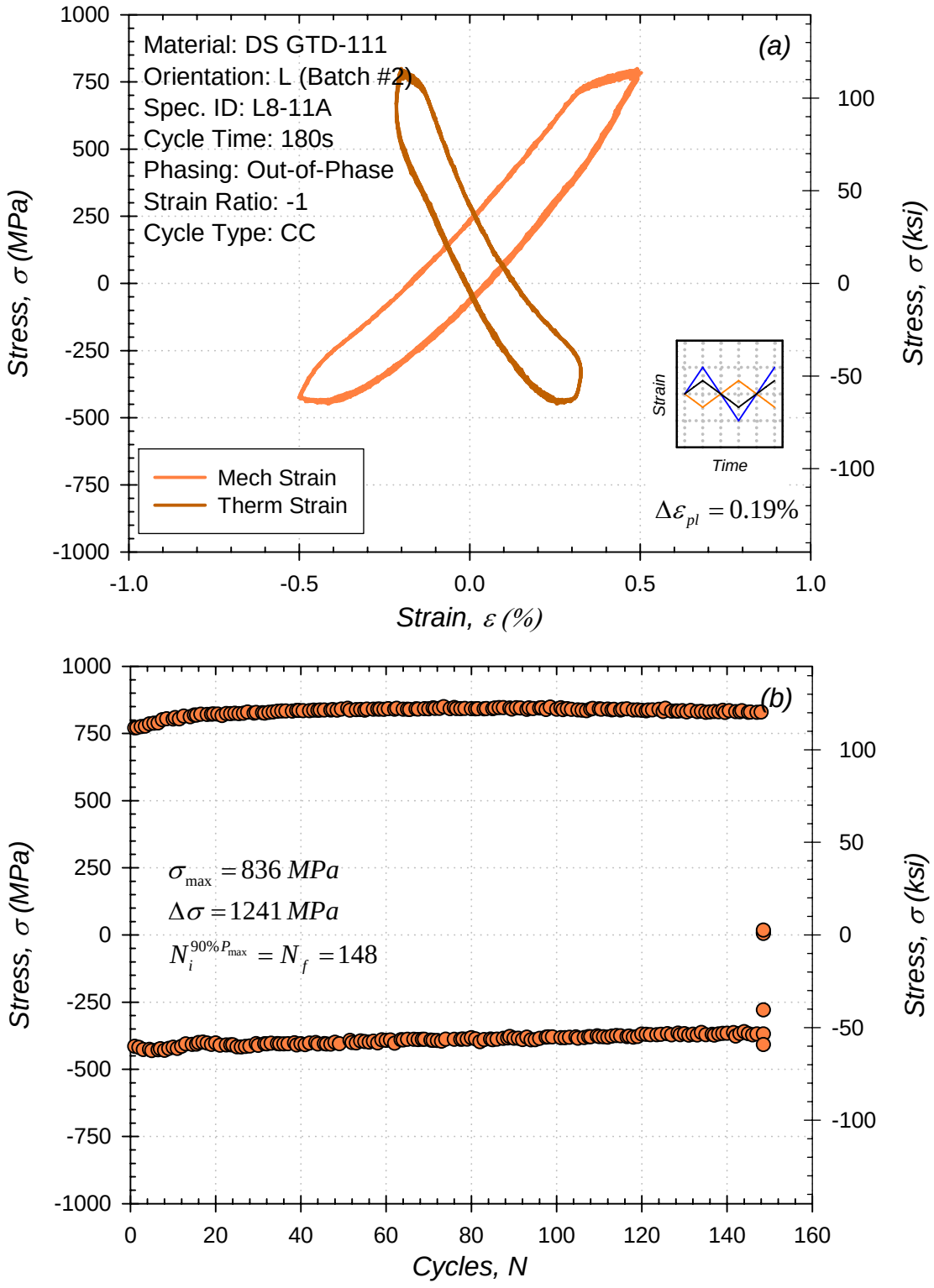


***Figure B.3:*** *(a) Initial stress-strain hysteresis loops and (b) stress history for TMF test with $T_{min}$ = 538°C and $T_{max}$ = 927°C.*

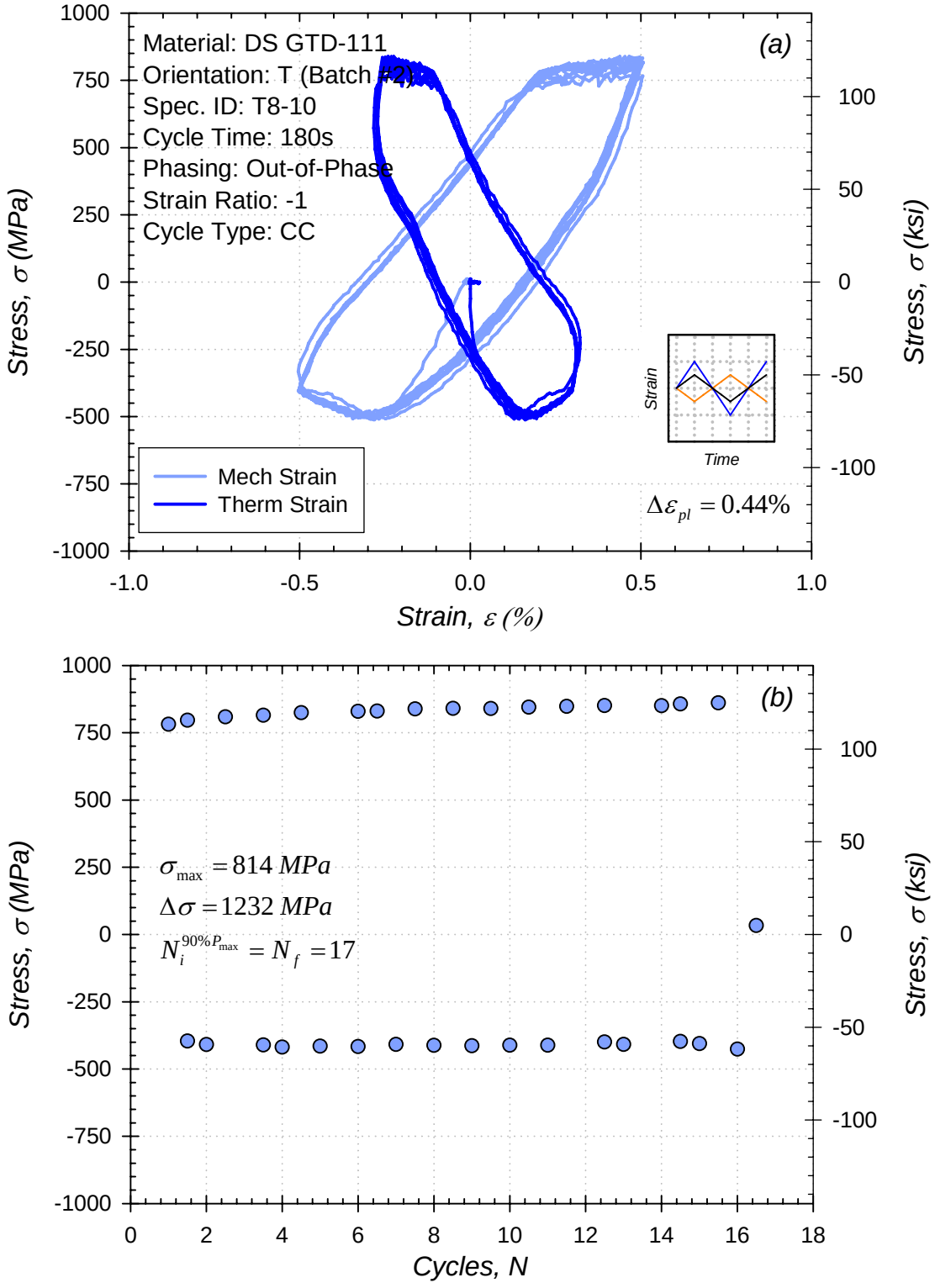


***Figure B.4:*** *(a) Initial stress-strain hysteresis loops and (b) stress history for TMF test with $T_{min}$ = 538°C and $T_{max}$ = 927°C.*

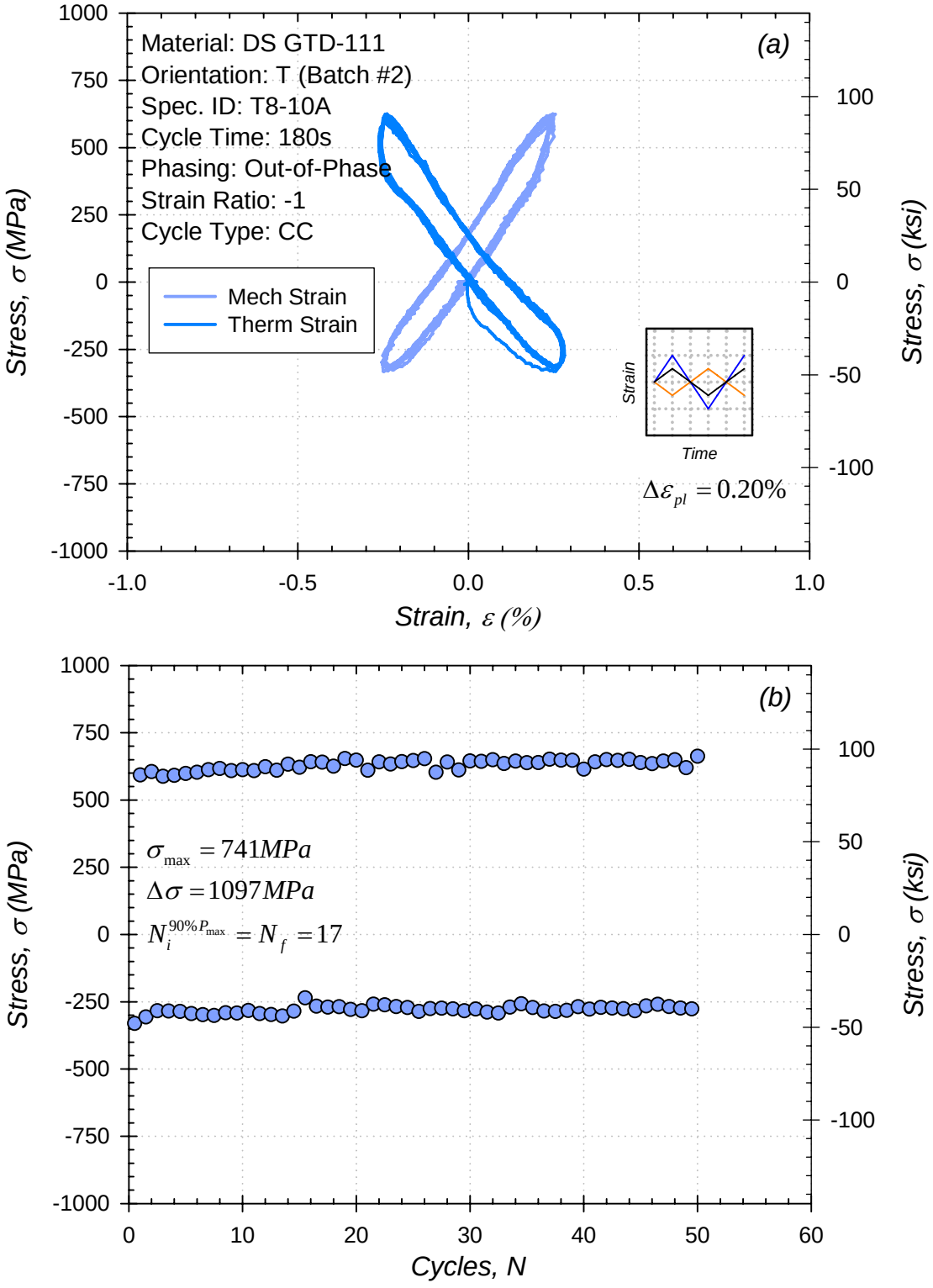


***Figure B.5:*** *(a) Initial stress-strain hysteresis loops and (b) stress history for TMF test with $T_{min}$ = 538°C and $T_{max}$ = 927°C.*

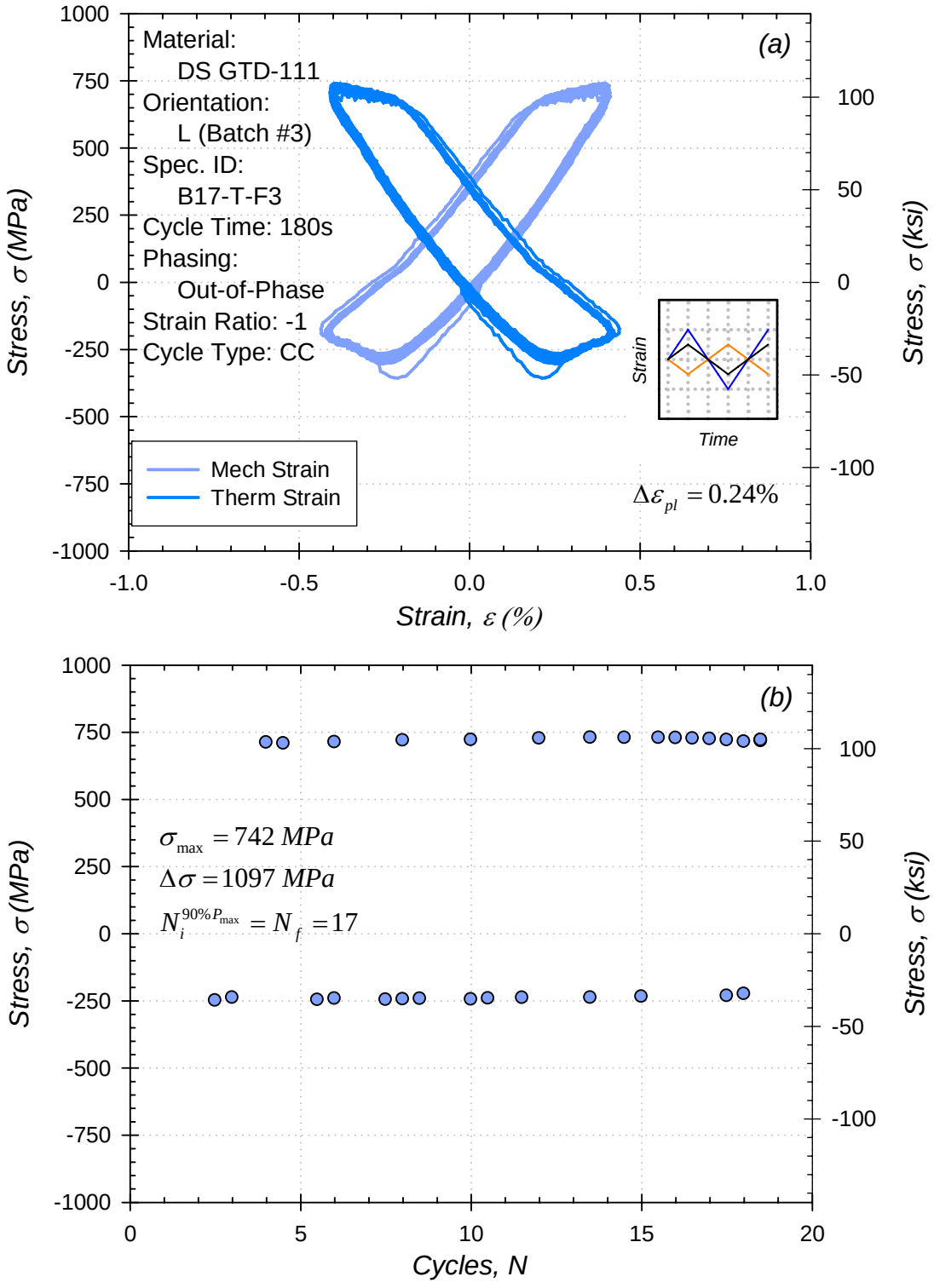


***Figure B.6:*** *(a) Initial stress-strain hysteresis loops and (b) stress history for TMF test with $T_{min}$ = 538°C and $T_{max}$ = 1038C.*

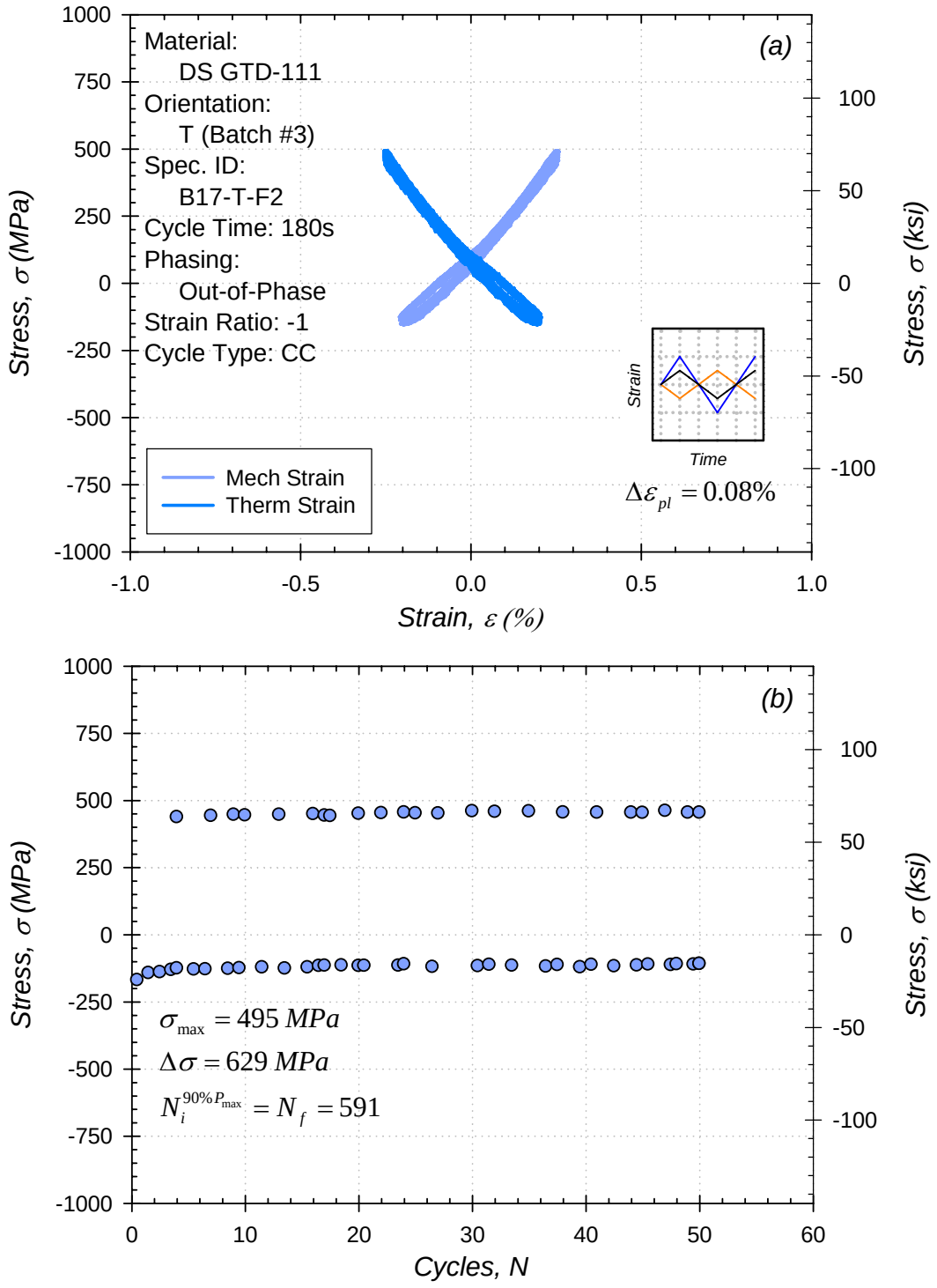


***Figure B.7:*** *(a) Initial stress-strain hysteresis loops and (b) stress history for TMF test with $T_{min}$ = 788°C and $T_{max}$ = 1038°C.*

# APPENDIX C

## PRE-EXPOSED AND ALTERNATE ENVIRONMENT LOW CYCLE FATIGUE TEST CURVES

(Chronologically Ordered)

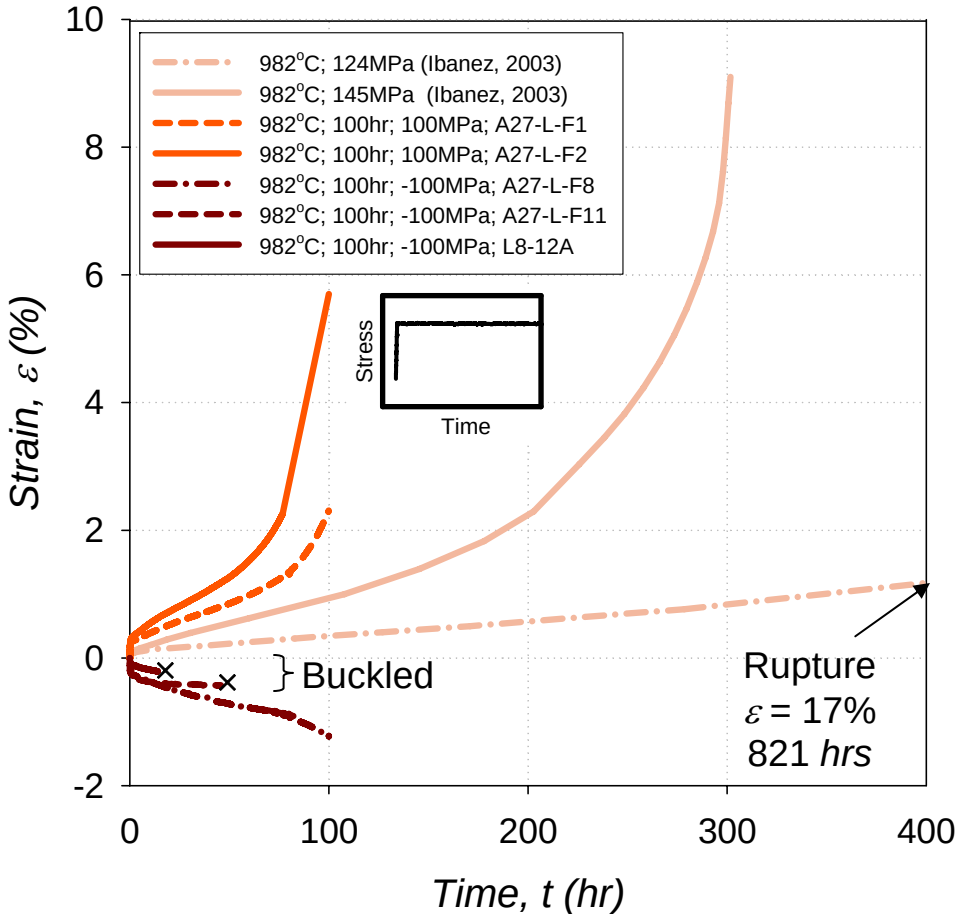


***Figure C.1:*** *Creep deformation until 100hr or rupture of L-oriented DS GTD-111 at 982℃.*

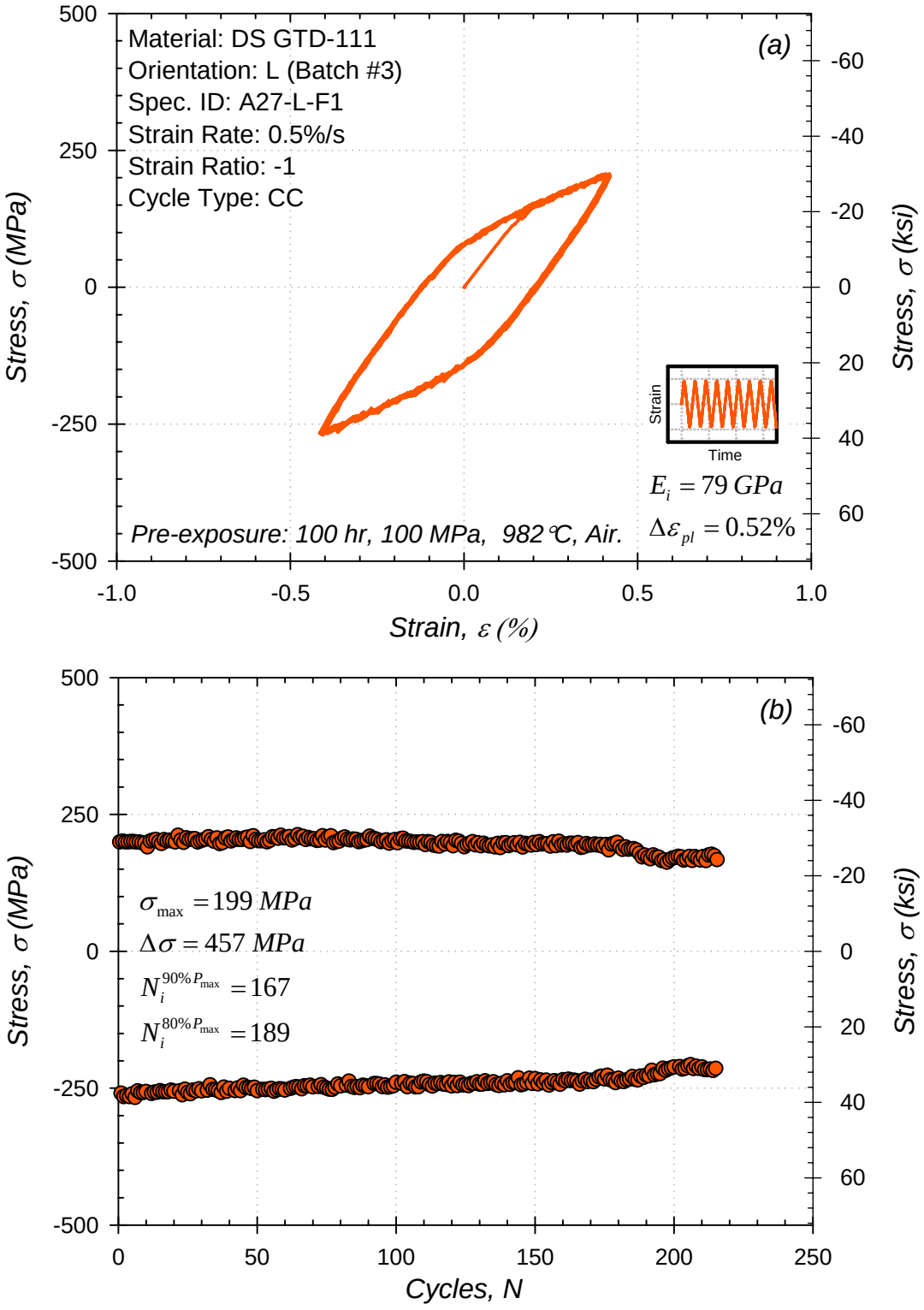


***Figure C.2:*** *(a) Initial stress-strain hysteresis loops and (b) stress history for low cycle fatigue test at 871°C.*

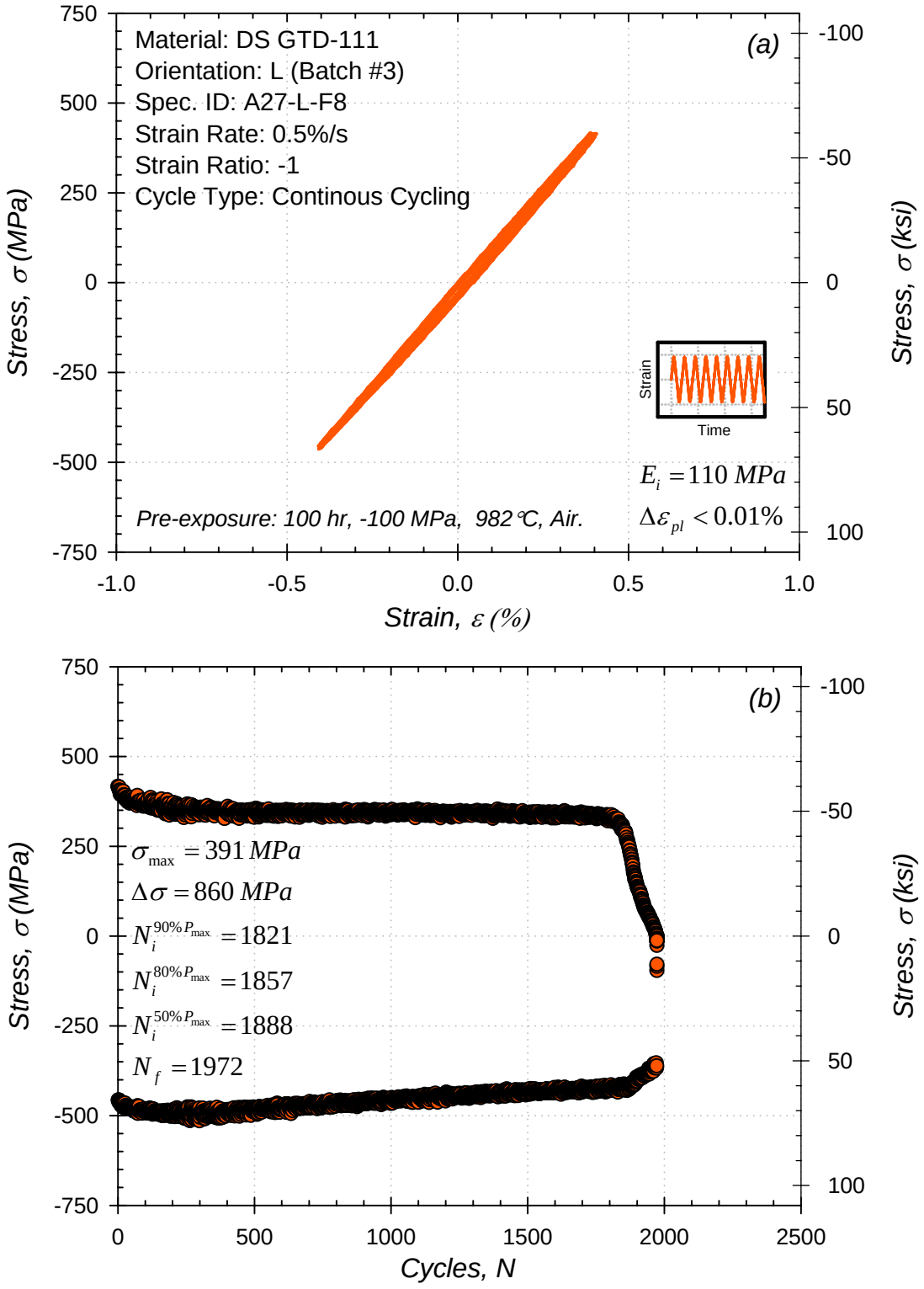


***Figure C.3:*** *(a) Initial stress-strain hysteresis loops and (b) stress history for pre-exposed low cycle fatigue test at 871°C.*

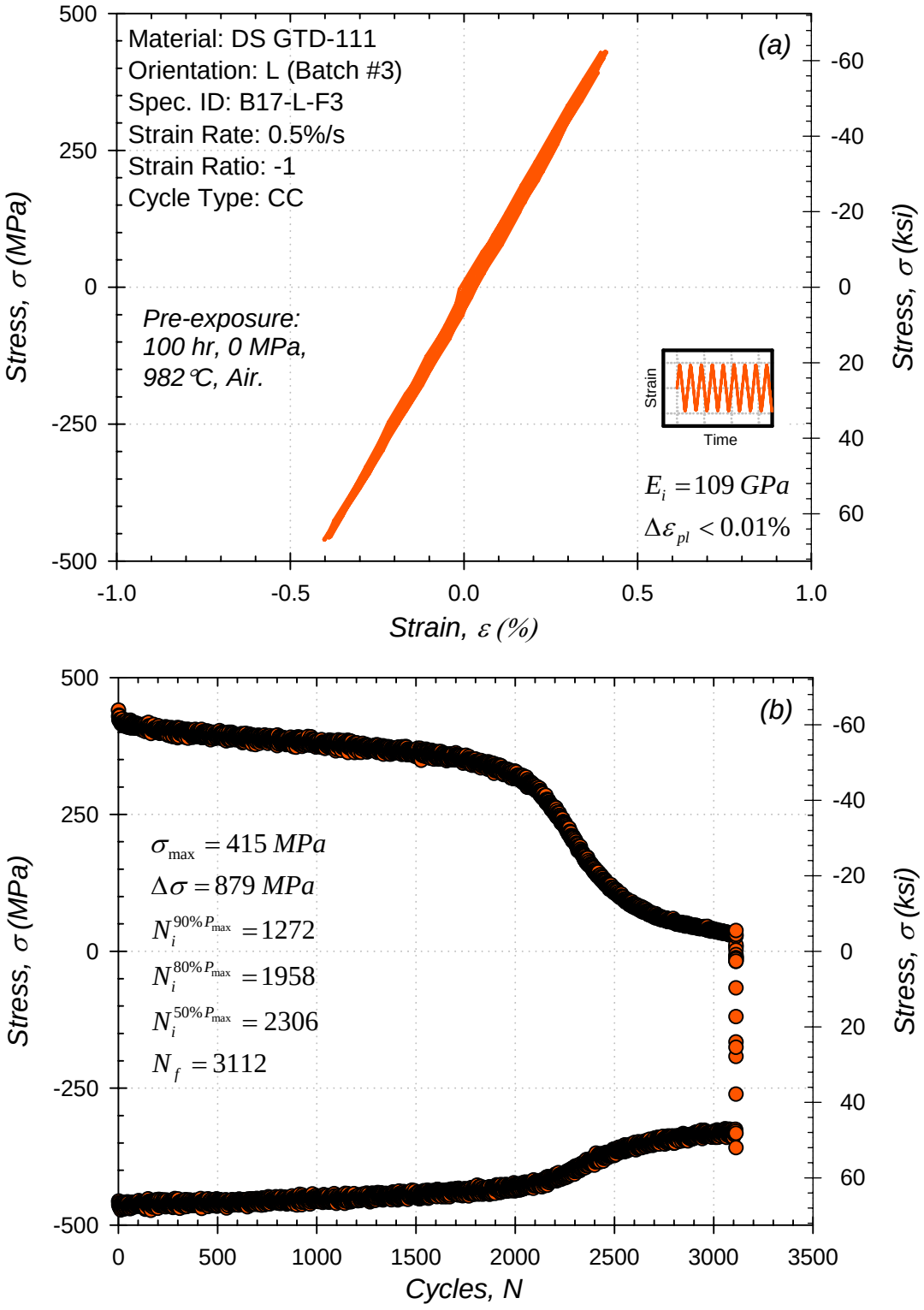


***Figure C.4:*** *(a) Initial stress-strain hysteresis loops and (b) stress history for low cycle fatigue test at 871°C.*

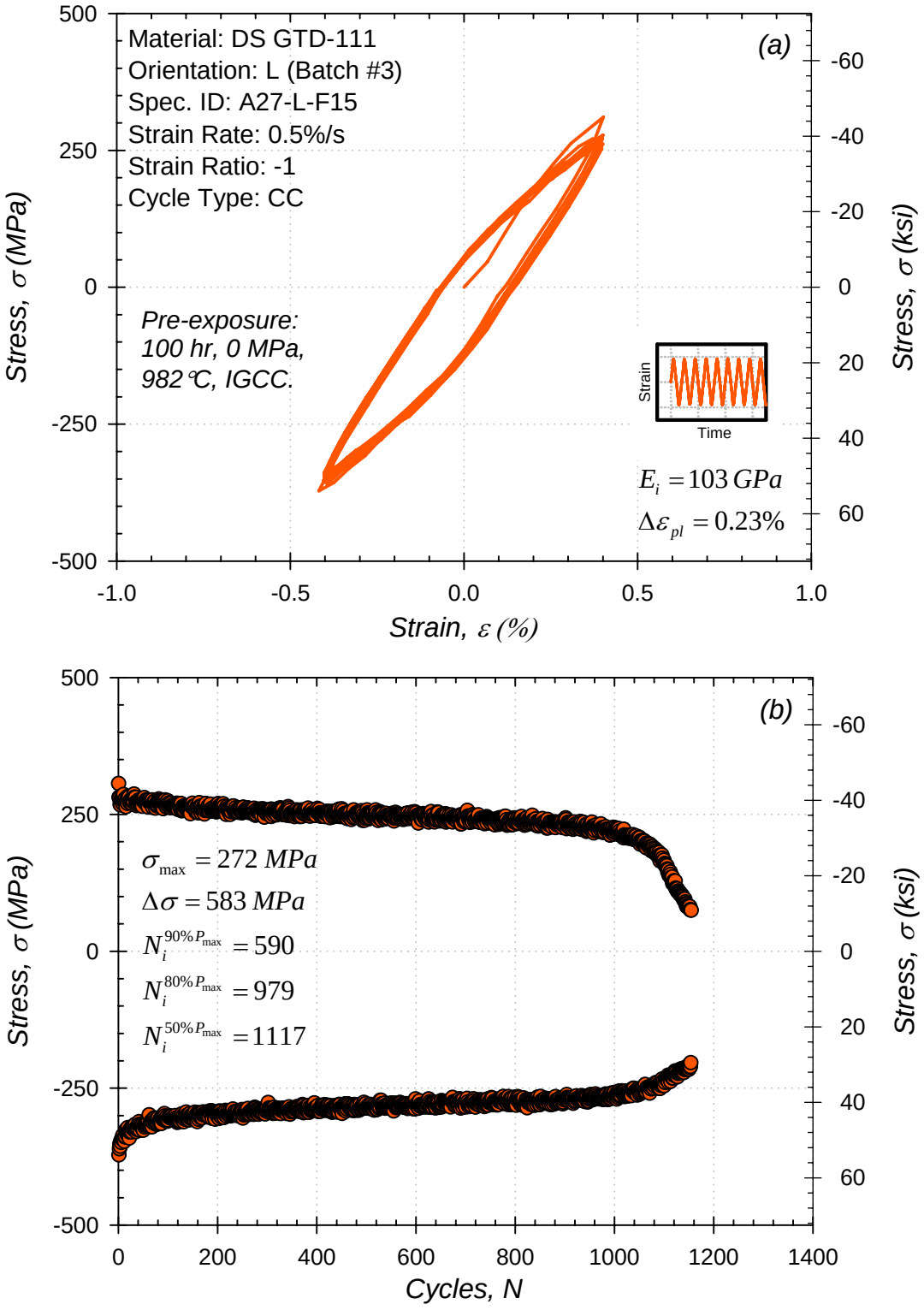


***Figure C.5:*** *(a) Initial stress-strain hysteresis loops and (b) stress history for low cycle fatigue test at 871°C.*

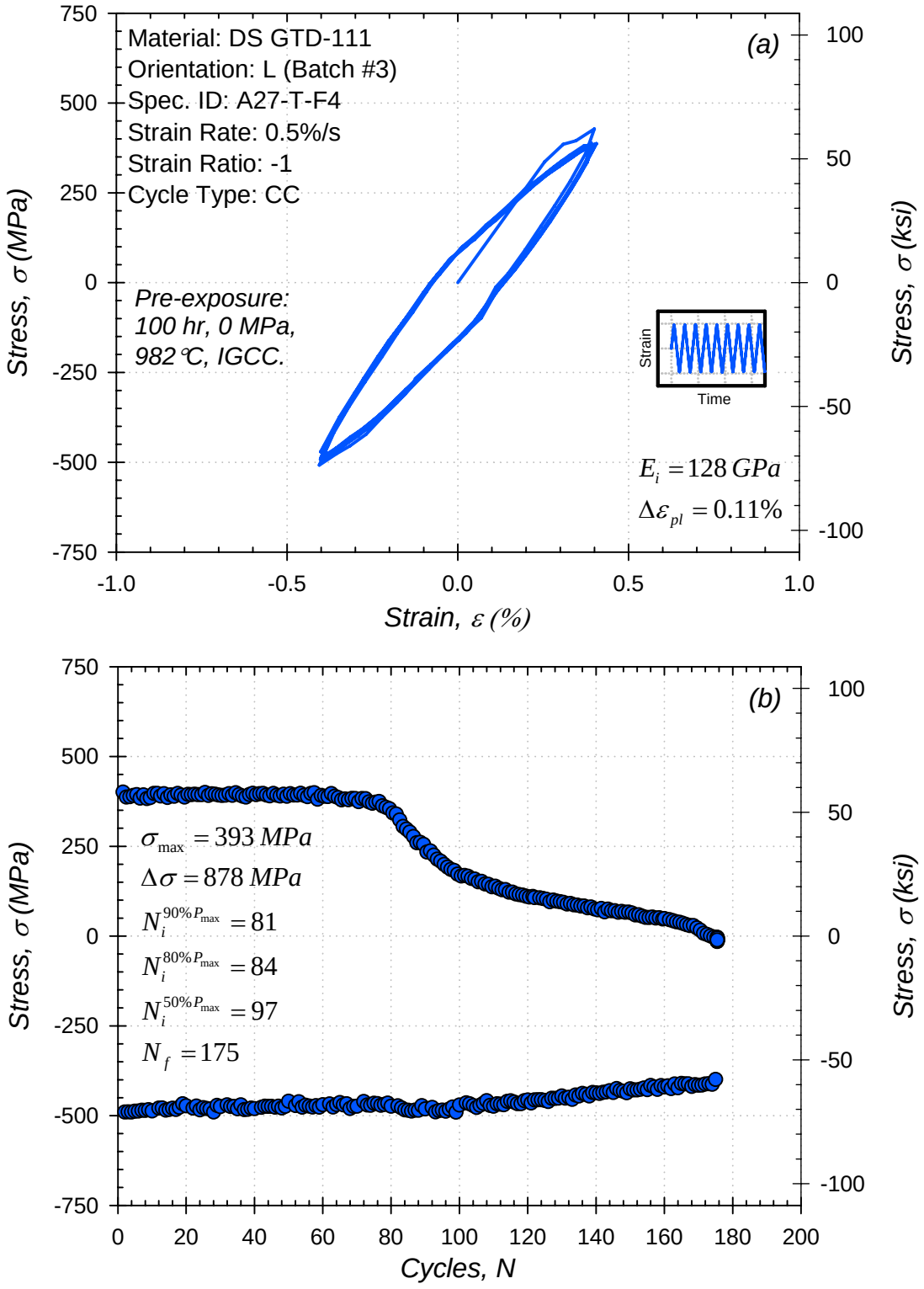


***Figure C.6:*** *(a) Initial stress-strain hysteresis loops and (b) stress history for low cycle fatigue test at 871°C.*

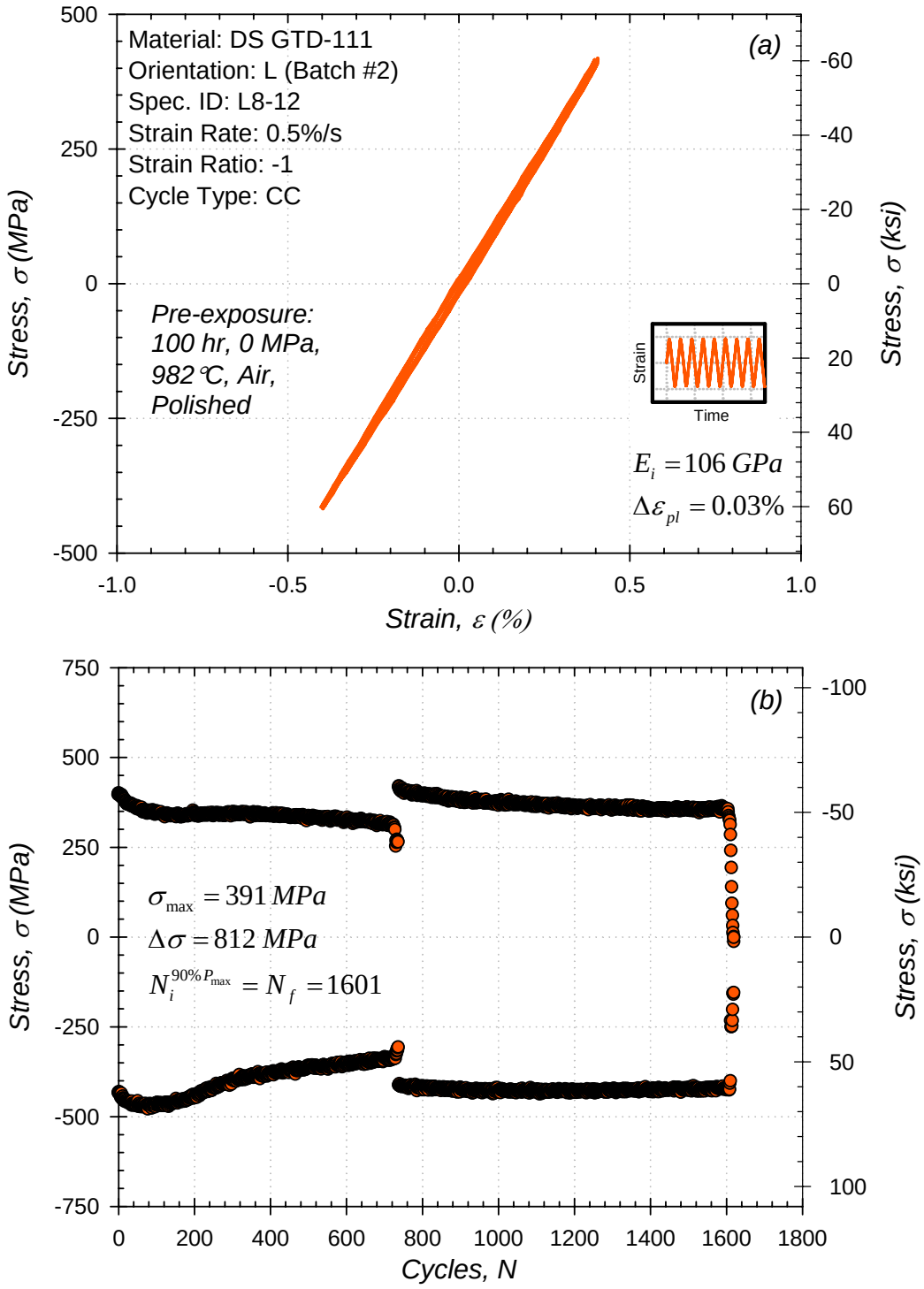


***Figure C.7:*** *(a) Initial stress-strain hysteresis loops and (b) stress history for low cycle fatigue test at 871°C.*

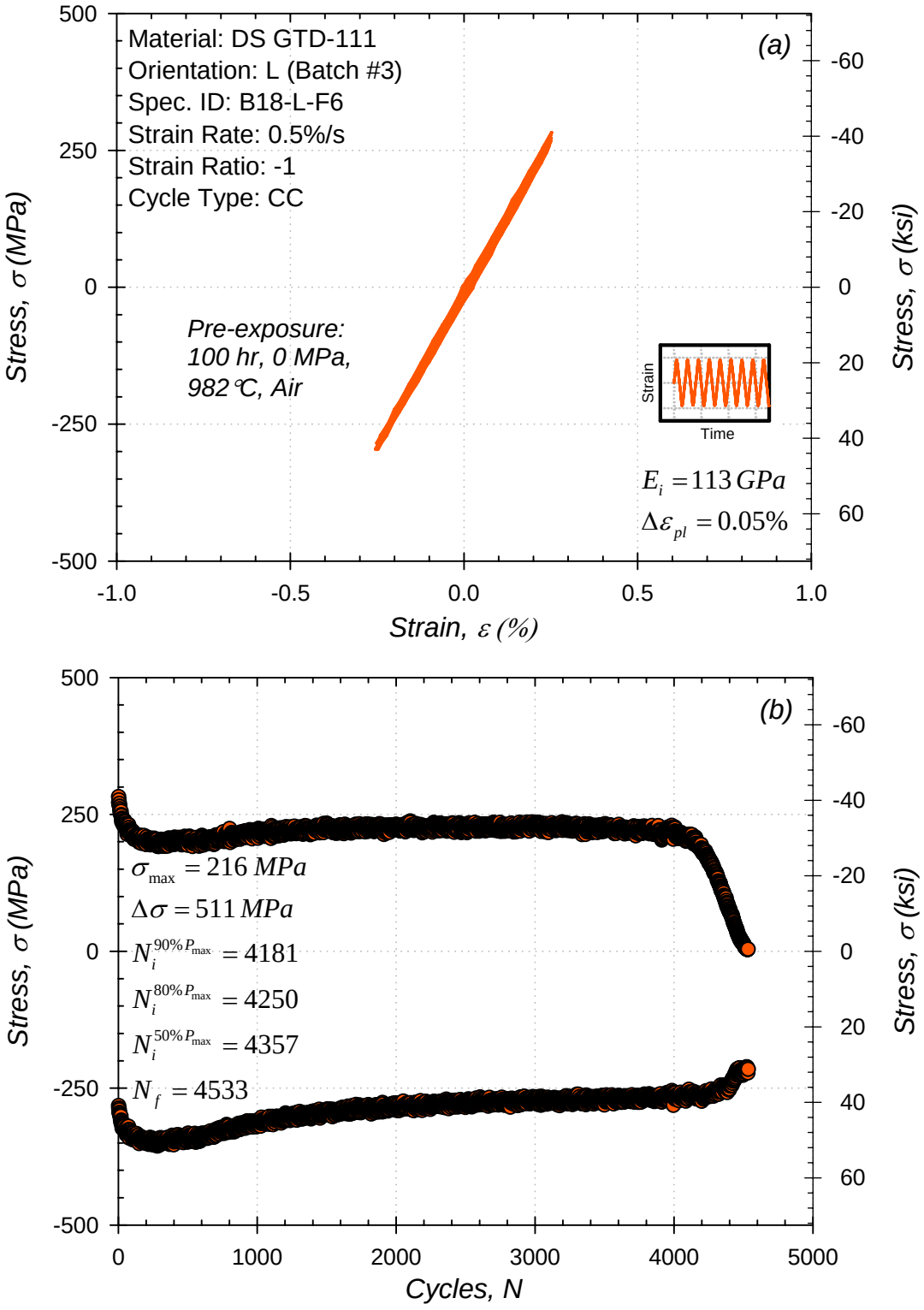


***Figure C.8:*** *(a) Initial stress-strain hysteresis loops and (b) stress history for low cycle fatigue test at 871°C.*

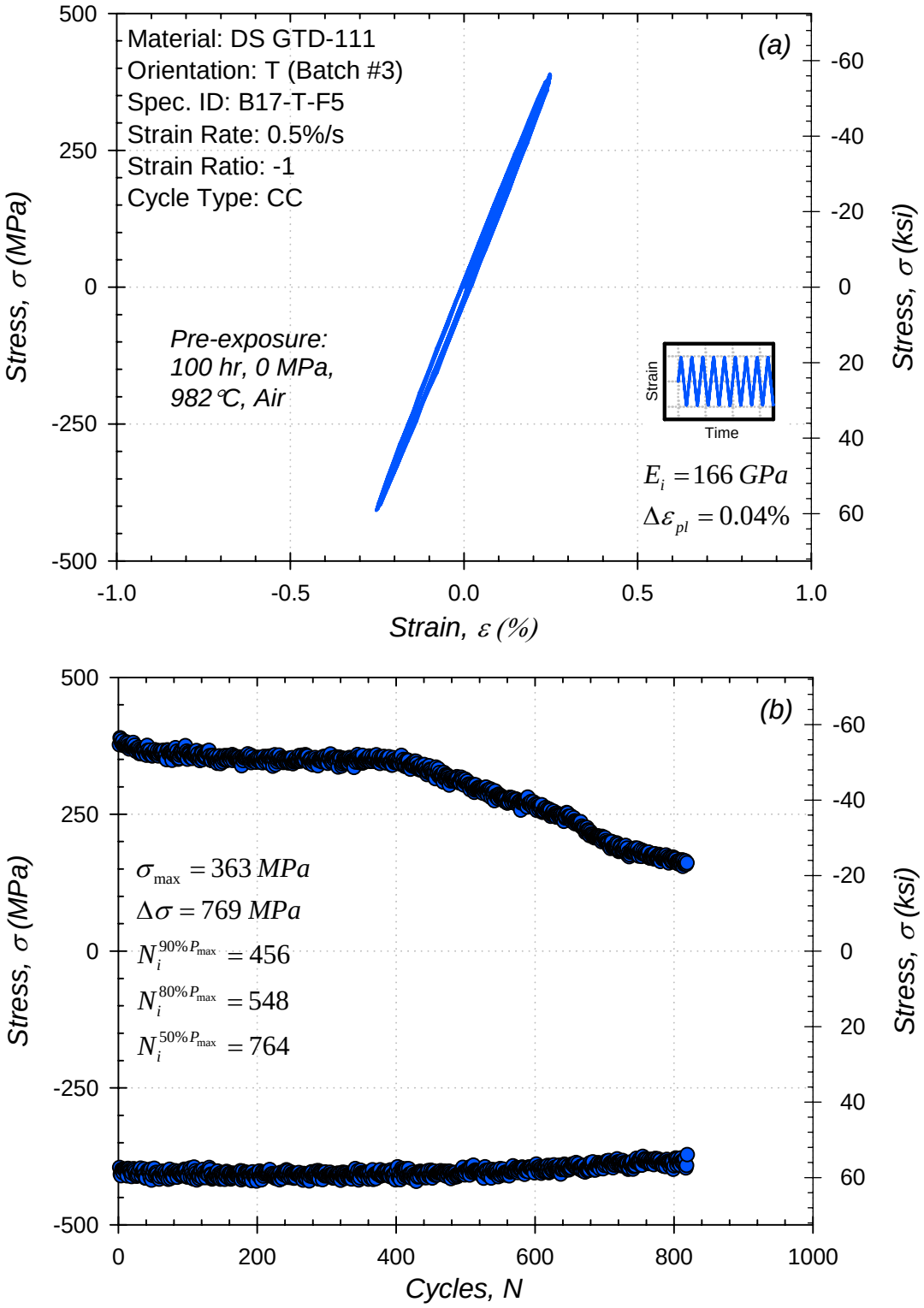


***Figure C.9:*** *(a) Initial stress-strain hysteresis loops and (b) stress history for low cycle fatigue test at 871°C.*

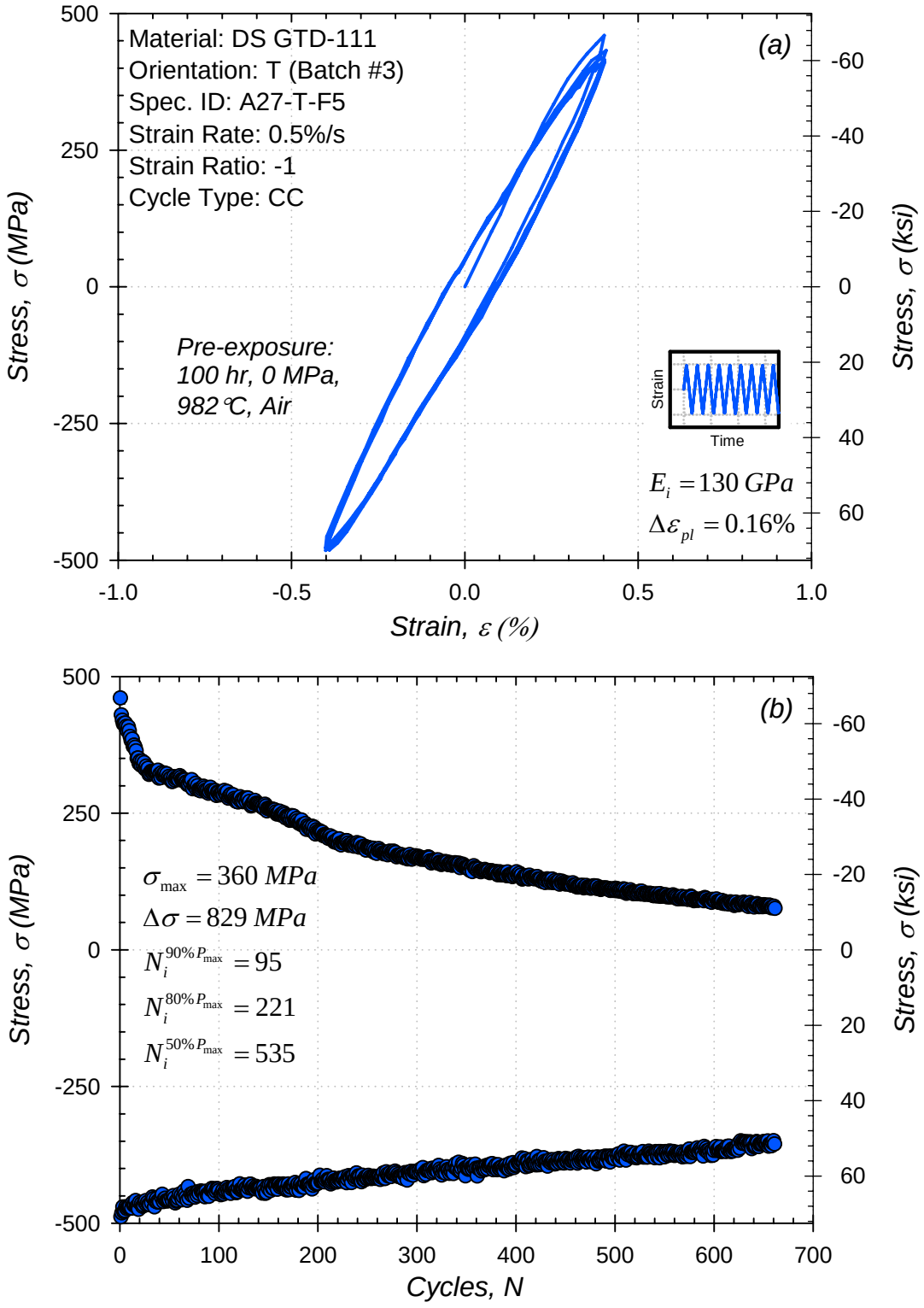


***Figure C.10:*** *(a) Initial stress-strain hysteresis loops and (b) stress history for low cycle fatigue test at 871°C.*

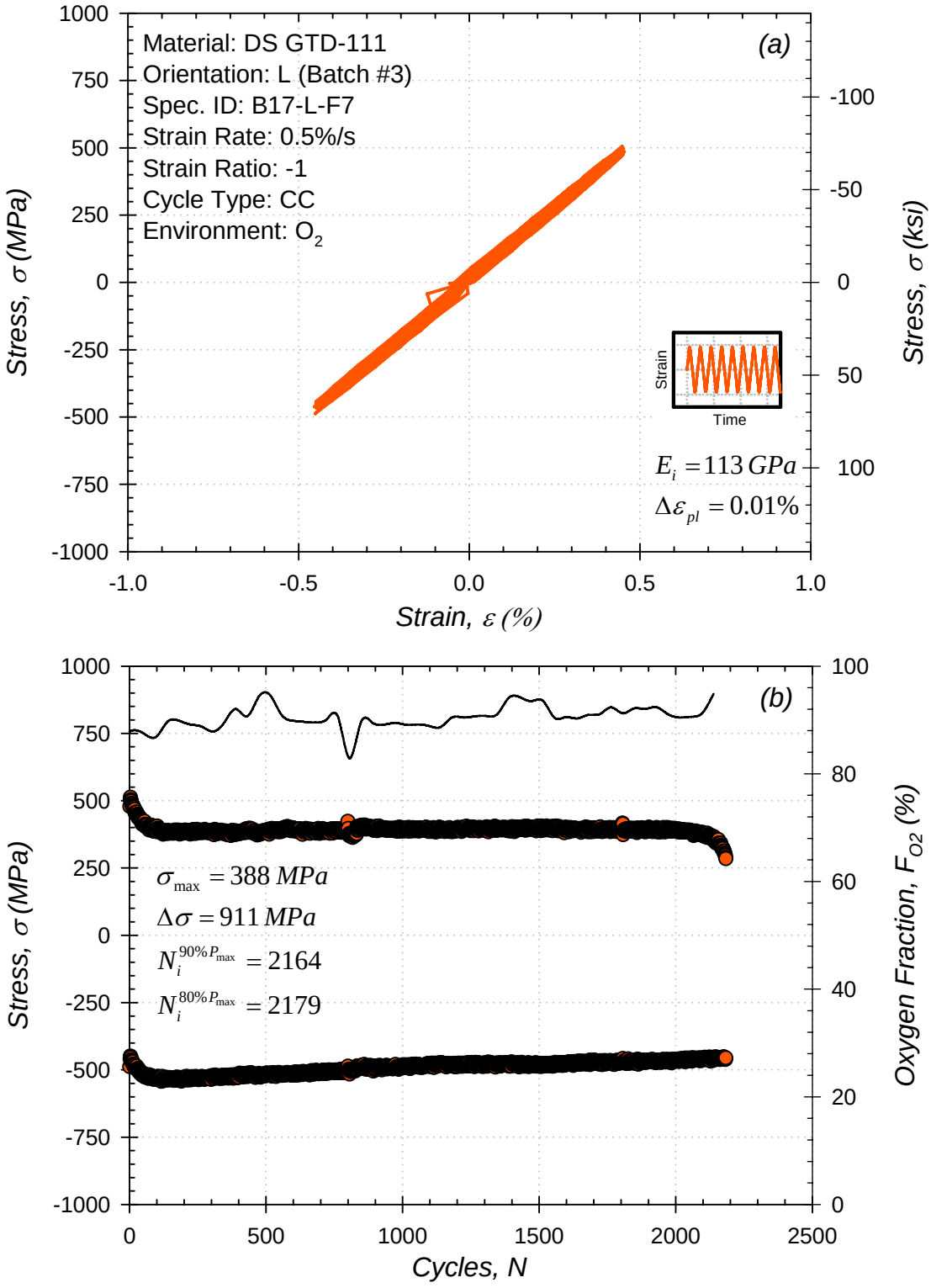


***Figure C.11:*** *(a) Initial stress-strain hysteresis loops and (b) stress and oxygen fraction history for low cycle fatigue test at 871°C.*

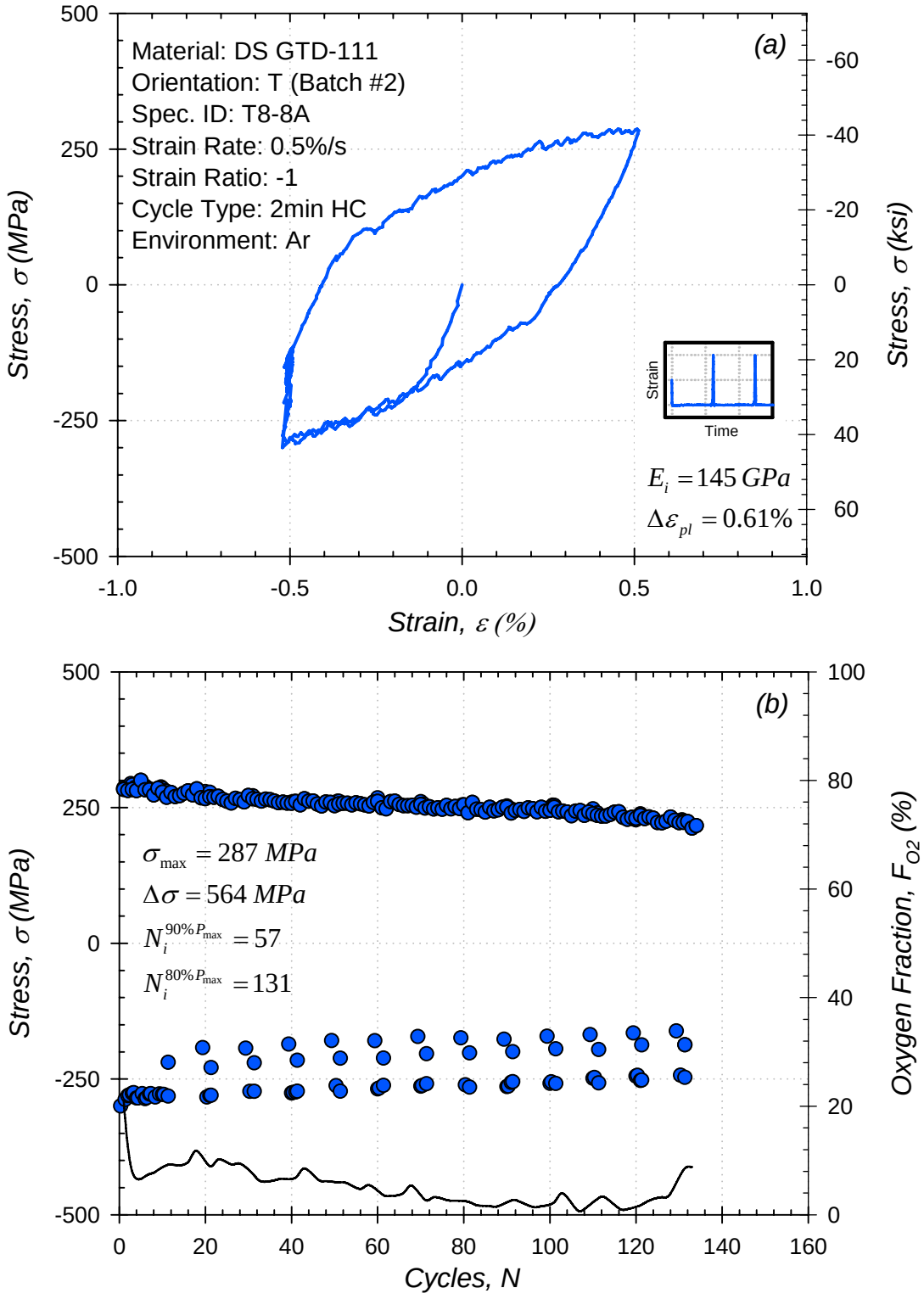


***Figure C.12:*** *(a) Initial stress-strain hysteresis loops and (b) stress and oxygen fraction history for low cycle fatigue test at 1038°C.*

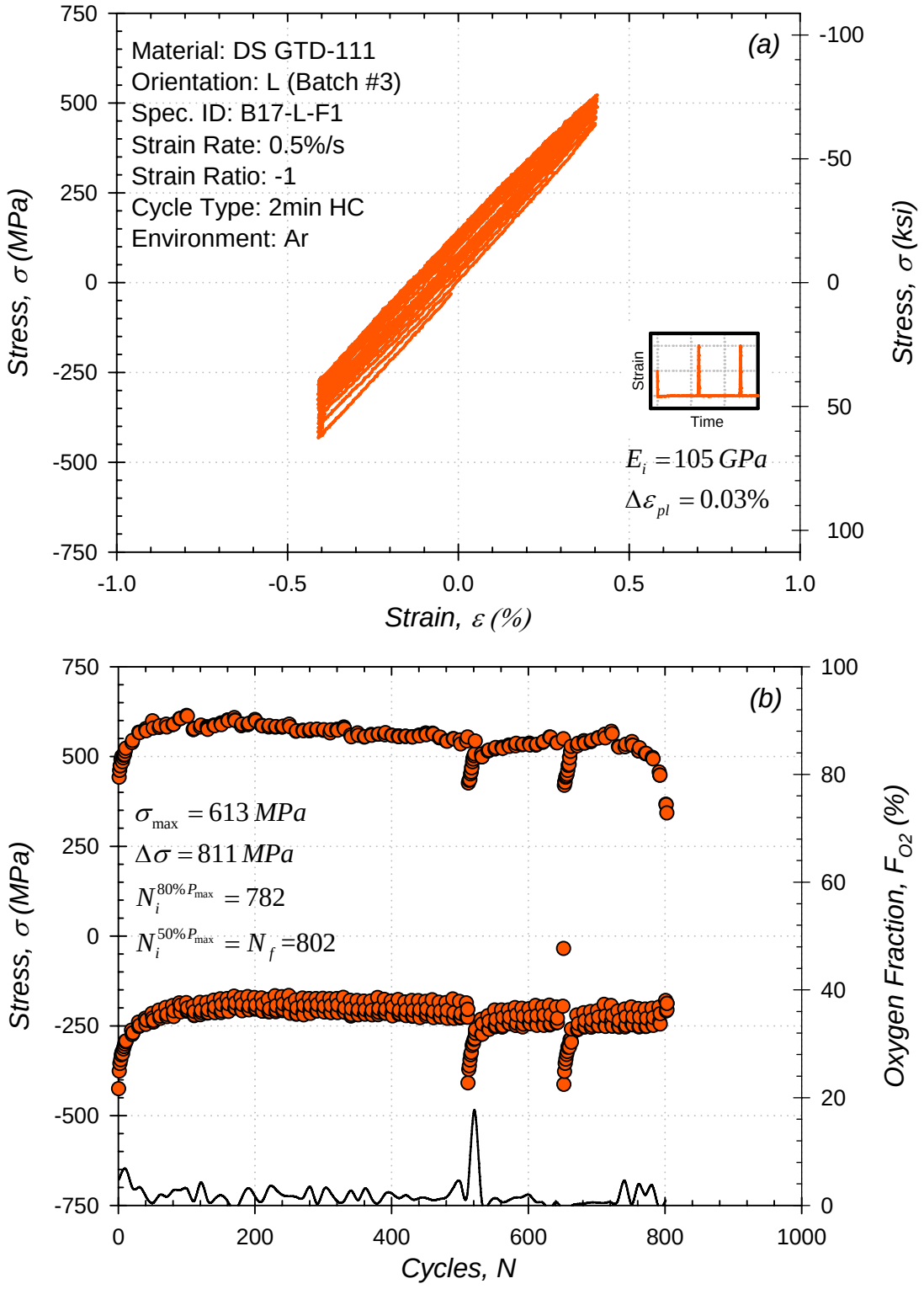


***Figure C.13:*** *(a) Initial stress-strain hysteresis loops and (b) stress and oxygen fraction history for low cycle fatigue test at 871°C.*

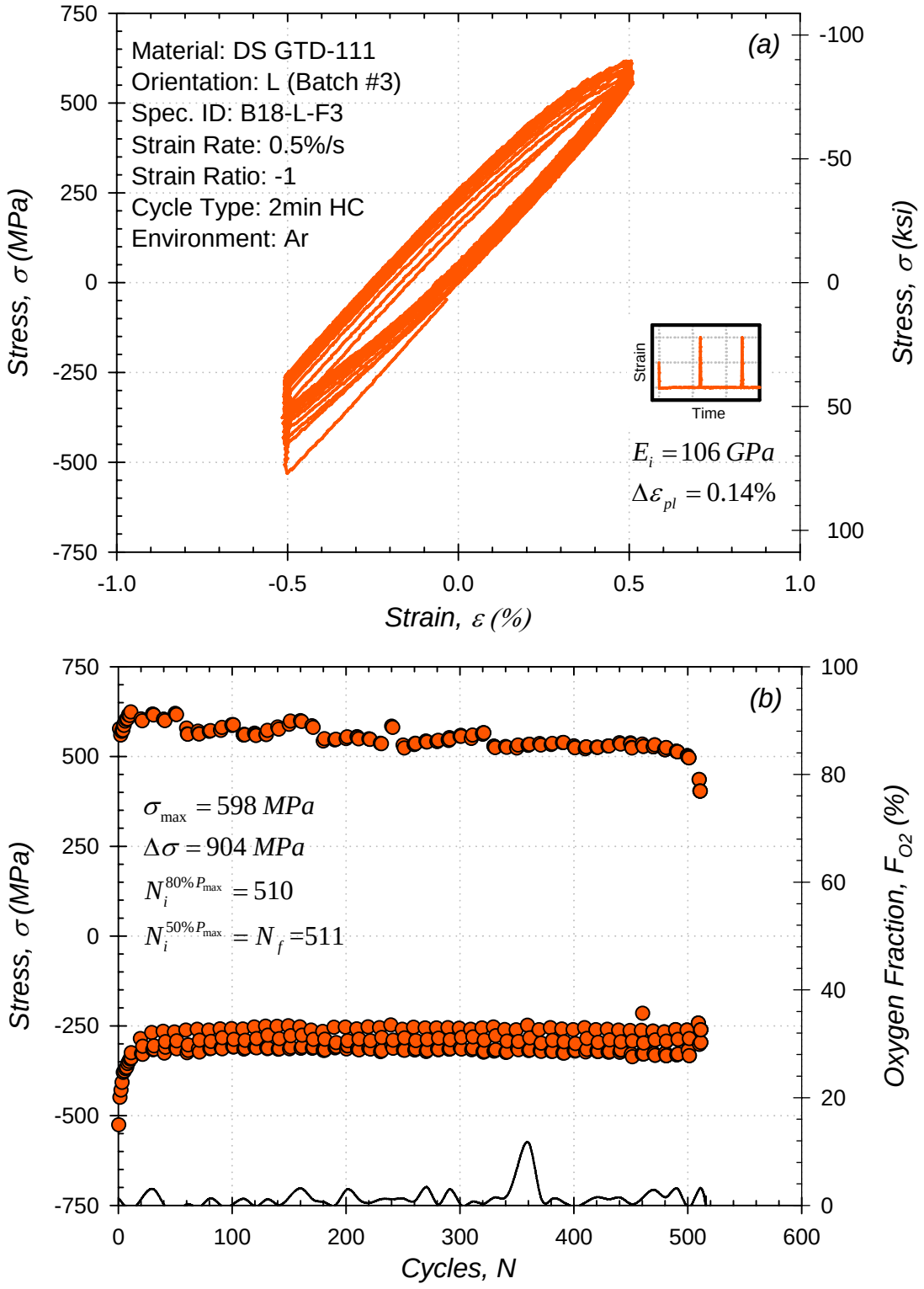


***Figure C.14:*** *(a) Initial stress-strain hysteresis loops and (b) stress and oxygen fraction history for low cycle fatigue test at 871°C.*

# APPENDIX D

## CREEP TEST CURVES
**(Ordered by Temperature)**

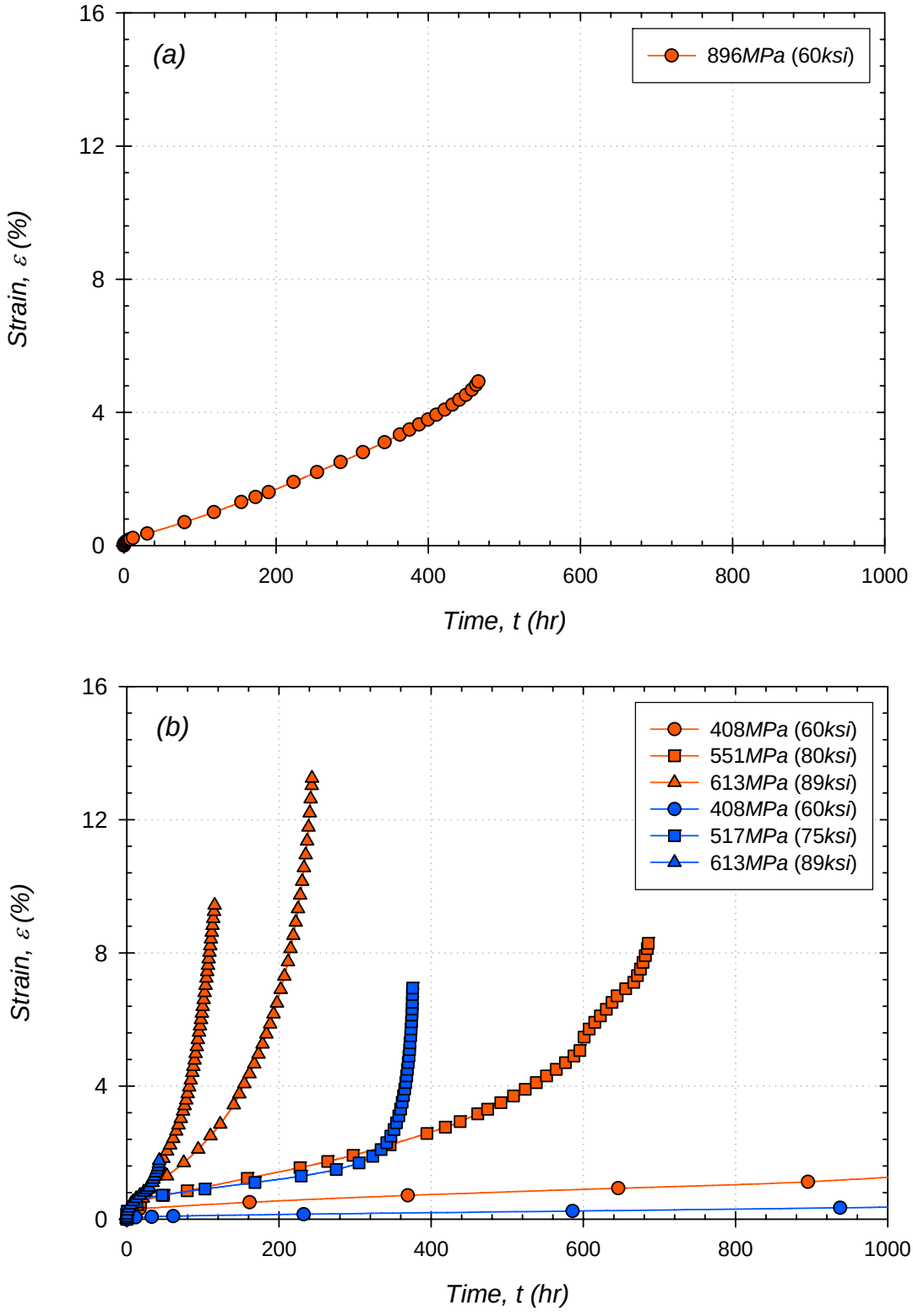


***Figure D.1:*** *Creep deformation of L (orange) and T-oriented (blue) DS GTD-111 at (a) 649℃ (1200℉) and (b) 760℃ (1400℉).*

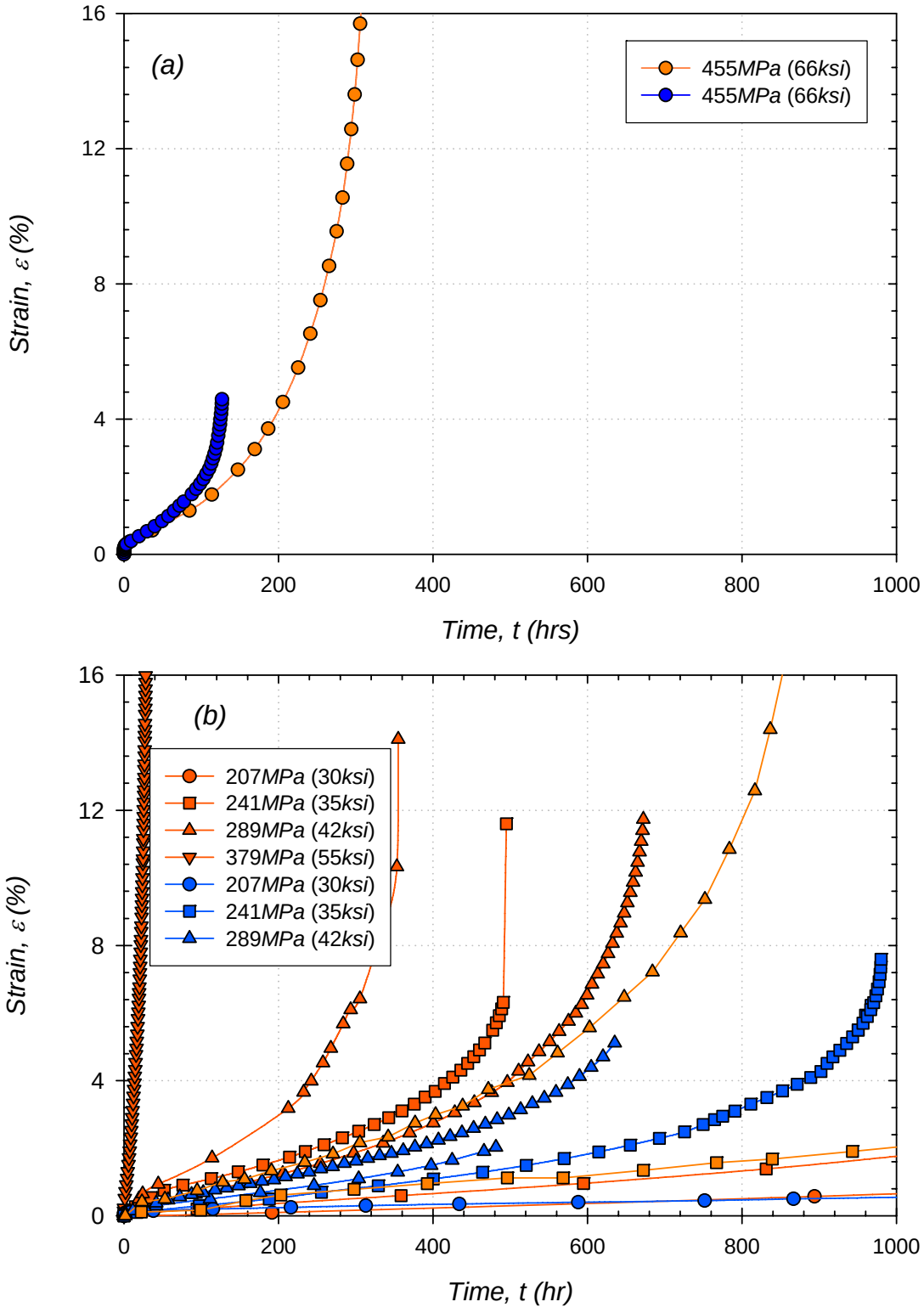


***Figure D.2:*** *Creep deformation of L (orange) and T-oriented (blue) DS GTD-111 at (a) 816℃ (1600℉) and (b) 871℃ (1600℉).*

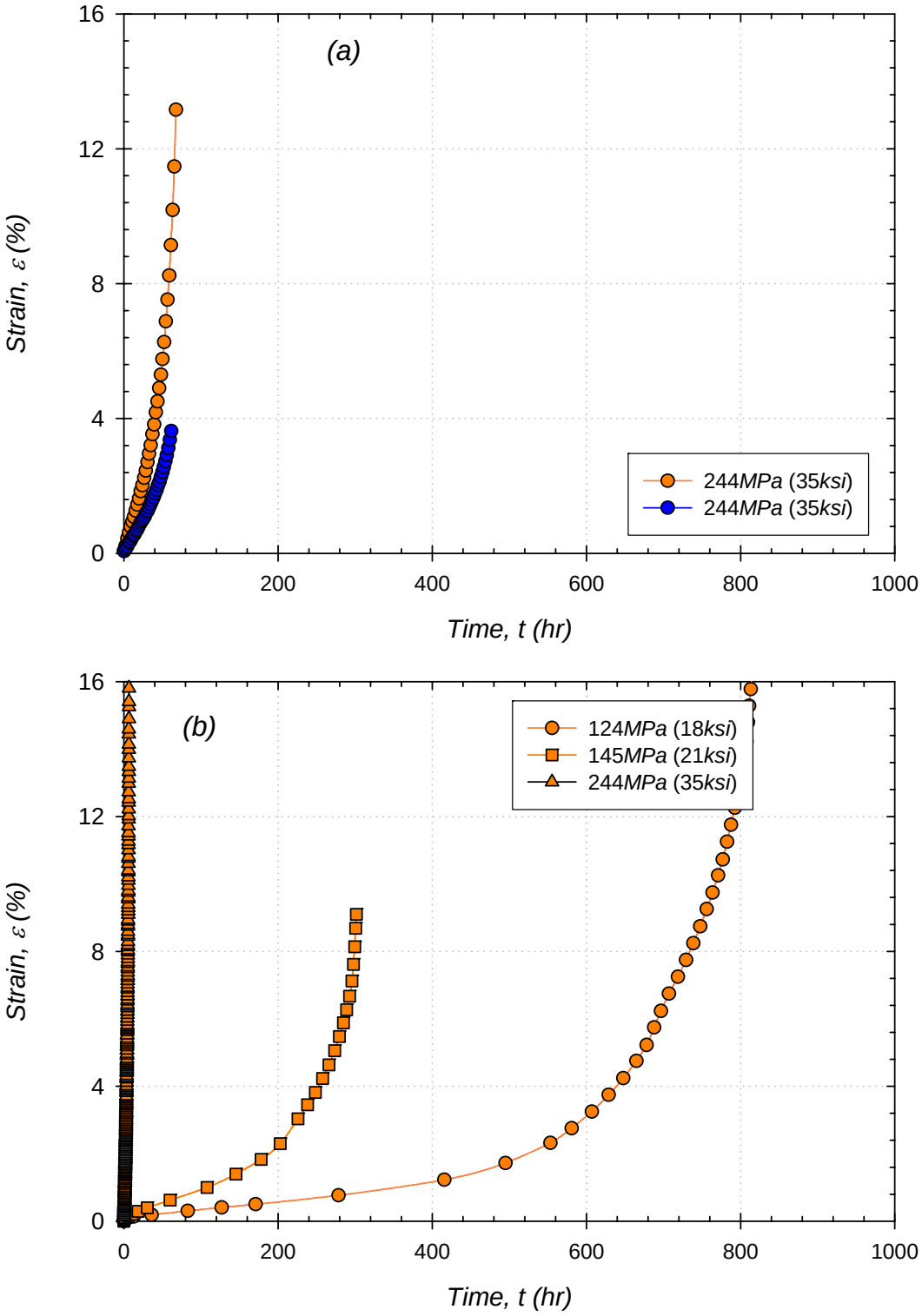


***Figure D.3:*** *Creep deformation of L (orange) and T-oriented (blue) DS GTD-111 at (a) 940℃ (1724℉) and (b) 982℃ (1800℉).*

# APPENDIX E

# NUMERICAL SIMULATION

***Table E.1:*** *Modeled response of DS GTD-111 under fatigue ($R_\varepsilon$=-1, $\Delta T$=0, $\dot{\varepsilon}$= 0.5%/s).*

| Temperature, *T* | | | L-oriented | | | T-oriented | | |
|---|---|---|---|---|---|---|---|---|
| °C | °F | Total Strain Range, $\Delta\varepsilon$ (%) | Plastic Strain Range, $\Delta\varepsilon_{pl}$ (%) | Max Stress, $\sigma_{max}$ (MPa) | Stress Range, $\Delta\sigma$ (MPa) | Plastic Strain Range, $\Delta\varepsilon_{pl}$ (%) | Max Stress, $\sigma_{max}$ (MPa) | Stress Range, $\Delta\sigma$ (MPa) |
| 649 | 1200 | 0.25 | 0.0008 | 145 | 289 | 0.0008 | 221 | 441 |
| | | 0.50 | 0.0032 | 291 | 578 | 0.0028 | 443 | 882 |
| | | 0.75 | 0.0073 | 437 | 867 | 0.0791 | 588 | 1191 |
| | | 1.00 | 0.0129 | 584 | 1157 | 0.2154 | 685 | 1392 |
| | | 1.50 | 0.0682 | 852 | 1682 | 0.5857 | 806 | 1623 |
| | | 2.00 | 0.3698 | 965 | 1915 | 1.0396 | 851 | 1705 |
| | | 3.00 | 1.1007 | 1129 | 2231 | 2.0024 | 890 | 1771 |
| | | 4.00 | 2.0265 | 1178 | 2319 | 2.9849 | 909 | 1802 |
| 760 | 1400 | 0.25 | 0.0008 | 134 | 268 | 0.0008 | 198 | 395 |
| | | 0.50 | 0.0033 | 269 | 536 | 0.0038 | 396 | 788 |
| | | 0.75 | 0.0073 | 405 | 804 | 0.0552 | 552 | 1103 |
| | | 1.00 | 0.0129 | 541 | 1071 | 0.1560 | 666 | 1340 |
| | | 1.50 | 0.1046 | 789 | 1517 | 0.4328 | 844 | 1694 |
| | | 2.00 | 0.3427 | 943 | 1801 | 0.8334 | 928 | 1852 |
| | | 3.00 | 1.0558 | 1127 | 2114 | 1.7762 | 980 | 1943 |
| | | 4.00 | 2.0217 | 1149 | 2151 | 2.7557 | 1001 | 1976 |
| 871 | 1600 | 0.25 | 0.0005 | 115 | 230 | 0.0008 | 161 | 320 |
| | | 0.50 | 0.0020 | 231 | 459 | 0.0025 | 321 | 640 |
| | | 0.75 | 0.0036 | 346 | 688 | 0.0385 | 460 | 916 |
| | | 1.00 | 0.0207 | 454 | 903 | 0.1358 | 556 | 1113 |
| | | 1.50 | 0.2319 | 586 | 1169 | 0.4654 | 670 | 1332 |
| | | 2.00 | 0.5400 | 677 | 1346 | 0.9237 | 698 | 1386 |
| | | 3.00 | 1.4439 | 726 | 1434 | 1.8974 | 716 | 1420 |
| | | 4.00 | 2.4407 | 728 | 1438 | 2.8857 | 724 | 1435 |
| 982 | 1800 | 0.25 | 0.0005 | 108 | 216 | 0.0021 | 167 | 335 |
| | | 0.50 | 0.0125 | 211 | 422 | 0.0947 | 274 | 548 |
| | | 0.75 | 0.0822 | 289 | 579 | 0.2653 | 326 | 656 |
| | | 1.00 | 0.2080 | 341 | 686 | 0.4572 | 366 | 734 |
| | | 1.50 | 0.5292 | 421 | 841 | 0.8899 | 413 | 826 |
| | | 2.00 | 0.9584 | 454 | 902 | 1.3612 | 433 | 864 |
| | | 3.00 | 1.9403 | 462 | 918 | 2.3408 | 448 | 892 |
| | | 4.00 | 2.9399 | 463 | 918 | 3.3334 | 453 | 903 |
| 1038 | 1900 | 0.25 | 0.0010 | 102 | 205 | 0.0091 | 154 | 311 |
| | | 0.50 | 0.0394 | 189 | 379 | 0.1541 | 223 | 446 |
| | | 0.75 | 0.1969 | 228 | 456 | 0.3604 | 251 | 503 |
| | | 1.00 | 0.4076 | 244 | 488 | 0.5783 | 271 | 544 |
| | | 1.50 | 0.8410 | 270 | 543 | 1.0301 | 302 | 606 |
| | | 2.00 | 1.2809 | 294 | 592 | 1.4958 | 324 | 651 |
| | | 3.00 | 2.1886 | 334 | 668 | 2.4556 | 351 | 703 |
| | | 4.00 | 3.1330 | 358 | 714 | 3.4374 | 364 | 727 |

***Table E.2:*** *Modeled response of DS GTD-111 under fatigue ($R_\varepsilon$=-1, $\Delta T$=0).*

| Temperature, *T* | | Total Strain Range, $\Delta\varepsilon$ (%) | Strain Rate, $\dot{\varepsilon}$ (%/s) | L-oriented | | | T-oriented | | |
|---|---|---|---|---|---|---|---|---|---|
| °C | °F | | | Plastic Strain Range, $\Delta\varepsilon_{pl}$ (%) | Max Stress, $\sigma_{max}$ (MPa) | Stress Range, $\Delta\sigma$ (MPa) | Plastic Strain Range, $\Delta\varepsilon_{pl}$ (%) | Max Stress, $\sigma_{max}$ (MPa) | Stress Range, $\Delta\sigma$ (MPa) |
| 649 | 1200 | 0.50 | 0.01 | 0.000 | 323 | 643 | 0.0026 | 440 | 882 |
| | | | 0.50 | 0.000 | 323 | 643 | 0.0028 | 443 | 882 |
| | | | 25.00 | 0.000 | 323 | 643 | - | - | - |
| | | 1.00 | 0.01 | 0.009 | 651 | 1280 | 0.2374 | 664 | 1353 |
| | | | 0.50 | 0.000 | 650 | 1286 | 0.2194 | 678 | 1385 |
| | | | 25.00 | 0.000 | 650 | 1287 | - | - | - |
| | | 2.00 | 0.01 | 0.651 | 928 | 1775 | 1.0721 | 821 | 1646 |
| | | | 0.50 | 0.602 | 966 | 1838 | 1.0416 | 848 | 1701 |
| | | | 25.00 | 0.570 | 990 | 1884 | - | - | - |
| 760 | 1400 | 0.50 | 0.01 | 0.000 | 269 | 536 | 0.0124 | 387 | 773 |
| | | | 0.50 | 0.000 | 269 | 536 | 0.0039 | 395 | 788 |
| | | | 25.00 | 0.000 | 269 | 536 | - | - | - |
| | | 1.00 | 0.01 | 0.005 | 540 | 1068 | 0.1946 | 630 | 1276 |
| | | | 0.50 | 0.000 | 541 | 1071 | 0.1585 | 662 | 1336 |
| | | | 25.00 | 0.000 | 541 | 1071 | - | - | - |
| | | 2.00 | 0.01 | 0.440 | 889 | 1715 | 0.8951 | 879 | 1750 |
| | | | 0.50 | 0.351 | 940 | 1801 | 0.8355 | 925 | 1848 |
| | | | 25.00 | 0.303 | 953 | 1834 | - | - | - |
| 871 | 1600 | 0.50 | 0.01 | 0.001 | 231 | 460 | 0.0242 | 304 | 612 |
| | | | 0.50 | 0.000 | 231 | 460 | 0.0026 | 321 | 640 |
| | | | 25.00 | 0.000 | 231 | 460 | - | - | - |
| | | 1.00 | 0.01 | 0.154 | 399 | 802 | 0.2461 | 481 | 969 |
| | | | 0.50 | 0.016 | 458 | 913 | 0.1412 | 549 | 1106 |
| | | | 25.00 | 0.000 | 464 | 919 | - | - | - |
| | | 2.00 | 0.01 | 0.827 | 575 | 1147 | 1.1078 | 576 | 1147 |
| | | | 0.50 | 0.543 | 699 | 1392 | 0.9246 | 696 | 1384 |
| | | | 25.00 | 0.402 | 746 | 1491 | - | - | - |
| 982 | 1800 | 0.50 | 0.01 | 0.172 | 150 | 303 | 0.2351 | 176 | 358 |
| | | | 0.50 | 0.018 | 211 | 428 | 0.0970 | 270 | 545 |
| | | | 25.00 | 0.000 | 217 | 433 | - | - | - |
| | | 1.00 | 0.01 | 0.553 | 204 | 415 | 0.6424 | 239 | 484 |
| | | | 0.50 | 0.309 | 317 | 638 | 0.4595 | 362 | 731 |
| | | | 25.00 | 0.086 | 406 | 812 | - | - | - |
| | | 2.00 | 0.01 | 1.411 | 275 | 553 | 1.5692 | 291 | 583 |
| | | | 0.50 | 1.120 | 412 | 825 | 1.3621 | 432 | 863 |
| | | | 25.00 | 0.862 | 511 | 1023 | - | - | - |
| 1038 | 1900 | 0.50 | 0.01 | 0.246 | 112 | 225 | 0.3030 | 126 | 254 |
| | | | 0.50 | 0.056 | 192 | 390 | 0.1557 | 220 | 444 |
| | | | 25.00 | 0.001 | 206 | 411 | - | - | - |
| | | 1.00 | 0.01 | 0.681 | 138 | 280 | 0.7519 | 158 | 320 |
| | | | 0.50 | 0.453 | 243 | 488 | 0.5797 | 269 | 542 |
| | | | 25.00 | 0.157 | 363 | 724 | - | - | - |
| | | 2.00 | 0.01 | 1.579 | 183 | 374 | 1.6811 | 203 | 411 |
| | | | 0.50 | 1.337 | 294 | 593 | 1.4969 | 323 | 649 |
| | | | 25.00 | 1.028 | 417 | 835 | - | - | - |

***Table E.3:*** *Modeled response of DS GTD-111 under fatigue ($\Delta T=0$, $\dot{\varepsilon}= 0.5\%/s$).*

| Mean Strain, $\varepsilon_m$ | Temperature, $T$ | | Total Strain Range, $\Delta\varepsilon$ (%) | L-oriented | | | T-oriented | | |
|---|---|---|---|---|---|---|---|---|---|
| | °C | °F | | Plastic Strain Range, $\Delta\varepsilon_{pl}$ (%) | Max Stress, $\sigma_{max}$ (MPa) | Stress Range, $\Delta\sigma$ (MPa) | Plastic Strain Range, $\Delta\varepsilon_{pl}$ (%) | Max Stress, $\sigma_{max}$ (MPa) | Stress Range, $\Delta\sigma$ (MPa) |
| *Tensile Mean Strain, $R_\varepsilon = 0$* | 760 | 1400 | 0.25 | 0.00E+00 | 269 | 269 | 1.75E-03 | 395 | 399 |
| | | | 0.50 | 3.27E-05 | 541 | 541 | 9.09E-03 | 662 | 806 |
| | | | 0.75 | 2.86E-03 | 783 | 831 | 2.18E-02 | 824 | 1151 |
| | | | 0.80 | 3.07E-03 | 813 | 886 | 3.21E-02 | 847 | 1214 |
| | | | 1.00 | 3.59E-03 | 919 | 1105 | 8.92E-02 | 910 | 1437 |
| | | | 1.20 | 4.66E-03 | 1001 | 1324 | 1.80E-01 | 943 | 1608 |
| | | | 1.50 | 1.05E-01 | 1081 | 1684 | 3.73E-01 | 969 | 1772 |
| | | | 2.00 | 3.33E-01 | 1133 | 1965 | 7.82E-01 | 990 | 1901 |
| | | | 3.00 | 1.02E+00 | 1149 | 2127 | 1.72E+00 | 1012 | 1969 |
| | | | 4.00 | 1.94E+00 | 1150 | 2150 | 2.67E+00 | 1023 | 1995 |
| | 871 | 1600 | 0.25 | 2.56E-05 | 231 | 231 | 2.65E-03 | 321 | 325 |
| | | | 0.50 | 4.81E-03 | 458 | 481 | 2.53E-02 | 549 | 675 |
| | | | 0.75 | 8.46E-03 | 598 | 736 | 2.50E-02 | 653 | 994 |
| | | | 0.80 | 9.06E-03 | 617 | 785 | 1.55E-02 | 663 | 1046 |
| | | | 1.00 | 2.20E-02 | 677 | 970 | 6.57E-02 | 688 | 1196 |
| | | | 1.20 | 8.91E-02 | 715 | 1157 | 1.93E-01 | 700 | 1287 |
| | | | 1.50 | 2.23E-01 | 742 | 1320 | 4.34E-01 | 709 | 1358 |
| | | | 2.00 | 5.18E-01 | 754 | 1434 | 8.93E-01 | 718 | 1400 |
| | | | 3.00 | 1.38E+00 | 757 | 1490 | 1.85E+00 | 727 | 1428 |
| | | | 4.00 | 2.33E+00 | 757 | 1494 | 2.80E+00 | 730 | 1440 |
| *Compressive Mean Strain, $R_\varepsilon = -\infty$* | 760 | 1400 | 0.25 | 7.27E-15 | 0 | 266 | 3.41E-05 | 4 | 395 |
| | | | 0.50 | 1.14E-04 | 0 | 530 | 3.44E-03 | 136 | 797 |
| | | | 0.75 | 2.89E-03 | 82 | 810 | 2.72E-02 | 328 | 1146 |
| | | | 0.80 | 3.07E-03 | 111 | 864 | 3.74E-02 | 369 | 1209 |
| | | | 1.00 | 3.55E-03 | 241 | 1081 | 9.97E-02 | 530 | 1429 |
| | | | 1.20 | 5.90E-03 | 397 | 1300 | 2.00E-01 | 660 | 1590 |
| | | | 1.50 | 1.21E-01 | 714 | 1674 | 4.01E-01 | 801 | 1753 |
| | | | 2.00 | 3.54E-01 | 958 | 1951 | 8.27E-01 | 916 | 1884 |
| | | | 3.00 | 1.10E+00 | 1126 | 2128 | 1.81E+00 | 974 | 1954 |
| | | | 4.00 | 2.10E+00 | 1149 | 2152 | 2.83E+00 | 998 | 1981 |
| | 871 | 1600 | 0.25 | 2.50E-05 | 0 | 229 | 7.41E-04 | 4 | 322 |
| | | | 0.50 | 4.68E-03 | 23 | 471 | 1.93E-02 | 126 | 667 |
| | | | 0.75 | 8.45E-03 | 139 | 723 | 1.95E-02 | 347 | 989 |
| | | | 0.80 | 9.04E-03 | 169 | 771 | 1.03E-02 | 389 | 1042 |
| | | | 1.00 | 2.25E-02 | 298 | 959 | 7.10E-02 | 520 | 1197 |
| | | | 1.20 | 9.36E-02 | 456 | 1153 | 2.01E-01 | 601 | 1289 |
| | | | 1.50 | 2.34E-01 | 597 | 1321 | 4.50E-01 | 662 | 1359 |
| | | | 2.00 | 5.28E-01 | 702 | 1438 | 9.27E-01 | 695 | 1401 |
| | | | 3.00 | 1.47E+00 | 755 | 1493 | 1.93E+00 | 715 | 1429 |
| | | | 4.00 | 2.50E+00 | 757 | 1496 | 2.96E+00 | 723 | 1440 |

***Table E.4.a:*** *Modeled response of DS GTD-111 under creep-fatigue ($\Delta\varepsilon$ = 0.5%, $R_\varepsilon$=-1, $\Delta T$=0, $\dot{\varepsilon}$= 0.5%/s).*

| | Temperature, $T$ | | | L-oriented | | | | T-oriented | | | |
|---|---|---|---|---|---|---|---|---|---|---|---|
| Hold Type | °C | °F | Hold Time, $t_h$ (min) | Plastic Strain Range, $\Delta\varepsilon_{pl}$ (%) | Max Stress, $\sigma_{max}$ (MPa) | Relaxed Stress, $\sigma_r$ (MPa) | Stress Range, $\Delta\sigma$ (MPa) | Plastic Strain Range, $\Delta\varepsilon_{pl}$ (%) | Max Stress, $\sigma_{max}$ (MPa) | Relaxed Stress, $\sigma_r$ (MPa) | Stress Range, $\Delta\sigma$ (MPa) |
| Tensile Dwell | 649 | 1200 | 2 | 0.003 | 323 | 322 | 643 | 0.006 | 443 | 422 | 899 |
| | | | 10 | 0.003 | 323 | 322 | 643 | 0.011 | 443 | 410 | 906 |
| | | | 50 | 0.003 | 323 | 322 | 643 | 0.016 | 443 | 392 | 917 |
| | | | 1250 | 0.003 | 323 | 322 | 643 | 0.028 | 443 | 348 | 937 |
| | | | 6250 | 0.003 | 323 | 322 | 644 | 0.032 | 443 | 329 | 945 |
| | 760 | 1400 | 2 | 0.003 | 269 | 269 | 536 | 0.007 | 395 | 351 | 806 |
| | | | 10 | 0.003 | 269 | 269 | 536 | 0.014 | 395 | 332 | 816 |
| | | | 50 | 0.003 | 269 | 269 | 536 | 0.019 | 395 | 314 | 825 |
| | | | 1250 | 0.003 | 269 | 269 | 536 | 0.027 | 395 | 290 | 836 |
| | | | 6250 | 0.003 | 269 | 269 | 536 | 0.029 | 395 | 284 | 839 |
| | 871 | 1600 | 2 | 0.018 | 231 | 211 | 479 | 0.036 | 321 | 250 | 690 |
| | | | 10 | 0.030 | 231 | 199 | 490 | 0.043 | 321 | 234 | 700 |
| | | | 50 | 0.038 | 231 | 191 | 498 | 0.049 | 321 | 222 | 707 |
| | | | 1250 | 0.047 | 231 | 183 | 506 | 0.055 | 321 | 210 | 714 |
| | | | 6250 | 0.048 | 231 | 181 | 508 | 0.056 | 321 | 207 | 716 |
| | 982 | 1800 | 2 | 0.050 | 211 | 90 | 477 | 0.076 | 270 | 103 | 574 |
| | | | 10 | 0.053 | 211 | 78 | 480 | 0.074 | 270 | 92 | 577 |
| | | | 50 | 0.055 | 211 | 71 | 481 | 0.073 | 270 | 85 | 578 |
| | | | 1250 | 0.057 | 211 | 64 | 483 | 0.072 | 270 | 78 | 580 |
| | | | 6250 | 0.057 | 211 | 63 | 483 | 0.071 | 270 | 77 | 580 |
| | 1038 | 1900 | 2 | 0.004 | 191 | 63 | 408 | 0.146 | 220 | 68 | 457 |
| | | | 50 | 0.004 | 190 | 54 | 409 | 0.145 | 220 | 60 | 458 |
| | | | 10 | 0.004 | 190 | 49 | 409 | 0.144 | 220 | 55 | 459 |
| | | | 1250 | 0.004 | 190 | 45 | 409 | 0.144 | 220 | 51 | 459 |
| | | | 6250 | 0.004 | 190 | 44 | 409 | 0.144 | 220 | 50 | 460 |
| Compressive Dwell | 649 | 1200 | 2 | 0.000 | 323 | -319 | 643 | 0.004 | 450 | -428 | 889 |
| | | | 10 | 0.000 | 323 | -319 | 643 | 0.007 | 456 | -417 | 895 |
| | | | 50 | 0.000 | 323 | -319 | 643 | 0.012 | 465 | -400 | 904 |
| | | | 1250 | 0.002 | 326 | -317 | 646 | 0.024 | 485 | -355 | 924 |
| | | | 6250 | 0.006 | 331 | -312 | 651 | 0.028 | 493 | -336 | 932 |
| | 760 | 1400 | 2 | 0.000 | 269 | -266 | 536 | 0.009 | 412 | -351 | 804 |
| | | | 10 | 0.000 | 269 | -266 | 536 | 0.015 | 422 | -332 | 814 |
| | | | 50 | 0.000 | 269 | -266 | 536 | 0.021 | 431 | -315 | 823 |
| | | | 1250 | 0.000 | 269 | -266 | 536 | 0.029 | 443 | -291 | 835 |
| | | | 6250 | 0.000 | 269 | -266 | 536 | 0.031 | 447 | -284 | 838 |
| | 871 | 1600 | 2 | 0.021 | 251 | -209 | 479 | 0.039 | 373 | -249 | 691 |
| | | | 10 | 0.034 | 262 | -198 | 491 | 0.047 | 383 | -233 | 701 |
| | | | 50 | 0.043 | 270 | -190 | 499 | 0.053 | 390 | -221 | 708 |
| | | | 1250 | 0.052 | 278 | -182 | 507 | 0.059 | 398 | -209 | 716 |
| | | | 6250 | 0.054 | 280 | -180 | 509 | 0.060 | 400 | -206 | 718 |
| | 982 | 1800 | 2 | 0.052 | 270 | -90 | 478 | 0.075 | 307 | -104 | 575 |
| | | | 10 | 0.056 | 272 | -78 | 481 | 0.073 | 309 | -92 | 577 |
| | | | 50 | 0.058 | 274 | -71 | 483 | 0.071 | 311 | -85 | 579 |
| | | | 1250 | 0.059 | 276 | -64 | 484 | 0.070 | 312 | -79 | 580 |
| | | | 6250 | 0.060 | 276 | -63 | 484 | 0.070 | 312 | -77 | 581 |
| | 1038 | 1900 | 2 | 0.003 | 220 | -63 | 409 | 0.145 | 239 | -69 | 458 |
| | | | 10 | 0.002 | 220 | -54 | 409 | 0.144 | 240 | -61 | 459 |
| | | | 50 | 0.002 | 221 | -49 | 409 | 0.144 | 241 | -56 | 459 |
| | | | 1250 | 0.002 | 221 | -45 | 409 | 0.143 | 241 | -51 | 460 |
| | | | 6250 | 0.002 | 221 | -44 | 409 | 0.143 | 241 | -50 | 460 |

***Table E.4.b:*** *Modeled response of DS GTD-111 under creep-fatigue ($\Delta\varepsilon$ = 1.0%, $R_\varepsilon$=-1, $\Delta T$=0, $\dot{\varepsilon}$= 0.5%/s).*

| | Temperature, $T$ | | | L-oriented | | | | T-oriented | | | |
|---|---|---|---|---|---|---|---|---|---|---|---|
| Hold Type | °C | °F | Hold Time, $t_h$ (min) | Plastic Strain Range, $\Delta\varepsilon_{pl}$ (%) | Max Stress, $\sigma_{max}$ (MPa) | Relaxed Stress, $\sigma_r$ (MPa) | Stress Range, $\Delta\sigma$ (MPa) | Plastic Strain Range, $\Delta\varepsilon_{pl}$ (%) | Max Stress, $\sigma_{max}$ (MPa) | Relaxed Stress, $\sigma_r$ (MPa) | Stress Range, $\Delta\sigma$ (MPa) |
| Tensile Dwell | 649 | 1200 | 2 | 0.002 | 650 | 630 | 1301 | 0.213 | 681 | 614 | 1396 |
| | | | 10 | 0.004 | 650 | 610 | 1308 | 0.212 | 679 | 592 | 1398 |
| | | | 50 | 0.007 | 650 | 580 | 1313 | 0.210 | 678 | 563 | 1402 |
| | | | 1250 | 0.018 | 650 | 496 | 1327 | 0.202 | 678 | 490 | 1416 |
| | | | 6250 | 0.024 | 650 | 461 | 1335 | 0.199 | 678 | 460 | 1421 |
| | 760 | 1400 | 2 | 0.009 | 541 | 516 | 1095 | 0.144 | 662 | 554 | 1360 |
| | | | 10 | 0.027 | 541 | 493 | 1115 | 0.138 | 662 | 518 | 1369 |
| | | | 50 | 0.039 | 541 | 473 | 1128 | 0.132 | 662 | 487 | 1378 |
| | | | 1250 | 0.053 | 541 | 442 | 1143 | 0.124 | 662 | 446 | 1390 |
| | | | 6250 | 0.057 | 541 | 431 | 1147 | 0.122 | 662 | 435 | 1394 |
| | 871 | 1600 | 2 | 0.052 | 458 | 307 | 975 | 0.103 | 549 | 361 | 1155 |
| | | | 10 | 0.064 | 458 | 279 | 986 | 0.097 | 549 | 331 | 1163 |
| | | | 50 | 0.071 | 458 | 262 | 993 | 0.093 | 549 | 312 | 1168 |
| | | | 1250 | 0.078 | 458 | 245 | 1000 | 0.090 | 549 | 293 | 1172 |
| | | | 6250 | 0.080 | 458 | 241 | 1001 | 0.089 | 549 | 289 | 1173 |
| | 982 | 1800 | 2 | 0.242 | 316 | 130 | 658 | 0.451 | 360 | 153 | 743 |
| | | | 10 | 0.240 | 316 | 117 | 660 | 0.451 | 359 | 139 | 743 |
| | | | 50 | 0.238 | 316 | 109 | 661 | 0.451 | 359 | 131 | 743 |
| | | | 1250 | 0.237 | 316 | 102 | 662 | 0.450 | 359 | 122 | 744 |
| | | | 6250 | 0.237 | 316 | 101 | 662 | 0.450 | 359 | 120 | 744 |
| | 1038 | 1900 | 2 | 0.399 | 243 | 85 | 495 | 0.575 | 268 | 96 | 548 |
| | | | 10 | 0.398 | 243 | 76 | 496 | 0.575 | 268 | 86 | 548 |
| | | | 50 | 0.398 | 243 | 71 | 496 | 0.575 | 268 | 80 | 548 |
| | | | 1250 | 0.398 | 243 | 66 | 496 | 0.575 | 267 | 73 | 548 |
| | | | 6250 | 0.398 | 243 | 65 | 496 | 0.575 | 267 | 72 | 548 |
| Compressive Dwell | 649 | 1200 | 2 | 0.042 | 705 | -582 | 1341 | 0.208 | 703 | -623 | 1398 |
| | | | 10 | 0.051 | 717 | -560 | 1353 | 0.207 | 707 | -600 | 1399 |
| | | | 50 | 0.058 | 725 | -531 | 1361 | 0.206 | 713 | -570 | 1401 |
| | | | 1250 | 0.074 | 746 | -452 | 1382 | 0.197 | 730 | -494 | 1417 |
| | | | 6250 | 0.081 | 755 | -419 | 1391 | 0.193 | 736 | -463 | 1424 |
| | 760 | 1400 | 2 | 0.042 | 587 | -487 | 1117 | 0.141 | 696 | -556 | 1356 |
| | | | 10 | 0.065 | 612 | -462 | 1141 | 0.133 | 707 | -517 | 1368 |
| | | | 50 | 0.081 | 628 | -442 | 1158 | 0.127 | 718 | -484 | 1379 |
| | | | 1250 | 0.099 | 647 | -412 | 1177 | 0.118 | 733 | -442 | 1393 |
| | | | 6250 | 0.104 | 653 | -401 | 1183 | 0.115 | 737 | -430 | 1397 |
| | 871 | 1600 | 2 | 0.063 | 529 | -304 | 978 | 0.097 | 616 | -359 | 1157 |
| | | | 10 | 0.076 | 541 | -277 | 989 | 0.090 | 624 | -330 | 1165 |
| | | | 50 | 0.084 | 548 | -260 | 997 | 0.087 | 629 | -311 | 1170 |
| | | | 1250 | 0.092 | 555 | -244 | 1004 | 0.083 | 634 | -292 | 1175 |
| | | | 6250 | 0.093 | 557 | -240 | 1005 | 0.082 | 635 | -288 | 1176 |
| | 982 | 1800 | 2 | 0.239 | 346 | -130 | 659 | 0.450 | 386 | -153 | 743 |
| | | | 10 | 0.236 | 348 | -117 | 661 | 0.450 | 387 | -140 | 744 |
| | | | 50 | 0.235 | 349 | -110 | 662 | 0.449 | 388 | -131 | 744 |
| | | | 1250 | 0.234 | 350 | -103 | 663 | 0.449 | 389 | -123 | 744 |
| | | | 6250 | 0.234 | 351 | -101 | 663 | 0.449 | 389 | -121 | 745 |
| | 1038 | 1900 | 2 | 0.397 | 255 | -85 | 495 | 0.575 | 282 | -96 | 548 |
| | | | 10 | 0.397 | 255 | -76 | 496 | 0.575 | 282 | -87 | 548 |
| | | | 50 | 0.396 | 256 | -71 | 496 | 0.574 | 283 | -80 | 549 |
| | | | 1250 | 0.396 | 256 | -67 | 497 | 0.574 | 283 | -74 | 549 |
| | | | 6250 | 0.396 | 256 | -66 | 497 | 0.574 | 283 | -73 | 549 |

***Table E.4.c:*** *Modeled response of DS GTD-111 under creep-fatigue ($\Delta\varepsilon$ = 2.0%, $R_\varepsilon$=-1, $\Delta T$=0, $\dot{\varepsilon}$= 0.5%/s).*

| Hold Type | Temperature, $T$ °C | Temperature, $T$ °F | Hold Time, $t_h$ (min) | L-oriented Plastic Strain Range, $\Delta\varepsilon_{pl}$ (%) | L-oriented Max Stress, $\sigma_{max}$ (MPa) | L-oriented Relaxed Stress, $\sigma_r$ (MPa) | L-oriented Stress Range, $\Delta\sigma$ (MPa) | T-oriented Plastic Strain Range, $\Delta\varepsilon_{pl}$ (%) | T-oriented Max Stress, $\sigma_{max}$ (MPa) | T-oriented Relaxed Stress, $\sigma_r$ (MPa) | T-oriented Stress Range, $\Delta\sigma$ (MPa) |
|---|---|---|---|---|---|---|---|---|---|---|---|
| Tensile Dwell | 649 | 1200 | 2 | 0.583 | 967 | 846 | 1848 | 1.040 | 850 | 748 | 1704 |
| | | | 10 | 0.581 | 965 | 816 | 1850 | 1.040 | 849 | 719 | 1705 |
| | | | 50 | 0.580 | 963 | 775 | 1852 | 1.039 | 849 | 682 | 1705 |
| | | | 1250 | 0.575 | 958 | 675 | 1858 | 1.039 | 847 | 590 | 1706 |
| | | | 6250 | 0.574 | 956 | 634 | 1860 | 1.039 | 846 | 554 | 1706 |
| | 760 | 1400 | 2 | 0.328 | 932 | 791 | 1818 | 0.831 | 924 | 751 | 1854 |
| | | | 10 | 0.326 | 926 | 745 | 1821 | 0.830 | 922 | 700 | 1856 |
| | | | 50 | 0.323 | 920 | 705 | 1824 | 0.830 | 921 | 655 | 1857 |
| | | | 1250 | 0.314 | 919 | 648 | 1834 | 0.829 | 919 | 598 | 1858 |
| | | | 6250 | 0.311 | 919 | 632 | 1837 | 0.829 | 919 | 582 | 1858 |
| | 871 | 1600 | 2 | 0.476 | 695 | 436 | 1412 | 0.922 | 695 | 427 | 1388 |
| | | | 10 | 0.474 | 694 | 398 | 1414 | 0.921 | 694 | 387 | 1388 |
| | | | 50 | 0.473 | 694 | 374 | 1415 | 0.921 | 694 | 361 | 1389 |
| | | | 1250 | 0.472 | 693 | 352 | 1416 | 0.921 | 694 | 336 | 1389 |
| | | | 6250 | 0.472 | 693 | 348 | 1416 | 0.921 | 694 | 331 | 1389 |
| | 982 | 1800 | 2 | 1.037 | 411 | 188 | 835 | 1.360 | 432 | 194 | 866 |
| | | | 10 | 1.037 | 411 | 174 | 835 | 1.360 | 432 | 179 | 866 |
| | | | 50 | 1.036 | 411 | 165 | 836 | 1.360 | 432 | 170 | 866 |
| | | | 1250 | 1.036 | 411 | 158 | 836 | 1.360 | 432 | 160 | 866 |
| | | | 6250 | 1.036 | 411 | 156 | 836 | 1.360 | 432 | 158 | 866 |
| | 1038 | 1900 | 2 | 1.274 | 293 | 123 | 598 | 1.494 | 323 | 130 | 653 |
| | | | 10 | 1.274 | 293 | 114 | 598 | 1.494 | 323 | 119 | 653 |
| | | | 50 | 1.274 | 293 | 109 | 598 | 1.494 | 323 | 112 | 653 |
| | | | 1250 | 1.273 | 293 | 104 | 598 | 1.494 | 323 | 105 | 653 |
| | | | 6250 | 1.273 | 293 | 103 | 598 | 1.494 | 323 | 103 | 653 |
| Compressive Dwell | 649 | 1200 | 2 | 0.564 | 995 | -761 | 1848 | 1.033 | 857 | -747 | 1705 |
| | | | 10 | 0.562 | 999 | -733 | 1850 | 1.033 | 858 | -717 | 1706 |
| | | | 50 | 0.559 | 1005 | -697 | 1854 | 1.032 | 860 | -679 | 1707 |
| | | | 1250 | 0.553 | 1018 | -606 | 1862 | 1.031 | 865 | -586 | 1710 |
| | | | 6250 | 0.549 | 1023 | -568 | 1867 | 1.030 | 867 | -549 | 1711 |
| | 760 | 1400 | 2 | 0.282 | 1002 | -705 | 1841 | 0.824 | 941 | -738 | 1857 |
| | | | 10 | 0.269 | 1015 | -660 | 1855 | 0.823 | 944 | -686 | 1859 |
| | | | 50 | 0.259 | 1026 | -620 | 1866 | 0.822 | 947 | -641 | 1861 |
| | | | 1250 | 0.246 | 1040 | -570 | 1879 | 0.820 | 951 | -583 | 1863 |
| | | | 6250 | 0.243 | 1043 | -556 | 1883 | 0.820 | 952 | -567 | 1863 |
| | 871 | 1600 | 2 | 0.461 | 736 | -430 | 1414 | 0.916 | 705 | -423 | 1389 |
| | | | 10 | 0.459 | 739 | -393 | 1417 | 0.916 | 706 | -383 | 1389 |
| | | | 50 | 0.458 | 741 | -370 | 1418 | 0.915 | 707 | -358 | 1389 |
| | | | 1250 | 0.457 | 742 | -348 | 1419 | 0.915 | 707 | -334 | 1390 |
| | | | 6250 | 0.456 | 743 | -344 | 1419 | 0.915 | 707 | -328 | 1390 |
| | 982 | 1800 | 2 | 1.035 | 430 | -187 | 835 | 1.359 | 438 | -194 | 866 |
| | | | 10 | 1.034 | 431 | -173 | 836 | 1.359 | 438 | -179 | 866 |
| | | | 50 | 1.034 | 431 | -165 | 836 | 1.359 | 439 | -170 | 867 |
| | | | 1250 | 1.033 | 432 | -157 | 837 | 1.359 | 439 | -160 | 867 |
| | | | 6250 | 1.033 | 432 | -156 | 837 | 1.359 | 439 | -158 | 867 |
| | 1038 | 1900 | 2 | 1.272 | 308 | -123 | 598 | 1.494 | 332 | -130 | 653 |
| | | | 10 | 1.272 | 308 | -114 | 599 | 1.493 | 332 | -119 | 653 |
| | | | 50 | 1.272 | 309 | -109 | 599 | 1.493 | 332 | -112 | 653 |
| | | | 1250 | 1.272 | 309 | -105 | 599 | 1.493 | 332 | -105 | 653 |
| | | | 6250 | 1.272 | 309 | -103 | 599 | 1.493 | 332 | -103 | 653 |

***Table E.5.a:*** *Modeled response of L-oriented DS GTD-111 under TMF ($t_{tc}$=180s, $R_{\varepsilon}$=-1, $T_{min}$=538°C).*

| Phasing | Max Temp., $T_{max}$ °C | Max Temp., $T_{max}$ °F | Mechanical Strain Range, $\Delta\varepsilon_m$ (%) | Plastic Strain Range, $\Delta\varepsilon_{pl}$ (%) | Thermal Strain Range, $\Delta\varepsilon_{th}$ (%) | Mean Stress, $\sigma_m$ (MPa) | Max Stress, $\sigma_{max}$ (MPa) | Stress Range, $\Delta\sigma$ (MPa) |
|---|---|---|---|---|---|---|---|---|
| In-Phase (0°) | 927 | 1700 | 0.25 | 0.00 | 0.54 | -3 | 137 | 302 |
| | | | 0.50 | 0.04 | 0.54 | -64 | 222 | 613 |
| | | | 1.00 | 0.14 | 0.54 | -177 | 337 | 1088 |
| | | | 2.00 | 0.85 | 0.54 | -133 | 596 | 1571 |
| | | | 4.00 | 2.73 | 0.55 | -41 | 1009 | 2060 |
| | 1038 | 1900 | 0.28 | 0.06 | 0.70 | -66 | 108 | 341 |
| | | | 0.50 | 0.15 | 0.70 | -176 | 107 | 621 |
| | | | 1.00 | 0.36 | 0.71 | -250 | 223 | 1007 |
| | | | 1.99 | 1.04 | 0.71 | -162 | 449 | 1431 |
| | | | 3.99 | 2.94 | 0.71 | -42 | 905 | 1962 |
| Out-of-Phase (180°) | 927 | 1700 | 0.26 | 0.00 | 0.54 | 2 | 169 | 303 |
| | | | 0.51 | 0.04 | 0.54 | 60 | 403 | 627 |
| | | | 1.01 | 0.14 | 0.54 | 171 | 772 | 1092 |
| | | | 2.01 | 0.87 | 0.54 | 125 | 970 | 1529 |
| | | | 4.01 | 2.74 | 0.54 | 51 | 1051 | 2029 |
| | 1038 | 1900 | 0.27 | 0.00 | 0.70 | 22 | 224 | 317 |
| | | | 0.50 | 0.02 | 0.70 | 123 | 483 | 602 |
| | | | 1.00 | 0.26 | 0.70 | 170 | 773 | 937 |
| | | | 2.00 | 1.06 | 0.70 | 115 | 972 | 1330 |
| | | | 4.00 | 2.97 | 0.70 | 42 | 1066 | 1894 |

***Table E.5.b:*** *Modeled response of T-oriented DS GTD-111 under TMF ($t_{tc}$=180s, $R_{\varepsilon}$=-1, $T_{min}$=538°C).*

| Phasing | Max Temp., $T_{max}$ °C | Max Temp., $T_{max}$ °F | Mechanical Strain Range, $\Delta\varepsilon_m$ (%) | Plastic Strain Range, $\Delta\varepsilon_{pl}$ (%) | Thermal Strain Range, $\Delta\varepsilon_{th}$ (%) | Mean Stress, $\sigma_m$ (MPa) | Max Stress, $\sigma_{max}$ (MPa) | Stress Range, $\Delta\sigma$ (MPa) |
|---|---|---|---|---|---|---|---|---|
| In-Phase (0°) | 927 | 1700 | 0.25 | 0.00 | 0.54 | -28 | 170 | 416 |
| | | | 0.50 | 0.01 | 0.54 | -133 | 257 | 821 |
| | | | 1.00 | 0.30 | 0.54 | -174 | 429 | 1252 |
| | | | 1.99 | 1.17 | 0.55 | -81 | 777 | 1716 |
| | | | 3.99 | 3.08 | 0.55 | -12 | 949 | 1941 |
| | 1038 | 1900 | 0.28 | 0.00 | 0.71 | -116 | 122 | 463 |
| | | | 0.50 | 0.06 | 0.71 | -220 | 161 | 786 |
| | | | 1.00 | 0.37 | 0.71 | -223 | 314 | 1162 |
| | | | 1.99 | 1.25 | 0.72 | -96 | 664 | 1604 |
| | | | 3.98 | 3.17 | 0.72 | -15 | 919 | 1910 |
| Out-of-Phase (180°) | 927 | 1700 | 0.26 | 0.00 | 0.54 | 17 | 249 | 418 |
| | | | 0.51 | 0.02 | 0.54 | 111 | 563 | 824 |
| | | | 1.01 | 0.31 | 0.54 | 152 | 815 | 1206 |
| | | | 2.01 | 1.18 | 0.54 | 81 | 920 | 1654 |
| | | | 4.01 | 3.10 | 0.54 | 19 | 964 | 1904 |
| | 1038 | 1900 | 0.28 | 0.01 | 0.70 | 60 | 316 | 422 |
| | | | 0.51 | 0.07 | 0.71 | 136 | 584 | 724 |
| | | | 1.01 | 0.39 | 0.71 | 140 | 825 | 1037 |
| | | | 2.00 | 1.27 | 0.70 | 72 | 918 | 1461 |
| | | | 4.00 | 3.19 | 0.70 | 20 | 981 | 1863 |

***Table E.6:*** *Modeled response of DS GTD-111 at various orientations ($R_\varepsilon$=-1, T=871 °C, $\Delta\varepsilon$=2.0%).*

| Orientation, $\omega$ | | | Plastic Strain Range, $\Delta\varepsilon_{pl}$ (%) | Max Stress, $\sigma_{max}$ (MPa) | Stress Range, $\Delta\sigma$ (MPa) | Yield Strength, $\sigma_o$ (MPa) | Elastic Modulus, *E (Gpa)* |
|---|---|---|---|---|---|---|---|
| Symbolic | Radians | Degrees | | | | | |
| 0 | 0.00 | 0 | 0.597 | 679 | 1374 | 649 | 93 |
| π/12 | 0.26 | 15 | 0.945 | 706 | 1409 | 664 | 136 |
| π/6 | 0.52 | 30 | 1.045 | 725 | 1447 | 676 | 156 |
| π/4 | 0.79 | 45 | 1.098 | 744 | 1487 | 681 | 169 |
| π/3 | 1.05 | 60 | 1.049 | 730 | 1457 | 679 | 155 |
| 5π/12 | 1.31 | 75 | 0.816 | 708 | 1415 | 667 | 121 |
| π/2 | 1.57 | 90 | 0.924 | 678 | 1350 | 648 | 122 |

## *REFERENCES*


Ai, S. H., Xia, Y. B. and Tian, J. F. (1998). "The Creep and Fracture Behavior of Two Nickel-Based Superalloys." *Acta Metallurgica Sinica*, Vol. 11, No. 6, pp. 425-428.

Alexandre, F., Deyber, S. and Pineau, A. (2004). "Modelling the Optimum Grain Size on the Low Cycle Fatigue Life of a Ni Based Superalloy in the Presence of Two Possible Crack Initiation Sites." *Scripta Materialia*, Vol. 50, pp. 25-30.

Antolovich, S. D., Baur, R. and Liu, S. (1980). "A Mechanistically Based Model for High Temperature LCF of Ni Base Superalloys." *Superalloys '80 (4th International Symposium)*. J. K. Tien, Ed., Seven Springs, PA, pp. 605-613.

Antolovich, S. D., Liu, S. and Baur, R. (1981a). "Low Cycle Fatigue Behavior of Rene 80 at Elevated Temperature." *Metallurgical and Materials Transactions A*, Vol. 12, pp. 473-481.

Antolovich, S. D., Rosa, E. and Pineau, A. (1981b). "Low Cycle Fatigue of Rene 77 at Elevated Temperatures." *Materials Science and Engineering*, Vol. 47, No. 1, pp. 47-57.

Beardmore, P., Davirs, R. G. and Johnston, T. L. (1969). "On Temperature Dependence of Flow Stress of Nickel-base Alloys." *Transactions of the Metallurgical Society of The American Institute of Mining, Metallurgical, and Petroleum Engineers*, Vol. 245, No. 7, pp. 1537-1545.

Beck, T., Ratchev, R., Moalla, M., Lang, K.-H. and Löhe, D. (2002). "Lifetime, Cyclic Deformation and Damage Behaviour of Mar-M-247 CC under In-Phase, Out-of-Phase and Phase-Shift TMF Loadings". *Temperature-Fatigue Interaction*. L. Rémy and J. Petit, Eds., Elsevier Science Ltd. and ESIS**,** pp. 115-124.

Bernstein, H. L., Grant, T. S., McClung, R. C. and M., A. J. (1993). "Prediction of Thermal Mechanical Fatigue Life for Gas Turbine Blades in Electric Power Generation". *Thermomechanical Fatigue Behavior of Materials, STP 1186*. H. Sehitoglu, Ed., Philadelphia, PA, American Society for Testing and Materials**,** pp. 212-238.

Bettge, D. and Österle, W. (1999). "Cube slip in near-[111] oriented speciments of a single-crystal nickel-base superalloy." *Scripta Materialia*, Vol. 40, No. 4, pp. 389-395.

Bilby, B., Bullough, R. and Smith, E. (1955). "Continuous Distributions of Dislocations: A New Application of the Methods of Non-Riemannian Geometry." *Proc. Royal Society*, Vol. A231, pp. 263-273.

Birks, N. and Meier, G. H. (1983). *Introduction to high temperature oxidation of metals*. London, Edward Arnold Publishers.

Boubidi, P. and Sievert, R. (2002). "Experimental and Numerical Investigations of Macro-crack Initiation under Low-Cycle Fatigue Loading at Notches in a Single Crystal Superalloy at High Temperature." *CAMP2002: High-Temperature Fatigue*. G. Biallas et al., Eds., Bad Lippspringe, Germany, pp. 127-141.

Bouhanek, K., Oquab, D. and Pieraggi, B. (1997). "High Temperature Oxidation of Single Crystal Ni-Base Superalloys." *Materials Science Forum*, Vol. 251-254, pp. 33-40.

Bruce, D. and Hancock, P. (1969). "Mechanical Properties and Adhesion of Surface Oxide Films on Iron and Nickel Measured During Growth." *Journal Institute of Metals*, Vol. 97, pp. 148-155.

Bulloch, J. H. and Callagy, A. G. (2000). "Assessment of a premature failure in a gas turbine part." *Engineering Failure Analysis*, Vol. 7, No. 6, pp. 411-426.

Castillo, R., Koul, A. K. and Toscano, E. H. (1987). "Lifetime Prediction under Constant Load Creep Conditions for a Cast Ni-base Superalloy." *Journal of Engineering for Gas Turbines and Power, Transactions of the ASME*, Vol. 109, No. 1, pp. 99-106.

Chan, K. S., Cheruvu, N. S. and Leverant, G. R. (1999). "Coating Life Prediction for Combustion Turbine Blades." *Journal of Engineering for Gas Turbines and Power*, Vol. 121, pp. 484-488.

Chang, J.-C., Yun, Y.-H., Choi, C. and Kim, J.-C. (2003). "Failure analysis of gas turbine buckets." *Engineering Failure Analysis*, Vol. 10, No. 5, pp. 559-567.

Cheruvu, N. S., Chan, K. S. and Leverant, G. R. (2000). "Cyclic Oxidation Behavior of Aluminide, Platinum Modified Aluminide, and MCrAlY Coatings on GTD-111." *Journal of Engineering for Gas Turbines and Power*, Vol. 122, pp. 50-54.

Chieragatti, R. and Rémy, L. (1991). "Influence of orientation on the low cycle fatigue of MAR-M 200 single crystals at 650$^{o}$C. I. Fatigue life behaviour." *Materials Science & Engineering A*, Vol. 141, No. 1, pp. 1-9.

Christ, H.-J. and Schöler, K. (2004). "Effect of prestraining on high-temperature fatigue behaviour of two Ni-base superalloys." *Zeitschrift fuer Metallkunde*, Vol. 95, No. 6, pp. 542-550.

Coffin, L. F. (1977). "Fatigue at High Temperature." *Fourth International Conference on Fracture*. Waterloo, Ont., Canada, Pergamon, pp. 263-292.

Daleo, J. A. and Wilson, J. R. (1998). "GTD111 Alloy Matieral Study." *Journal of Engineering for Gas Turbines and Power*, Vol. 120, pp. 375-382.

Das, D. K., Singh, V. and Joshi, S. V. (2003). "High Temperature Oxidation Behaviour of Directionally Solidified Nickel Base Superalloy CM-247LC." *Materials Science and Technology*, Vol. 19, No. 6, pp. 695-708.

Dettenwanger, F., Schumann, E., Rakowski, J., Meier, G. H. and Ruehle, M. (1997). "Development and Microstructure of the Al-depleted Layer of Oxidized TiAl." *Materials and Corrosion*, Vol. 48, No. 1, pp. 23-27.

Dong, J. X., Sawada, K., Yokokawa, K. and Abe, F. (2001). "Internal Nitridation Behavior During Long-Term Creep in a Nickel-Base Superalloy." *Scripta Materialia*, Vol. 44, pp. 2641-2646.

Duquette, D. J. and Gell, M. (1971). "The Effect of Environment on the Mechanism of Stage I Fatigue Fracture." *Metallurgical Transactions*, Vol. 2, pp. 1325-1331.

Duquette, D. J. and Gell, M. (1972). "The effects of environment on the elevated temperature fatigue behavior of nickel-base superalloy single crystals." *Metallurgical Transactions*, Vol. 3, pp. 1899-1905.

Embley, G. T. and Russell, E. S. (1984). "Thermal-Mechanical Fatigue of Gas Turbine Bucket Alloys." *First Parsons International Turbine Conference.*, Dublin, Parsons Press, pp. 157-164.

Evans, H. E. (1994). "Modelling Oxide Spallation." *Materials Under High Temperature*, Vol. 12, No. 2-3, pp. 219-227.

Evans, H. E. and Taylor, M. P. (1997). "Creep Relaxation and the Spallation of Oxide Layers." *Surface and Coatings Technology*, Vol. 94-95, pp. 27-33.

Fleury, E. and Rémy, L. (1994). "Behavior of nickel-base superalloy single crystals under thermal-mechanical fatigue." *Metallurgical and Materials Transactions A*, Vol. 25, No. 1, pp. 99-109.

Gallerneau, F., Nouailhas, D. and Chaboche, J. L. (1996). "A Fatigue Damage Model Including Interaction Effects with Oxidation and Creep Damages." *Fatigue '96*. Berlin, Germany, pp. 861-866.

Gordon, A. P., Neu, R. W. and McDowell, D. L. (2002). "GEPS Annual Report on Low Cycle Fatigue of GTD-111 DS." Georgia Institute of Technology, Atlanta, GA.

Gunturi, S. S. K., MacLachlan, D. W. and Knowles, D. M. (2000). "Anisotropic Creep in CMSX-4 in Orientations Distant from <001>." *Materials Science and Engineering A*, Vol. A289, pp. 289-298.

Guo, J. T., Yuan, C., Yang, H. C., Lupinc, V. and Maldini, M. (2001). "Creep-Rupture Behavior of a Directionally Solidified Nickel-Base Superalloy." *Metallurgical and Materials Transactions A*, Vol. 32A, pp. 1103-1110.

Harada, H., Yamazaki, M., Koizumi, Y., Sakuma, N., Furuya, N. and Kamiya, H. (1982). "Alloy Design for Nickel-base Superalloys." *High Temperature Alloys for Gas Turbines*. F. Julich, Ed., Liege, Belgium, D. Reidel Publishing Co., pp.

Hasebe, T., Sakane, M. and Ohnami, M. (1992). "Elastic Anisotropic of Directioally Solidified Superalloy." *Journal of Engineering Materials and Technology*, Vol. 114, pp. 162-167.

Hayes, R. W., Smith, D. F., Wanner, E. A. and Earthman, J. C. (1994). "Effect of environment on the rupture behavior of alloys 909 and 718." *Materials Science and Engineering A*, Vol. 177, No. 1-2, pp. 43-53.

Hertzberg, R. W. (1996). *Deformation and Fracture of Engineering Materials*. New York, J. Wiley & Sons.

Hou, J., Wicks, B. J. and Antoniou, R. A. (2002). "An investigation of fatigue failures of turbine blades in a gas turbine engine by mechanical analysis." *Engineering Failure Analysis*, Vol. 9, No. 2, pp. 201-211.

Huron, E. S. (1986). "High Temperature Monotonic and Cyclic Deformation in a Directionally-Solidified Nickel-Base Superalloy." Technical Report 86-C-19, Georgia Institute of Technology, Atlanta, GA.

Hyzak, J. M. and Bernstein, I. M. (1982a). "Effects of Defects on the Fatigue Crack Initiation Process in Two P/M Superalloys - 1. Fatigue Origins." *Metallurgical Transactions*, Vol. 13, No. 1, pp. 33-43.

Hyzak, J. M. and Bernstein, I. M. (1982b). "Effects of Defects on the Fatigue Crack Initiation Process in Two P/M Superalloys - 2. Surface-Subsurface Transition." *Metallurgical Transactions A*, Vol. 13, No. 1, pp. 45-52.

Ibanez, A. R. (2003). "Modeling Creep Behavior in a Directionally Solidified Nickel Base Superalloy." PhD Thesis, Georgia Institute of Technology, Atlanta, GA.

Kachanov, L. M. (1958). "Rupture Time Under Creep Conditions." *Izvestiya Akademiya Nauk USSR*, Vol. 8, pp. 26-31.

Kalluri, S., Halford, G. R. and McGaw, M. A. (1996). "Prestraining and its influence on subsequent fatigue life." *Proceedings of the 1994 3rd Symposium on Advances in Fatigue Lifetime Predictive Techniques, May 16-17 1994*. Montreal, Que, Can, ASTM, Conshohocken, PA, USA, pp. 328-341.

Khanna, A. S. (2002). *Introduction to High Temperature Oxidation and Corrosion*. Materials Park, Ohio, ASM International.

Kim, T. K., Yu, J. and Jeon, J. Y. (1992). "Creep rupture in a nickel-based superalloy." *Metallurgical Transactions A*, Vol. 23, No. 9, pp. 2581-2587.

Koster, A., Alam, A. M. and Rémy, L., Eds. (2002). *A Physical-Base Model for Life Prediction of Single Crystal Turbine Blades under Creep-Fatigue Loading and Thermal Transient Conditions*. Temperature-Fatigue Interaction, Elsevier Science.

Kowalewski, R. and Mughrabi, H. (2000). "Thermo-mechanical and isothermal fatigue of a coated columnar-grained directionally solidified nickel-base superalloy." *The Symposium of 'Thermo-Mechanical Fatigue Behavior of Materials*. Norfolk, VA, ASTM, Conshohocken, PA, pp. 3-17.

Krupp, U. and Christ, H.-J. (2000). "Selective Oxidation and Internal Nitridation During Temperature Exposure of Single-Crystalline Nickel-Base Superalloys." *Metallurgical and Materials Transactions A*, Vol. 31, pp. 47-56.

Kurz, W. and Fisher, D. J. (1998). *Fundamentals of Solidification*. Switzerland, Trans Tech Publications.

Larson, F. R. and Miller, J. (1952). "Time-temperature relationship for rupture and creep stresses." *American Society of Mechanical Engineers -- Transactions*, Vol. 74, No. 5, pp. 765-771.

Lee, H. (1969). "Elastic plastic deformations at finite strains." *Journal of Applied Mechanics*, Vol. 36, pp. 1-6.

Leverant, G. R. and Bernard, H. K. (1970). "The Mechanism of Creep in Gamma Prime Precipitation-Hardened Nickel-Base Alloys at Intermediate Temperatures." *Metallurgical Transactions*, Vol. 8, No. 3, pp. 125-133.

Leverant, G. R., Gell, M. and Hopkins, S. W. (1971). "Effect of strain rate on the flow stress and dislocation behavior of a precipitation-hardened nickel-base alloy." *Materials Science and Engineering*, Vol. 8, No. 3, pp. 125-33.

Li, M. H., Sun, X. F., Li, J. G., Zhang, Z. Y., Jin, T., Guan, H. R. and Hu, Z. Q. (2003). "Oxidation of a Single-Crystal Ni-Base Superalloy in Air I: At 800 and 900C." *Oxidation of Metals*, Vol. 59, No. 5/6, pp. 591-605.

Lvov, G., Levit, V. I. and Kaufman, M. J. (2004). "Mechanism of Primary MC Carbide Decomposition." *Metallurgical and Materials Transactions A*, Vol. 35, pp. 1669-1679.

Lvova, E. and Norsworthy, D. (2001). "Influence of Service-Induced Microstructural Changes on the Aging Kinetcis of Rejuventated Ni-based Superalloy Gas Turbine

Blades." *Journal of Materials Engineering and Performance*, Vol. 10, No. 3, pp. 299-313.

MacLachlan, D. W. and Knowles, D. M. (2000). "Creep-Behavior Modeling of the Single-Crystal Superalloy CMSX-4." *Metallurgical and Materials Transactions A*, Vol. 31, pp. 1401-1411.

MacLachlan, D. W., Wright, L. W., Gunturi, S. and Knowles, D. M. (2001). "Constitutive modelling of anisotropic creep deformation in single crystal blade alloys SRR99 and CMSX-4." *International Journal of Plasticity*, Vol. 17, No. 4, pp. 441-467.

Malpertu, J. L. and Rémy, L. (1990). "Influence of test parameters on the thermal-mechanical fatigue behavior of a superalloy." *Metallurgical Transactions A*, Vol. 21, No. 2, pp. 389-399.

Manson, S. S. and Halford, G. R. (1981). "Practical implementation of the double linear damage rule and damage curve approach for treating cumulative fatigue damage." Vol. 17, No. 2, pp. 169-192.

Manson, S. S. and Halford, G. R. (1985). "Re-examination of cumulative fatigue damage analysis - an engineering perspective." *Engineering Fracture Mechanics*, Vol. 25, No. 5-6, pp. 539-571.

Marchionni, M., Osinkolu, G. A. and Maldini, M. (1996). "High Temperature Cyclic Deformation of a Directionally Solidified Ni-Base Superalloy." *Fatigue and Fracture of Engineering Materials and Structures*, Vol. 19, No. 8, pp. 955-962.

Mazur, Z., Luna-Ramirez, A., Juarez-Islas, J. A. and Campos-Amezcua, A. (2005). "Failure analysis of a gas turbine blade made of Inconel 738LC alloy." *Engineering Failure Analysis*, Vol. 12, No. 3, pp. 474-486.

McDowell, D. L. (1992). "A Nonlinear Kinematic Hardening Theory for Cyclic Thermoplasticity and Thermoviscoplasticity." *International Journal of Plasticity*, Vol. 8, pp. 695-728.

McGinty, R. D. (2001). "Multiscale Representation of Polycrystalline Inelasticity." PhD Thesis, Georgia Institute of Technology, Atlanta, GA.

Meric, L., Poubanne, P. and Cailletaud, G. (1991). "Single Crystal Modeling for Structural Calculations Part 1 - Model Presentation." *Journal of Engineering Materials and Technology (Transactions of the ASME)*, Vol. 162, No. 113, pp. 162-170.

Miller, M. P., McDowell, D. L. and Oemke, R. L. T. (1992). "A Creep-Fatigue-Oxidation Microcrack Propagation Model for Thermomechanical Fatigue." *Journal of Engineering Materials and Technology (Transactions of the ASME)*, Vol. 114, pp. 282-288.

Murakumo, T., Kobayashi, T., Koizumi, Y. and Harada, H. (2004). "Creep Behavior of Ni-base Single-Crystal Superalloys with Various γ' Volume Fraction." *Acta Materialia*, Vol. 52, pp. 3737-3744.

Nabarro, F. R. N., Cress, C. M. and Kotschy, P. (1996). "Thermodynamic driving force for rafting in superalloys." *Acta Materialia*, Vol. 44, No. 8, pp. 3189-3198.

Nakasone, Y., Hiraga, K. and Tanabe, T. (1992). "Creep Crack Growth Behavior in Ni-Base Superalloys in 1,273 K Helium Gas Environment." *Journal of Nuclear Science and Technology*, Vol. 29, pp. 422-426.

Nategh, S. and Sajjadi, S. A. (2003). "Dislocation Network Formation During Creep in Ni-base Superalloys." *Materials Science and Engineering A*, Vol. 339, pp. 103-108.

Nazmy, M., Denk, J., Baumann, R. and Kunzler, A. (2003). "Environmental effects on tensile and low cycle fatigue behavior of single crystal nickel base superalloys." *Scripta Materialia*, Vol. 48, No. 5, pp. 519-524.

Nazmy, M. Y. and Wuthrich, C. (1983). "Creep Crack Growth in IN-738 and IN-939 Nickel-base Superalloys." *Materials Science and Engineering*, Vol. 61, pp. 119-125.

Neu, R. W. and Sehitoglu, H. (1989a). "Thermomechanical Fatigue, Oxidation and Creep: Part I. Damage Mechanisms." *Metallurgical Transactions A*, Vol. 20, pp. 1755-1767.

Neu, R. W. and Sehitoglu, H. (1989b). "Thermomechanical Fatigue, Oxidation and Creep: Part II Life Prediction." *Metallurgical Transactions A*, Vol. 20, pp. 1755-1767.

Neuner, F. C., Ulrich, T. and Mughrabi, H. (2002). "Enhancement of Thermomechanical Fatigue Resistance of a Monocrystalline Nickel-Base Superalloy by Pre-Rafting". *Thermomechanical Fatigue Behavior of Materials, STP 1428*. M. A. McGaw et al., Eds., West Conshocken, PA, American Society of Testing and Materials.

Nicholls, J. R., Evans, H. E. and Saunders, R. J. (1996). "Fracture and Spallation of Oxides." *Materials at High Temperatures*, Vol. 14, No. 1, pp. 5-13.

Nomoto, A., Yaguchi, M. and Ogata, T. (2000). "Study of Creep Properties and Microstructural Relation in Directionally Solidified Nickel Base Superalloy." *Key Engineering Materials*, Vol. 171-174, pp. 569-576.

Ohno, N., T. Mizuno, Kawaji, H. and Okada, I. (1992). "Multiaxial creep of a nickel-base directionally solidified alloy: anisotropy and simulation." *Acta Metallurgica et Materialia*, Vol. 40, No. 3, pp. 559-567.

Okada, M., Tsutsumi, M., Kitamura, T. and Ohtani, R. (1998). "Initiation and growth of small cracks in directionally solidified Mar-M247 under creep-fatigue. Part I: Effect of

microstructure." *Fatigue and Fracture of Engineering Materials & Structures*, Vol. 21, No. 6, pp. 741-750.

Okazaki, M., Tabata, T. and Nohmi, S. (1990). "Intrinsic Stage I Crack Growth of Directionally Solidified Ni-Base Superalloys During Low-Cycle Fatigue at Elevated Temperature." *Metallurgical Transactions A*, Vol. 21, pp. 2201-2208.

Okazaki, M. and Yamazaki, Y. (1999). "Creep-fatigue small crack propagation in a single crystal Ni-base superalloy, CMSX-2 microstructural influences and environmental effects." *International Journal of Fatigue*, Vol. 21, No. SUPPL, pp. 79-86.

Organ, F. E. and Gell, M. (1971). "Effect of Frequency on the Elevated Temperature Fatigue of a Nickel-Base Superalloy." *Metallurgical Transactions*, Vol. 2, No. 4, pp. 943-952.

Osterle, W., Bettge, D., Fedelich, B. and Klingelhoffer, K. (2000). "Modelling the orientation and direction dependence of the critical resolved shear stress of Nickel-base superalloy single crystals." *Acta Materialia*, Vol. 48, pp. 689-700.

Ott, M. and Mughrabi, H. (1999). "Dependence of the high-temperature low-cycle fatigue behavior of the monocrystalline nickel-base superalloys CMSX-4 and CMSX-6 on the γ/γ'-morphology." *Materials Science and Engineering A*, Vol. 272, pp. 24-30.

Park, M., Hwang, Y.-H., Choi, Y.-S. and Kim, T.-G. (2002). "Analysis of a J69-T-25 engine turbine blade fracture." *Engineering Failure Analysis*, Vol. 9, No. 5, pp. 593-601.

Ramachandran, J. and Conway, M. C. (1996). "MS6001FA – An Advanced-Technology 70-MW Class 50/60Hz Gas Turbine." Technical Report GER-3765B, GE Power Systems, Schenectady, NY.

Reger, M. and Rémy, L. (1988). "Fatigue oxidation interaction in IN 100 superalloy." *Metallurgical Transactions A*, Vol. 19, No. 9, pp. 2259-2268.

Rémy, L., Bernard, H., Malpertu, J. L. and Rezai-Aria, F. (1993). "Fatigue Life Prediction Under Thermal-Mechanical Loading in a Nickel-Base Superalloy". *Thermomechanical Fatigue Behaviour of Materials, STP 1186*. H. Sehitoglu, Ed., Philadelphia, PA, American Society of Mechanical Engineers**,** pp. 3-16.

Rémy, L., Koster, A., Chataigner, E. and Bickard, A. (2000). "Symposium Thermal-mechanical Fatigue and the Modelling of Materials Behaviour Under Thermal Transients." *Thermo-mechanical Fatigue Behavior of Materials, STP 1371*. H. Sehitoglu and H. J. Maier, Eds., Norfolk, VA, American Society for Testing and Materials, pp. 223-238.

Reuchet, J. and Rémy, L. (1983). "Fatigue Oxidation Interaction in a Superalloy - Application to Life Prediction in High Temperature Low Cycle Fatigue." *Metallurgical Transactions A*, Vol. 14, No. 1, pp. 141-149.

Riedel, H. R. (1987). *Fracture at High Temperatures*. New York, Springer-Verlag Berlin Heidelberg.

Rong, T. S., Jones, I. P. and Smallman, R. E. (1997). "Pre-creep strain on single crystal $Ni_3Al$." *Acta Materialia*, Vol. 45, No. 5, pp. 2139-2145.

Sajjadi, S. A. and Nategh, S. (2001). "A High Temperature Deformation Mechanism Map for the High Performance Ni-base Superalloy GTD-111." *Materials Science and Engineering A*, Vol. 307, pp. 158-164.

Sajjadi, S. A., Nategh, S. and Guthrie, R. I. L. (2002). "Study of Microstructure and Mechanical Properties of High Performance Ni-base Superalloy GTD-111." *Materials Science and Engineering A*, Vol. 325, pp. 484-489.

Sajjadi, S. A., Nategh, S., Isac, M. and Zebarjad, S. M. (2004). "Tensile deformation mechanisms at different temperatures in the Ni-base superalloy GTD-111." *Journal of Materials Processing Technology*, Vol. 155-156, No. 30, pp. 1900-1904.

Saxena, A. (2002). "Gas turbine engine prognostics and equipment health management." Project No. E-18-637, Georgia Institute of Technology, Atlanta, GA.

Schilke, P. W. (2004). "Advanced Gas Turbine Materials and Coatings." GER-3569G, GE Energy, Schenectady.

Schöler, K. and Christ, H.-J. (1998). "Effect of predeformation on the high-temperature low cycle fatigue behaviour of polycrystalline Ni-base superalloys." *4th International Conference on Low Cycle Fatigue and Elasto-Plastic Behaviour of Materials*. K.-T. Rie and P. D. Portella., Eds., Garmisch-Partenkirchen, Germany, Elsevier, pp. 345-50.

Sehitoglu, H. (1992). "Thermo-mechanical Fatigue Life Prediction Methods". *Advances in Fatigue Lifetime Predictive Techniques, STP 1122*. M. R. Mitchell and R. W. Landgraf, Eds., San Francisco, American Society for Testing and Materials**,** pp. 47-76.

Sehitoglu, H. and Boismier, D. A. (1990a). "Thermo-Mechanical Fatigue of Mar-M247: Part 1-Experiments." *Journal of Engineering Materials and Technology*, Vol. 112, No. 1, pp. 68-79.

Sehitoglu, H. and Boismier, D. A. (1990b). "Thermo-Mechanical Fatigue pf Mar-M247: Part 2-Life Prediction." *Journal of Engineering Materials and Technology*, Vol. 112, No. 1, pp. 80-89.

Shahinan, P. and Sadananda, K. (1989). "Creep and Fatigue Crack Growth Behavior of Some Cast Nickel-base Alloys." *Materials Science and Engineering A*, Vol. 108, pp. 131-140.

Sharke, P. (2000). "Lost and Foundry." *Mechanical Engineering*, Vol. 122, No. 9, pp. 62-67.

Sheh, M. Y. and Stouffer, D. C. (1988). "Anisotropic constitutive model for Nickel-base Single Crystal Superalloys." *NASA*, Vol. Technical Report No. CR-182157, pp.

Shenoy, M. M., Gordon, A. P., McDowell, D. L. and Neu, R. W. (2005). "Thermomechanical fatigue behavior of a directionally solidified Ni-base superalloy." *Journal of Engineering Materials and Technology, Transactions of the ASME*, Vol. 127, No. 3, pp. 325-336.

Sinharoy, S., Virro-Nic, P. and Milligan, W. W. (2001). "Deformation and strength behavior of two nickel-base turbine disk alloys at 650$^{o}$C." *Metallurgical and Materials Transactions A*, Vol. 32, No. 8, pp. 2021-2032.

Srinivas, S., Pandey, M. C. and Taplin, D. M. R. (1995). "Air-Environment-Creep Interaction in a Nickel Base Superalloy." *Engineering Failure Analysis*, Vol. 2, No. 3, pp. 191-196.

Sun, Y. Q. and Hazzledine, P. M. (1996). "Geometry of dislocation glide in L12 - phase: TEM observations." *Dislocations in Solids*, Vol. 10, pp. 27-68.

Sung, P. K. and Poirier, D. R. (1998). "Estimation of densities and coefficients of thermal expansion of solid Ni-base superalloys." *Materials Science & Engineering A*, Vol. 245, No. 1, pp. 135-141.

Taira, S. (1973). "Relationship between Thermal Fatigue and Low-Cycle Fatigue at Elevated Temperature". *Fatigue at Elevated Temperatures, STP 520*. A. E. Carden et al., Eds., Philadelphia, American Society for Testing and Materials**,** pp. 80-101.

Thompson, N., Wadsworth, N. J. and Louat, N. (1956). "The Origin of Fatigue Fracture in Copper." *Philosphical Magazine*, Vol. 1, pp. 113-126.

Tong, J., Dalby, S., Byrne, J., Henderson, M. B. and Hardy, M. C. (2001). "Creep, Fatigue and Oxidation in Crack Growth in Advanced Nickel Base Superalloys." *International Journal of Fatigue*, Vol. 23, pp. 897-902.

Trexler, M. D. and Sanders, T. H. (2002). "Investigation of Microstructural Evolution in GTD-111." Georgia Institute of Technology, Atlanta, GA.

Valerio, P., Gao, M. and Wei, R. P. (1994). "Environmental Enhancement of Creep Crack Growth in Inconel 718 by Oxygen and Water Vapor." *Scripta Metallurgica et Materialia*, Vol. 30, No. 10, pp. 1269-1274.

Vasseur, E. and Rémy, L. (1994). "High temperature low cycle fatigue and thermal-mechanical fatigue behaviour of an oxide-dispersion-strengthened nickel-base superalloy." *Materials Science and Engineering A*, Vol. 184, No. 1, pp. 1-5.

Vitek, V., Pope, D. P. and Bassani, J. L. (1996). "Superalloys (Ni base) and dislocations - An Introduction." *Dislocations in Solids*, Vol. 10, pp. 135-186.

Woodford, D. A. (1996). "Creep design analysis of silicon nitride using stress relaxation data." *Materials & Design*, Vol. 17, No. 3, pp. 127-132.

Woodford, D. A. (1997). "Creep Analysis of Directionally-Solidified GTD111 based on Stress Relaxation Testing." *Materials at High Temperature*, Vol. 14, No. 4, pp. 413-420.

Woodford, D. A. and Stiles, D. (1997). "High-Temperature Performance Evaluation of a Directionally-Solidified Nickel-Base Superalloy." *Journal of Materials Engineering and Performance*, Vol. 6, No. 4, pp. 521-533.

Wright, P. K. (1988). "Oxidation-Fatigue Interactions in a Single-Crystal Superalloy". *Low Cycle Fatigue, STP 942*. H. D. Solomon et al., Eds., Philadelphia, American Society for Testing and Materials**,** pp. 558-575.

Wright, P. K. and Anderson, A. F. (1980). "Influence of Orientation on the Fatigue of Directionally Solidified Superalloys." *4th International Symposium on Superalloys*. J. K. Tien et al., Eds., Seven Springs, PA, American Society for Materials, pp. 689-698.

Yao, X. X., Fang, Y., T., K. H. and Choi, J. (1997). "The Microstructural Characterisitcs in a Newly Developed Nickel-Base Superalloy." *Materials Characterization*, Vol. 38, pp. 97-102.

Yue, Z. F., Lu, Z. Z. and Zheng, C. Q. (1996). "Evaluation of creep damage behavior of Nickel-base directionally solidified superalloys with different crystallographic orientation." *Theoretical and Applied Fracture Mechanics*, Vol. 25, pp. 127-138.

Zamrik, S. Y. and Renauld, M. L. (2000). "Thermo-mechanical Out-of-Phase Fatigue Life of Overlay Coated IN-738LC Gas Turbine Material." *Thermomechanical Fatigue Behaviour of Materials, STP 1371*. H. Sehitoglu and H. J. Maier, Eds., American Society for Testing and Materials, pp.

# VITA

Ali P. Gordon, son of Mary F. Gordon and H. Antony Cramer, was born on July, 25th, 1974 in Washington, District of Columbia. There he attended Wilson Senior High School. Afterwards, he matriculated to Morehouse College in Atlanta, Georgia. With support from the Atlanta University Center Dual-Degree Engineering Program, he commenced studies at the Georgia Institute of Technology after three years. In 1997, he graduated from Morehouse with a Bachelor's of Science degree in Mathematics and from Georgia Tech with Bachelor's degree in Mechanical Engineering. Three months later, Ali commenced his graduate studies within the George W. Woodruff School of Mechanical Engineering under the direction of Dr. David L. McDowell. During this time he worked in the area of time dependent fracture mechanics of bimaterials. In 2000, he graduated with a Master's of Science Degree in Mathematics. His doctoral studies were co-advised by Drs. David L. McDowell and Richard W. Neu.

In addition to his graduate studies at Georgia Tech, Ali served as a Senator in the Georgia Tech Graduate Student Government Association (SGA) and was later appointed as the Vice President of Finance of the Graduate SGA and to the Graduate Judiciary Cabinet. In 2003, he co-founded the Georgia Tech Graduate Technical ($GT^2$) Symposium which is now an on-going event. He is a member of the American Society of Mechanical Engineers (ASME), the American Society of Testing and Materials (ASTM), and the American Society for Engineering Education (ASEE).

Ali married the former Angelita J. Bush on October 12th, 2003 in Atlanta. Their children are Kayla Patrice and Celina Alita. After graduation with his doctorate, Ali will accept a position as an Assistant Professor in the Department of Mechanical, Materials and Aerospace Engineering at the University of Central Florida located in Orlando.